
http://sf2a.oamp.fr
Semaine de l'Astrophysique
21-24 juin 2010
Marseille, la Canebière
Journées de la SF2A
Ateliers communs SAIt/SF2A
"Resolved Stellar Populations"
"Adaptive Optics"
Evènements publics
Prix jeunes chercheurs HP/AMD/SF2A
Prix EDP/SF2A
Conférence publique
R. Pansard-Besson & P. Léna
"Tours du monde, tours du ciel"
Comité local
V. Blanc
S. Boissier
T. Botti
O. Ilbert
B. Le Roux
D. Russeil
L. Tasca
Conseil SF2A
F. Allard
S. Basa
J. Braine
D. Burgarella
C. Charbonnel
M. Heydari-Malayeri
J. Knödlseder
B. Lefloch
D. Rouan
R. Samadi
D. Valls-Gabaud
H. Wozniak
SF2A
LAM
LABORATOIRE D'ASTROPHYSIQUE DE MARSEILLE
OAMP
VILLE DE MARSEILLE
INSU
CONSEIL GENERAL DES BOUCHES-DU-RHÔNE
Provence-Alpes-Côte d'Azur, notre région
EDP SCIENCES

Contents

PARTICIPANT LIST

Nathalie Alleq (nathalie.alleq etumel.univmed.fr)
Danielle Alloin (danielle.alloin cea.fr)
Philippe Amram (philippe.amram oamp.fr)
Frédéric Arenou (frederic.arenou obspm.fr)
Luc Arnold (luc.arnold oamp.fr)
Dominique Aubert (dominique.aubert unistra.fr)
Carine Babusiaux (carine.babusiaux obspm.fr)
David Bancelin (bancelin imcce.fr)
Pierre Barge (pierre.barge oamp.fr)
Stéphane Basa (stephane.basa oamp.fr)
Laurène Beauvalet (beauvalet imcce.fr)
Julien Bel (julien.bel cpt.univ-mrs.fr)
Dominique Bockelee-morvan (dominique.bockelee obspm.fr)
Isabelle Boisse (iboisse iap.fr)
Samuel Boissier (samuel.boissier oamp.fr)
Jérémie Boissier (boissier iram.fr)
Piercarlo Bonifacio (Piercarlo.Bonifacio obspm.fr)
Daniel Bonneau (daniel.bonneau oca.eu)
Sylvain Bontemps (bontemps obs.u-bordeaux1.fr)
Thierry Botti (thierry.botti oamp.fr)
Gwenaël Boué (boue imcce.fr)
Francois Bouchy (bouchy iap.fr)
Thomas Bourquin (thomas.bourquin oamp.fr)
Angela Bragaglia (angela.bragaglia oabo.inaf.it)
Jonathan Braine (braine obs.u-bordeaux1.fr)
Matthieu Brangier (matthieu.brangier obspm.fr)
Richard Britto (britto tifr.res.in)
Véronique Buat (veronique.buat oamp.fr)
Eric Buchlin (eric.buchlin ias.u-psud.fr)
Denis Burgarella (denis.burgarella oamp.fr)
Adeline Buzzi (buzzi cpt.univ-mrs.fr)
Nahuel Cabral (nahuel.cabral space.unibe.ch)
Laurent Cambresy (cambresy astro.unistra.fr)
Marcel Carbilet (marcel.carbillet unice.fr)
John Carr (carr cppm.in2p3.fr)
Baptiste Cecconi (baptiste.cecconi obspm.fr)
Benoît Cerutti (benoit.cerutti obs.ujf-grenoble.fr)
Merieme Chadid (chadid unice.fr)
Corinne Charbonnel (corinne.charbonnel unige.ch)
Sébastien Charnoz (charnoz cea.fr)
Manal Chebbo (manal.chebbo oamp.fr)
Laurent Chemin (chemin obs.u-bordeaux1.fr)

Andrea Chiavassa (chiavass MPA-Garching.MPG.de)
Bruno Christophe (bruno.christophe onera.fr)
Laure Ciesla (laure.ciesla oamp.fr)
Marine Ciesla (marine.ciesla oamp.fr)
Nicolas Clerc (nicolas.clerc m4x.org)
Johan Comparat (johan.comparat oamp.fr)
Anne Coupeaud (anne.coupeaud cesr.fr)
Régis Courtin (regis.courtin obspm.fr)
Stéphanie Courty (courty obs.univ-lyon1.fr)
Nicolas Crouzet (crouzet oca.eu)
Jean-Gabriel Cuby (jean-gabriel.cuby oamp.fr)
Olga Cucciati (olga.cucciati oamp.fr)
Rémi De Guiran (rdeguira ujf-grenoble.fr)
Thibaut Decressin (decress1 astro.uni-bonn.de)
Sébastien Deheuvels (sebastien.deheuvels obspm.fr)
Omar Delaa (omar.delaa obs-azur.fr)
Florent Deleflie (Florent.Deleflie obs-azur.fr)
Magali Deleuil (magali.deleuil oamp.fr)
Xavier Delfosse (Xavier.Delfosse obs.ujf-grenoble.fr)
Philippe Delorme (pd10 st-andrews.ac.uk)
Audrey Delsanti (audrey.delsanti oamp.fr)
Luc Di Gallo (luc.digallo obspm.fr)
Emiliano Diolaiti (emiliano.diolaiti oabo.inaf.it)
Kjetil Dohlen (kjetil.dohlen oamp.fr)
Damien Dornic (dornic cppm.in2p3.fr)
Catherine Dougados (catherine.dougados obs.ujf-grenoble.fr)
Guillaume Dubus (Guillaume.Dubus obs.ujf-grenoble.fr)
Pierre-Alain Duc (paduc cea.fr)
Thierry Dudok De Wit (ddwit cnrs-orleans.fr)
Anne Dutrey (Anne.Dutrey obs.u-bordeaux1.fr)
Kacem El Hadi (kacem.elhadi oamp.fr)
Nicolas Epchtein (epchtein unice.fr)
Lise Escande (escande cenbg.in2p3.fr)
Cyril Escolano (cyril.escolano oamp.fr)
Nicolas Fabas (nicolas.fabas univ-montp2.fr)
Edith Falgarone (edith lra.ens.fr)
Emeric Falize (Emeric.Falize obspm.fr)
Benoit Famaey (benoit.famaey astro.unistra.fr)
Marianne Faurobert (marianne.faurobert unice.fr)
Jonathan Ferreira (Jonathan.Ferreira obs.ujf-grenoble.fr)
Bernard Foing (Bernard.Foing esa.int)
Sébastien Fromang (sebastien.fromang cea.fr)
Stefano Gabici (stefano.gabici apc.univ-paris7.fr)
Yves Gallant (gallant lpta.in2p3.fr)
Sébastien Galtier (sebastien.galtier ias.fr)
Jean-Christophe Gazzano (Jean-Christophe.Gazzano oamp.fr)
Vincent Génot (vincent.genot cesr.fr)
Marwan Gebran (mgebran am.ub.es)
Bruce Gendre (gendre asdc.asi.it)
Piotto Giampaolo (giampaolo.piotto unipd.it)
Elodie Giovannoli (elodie.giovannoli oamp.fr)
Bono Giuseppe (bono roma2.infn.it)
Olivier Godet (godet cesr.fr)
Bertrand Goldman (goldman mpia.de)
Jean-François Gonzalez (Jean-Francois.Gonzalez ens-lyon.fr)

Manuel Goubet (manuel.goubet univ-lille1.fr)
Corinne Goy (corinne.goy lapp.in2p3.fr)
Morgan Gray (gray.morgan neuf.fr)
Cécile Gry (cecile.gry oamp.fr)
Jérôme Guilet (jerome.guilet cea.fr)
Sylvain Guiriec (sylvain.guiriec lpta.in2p3.fr)
Mélanie Guittet (melanie.guittet obspm.fr)
Emilie Habart (emilie.habart ias.u-psud.fr)
Murad Hamidouche (mhamidouche sofia.usra.edu)
Mathieu Havel (mathieu.havel oca.eu)
Misha Haywood (Misha.Haywood obspm.fr)
Guillaume Hébrard (hebrard iap.fr)
Fabrice Herpin (herpin obs.u-bordeaux1.fr)
Daniel Hestroffer (hestro imcce.fr)
Vanessa Hill (Vanessa.Hill oca.eu)
Tracey Hill (tracey.hill cea.fr)
Sacha Hony (sacha.hony cea.fr)
Rodrigo Ibata (ibata astro.u-strasbg.fr)
Olivier Ilbert (olivier.ilbert oamp.fr)
Pascale Jablonka (pascale.jablonka epfl.ch)
Agnieszka Jacholkowska (Agnieszka.Jacholkowska cern.ch)
Laurent Jorda (laurent.jorda oamp.fr)
Martin Kilbinger (martin.kilbinger universe-cluster.de)
Karl-Ludwig Klein (ludwig.klein obspm.fr)
Alexis Klutsch (klutsch astrax.fis.ucm.es)
Jurgen Knodlseder (knodlseder cesr.fr)
Georges Kordopatis (gkordo oca.eu)
Petr Kuchynka (kuchynka imcce.fr)
Benjamin L'huillier (benjamin.lhuillier obspm.fr)
Nadège Lagarde (Nadege.Lagarde unige.ch)
Rosine Lallement (rosine.lallement latmos.ipsl.fr)
Astrid Lamberts (astrid.lamberts obs.ujf-grenoble.fr)
Marie Laslandes (marie.laslandes oamp.fr)
Julien Lavalle (lavalle to.infn.it)
Vincent Le Brun (vincent.lebrun oamp.fr)
Olivier Le Contel (olivier.lecontel lpp.polytechnique.fr)
David Le Mignant (david.lemignant oamp.fr)
Brice Le Roux (brice.leroux oamp.fr)
Agnès Lèbre (agnes.lebre univ-montp2.fr)
John Leibacher (john.leibacher ias.u-psud.fr)
Jean Louis Lemaire (jean-louis.lemaire obspm.fr)
Gérard Lemaitre (gerard.lemaitre oamp.fr)
Agnès Levy (agnes.levy onera.fr)
Cedric Leyrat (cedric.leyrat obspm.fr)
Anne-Lise Maire (Anne-Lise.Maire obspm.fr)
Hervé Manche (manche imcce.fr)
Lucie Maquet (maquet imcce.fr)
Alexandre Marcowith (Alexandre.Marcowith lpta.in2p3.fr)
Sébastien Maret (sebastien.maret obs.ujf-grenoble.fr)
Jean-baptiste Marquette (marquett iap.fr)
Douglas Marshall (douglas.marshall cesr.fr)
Pierrick Martin (martinp mpe.mpg.de)
Jean-Michel Martin (jean-michel.martin obspm.fr)
Claire Martin-zaidi (claire.martin-zaidi obs.ujf-grenoble.fr)
Fabrice Martins (martins graal.univ-montp2.fr)

Nicolas Mauron (mauron graal.univ-montp2.fr)
Christian Mazelle (Christian.Mazelle cesr.fr)
Héloise Méheut (hmeheut apc.univ-paris7.fr)
Thibault Merle (thibault.merle oca.eu)
Gilles Metris (Gilles.Metris obs-azur.fr)
Antonino Milone (antonino.milone unipd.it)
Rémi Monceau-Baroux (Remi.Monceau-Baroux lpta.in2p3.fr)
Richard Monier (Richard.Monier unice.fr)
Thierry Montmerle (montmerle iap.fr)
Raphael Moreno (raphael.moreno obspm.fr)
Fabrice Mottez (fabrice.mottez obspm.fr)
David Mouillet (david.mouillet obs.ujf-grenoble.fr)
Arielle Moullet (arielle.moullet obspm.fr)
Denis Mourard (denis.mourard oca.eu)
Benoit Mours (mours lapp.in2p3.fr)
Claire Moutou (Claire.Moutou oamp.fr)
Mamadou N'diaye (mamadou.ndiaye oamp.fr)
Quang Nguyen-Luong (quang.nguyen-luong cea.fr)
Jérome Novak (Jerome.Novak obspm.fr)
Micaela Oertel (micaela.oertel obspm.fr)
Francesco Palermo (palermo df.unipi.it)
Sébastien Peirani (peirani iap.fr)
Céline Péroux (celine.peroux gmail.com)
Patrick Peter (peter iap.fr)
Pascal Petit (petit ast.obs-mip.fr)
Pierre-Olivier Petrucci (pierre-olivier.petrucci obs.ujf-grenoble.fr)
Jérôme Pety (pety iram.fr)
Bernard Pichon (Bernard.Pichon oca.eu)
Francis Pierron (francis.pierron obs-azur.fr)
Christophe Pinte (christophe.pinte obs.ujf-grenoble.fr)
Frédéric Piron (piron lpta.in2p3.fr)
Thierry Pradier (pradier in2p3.fr)
Denis Puy (Denis.Puy univ-montp2.fr)
Séverine Raimond (severine.raimond latmos.ipsl.fr)
Arvind Rajpurohit (arvind obs-besancon.fr)
Francois Raulin (francois.raulin lisa.univ-paris12.fr)
Matthieu Renaud (mrenaud lpta.in2p3.fr)
Céline Reylé (celine obs-besancon.fr)
Isabelle Ristorcelli (Isabelle.Ristorcelli cesr.fr)
Annie Robin (annie.robin obs-besancon.fr)
Brigitte Rocca-Volmerange (rocca iap.fr)
Florent Rostagni (florent.rostagni oca.eu)
Daniel Rouan (daniel.rouan obspm.fr)
Evelyne Roueff (evelyne.roueff obspm.fr)
Boud Roukema (boud astro.uni.torun.pl)
Frédéric Royer (frederic.royer obspm.fr)
Réza Samadi (reza.samadi obspm.fr)
Alexandre Santerne (alexandre.santerne oamp.fr)
Luca Santoro (santoro oca.eu)
Marc Sauvage (marc.sauvage cea.fr)
Nicola Schneider-Bontemps (nschneid cea.fr)
Angelica Sicard-Piet (angelica.sicard onera.fr)
Geneviève Soucail (soucail ast.obs-mip.fr)
Philippe Stee (Philippe.Stee oca.eu)
Clement Surville (clement.surville oamp.fr)

Michel Tagger (michel.tagger cnrs-orleans.fr)
Michel Tallon (mtallon obs.univ-lyon1.fr)
Lidia Tasca (lidia.tasca oamp.fr)
Wing-Fai Thi (WingFai.Thi obs.ujf-grenoble.fr)
KiliÇoglu Tolgahan (tolgahan astro1.science.ankara.edu.tr)
Laurence Tresse (laurence.tresse oamp.fr)
Catherine Turon (catherine.turon obspm.fr)
David Valls-Gabaud (david.valls-gabaud obspm.fr)
Jean-Claude Valtier (jean-claude.valtier oca.eu)
Véronique Van Elewyck (elewyck apc.univ-paris7.fr)
Peggy Varniere (varniere apc.univ-paris7.fr)
Christian Veillet (veillet cfht.hawaii.edu)
Simon Verley (simon ugr.es)
Jean-Claude Vial (vial ias.fr)
Alain Vienne (vienne imcce.fr)
Arthur Vigan (arthur.vigan oamp.fr)
Nicole Vilmer (nicole.vilmer obspm.fr)
Valentine Wakelam (wakelam obs.u-bordeaux1.fr)
Laurent Wiesenfeld (laurent.wiesenfeld obs.ujf-grenoble.fr)
Gérard Williger (gerard.williger unice.fr)
Clare Worley (cworley oca.eu)
Marie Ygouf (marie.ygouf onera.fr)
Annie Zavagno (annie.zavagno oamp.fr)
Claude Zeippen (claude.zeippen obspm.fr)
Julien Zoubian (julien.zoubian oamp.fr)

SF2A

Common session

THE EUROPEAN ELT: STATUS REPORT

J.-G. Cuby[1]

Abstract. This paper provides a brief status report on the European Extremely Large Telescope (E-ELT) as presented at the annual meeting of the French Astronomical Society (SF2A) held in Marseille in June 2010. The project is now proceeding to the end of its Phase B that lasted four years, the results of which will form the basis of the proposal for construction that will be submitted to the ESO council for approval. The decision is expected to be taken in 2011. In parallel to the Telescope Phase B, Instrument Phase A studies have been completed from which a comprehensive instrumentation plan could be drawn.

Keywords: telescope, instrumentation

1 Introduction

The last report on the European Extremely Large Telescope (E-ELT) situation at the Annual Meeting of the SF2A was in 2006, four years ago. Since then the project has been formally kicked into Phase B after the 'Towards the E-ELT' conference that took place in Marseille in November 2006, de facto marking the start of the E-ELT project as we know it today. Since then, this Phase B is about to be completed : several key industrial studies, some of them including the manufacturing of prototypes, have been performed ; ten instrument and adaptive optics phase A studies have been completed ; the site has been selected ; funding scenarios have been elaborated. This paper provides an ultra-short status report on some of these aspects.

2 The E-ELT project

2.1 The telescope

The ASTRONET Infrastructure Roadmap identified the European Extremely Large Telescope (E-ELT) as the first of two top-priority facilities to be implemented in the coming decade. The E-ELT will be a ground-based astronomical observatory with a 42-meter diameter segmented mirror. The design features a filled aperture mirror with an area of 1,300 m^2, and an original 5-mirror design that includes a 6-m secondary convex mirror (M2), a 2.5-m adaptive optics mirror (M4), and a 2.5-m tip-tilt mirror (M5). Adaptive Optics is fully integrated in the telescope design (M4), and by default the telescope will operate in Ground Layer Adaptive Optics (GLAO) mode.

The ESO budget for the Phase B was of the order of 60 M€and further funding was available through the FP6 and FP7 European programmes. This allowed carrying out a number of industrial studies for key elements of the telescope. Two contracts have been placed for the manufacturing of seven prototype segments of the primary mirror (at the extreme edge of the primary mirror). Other studies have been performed and prototype developed for the M4 adaptive mirror which is one of the most delicate elements of the project. Several studies were performed in industry for the telescope structure and for the dome.

The outcome of these studies have allowed to improve the technology readiness level of the project and to accurately estimate its cost and the schedule for its construction.

[1] Laboratoire d'Astrophysique de Marseille, OAMP, Université Aix-Marseille & CNRS, 38 rue Frédéric Joliot Curie, 13388 Marseille cedex 13, France

2.2 The instruments

Eight Phase A instrument studies have been performed, as well as two studies for the Multi-Object and Laser Tomography Adaptive Optics (MCAO and LTAO) modules. Table 1 shows the instrument names, basic properties and main scientific objectives that have been studied as part of the E-ELT phase B programme.

These studies were performed in the timeframe 2008-2009. The results of these studies should allow to draw a comprehensive instrumentation plan, based on the scientific priorities of the project in its first decade of operations and beyond.

Table 1. Instrument studied in Phase A.

Name	Type	Spectral Range (μm)	Field (linear) and sampling (mas.pix^{-1})	Spectral Resolution	Adaptive Optics mode	Scientific drivers
MICADO	Diffraction Limited Imager	0.8 - 2.4	1' 1–4	10–100	MCAO	Black Holes Galactic Center Globular Clusters Resolved Stellar Pops.
HARMONI	IFU	0.8 -2.4	1" – 10" 4 – 40	4000-20000	SCAO LTAO	Stellar disks Star forming regions Resolved Stellar Pops. Black Holes
EAGLE	Multi-IFU ($\sim$ 20)	0.8 - 2.4	$\sim$ 7' 40	4000-10000	GLAO MOAO	First Galaxies Evolution of Galaxies Resolved Stellar Pop.
CODEX	High Resolution High Stability Spectrograph	0.4-0.7	1"	$>$ 120000	–	Expansion of the Universe Extrasolar twin earths Variability of physical ctes
METIS	Imager & Spectrograph	3.5 – 14	18" 15–30	5 5000 100,000	SCAO LTAO	Solar System Extrasolar planets Planet Formation Growth of SMBHs
EPICS	High Contrast Imager	0.6-1.8	2" - 4" 2	$>$ 50 3,000 20,000	XAO	Extrasolar Planets Stellar Disks Planet formation
OPTIMOS	MOS (>100)	0.4-1.7	$\sim$ 7' 5	1000-10000	GLAO	Resolved stellar Pops. Evolution of galaxies Evolution of galaxies
SIMPLE	High Resolution Spectrograph	0.8-2.4	Slit 0.027"$\times$ 4"	>100000	SCAO	Exoplanets Stellar populations High-z IGM

2.3 The site

Several sites were in consideration for hosting th E-ELT: La Palma in the Canary islands, and Cerro Armazones (see figure 1), Cerro Tolonchar and other sites in the vicinity of Paranal and Armazones in Chile. Other sites were considered in Morocco and in Argentina. A Site Selection Advisory Committee was established to assist ESO in analyzing the data from the site testing campaigns and to make recommendations. Some of the sites were tested by ESO and the others by the Thirty Meter Telescope (TMT) project, and the data were shared between the two teams under the terms of a collaborative agreement.

2.4 Cost and schedule

An internal ESO review took place in the fall of 2010 to review the results and findings of the Phase B. The results of this review will be folded in the proposal for construction that will be presented to the ESO council

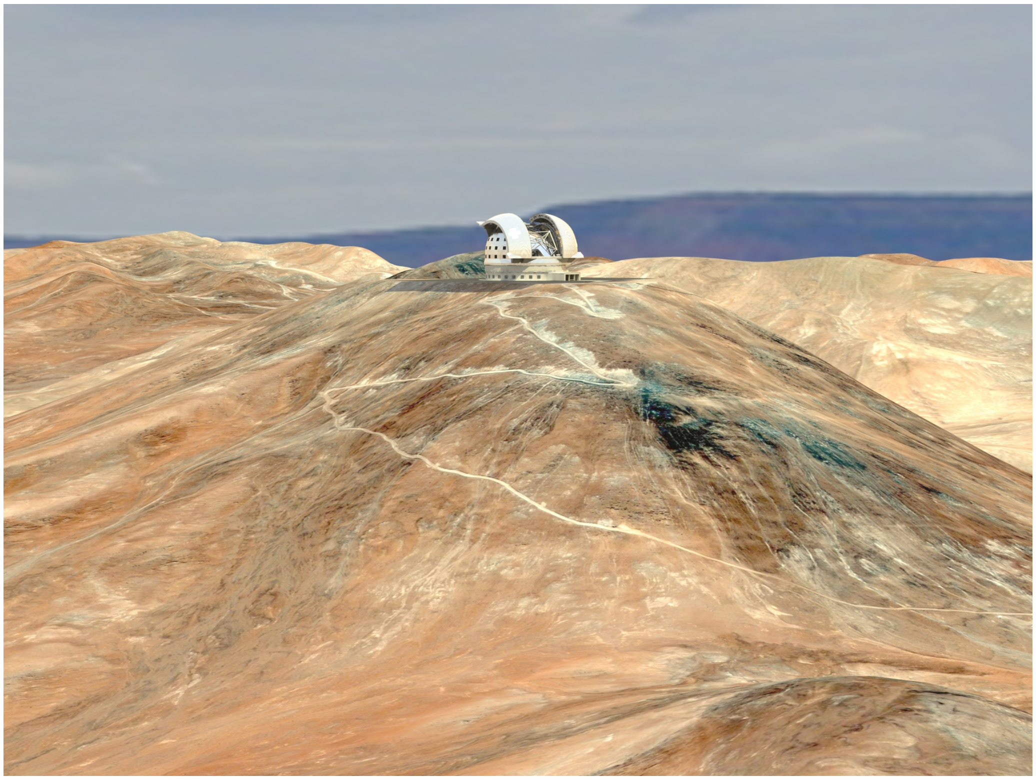

Fig. 1. Impression of the E-ELT atop Cerro Armazones

in 2011 for approval. The anticipated cost of the project is likely to exceed one billion Euros (the precise cost estimate that will be submitted to council is unknown at time of writing this status report). This cost largely exceeds what is available in the long range plan of ESO, and it is therefore necessary to find major partners that would join the project and/or ESO as well as increasing the financial contribution of the current member states. Financing the project is the most outstanding issue remaining to be resolved before the project can be officially launched.

3 French E-ELT activities

A working group was setup by INSU in 2004 to coordinate the ELT activities in France back at a time when the E-ELT project did not exist, with the ESO OWL 100-m telescope project and the Euro50 project promoted in some European countries. With the clarification of the European landscape in 2006 and the launch of the first instrument studies while the project was steadily proceeding into phase B, the activities of the working group were terminated and de facto replaced by the participation into several instrument Phase A studies.

The participation of French institutes in the instrument Phase A studies were:

- The Centre de Recherche Astronomique de Lyon (CRAL) was CoI of HARMONY
- The Laboratoire d'Études spatiales et d'instrumentation en astrophysique (LESIA) was participating as Co-I to MICADO, ATLAS and EAGLE.
- The "Galaxies, Etoiles, Physique, Instrumentation" (GEPI) was PI of one of the two competitive OPTIMOS phase A studies, and was participating as Co-I to ATLAS and EAGLE
- The Laboratoire d'Astrophysique de Marseille (LAM) was PI of EAGLE, PI of the other OPTIMOS Phase A study, participated to EPICS and had a minor contribution to ATLAS
- The Service d'Astrophysique of the Commissariat à l'énergie Atomique (SAp/AIM/CEA Saclay) was Co-I of METIS

- The Laboratoire d'Astrophysique de l'Observatoire de Grenoble (LAOG) was Co-I of EPICS
- ONERA was PI of ATLAS, CoI of MAORY, EAGLE and participated to the studies of HARMONY and OPTIMOS

In September 2010, ESO has announced to the instrument PIs its intentions concerning the selection of the E-ELT instruments. The two first light instruments have been selected, namely HARMONI and MICADO. No decision is taken for the suite of instruments that will follow, and a notional plan indicates that the third instrument could be selected in 2012 or 2013 for a start of construction in 2014, while other instruments would start at approximately 2-year intervals thereafter.

4 Conclusion

The E-ELT is the top priority project for the European community, as clearly expressed in the ASTRONET roadmap. The project Phase B is nearing completion, and a formal proposal for construction will ensue. Major industrial studies have been completed for the sub-systems that are critical to the project, increasing the overall Technology Readiness Level of the whole project and allowing ESO to better estimate the cost and schedule for its construction. Drawing a comprehensive instrumentation plan that would clarify what the scientific priorities of the project are for its first decade of operations remains to be elaborated.

SF2A 2010
S. Boissier, M. Heydari-Malayeri, R. Samadi and D. Valls-Gabaud (eds)

STRATOSPHERIC OBSERVATORY FOR INFRARED ASTRONOMY

M. Hamidouche[1], E. Young[1], P. Marcum[2] and A. Krabbe[3]

Abstract. We present one of the new generations of observatories, the Stratospheric Observatory For Infrared Astronomy (SOFIA). This is an airborne observatory consisting of a 2.7-m telescope mounted on a modified Boeing B747-SP airplane. Flying at an up to 45,000 ft (14 km) altitude, SOFIA will observe above more than 99 percent of the Earth's atmospheric water vapor allowing observations in the normally obscured far-infrared. We outline the observatory capabilities and goals. The first-generation science instruments flying on board SOFIA and their main astronomical goals are also presented.

Keywords: SOFIA, infrared, instrumentation, airborne observatory

1 Introduction

SOFIA (Stratospheric Observatory For Infrared Astronomy) consists of a 2.7-meter telescope mounted in a modified Boeing 747SP aircraft. SOFIA is a joint project of NASA and the Deutsches Zentrum für Luft und Raumfahrt (DLR). Operations costs and observing time will be shared by the United States (80%) and Germany (20%). It is a near-space observatory that comes home after every flight. Flying at altitudes up to 45,000 ft (14 km), SOFIA observes from above more than 99% of Earth's atmospheric water vapor. SOFIA will begin science observations in 2011. It will offer the international astronomical community approximately 1000 science observing hours per year for two decades, when full operational capabilities are reached in 2014. Science proposals will be open to the international community. In this paper, we focus on SOFIA scientific capabilities.

2 SOFIA Performance

The first generation science instruments are being tested or under development by different institutions in both the US and Germany, including imaging cameras and spectrographs as well as imaging cameras with spectrometers. SOFIA will observe at wavelengths from 0.3 μm up to 1600 μm. It will be capable of high resolution spectroscopy (R $> 10^4$) at wavelengths between 5 and 240 μm (Figure 1). The 8 arcminute diameter field of view will ultimately allow use of very large format detector arrays. SOFIA will provide diffraction limited imaging long-ward of 15 μm. After Herschel's cryogen depletion, SOFIA will be the only telescope covering the 30 to 300 μm wavelength range in the next years.

3 SOFIA Uniqueness for Astronomy

One of its great strengths is that its scientific instruments can be exchanged regularly to accommodate changing science requirements and new technologies. Furthermore, large, massive, complex and sophisticated instruments with substantial power and heat dissipation needs can be flown on SOFIA, and thus increasing SOFIAs science productivity.

SOFIA has unique capabilities for studying transient events. The observatory can operate from air-bases worldwide to respond to new discoveries in both the northern and southern hemispheres. SOFIA has the flexibility to respond to events such as supernovae and nova explosions, cometary impacts, comet apparitions,

[1] USRA - NASA Ames Research Center, MS N211-3, Moffett Field, CA 94035
[2] NASA Ames Research Center, MS 211-1, Moffett Field, CA 94035
[3] Deutsches SOFIA Institut, Pfaffenwaldring 31, 70569 Stuttgart, Germany

eclipses, occultations, near Earth objects, activity in Active Galactic Nuclei, and activity in luminous variable stars. SOFIA's wide range of instruments will facilitate a coordinated science program through analysis of specific targets. No other observatory operating in SOFIAs wavelength range can provide such a large variety of available instruments for such a long period of time. A particular advantage of SOFIA is that it will be able to access events unavailable to many space observatories because of the viewing constraints imposed by their orbits. For example, SOFIA can observe astrophysical events which occur closer to the Sun than most spacecrafts can. This will enable temporal monitoring of supernovae, novae, and variable stars throughout the year. SOFIAs 20-year operational lifetime will enable long term temporal studies and followup of work initiated by SOFIA itself and by other observatories. Many space missions are relatively short compared with the critical cycle of observation, analysis, and further observation. The Herschel observatory will raise scientific questions that will benefit from followup observations well after their missions have ended. SOFIA will keep the community engaged in fundamental science research until the next generation of missions is launched.

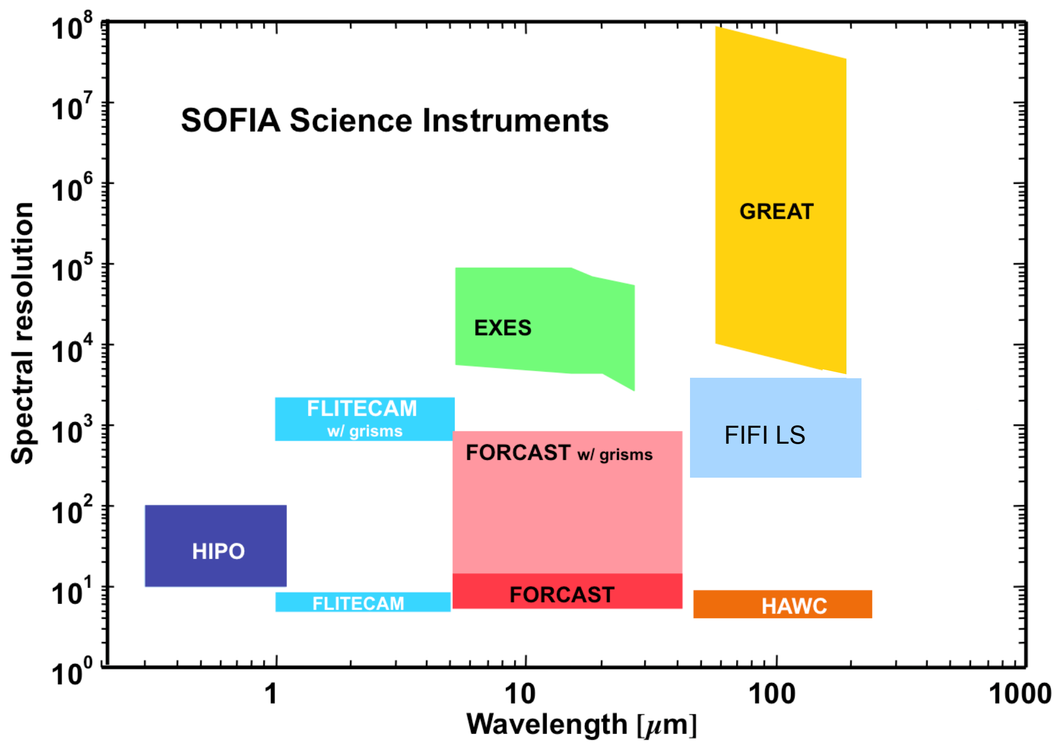

Fig. 1. SOFIA first generation instruments shown in a plot of spectral resolution vs. the wavelength.

SF2A 2010
S. Boissier, M. Heydari-Malayeri, R. Samadi and D. Valls-Gabaud (eds)

A CHANDRA CENSUS OF C2D YSOS: EVOLUTION OF X-RAY EMISSION

M. Hamidouche[1], M. Jacobson[2] and L.W. Looney[2]

Abstract. We present an analytical study of a large sample of ∼109 young stellar objects in the X-ray. Our objects were detected in X-ray independent of age. Unexpectedly, the X-ray energy is somewhat correlated with the ages. It decreases with time and with column density, while it should increase. We conclude that the youngest protostars, Class 0/I, emit X-rays in the 1-8 keV band. The deeply embedded sources with the strongest accretion activity are detected in the hard-band (> 2keV) only. Due to extinction, their soft X-rays are not detected. To explain the decline in energy, we suggest that within a timescale of few Myrs the corona cools down via the accretion material.

Keywords: infrared: stars, stars: magnetic field, pre-main-sequence stars, protostars, X-rays: stars

1 Introduction

X-ray emission of pre-main-sequence T Tauri stars has been extensively studied over the last decades. The observed X-rays are explained to be from the coronal emission Preibisch (2007). In this study, we further investigate the X-ray emission processes of such objects and its evolution since their youngest ages. We present a study of a large sample of young stellar objects (YSO) in the infrared and X-ray to probe their X-ray energy regime evolution from the youngest embedded and strongly accreting Class 0 objects into the non-accreting Class III objects. We track their X-ray activity during their lifetime, and thus the role of the accretion.

2 Analysis

We cross-correlated the data archive of YSO from the infrared Spitzer c2d legacy project (Evans et al. 2003) with CHANDRA X-ray observations from the web based archive (Wolk & Spitzbart 2007) ANCHOR (AN archive of Chandra Observations of Regions of star formation). We spatially matched 109 detected YSOs within 4" from three star-forming regions : NGC 1333, Serpens, and ρ-Ophiuchus. We determine their ages from infrared spectral indices α and classify them from Class 0 to III, using the color-color diagram with the four IRAC bands [3.6]-[4.5] and [5.8]-[8.0]. We used the SED online fitting tool developed by Robitaille et al. (2007) to deduce the envelope accretion rate and the age. We obtain the column density n_e and the X-ray energy from ANCHOR X-ray data.

3 Discussion

The column density decreases with the derived infrared index, or the more evolved Class II/III objects are less embedded. These results show that our study is robust since our parameters are consistent with their physical implication. Overall, the infrared index α is slightly correlated with the stellar age. On the other hand, it is well correlated with the accretion rate. Nevertheless, we should point out that we have much less data for the older YSO than for the youngest ones. They are also scattered in the plot and it is difficult to determine any correlation.

[1] USRA - NASA Ames Research Center, MS N211-3, Moffett Field, CA 94035
[2] Astronomy Department, U. of Illinois at Urbana-Champaign, Urbana, IL 61801

4 Conclusion

We deduce in this study of 109 YSO that they all emit X-rays independently of their ages. Unexpectedly, the X-ray energy is somewhat correlated with the infrared indices (Figure 1), and thus it is anti-correlated with the ages. It decreases with time and column density, while it was expected to increase. We find that the youngest YSO protostars (Class I) emit X-rays in the ∼1-8 keV band. Interestingly, we do not see an apparent evidence that Class 0 objects have X-ray emission. The deeply embedded sources with the strongest accretion activity are detected in the hard-band (> 2keV) only. Due to extinction, their soft X-rays are not detected. To explain the decline in energy, one could consider that within a timescale of few Myrs the corona cools down via the accretion material, as seen in the pre-main-sequence Herbig AeBe stars (Hamidouche et al. 2008). As a result, the older YSO (Class II/III) emit only in the soft-band.

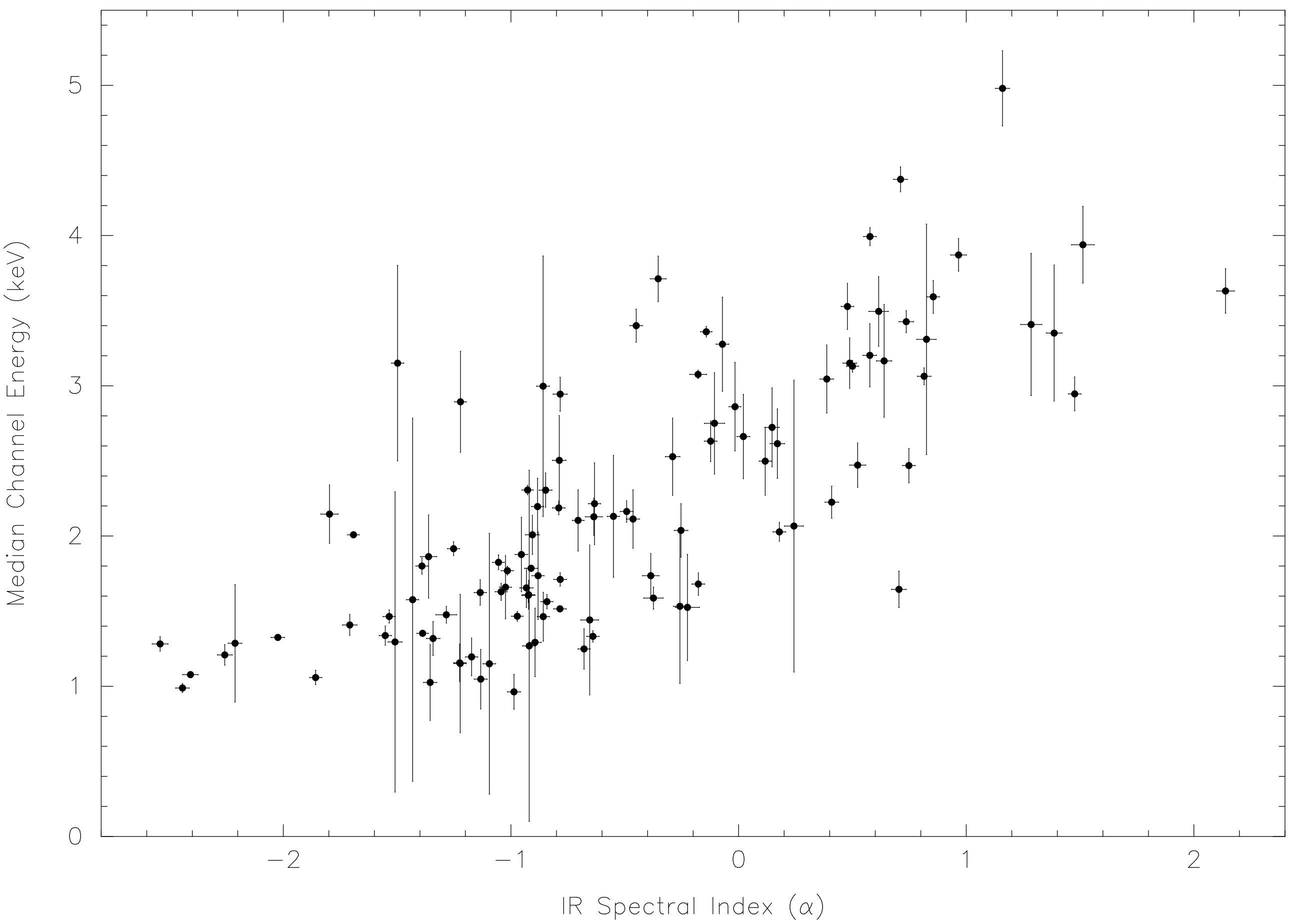

Fig. 1. X-ray energy of the YSO as a function of their infrared indices, showing an almost-linear correlation. This indicates that during the evolution of the YSOs, their X-ray energy becomes softer.

References

Evans, II, N. J. et al., 2003, PASP, 115, 965-980

Hamidouche, M., Wang, S., Looney, L.W., 2007, AJ, 135, 1474

Preibisch, T., 2007, Memorie della Società Astronomica Italiana, v.78, p.332

Robitaille, T. P., Whitney, B. A., Indebetouw, R., Wood, K., 2007, ApJS, 169, 328

Wolk, S.J., Spitzbart, B.D., Highlights of Astronomy, v. 14, p. 587

SF2A 2010
S. Boissier, M. Heydari-Malayeri, R. Samadi and D. Valls-Gabaud (eds)

GALAXY FORMATION: MERGER VS GAS ACCRETION

B. L'Huillier[1], F. Combes[1] and B. Semelin[1]

Abstract. According to the hierarchical model, small galaxies form first and merge together to form bigger objects. In parallel, galaxies assemble their mass through accretion from cosmic filaments. Recently, the increased spatial resolution of the cosmological simulations have emphasised that a large fraction of cold gas can be accreted by galaxies. In order to compare the role of both phenomena and the corresponding star formation history, one has to detect the structures in the numerical simulations and to follow them in time, by building a merger tree.

Keywords: galaxy: formation, galaxy: dark matter, galaxy: ISM

1 Introduction

Recent simulations (Kereš et al. (2005) for example) have emphasised the role of smooth cold accretion on galaxy formation. We aim at comparing the roles of mergers and gas accretion on galaxy growth by studying numerical simulations.

2 The simulations

We use a set of TreeSPH multizoom simulations (Semelin & Combes 2002, 2005), starting with a low resolution cosmological simulation, and resimulating regions of interest at higher resolution. The box radius is 8.30 Mpc (comoving), the mass resolution is $3 \times 10^7\ M_\odot$ for baryons and $1.4 \times 10^8\ M_\odot$ for DM particles, and the gravitational smoothing is $\varepsilon = 6.25$ kpc. There are 90 outputs spaced by 100 Myr from $z \sim 29$ to $z \sim 0.41$, which enables us to follow particles from one output to the other.

3 Structure detection and merger tree

We use AdaptaHOP (Aubert et al. 2004; Tweed et al. 2009) to detect the DM haloes and subhaloes hierarchy. We also use AdaptaHOP to detect the baryonic galaxies [*], with a better adapted set of parameters: we use for the density threshold above which structures are detected $\rho_{\mathrm{T}} = 1000$ (times the mean density of the simulation) instead of 81 for DM. We also check that the results do not vary too much with the choice of ρ_{T}.

In the following, we are only interested in baryonic particles and structures. At each timestep, baryonic particles either belong to a structure (galaxy or satellite), or are diffuse and belong to the background. To compute the mass gained by the main galaxy at each timestep, we sum the mass of all the particles entering the structure, and we count as *smooth accretion* particles that belonged to the background at the previous timestep, and as *merger* particles that belong to another structure. Particles can also leave the main galaxy for another structure, generally for a satellite (*fragmentation*) or for the background (*evaporation*). We then have to substract *fragmentation* to *merger* and *evaporation* to *accretion*.

One of the main problems while building a merger tree is the so-called *flyby issue*: when structures are too close one to another, they are undistinguishable for the structure finder. Thus two structures can be separated at a given timestep, merged at the following, and separated again later. Such an example can be seen in figure 1,

[1] LERMA, Observatoire de Paris, UPMC, 61 avenue de l'Observatoire, 75014 Paris, France

[*]Screenshots of the simulations and of the structures found by AdaptaHOP as well as an example of merger tree can be seen at `http://aramis.obspm.fr/~blhuill/research.html`

left: the red upper curve (satellites) grows, then decreases when the satellite flies away from the central galaxy, then the curve increases again when the satellite comes back.

Thus with our technique, when particles enter the main galaxy, they are counted positively, and negatively when they leave, which enables us to compute the total mass origin of the main galaxy (figure 1, right).

4 Results

We measure the smooth accretion and the merger fractions of several galaxies, as shown in figure 1, right and table 1.

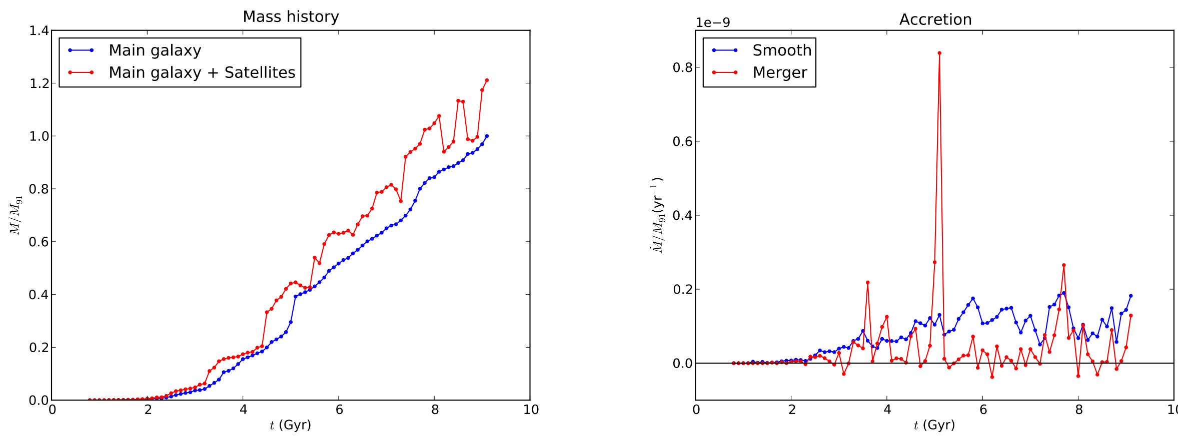

Fig. 1. *Left:* Baryonic mass evolution of a galaxy normalised by the galaxy mass at $t = 9.1$ Gyr. *Right:* Incoming mass by time unit. The blue curve shows mass smoothly accreted, the red curve shows the mass gained through mergers.

Table 1. Fraction of smooth accretion within the total assembled mass for different central galaxies. The first galaxy has $f_{\rm acc} > 1$, which means that the galaxy loses more mass during merger envents due to fragmentation that it gains.

galaxy	1	2	3	4	5	6
Mass ($10^{11} M_\odot$)	107.5	244.81	140.81	1.73	143.40	8.98
Accretion fraction	1.04*	0.65	0.67	0.52	0.95	0.71

5 Conclusions

The study of these simulations shows that baryonic mass assembly of galaxies seems to be dominated by smooth accretion, although we still have to perform further consistency tests. The next step is to perform statistical studies to confirm the preliminary results, then further physical exploitation can be made such as the role of the environment on the SFR.

BL would like to thank D. Tweed and S. Colombi for stimulating discussions.

References

Aubert, D., Pichon, C., & Colombi, S. 2004, MNRAS, 352, 376

Kereš, D., Katz, N., Weinberg, D. H., & Davé, R. 2005, MNRAS, 363, 2

Semelin, B. & Combes, F. 2002, Astronomy and Astrophysics, 388, 826

Semelin, B. & Combes, F. 2005, Astronomy and Astrophysics, 441, 55

Tweed, D., Devriendt, J., Blaizot, J., Colombi, S., & Slyz, A. 2009, A&A, 506, 647

LA SOCIÉTE FRANÇAISE D'EXOBIOLOGIE

F. Raulin[1]

Résumé. L'exobiologie est une jeune science, très pluridisciplinaire qui, de façon générale, a pour objet l'étude de la vie dans l'univers. Plus précisément, elle inclut l'étude des conditions et des processus qui ont permis l'émergence du vivant sur notre planète, et ont pu oumo pourraient le permettre ailleurs, l'étude de l'évolution de la matière organique vers des structures complexes dans l'univers, et les recherches qui concernent la distribution de la vie sous toutes les formes qu'elle pourrait revêtir, et son évolution. La Société Française d'Exobiologie a été fondée en mai 2009. Elle a pour buts principaux de fédérer les recherches en exobiologie au niveau français en facilitant l'établissement de contacts interdisciplinaires entre les chercheurs français et faire connaître et expliquer l'exobiologie pour satisfaire la demande socio culturelle provenant d'un public diversifié, par le biais de conférences, d'ateliers, d'expositions. La SFE est reconnue comme Société savante. Elle compte actuellement 140 membres et vient d'organiser son premier colloque national d'exobiologie à Biarritz.

Keywords: astrobiologie, bioastronomie, chimie organique extraterrestre, exobiologie, ISSOL, NAI, origine de la vie, SFE

1 L'exobiologie

C'est pendant le développement du programme Apollo de la NASA que le mot ≪ exobiologie ≫ est apparu dans la communauté scientifique. La NASA avait alors constitué un groupe de travail pour étudier la question d'une éventuelle vie sur la Lune et son interaction possible avec la vie terrestre. Le président de ce groupe, le microbiologiste Joshua Lederberg, Lauréat du prix Nobel de Médecine en 1958, introduisit alors le mot ≪ exobiologie ≫ pour désigner la science qui s'intéresse à la vie extraterrestre.

L'hypothèse de la présence possible sur notre satellite naturel de micro-organismes extraterrestres vivants est aujourd'hui abandonnée. En revanche, l'exobiologie est restée et est à présent une science en pleine expansion. En fait, six ans seulement après le premier pas de l'Homme sur la Lune, la NASA lançait la mission Viking vers Mars. Chacune des deux sondes Viking qui se posèrent à la surface de la planète rouge l'été 1976 incluait les premières expériences exobiologiques de l'exploration spatiale : trois instruments spécifiquement destinés à mettre en évidence une activité biologique dans le sol martien. Depuis, le domaine de l'exobiologie a considértablement évolué, sous l'impulsion de microbiologistes mais aussi de chimistes et d'astrophysiciens, comme Carl Sagan.

Aujourd'hui l'exobiologie a largement repoussé ses frontières. Ce domaine englobe à présent l'étude de l'origine, de la distribution et de l'évolution de la vie dans l'univers, ainsi que des processus et structures qui sont liés à la vie. L'exobiologie est donc devenue en fait l'étude de la vie dans l'Univers. Elle est largement représentée au sein de l'ISSOL (International Society for the Study of the Origin of Life), par les chimistes, physico-chimistes et planétologues qui s'occupent de chimie prébiotique, terrestre et extraterrestre, et les microbiologistes qui s'intéressent aux origines de la vie et aux biosignatures. L'ISSOL, qui regroupe plus de 500 scientifiques travaillant dans ces domaines, organise une conférence triennale sur ces thématiques.

En parallèle, la communauté des astronomes et principalement des radioastronomes s'intéressant aux expériences ≪ SETI ≫ (Search for Extraterrestrial Intelligence), a introduit au début des années 1980 l'appellation ≪ Bioastronomie ≫. Elle a aussi convaincu l'Union astronomique internationale de créer une commission (Commission 51) sur cette thématique. Cette communauté organise depuis une conférence internationale tous les trois ans.

∗. [1] LISA - CNRS / Univ. Paris Est Créteil / Univ. Paris Diderot /I PSL 61 Avenue Général de Gaulle, 94000 Créteil

Plus récemment, au milieu des années 1990, la NASA a introduit le terme ≪ Astrobiologie ≫ pour désigner un domaine scientifique quasi identique et a crée son programme d'instituts virtuels d'astrobiologie (NASA Astrobiology Institute ou NAI) qui réunit aujourd'hui quatorze centres aux États-Unis, avec de larges collaborations internationales.
En fait ces trois appellations sont quasi-synonymes et désignent la science qui recherche des formes de vie extraterrestres et qui étudie les origines de la vie terrestre. Ce vaste domaine de recherches pluridisciplinaires, fait appel aux sciences de l'Univers, aux sciences de la Terre, à la physique, à la chimie et à la biologie ainsi qu'à des sciences sociales comme la sociologie et l'épistémologie. Cette recherche se double d'une composante socio culturelle importante, tournée vers la société et inclut l'explication de ces recherches à un public aussi large que possible.
Les approches sont nombreuses (Fig. 1). Elles comprennent bien sûr la recherche de vie ou de signatures biologiques, présentes ou passées, ailleurs que sur Terre. Cette recherche peut se faire dans le système solaire par télédétection ou, depuis peu, grâce au développement des technologies spatiales, par mesures in situ. Elle peut aussi se faire hors du système solaire, par l'approche SETI et devrait pouvoir se faire dans un futur proche, par la détermination de la composition des atmosphères des exoplanètes. Mais l'exobiologie inclut aussi l'étude du seul exemple de vie dont nous disposions pour l'instant : la vie terrestre : son ou ses origines, sa diversité et son évolution dans des conditions extrêmes. La vie terrestre est l'aboutissement d'une évolution chimique de composés organiques (carbonés) en présence d'eau liquide, et sous flux d'énergie. L'exobiologie comprend aussi l'étude de la chimie organique dans des environnements extraterrestres.

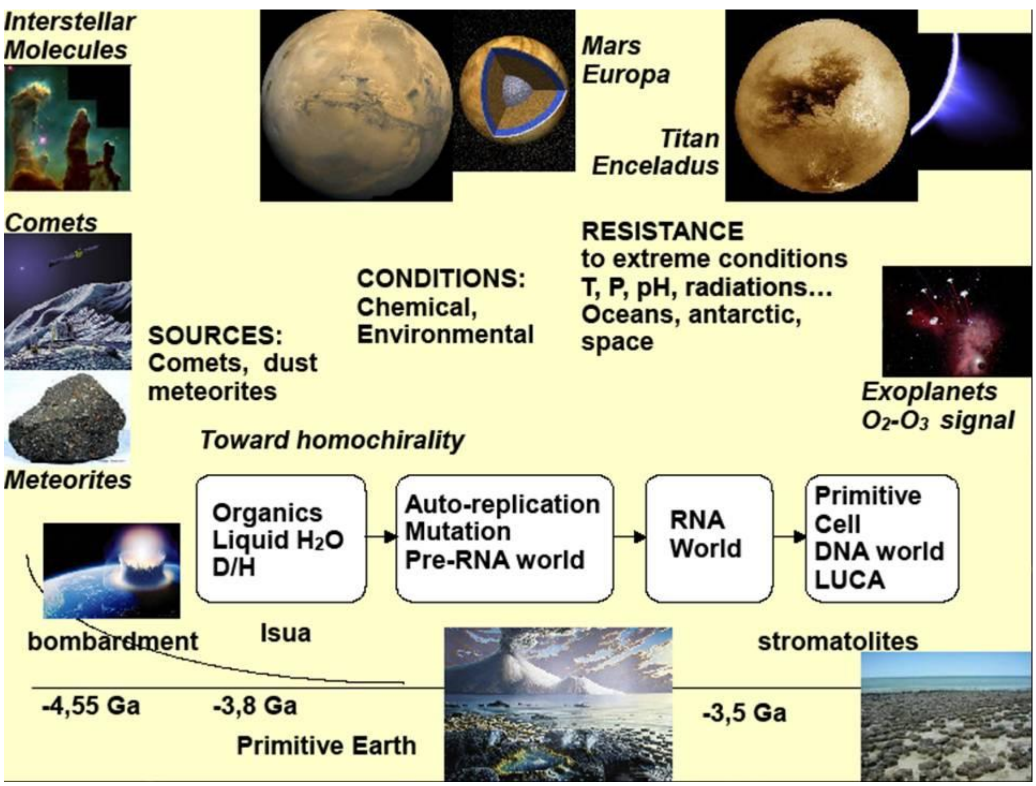

Figure 1. Les différentes approches de l'exobiologie. L'origine de la vie sur Terre (origine des ingrédients carbonés – météorites, comètes, milieu interstellaire - chimie prébiotique vers un monde pré-ARN, le monde ARN, puis LUCA, ≪Last Universal Commun Ancestor≫, et le monde ADN actuel). L'étude des conditions sur la Terre primitive et la recherche des traces de vie les plus anciennes. La recherche de signatures biologiques ou prébiotiques sur les objets du système solaire : Mars, Europe, Titan et Encelade, et hors du système solaire avec l'étude des exoplanètes.

2 La SFE

En France, l'exobiologie est une discipline en plein essor se fondant sur les travaux de nombreux chercheurs individuels et quelques équipes, œuvrant essentiellement au sein de laboratoires institutionnels dont ce n'est pas

l'activité principale.
La coordination des exobiologistes français et de leurs thèmes de recherche s'est faite essentiellement au sein du Groupement de Recherche ≪ Exobiologie ≫ du CNRS. A l'expiration de ce GDR, il est apparu important de créer une structure pérenne sous la forme d'une Société Française d'Exobiologie dont le but est de promouvoir l'ensemble des activités de cette discipline, de créer une réelle structure fédérative des scientifiques, des instituts de recherche ainsi que des universités, tous engagés dans cette discipline et d'assurer une ouverture aussi large que possible vers la société. C'est ainsi qu'a été créée en mai 2009 la Société Française d'Exobiologie (SFE), sous forme d'une association type ≪loi 1901≫.
Les buts de la Société sont de :

- Contribuer à fédérer les recherches en exobiologie au niveau français en facilitant l'établissement de contacts inter-disciplinaires entre les chercheurs français pour renforcer les collaborations existantes et en créer de nouvelles ;
- participer activement aux travaux de prospective scientifique en exobiologie menés par les organismes nationaux, internationaux ou fédératifs ;
- participer à la promotion, à la défense et à la diffusion de l'exobiologie en Europe, intervenir dans les organisations scientifiques internationales et soutenir les initiatives francophones dans le domaine ;
- sensibiliser les jeunes scientifiques à cette science et les orienter vers ce domaine de recherches pluridisciplinaire ;
- créer et gérer un site Internet présentant le potentiel français et les possibilités d'expertise offertes ;
- faire connaître et expliquer l'exobiologie à tous les publics et satisfaire la demande socio culturelle provenant d'un public diversifié, par le biais de conférences, d'ateliers, d'expositions ;
- solliciter des aides financières pour atteindre les objectifs de la Société ; susciter le mécénat de particuliers ou de personnes morales, aboutissant par exemple à la création de prix d'excellence ou de bourses d'études ou de recherches

Le siège social de la SFE est fixé à l'Observatoire de Bordeaux. L'assemblée générale fondatrice de la SFE a eu lieu dans la salle de l'Espace du CNES, à Paris le 8 juillet 2009. Elle a réuni près de 100 participants qui ont élu un Conseil d'Administration, constitué de 12 membres. Celui-ci a élu le bureau (Fig. 2).

Figure 2. Bureau et Conseil d'Administration (2009-2011) de la SFE

La SFE comprend actuellement 140 membres, incluant des membres titulaires et associés. Les membres titulaires sont des personnes physiques, impliquées activement dans des recherches en exobiologie au moment de leur adhésion. Les membres associés sont des professionnels ou étudiants qui ne sont pas engagés activement dans une recherche en exobiologie mais qui s'y intéressent. Une grande partie des membres (43%) sont liés à l'INSU, 27% à la chimie (INSB), 17% aux sciences de la vie (INSB) et 7% à SHS.
Depuis mai 2009, la SFE a :

– créé son site internet (`http://www.exobiologie.fr/`), qui diffuse des informations sur l'actualité exobiologique permettant en particulier aux percées scientifiques de circuler au travers des frontières des champs disciplinaire impliqués,
– participé à de nombreuses manifestations scientifiques (Fête de la Science 2009, partenariat avec le CNES dans l'opération de vulgarisation « L'arbre à palabre » ; et 2010 : partenariat avec Ars Mathematica / CSI /.
– participé à de nombreuses activités d'enseignement/valorisation/diffusion (projets de lycéens/étudiants liés à l'Exobiologie, ateliers de Travail thématiques, rencontres exobiologiques pour doctorants (Red'10 et 11), ouvrages de synthèse (Encyclopedia of Astrobiology, Springer).
– demandé et obtenu du MESR le label de «Société Savante».
– organisé son premier colloque national d'exobiologie.

Ce colloque, «Rencontres SFE 2010» a eu lieu à Biarritz du 27 au 30 septembre 2010 et a réuni près de 60 personnes. Il avait pour objectifs de réunir, renforcer et fédérer la communauté exobiologique française, de permettre un bilan des avancées et établir une prospective au niveau national dans le domaine de l'exobiologie tout en encourageant les jeunes exobiologistes et en valorisant leurs travaux.
Cinq thèmes principaux ont été couverts par des conférences invitées, des présentations orales et des posters :

1 Terre primitive et premières molécules
2 Briques du vivant et chimie prébiotique
3 Transition vers le vivant et évolution précoce de la vie
4 Exobiologie du système solaire
5 Exoplanètes et habitabilité

Une table ronde a été organisée sur les jalons chronologiques dans le domaine des origines de la vie. Les aspects épistémologie/histoire et philosophie des sciences ont aussi été discutés.

3 Perspectives

Beaucoup des activités de la SFE ont été menées en étroite collaboration avec la SF2A. En effet, traditionnellement, l'exobiologie a toujours eu un lien fort avec l'astronomie/l'astrophysique. Plusieurs des membres de la SFE sont issus de la communauté astrophysique et sont aussi membres de la SF2A Aussi la SFE souhaite développer cette collaboration entre les deux sociétés savantes. C'est ainsi que la SFE a pu présenter ses activités lors du colloque de la SF2A à Marseille en juillet 2010, et la SF2A les siennes lors du colloque de la SFE à Biarritz.
La SFE a établi depuis fin 2009 un partenariat avec le NAI (NASA Astrobiology institute (cf. `http://astrobiology.nasa.gov/nai/`)) et participe avec les membres du NAI et les autres structures partenaires à la création d'une Union Internationale d'Astrobiologie.
En parallèle, la SFE est largement impliquée dans l'organisation de la première conférence jointe de l'ISSOL et de la Commission 51 de l'Union Astronomique Internationale. Ces deux structures avaient l'habitude d'organiser indépendamment une conférence internationale tous les trois ans. Compte tenu du large recouvrement entre les communautés concernées, pour faciliter les échanges entre ces communautés et éviter la multiplication des conférences sur des sujets proches voire identiques, plusieurs membres français de l'ISSOL, actuellement membres de la SFE ont fortement milité pour une conférence jointe. Au bout de 8 ans d'effort, ils ont réussi à convaincre les deux organismes. Ainsi, pour la première fois depuis qu'elles existent (plus de 40 ans en ce qui concerne l'ISSOL) l'ISSOL et la Commission 51 de l'IAU ont décidé d'organiser leur conférence triennale en commun. Plusieurs propositions on été faites, émanant de la Russie, de la France et du Japon, pour l'organisation de cette manifestation scientifique. C'est la proposition française, coordonnée par Murielle Gargaud (Observatoire de Bordeaux) et Robert Pascal (Université de Montpellier), qui a été sélectionnée. C'est donc la communauté exobiologique française, structurée autour de la SFE, qui a l'honneur et la responsabilité d'organiser cette grande conférence internationale «ORIGINS 2011» (`http://www.origins2011.univ-montp2.fr/`). Elle aura lieu à Montpellier, du 3 au 8 juillet 2011.

Figure 3. Une partie des exobiologistes présents aux Rencontres SFE 2011 (Biarritz, 30 septembre)

Les précédentes manifestations scientifiques internationales du domaine se sont déroulées de manières séparées à Florence (ISSOL 2008) et à Puerto-Rico (Bioastronomy 2007) avec des audiences respectives de 450 et 300 participants. La fusion de ces 2 grandes conférences internationales, associée à un projet de création d'une Union Internationale d'Astrobiologie (qui sera discutée à Montpellier par l'ensemble des participants) permet une estimation d'environ 700 participants.

4 Récapitulatif des adresses internet

– NAI : `http://astrobiology.nasa.gov/nai/`
– ISSOL : `http://issol.org/`
– SFE : `http://www.exobiologie.fr/` ,
– ORIGINS : `http://www.origins2011.univ-montp2.fr/`

ASA

Action Spécifique ALMA

SF2A 2010
S. Boissier, M. Heydari-Malayeri, R. Samadi and D. Valls-Gabaud (eds)

PROTOPLANETARY DISKS IN THE (SUB)MILLIMETER: PAVING THE ROAD TO ALMA

J.-F. Gonzalez[1], S. T. Maddison[2], C. Pinte[3], É. Pantin[4], L. Fouchet[5] and F. Ménard[3]

Abstract. ALMA (Atacama Large Millimeter/submillimeter Array) holds the promise of revolutionizing our view of the Universe and in particular that of the planet formation process via unprecedented observations of protoplanetary disks. Preparing for its arrival is of utmost importance to ensure an optimal exploitation of its capabilities. In that view, we are following two roads. First, we are undertaking a observing campaign at millimeter wavelengths of southern disks with ATCA (Autralia Telescope Compact Array) to complement our existing multi-wavelength, multi-technique data and accurately model these sources to prepare followup observations with ALMA. Second, we numerically model the evolution of dust in the presence of an embedded planet in a typical Classical T Tauri star (CTTS) disk. We find that a system with a given stellar, disk and planetary mass will have a completely different appearance depending on the grain size and that such differences will be detectable in the millimeter domain with ALMA. Dust accumulates at the edges of the planetary gap where its density exceeds that of the gas phase, gap edges therefore appear as potential sites for the formation of additional planets.

Keywords: protoplanetary disks, planet-disk interactions, hydrodynamics, submillimeter: planetary systems

1 Introduction

Following the discovery of the first planet around a solar-type star, 51 Peg (Mayor & Queloz 1995), and the subsequent search for exoplanets, with 493 detected to date*, the field of planet formation has been blooming in recent years. In this context, protoplanetary disks have been extensively studied, but a number of unknowns remain.

The ANR-funded "Dust disks" consortium (PI: F. Ménard, LAOG, co-PIs: J.-F. Gonzalez, CRAL, and S. Charnoz, CEA Sacaly) aims at bringing answers to some fundamental questions about protoplanetary disks: what is their structure? Can one reproduce all their observables with a single model? Are their masses and densities sufficient to form planets? Where and how do grains grow in disks to form planets? On what timescales? To that end, three axes are developped: (i) the acquisition of multi-wavelengths and multi-technique (imaging, polarimetry, spectroscopy, interferometry) data for a sample of disks and their interpretation in the framework of a single model per source, (ii) the analysis of these models to infer the disk properties as a function of their environment (stellar mass, age, ...) and derive the dust evolution (migration, settling, growth) signatures, and (iii) the numerical simulation of these disks with hydrodynamical codes to compute the formation of planets from realistic initial conditions and to obtain the signatures left by the presence of planets to predict the observables that upcoming instruments, such as ALMA, will have access to. One of the recent results is the modelling of the complex structure of the disk of HD 100546 by a tenuous inner disk, a gap from 4 to 13 AU, and a massive outer disk (Benisty et al. 2010).

[1] Université de Lyon, Lyon, F-69003, France; Université Lyon 1, Villeurbanne, F-69622, France; CNRS, UMR 5574, Centre de Recherche Astrophysique de Lyon; École normale suprieure de Lyon, 46, allée d'Italie, F-69364 Lyon Cedex 07, France
[2] Centre for Astrophysics and Supercomputing, Swinburne Institute of Technology, PO Box 218, Hawthorn, VIC 3122, Australia
[3] Laboratoire d'Astrophysique de Grenoble, CNRS/UJF UMR 5571, B.P. 53, 38041 Grenoble Cedex 9, France
[4] Laboratoire AIM, CEA/DSM-CNRS-Université Paris Diderot, IRFU/Service d'Astrophysique, Bât.709, CEA-Saclay, 91191 Gif-sur-Yvette Cedex, France
[5] Physikalisches Institute, Universitt Bern, CH-3012 Bern, Switzerland

*`http://exoplanet.eu/`

The evolution of the gas component of these disks is currently being investigated by the "GASPS" (Gas in Protoplanetary Disks, PI: B. Dent, ALMA Chile) Open-Time Key Program for the Herschel Space Observatory. It adresses the fundamental questions of the timescales of the gas evolution as well as the radiative interactions between gas and dust. It will survey a total of 250 disks with the PACS instrument, observing key tracers: lines (notably O I at 63 μm) and photometry. It will provide a statistical study of the combined evolution of gas and dust from young disks to debris disks, associated with a modelling effort using a grid of 300,000 models. Among its first results, the modelling of the dust component of HD 169142 has given constraints on the disk structure, with a gap at 10 AU, and on the fraction of PAHs, while that of the gas has shown a weak UV excess, that the main heating source is the PAHs, and has constrained the gas-to-dust ratio to 20–50 (Meeus et al. 2010).

2 Millimeter interferometry with ATCA

To complement the data sample covering visible to submillimeter wavelengths obtained in the "Dusty Disks" and "GASPS" programs and prepare future observations with ALMA, we have started an initiative to obtain additional data at larger wavelengths, in the millimetric range, that are sensitive to coalesced grains. This allows to obtain a reliable tracer of the grain growth process, precursor of planet formation. A striking example is that of the disk of HD 97048 which shows at 450 μm a flux that is 10 times larger than that expected from models based on shorter-wavelength data.

ATCA (Australia Telescope Compact Array), an interferometer comprising six 22 m-antennas which covers wavelengths from 3 mm to 20 cm with baselines of up to 6 km, is ideally suited for a followup of the sources we have been observing. Located in the southern hemisphere, it allows to observe disks that are inaccessible to the PdBI in the French Alps or the SMA in Hawaii. ATCA is therefore a precious asset to prepare the observations and modelling of a large number of disks: a good prior knowledge of the sources will be essential to secure followup observations with ALMA and complement the wavelength and $u - v$ coverages.

We have started an observing campaign with ATCA, with two components: the first is a mapping program of protoplanetary disks in the millimeter to complement the set of multi-wavelenght data already obtained by the consortium and better constrain the models for each source, and in particular grain growth. The second is a debris disk observation program at 3 mm, aiming at constraining the location of millimeter grains, which are the main contributors to the disk mass, and to break the degeneracy between mass, temperature and opacity. The morphology of the dust population can also trace the presence of planets, thus yielding constraints to their formation process at a later stage than observations of protoplanetary disks. We have obtained observing time in two runs in May and September 2010, the data is currently begin reduced. Figure 1 shows an example of the capabilities of ATCA on the disk of β Pic.

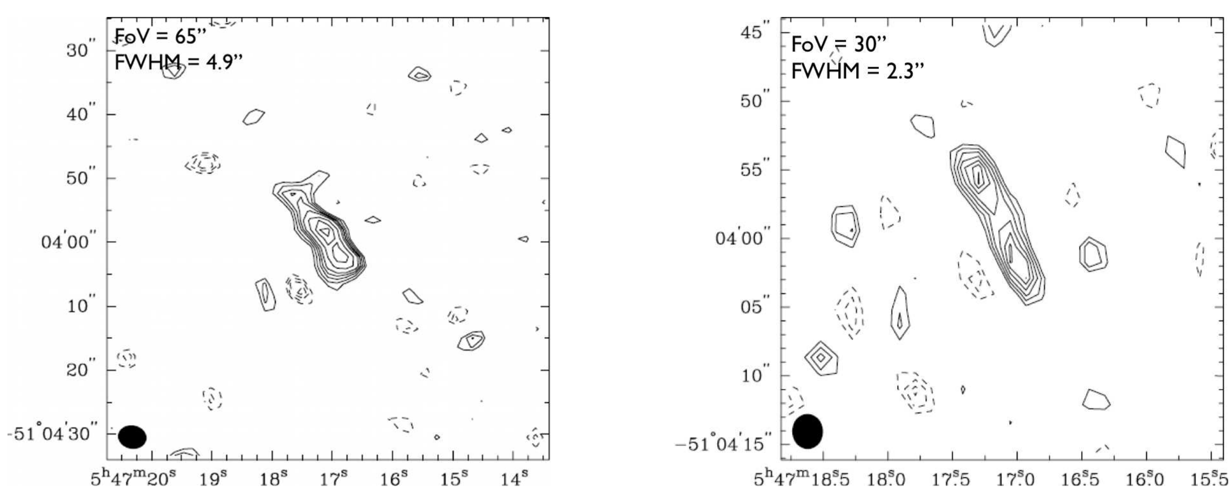

Fig. 1. ATCA contours of the β Pic disk. **Left**: 3 mm map (93+95 GHz). **Right**: 7 mm map (43+45 GHz).

3 Planet gaps in the dust layer of protoplanetary disks

Gaps carved by planets in gas disks have been well studied theoretically and numerically (see Papaloizou et al. 2007, for a review). More recent work (Paardekooper & Mellema 2006; Fouchet et al. 2007) has shown that gaps are more pronounced in the dust layer of a Minimum Mass Solar Nebula (MMSN) disk. Here we study the formation of gaps in dusty CTTS disks, motivated by their observability with ALMA which has been shown by (Wolf & D'Angelo 2005) assuming perfect mixing of gas and dust. We consider dust grains in the size range where gas drag has the strongest effect on their dynamics and which ALMA will be able to detect.

We use our 3D, two-phase (gas+dust), non self-gravitating, locally isothermal smoothed particle hydrodynamics (SPH) code (Barrière-Fouchet et al. 2005) to model the evolution of dust grains under the influence of gas drag in the Epstein regime. Our standard disk orbits a 1 $M_\odot$ star, has a mass $M_{\rm disk} = 0.02\ M_\odot$ and a viscosity $\alpha \simeq 0.01$, and extends from 4 to 160 AU. It contains 1% of 1 mm-sized dust grains by mass and a 5 $M_{\rm J}$ planet at 40 AU. The simulations include 400,000 SPH particles and are evolved for 100 planet orbits ($\sim 26,000$ yr). We vary the grain size s (100 μm to 10 cm) and planet mass $M_{\rm p}$ (0.1 to 5 $M_{\rm J}$).

Our previous work on planet-less disks (Barrière-Fouchet et al. 2005) showed that tiny grains are coupled to the gas and follow its evolution, while large grains are decoupled and follow their own orbits. For intermediate sizes around $s_{\rm opt}$ (optimal size depending on the nebula parameters, 1 mm-1 cm for our CTTS disk), gas drag is most efficient and grains settle to the midplane and migrate radially.

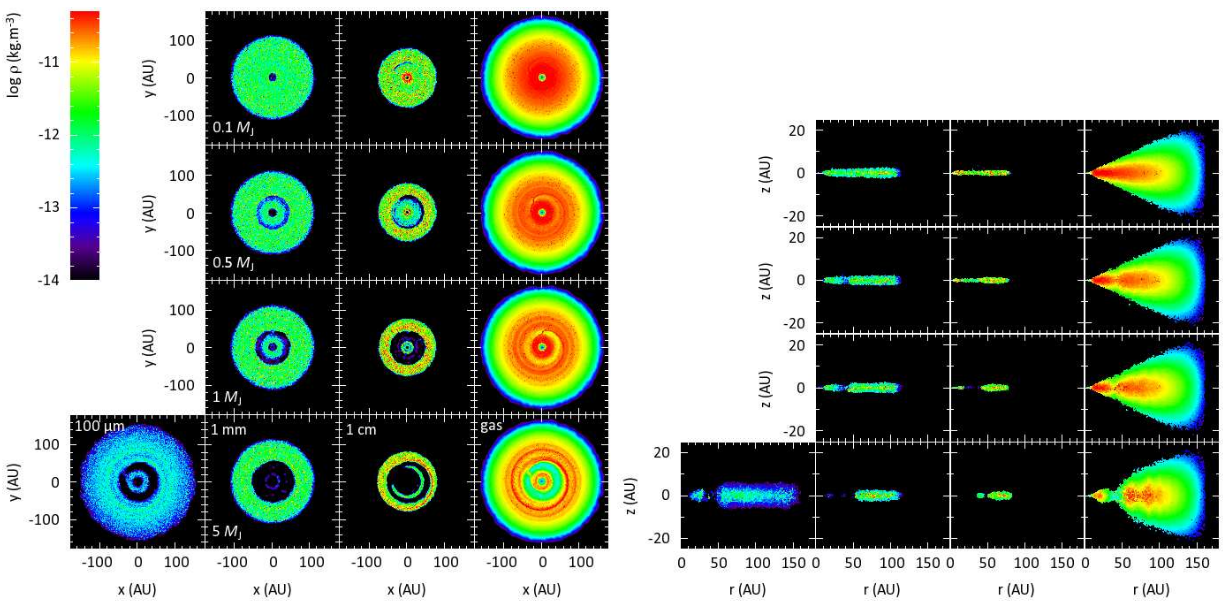

Fig. 2. Density maps in midplane (left panel) and meridian plane (right panel) cuts of the disks. The three leftmost columns show the dust density for $s = 100\ \mu$m, 1 mm and 1 cm, from left to right, and the right hand column shows the gas density. The rows show simulations with $M_{\rm p} = 0.1$, 0.5, 1 and 5 $M_{\rm J}$, from top to bottom.

Gap opening depends on the disk scale height H (Crida et al. 2006) and is easier in the settled dust layer than in the flared gas disk, as seen in Fig. 2. Gaps are deeper and wider for (1) larger grains (with smaller H) and (2) more massive planets. Larger planet masses are required to open a gap in the gas phase than in the dust. While a 0.5 $M_{\rm J}$ planet only slightly affects the gas phase, it carves a deep gap in the dust. Grains can be seen trapped in corotation only for the most massive 5 $M_{\rm J}$ planet (see Fouchet et al. 2010, for details).

4 Observability of planet gaps with ALMA

Wolf & D'Angelo (2005) showed that gaps carved by 1 $M_{\rm J}$ planets should be detectable by ALMA up to 100 pc. However, they used 2D simulations of a planet in a gas disk and assumed that dust grains were perfectly mixed with the gas before performing 3D radiative transfer calculations to obtain synthetic images at the shortest ALMA wavelength (350 μm) and therefore the highest spatial resolution.

We use the dust distributions obtained from our 3D SPH simulations for each grain size as an input to the 3D radiative transfer code MCFOST (Pinte et al. 2006) to compute synthetic scattered light images at several ALMA wavelengths. We reconstruct a grain size distribution described by a power law of index -3.5. Outside the size range of our SPH simulations, small grains are assumed to be perfectly coupled to the gas and large grains are omitted because their contribution to scattered light at those wavelengths is negligible. We also compute images assuming grains of all sizes follow the gas in order to highlight the important effect of gas drag. The resulting synthetic images are then passed on to the CASA simulator for ALMA and are shown in Fig. 3 for array configuration 20 (longest baseline $\sim$ 4 km). They reproduce the decreasing spatial resolution as wavelength increases.

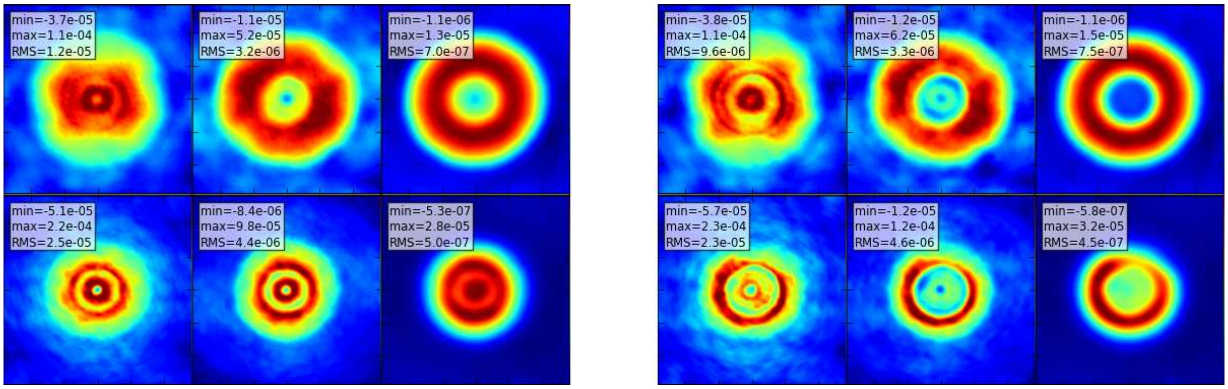

Fig. 3. ALMA synthetic images of the CTTS disk with a 1 M_{J} (left pannel) and 5 M_{J} (right pannel) planet for $\lambda = 850$, 1300 and 2700 μm, from left to right, for array configuration 20 (longest baseline $\sim$ 4 km). **Top**: naïve well-mixed assumption. **Bottom**: self-consistently included aerodynamic drag.

The images from the realistic case with aerodynamic drag (bottom row of Figs. 3 and 4) display notable features. The extent of the disk varies with wavelength, reflecting the location of different grain sizes in the disk (as grains with sizes closest to the wavelength contribute the most). The disk asymmetry caused by the spiral wave in the 5 M_{J} planet case is clearly visible and can provide a constraint on the angular position of the planet. Finally, the gap has a much higher contrast in the realistic case than in the naïve mixed case: it is deeper and its edges are denser and brighter. Even for the 1 M_{J} planet, it is still visible at the lowest resolution, whereas the naïve mixed case would only show a central hole. Gaps carved by lighter planets will therefore be much easier to detect than anticipated.

5 Conclusions

To prepare future observations with ALMA and identify the optimal setup, we observe southern protoplanetary disks with the ATCA interferometer at longer wavelengths, and thus constrain the source models. In parallel, we numerically model planet gaps in dusty disks and find that they are more striking and require a smaller planet mass to form in the dust phase than in the gas. They are wider and deeper for larger grains, both in MMSN (Fouchet et al. 2007) and in CTTS (Fouchet et al. 2010) disks. The variety of structures seen for different s and M_{p} are visible in the synthetic images and future ALMA observations will be able to constrain both parameters. Gaps will be detectable for lighter planets than anticipated.

This research was supported by the *Programme National de Physique Stellaire*, the *Programme National de Planétologie* and the *Action Spécifique ALMA* of CNRS/INSU, France, the *Agence Nationale de la Recherche* (ANR) of France through contract ANR-07-BLAN-0221, the Swinburne University Research Development Grant Scheme, the Australia-France co-operation fund in Astronomy (AFCOP), and the Swiss National Science Foundation through a Maria Heim-Voegtlin fellowship. Simulations presented here were run on the Swinburne supercomputer (`http://astronomy.swin.edu.au/supercomputing`) and the Fostino cluster at LAOG.

References

Barrière-Fouchet L., Gonzalez J.-F., Murray J. R., Humble R. J., & Maddison S. T. 2005, A&A 443, 185

Benisty M., Tatulli E., Ménard F., & Swain M. R. 2010, A&A 511, A75

Crida A., Morbidelli A., & Masset F. 2006, Icarus 181, 587

Fouchet L., Maddison S. T., Gonzalez J.-F., & Murray J. R. 2007, A&A 474, 1037

Fouchet L., Gonzalez J.-F., & Maddison S. T. 2010, A&A 518, A16

Mayor, M. & Queloz, D. 1995, Nature 378, 355

Meeus G., Pinte C., Woitke P. et al. 2010, A&A 518, L124

Paardekooper S.-J. & Mellema G. 2006, A&A 453, 1129

Papaloizou J. C. B., Nelson R. P., Kley, W., Masset, F. S., & Artymowicz, P. 2007, Protostars and Planets V, p. 655
Pinte C., Ménard F., Duchêne G., & Bastien P. 2006, A&A 459, 797
Stepinski T. F. & Valageas P. 1997, A&A 319, 1007
Wolf S. & D'Angelo G. 2005, ApJ 619, 1114

AS GAIA - PNCG

Stellar populations and modelisation of the Galaxy

SF2A 2010
S. Boissier, M. Heydari-Malayeri, R. Samadi and D. Valls-Gabaud (eds)

THE CATALOG OF RADIAL VELOCITY STANDARD STARS FOR THE GAIA RVS: STATUS AND PROGRESS OF THE OBSERVATIONS

L. Chemin[1], C. Soubiran[1], F. Crifo[2], G. Jasniewicz[3], L. Veltz[4], D. Hestroffer[5], S. Udry[6], J. Berthier[5], A. Vigneron[5], D. Katz[2] and A. Siebert[7]

Abstract. A new full-sky catalog of Radial Velocity standard stars is being built for the determination of the Radial Velocity Zero Point of the RVS on board of Gaia. After a careful selection of 1420 candidates matching well defined criteria, we are now observing all of them to verify that they are stable enough over several years to be qualified as reference stars. We present the status of this long-term observing programme on three spectrographs : SOPHIE, NARVAL and CORALIE, complemented by the ELODIE and HARPS archives. Because each instrument has its own zero-point, we observe intensively IAU RV standards and asteroids to homogenize the radial velocity measurements. We can already estimate that 8% of the candidates have to be rejected because of variations larger than the requested level of 300 m s^{-1}.

Keywords: Gaia, Milky Way, stars, asteroids, radial velocity, high-resolution spectroscopy

1 Introduction

The purpose of this new spectroscopic catalog of standard stars is to calibrate the future radial velocities measured by the Radial Velocity Spectrometer (RVS) on board of the Gaia satellite (see e.g. Jasniewicz et al. 2010, and references therein). We refer to Crifo et al. (2009, 2010) for a complete description of the selection criteria and of the ground observations of the 1420 candidates as reference stars.

2 Status of the observations

A total of 4035 measurements is currently available for 1330 stars. It consists in new and archived observations performed with the NARVAL (98 measurements), CORALIE (688), SOPHIE (902), ELODIE (1057) and HARPS (1290) high-resolution spectrographs. Figure 1 (left panel) represents the spatial distribution in the equatorial frame of the number of measurements already obtained for the 1420 candidates. The majority of stars still lacking observations is located in the Southern part of the sky, because the Southern programme on CORALIE started later. In the North ($\delta > -15^{\circ}$), ∼200 stars still lack a second measurement. The Northern programme should be completed in 2011.

3 Preliminary results

- ***Radial velocities of stars:*** We have first compared the radial velocities of 320 stars we have in common with Nidever et al. (2002). A mean difference of -40 m s^{-1} exists between both studies. This illustrates the zero-point issue that has to be solved for the calibration of the RVS (Jasniewicz et al. 2010). Among

[1] Laboratoire d'Astrophysique de Bordeaux, UMR 5804 (CNRS, Université Bordeaux 1), 33271 Floirac Cedex, France
[2] Observatoire de Paris, GEPI, UMR 8111 (CNRS , Université Denis Diderot Paris 7), 92195 Meudon, France
[3] GRAAL, UMR5024, (CNRS, Université Montpellier 2), 34095 Montpellier Cedex 05, France
[4] Astrophysikalisches Institut Potsdam, Potsdam, An der Sternwarte 16, D-14482 Potsdam, Germany
[5] Observatoire de Paris, IMCCE, UMR8028 (CNRS, Université Pierre & Marie Curie Paris 6), 75014, Paris, France
[6] Observatoire de Genève, 51 Ch. des Maillettes, 1290 Sauverny, Switzerland
[7] Observatoire Astronomique de Strasbourg, UMR 7550 (CNRS, Université de Strasbourg), 67000, Strasbourg, France

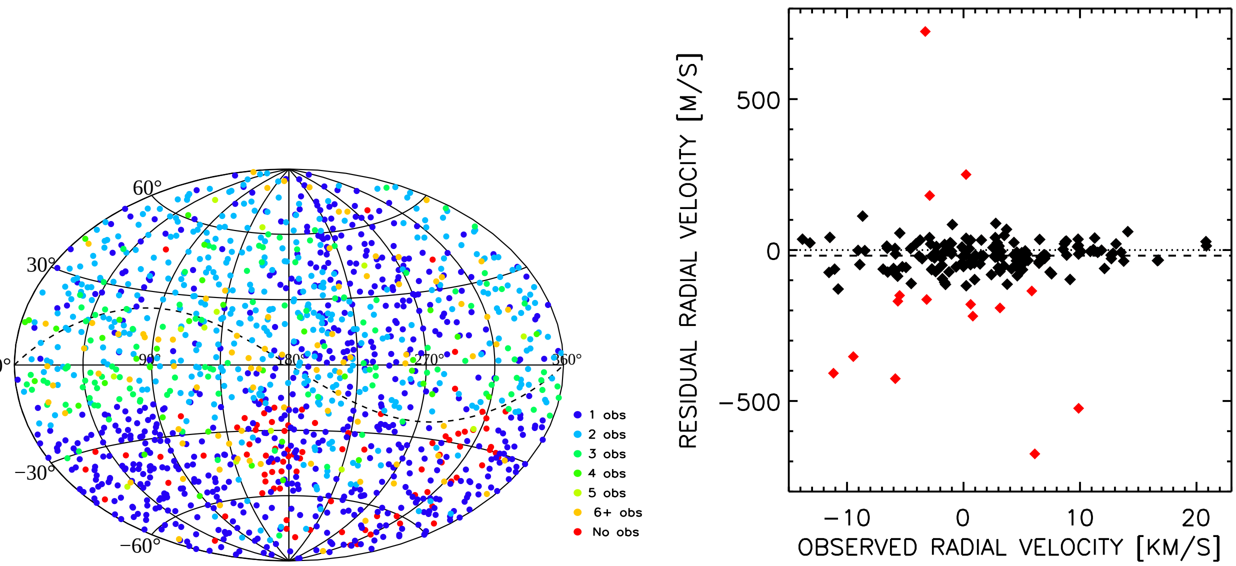

Fig. 1. *Left panel:* Number of ground-based observations of Gaia-RVS reference stars performed as of June 2010. The ecliptic is shown as a dashed line. *Right panel:* Residual velocities (observed - theoretical) for asteroids as a function of their observed velocities. The red dots deviate by more than 3σ.

those 320 stars 27 objects deviate by more than $\sim$300 m s^{-1}. Such a discrepancy between both studies may be due to variable stars that should not be considered as standard objects in a future analysis.

We have also done a preliminary statistical analysis our catalog. When selecting a sub-sample of 673 candidates for which at least two measurements have been performed it is seen that the velocity for $\sim$72% of them does not vary by more than 100 m s^{-1} during a time baseline of 0.5-2 years. Such a stability of radial velocities is very important to get the most accurate calibration of the RVS. The time variability of the catalog will be studied during the whole lifetime of the Gaia mission. Notice that $\sim$8% of the 673 stars exhibit a velocity variation of more than 300 m s^{-1}. Those objects likely correspond to variable stars.

- ***Radial velocities of asteroids:*** Observations of asteroids are very important for this project because they will allow the derivation of the zero point of the radial velocities for all reference sources. 171 measurements of 70 asteroids have been performed until now with SOPHIE. Their velocities have been compared with the theoretical values (Fig. 1, right panel) which have been derived using the MIRIADE webservice of the virtual observatory at IMCCE. The scatter of the residual (observed minus calculated) velocity is $\sigma \sim 45$ m s^{-1}. Points that are more deviant than 3σ (red symbols) correspond all to low signal-to-noise observations due to bad transparency conditions, or to badly derived velocity centroids due to e.g. double peaks in the cross-correlation function (observing conditions, contamination by the moon, ...). We are currently investigating the correlations of the observed and computed velocities with the physical properties of the asteroids (diameter, shape, rotation, phase, etc).

We are very grateful to the AS-Gaia, the PNPS and PNCG for the financial support and help in this project.

References

Crifo F., Jasniewicz G., Soubiran C., et al., 2009, SF2A 2009 conference proceedings, 267

Crifo F., Jasniewicz G., Soubiran C., et al., 2010, A&A, accepted, in press

Jasniewicz G., Crifo F., Soubiran C., et al., 2010, ELSA 2010 conference proceedings, in press

Nidever D. L., Marcy G. W., Butler R. P., Fischer D. A., Vogt S. S., 2002, ApJS, 141, 503

SF2A 2010
S. Boissier, M. Heydari-Malayeri, R. Samadi and D. Valls-Gabaud (eds)

SED FITTING OF NEARBY GALAXIES IN THE HERSCHEL REFERENCE SURVEY

L. Ciesla[1], A. Boselli[1], V. Buat[1], L. Cortese[2], R. Auld[2], M. Baes[2], G.J. Bendo[2], S. Bianchi[2], J. Bock[2], D.J. Bomans[2], M. Bradford[2], N. Castro-Rodriguez[2], P. Chanial[2], S. Charlot[2], M. Clemens[2], D. Clements[2], E. Corbell[2], A. Cooray[2], D. Cormie[2], A. Dariush[2], J. Davies[2], I. De Looze[2], S. di Serego Alighieri[2], E. Dwek[2], S. Eales2, D. Elbaz[2], D. Fadda[2], J. Fritz[2], M. Galametz[2], F. Galliano[2], D.A. Garcia-Appadoo[2], G. Gavazzi[2], W. Gear[2], C. Giovanardi[2], J. Glenn[2], H. Gomez[2], M. Griffin[2], M. Grossi[2], S. Hony[2], T.M. Hughes[2], L. Hunt[2], K. Isaak[2], A. Jones[2], L. Levenson[2], N. Lu[2], S.C. Madden[2], B. O'Halloran[2] , K. Okumura[2], S. Oliver[2], M. Page[2], P. Panuzzo[2], A. Papageorgiou[2], T. Parkin[2], I. Perez-Fournon[2], D. Pierini[2], M. Pohlen[2], N. Rangwala[2], E. Rigby[2], H. Roussel[2], A. Rykala[2], S. Sabatini[2], N. Sacchi[2], M. Sauvage[2], B. Schulz[2], M. Schirm[2], M.W.L. Smith[2], L. Spinoglio[2], J. Stevens[2], S. Sundar[2], M. Symeonidis[2], M. Trichas[2], M. Vaccari[2], J. Verstappen[2], L. Vigroux[2], C. Vlahakis[2], C. Wilson[2], H. Wozniak[2], G. Wright[2], E.M. Xilouris[2], W. Zeilinger[2] and S. Zibetti [2]

Abstract. We compute UV to radio continuum spectral energy distributions of 51 nearby galaxies recently observed with SPIRE onboard Herschel and present infrared colours (in the $25 - 500\mu$m spectral range). SPIRE data of normal galaxies are well reproduced with a modified black body (β=2) of temperature $T\simeq$ 20 K. In ellipticals hosting a radio galaxy, the far-infrared (FIR) emission is dominated by the synchrotron nuclear emission. The colour temperature of the cold dust is higher in quiescent E-S0a than in star-forming systems probably because of the different nature of their dust heating sources (evolved stellar populations, X-ray, fast electrons) and dust grain properties.

Keywords: galaxies: ISM, spiral, elliptical and lenticular, infrared: galaxies

1 Introduction

By constructing the spectral energy distribution (SED) of any extragalactic source, its energetic output can be determined. The stellar component emits from the UV to near-infrared (NIR) domain, young and massive stars dominating the UV and old stars the NIR. Dust, produced by the aggregation of metals injected into the interstellar medium (ISM) by massive stars through stellar winds and supernovae, efficiently absorbs the stellar light, in particular that at short wavelengths, and re-emits it in the infrared domain (5μm-1mm). At longer wavelengths, the emission of normal galaxies is generally dominated by the loss of energy of relativistic electrons accelerated in supernovae remnants (Lequeux 1971; Kennicutt 1983) (synchrotron emission). SEDs are crucial for quantifying dust extinction and reconstructing the intrinsic distribution of the different stellar populations within galaxies. In particular, the importance of the infrared domain explored by Herschel resides in the dust that, by means of the absorption and scattering of UV, optical and NIR photons, modifies the stellar spectra of galaxies. The interpretation of the infrared SEDs of normal galaxies has already been the subject of several studies (e.g. Dale et al. 2007; Chary & Elbaz 2001) even within the Virgo cluster region (Boselli et al. 1998; 2003) which were limited in the infrared domain to $\lambda \leq 170$ μm (domain covered by ISO or Spitzer) With the Herschel data, we can extend to the sub-mm domain ($\lambda \leq 500$ μm) where the emission is dominated by the coldest dust component. This domain is crucial for determining galaxy properties such as the total mass of dust, and an accurate total infrared luminosity. Galaxies analysed in this work were observed

[1] Laboratoire d'Astrophysique de Marseille, UMR6110 CNRS, 38 rue F.Joliot-Curie, F-13388 Marseille France
[2] Members of the Herschel/SPIRE guaranteed time Extragalactic Working Group (SAG2)

during the Herschel (Pilbratt et al. 2010) SPIRE (Griffin et al. 2010) science demonstration phase mainly as part of the Herschel Reference Survey (HRS), a guaranteed time key project designed to observe with SPIRE a volume-limited, K-band-selected, complete sample of nearby galaxies (Boselli et al. 2010), and the Herschel Virgo Cluster Survey (HeViCS), an open time key project focused on covering 60 sq.deg. of the Virgo cluster with PACS and SPIRE (Davies et al. 2010). The results of this analysis have been presented in Boselli et al. (2010b).

2 Far infrared colours

We determine the IR colours of the galaxies in order to quantify their spectral properties combining SPIRE and IRAS flux densities (Fig. 1). These colour diagrams indicate that in star-forming galaxies the flux density ratios $f60/f500$, $f25/f250$, or $f100/f250$ are strongly correlated with the generally used IRAS colour index $f60/f100$ (panels a, b and c). However, the dynamic range covered by $f60/f500$ is a factor of about 30 larger than that covered by the $f60/f100$ flux density ratio. The colour index is thus a powerful tracer of the average temperature of the dust component. Starburst galaxies, generally defined to have $f60/f100 > 0.5$ (Rowan-Robinson & Crawford 1989), show $f60/f500$ spanning from ~ 3 to ~ 30 and Sa-Sb have $f60/f500$ colours generally colder than Sbc-Scd, Sd, Im, BCD, and Irr. Early-types with a synchrotron-dominated IR emission (M87, M84) are well separated in all colour diagrams with respect to the other dust-dominated E-S0a. Therefore, we can use colour diagrams in order to identify and discriminate radio galaxies from the remaining early-types. The remaining early-types have colour indices indicating that the cold dust temperature is higher than in star-forming systems.

Figure 1 also shows that, despite possible uncertainties in the absolute flux calibration (15 %), the empirical SEDs of Dale & Helou (2002), Chary & Elbaz (2001), and Boselli et al. (2003), cover only qualitatively the wide range of infrared colours observed in our sample (even excluding the radio galaxies M87 and M84), underpredict the $f250/f350$ ratio for a given $f100/f250$ ratio (d), and do not reproduce the coldest colour temperatures observed in the diagram $f350/f500$ versus $f250/f350$ (f).

3 Spectral Energy Distribution

As a representative example of the target galaxies, we show the SED of two late-type galaxies (Fig2), M100 (NGC4321) and NGC4438, and two ellipticals (Fig3), M87 (NGC486) and M86 (NGC4406). The SED has been computed by combining data available in the literature. We match the 100μm IRAS data with a modified black body (β=2) of temperature $T \simeq 20$ K (magenta dashed line) and the radio data with a power law. Despite their very different morphology (M100 is a normal spiral galaxy while NGC4438 is a strongly interacting system), these two objects have quite similar SEDs. Contrarily, the galaxies M87 and M86 are both bright ellipticals but characterized by very different SEDs. In M87, the submilimeter emission detected by Herschel is due to synchrotron (Baes et al. 2010), while in M86 it is due to the cold dust nearbly falling into the galaxy after its interaction with nearby companions (Gomez et al. 2010). These different SEDs for galaxies of the same morphological type clearly explain why galaxies of a given type have so different infrared colours.

4 Conclusions

The infrared colour index $f60/f500$ is more capable of detecting a starburst than $f60/f100$ due to a larger dynamical range. Normal galaxies show a gradual increase in their dust temperature along the Hubble sequence, from Sa to Sc-Im-BCD with the exception of E-S0a, where the dust temperature is higher than in star-forming systems probably because of the different nature of their dust heating sources. SPIRE colours can be used to discriminate thermal from synchrotron emission in radio galaxies. SED of radio galaxies clearly show the far-infrared dominated by the synchrotron emission. In normal galaxies, the modified black body seems to well reproduce the SPIRE data but it has to be detailed with a proper fit using the CIGALE code (Code Investigating GALaxy Emission, Noll et al. 2009).

References

Baes, M. et al. 2010, ApJ, 652, 283
Bendo, G. et al. 2010, A&A, 518, L65

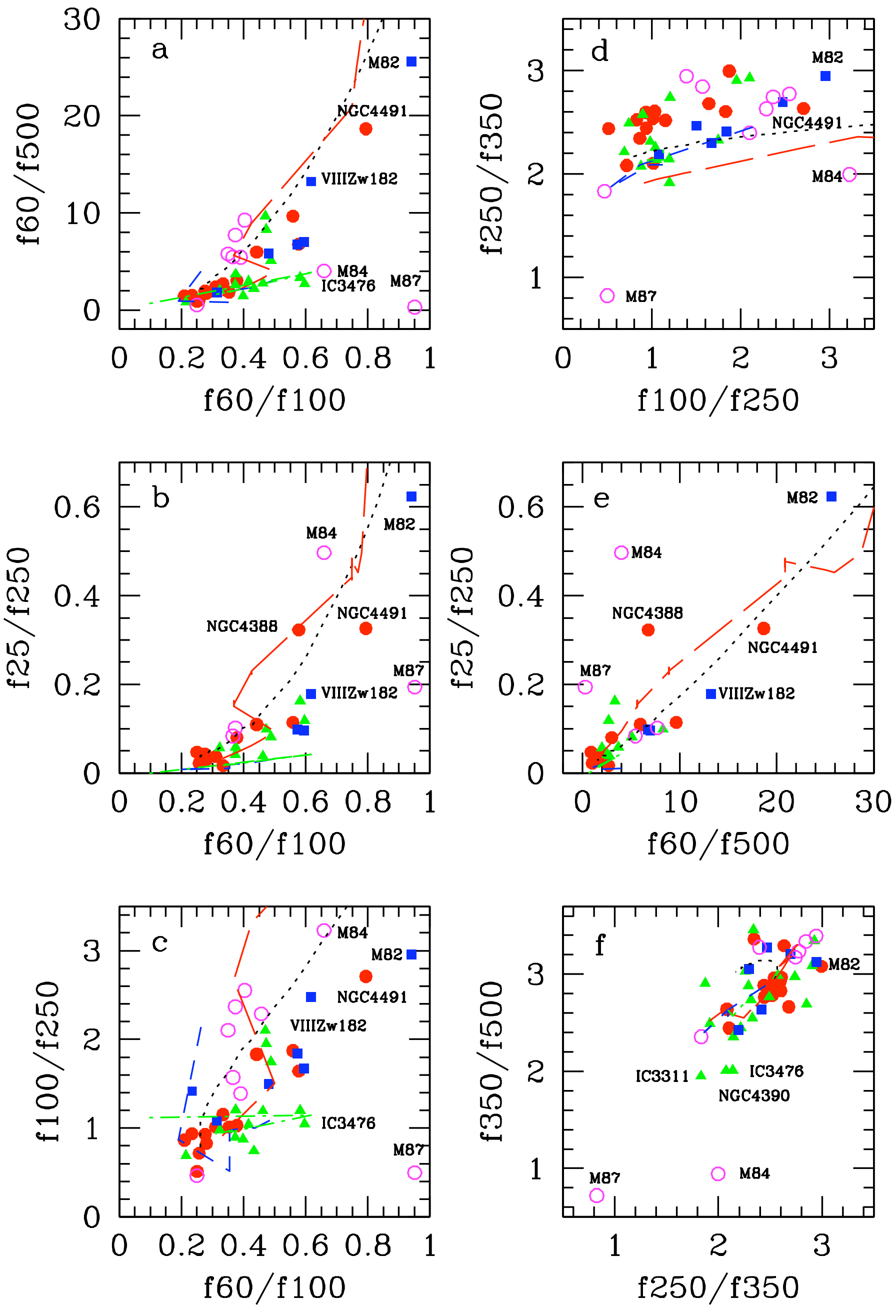

Fig. 1. The infrared colours of our targets. Galaxies are coded according to their morphological type: magenta empty circles for E-S0a, red filled circles for Sa-Sb, green triangles for Sbc- Scd, blue squares for Sd, Im, BCD, and Irr galaxies. The black dotted line indicates the colour expected from the Dale & Helou (2002) empirical SED, the red long-dashed line those from Chary & Elbaz (2001), the blue-short dashed, and the green dashed-dotted line the colours of the morphology- and luminosity-dependent templates of Boselli et al. (2003).

Boselli, A. and Gavazzi, G. 2006, PASP, 118, 517
Boselli, A., Lequeux, J., Sauvage, M., et al. 1998, A&A, 335, 53
Boselli, A., Gavazzi, G., Donas, J., Scodeggio, M. 2001, AJ, 121, 753
Boselli, A., Gavazzi, G., Sanvito, G., 2003, A&A, 402, 37
Boselli, A., Cortese, L., Deharveng, JM., et al. 2005, ApJ, 629, L29
Boselli, A., Boissier, S., Cortese, L., Buat, V., Hughes, T., Gavazzi, G. 2009, ApJ, 706, 1527
Boselli, A., Eales, S., Cortese, L., et al. 2010, PASP, 122, 261

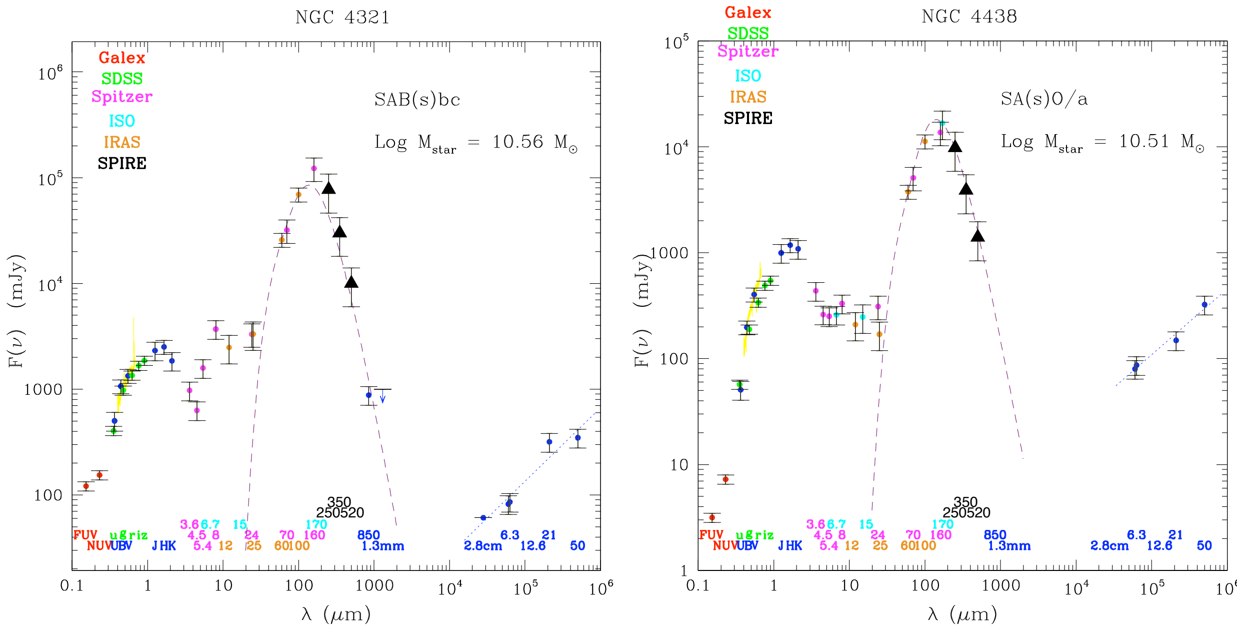

Fig. 2. The UV to radio SED of M100 (NGC4321) and NGC4438. Points are coloured according to the origin of the data. Black triangles are for Herschel-SPIRE data, red dots for GALEX data, green dots for SDSS data, magenta for Spitzer-IRAC and MIPS data, orange dots for IRAS data. Blue dots correspond to data from NED. The magenta dashed line shows a modified black body (β=2) of temperature $T \simeq$ 20 K matching the 100μm IRAS data, while the blue dotted-line indicates the radio power law spectrum due to synchrotron emission. We fit the radio data with a power law (blue dotted-line).

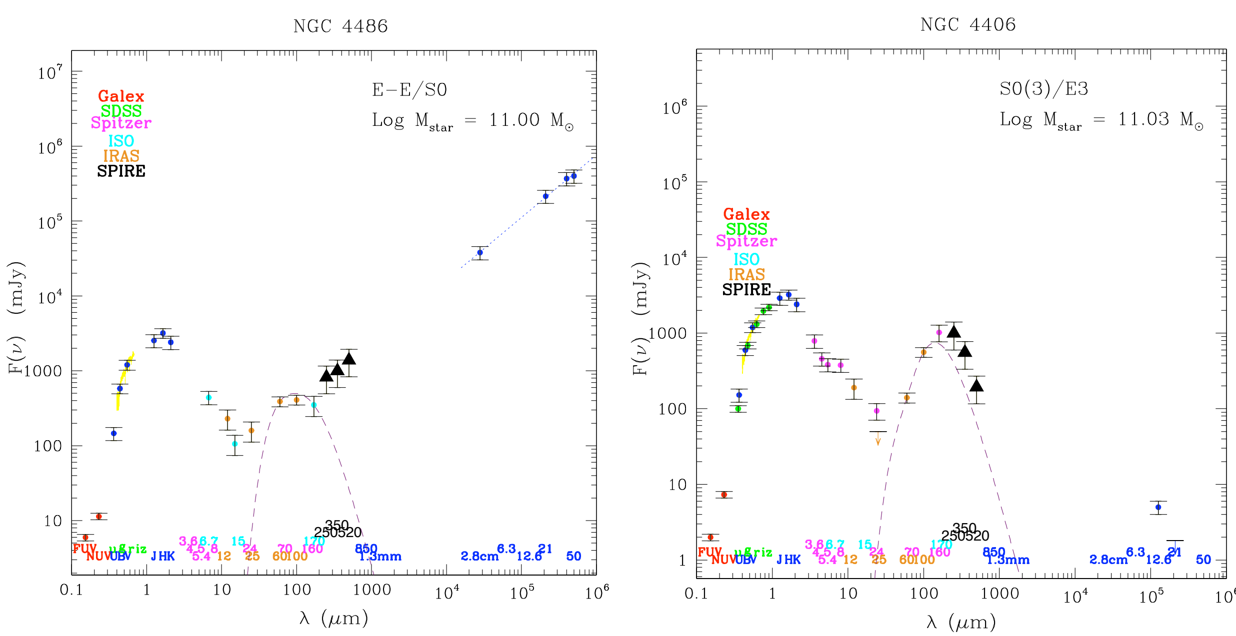

Fig. 3. The UV to radio SED of M87 (NGC4486) and M86 (NGC4406). Points are coloured according to the origin of the data. Black triangles are for Herschel-SPIRE data, red dots for GALEX data, green dots for SDSS data, magenta for Spitzer-IRAC and MIPS data, orange dots for IRAS data. Blue dots correspond to data from NED. The magenta dashed line shows a modified black body (β=2) of temperature $T \simeq$ 20 K matching the 100μm IRAS data while the blue dotted-line indicates the radio power law spectrum due to synchrotron emission.

Boselli, A., Ciesla, L., Buat, V., et al. 2010, A&A, 518, L61
Chary, R. and Elbaz, D. 2001, ApJ, 556, 562
Cortese, L., Davies, J., Pohlen, M., et al. 2010, A&A, 518, L63
Dale, D., Gil de Paz, A., Gordon, K., et al. 2007, ApJ, 655, 863
Dale, D. & Helou, G. 2002, ApJ, 576, 159
Davies, J., Baes, M., Bendo, G., et al. 2010, A&A, 518, L48
Draine, B. and Li, A. 2007, ApJ, 657, 810
Draine, B., Dale, D., Bendo, G., et al. 2007, ApJ, 663, 866
Galliano, F., Madden, S., Jones, A., Wilson, C., Bernard, J. 2005, A&A, 434, 867
Gavazzi, G., Boselli, A., Donati, A., Franzetti, P., Scodeggio, M. 2003, A&A, 400, 451
Gomez, H. et al. 2010, A&A, 518, L45
Griffin, M., et al. 2010, A&A, 518, L3
Kennicutt, R. 1983, A&A, 120, 219
Lequeux, J. 1971, A&A, 15, 42
Noll, S., Burgarella, D., Giovannoli, E., Buat, V. et al. 2009, A&A, 507, 1793
O'Connell, R. 1999, A&A, 37, 603
Pilbratt, G., et al. 2010, A&A, 518, L1
Pohlen, M., et al. 2010, A&A, 518, L72
Rowan-Robinson, M., Crawford, J. 1989, MNRAS, 238, 523
Swinyard, B., Ade, P, Baluteau, J.P., et al. 2010, A&A, 518, L4
Wolfire, M., Hollenbach, D., McKee, C., Tielens, A., Bakes, E. 1995, ApJ, 443, 152

SF2A 2010
S. Boissier, M. Heydari-Malayeri, R. Samadi and D. Valls-Gabaud (eds)

DYNAMICAL MODELING OF THE GALAXY AND STELLAR MIGRATION IN THE DISK

B. Famaey[1] and I. Minchev[2]

Abstract. We exhibit the local and global effects of the non-axisymmetry of the Milky Way potential. In addition to creating moving groups in the Solar neighborhood, we show that spiral structure interacting with a central bar is an effective mechanism for mixing the whole stellar disk radially. This spiral-bar resonance overlap mechanism accounts for the absence of age-metallicity relation in the solar neighborhood, can create extended disks in both Milky Way-mass and low-mass galaxies, and could also be responsible for the formation of a thick disk component early-on in the Galaxy evolution.

Keywords: galaxy: kinematics and dynamics, galaxy: evolution

1 Introduction

Our Milky Way Galaxy is a unique laboratory in which to study galactic structure and evolution. The story of the efforts to obtain stellar kinematic data nicely illustrates how theoretical progress and data acquisition have to go hand in hand if one wants to gain insight into the structure and history of the Galaxy. Until recently, most observational studies have been limited to the solar neighbourhood. The zeroth order approximation for modelling these kinematic data assumes an axisymmetric model, in which the Local Standard of Rest is on a perfectly circular orbit. However, the local velocity field in the solar neighbourhood already displays signatures of the non-axisymmetry of the Galactic potential in the form of stellar moving groups containing stars of very different ages and chemical compositions (Famaey et al. 2005, 2007, 2008), the most prominent being the Hyades stream, the Sirius stream, and the Hercules stream (see Fig. 1 left panel). Here we investigate how to reproduce these streams with a bar and a spiral pattern, and how the combined effect of the bar and the spiral can cause radial migrations in the disk. Future astrometric and spectroscopic surveys will allow radical progress in our understanding of these effects of the non-axisymmetry of the Galactic potential.

2 Moving groups

Kalnajs (1991) suggested that the bar could cause the velocity distribution in the vicinity of the 2:1 outer Lindblad resonance (OLR) to become bimodal, due to the coexistence of orbits elongated along and perpendicular to the bars major axis. Today, we know that this mechanism does account for the Hercules stream (Dehnen 2000) as well as for some low-velocity streams such as the Pleiades (Minchev et al. 2010a). Quillen & Minchev (2005) also showed that the 4:1 ultra-harmonic (or second order) ILR of a 2-armed spiral structure* splits the velocity distribution into two features corresponding to two orbital families, one of them consistent with the Hyades. Test-particle simulations of a stellar disk consistent with the Milky Way kinematics, perturbed by a 2-armed spiral pattern (simulation parameters can be found in Minchev & Quillen 2007) showed that we could indeed reproduce the position of the Hyades stream in velocity-space only when the Sun is near the 4:1 ILR. The beauty of this simulation is that, while reproducing the Hyades stream, the other orbital family creates another remarkable feature in velocity space around $(U, V) \approx (10, 0)$ km/s, which is consistent with the Sirius stream (see Fig. 1, right panel). In order to reproduce the observed streams, the Sun should thus be at the same time close to the 2:1 OLR of the bar and 4:1 ILR of the spiral pattern. Since it has long been known that in the case of resonance overlap the last KAM surface between the two resonances is destroyed, resulting in chaotic behaviour, we expect that such a resonance overlap could give rise to radial migration of stars in the disk.

[1] Observatoire Astronomique, Université de Strasbourg, CNRS UMR 7550, F-67000 Strasbourg, France
[2] Astrophysikalisches Institut Potsdam, An der Sterwarte 16, D-14482 Potsdam, Germany

*Observations indicate that the Milky Way has a 4-armed structure, but with 2 more prominent arms

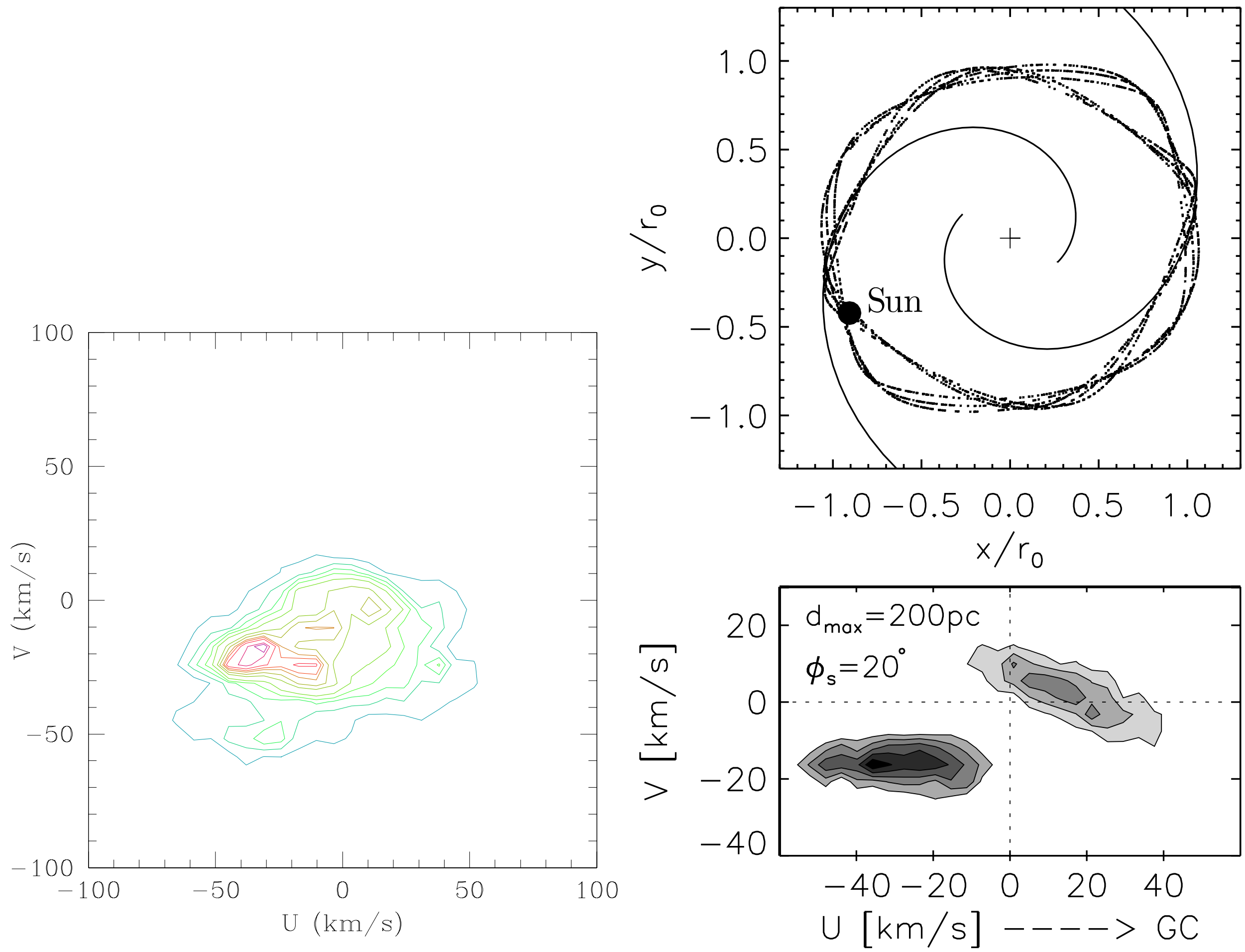

Fig. 1. Left Panel – Isocontours for the Geneva-Copenhagen survey (see Famaey et al. 2007) in the UV-plane (U is the velocity w.r.t. to the Sun in the direction of the Galactic center and V in the direction of Galactic rotation): the contours correspond respectively to 0.5, 0.8, 1.2, 1.5, 1.9, 2.6, 3.1, 3.5, 3.8, 4.2, 4.7, 5. stars/(km/s)^2. The Hyades stream, at $U \simeq -40$ km/s and $V \simeq -20$ km/s, and the Sirius stream at $U \simeq 10$ km/s and $V \simeq 0$ km/s are prominent features. The Pleiades stream is also visible at $U \simeq -15$ km/s and $V \simeq -20$ km/s, and the Hercules stream at $V \simeq -50$ km/s. **Top Right panel** – The effect of a 2-armed spiral structure on orbits near the 4:1 ILR. Note the splitting into 2 families of closed orbits in the frame moving with the (trailing) spiral pattern. For a Sun orientation at 20° with respect to a concave arm, both orbital families enter the solar neighborhood stellar velocity distribution (black filled circle). The galactocentric axes are in units of r_0 (the galactocentric radius of the Sun). **Bottom Right panel** – The effect on the UV-plane for the configuration shown in the top panel (selecting test particles in a 200 pc circle around the Sun). Each orbital family gives rise to a stream in velocity space. We can associate the dense clump at $(U, V) \approx (-40, -20)$ km/s with the Hyades and the shallow one at $(U, V) \approx (10, 0)$ km/s with Sirius.

3 Stellar migration

We have subsequently shown (Minchev & Famaey 2010) that a strong exchange of angular momentum indeed occurs when a stellar disk is perturbed by a central bar and spiral structure simultaneously (see Fig. 2). By using test-particle simulations, we confirmed that this effect was due to the overlap of first and second order resonances of each perturber, and showed that the mechanism was efficient throughout the whole disk, as such overlaps happen evrywhere. Beforehand, it was believed that radial mixing was solely caused by transient spirals (Sellwood & Binney 2002). The efficiency of the new spiral-bar mechanism was confirmed in fully self-consistent, Tree-SPH simulations, as well as high-resolution pure N-body simulations (Minchev et al. 2010b, see Fig. 3).

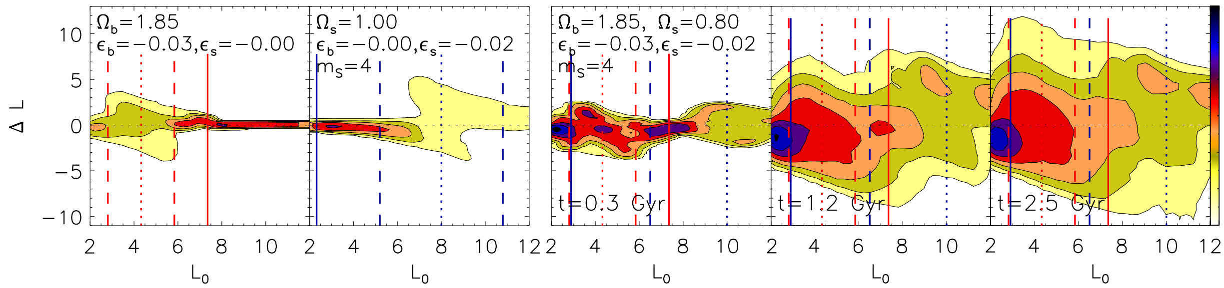

Fig. 2. Changes in the (vertical component of the) angular momentum, ΔL, as a function of the initial angular momentum, L_0. From left to right the first 2 panels show the effect of a bar or a spiral only, respectively, with parameters consistent with the Milky Way. The simultaneous propagation of the same perturbers is shown in the following 3 panels for $t = 0.3 - 2.5$ Gyr. The dotted lines show the corotation radii. The 2:1 and 4:1 LRs are indicated by the solid and dashed lines respectively (bar=red, spiral=blue). Figure is from Minchev & Famaey (2010).

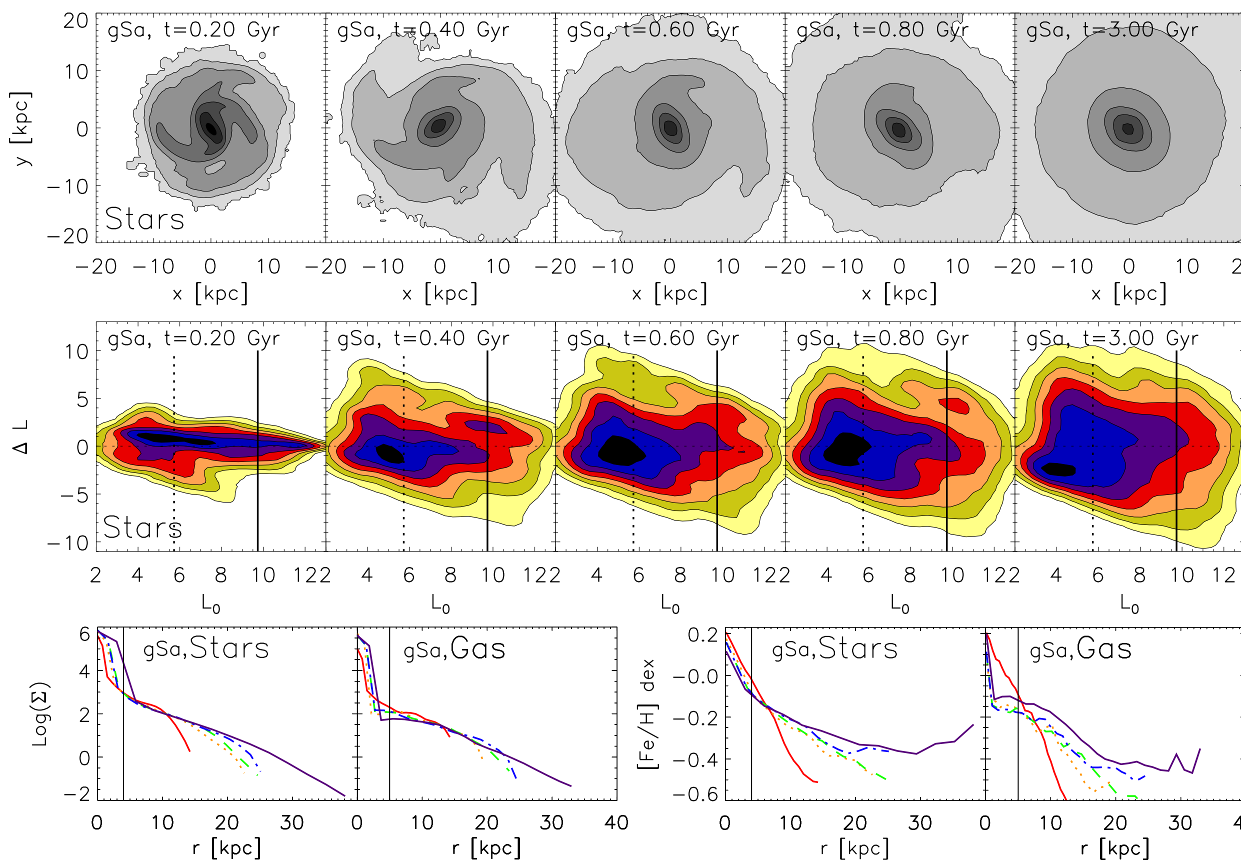

Fig. 3. Results of a Tree-SPH simulation, studying the exchange of angular momentum due to resonance overlap of bar and spiral. **Top row:** Time development of the stellar disk density contours of a giant Sa galaxy. **Second row:** ΔL as a function of the initial angular momentum, L_0. **Bottom row:** The evolution of the radial profiles of surface density (left) and metallicity (right) for the stellar and gaseous disks. The initial disk scale-lengths are indicated by the solid lines. The 5 time steps shown are as in the top row, indicated by solid red, dotted orange, dashed green, dotted-dash blue and solid purple, respectively, from Minchev et al. (2010b).

4 Conclusions

In order to reproduce the local velocity distribution of stars, the Sun should lie close to inner and outer Lindblad resonances of the spiral and bar, respectively. We showed that such a resonance overlap leads to radial migration of stars. This happens throughout the whole disk, as other resonances do overlap too (see Fig. 2). This new theoretical mechanism for stellar migrations could be up to an order of magnitude more effective than the transient spirals mechanism. This effect is non-linear, strongly dependent on the strengths of the perturbers. The signature of this mechanism is a bimodality in the changes of angular momentum in the disk with maxima near the bar's corotation and its outer Lindblad resonance (Figs. 2 and 3). This is true regardless of the spiral pattern speed. This migration mechanism can create extended disks in both Milky Way-mass (Fig. 2) and low-mass galaxies, such as NGC 300 and M33, and it could also be responsible for the formation of a thick disk component early on in the galaxy evolution (Minchev et al., in preparation, see also Schoenrich & Binney 2009). However, important constraints on the mechanism come from the fact that it heats the disk too, and should not overheat it as compared to what is observed. We finally note that the most promising technique to put constraints on this mechanism in the Milky Way is "chemical tagging" (e.g., Bland-Hawthorn et al. 2010) which will become possible with the forthcoming spectroscopic survey HERMES, coupled with the precise astrometric measurements from GAIA.

References

Bland-Hawthorn J., et al., 2010, ApJ, 713, 166
Dehnen W., 2000, AJ, 119, 800
Famaey B., et al., 2005, A&A, 430, 165
Famaey B., et al., 2007, A&A, 461, 957
Famaey B., et al., 2008, A&A, 483, 453
Kalnajs A., 1991, in Sundelius B., ed., Dynamics of Disc Galaxies, Goteborgs Univ., p.323
Minchev I., Quillen A., 2007, MNRAS, 377, 1163
Minchev I., Famaey B., 2010, ApJ, 722, 112
Minchev I., et al., 2010a, MNRAS, 407, 2122
Minchev I., et al., 2010b, arXiv:1006.0484
Quillen A., Minchev I., 2005, AJ, 130, 576
Schoenrich R., Binney J., 2009, MNRAS, 399, 1145
Sellwood J., Binney J., 2002, MNRAS, 336, 785

SF2A 2010
S. Boissier, M. Heydari-Malayeri, R. Samadi and D. Valls-Gabaud (eds)

POPULATION SYNTHESIS MODELLING OF LUMINOUS INFRARED GALAXIES AT INTERMEDIATE REDSHIFT

E. Giovannoli[1], V. Buat[1], S. Noll[2], D. Burgarella[1] and B. Magnelli[3]

Abstract. Luminous InfraRed Galaxies (LIRGs) are particularly important for studying the build-up of the stellar mass from z=1 to z=0, and for determining physical properties of these objects at redshift 0.7. The global star formation rate (SFR) at $z \sim 0.7$ is mainly produced by LIRGs. We perform a multiwavelength study of an LIRGs sample in the Extended Chandra Deep Field South at z=0.7, selected at 24 μm by MIPS onboard *Spitzer Space Telescope* and detected in 17 filters. Data go from the near-ultraviolet to the mid-infrared. We distinguish a subsample of galaxies detected at 70 μm, which we compare to the rest of the sample to investigate the relative importance of this wavelength in determining of the physical parameters.

Keywords: galaxies evolution, infrared, Bayesian analysis, stellar content, SED-fitting

1 Introduction

Luminous InfraRed Galaxies (LIRGs) are commonly defined as galaxies whose infrared (IR, 8-1000 μm) emission is higher than $10^{11}L_\odot$ and lower than $10^{12}L_\odot$. A z ∼1 only 30% of LIRGs exhibit features linked to violent merging (Bell et al. 2007), (Zheng et al. 2007) : most of them look like bright spirals that experience a secular evolution without violent events. This morphological difference between local and distant LIRGs is corroborated by the analysis of their star formation rate (SFR). Whereas local LIRGs are experiencing a strong starburst, distant LIRGs do not seem to strongly depart from the mean SFR - stellar mass ($M_\star$) relation found at z=1 (Elbaz et al. 2007).

2 Analysis of a LIRGs sample

We apply a multiwavelength analysis from the far-ultraviolet (FUV) to the IR, based on SED (Spectral Energy Distribution)-fitting, on a sample of z=0.7 LIRGs selected at 24 μm (Giovannoli et al., 2010). Our aim is to study this galaxy sample, representative of LIRGs at intermediate redshift, in a very homogeneous and systematic way to determine the main characteristics of their stellar populations and dust emission. We study LIRGs with the SED-fitting code CIGALE (Code Investigating GALaxy Emission * : Noll et al. 2009b, Burgarella et al. 2005), which provides an estimation of physical parameters of galaxies thanks to a Bayesian-like analysis. The stellar populations synthesis code of Maraston et al. (2005) is adopted to model the stellar emission (UV, optical, and NIR wavelengths). The created stellar population spectra are then attenuated by using a synthetic Calzetti-based attenuation law (Calzetti et al. 2000) before adding the dust emission as given by the infrared SED library (semi-empirical one-parameter models of Dale & Helou (2002)).

Figure 1 shows distributions for the parameters related to the star formation history and the attenuation ($M_\star$, infrared luminosity L_{dust}, SFR, attenuation in the V-band A_V, fraction in mass of the young stellar population f_{ySP}, and fraction of AGN f_{AGN}) calculated with the Bayesian-like analysis in CIGALE, for the subsample detected at 70 μm and for the whole sample. The masses found for the 70 μm sample are shifted towards higher masses then in the total sample. We observe a similiar situation for L_{dust} and the SFR; the values are in the range [10^{11} ; 10^{12}] $L_\odot$ and [10 ; 92] $M_\odot.yr^{-1}$, respectively, with mean values higher than ones found for the total sample. This shift is expected because of the 70 μm detection limit

[1] Laboratoire d'Astrophysique de Marseille, OAMP, Université Aix-Marseille, CNRS, 38 rue Frédéric Joliot-Curie, 13388 Marseille cedex 13, France
[2] Institut für Astro- und Teilchenphysik, Universität Innsbruck, Technikerstr. 25/8, 6020 Innsbruck, Austria
[3] Max-Planck-Institut für Extraterrestrische Physik (MPE), Postfach 1312, 85741 Garching, Germany.
*Web address to use CIGALE : `http://www.oamp.fr/cigale/`

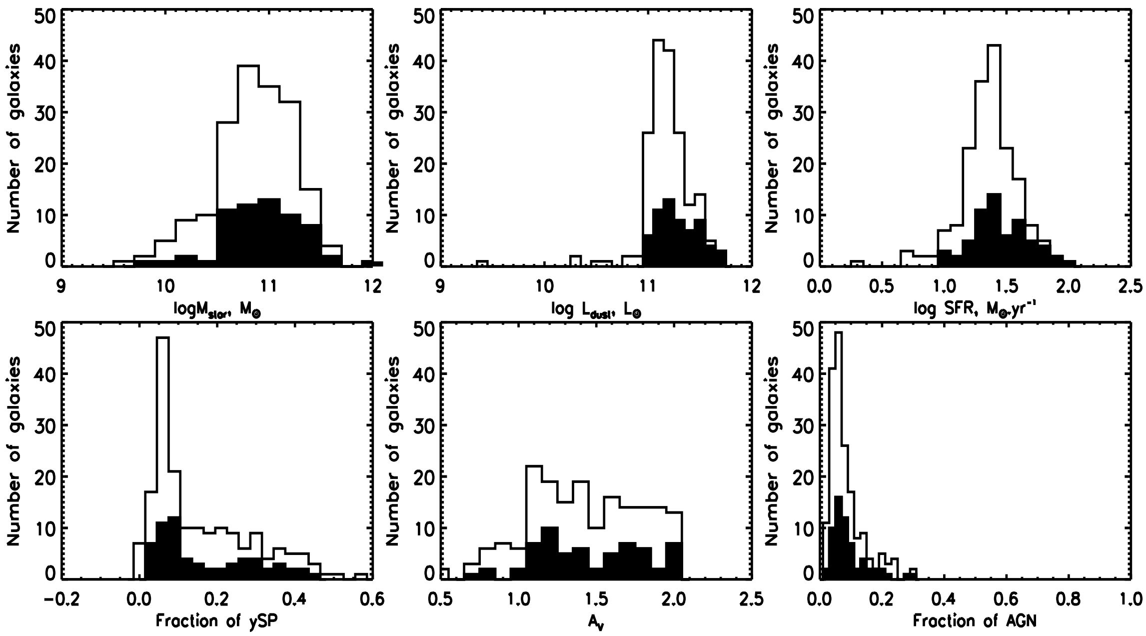

Fig. 1. Bayesian results of the code for the following parameters : $M_\star$, L_{dust}, SFR, A_V, f_{ySP}, f_{AGN}. The empty histogram represents the total sample and the full one represents the 70 μm sample.

(2.7 mJy at 5σ): at this wavelength, we only detect luminous and massive galaxies. The distribution of f_{ySP} is broad with a long tail towards high values, and A_V lies between 0.5 and 2.1 mag with very few objects under 1.0 mag and quite a homogeneous distribution between 1.0 and 2.0.

Galaxies in the total sample have $M_\star$ between 10^{10} and 10^{12} $M_\odot$ with a peak at $10^{10.8} M_\odot$. We find the SFR between 3 and 92 $M_\odot yr^{-1}$ with a peak at 23 $M_\odot yr^{-1}$. For f_{ySP} and A_V, we observe the same distribution as for the 70 μm sample. For both samples, f_{AGN} is relatively low, between 0.0 and 0.3 with the majority of the objects in the interval [0;0.1]. We consider that there is a definite contamination of L_{dust} by an AGN when $f_{AGN} > 15\%$, because a contamination lower than15% does not significantly modify the total IR emission.

3 Conclusions

We fit the SEDs of our sample of LIRGs with the CIGALE code, which combines stellar and dust emissions in a physical way. This study is the first use of CIGALE at a redshift higher than 0. The multiwavelength data analysis performed in this study provides reliable estimates of several physical parameters based on a Bayesian-like analysis.

References

Bell, E. F., Zheng, X. Z, Papovich, C. et al., 2007, ApJ, 663, 834

Buat, V., Takeuchi, T. T., Iglesias-Páramo, J, et al. 2007, ApJS, 173, 404

Buat, V., Boissier, S., Burgarella, D., et al. 2008, A&A, 483, 107

Burgarella, D., Buat, V. & Iglesias-Páramo, J. 2005, MNRAS, 1413,1425

Calzetti, D., Armus, L., Bohlin, R. C., et al. 2000, 533, 682

Dale, D. & Helou, G. 2002, ApJ, 576,159

Elbaz, D., Daddi, E., Le Borgne, et al., 2007, A&A ,468, 33

Giovannoli, E., Buat, V., Noll., S., Burgarella, D., Magnelli, B., 2010, arXiv,1006,5555

Maraston, C., 2005, MNRAS, 362, 799

Noll, S., Burgarella., D., Giovannoli, E., et al., 2009, A&A, 507, 1793

Zheng, X. Z., Dole, H., Bell, E. F., et al, 2007, ApJ, 670, 301

COSMOLOGICAL SIMULATIONS AND GALAXY FORMATION: PROSPECTS FOR HST/WFC3

S. Peirani[1], R.M. Crockett[2], S. Geen[2], S. Khochfar[3], S. Kaviraj[2,4] and J. Silk[2]

Abstract. The star formation history of nearby early-type galaxies is investigated via numerical modelling. Idealized hydrodynamical N-body simulations with a star formation prescription are used to study the minor merger process between a giant galaxy (host) and a less massive spiral galaxy (satellite). We find that the evolution of the star formation rate is extended over several dynamical times and shows peaks which correspond to pericentre passages of the satellite. The newly formed stars are mainly located in the central part of the satellite remnant while the older stars of the initial disc are deposited at larger radii in shell-like structures. Synthetic 2D images in J, H, NUV, Hβ and V bands, using the characteristic filters of the Wide Field Camera 3 (WFC3) on the Hubble Space Telescope, reveal that residual star formation induced by gas-rich minor mergers can be clearly observed during and after the final plunge, especially in the near-ultraviolet band, for interacting systems at ($z \leq 0.023$) over moderate numbers of orbits (for more details see Peirani et al. 2010).

Keywords: formation, galaxies: interactions, galaxies: structure, galaxies: kinematics and dynamics, galaxies: photometry, methods: N-body simulations

1 Introduction

Understanding the formation of early-type galaxies (ETGs), and in particular their star formation history, is of crucial importance for setting strong constraints on models of galaxy formation. It is now well known that ETGs have considerable substructure (e.g. from SAURON and GALEX) which is interpreted as a result of mergers in the past several gigayears. To study this plausible process, we have compared the ultra-violet (UV) colours of nearby ($0.05 \leq z \leq 0.06$) early-type galaxies with synthetic photometry derived from numerical simulations of minor mergers, with reasonable assumption for the ages, metallicities and dust properties of the merger progenitors (Kaviraj et al. 2009). We found that the large scatter in the ultra-violet colours of intermediate mass early-type galaxies in the local universe and the inferred low-level recent star formation in this objects can be reproduced by minor mergers in the standard ΛCDM cosmology. In the present work, our aim is to study the evolution of the internal structure of these objects using the same methodology but with higher mass resolution, in order to help understand in more detail the observational signatures of satellite minor merger events with different mass ratios, gas-fractions and orbital configurations. This work is also motivated by the recent installation on the Hubble Space Telescope (HST) of NASA's Wide Field Camera 3 (WFC3*) whose optical design provides a large field of view and high sensitivity over a broad wavelength range, excellent spatial resolution and a stable and accurate photometric performance. It features two independent imaging cameras, a UV/optical channel (UVIS) and a near-infrared channel (IR).

[1] Institut d'Astrophysique de Paris, 98 bis Bd Arago, 75014 Paris, France - Unité mixte de recherche 7095 CNRS - Université Pierre et Marie Curie
[2] Department of Physics, University of Oxford, Denys Wilkinson Building, Keble Road, Oxford OX1 3RH, UK
[3] Max Planck Institut für extraterrestrische Physik, p.o. box 1312, D-85478 Garching, Ge rmany
[4] Blackett Laboratory, Imperial College London, South Kensington Campus,London SW7 2AZ
*`http://www.stsci.edu/hst/wfc3`

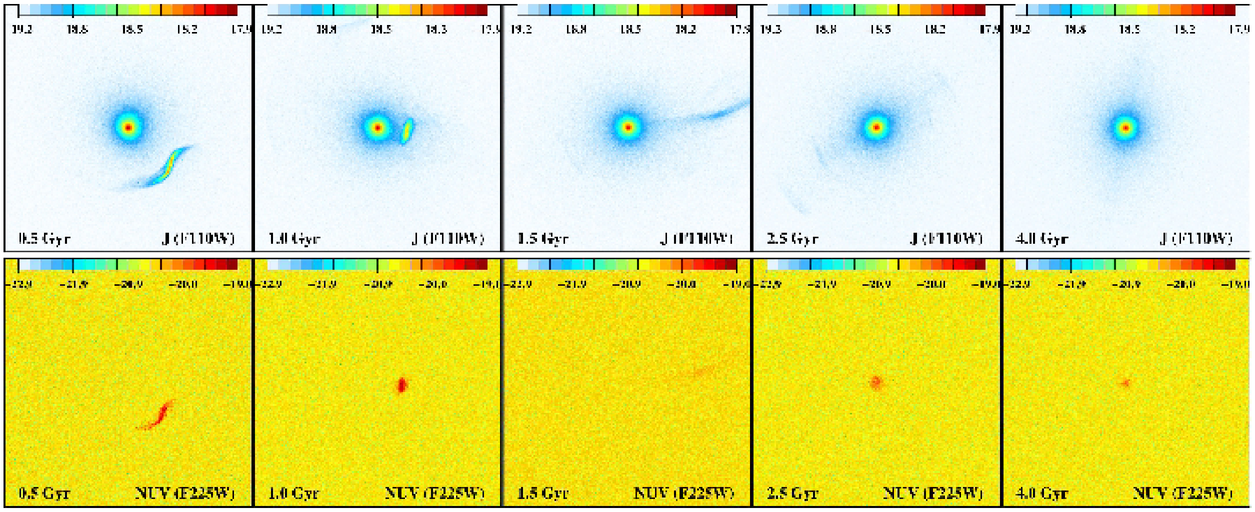

Fig. 1. The evolution of synthetic images through J (first line) and NUV (second line) assuming the observed system at $z \sim 0.023$. the magnitude units given as measures of spectral flux are $W\,m^{-2}$, and in all synthetic images, we use a logarithmic scale.

2 Evolution of WFC3 bands

In order to produce synthetic images, we have assumed our galaxy system to be in the local universe. The galaxy pair is supposed to be at a redshift $z \sim 0.023$ (or equivalently at a luminosity distance of $D = 100$ Mpc) in order to facilitate comparisons with future observational data. In Fig.1, we present the grid map derived by our numerical modelling through the J and NUV bands. From the J band, it appears that it is possible to resolve the host elliptical galaxy and the satellite remnant, in particular the shell structure which is mainly composed of old stars. However, this latter tends to disappear at $t = 4.0$ Gyr. From the NUV band, the ongoing star formation regions can be clearly followed. In particular, after the final plunge, ongoing star formation located at the center of the galaxy can be clearly observed.

Thus, the combination of IR and UVIS images allows us to separate different stellar populations and then distinguish the most bound part of the satellite remnant, composed of young stars, from the host galaxy, composed of older stars. This combination also gives useful clues on the formation of ETGs: while the shell structure revealed in IR images support a past merger scenario, evidence or not of the presence of young stars in UVIS images bring additional constraints on the wetness/dryness of the merger.

3 Conclusions

The present work shows that minor mergers induce amounts of star formation in ETGs which can be measured through UV bands. WFC3 represents the best instrument to study these minor merger events because it has a matching UV and optical FOV and gives the resolution to see young substructures (which would not be possible with GALEX for instance). The previous ACS/HRC UV detectors had a tiny FOV so it was not possible to study a galaxy up to 1 effective radius because one would get the whole galaxy in the optical image and only a fraction of its core using the UV. With WFC3, it is now possible to map the entire galaxy in both the UV and optical making it possible for the first time to perform spatially resolved star formation histories in ETGs at low redshift using the UV. Moreover the ability to see the young substructures is important because it rules out UV flux from old sources such as horizontal branch stars (which would follow the optical light profile).

References

Kaviraj, S., Peirani, S., Khochfar, S., Silk, J., & Kay, S. 2009, MNRAS, 394, 1713, K09

Peirani, S., Crockett, R. M., Geen, S., Khochfar, S., Kaviraj, S., & Silk, J. 2010, MNRAS, 405, 2327

SF2A 2010
S. Boissier, M. Heydari-Malayeri, R. Samadi and D. Valls-Gabaud (eds)

3D TOMOGRAPHY OF LOCAL INTERSTELLAR GAS AND DUST

S. Raimond[1], R. Lallement[1] and J-L. Vergely[2]

Abstract. Interstellar absorption data and Strömgren photometric data for target stars possessing a Hipparcos parallax have been combined to build a 3D tomography of local gas and dust. We show the latest inverted 3D distributions within 250 pc, compare gas and dust maps and discuss the present limitations and work in progress. Gaia extinction data and follow-up ground-based stellar spectra (e.g. with GYES at the CFHT) will provide a far larger database that should allow a 3D tomography of much higher quality and extended to much larger distances.

Keywords: galaxy: solar neighborhood, ISM: atoms, ISM: clouds

1 Introduction

The nearby interstellar medium plays several important roles in astrophysics. It is a tool for studying the evolution of the ISM, it provides the local conditions for photons and particles transport, it is a foreground which needs to be removed for studying specific objects, it is the ambient medium which governs limit conditions for a specific object and also the context environning such an object, etc. We present here studies of the gas and dust 3D distribution in the local interstellar medium (by local we mean here the interstellar medium within 250 pc).

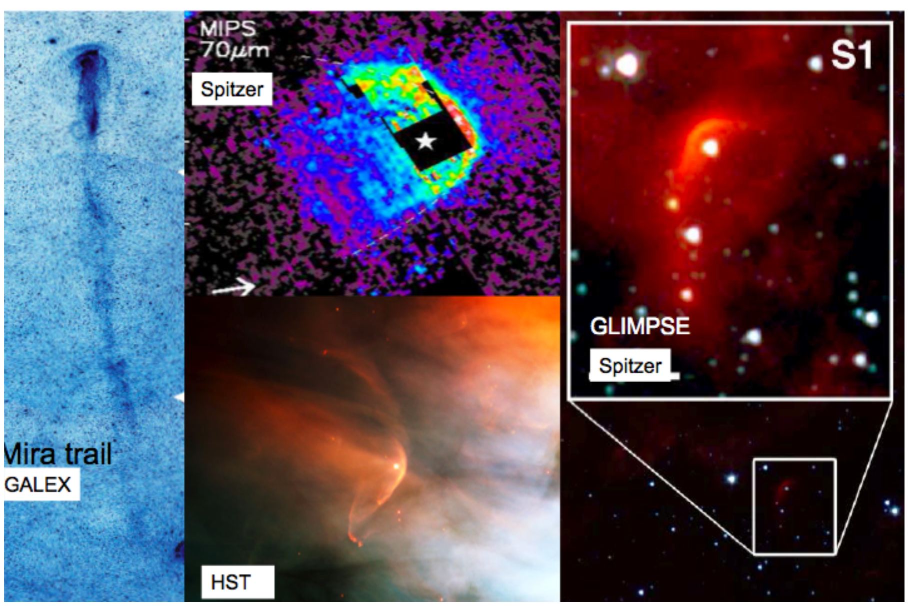

Fig. 1. Examples of interaction regions between stars and their surrounding environment. Stars collide the surrounding gas inducing a compression area. The knowledge of the ambient medium helps modeling the interaction.

[1] LATMOS, CNRS UMR 8190, 78280 Guyancourt, France
[2] ACRI-ST, 06904 Sophia Antipolis, France

2 Means of study

This work is based on NaI and CaII interstellar absorption lines in nearby star spectra and extinction obtained by Strömgren photometry. Both types of data can be inverted to get a 3D tomography of gas and dust. In addition, absorption lines assembled in an interstellar absorption database are a tool to distinguish between foreground absorption and local lines when studying objects by means of spectroscopy.

Fig. 2 illustrates an example of typical absorption lines.

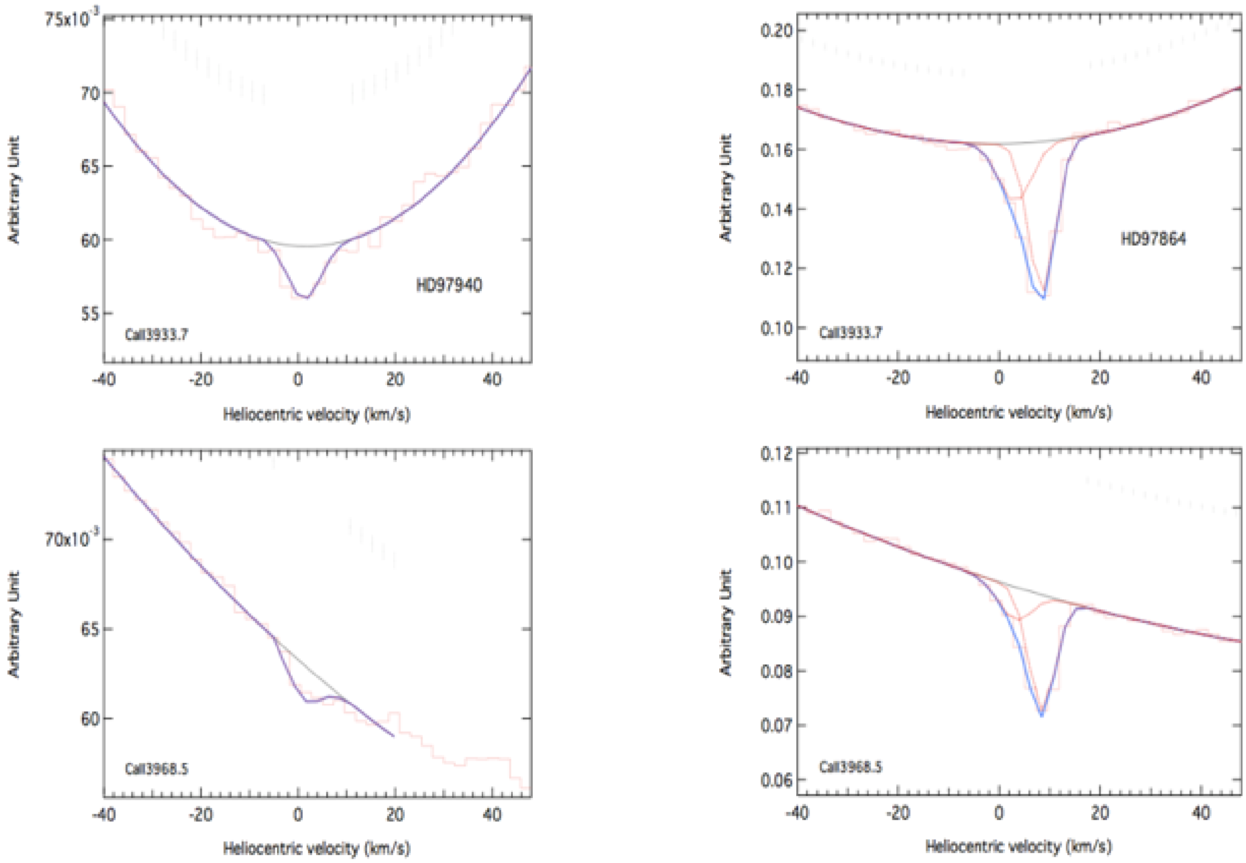

Fig. 2. Examples of CaII absorption lines of two stars in the same line of sight (the K line at 3934Å is on the top and the H line at 3968Å is on the bottom). On the left, HD97940 located at 85pc. A line is observed at about 2 km/s therefore a cloud begins before 85pc at this velocity. On the right, HD97864 located at 92pc. The same line is observed at about 2 km/s and a new one is detected around 9 km/s so the cloud beginning before 85pc is still present and another one at a velocity of about 9 km/s begins between 85 and 92pc.

3 Comparison of the different tracers

Gas and dust data can be combined with distances to the target stars to reconstruct by means of sophisticated inversion tools the gas and dust distributions in three dimensions. The obtained maps of the local interstellar medium reveal the so-called *Local Bubble*, a region devoid of dense gas that surrounds the Sun. Because of the difficulty to represent these distributions in three dimensions we show several cuts in the data cubes.

The different tracers are NaI, CaII and extinction. NaI is the tracer of dense and neutral gas, CaII is the tracer of dense neutral and also ionized gas and extinction locates the dust. We compare the results obtained with the different tracers in the meridian plane, i.e. the plane perpendicular to the galactic plane containing the Sun and the galactic center. These are shown in Fig. 3.

In all the cases, the Local Bubble surrounding the Sun is about 200pc wide in the galactic plane. This cavity is surrounded by large dense clouds: Ophiucus, Chamaeleon, Coalsack or Taurus. The maps reveal two chimneys towards the halos and the cavity is tilted perpendicularly to the plane of the Gould Belt which is a ring of young stars and star forming regions tilted of about 20° towards the Galactic Center.

Within the Local Bubble neither NaI nor dust significant concentration is present, however it contains many diffuse clouds revealed in the CaII maps. These clouds are too ionized for being visible in NaI and too tenuous to be visible in extinction but they are detected thanks to CaII which traces the ionized gas.

The maps present strong similarities but also differences that may reflect gas states but also poor precision due to the limited amount of stars available for the inversion. Two articles are based on these maps, one comparing NaI and CaII (Welsh et al. 2010) and the other comparing NaI and extinction (Vergely et al. 2010).

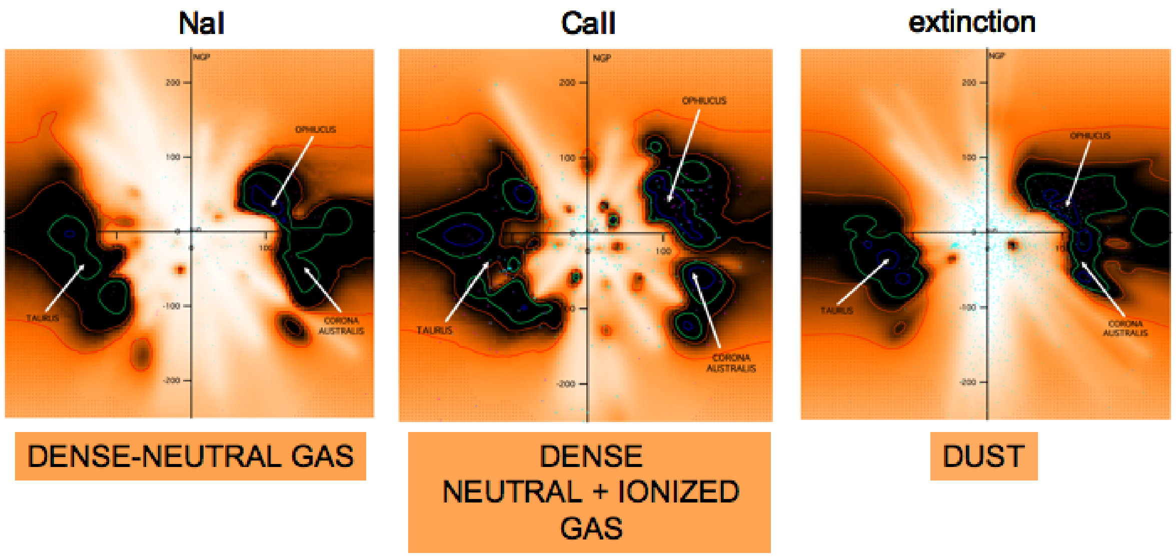

Fig. 3. Comparison of the local interstellar medium in the meridian plane. In each cut, the Galactic Center is on the right and the North Galactic Pole is on the top. Black indicates an important density whereas white represents diffuse regions. On the left, the map with NaI. On the middle, the map with CaII. On the right, the map with extinction.

4 Comparison between integrated gas and dust

In Fig. 4 neutral gas (on the left) and dust (on the middle) integrated back within the 3D cubes between the Sun and 200 pc are represented in aitoff projection. Important similarities are visible between the total columns of neutral gas traced by neutral sodium and dust opacities. On the right of Fig. 4, dotted lines representing integrated dust until 200pc are superimposed on the map showing the dust emission integrated to infinity derived from infrared data (Finkbeiner et al. 1999). Firstly, isocontours correspond very well with the map, showing that the inversion method is robust in spite of the limited amount of stars. Secondly, since the isocontours are well matching the map at moderate and high latitude, this means that the majority of the dust observed on the map of Finkbeiner et al. 1999 is located within 200pc.

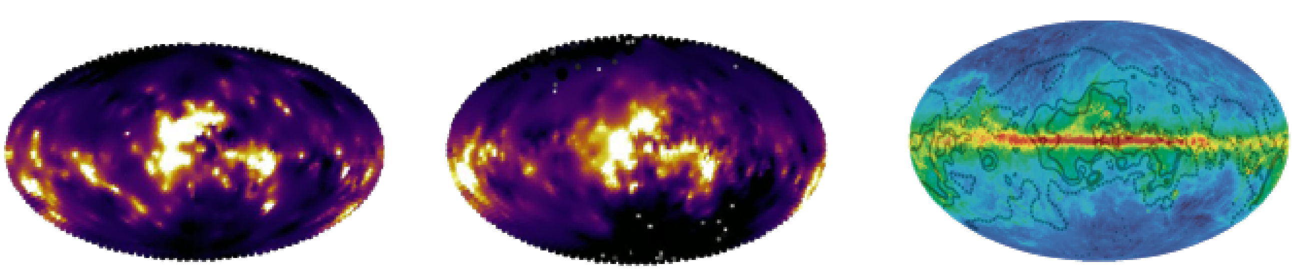

Fig. 4. Neutral gas (on the left) and dust (on the middle) integrated between the Sun and 200pc. On the right, map of the total column of dust, i.e. integrated to infinity (Finkbeiner et al. 1999). Dotted lines representing integrated dust until 200pc are superimposed.

5 Determination of the distance towards nearby structures

One of the interests of these inversions is the possibility to identify nearby structures seen in 2D maps and obtain an information on their distance, based on the kinematics. In particular, some clouds seen in the 21 cm HI data maps from the LAB Survey (Kalberla et al. 2005) are studied by comparing HI emission and NaI absorption velocities of the stars belonging to the database in the direction of the clouds. An example is presented in Fig. 5.

The map on the left in Fig. 5 presents a structure seen in HI emission between -10 and 0 km/s LSR. In order to define its distance, all the stars in this region are superimposed on the map and for each of them, we note the distance of the star and whether or not NaI is observed in absorption in this velocity interval.

We remark in this example that until 75pc, the stars don't present NaI absorption on their line of sight whereas from 75pc, all of them present NaI absorption lines around -3 km/s LSR. This means that the structure at -3 km/s LSR begins at around 75pc .

The spectra of the top and of the bottom of Fig. 5 illustrate respectively the NaI absorption spectrum of a star more distant than 75pc in the region and the HI emission spectrum in the same direction. This is an example showing that gas in the structure has a velocity around -3 km/s LSR. It would be the same with the NaI absorption and HI emission spectra of each star more distant than 75pc.

The cut on the right in Fig. 5 shows the structure seen in the same sky region in the NaI cube. It begins at 75pc, which is consistent with the distance found previously from the kinematics and allows the identification. Indeed, by using two methods based on different data, the first being the localization by velocity criteria and the second being the localization in the NaI cube only by absorption growth with distance criteria, the same result is obtained.

This identified region corresponds to the high latitude molecular clouds known as MBM53, MBM54 and MBM55 (Magnani et al. 1985). (Magnani et al. mapped the sky looking for high latitude clouds emitting CO and named them MBM.) Their initial estimated distance was 150pc (Welty et al. 1989). At that time, the stars did not have Hipparcos parallax, so the distance of the cloud was badly estimated. Here we have improved the localization of the structure and shown that it is much closer than previously thought.

This analysis is currently extended to other dense clouds by comparing the NaI interstellar absorptions and the HI emission and by searching the clouds in the data cubes.

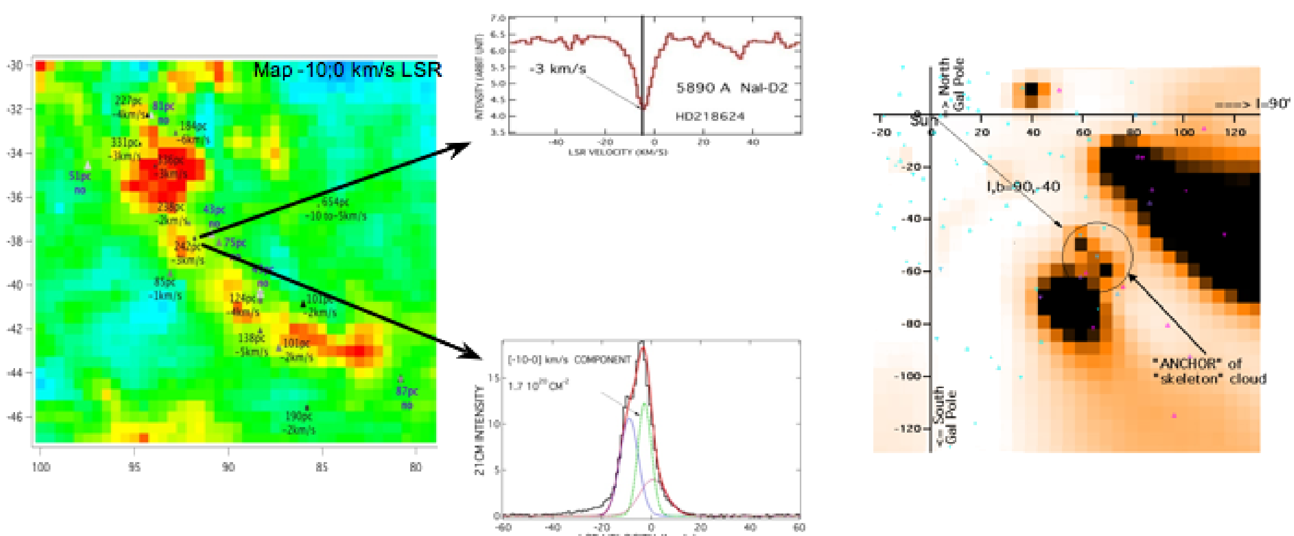

Fig. 5. Determination of the distance of a structure located at $l = 90°$ and $b = -40°$. On the left, the structure seen in HI emission in the velocity interval between -10 and 0 km/s LSR. On the top, NaI absorption spectrum of one of the stars more distant than the cloud with an absorption velocity around -3 km/s LSR. On the bottom, HI emission spectrum in the same direction with one of the peak around -3 km/s LSR. On the right, cut in the NaI cube at the good coordinates. The structure is visible and begins at 75pc.

6 Perspectives

Tomographic methods applied to local ISM dust and gas have been tested and validated on the current available absorption and extinction databases. In order to improve the accuracy and spatial resolution of the 3D maps, it is mandatory to increase the stellar databases, and have access to corresponding reliable parallaxes for the target stars. The GAIA mission and follow-up ground-based spectroscopic data with GYES will provide such considerably larger and better data sets. Combinations of the 3D distributions with 2D spectral maps should in addition allow to replace the roughly spherical clouds obtained by inversion by more realistic shapes.

References

Welsh, B. Y., Lallement, R., Vergely, J-L., Raimond, S. 2010, A&A, 510, 54

Vergely, J-L., Valette, B., Lallement, R., Raimond, S. 2010, A&A in press

Finkbeiner, D. P., Davis, M., Schlegel, D. J. 1999, ApJ, 524, 867

Kalberla, P.M.W., Burton, W.B., Hartmann, D., Arnal, E.M., Bajaja, E., Morras, R., Pöppel, W.G.L. 2005, A&A, 440, 775

Magnani, L., Blitz, L., Mundy, L. 1985, ApJ, 295, 402

Welty, D. E., Hobbs, L. M., Penprase, B.E., Blitz, L. 1989, ApJ, 346, 232

SF2A 2010
S. Boissier, M. Heydari-Malayeri, R. Samadi and D. Valls-Gabaud (eds)

THE BESANÇON GALAXY MODEL: COMPARISONS TO PHOTOMETRIC SURVEYS AND MODELLING OF THE GALACTIC BULGE AND DISC

C. Reylé[1], A. C. Robin[1], M. Schultheis[1] and D.J. Marshall[2]

Abstract. Exploring the in-plane region of our Galaxy is an interesting but challenging quest, because of the complex structure and the highly variable extinction. We here analyse photometric near-infrared data using the Besançon Galaxy Model in order to investigate the shape of the disc and bulge. We present new constraints on the stellar disc, which is shown to be asymmetric, and on the bulge, which is found to contain two populations. We present how the Galaxy model is used in the framework of the preparation of the Gaia mission.

Keywords: stellar population model, bulge, disc, large scale survey, Gaia

1 Introduction

The population synthesis approach aims at assembling together current scenarii of galaxy formation and evolution, theory of stellar formation and evolution, models of stellar atmospheres and dynamical constraints, in order to make a consistent picture explaining currently available observations of different types (photometry, astrometry, spectroscopy) at different wavelengths. The validity of any Galactic model is always questionable, as it describes a smooth Galaxy, while inhomogeneities exist, either in the disc or the halo. The issue is not to make a perfect model that reproduces the known Galaxy at any scale. Rather one aims at producing a useful tool to compute the probable stellar content of large data sets and therefore to test the usefulness of such data to answer a given question in relation with Galactic structure and evolution. Modelling is also an effective way to test alternative scenarii of galaxy formation and evolution.

In section 2, we give a brief description of the model. In section 3 we describe recent and future analysis of near-infrared data with the model. In section 4 we describe the use of the model for the preparation of the Gaia mission.

2 The Besançon Galaxy model: ingredients and recipe

The main scheme of the model is to reproduce the stellar content of the Galaxy, using some physical assumptions and a scenario of formation and evolution. We essentially assume that stars belong to four main populations : the thin disc, the thick disc, the stellar halo, and the outer bulge. The modelling of each population is based on a set of evolutionary tracks, assumptions on density distributions, constrained either by dynamical considerations or by empirical data, and guided by a scenario of stellar formation and evolution, that is to say assumptions on the initial mass function (IMF) and the star formation rate (SFR) history for each population. The originality of the Besançon model, as compared to a few other population synthesis models presently available for the Galaxy, is the dynamical self-consistency. The Boltzmann equation allows the scale height of an isothermal and relaxed population to be constrained by its velocity dispersion and the Galactic potential (Bienaymé et al.1987). The use of this dynamical constraint avoids a set of free parameters and gives the model an improved physical credibility. More detailed descriptions on these constraints can be found in Robin et al. 2003. Simulations can be performed on-line.*

[1] Observatoire de Besançon, Institut Utinam, UMR CNRS 6213, BP 1615, 25010 Besançon Cedex, France
[2] Centre d'Etude Spatiale des Rayonnements, UMR 5187, 9, av du Colonel Roche, BP 44346, 31028 Toulouse Cedex 4, France
*`http://model.obs-besancon.fr`

Observational tests have been made in many directions in the optical, mostly at high latitudes, a few directions to magnitudes V=24-25 (Robin et al. 2000, Reylé & Robin 2001, Schultheis et al. 2006, Robin et al. 2008). An all-sky comparison has been made with the Guide Star Catalogue 2 (GSC2, see Fig. 1). The model has also been constrained using near-infrared data (Picaud & Robin, Reylé et al. 2009), X-ray data (Guillout et al. 1996), and UV (Todmal et al. 2010).

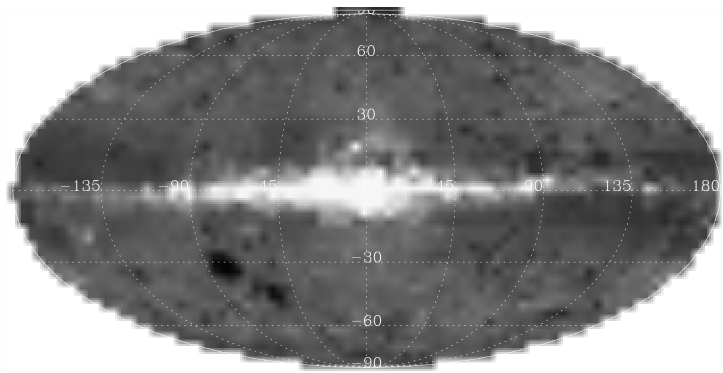

Fig. 1. Relative difference map, (model - GSC2)/GSC2, on a log scale, to magnitude V=17. The agreement is at 10% outside plane. Most of the discrepancy between the model and the observations are within of the Galactic plane, probably due to inadequate extinction in the plane (Drimmel et al. 2003).

3 Constraints on the external disc and central regions

The 2MASS survey is a powerful tool to study large scale structure in the Galaxy, particularly in the Galactic plane because NIR data are well suitable to study stellar populations in regions of medium to high extinction. A good estimate of the extinction is required to understand the structure in the Galactic plane. In the following studies, we used a three dimensional extinction map of the Galaxy (Marshall et al. 2006).

From the comparison of 2MASS star counts with the Besançon Galaxy model, we investigated the warp feature followed by stars (Reylé et al. 2009). We modelled the warp as a simple S-shape symmetrical but found that the warp is not symmetrical: the simple model reproduces well the northern side of the warp (positive longitudes), but not the southern side. The results also show that the stellar warp is less marked in stars than in the HI gas. Our result is well in agreement with studies in external galaxies, where van der Kruit (2007) noted that stellar discs look flatter than gas layers. This is understandable in a scheme where the HI warps start close to the truncation radius, truncation seen in the exponential distribution of stars which may be due to a threshold effect in the star formation efficiency.

Since the discovery of a triaxial structure in the Galactic central regions from COBE, numerous attempts have been done in order to characterize this structure and to investigate its origin. It is still unclear whether this structure had its origin from the early formation of the spheroid (as a typical bulge, similar to ellipsoidal galaxies) or was formed by a bar instability later in the disc. The question of formation history is crucial and necessary to investigate, as our Galaxy is a benchmark for understanding formation of disc galaxies. Thanks to the ability of the model to simulate the stellar populations as they are seen in surveys, we compared model simulations with 2MASS star counts in all the region covered by the outer bulge. We show evidence for two independent structures, a triaxial bulge and a long and narrow structure which angles are different (Fig. 2, Robin et al., in prep.). Further studies are needed to confirm these preliminary conclusions, in particular kinematical data, helpful in understanding the dynamics, especially to measure the rotation and velocity dispersions of these populations.

4 The Besançon Galaxy model for the preparation of the Gaia mission

Preparing the Gaia mission requires large efforts dedicated to simulations of the observations. Several simulators have been constructed, generating telemetry, images, or the final database. All these tools use a Universe Model containing essentially the astronomical sources to be seen by Gaia and their characteristics, as well as a Relativity model and a radiation model for estimating the potential damage to the CCDs. The stellar content

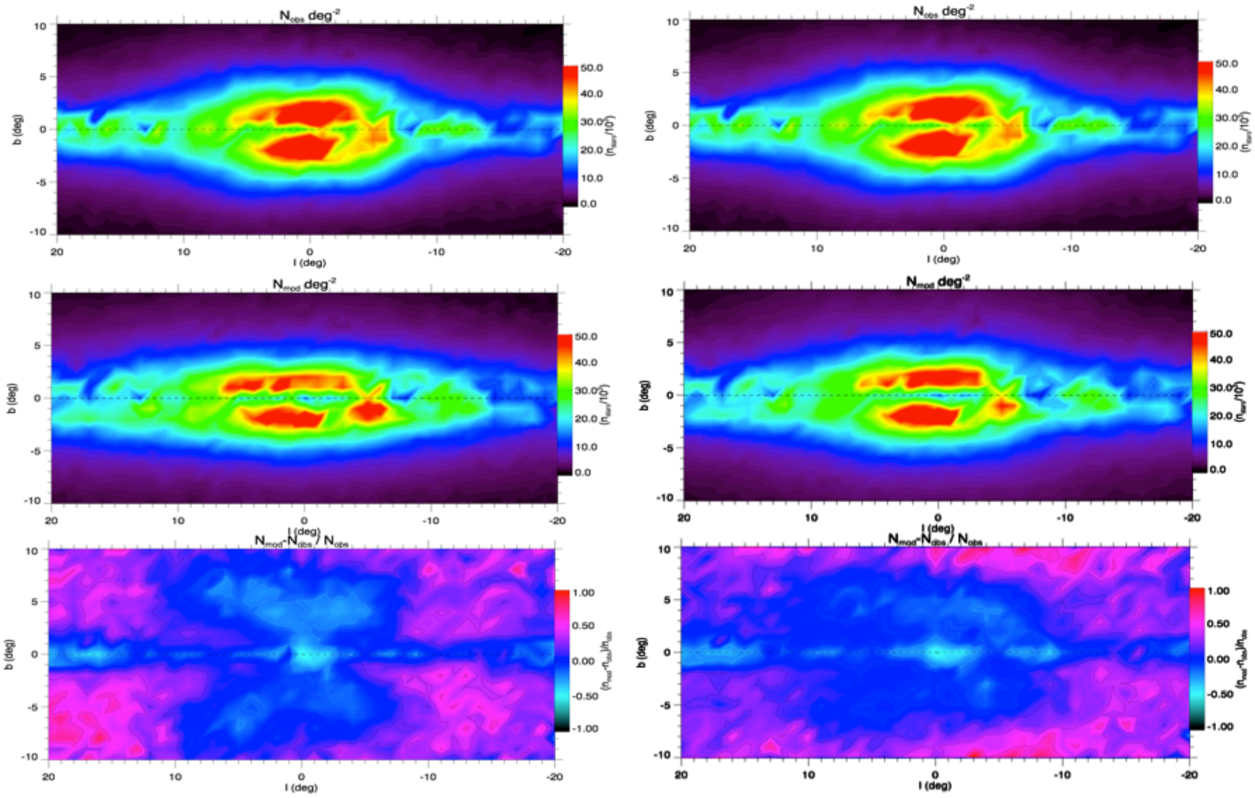

Fig. 2. Star counts up to magnitude K=12 from 2MASS data (top) compared with 2 models (middle panels) and residuals (Nmod-Nobs)/Nobs (bottom). Left: model with 1 bulge population. Right: model with 2 populations : a triaxial bulge and a thin elongated structure. In pink the excess in the model is at the level of 70%. The light blue corresponds to a lack in the model at the level of 50%. The 2-population model allows to nicely reproduce the boxy shape of the outer bulge region, while the 1-population model leaves significant X-shaped residuals. Near the Galactic center the nuclear bar population is missing in the model. The residuals in the outer region are not much significant due to the small number of stars in each bin.

of the Universe Model is simulated using the Besançon Galaxy model (Isasi et al. 2010). Fig. 3 shows the expected density of stars to magnitude G=20 as a function of galactic coordinates. The expected total number of stars is 1.3×10^9 (8.7×10^8 disc stars, 2.6×10^8 thick disc stars, 15×10^6 halo stars, and 10^8 bulge stars). Fig. 4 gives the expected number of stars as a function of spectral type and luminosity class. The right panel in Fig. 3 shows the expected density of stars in the (X,Y) plane, centered on the Sun. The sharp radius towards the anticenter is due to the cut-off radius of the thin disc at 14 kpc (from Ruphy et al. 1996). The Gaia data will bring a strong constraint on the shape and radius of the disc, as well as on many other parameters.

5 Conclusions

Population synthesis models are useful tools for data interpretation. Although imperfect they allow a better understanding of galactic structure and evolution, eases the interpretation, and is useful for the preparation of future surveys. Gaia will obtain distance, proper motions of more than 1 billion stars (about 1% of the Galaxy) as well as astrophysical parameters, radial velocities for about 250 million stars, and abundances for a few million stars. It will be a challenge to fit Gaia data with (simplistic) models! Since then, efforts have to been made to get stellar population models with self-consistent dynamical modelling.

References

Bienaymé, O., Robin, A. C., Crézé, M. 1987, A&A, 180, 94

Drimmel, R., Cabrera-Lavers, A., López-Corredoira, M. 2003, A&A, 409, 205

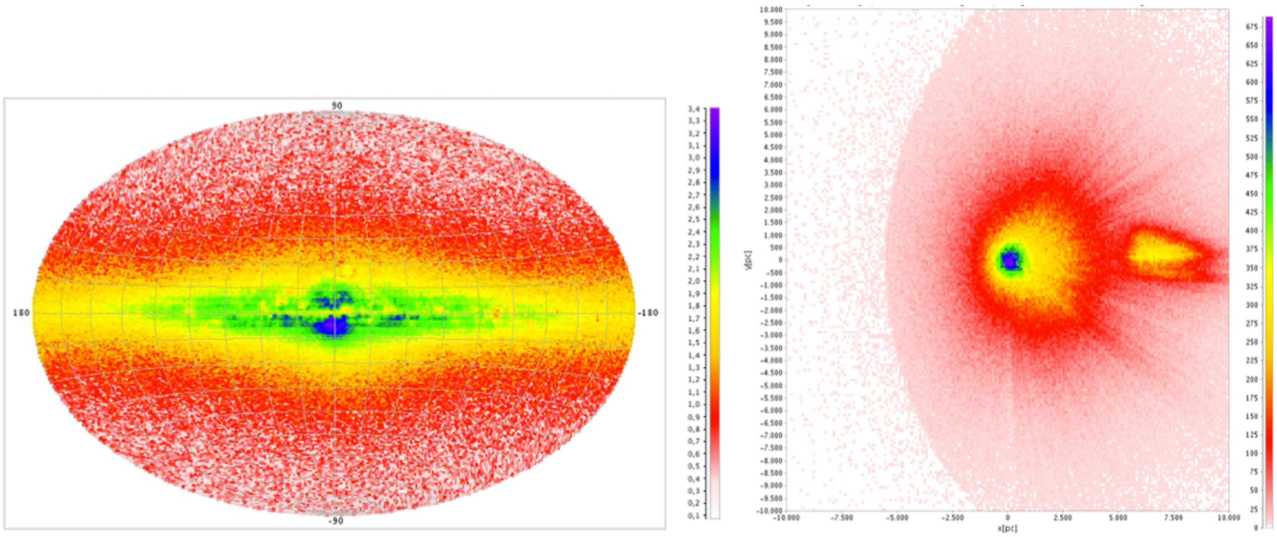

Fig. 3. Left: Expected total sky density (log of the number of objects per square degree) to magnitude G=20 from the Gaia Universe Model simulations (GUMS). Right: Expected total sky density in the X,Y plane, centered on the Sun.

spectralType	Total
O	3
B	3589
A	24916
F	296763
G	473337
K	349763
M	99937
L	1
Be	0
WR	0
AGB	9817
Other	1183
Total	1259309

lumClass	Total
BrightGiant	8812
Giant	173305
MainSequence	885651
Other	401
PreMainSequence	4584
SubGiant	185774
SuperGiant	18
WhiteDwarf	764
Total	1259309

Fig. 4. Expected number of stars $\times 10^{-3}$ at magnitude G=20 from the Gaia Universe Model simulations (GUMS).

Guillout, P., Haywood, M., Motch, C., Robin, A. C. 1996, A&A, 316, 89

Isasi, Y., Figueras, F., Luri, X., Robin, A. C. 2010, Highlights of Spanish Astrophysics V, 415

Marshall, D. J., Robin, A. C., Reylé, C., Schultheis, M., Picaud, S. 2006, A&A, 453, 635

Picaud, S., & Robin, A. C. 2004, A&A, 428, 891 bibitemReylé, C., Robin, A. C. 2001, A&A, 373, 886

Reylé, C., Marshall, D.J., Robin A.C., Schultheis, M. 2009, A&A 495, 819

Robin, A. C., Reylé, C., Crézé, M. 2000, A&A, 359, 103

Robin, A. C., Reylé, C., Derrière, S., Picaud, S. 2003. A&A, 409, 523 -540

Robin, A. C., Rich, R. M., Aussel, H. et al. 2007, ApJS, 172, 545

Ruphy, S., Robin, A.C., Epchtein, N., Copet, E., Bertin, E., Fouqué, P., Guglielmo, F. 1996, A&A, 313, L21

Schultheis, M., Robin, A. C., Reylé, C., McCracken, H. J., Bertin, E., Mellier, Y., Le Fèvre, O. 2006, A&A, 447, 185

Todmal, S.S, Gosh, S.K., Ojha, D.K., Robin, A.C. 2010, Bull. Astr. Soc. India, 1, 205

van der Kruit, P.C., 2008, in Formation and Evolution of Galaxy Disks, ASP Conference Series, Eds. J. G. Funes, S.J., E. M. Corsini

SF2A 2010
S. Boissier, M. Heydari-Malayeri, R. Samadi and D. Valls-Gabaud (eds)

GALACTIC PLANE IMAGE SHARPNESS AS A CHECK ON COSMIC MICROWAVE BACKGROUND MAPMAKING

B. F. Roukema[1]

Abstract. The largest uncollapsed inhomogeneity in the observable Universe is statistically represented in the quadrupole signal of the cosmic microwave background (CMB) sky maps as observed by the Wilkinson Microwave Anisotropy Probe (WMAP). The constant temporal offset of −25.6 ms between the timestamps of the spacecraft attitude and observational data records in the time-ordered data (TOD) of the WMAP observations was suspected to imply that previously derived all-sky CMB maps are erroneous, and that the quadrupole is in large part an artefact. The optimal focussing of bright objects in the Galactic Plane plays a key role in showing that no error occurred at the step of mapmaking from the calibrated TOD. Instead, the error had an effect when the uncalibrated TOD were calibrated. Estimates of the high-latitude quadrupole based on the wrongly calibrated WMAP maps are overestimated by about 15–60%.

Keywords: cosmic background radiation, galaxy: center, galaxy: disk, techniques: image processing

Although the primary aim of cosmic microwave background (CMB) all-sky observation missions is cosmological, the Galaxy constitutes a major component of the resulting data set. Liu & Li (2010) reconstituted all-sky maps from Wilkinson Microwave Anisotropy Probe (WMAP, Bennett et al. 2003) time-ordered data (TOD) and suggested that the quadrupole present in the official versions of the maps is mostly an artefact, since their own maps had a weaker quadrupole. They later traced this to a timing offset of −25.6 ms between the timestamps of the spacecraft attitude and observational data records in the calibrated TOD files (Liu et al. 2010). Since the offset is also present in the uncalibrated TOD files, it could have affected either (i) the calibration step or (ii) the mapmaking step.

The WMAP 3-year calibrated TOD were compiled into maps using Liu et al. (2010)'s publicly available data analysis pipeline*, and patched for using the GNU Data Language (GDL) and for two different timing error tests. In both cases, the timing offset, written as a multiple δt of an exposure time in a given waveband, where $\delta t = 0.5$ corresponds to the timing offset used by the WMAP collaboration, was varied in order to detect its effect on a relevant statistic of the maps. Testing an error at step (i) was done by creating low-resolution maps and finding the maps with the least variance per pixel (Roukema 2010b).† Testing an error at step (ii) was done by calculating high-resolution maps that included sub-cosmological objects, and finding the best focussed maps (Roukema 2010a).‡ The results, summarised in Table 1, showed to very high significance that the error affected the calibration step, but did not affect the mapmaking step directly. However, maps made from the wrongly calibrated data necessarily include the calibration error. For example, estimates of the high-latitude quadrupole based on the wrongly calibrated WMAP maps are overestimated by about 15–60% (Roukema 2010b). Figures 1 and 2 illustrate the sharpest focus test.

References

Bennett, C. L., Halpern, M., Hinshaw, G., et al. 2003, ApJSupp, 148, 1, [arXiv:astro-ph/0302207]
Liu, H., & Li, T. 2010, ArXiv e-prints, [arXiv:0907.2731]
Liu, H., Xiong, S., & Li, T. 2010, ArXiv e-prints, [arXiv:1003.1073]
Roukema, B. F. 2010a, A&A, 518, A34, [arXiv:1004.4506]
Roukema, B. F. 2010b, A&A, submitted, [arXiv:1007.5307]

[1] Toruń Centre for Astronomy, Nicolaus Copernicus University, ul. Gagarina 11, 87-100 Toruń, Poland
*http://cosmocoffee.info/viewtopic.php?p=4525, http://dpc.aire.org.cn/data/wmap/09072731/release_v1/source_code/v1/
†http://cosmo.torun.pl/GPLdownload/LLmapmaking_GDLpatches/LLmapmaking_GDLpatches_0.0.4.tbz
‡http://cosmo.torun.pl/GPLdownload/LLmapmaking_GDLpatches/LLmapmaking_GDLpatches_0.0.3.tbz

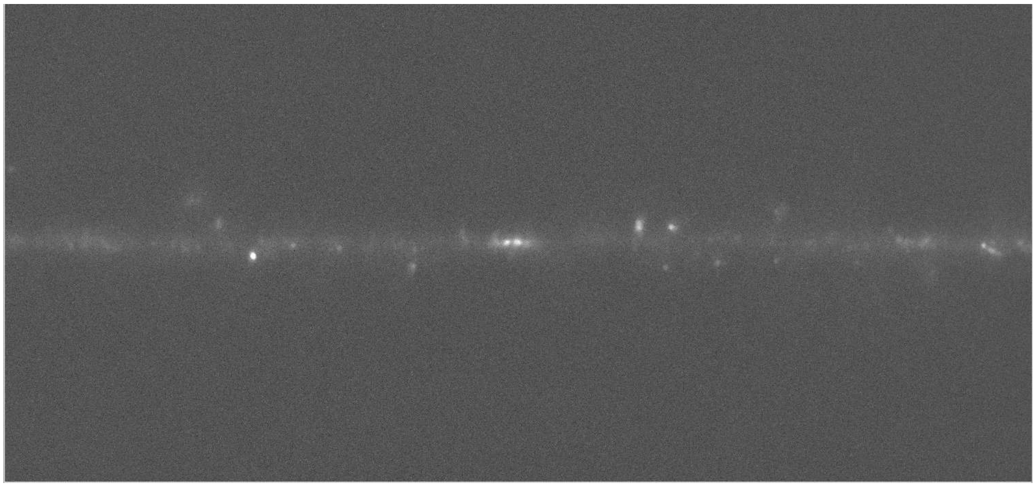

Fig. 1. Correctly focussed ($\delta t = 0.5$, Roukema 2010a) but wrongly calibrated (Roukema 2010b) WMAP W band (94 GHz) image of the $53.0° \times 24.7°$ region centred at the Galactic Centre (North up, East left), after monopole and dipole subtraction, on a grey scale ranging from black (-20 mK) to white (+40 mK). To zoom in, see Fig. 4, Roukema (2010a).

Table 1. Comparison of sharpest focus and minimum variance methods of testing for a timing offset error.

short name	minimum variance	sharpest focus
reference	Roukema (2010b)	Roukema (2010a)
step to understand	uncal. TOD $\rightarrow$ cal. TOD	cal. TOD $\rightarrow$ map
step analysed	cal. TOD $\rightarrow$ map	cal. TOD $\rightarrow$ map
planets & Gal. Plane	excluded	included
N_{side}	8	2048
statistic	variance per pixel	brightness of 503-rd brightest pixel
max/min	min	max
rejected hypothesis	$\delta t = 0.5$ rejected at 8.5σ	$\delta t = 0$ rejected at 4.6σ
accepted hypothesis	$(\delta t - 0.5) \times 52.1$ ms $= -25.6$ ms	$\delta t = 0.5$
conclusion	calibration step wrong	mapmaking step right

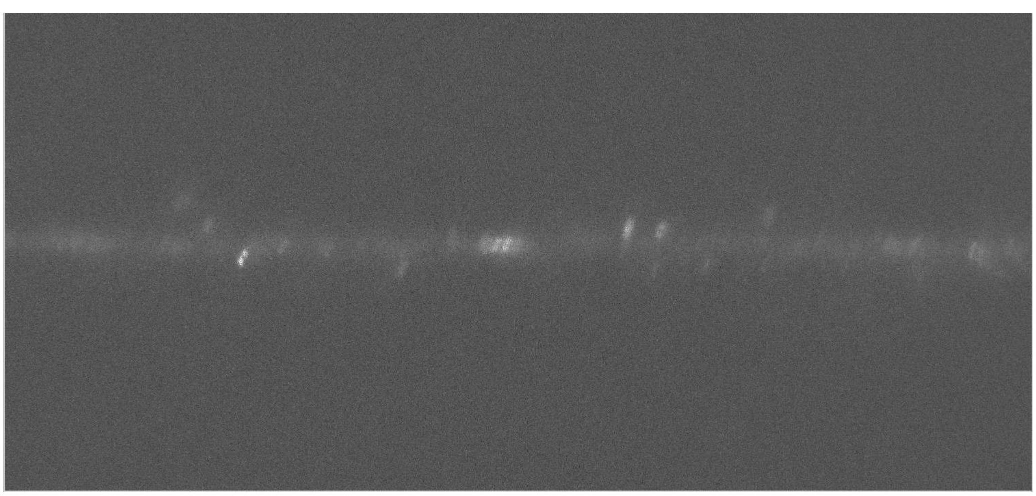

Fig. 2. Wrongly focussed, wrongly calibrated WMAP W band image, as for Fig. 1, with a timing offset $\delta t = -5$, i.e. exaggerated by a factor of ten beyond that which generated the calibration error. To zoom in, see Fig. 2, Roukema (2010a).

SF2A 2010
S. Boissier, M. Heydari-Malayeri, R. Samadi and D. Valls-Gabaud (eds)

THE HERSCHEL VIEW OF HII REGIONS IN M 33 (HERM33ES)

S. Verley[1], M. Relaño[1], C. Kramer[2], E.M. Xilouris[3], M. Boquien[4], D. Calzetti[4], F. Combes[5], C. Buchbender[2], J. Braine[6], G. Quintana-Lacaci[2], F.S. Tabatabaei[7], S. Lord[8], F. Israel[9], G. Stacey[10] and P. van der Werf[9]

Abstract. Within the framework of the HERM33ES Key Project (Kramer et al. 2010), using the high resolution and sensitivity of the Herschel photometric data, we study the compact emission in the Local Group spiral galaxy M 33. We present a catalogue of 159 compact emission sources in M 33 identified by SExtractor in the 250 μm SPIRE band which is the one that provides the best spatial resolution. We measure fluxes at 24 μm and Hα for those 159 extracted sources. We find a very strong Pearson correlation coefficient with the MIPS 24 μm emission ($r_{24} = 0.94$) and a rather strong correlation with the Hα emission, although with more scatter ($r_{H\alpha} = 0.83$). Due to the very strong link between the 250 μm compact emission and the 24 μm and Hα emissions, by recovering the star formation rate from standard recipes for HII regions, we are able to provide star formation rate calibrations based on the 250 μm compact emission alone. Finally, the morphological study of a set of three Hα shells shows that there is a displacement between far-ultraviolet and the SPIRE bands, while the Hα structure is in general much more coincident with the cool dust.

Keywords: galaxies: individual: M 33, galaxies: ISM, local group, galaxies: spiral

1 SPIRE 250 μm calibration of the star formation rate for HII regions in M 33

In order to create a catalogue of compact emission sources in the SPIRE 250 μm band, we use the SExtractor software (Bertin & Arnouts 1996). The photometry of the 159 extracted sources is computed using the parameter FLUX_ISO given by SExtractor, which uses isophotal photometry (sum of all the pixels above a threshold given by the lowest isophot: 16 times the background r.m.s.). Since most of the extracted objects are along the spiral pattern of the galaxy, we believe many of the sources may be directly linked to star formation (SF). This suggests that the SPIRE 250 μm compact emission could be a reliable SF tracer in the vicinity of HII regions. Therefore, we concentrate our preliminary work on the 250 μm compact emission and compare its properties with standard SF tracers such as the Hα emission line and the 24 μm compact emission linked to HII regions (Calzetti et al. 2005, 2007, 2010; Verley et al. 2009, 2010a). To recover the Hα+24 μm SF rate (SFR), our best fit leads to:

$$\mathrm{SFR}\ [\mathrm{M}_\odot\,\mathrm{yr}^{-1}] = 8.71 \times 10^{-45} L(250\,\mu\mathrm{m})^{1.03} \quad , \tag{1.1}$$

where $L(250\,\mu\mathrm{m})$ is in erg s^{-1}. To recover the SFR(24), we need the following calibration:

$$\mathrm{SFR}\ [\mathrm{M}_\odot\,\mathrm{yr}^{-1}] = 3.47 \times 10^{-44} L(250\,\mu\mathrm{m})^{1.02} \quad , \tag{1.2}$$

also with $L(250\,\mu\mathrm{m})$ in erg s^{-1}. The uncertainties are 0.04 and 0.03 for the exponents in Eqs. 1.1 and 1.2, respectively, while the calibration constants have uncertainties of 4.0 and 2.7%, respectively. Please, see Verley et al. (2010b) for more information.

[1] Dept. Física Teórica y del Cosmos, Universidad de Granada, Spain
[2] Instituto Radioastronomia Milimetrica (IRAM), Av. Divina Pastora 7, Nucleo Central, E-18012 Granada, Spain
[3] Institute of Astronomy and Astrophysics, National Observatory of Athens, P. Penteli, 15236 Athens, Greece
[4] Department of Astronomy, University of Massachusetts, Amherst, MA 01003, USA
[5] Observatoire de Paris, LERMA, 61 Av. de l'Observatoire, 75014 Paris, France
[6] Lab. d'Astrophysique, Université 1 et Observatoire de Bordeaux, OASU, UMR 5804, CNRS/INSU, Floirac F-33270, France
[7] Max-Planck-Institut für Radioastronomie (MPIfR), Auf dem Hügel 69, D-53121 Bonn, Germany
[8] Infrared Processing and Analysis Center, MS 100-22 California Institute of Technology, Pasadena, CA 91125, USA
[9] Leiden Observatory, Leiden University, PO Box 9513, NL 2300 RA Leiden, The Netherlands
[10] Department of Astronomy, Cornell University, Ithaca, NY 14853, USA

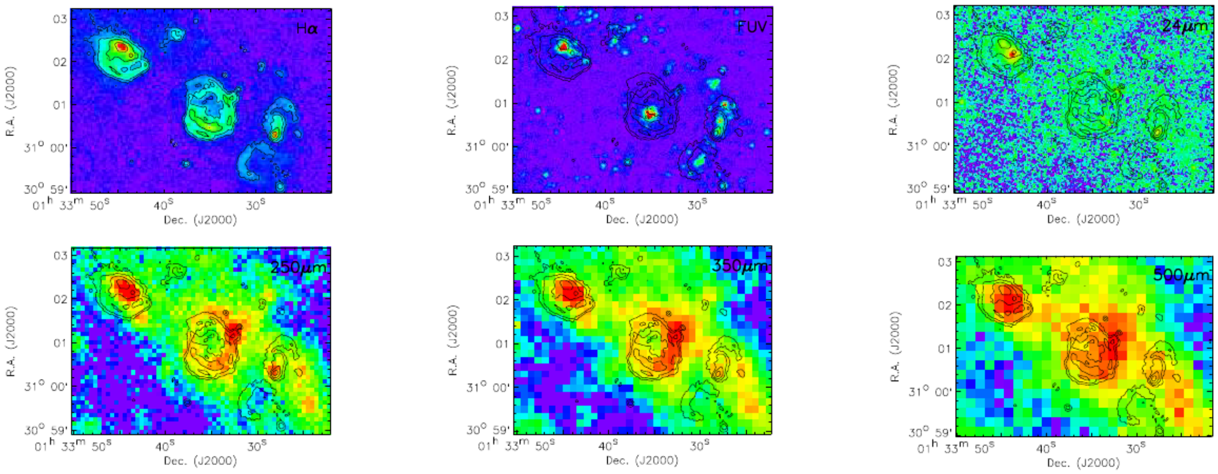

Fig. 1. Continuum-subtracted Hα image of a set of large shells in the outer north part of M 33 (top left). Contours are overlaid in this image to better enhance the shell features (levels are at 20, 49, 122, 300 of Hα emission measure) and repeated in the other images for comparison.

2 SPIRE emission distributions for HII regions

Taking advantage of the unprecedented Herschel resolution at the SPIRE wavelength bands, we also focus on a more precise study of some striking Hα shells in the northern part of the galaxy (see Fig. 1). The morphological study of the Hα shells shows a displacement between far-ultraviolet, Hα, and the SPIRE bands. The different locations of the Hα and far-ultraviolet emissions with respect to the SPIRE cool dust emission leads to a dynamical age of a few Myr for the Hα shells and the associated cool dust (Relaño & Beckman 2005).

We refer the reader to Kramer et al. (2010); Braine et al. (2010); Boquien et al. (2010) for more details about the overall `HERM33ES` preliminary results, as well as for a first presentation of the PACS and SPIRE maps of the entire galaxy, together with spatially averaged spectral energy distributions.

This work was partially supported by a Junta de Andalucía Grant FQM108, a Spanish MEC Grant AYA-2007-67625-C02-02, and a Juan de la Cierva fellowship. This research was supported by an MC-IEF within the 7$^{\text{th}}$ European Community Framework Programme.

References

Bertin, E. & Arnouts, S. 1996, A&AS, 117, 393
Boquien, M., Calzetti, D., Kramer, C., et al. 2010, A&A, 518, L70
Braine, J., Gratier, P., Kramer, C., et al. 2010, A&A, 518, L69
Calzetti, D., Kennicutt, R. C., Engelbracht, C. W., et al. 2007, ApJ, 666, 870
Calzetti, D., Kennicutt, Jr., R. C., Bianchi, L., et al. 2005, ApJ, 633, 871
Calzetti, D., Wu, S., Hong, S., et al. 2010, ApJ, 714, 1256
Kramer, C., Buchbender, C., Xilouris, E. M., et al. 2010, A&A, 518, L67
Relaño, M. & Beckman, J. E. 2005, A&A, 430, 911
Verley, S., Corbelli, E., Giovanardi, C., & Hunt, L. K. 2009, A&A, 493, 453
Verley, S., Corbelli, E., Giovanardi, C., & Hunt, L. K. 2010a, A&A, 510, A64
Verley, S., Relaño, M., Kramer, C., et al. 2010b, A&A, 518, L68

ASHRA - SAIt

High Angular Resolution

SF2A 2010
S. Boissier, M. Heydari-Malayeri, R. Samadi and D. Valls-Gabaud (eds)

THE CAOS PROBLEM-SOLVING ENVIRONMENT: LAST NEWS

M. Carbillet[1], G. Desiderà[2], É. Augier[1], A. La Camera[2], A. Riccardi[3], A. Boccaletti[4], L. Jolissaint[5] and D. Ab Kadir[1]

Abstract. We present recent developments of the `CAOS` problem-solving environment (PSE), an `IDL`-based software tool complete of a global graphical interface, a general utilities library, and different specialized scientific packages going from end-to-end and analytical simulations to image simulation/reconstruction, with specialization to given instruments.

Keywords: adaptive optics, numerical simulations, image reconstruction, LINC-NIRVANA, SPHERE

Introduction

The name `CAOS` ("Code for Adaptive Optics Systems") was originally used to describe the `Software Package CAOS` which permits end-to-end numerical modeling of adaptive optics (AO) systems. Since a few years it also describes the `CAOS` problem-solving environment (PSE), which allows to clearly separate in its own bosom the scientific part of the original `Software Package CAOS` from the global interface and global structure of the tool, permitting also to complete the whole suite with a number of other `Software Packages` covering a wider area of astronomical-optics-related scientifical topics: image reconstruction/deconvolution with the `Software Package AIRY` ("Astronomical Image Reconstruction in interferometrY"), deconvolution specialized for the LBT LINC-NIRVANA instrument with the `Software Package AIRY-LN` ("`AIRY` for LINC-NIRVANA"), simulation of the data delivered by the VLT SPHERE instrument with the `Software Package SPHERE`, analytical AO modeling with the `Software Package PAOLAC` ("`PAOLA` within CAOS"), and multiple-reference AO simulations with the `Software Package MAOS` ("Multiple-reference Adaptive Optics Simulations").

The `CAOS` PSE is composed of a global graphical interface (the `CAOS Application Builder`, which permits to connect together modules from the various `Software Packages` installed), a library of utilities (the `CAOS Library`), and the `Software Packages` (each of them being a collection of modules). Within the `CAOS Application Builder`, the modules from each `Software Package` can be selected and placed in order to compose a simulation project by combining together the modules and defining the corresponding data flow. The `IDL` code implementing the simulation program is automatically generated and the whole structure of the simulation is saved as a project that can be restored for latter modifications and/or parameters upgrading.

The `CAOS Library` and the `CAOS Application Builder`

Since the first (and last) global presentation of the CAOS PSE (Carbillet et al. 2004), the `CAOS Library` has been completed with routines permitting to deal with low-light-level (LLL) CCDs, and a global noise addition routine usable from any `Software Package` in the same exact manner. On its side, the `CAOS Application Builder` has benefited from important debugging, leading to a very stable version of it since 6.0. In addition, since version 7.0, and by taking advantage from the Virtual Machine feature of `IDL`, one can also now build an IDL-licence-free executable made from any simulation project and which can be run afterwards on machines with neither the `CAOS` PSE installed, nor even `IDL` licensed.

[1] UMR 6525 H. Fizeau, Université de Nice Sophia Antipolis/CNRS/OCA, Parc Valrose, 06108 Nice Cedex 2, France
[2] Dipartimento di Informatica e Scienza dell'Informazione, Università di Genova, Via Dodecaneso 35, 16146 Genova, Italy
[3] Istituto Nazionale di AstroFisica - Osservatorio Astrofisico di Arcetri, Largo Enrico Fermi 5, 50125 Firenze, Italy
[4] UMR 8109 LESIA, Observatoire de Meudon/CNRS, 5 Place Jules Jansen, 92195 Meudon, France
[5] aquilAOptics, Rue de la Châtellenie 4, 1635 La Tour-de-Trême, Switzerland

The `Software Package CAOS` - end-to-end AO modeling

This is the original part of the whole `CAOS` PSE. It has been deeply described in a paper published in 2005 (Carbillet et al. 2005) (see also Carbillet and Riccardi (2010a) for the wavefront generation issue), and it is clearly now in a full exploitation phase. Recent developments mainly include densified-pupil capabilities and the possibility of using the LLLCCD routines when simulating the pyramid sensor (Carbillet and Riccardi 2010b).

The `Software Package AIRY` - image simulation & reconstruction

Developments since the original paper (Correia et al. 2002) were numerous and concerned, among others, blind deconvolution implementation, regularizations, accelerations, point-spread function extraction, high-dynamic-range and super-resolution capabilities assessments, boundary effects mitigation, etc. Next to come are a new module for Strehl-constrained blind deconvolution (Desiderà and Carbillet 2009), another one for the rotation of images, and modifications to the existing modules in order to simulate multi-frame images and common CCD defects (and associated data reduction).

The `Software Package PAOLAC` - analytical AO modeling

This is the last developed package of the whole `CAOS` PSE. It is completely based on the well-known analytical model `PAOLA` (Jolissaint et al. 2006), being a simple embedment of it (Carbillet et al. 2010). Further work includes extending the existing modules to the whole capabilities offered by the original code `PAOLA` and implementation of its brand new close-loop feature (Jolissaint 2010).

Other packages

The `Software Package MAOS` is still in its β version, but some modules are being used for GLAO simulations (Carbillet et al. 2009).

On the other hand, the `Software Package SPHERE` (Carbillet et al. 2008) and the `Software Package AIRY-LN` (Desiderà et al. 2008), like the `Software Package PAOLAC`, were absolutely not foreseen in any way in 2004. But, unlike the other packages presented here, they are not publicly distributed because completely dedicated to a particular instrument: SPHERE on the VLT and LINC-NIRVANA on the LBT, respectively. While the `Software Package SPHERE` has already attained its final version and has been already well exploited, the `Software Package AIRY-LN` is in its plain development phase and begins to be exploited now.

Availability of the code

The whole `CAOS` PSE, except from its instrument-dedicated packages, is freely distributed, and can be downloaded from `http://fizeau.unice.fr/caos`.

References

Carbillet, M. & Riccardi, A. 2010a, to appear in App. Opt., 49, 31

Carbillet, M. & Riccardi, A. 2010b, submitted to App. Opt.

Carbillet, M., Vérinaud, C., Guarracino, M. et al., 2004, SPIE Proc., 5490, 550

Carbillet, M., Vérinaud, C., Femenía, B. et al., 2005, Mon. Not. R. Astron. Soc., 356, 1263

Carbillet, M., Boccaletti, A., Thalmann, Ch. et al., 2008, SPIE Proc., 7015, 70156Z

Carbillet, M., Maire, A.L., Le Roux, B. et al., 2009, EAS Pub. Series, 40, 157

Carbillet, M., Jolissaint, L., Maire, A.L. 2010, EDP Sciences (`ao4elt.edpsciences.org`), 03006

Correia, S., Carbillet, M., Boccacci, P. et al. 2002, Astron. Astrophys., 387, 733

Desiderà, G. & Carbillet, M. 2009, A&A, 507, 1759

Desiderà, G., La Camera, A., Boccacci, P. et al., 2008, SPIE Proc., 7013, 701340

Jolissaint, L. 2010, Journal of the European Optical Society, Rapid Publications, in press

Jolissaint, L., Véran, J.P., Conan, R. 2006, J. Opt. Soc. Am. A, 23, 382

THE MULTI-CONJUGATE ADAPTIVE OPTICS MODULE FOR THE E-ELT

E. Diolaiti[1], J.-M. Conan[2], I. Foppiani[1,3], E. Marchetti[4], A. Baruffolo[5], M. Bellazzini[1], G. Bregoli[1], C. R. Butler[6], P. Ciliegi[1], G. Cosentino[3], B. Delabre[4], M. Lombini[1,3], C. Petit[2], C. Robert[2], P. Rossettini[7], L. Schreiber[3], R. Tomelleri[7], V. Biliotti[8], S. D'Odorico[4], T. Fusco[2], N. Hubin[4] and S. Meimon[2]

Abstract. The Multi conjugate Adaptive Optics RelaY (MAORY) for the European Extremely Large Telescope is designed to compensate the effects of the atmospheric turbulence over a 2 arcmin field of view in the wavelength range 0.8-2.4 micron. The wavefront correction is performed by three deformable mirrors driven by a wavefront sensing system based on laser and natural guide stars. Accurate relative photometry and astrometry and infrared spectroscopy are the key science applications of the adaptive optics module with its client instruments.

Keywords: Extremely Large Telescopes, E-ELT, multi-conjugate adaptive optics, laser guide stars, sky coverage

1 Introduction

MAORY (acronym for Multi-conjugate Adaptive Optics RelaY) is a post-focal adaptive optics module for the European Extremely Large Telescope (E-ELT) (Gilmozzi and Spyromilio 2008). A Phase-A study of this module was carried out by a consortium formed by Istituto Nazionale di Astrofisica (INAF) and Office National d'Etudes et de Recherches Aerospatiales (ONERA) in the framework of the E-ELT instrumentation studies (Ramsay et al. 2010) sponsored by the European Organisation for Astronomical Research in the Southern Hemisphere.

The E-ELT high angular resolution camera MICADO (Davies et al. 2010) is a candidate client instrument of MAORY. It requires an image correction of high quality and uniformity across a 53×53 arcsec^2 field of view in the wavelength range 0.8-2.4 μm. Accurate relative photometry and astrometry are key science drivers of MICADO which requires reliable and stable adaptive optics correction with calibrations limited to low order distortion compensation. Infrared spectroscopy is also a potential application of MAORY: a possible client instrument is SIMPLE, a single field high resolution spectrograph (Origlia et al. 2010). During the Phase-A study other instrumental concepts were considered, exploiting the energy concentration of the point spread function provided by MAORY: a wide field imaging camera with reduced angular resolution with respect to MICADO and a multi-object infrared spectrograph. Having in mind these concepts, a target science field of view of 120 arcsec diameter was considered for the module design and performance optimization. High sky coverage is a request common to all science instruments.

MAORY is based on Multi-Conjugate Adaptive Optics (MCAO), a concept proposed by Beckers (1989) and proven on sky by MAD, the MCAO demonstrator for the Very Large Telescope (Marchetti et al. 2008). The atmospheric turbulence is corrected by three deformable mirrors conjugated at different ranges: in this way the

[1] INAF - Osservatorio Astronomico di Bologna, 40127 Bologna, Italy
[2] ONERA, 92322 Chatillon, France
[3] Università di Bologna, Dipartimento di Astronomia, 40127 Bologna, Italy
[4] ESO, 85748 Garching, Germany
[5] INAF - Osservatorio Astronomico di Padova, 35122 Padova, Italy
[6] INAF - Istituto di Astrofisica Spaziale e Fisica Cosmica, 40129 Bologna, Italy
[7] Tomelleri s.r.l., 37069 Villafranca, Italy
[8] INAF - Osservatorio Astrofisico di Arcetri, 50125 Firenze, Italy

module design provides a performance of high quality and uniformity over the science field. The deformable mirrors are driven in closed loop by a wavefront sensing system based on Laser Guide Stars (LGS) and Natural Guide Stars (NGS). These general design choices are similar to those adopted in other MCAO systems as GeMS for the Gemini telescope (Ellerbroek et al. 2003) and NFIRAOS for the Thirty Meter Telescope (Herriot et al. 2010).

2 Design overview

The foreseen location of MAORY is a bent focus on the E-ELT Nasmyth platform (Figure 1). From the optical design point of view the MCAO module is a unit magnification finite conjugate relay based on off-axis aspheric mirrors. The splitting of the science and LGS beams in the optical relay is accomplished by means of a dichroic, that transmits the LGS light (wavelength 0.589 μm) and reflects the science channel light (wavelength longer than 0.6 μm). The LGS beam transmitted by the dichroic is focused by a refractive objective. Assuming high performance optical coatings, based on multi-layer protected silver, the thermal background of MAORY is expected to have an acceptable impact on the currently foreseen science instruments: for this reason as a baseline MAORY is not cooled. This choice might have to be re-assessed in the future, depending on refined or new science instrument requirements. The post-focal relay feeds two output focal stations: a gravity invariant port underneath the optical bench, providing mechanical derotation for a light instrument as MICADO, and a lateral port on a side of the bench to feed an instrument standing on the Nasmyth platform, detached from the module.

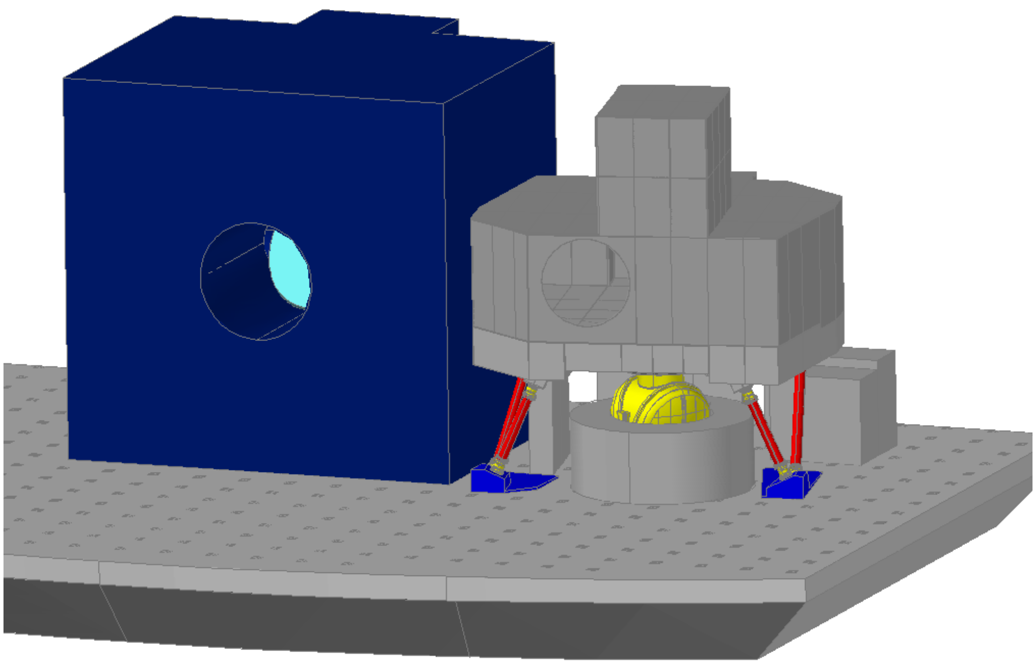

Fig. 1. Layout of MAORY on the E-ELT Nasmyth platform. The telescope pre-focal station is on the left part of the picture; MAORY is on the right. MICADO is shown underneath the optical bench of MAORY.

MAORY features three levels of wavefront correction: the telescope adaptive mirror M4, optically conjugated to few hundred meters above the telescope pupil and complemented by the telescope field stabilization mirror M5, and two post-focal deformable mirrors, conjugated to 4 km and 12.7 km from the telescope entrance pupil and located in the optical relay of MAORY. High-order wavefront sensing is performed by means of six sodium LGSs, arranged on a circle of 120 arcsec angular diameter. The LGSs are assumed to be projected from the telescope edge: this choice translates into a slightly higher slope measurement error than central projection, due to the larger perspective spot elongation, however it allows to get rid of the so-called fratricide effect among different guide stars, related to Rayleigh scattering of the laser light in the atmosphere. Six Shack-Hartmann wavefront sensors of order 84×84 subapertures are used to sense the LGS wavefronts by means of advanced spot position measurement algorithms in order to mitigate the impact of the spot elongation effect. The LGS wavefront sensor measurements are complemented by three NGSs, searched over a technical field of up to 160 arcsec diameter. The light of wavelength 1.5-1.8 μm is used for fast tip-tilt and focus measurement, providing the necessary information to solve the LGS tip-tilt indetermination problem and to retrieve the LGS focus which is affected by the sodium altitude instability. The high order correction achieved at these wavelengths by means of the LGS wavefront sensor ensures a spot shrinking which allows to exploit faint NGSs, translating into a high sky coverage. The light of wavelength 0.6-0.9 μm of the NGSs feeds a so-called Reference wavefront sensor of order $\sim$10$\times$10 subapertures, operated at temporal frequencies in the range 0.1-1 Hz, used to monitor the LGS non common path aberrations related to the sodium layer profile variability. A high order engineering mode of the Reference wavefront sensor is foreseen as well, allowing a NGS-based MCAO correction to be performed. The baseline strategy for the MCAO correction loop is pseudo open loop control (Gilles 2005), representing a good compromise in terms of performance and computational complexity between an optimal approach as linear quadratic gaussian control and a plain least squares approach.

3 Performance

The estimated performance of the MCAO module is shown in Figure 2 as a function of the angular distance from the field center at four wavelengths (K_s: 2.16 μm, H: 1.65 μm, J: 1.215 μm, I: 0.9 μm) for two atmospheric turbulence conditions (median seeing: 0.8 arcsec; good seeing: 0.6 arcsec).

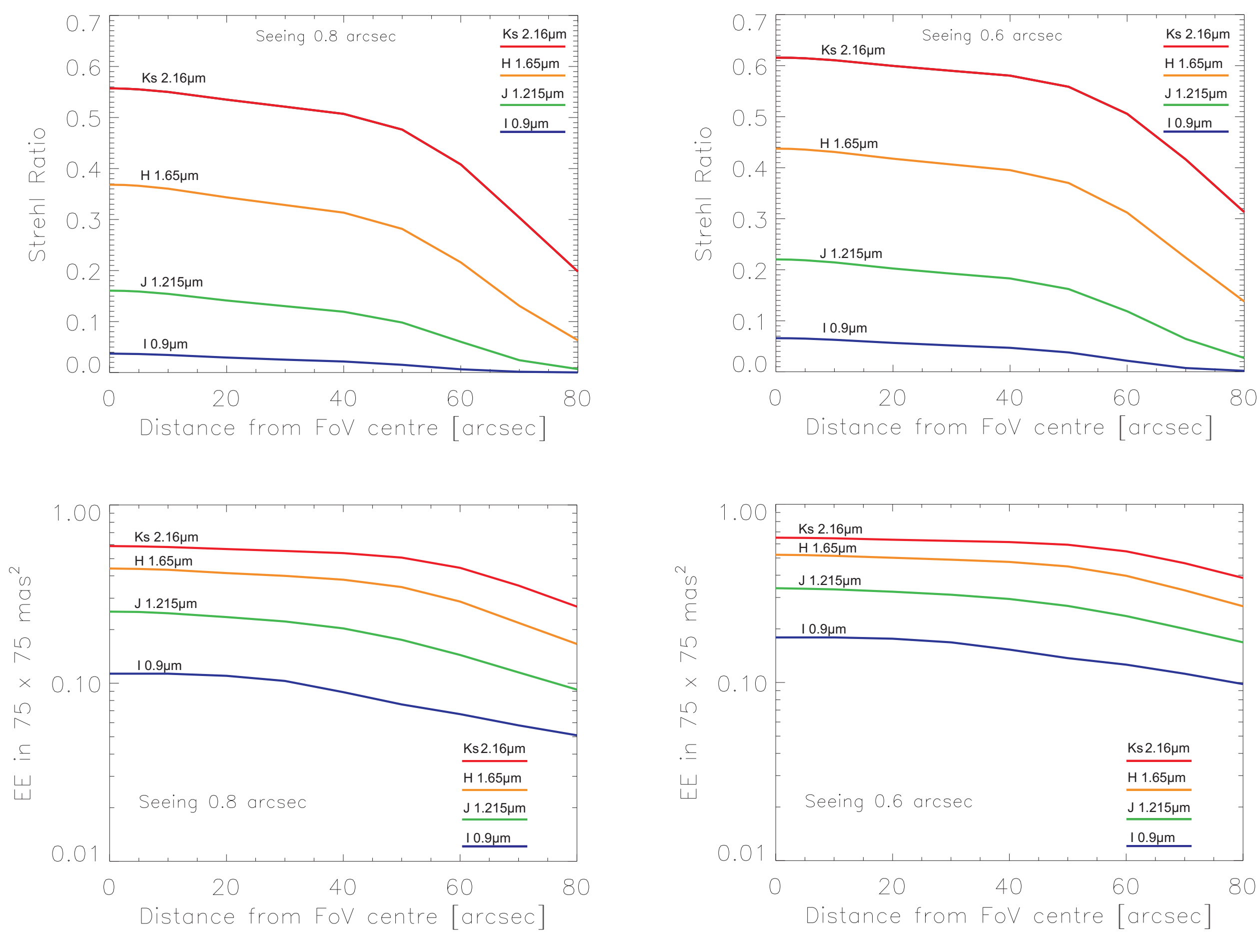

Fig. 2. MCAO module correction performance. Above: Strehl Ratio. Below: point spread function Ensquared Energy in 75$\times$75 mas^2. Left: seeing FWHM 0.8 arcsec. Right: seeing FWHM 0.6 arcsec.

The performance is remarkably uniform out to a radial distance of approximately 60 arcsec corresponding to the optimization field of view. For median seeing conditions the point spread function Ensquared Energy in a 75×75 mas^2 square slit, an interesting performance metric for a spectrograph, is higher than 30% in H band on average over the 120 arcsec field.

On the basis of a study on simulated images, accounting for point spread function shape, field variation and seeing dependency, it was shown that the relative photometric accuracy (0.02-0.03 mag RMS) and the relative astrometric accuracy (0.05-0.1 milli-arcsec) required by MICADO are both achievable. A more detailed analysis of the attainable accuracy, including all atmospheric effects, shall be pursued further in the future. To assist the data analysis a study was started to develop a point spread function model including the field variation.

The sky coverage at the North Galactic Pole for median seeing is shown in Table 1. It was estimated on the basis of Monte Carlo simulations of random asterisms with star densities derived from the TRILEGAL code v1.2 (Girardi et al. 2005). Anisoplanatic effects, measurement noise and temporal error were considered; windshake, a major contributor to image jitter, was included in the calculation of the temporal error, assuming a Kalman filter taking into account the windshake statistical properties. Stars as faint as magnitude H=21 were used: currently available infrared star catalogues do not reach this magnitude limit, but it was assumed that such catalogues will be available by the time the E-ELT will be operating or that it will be possible to make a pre-imaging of the target field. The sky coverage in the table is expressed in terms of the percentage of sky at the North Galactic Pole where a given minimum performance averaged over the MICADO field is achieved. The first line of the table corresponds to the nominal performance shown in Figure 2 for median seeing. The sky coverage shown here relies on a solid basis: the relatively good correction performance achieved in closed loop over the whole NGS search field.

Strehl Ratio				Sky coverage
K_s	H	J	I	
0.53	0.34	0.14	0.03	39%
0.51	0.32	0.13	0.03	50%
0.41	0.22	0.06	0.01	80%

Table 1. Sky coverage at the North Galactic Pole.

More detailed information about MAORY may be found in Diolaiti et al. (2010), Foppiani et al. (2010) and on the project web page `www.bo.astro.it/maory`.

This work was supported by the European Community (Framework Programme 6, ELT Design Study, contract N. 011863; Framework Programme 7, Preparing for the Construction of the European Extremely Large Telescope, contract N. INFRA-2007-2.2.1.28) and by the European Organization for Astronomical Research in the Southern Hemisphere (Agreement No 16669/ESO/INS/07/17243/LCO).

References

Beckers, J.M. 1989, Proc. SPIE, 1114, 215

Davies, R., Ageorges, N., Barl, L. et al. 2010, Proc. SPIE, 7735, 77352A

Diolaiti, E., Conan, J.-M., Foppiani, I. et al. 2010, Proc. SPIE, 7736, 77360R

Ellerbroek, B.L., Rigaut, F.J., Bauman, B.J. et al. 2003, Proc. SPIE, 4839, 55

Foppiani, I., Diolaiti, E., Baruffolo, A. et al. 2010, Proc. SPIE, 7736, 77362Z

Gilles, L. 2005, Applied Optics, 44, 993

Gilmozzi, R., & Spyromilio, J. 2008, Proc. SPIE, 7012, 701219

Girardi, L., Groenewegen, M.A.T., Hatziminaoglou, E. et al. 2005, A&A, 463, 895

Herriot, G., Andersen, D., Atwood, J. et al. 2010, Proc. SPIE, 7736, 77360B

Marchetti, E., Brast, R., Delabre, B. et al. 2008, Proc. SPIE, 7015, 70150F

Origlia, L., Oliva, E., Maiolino, R. et al. 2010, Proc. SPIE, 7735, 77352B

Ramsay, S., D'Odorico, S., Casali, M. et al. 2010, Proc. SPIE, 7735, 773524

SF2A 2010
S. Boissier, M. Heydari-Malayeri, R. Samadi and D. Valls-Gabaud (eds)

SIMULATIONS OF WAVE FRONT MEASUREMENTS AND TOMOGRAPHY FOR EXTREMELY LARGE TELESCOPES

M. Chebbo[1], B. Le Roux[2], J.F. Sauvage[3] and T. Fusco[4]

Abstract. The control of AO systems dedicated to ELT is a difficult problem related to the large number of degrees of freedom. The standard and most used adaptive optics AO control starting from the integrator to the LQG are not useful in such a case. In fact, for future Extremely Large Telescope (ELTs) the number of degrees of freedom is very large related to the large diameter of the ELTs and the emergence of new architectures for the AO systems. So that the necessary computational power for real time control RTC on such systems is currently unattainable when using these control methods. Thus, more efficient algorithms are required. We present simulation results of a tomographic AO system in the configuration of EAGLE instrument (multi-object adaptive optics).

Keywords: adaptive optics, inverse problem, reconstruction, sparse matrix

1 Introduction

In this article we describe an adaptive optics simulation platform, which can be used to simulate adaptive optics systems on the largest proposed future extremely large telescopes ELT. This simulator is based on a sparse library created by RALPH Flicker, it's a sparse Operations with Yorick/IDL originates from a collection of IDL/C routines that are used together for a specific purpose: efficient wave front reconstruction in adaptive optics simulations*.We introduce a solution for a fast wavefront recontructions and then the results for simulations and reconstructions done over an octopro 2.1GHZ.

2 E2E CAOS simulations

The CAOS "system" (Code for Adaptive Optics Systems) is properly said a Problem Solving Environment (PSE) (Carbillet et al. 2004). MAOS (that stands for Multiconjugate Adaptive Optics Simulations) developped for multi-reference multiconjugate AO studies purpose. PAOLAC which is a simple CAOS interface for the analytic IDL code PAOLA (Carbillet et al. 2005) . The first step of our work consisted in validating the computing capabilities for ELT simulations. First of all, using a standard biprocessor computer, we simulated classical adaptive optics with CAOS for different telescope diameters, from 8m to 28m. For larger telescopes, the biprocessor computer was not able to make the simulation (see Figure1) . Our second step consisted in simulating classical adaptive optics on an octoprocessor computer so that we reached a 42m telescope . We present the simulation time for the different simulation reached by a bi and octoprocessor. For a 42m, 8 hours of simulation are required. Moreover the simulation of GLAO FOR 28m telescope on an octoprocessor, using 4 guide stars on the border of a 40 arcmin field of view. The deformable mirror is 31×31 actuators and the Shack-Hartmann WFS is 30×30 sub-apertures. The atmosphere is composed of 4 turbulent layers at 10, 100, 1000 and 5000 m of altitude the E2E simulation times tooks 1 day. As a conclusion, the dramatic increase of the number of degrees of freedom while simulation AO for the ELT makes our work more difficult using CAOS. For those reasons we are going to introduce the SOY/I library created by Ralf-Flicker in the purpose of an efficient wave front reconstruction in adaptive optics simulations.

[1] Laboratoire d'Astrophysique de Marseille
[2] Laboratoire d'Astrophysique de Marseille
[3] ONERA, BP 72, 92322 Chatillon cedex, France
[4] ONERA, BP 72, 92322 Chatillon cedex, France

*see Ralf Flicker's site `http://homepage.mac.com/rflicker/soy.htm`

3 Modelization of a Shack-Hartmann

The purpose of this chapter is to analyse the noise introduced by a SH on the slopes of an incident WF and to reconstruct a wave front given the measurements, all by using the real matrix and the generalized inverse.

In fact, a model of the wave front sensor allows to link the measurement S to the incoming phase ϕ. It can be written as

$$S = D\Phi$$

3.1 Zonal approach

In order to determine the matrix D of N*M elements, we are going to use the finite difference to express the slopes in terms of the discrets phase values. Considering the Shack-Hartmann with square subaperatures, and by using the Frieds model (Rousset 1999) :

$$S^x_{ij} = [(\phi_{i+1j+1} + \phi_{i+1j}) - (\phi_{ij} + \phi_{ij+1})]/2d$$
$$S^y_{ij} = [(\phi_{i+1j+1} + \phi_{ij+1}) - (\phi_{ij} + \phi_{i+1j})]/2d$$

Where D is the interaction matrix. Created by four diagonals corresponding to the response of WFS on each phase ϕ_{ij} at the corner of each subaperature. So the elements of D are $\pm(2d)^{-1}$ or 0. By using the inverse problem and given the measurement we are able to estimate the phase:

$$\hat{\phi} = D^{\dagger} S$$
$$D^{\dagger} = (D^T D)^{-1} D^T$$

We verify in Figure 2 that the power spectral density introduced by the subaperatures of a Shack-Hartmann in the phase slopes follows the inverse of the square of the special frequency.

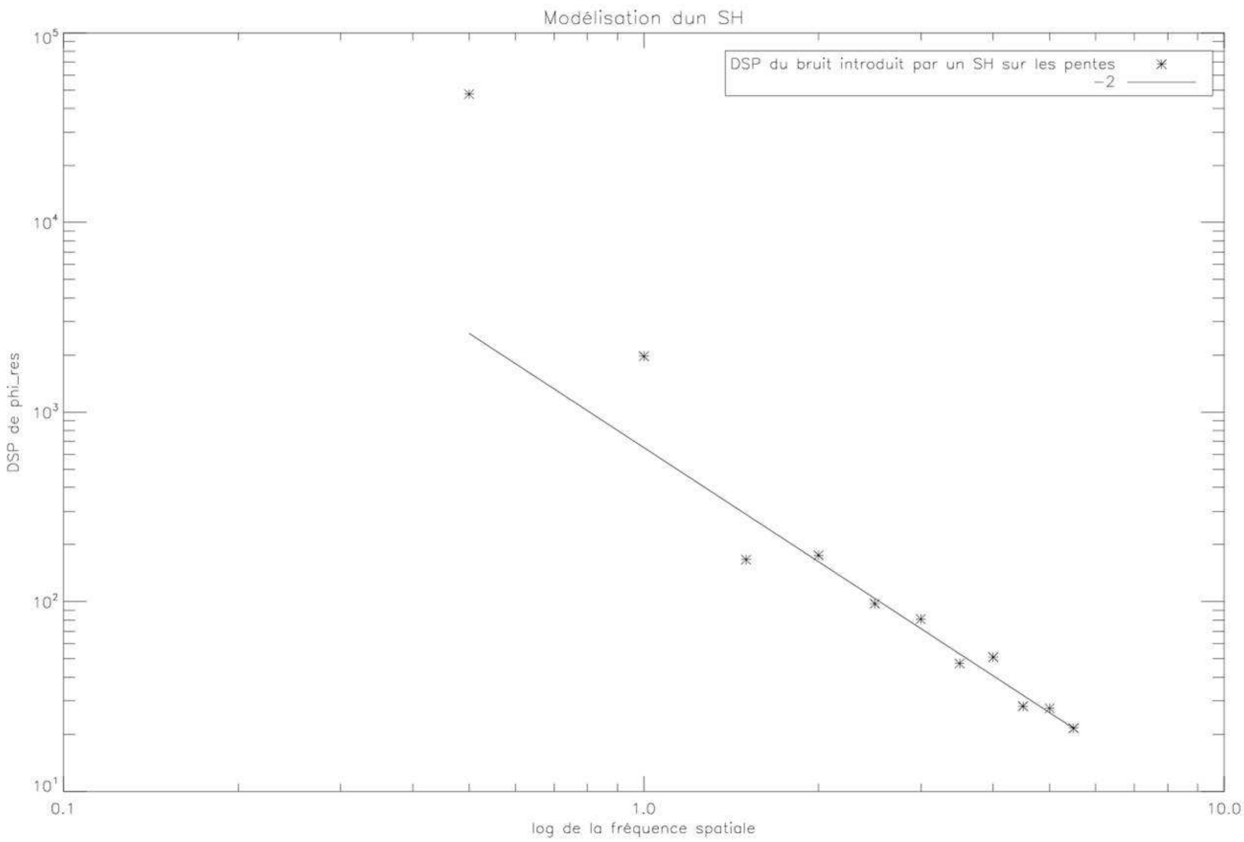

Fig. 1. DSP on the meausurement intruduced by a SH

4 E2E Sparse Matrix Simulator

4.1 Volume phase reconstruction

We generate a turbulent phase corresponding to each layer (see Figure 4), then we build a matrix in a sparse format giving the number of none zero elements to be stored for each direction and each layer. This matrix provides the projection of the phase in the pupille coming from all the analyses directions, supposed that we have 3 layers and 5 directions this matrix is $(N^2 \times 5, N^2 \times 3)$

$$\phi_a = I\phi_c$$

The estimation of the wave front given the measurement in the different directions is an inverse problem which must be solved using proper regularization in order to improve the quality of the solution while avoiding noise amplification or ambiguity due to missing data. Estimating the phase requires the inversion of the covariance matrix, moreover for the ELT the number of actuators being considered is in the range $10^4 - 10^5$, so the inversion of the covariance matrix using the present methods needs a lot of time to calculate and a huge memory to store, moreover those present reconstructor scales more than $O(N^2)$.

$$\hat{\phi} = (I^T I)^{-1} I^T \phi_{mes}$$

To avoid the direct matrix inversion we propose to use an iterative method with Jacobi preconditioner to solve the linear system :

$$(I^T I)\hat{\phi} = I^T \phi_{mes}$$

Where the first factor is a symmetric positive definite sparse matrix, and the MVM (matrix-vector multiplications) is carried out sparsely by the `ruoxv(a,v)` function.

4.2 Simulation results

For a telescope 190×190 pixels in the metapupil, $R_0 = 0.159$m and RSB = 20 in 5 arcmin. We show the estimated phase in four layers as it is shown in Figure 5, given the measurements from Figure 3.

Fig. 2. The wave front measurement in nine directions for a 42 m in 5 arc min

As a conclusion of this section, we generate a turbulent wave front in the layers, using a projector matrix built in a sparse format and providing a bilinear interpolation we project the phase in the pupille, we add the wave front sensor noise, then using an iterative methode and the jacobi preconditioner we solve the linear probleme in order to estimate the phase corresponding to the different layers.

5 Computing time characterization of the E2E Sparse Matrix code

Since we are looking to simulate AO for ELT, its important to proove that we have a fast wave front reconstructor.

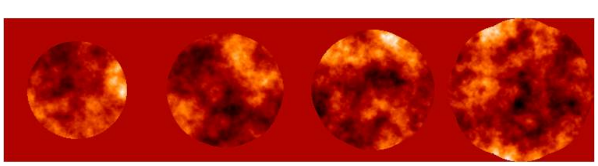

Fig. 3. Turbulent phase

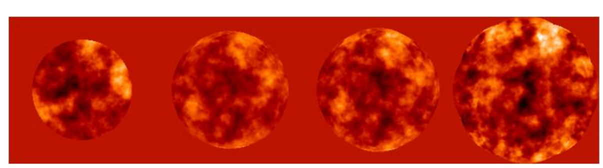

Fig. 4. estimated phase

Running on an octopro 2.1 GHZ and using the sparse End To End simulator we show in Figure 13 the result of the simulation for a different dimension of the telescope and where we reach the 42m for about 4min.

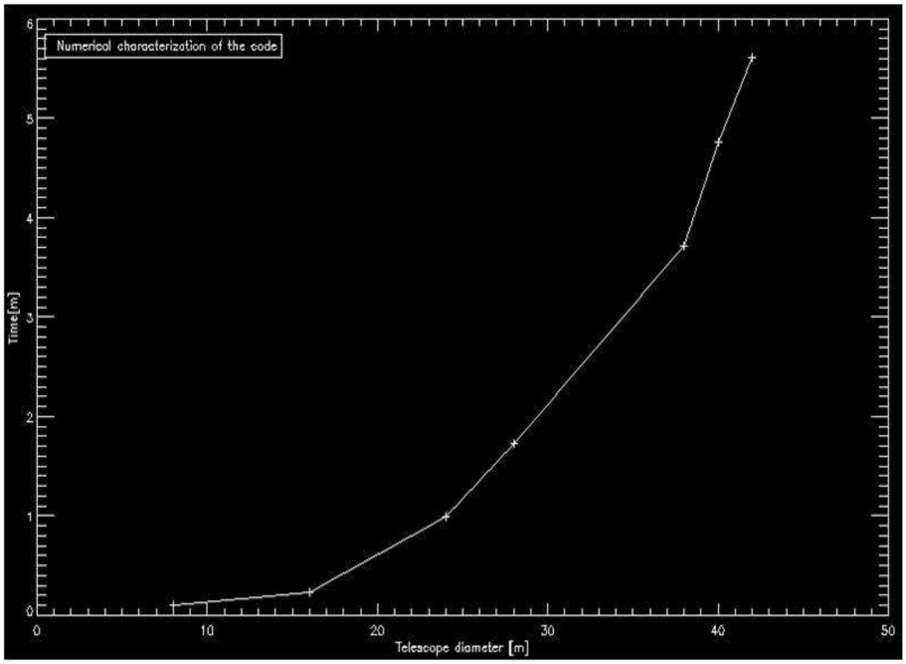

Fig. 5. Time characterization of the E2E sparse simulator

We demonstrate above the efficiency of the sparse matrix simulator for an AO system for the ELT, and as shown we are going 100 times fast then a CAOS E2E simulator running on the same octoprocessor.

6 Conclusion and perspective

We have presented an Adaptive Optics E2E simulator which includes a very fast wave front reconstruction which is dedicated for the Extremely Large Telescope.
Our code takes advantages of the SOY library, where we build the interaction and reconstruction matrix in a sparse format. Based on a script for solving linear systems by conjugate gradient with Jacobi preconditioner , our reconstruction matrix is computed very fast.
Moreover, this simulator is going 100 times faster then a present simulator running on the same octoprocessor. The objective of developing this code is to obtain an E2E simulator for wide field of view instruments for ELTs and more spcifically for an MOAO instrument such as Eagle on the E-ELT. The next step of our work, on which we are currently working to acheive this objective is the implementation of the laser guide stars and the wave front sensor such as Shack-Hartmann.

References

Carbillet, M., Vérinaud, C., Guarracino, M. et al. 2004, Proceedings of the SPIE, Volume 5490, 637

Carbillet, M., Vrinaud, C., Femenía, B. et al. 2005, MNRAS, 356, 1263

Rousset, G. 1999, in *Adaptive Optics in Astronomy*, F. Roddier (ed) (Cambridge: Cambridge University Press), p. 91

SOME RESULTS ON DISTURBANCE REJECTION CONTROL FOR AN ADAPTIVE OPTICS SYSTEM

J.-P. Folcher[1], A. Abelli[1], A. Ferrari[1] and M. Carbillet[1]

Abstract. Using linear quadratic gaussian (LQG) control theory, we propose a disturbance rejection control for an adaptive optics (AO) system. An a posteriori frequency analysis of the AO multivariable feedback system is carried out to check stability and robustness properties. We present numerical simulations to demonstrate the effectiveness of the proposed approach.

Keywords: adaptive optics, linear quadratic gaussian control, MIMO feedback analysis

1 LQG disturbance rejection control for an AO system

1.1 LQG state-space system

Deformable mirror (DM) and wavefront sensor (WFS) dynamics are assumed linear and determined by their influence matrices and pure delays (command input, measured output) as in Kulcsár et al. (2000). An autoregressive (AR) system describes the time evolution of the atmospheric wavefront. The obtained LQG discrete-time state-space system is diagonal and separates the plant dynamics (DM & WFS) and the disturbance dynamics (AR model). Thus, the AO control problem can be formulated as a LQG disturbance rejection control problem, see Bitmead et al. (1990); Folcher et al. (2010).

1.2 Control objectives & LQG design

Good adaptive optics performance (resulting in high Strehl ratios in the data) is obtained when the residual wavefront variance is weak. Keeping DM command input in an admissible range is also an important control objective. These two specifications can be translated in terms of the LQG cost criterion (to be minimized) for the given state-space system. The solution of the LQG problem, called the LQG controller, is simply the combination of a linear quadratic regulator (LQR) and a linear quadratic estimator (Kalman filter). The separation principle (see Kwakernaak and Sivan (1972); Anderson and Moore (1990)) guarantees that optimal state feedback gain and optimal observer gain can be computed independently. Moreover, for this specific disturbance rejection problem, the gains computation involve the resolution of reduced order Algebraic Riccati equations. This makes this control problem amenable to an efficient numerical solution.

2 Numerical simulations

2.1 Main parameters

For numerical modeling purposes, the `Software Package CAOS` Carbillet et al. (2005) is used to generate 1000×1 ms wavefronts propagated through an evolving 3-layers turbulent atmosphere (r_0=10 cm at λ=500 nm, $\mathcal{L}_0$=25 m, wind velocities=8–16 m/s). We consider an 8-m telescope, with 0.1 obstruction ratio. Wavefronts are projected over a Zernike polynomials base of size 15. DM controls perfectly low spatial frequencies: the influence matrix is $M_m = I_{n_b}$. An 8×8 (⇒52) subaperture Shack-Hartmann WFS (8×8 0.2" px/subap., λ_0=700 nm) is choosen. The WFS influence matrix M_w was previously determined numerically (interaction matrix computed through simulation of the AO system calibration).

[1] UMR 6525 H. Fizeau, Université de Nice Sophia Antipolis/CNRS/OCA, Parc Valrose, 06108 Nice Cedex 2, France

2.2 LQG controller design

The sampling period is T=1 ms, and command input and measured ouptut delays are considered unitary. The weighting matrice R, which defines the minimized LQG quadratic cost is fixed to R=10^{-2}. Two WFS noise levels are considered: V=$10^{-2}I$ (design 1) and V=$10^{-4}I$ (design 2), for which we obtain two candidate controllers. We invite the interested reader to consult the companion paper Folcher et al. (2010) for more details.

2.3 Frequency analysis of the AO multivariable feedback system

The residual wavefront variance control objective can be written in the frequency domain for given atmospheric wavefront's power spectral density, and WFS noise's power spectral density. This relation (see Kulcsár et al. (2000)) gives constraints on the frequency response of the residual wavefront rejection transfer function and the measurement noise rejection transfert function. The singular value plot of these highly multivariable transfer functions are given in the companion paper Folcher et al. (2010) for the two candidate controllers. Design 2 rejects better the residual wavefront, but is more sensitive to measurement noise. Singular values of residual wavefront rejection transfer function also exhibits a higher resonant factor which indicates a weak input stability margin. The frequency analysis selects the controller of design 1 as the final controller.

2.4 Time responses

Three components of the signal w_a (Zernike coefficients from the simulated atmospheric wavefronts) and residual wavefront coefficients w_r are plotted in Fig. 1. LQG controller rejects the atmospheric perturbation: residual wavefront coefficients w_r are reduced by a factor of 100.

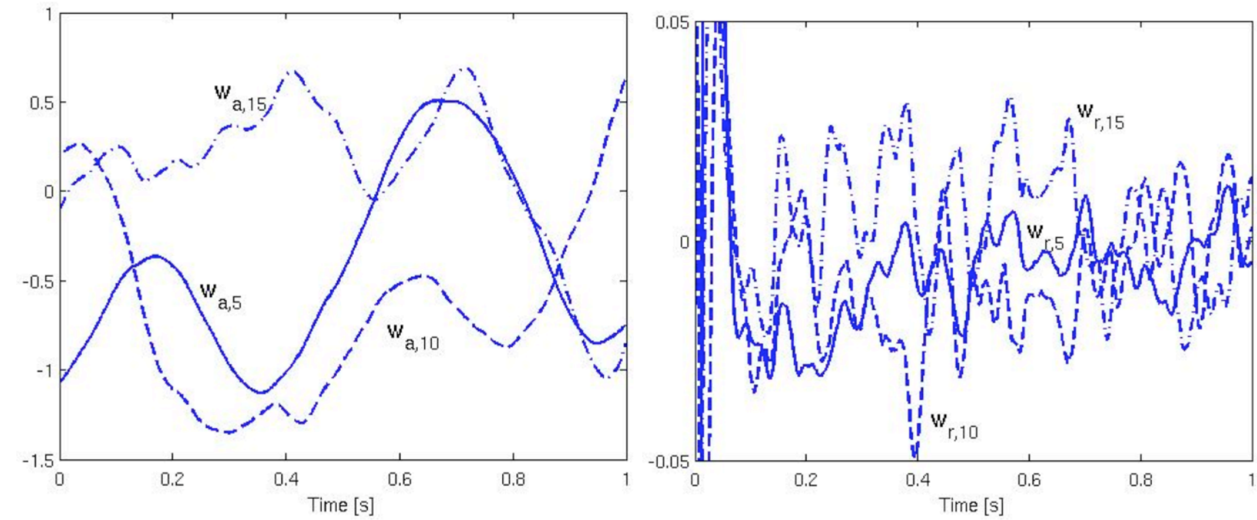

Fig. 1. Time evolution of w_a (on the left) and w_r (on the right) for the 5th mode (plain line), for the 10th mode (dashed line), and for the 15th mode (dashed-dot line).

As a result of this test simulation: on the 15 Zernike modes controlled, the total standard deviation drops down from ∼1030 nm to ∼30 nm (all modes standard deviation: ∼1150 nm, uncorrected modes: ∼500 nm).

References

Anderson, B., & Moore, J. B. 1990, Optimal Control: Linear Quadratic Methods, Prentice-Hall

Bitmead, R., Gevers, M., & Wertz, V. 1990, Adaptive Optimal Control: the Thinking Man's GPC, Prentice Hall.

Carbillet, M., Vérinaud, C. , Femenía, B., Riccardi, A., & Fini, L. 2005, MNRAS, 356, 1263

Folcher, J.-P., Abelli, A., Ferrari, A., & Carbillet, M. 2010, Adaptive Optics Systems II, Proceedings of SPIE, 7736-4F

Kulcsár, C., Raynaud, H.F., Petit, C., Conan, J.M., & de Lesegno, P.V. 2000, Appl. Opt, 39, 2525

Kwakernaak, H., & Sivan, R. 1972, Linear Optimal Control Systems, Wiley-Interscience New York.

SF2A 2010
S. Boissier, M. Heydari-Malayeri, R. Samadi and D. Valls-Gabaud (eds)

UTILIZATION OF THE ENSEMBLE KALMAN FILTER: AN OPTIMAL CONTROL LAW FOR THE ADAPTIVE OPTICS OF THE E-ELT

M. Gray[1] and B. Le Roux[1]

Abstract. Adaptive Optics (AO) systems require the implementation of techniques intended for real time identification of atmospheric turbulence. Nowadays there are several approaches. One of them is using the Kalman Filter (KF) and presents numerous advantages at the level of optimal control. However it will be impossible to install this process within the frame of an AO system for any ELT class telescope because of the quantitative leap in the number of parameters (high dimensional system) and consequently the quantitative leap in the cost in real time processes. First of all, we briefly give some backgrounds of AO on 8-10 m class telescopes and the utilization of the KF for an optimal control law. Then we present the Ensemble Kalman Filter (EnKF), a recent method tried and tested in Geophysics and which is particularly well suited for a transition to a very high number of parameters. After a description from a general point of view, we shortly present the numerical implementation and two main approaches for simplifying the matrix equations of the estimation in order to reduce the computational complexities of this technique. Finally, we propose some different perspectives and future works of this approach.

Keywords: adaptive optics, E-ELT, Kalman filter

1 Background

1.1 Adaptive Optics command on 8-10 m class telescopes

In a standard AO system, the wave front sensor which gives a measurement of the wave front shape is located after the corrector element, a Deformable Mirror (DM). The wave front sensor gives then access to the shape of the residual phase. From its measurements, one has to compute the new optimal voltages to apply on the DM. The whole system therefore works in a closed loop. The usual control law for classical AO on standard 8-10 m class telescopes is made of a simple integrator control law on which the integrator gain has eventually been optimized with respect of the signal to noise ratio, in order to minimize the propagation of the noise mode by mode. When the phase is decomposed on a basis of modes, it in fact appears that the signal to noise ratio can be different on each mode. It becomes then possible to adjust the integrator gain on each mode.
Unfortunately, this approach on special AO systems, such as wide field AO, does not allow to correct efficiently the turbulence because in those cases, some energetic modes have a very poor signal to noise ratio.
It becomes then necessary to estimate those modes and not only to filter them : the Kalman Filter (KF) based control law allows this estimation.

1.2 Utilization of the KF and notations used for the Multi Conjugate AO (MCAO) on 8-10 m class telescopes

On a 8-10 m class telescope, the KF based control law improves the performance of wide field of view AO systems (MCAO for example), thanks to its ability to estimate the badly seen modes (with a low signal to noise ratio). It is also very helpful in eXtreme AO systems to predict and compensate the telescope vibration's effects. We will use the notations and the structure of the control law presented for MCAO in Le Roux et al. (2004) and Petit et al. (2009). For the hidden state vector, we choose an expression with the turbulence phase at 3 successive instants and the DM's voltages at 2 successive instants :

[1] LAM/OAMP, Pôle de l'Étoile, site de Château-Gombert, 38 rue F. Joliot-Curie, 13388 Marseille Cedex 13, France

$$X_k = \left((\varphi^{tur}_{k+1})^T \quad (\varphi^{tur}_{k})^T \quad (\varphi^{tur}_{k-1})^T \quad (u_{k-1})^T \quad (u_{k-2})^T \right)^T$$

We have a linear state space model whose solution in the Gaussian case is given by the KF :

$$X^{(1)}_{k+1} = \begin{bmatrix} A_{tur} & 0 & 0 \\ Id & 0 & 0 \\ 0 & Id & 0 \end{bmatrix} X^{(1)}_k + \begin{bmatrix} Id \\ 0 \\ 0 \end{bmatrix} V_k \quad ; \quad X^{(2)}_{k+1} = \begin{bmatrix} 0 & 0 \\ Id & 0 \end{bmatrix} X^{(2)}_k + \begin{bmatrix} Id \\ 0 \end{bmatrix} u_k$$

and : $\quad Y_k = \begin{bmatrix} 0 & 0 & DM^L_\alpha \end{bmatrix} \times X^{(1)}_k + \begin{bmatrix} 0 & -DM^M_\alpha N \end{bmatrix} \times X^{(2)}_k + W_k$

The estimation of the predicting state vector is : $\hat{X}^{(1)}_{k+1/k} = A^{(1)} \times \hat{X}^{(1)}_{k/k-1} + A^{(1)} \times H_k \times [Y_k - \hat{Y}_{k/k-1}]$

with : $\hat{Y}_{k/k-1} = C^{(1)} \times \hat{X}^{(1)}_{k/k-1} + C^{(2)} \times X^{(2)}_k$

The Kalman gain is : $H_k = \Sigma^{(1)}_{k/k-1} C^{(1)T} \times [C^{(1)} \Sigma^{(1)}_{k/k-1} C^{(1)T} + \sum_w]^{-1}$

with the Riccati equation : $\Sigma^{(1)}_{k+1/k} = A^{(1)} \Sigma^{(1)}_{k/k-1} A^{(1)T} - A^{(1)} H_k C^{(1)} \Sigma^{(1)}_{k/k-1} A^{(1)T} + \sum_v$

1.3 Limitations of the KF for the AO systems of the E-ELT

Such a control law would be very helpful on an ELT class telescope. But it is becoming to much computing demanding, as the number of parameters increases dramatically. If the dimension n of the state vector is large (about 10^5 for the E-ELT), then computing and storing large n×n covariance matrices is impossible and the products for the estimation error's covariance matrices are even more problematic to work out.

2 The Ensemble Kalman Filter (EnKF) for the AO systems of ELT class telescopes

2.1 Presentation and theoretical concepts of the EnKF

The idea will be ***to use Monte Carlo samples*** and *not to use* the exact estimation error's covariance matrices. EnKF represents a distribution of the system state using a random sample, called an ensemble, and replace the covariance matrices by the sample covariance matrices computed from the ensemble.
EnKF is a Monte Carlo approximation of the KF which avoids evolving the real covariance matrices.
First of all, an initial ensemble of N_s elements is simulated as Independent Identically Distributed (IID) Gaussian random vectors with the same statistics as the initial condition X_0 : $\hat{X}^1_{0/0}$; ... ; $\hat{X}^{N_s}_{0/0}$
During the ***prediction step***, given the previous analysis ensemble, each ensemble element i is propagated independently according to the state equation (i is an integer from 1 to N_s) :

$$\hat{X}^i_{k/k-1} = A \times \hat{X}^i_{k-1/k-1} + V^i_k$$

We have to notice that IID random vectors V^i_k are simulated with the same statistics as the additive Gaussian model noise V_k in the original state's equation. We can then calculate :
the empirical estimation mean vector : $m^{N_s}_{k/k-1} = \frac{1}{N_s} \times \sum_{i=1}^{N_s} \hat{X}^i_{k/k-1}$
and the empirical estimation error's covariance matrix :

$$P^{N_s}_{k/k-1} = \frac{1}{N_s - 1} \times \sum_{i=1}^{N_s} (\hat{X}^i_{k/k-1} - m^{N_s}_{k/k-1})(\hat{X}^i_{k/k-1} - m^{N_s}_{k/k-1})^T$$

During the ***correction step***, given the previous forecast ensemble, each ensemble element i is updated independently according to the estimation equation :

$$\hat{X}^i_{k/k} = \hat{X}^i_{k/k-1} + H_k(P^{N_s}_{k/k-1}) \times [Y_k + W^i_k - C \times \hat{X}^i_{k/k-1}]$$

We have to notice that IID random vectors W^i_k are simulated with the same statistics as the additive Gaussian measurement noise W_k in the original observation's equation. But there are 2 approaches (see 3.3 and 3.4) : the covariance matrix $\sum_w$ can be obtained from the randomized data or from the real measurement errors.
We can then calculate :
the empirical Kalman gain matrix : $H_k(P^{N_s}_{k/k-1}) = P^{N_s}_{k/k-1} \times C^T \times [C \times P^{N_s}_{k/k-1} \times C^T + \sum_w]^{-1}$
the empirical estimation mean vector : $m^{N_s}_{k/k} = \frac{1}{N_s} \times \sum_{i=1}^{N_s} \hat{X}^i_{k/k}$
The ensemble covariance matrix $P^{N_s}_{k/k-1}$ is computed from all ensemble members together which introduces dependence and destroys the normality of the ensemble distribution. But Mandel et al. (2009) gives a mathematical proof of the convergence of the EnKF in the limit for large ensembles to the KF (large ensembles are in fact nearly IID and nearly normal). In Geophysics, they usually use a value of N_s between 50 to 100.

2.2 Utilization of the EnKF for the AO systems of the ELT class telescopes

The EnKF allows to bring on an ELT all the advantages of the state space formalism of a KF based control law. The ability of estimating the unseen modes for wide field AO remains critical. On an ELT class telescope, the ability to filter out vibration's modes thanks to an adapted state space model can also become fundamental, as the vibrations of an ELT class telescope is a critical issue.

3 Numerical Implementation of the EnKF

3.1 Implementation of the EnKF

It can be shown (Evensen (2003); Mandel (2006)) that, during the correction step, the *vectorial equation* can be rewritten with this new *matrix equation* :

$$\hat{X}_{k/k} = \hat{X}_{k/k-1} + \frac{Z_k(CZ_k)^T}{N_s-1} \times [\frac{(CZ_k)(CZ_k)^T}{N_s-1} + \Sigma_w]^{-1} \times [D_k - C\hat{X}_{k/k-1}]$$

with : $Z_k = \hat{X}_{k/k-1} \times [I_{N_s} - \frac{1}{N_s} \times J_{N_s}]$ and J_{N_s} a matrix with each element is equal to 1.

3.2 Computational Complexities of the EnKF

For the estimation of the computational complexity of this formula, we will only consider the number of multiplications. We just have to know that the multiplication of a matrix of size $n_1 \times n_2$ by a matrix of size $n_2 \times n_3$ has a *numerical cost of* $n_1 \times n_2 \times n_3$ *multiplications*. This cost is noticed : $O(n_1 \times n_2 \times n_3)$.
We have also to remind that : n is the number of coordinates in the state's vector X_k, p is the number of coordinates in the observation's vector Y_k, and N_s is the number of elements in the ensemble.

3.3 Evensen's Approach

The observations D_k are treated as random variables having a distribution with mean equal to the first-guess observations and covariance matrix equal to Σ_w (the simulated random measurement errors W_k^i have a mean equal to zero). We define the ensemble covariance matrix of the measurements as : $\Sigma_w = \frac{1}{N_s-1} \times \sum_{i=1}^{N_s} W^i W^{iT}$
As Evensen wrote : "the actual observation error covariance matrix is poorly known and the errors introduced by the ensemble representation can be made less than the initial uncertainty in the exact form of Σ_w. Further, the errors introduced by using an ensemble representation for Σ_w have less impact than the use of an ensemble representation of matrix $P_{k/k-1}^{N_s}$."
Using a Single Value Decomposition (SVD), a pseudo inversion and with the assumption of uncorrelated forecast elements and measurement errors, for the correction step, the new estimation's formula is :

$$\hat{X}_{k/k} = \hat{X}_{k/k-1} + Z_k(CZ_k)^T \times O_1(\Sigma\Sigma^T)^{\dagger} O_1^T \times [D_k - C\hat{X}_{k/k-1}]$$

The total computational complexity obtained is : $O(N_s^2 \times (n+p))$
which is **linear** and **suitable** for large values of n and p.

3.4 Mandel's Approach

The matrix Σ_w is the covariance matrix of the real measurement errors rather than the sample covariance matrix of the randomized data. Because Σ_w is always positive definite, there will be no difficulty to compute $\Sigma_w = SS^T$ (very low cost) and calculate the inverse Σ_w^{-1}. Moreover, there will be no need to use a pseudo inversion or a SVD on a large matrix.
Using the Sherman-Morrison-Woodbury formula and a Cholesky decomposition on a small matrix (its size is only $N_s \times N_s$), for the correction step, the new estimation's formula is :

$$\hat{X}_{k/k} = \hat{X}_{k/k-1} + \frac{Z_k(S^{-1}CZ_k)^T}{N_s-1}\{I_p - \frac{S^{-1}CZ_k}{N_s-1}[I_{N_s} + \frac{(S^{-1}CZ_k)^T(S^{-1}CZ_k)}{N_s-1}]^{-1}(S^{-1}CZ_k)^T\}S^{-1}[D_k - C\hat{X}_{k/k-1}]$$

The total computational complexity obtained is : $O(N_s^3 + N_s^2 \times (n+p))$
which is **linear** and **suitable** for large values of n and p.

3.5 Comparisons

These two implementation techniques have a **linear computational complexity** *in the number of degrees of freedom* $\boldsymbol{n}$ and *in the number of degrees of observation* $\boldsymbol{p}$ (with a proportional factor N_s^2).
However the method used by Mandel involves symmetric products of matrices which is numerically more stable and allows to save memory.
The problems using a low rank measurement error covariance matrix pointed out by Kepert (2004) are resolved in Evensen (2004) where he introduced a new Square Root implementation of the EnKF.

4 Conclusions

We have made a brief and simple description of two different efficient implementations of the EnKF (with a linear complexity) in order to use it as an optimal control law for the AO systems of the ELT class telescopes. This version described here involves randomization of data. But some alternative methods (without randomization of data) based on Square Root analysis schemes and the Ensemble Transform Kalman Filter (ETKF) seem to be very promising : some theoretical studies on the links between ETKF and the AO/MCAO for the E-ELT will be therefore deepened. The next step will be to adapt the current routines in order to implement them on our AO simulator for different numerical simulations. Then some works on the hardware and software design will be made to obtain precious gain in the real time identification. And finally, we will compare our results with those obtained in the other existing methods for the AO systems of ELT class telescopes.

References

Burgers, G. et al. 1998, Analysis Scheme in the Ensemble Kalman Filter, Monthly Weather Review, 126, 1719-1724

Evensen, G. 2003, The Ensemble Kalman Filter : Theorical Formulation and Practical Implementation, Ocean Dynamics, 53, 343-367

Evensen, G. 2004, Sampling Strategies and Square Root Analysis Schemes for EnKF, Ocean Dynamics, 54, 539-560

Evensen, G. 2009, Data assimilation : The Ensemble Kalman Filter, Springer Verlag, Berlin

Kepert, J. 2004, On ensemble representation of the observation-error covariance in the Ensemble Kalman Filter, Ocean Dynamics, 54, 561-569

Le Roux, B. et al. 2004, Optimal Control Law for Classical and Multiconjugate Adaptive Optics, J. Opt. Soc. Am. A., Vol 21, n° 7, 1261-1276

Mandel, J. 2006, Efficient Implementation of the Ensemble Kalman Filter, Center for Computational Mathematics Reports, N° 231

Mandel, J. et al. 2009, On the Convergence of the Ensemble Kalman Filter, `http://arxiv.org/abs/0901.2951`

Petit, C. et al. 2009, LQG control for Adaptive Optics and Multiconjugate Adaptive Optics : experimental and numerical analysis, J. Opt. Soc. Am. A., Vol 26, n° 6, 1307-1325

SPACE ACTIVE OPTICS: IN SITU COMPENSATION OF LIGHTWEIGHT PRIMARY MIRRORS' DEFORMATIONS

M. Laslandes[1], M. Ferrari[1], E. Hugot[1] and G. Lemaitre[1]

Abstract. The need for both high quality images and light structures is a constant concern in the conception of space telescopes. The goal here is to determine how an active optics system could be embarked on a satellite in order to correct the wave front deformations of the optical train. The optical aberrations appearing in a space environment are due to mirrors' deformations, with three main origins: the thermal variations, the weightlessness conditions and the use of large weightlighted primary mirrors. We are developing a model of deformable mirror as minimalist as possible, especially in term of number of actuators, which is able to correct the first Zernike polynomials in a specified range of amplitude and precision. Flight constraints as weight, volume and power consumption are considered. Firstly, such a system is designed according to the equations from the elasticity theory: we determine the geometrical and mechanical characteristics of the mirror, the location of the forces to be applied and the way to apply them. Then the concept is validated with a Finite Element Analysis, allowing to optimize the system by taking into account parameters absent from the theory. At the end, the mirror will be realized and characterized in a representative optical configuration.

Keywords: active optics, elasticity, aberrations correction, deformable mirror, space telescope

1 Introduction

The need for both high quality images and light structures is a constant concern in the conception of space telescopes. In this paper, we present an active optics system as a way to fulfill those two objectives. Indeed, active optics consists in controlling mirrors' deformations in order to improve the images quality (Freeman 1982). The two main applications of active optics techniques are the in-situ compensation of phase errors in a wave front by using a corrector deformable mirror (Wilson 1987) and the manufacturing of aspherical mirrors by stress polishing or by in-situ stressing (Hugot 2009). We will focus here on the wave-front correction. Indeed, the next generation of space telescopes will have lightweight primary mirrors; in consequence, they will be sensitive to the environment variations, inducing optical aberrations in the instrument.

An active optics system is principally composed of a deformable mirror, a wave-front sensor, a set of actuators deforming the mirror and control/command electronics. It is used to correct the wave-front errors due to the optical design, the manufacturing imperfections, the large lightweight primary mirrors' deflection in field gravity, the fixation devices, and the mirrors and structures' thermal distortions due to the local turbulence (Kendrew 2006). Active optics is based on the elasticity theory (Lemaitre 2009); forces and/or load are used to deform a mirror. Like in adaptive optics, actuators can simply be placed under the optical surface (Wilson 1987), but other configurations have also been studied: a systems simplification, inducing a minimization of the number of actuators can be achieved by working on the mirror design (Lemaitre 2009). For instance, in the so called Vase form Multimode Deformable Mirror (Lemaitre 2005), forces are applied on an external ring clamped on the pupil. With this method, there is no local effect due to the application of forces on the mirror's back face. Furthermore, the number of actuators needed to warp the mirror does not depend on the pupil size; it is a fully scalable configuration.

The insertion of a Vase form Multimode Deformable Mirror on the design of an optical instrument will allow correcting the most common low spatial frequency aberrations. This concept could be applied in a space telescope. A Finite Element Analysis of the developed model has been conducted in order to characterize the systems behavior and to validate the concept.

[1] Laboratoire d'Astrophysique de Marseille (CNRS and Université de Provence) - 38 rue F. Joliot Curie - 13388 Marseille cedex 13 - France

2 Vase form Multi-mode Deformable Mirror

2.1 Needs in space

Lightweight primary mirrors of space telescope will loose their best shape mainly because of the thermal dilatation and the weightlessness conditions (Kendrew 2006). It will induce Optical Path Differences (OPD) in the instrument corresponding to the first optical aberrations.
Following previous studies in close collaboration with the French space agency (CNES) and space industry, we can assume that correcting the first 9 optical modes Spherical3, Coma3, Astigmatism3&5, Trefoil5&7 and Tetrafoil7&9 is enough to significantly improve the wave-front quality. The rms amplitude of the wave-front to be corrected is chosen on the order of $\lambda = 632.8$ nm with a required precision of $\lambda/20$ rms in Wave-Front for each mode. The design of the correcting mirror for such an application has also to consider some particular constraints such as the weight, the volume, the power consumption or the resistance to the launch vibrations (CNES 1998).

2.2 Principles of deformation and design

A Vase form Multi-mode Deformable Mirror (VMDM) is composed of a circular meniscus, an outer ring of biggest thickness and k_m arms regularly clamped on the ring. The deformation of the pupil is obtain by applying a set of $2k_m$ forces located on the ring and at the end of each arm.
As demonstrated by Lemaitre (2005), such a system can compensate a set of Zernike polynomials verifying $n = m$ or $n = m + 2$ (with n and m the radial and azimuthal orders).Given the symmetry of the modes needed to be generated to meet our specifications, we have chosen to use a mirror with 12 arms, allowing creating the deformations in several orientations. Furthermore, in order to correct the spherical aberration, a central clamping on the back face of the mirror, fixed at its base, is added relatively to the usual VMDM design (Fig.1).
In order to have a light system, the dimensions of the studied mirror have been reduced to a minimum: the diameter of the equipped mirror (including the arms) is set to 130 mm. All the mirror's characteristics have been optimized to obtain the most efficient system possible. For that purpose, a Finite Element Analysis (FEA) has been performed.

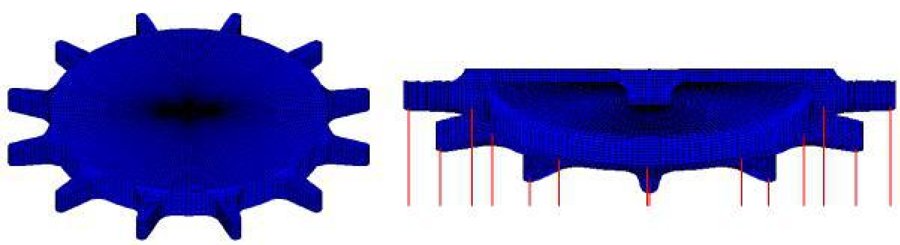

Fig. 1. Finite Elements model of the studied VMDM (77879 nodes, 63708 hexaedrical elements)

3 Correcting system performances

3.1 Influence Functions and Eigen Modes

Leaning on a VMDM's FEA model (Fig. 1), we develop a method to determine the needed forces using the phase decomposition on the mirror's influence functions base (Gray 2008; Paterson 2000). The influence function of an actuator, ϕ_i^{IF}, is the resulting mirror surface shape when that actuator is given a unit command. For a VMDM configuration, there are two types of influence functions: the deformation maps when we push the end of the arm, and when we push on the ring. The influence functions base gives also access to the system's eigen modes. They are shown in Figure2 They are very close to optical aberrations and represent an orthogonal base of the system: linear combinations of them give all the deformations that the system is able to produce. The modes are classified from the less to the more energetic.
The decomposition on the mirror's influence functions or eigen modes allows characterizing the mirror in a fast and accurate way. In the FEA model, we acquire the $2k_m$ influence functions. The decomposition of a phase map on this characteristic base permits to reconstruct the deformation that the system is able to generate. Comparing it to the initial phase, the precision of the correction is determined.

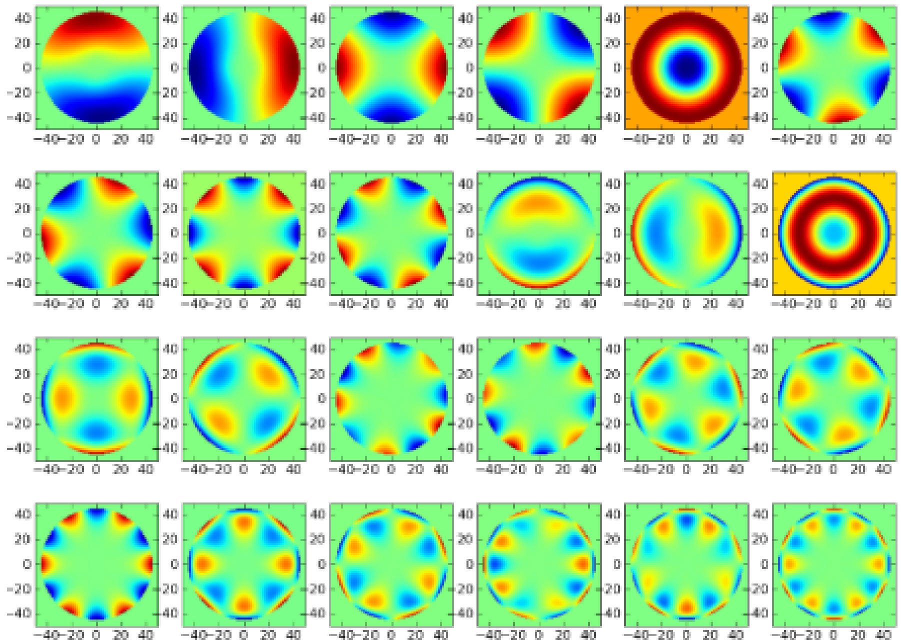

Fig. 2. Mirror's Eigen Modes

3.2 Precision of correction

The purity of each mode is determined by calculating the residues obtained when the aberration is corrected with an amplitude of λ. The results are presented in Figure3, left. With less than 2% of residues, the Coma3, Trefoil5 and Astigmatism3 are precisely corrected (WFE< $\lambda/60$ rms). Trefoil7, Tetrafoil7 and Astigmatism5 can be generated with 5% of residues and they are just at the $\lambda/20$ specification. On the other hand, the Spherical3 and Tetrafoil9 aberrations induce more residues (around $\lambda/8$). We can note that residues mainly come from the presence of the central clamping and from the difference between the modes' symmetry and the mirror symmetry. The residues projection on the Zernike polynomials base shows that they are composed of harmonics of the considered aberration.
The projection on the influence functions base gives the values of displacement to be applied in order to generate the given phase. Applying those values in the FEA model we can visualize the mirror deformation (Fig3, right). This last step allows us to validate the decomposition method and to study the system behavior (displacements, stress in the material etc.).

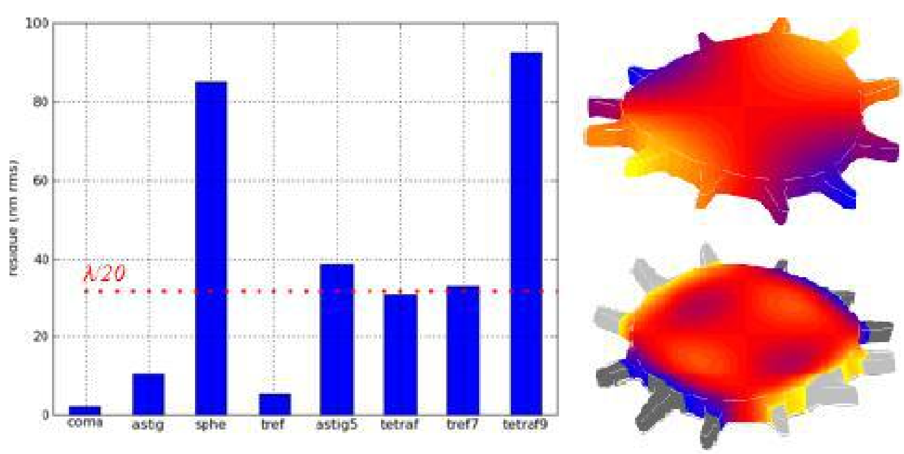

Fig. 3. Left: Residues for a modal correction of 1λ - Right: Mirror deformation corresponding to Astigmatism3&5

It is important to study the mirror's performances in a situation close to the real functioning of this correcting system. In such a case, the wave-front to be corrected will be a combination of the 8 modes presented before plus others minors terms. Because the generation of Spherical3 and Tetrafoil9 induces a too much residues, we decide to correct them only up to an amplitude of $\lambda/3$, so that the amount of residue is lower than $\lambda/20$ for each mode.
Firstly, we consider the worst case: the incident phase is composed of the 8 aberrations at their maximum amplitude. The residual error is then about $\lambda/8$ rms.
To have a representative idea of what the system can achieve, we calculate the residues after the correction of a random phase map. The OPD map is created by adding all the modes, balancing them with a random coefficient between 0 and their maximum corrigible amplitude. Studying the statistics after several random draws gives the expected mean precision achievable by the system. For 1000 random maps, the mean precision correction achieved is around $\lambda/15$ rms with a standard deviation of $\lambda/60$.

4 Conclusions

The very simple concept of Vase form Multimode Deformable Mirror seems to be applicable and very efficient to improve the wave-front quality in a space telescope. We have seen in this paper that it allows correcting, with a good quality, the first Zernike polynomials: Comas, Astigmatisms, Trefoils and Tetrafoils. The spherical aberration can also be generated with the presence of a central clamping on the mirror's back face. In addition, this holds the entire system. A system with 12 arms is preferred because it can easily create shapes of several symmetries. To characterize the system, we have considered the mirror's influence functions and eigen modes. Knowing these characteristics, the correction capabilities have been determined for each mode separately and for more representative phases. With this work, we have defined some specifications for the amplitudes that can be corrected in an efficient way.
The Comas3, Astigmatisms3&5, Trefoils5&7 and Terafoils7 are easily generated at amplitudes around 1λ rms with a precision better than $\lambda/20$ rms. The corrections of Spherical3 and Tetrafoils9 require more energy and are less precise; we choose to correct them at a maximal amplitude of $\lambda/3$ rms to obtain the same precision. The element inducing a significant part of the residues is the central clamping, but it allows the generation of Spherical3 despite the absence of an uniform load. Simulating the correction of random phase maps, the mean residual phase is around $\lambda/15$ rms.
Those results are promising for the application of such a concept to the compensation of the deformations in a large space telescope. The next step is to realize a prototype of this correcting mirror and test it in a representative configuration.

Acknowledgments
This study is performed with the support of a Ph.D grant from CNES (Centre National d'Etudes Spatiales) and Thales Alenia Space, within a project of the Research and Industry Optical Cluster 'PopSud/Optitec'.

References

CNES, 'Techniques & Technologies des Véhicules Spatiaux', Cours de Technologie Spatiale Volume 1, 1998

Freeman, R., Pearson, J., 'Deformable Mirrors for all Seasons and Reasons', Applied Optics, Vol. 21, No. 4, 1982

Gray, T., 'Minimizing High Spatial Frequency Residual in Active Space Telescope Mirrors', PhD Thesis, 2008

Hugot, E. et al, 'Active Optics: Stress Polishing of Toric Mirrors for the VLT SPHERE Adaptive Optics System', Applied Optics, Vol. 48, No. 15, 2009

Kendrew, S., 'Lightweight Deformable Mirrors for Ground- and Space-Based Imaging Systems', PhD Thesis, 2006

Lemaitre, G., 'Active Optics: Vase or Meniscus Multimode Deformable Mirrors and Degenerated Monomode Configurations', Meccanica 40, 233-249, 2005

Lemaitre, G. 'Astronomical Optics and Elasticity Theory Active Optics Methods', Springer, 2009

Paterson, C., Munro, I., Dainty, J.C., 'A Low Cost Adaptive Optics System Using a Membrane Mirror', Optics Express 175, Vol. 6, No. 9, 2000

Wilson, R., Franza, F., Noethe, L., 'Active Optics I. A System for Optimizing the Optical Quality and Reducing the Costs of Large Telescopes', Journal of Modern Optics, Vol. 34, No.4, 1987

SF2A 2010
S. Boissier, M. Heydari-Malayeri, R. Samadi and D. Valls-Gabaud (eds)

VISIBLE SPECTROSCOPY OF TERRESTRIAL EXOPLANETS WITH SEE-COAST

A.-L. Maire[1], R. Galicher[2], A. Boccaletti[1], J. Schneider[2], P. Baudoz[1] and the SEE-COAST team

Abstract. While more than 450 exoplanets have been discovered, mid-infrared photometry and near-infrared (NIR) low-resolution spectroscopy were obtained for a few transiting gazeous planets. Nevertheless, the transit method is limited to close-in planets ($\lesssim$0.1 AU). To study the chemical composition and structure of the atmosphere of wide-separated planets ($\gtrsim$1 AU), direct imaging is requested. To date, 12 planet candidates were detected by this method. In a near future (2011-2014), ground-based instruments (SPHERE, GPI, HiCIAO) and the James Webb Space Telescope (JWST) will survey a large sample of gazeous planets around young and M-dwarf stars in the solar neighborhood. To characterize terrestrial planets, extremely good and stable conditions as in space are required. Our team propose the SEE-COAST mission, a 1.5-m space telescope, that aims at visible spectro-polarimetry of mature giant and massive terrestrial planets. Here we briefly recall the principle of this mission and its objectives. We detailed the image analysis used to retrieve the planet spectra and we present the performance of SEE-COAST obtained by numerical simulations.

Keywords: exoplanets, high contrast imaging, coronagraph, imaging spectroscopy, numerical simulations

1 Exoplanet characterization

The exoplanet research passed from a detection stage to a characterization one with photometric and spectroscopic measurements of the atmosphere of transiting giant planets (see e.g. Swain et al. 2009; Tinetti et al. 2010). However, the transit method is more appropriated to close-in exoplanets ($\lesssim$0.1 AU). The other method to investigate the physical properties of exoplanets is direct imaging which is complementary to transits by studying the diversity of planet separations beyond 1 AU. This provides observational constraints to theoretical mechanisms of planetary formation. Nevertheless, this technique is difficult to carry out because it necessitates both high contrast and high angular resolution. The 12 planet candidates already detected have physical characteristics favorable to direct imaging like a large separation from the host star (>8 AU), a large mass (>1 M_{Jup}) and a young age (<300 Myr).

Planet finder instruments (2011) like SPHERE (Beuzit et al. 2006) on the Very Large Telescope, GPI (Macintosh et al. 2006) on the Gemini telescope and HiCIAO (Tamura et al. 2006) on the Subaru telescope, and the JWST (2014) will analyze a large sample of young giant planets down to the Jupiter mass in the NIR. Extremely large telescopes (∼2020) are expected to extend this sample towards less massive and mature planets ideally down to super-Earths (terrestrial planets with a mass up to 10 M_{Earth}). However, ground-based instruments will probably be unable to characterize telluric planets due to the limitations of adaptive optics in terms of long-time performance and stability, the day/night cycle and most of all the atmospheric absorption. Ambitious space projects like Darwin and Terrestrial Planet Finder concepts will be devoted to this objective but they are technically difficult and planned for the long-term (>2030). It is now mostly admitted that mid-term (2020−2022) precursory missions are required to prepare these missions. They will also be complementary to extremely large telescopes and other mid- and long-term planned instruments by addressing different science cases.

[1] Observatoire de Paris, LESIA, CNRS UMR 8109, 92195 Meudon, France
[2] Observatoire de Paris, LUTh, CNRS UMR 8102, 92195 Meudon, France

2 The SEE-COAST mission

In the context detailed in the previous section, our team propose a 1.5-m coronagraphic space telescope named SEE-COAST (Super-Earth Explorer - Coronagraphic Off-Axis Space Telescope). For further informations on the scientific objectives and instrumental concept, the reader is referred to the following papers: Schneider et al. (2006); Boccaletti et al. (2008); Schneider et al. (2009). Here we briefly recall the main characteristics of this mission. It aims at visible spectroscopy and polarimetry of a sample of giant and massive terrestrial exoplanets previously discovered by NIR direct imaging (SPHERE/GPI/HiCIAO), radial velocities or astrometry. The scientific motivation is twofold. First, the flux reflected (visible light) by a planet gives informations on the chemical composition of its atmosphere. It also depends on its radius, albedo and phase angle. With theoretical mass-radius relations, we can deduce the albedo which brings informations about the planet surface type. Then, the measurement of the degree of polarization of the reflected light completes the spectral data by providing informations on the physics of atmospheres (clouds, hazes and so on) and the existence of oceans at the surface (Stam 2008). SEE-COAST was proposed as a M-class mission to the first ESA Cosmic Vision call for proposals in 2007 but it was not selected. We will submit a slightly evolved project called SPICES (Spectro-Polarimetric Imaging and Characterization of Exoplanetary Systems) to the new call in december 2010.

Fig. 1 explains how to derive the SEE-COAST contrast and angular resolution requirements from its planet targets. It represents the planet/star contrast in reflected light for giant and telluric planets orbiting a G0V star at 0.4 μm. The blue, green and red vertical lines represent the contrast curves for a 1.5-m coronagraphic telescope characterized by a 2-λ/D inner working angle and a 10^{-10}-contrast for a star distance of 2, 10 and 20 pc. SEE-COAST must achieve a contrast of about 10^{-10} and have a diameter at least equal to 1.5 m to analyze massive telluric planets until $\sim$15 pc.

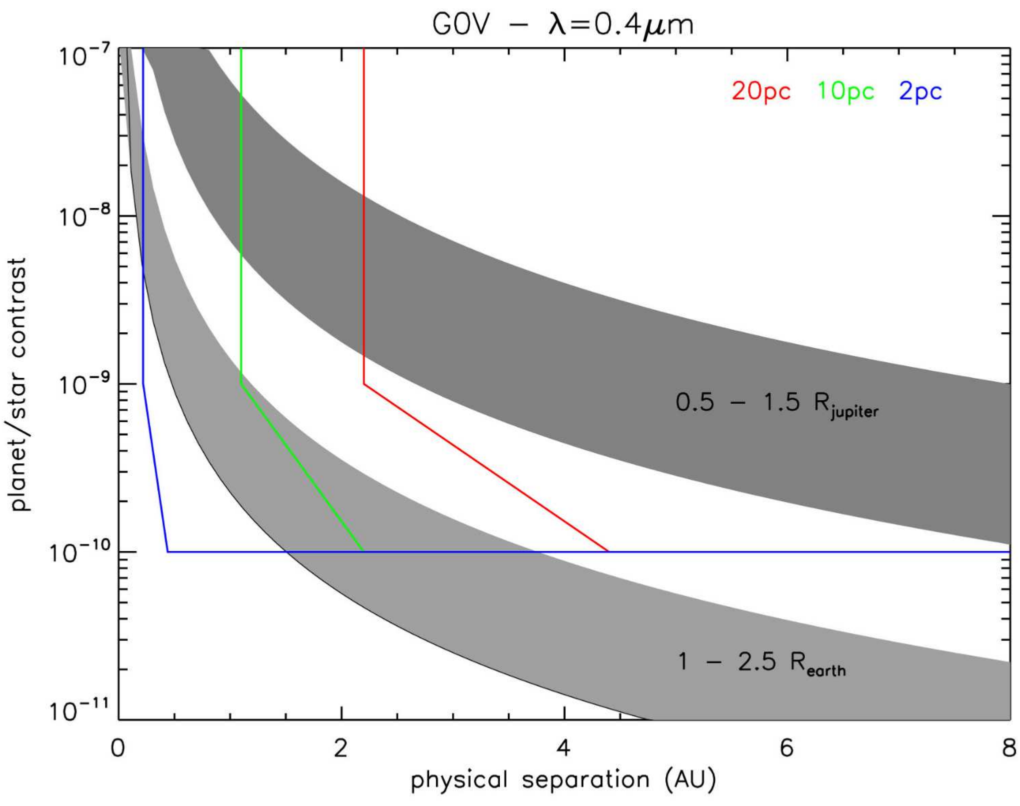

Fig. 1. SEE-COAST instrumental requirements derived from its planet targets.

2.1 Numerical simulations

Fig. 2 is a block diagram of the SEE-COAST instrumental baseline. It comprises an off-axis telescope, a coronagraph to attenuate the starlight, a deformable mirror (DM) and an integral field spectrometer (IFS) associated to a polarimeter. We use an off-axis telescope because the attenuation power of a coronagraph is degraded by a mirror obscuration. The coronagraph performance is also sensitive to the wavefront aberrations upstream it. In space, they are due to imperfections in the optical components which induce a "quasi-static" speckle field (Baudoz et al. 2006). We use a DM to correct for the mirror aberrations to avoid very stringent polishing constraints on it (<5 nm rms; for comparison the value for the HST is 20 nm rms but we aim to reach a slightly lower value for SEE-COAST). However, the DM correction is not perfect (finite number of actuators) and image analysis is required to remove the non-corrected speckles to detect faint planets. We use two techniques. At small separations ($\lesssim$10 λ/D), the self-coherent camera (SCC) distinguishes planets from speckles using the incoherence of the starlight with the planet light (Baudoz et al. 2006). The spectral deconvolution (SD) technique discriminates them because the speckle distance from the image center varies with the observation wavelength whereas the planet one does not (Sparks & Ford 2002). This technique is efficient for planet separations $\gtrsim$10 λ/D.

We chose a peculiar instrumental configuration for this paper. The main characteristics are a 1.5-m primary mirror, no central obscuration, 20-nm rms phase aberrations, no amplitude aberrations, a 32x32 DM, an achromatic four-quadrant phase mask coronagraph (Rouan et al. 2000) and a 30-channel IFS covering the 0.5−0.95 μm spectral bandwidth (spectral resolution of ∼49). We currently carry out simulations to refine the design for the ESA proposal in next december but it will not differ a lot from the current one.

2.2 First results

The left panel of Fig. 3 shows the SEE-COAST performance without photon noise before and after speckle calibration by the SCC. The calibration efficiency decreases with the angular separation because of the channel chromaticity (Baudoz et al. 2006). Then we study the impact of photon noise assuming that the observed source is a 10-pc G2V star, the global instrument transmission is 15% and the sole noise sources are speckle and photon noises. The right panel of Fig. 3 presents the performance after speckle calibration for two exposure times. After 10 hours, the profiles have achieved a contrast inferior to 10^{-8} between 1 and 7 λ/D but 72 hours are needed to reach a few 10^{-9}-contrast in the same region. As the instrument is limited by the sole photon noise, longer exposures enable to reach very high contrasts. This point will however limit SEE-COAST to the study of nearby systems ($\lesssim$25 pc).

To confirm the conclusions drawn from the 5-σ detection radial profiles, we introduced spectra of a Jupiter-like planet and a super-Earth orbiting a G2V star and calculated the signal-to-noise ratio (SNR) of the continuum and the spectral lines obtained with the SEE-COAST concept. The left panel of Fig. 4 shows the spectrum of a Jupiter-like planet at 2 AU at a 10-pc distance after 72 hours (model from Burrows et al. 2004). The right panel of Fig. 4 represents the spectrum of a super-Earth at 1 AU at a distance of 6 pc after 100 hours (model from Stam 2008). Note that the y-axis scale is different between the two plots. Table 1 gives the SNR of the main features of the Jupiter (top) and the super-Earth (bottom) spectra. For the Jupiter, we correctly measure the continuum <0.77 μm and the methane spectral line at 0.62 μm but not the other methane features. For the super-Earth, the continuum and the spectral lines of water at 0.72 μm and dioxygen at 0.76 μm are well retrieved but the SNR values for the 0.6-μm ozone line and the 0.82-μm water line are moderate.

Table 1. SNR for the continuum and the major spectral lines of the Jupiter-like planet (top) and the super-Earth (bottom) spectra.

Feature	continuum < 0.77 μm	0.62-μm CH_4 line	0.74-μm CH_4 line	0.89-μm CH_4 line
SNR	11.5 (mean)	12.8	2.8	2.3 (edges)

Feature	continuum	0.6-μm O_3 line	0.72-μm H_2O line	0.76-μm O_2 line	0.82-μm H_2O line
SNR	9.5 (mean)	4.8	11.8	13.9	6.5

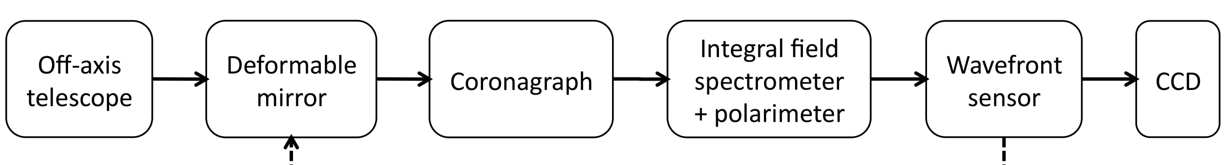

Fig. 2. Block diagram of the SEE-COAST instrumental baseline.

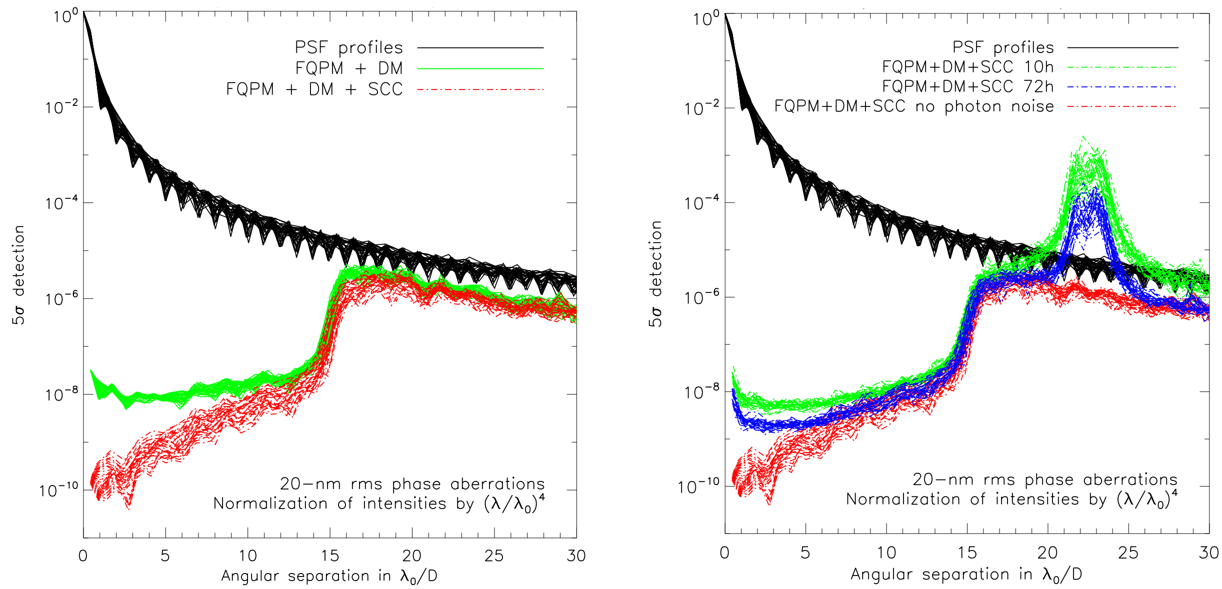

Fig. 3. 5-σ detection radial profiles of the SEE-COAST concept obtained before and after SCC speckle calibration without photon noise (left) and after SCC speckle calibration for two levels of photon noise and without photon noise (right).

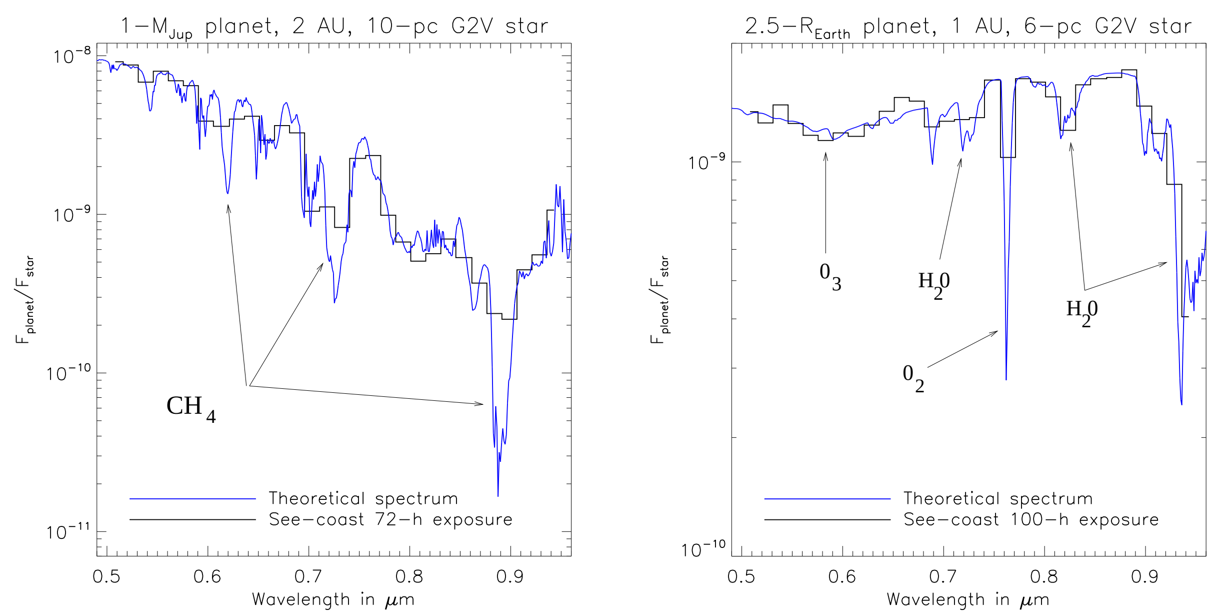

Fig. 4. Spectra of a Jupiter-like planet (left) and a super-Earth (right) measured by SEE-COAST.

3 Conclusions

The objective of the SEE-COAST spacecraft (now renamed SPICES) is the visible spectro-polarimetric characterization of Jupiter-like planets down to super-Earths. It will be complementary to future projects of NIR direct imaging and transit spectroscopy by dealing with different science cases. It will also be a precursor to ambitious Terrestrial Planet Finder concepts. In this paper, we presented the performance of a peculiar instrumental configuration without and with photon noise. Speckle noise is calibrated at a contrast level of about 10^{-10} very close to the star image ($\sim 2\ \lambda/D$). The instrument is limited by the sole photon noise and will be able to characterize only nearby targets ($\lesssim$25 pc). Then, we compared spectra of a Jupiter-like planet and a super-Earth retrieved by SEE-COAST with the theoretical ones: the continuum and the spectral features above a contrast of 10^{-9} are correctly measured in 3-4 days. Currently, we are refining the instrumental configuration for the next ESA proposal. We account for other types of aberrations (Fresnel propagation and amplitude aberrations) and other noise sources. Then, we will study the retrieval of planet spectra for different kinds of planets and stars both in spectroscopy and polarimetry.

References

Baudoz, P., Boccaletti, A., Baudrand, J., & Rouan, D. 2006, in IAU Colloq. 200: Direct Imaging of Exoplanets: Science & Techniques

Beuzit, J.-L., Feldt, M., Dohlen, K., et al. 2006, The Messenger, 125, 29

Boccaletti, A., Schneider, J., Tinetti, G., et al. 2008, in SF2A-2008, ed. C. Charbonnel, F. Combes, & R. Samadi, 61

Burrows, A., Sudarsky, D., & Hubeny, I. 2004, ApJ, 609, 407

Macintosh, B., Graham, J., Palmer, D., et al. 2006, in SPIE Conf. Series, Vol. 6272, 62720L

Rouan, D., Riaud, P., Boccaletti, A., Clénet, Y., & Labeyrie, A. 2000, PASP, 112, 1479

Schneider, J., Boccaletti, A., Mawet, D., et al. 2009, Exp. Astron., 23, 357

Schneider, J., Riaud, P., Tinetti, G., et al. 2006, in SF2A-2006, ed. D. Barret, F. Casoli, G. Lagache, A. Lecavelier, & L. Pagani, 429

Sparks, W. B. & Ford, H. C. 2002, ApJ, 578, 543

Stam, D. M. 2008, A&A, 482, 989

Swain, M. R., Vasisht, G., Tinetti, G., et al. 2009, ApJL, 690, L114

Tamura, M., Hodapp, K., Takami, H., et al. 2006, in SPIE Conf. Series, Vol. 6269, 62690V

Tinetti, G., Deroo, P., Swain, M. R., et al. 2010, ApJL, 712, L139

SF2A 2010
S. Boissier, M. Heydari-Malayeri, R. Samadi and D. Valls-Gabaud (eds)

EXPERIMENTAL ADVANCES IN PHASE MASK CORONAGRAPHY

M. N'Diaye[1,2], K. Dohlen[1], S. Cuevas[2], R. Soummer[3] and C. Sánchez[4]

Abstract. Stellar coronagraphy is a key technology for current and future instruments for exoplanet imaging and spectroscopy, both on the ground and in space. We pursue the research on coronagraphs based on circular phase-masks and report in this paper on recent advances in terms of the trade between spectral bandwidth and achievable contrast. Circular phase masks combined with colored apodizations prove to be promising options in such coronagraphic systems to reach high contrast gains within the search area over a wide band of wavelengths.

Keywords: high angular resolution, coronagraphy

1 Introduction

Detection by direct imaging and spectral analysis of the exoplanets represent some very exciting but challenging issues in contemporary astronomy. Once very high angular resolution images obtained, downstream high contrast imaging techniques are required to observe faint sources close to bright stars. In this context, several coronagraphic concepts were proposed these past few years to remove the light of an observed star.
Coronagraphs using phase masks prove to be very promising concepts since high contrast levels can theoretically be achieved with them at very small separations from an observed bright star. In particular, circular phase masks present the advantage to be less sensitive to the telescope central obscuration than other phase mask concepts, like the sectorised phase mask family (e.g. see Lloyd et al. 2003). The Roddier & Roddier phase mask (RRPM) was the first circular phase mask concept proposed within this approach (Roddier & Roddier 1997). In its apodized version, it can completely suppress the diffraction pattern of a monochromatic point source (Soummer et al. 2003a). This concept is however greatly limited when it deals with large spectral bandwidths. The Dual Zone phase mask (DZPM, Soummer et al. 2003b) constitutes an improvement of this RRPM since it was conceived to overcome the limits met by the RRPM in the presence of a polychromatic point source. The first design of the DZPM coronagraph has been realized considering a grey (or achromatic) apodization.
In this paper, we report an improvement of the DZPM coronagraphic design, replacing the grey by a colored (or chromatic) apodization, to increase the performance of the DZPM coronagraph over the whole considered spectral bandwidth. Theoretical contrast levels achieved by the colored apodized DZPM coronagraph will be compared with those of the grey apodized DZPM coronagraph and manufacturing aspects will be analyzed.

2 The DZPM coronagraph

Roddier & Roddier (1997) proposed an improvement of the classical Lyot coronagraph by replacing the opaque occulting mask by a small and transparent π-phase shifting mask (also called RRPM). They showed that if the core of the stellar diffraction pattern is delayed by a π-phase change, the original object wave and the wave diffracted by the phase mask interfere destructively within the geometrical pupil image, displacing most of the starlight into a halo surrounding the pupil. The rejected stellar light can be removed with the Lyot stop, leading to an important reduction of diffracted starlight in the final image projected onto a detector. A perfect starlight

[1] Laboratoire d'Astrophysique de Marseille, UMR6110, CNRS/Université de Provence, France
[2] Instituto de Astronomía, Universidad Nacional Autónoma de México (UNAM), Mexico
[3] Space Telescope Science Institute, 3700 San Martin Drive, Baltimore, MD 21218, USA
[4] Centro de Ciencias Aplicadas y Desarrollo Tecnológico, UNAM, Mexico

extinction can theoretically be reached in the monochromatic case with the addition of an optimized entrance pupil apodization(Soummer et al. 2003a).
Soummer et al. (2003b) proposed to modify the mask design to reach a quasi-perfect suppression of the star image over a large spectral bandwidth. He introduced a second annular phase mask to the initial phase mask, what leads to the design of a so-called dual-zone phase mask (DZPM) with two non π phase shifts. As for the RRPM, the contrast gain reached with the DZPM is improved by adding an entrance pupil apodization. The introduction of an entrance pupil apodization allows one to smooth the direct wave and make it match well with the sum of the waves diffracted by the two zones of the DZPM. The addition of a phase apodization typically in the form of mask defocus also leads to a closer null sum of the waves and then, an improvement of the coronagraphic performance.
In order to keep on improving the DZPM coronagraph performance, we propose to replace the grey by a colored apodization and thus, optimize the apodization transmission function at each wavelength within our spectral bandwidth.

3 Numerical simulations

For our numerical simulations, a circular aperture with $D = 42\,\mathrm{m}$ diameter and $\eta = 30\%$ central obscuration (E-ELT case) is considered. We assume a central wavelength $\lambda_0 = 1.65\,\mu\mathrm{m}$ and a bandwidth of 25.4% (H-band case). Concerning our optimization, the monochromatic intensity of the coronagraphic and non coronagraphic images is calculated at 5 wavelengths: $1.49\,\mu$m, $1.57\,\mu$m, $1.65\,\mu$m, $1.73\,\mu$m and $1.81\,\mu$m. For each wavelength λ, we average the intensity of the coronagraphic and non coronagraphic images over an annulus from $2\,\lambda_0/D$ to $10\,\lambda_0/D$ from the main optical axis. The averaged attenuation is obtained calculating the ratio of these mean intensity values. Once this done, we compute a merit function to estimate the quadratic sum of the averaged attenuations reached at each wavelength. A numerical least-squares method is used to obtain the DZPM parameters that maximize our merit function and therefore, achieve the best attenuation for simultaneously all the wavelengths of our study.

3.1 Numerical models analyzed for this study

Five numerical models for the DZPM coronagraph are studied here and involve several parameters. The mask diameters d_1 and d_2 and the phase steps, given in optical path difference OPD_1 and OPD_2, constitute the common characteristics to all of our concepts. The other parameters are related to the amplitude and phase apodization of the entrance pupil and can be grey (achromatic) or colored (chromatic) depending on the considered model. For the phase apodization, we work with radially symmetric aberrations of the first order and therefore, it can be obtained physically by defocussing the mask.
–The 1^{st} and 2^{nd} models are related to a grey apodized DZPM coronagraph. Their apodization parameters are then constant and estimated considering the best on-axis starlight extinction and the merit function defined above, for the 1^{st} and 2^{nd} models respectively.
–The 3^{rd} model is a colored apodized DZPM coronagraph and thus, the apodization parameters are chromatic and optimized independently at each wavelength of our study considering the merit function defined above.
–The 4^{th} and 5^{th} models constitute possible physical implementations of the 3^{rd} model. For the colored apodizer of the 4^{th} and 5^{th} models, we adopt a design using an absorbing material like color filter glass and an assembly based on a metallic thin film deposited on a silica substrate respectively.

3.2 Choice of the metal for the 5^{th} model

Preliminary studies have been realized to determine the choice of the metal for the 5^{th} model, see Figure 1. We have considered the chromatic extinction coefficient of different metals and a controlled thin film thickness of the used metal for different normalized radial distances r. Figure 1 is limited to the case $r = 0.324$ but results are quite similar for other radial distances and lead to the same conclusion. Using silver allows us to reach the closest amplitude apodization to that obtained with the 4^{th} model for all the wavelengths of our study. In the following, silver will be the metal considered for our simulations.

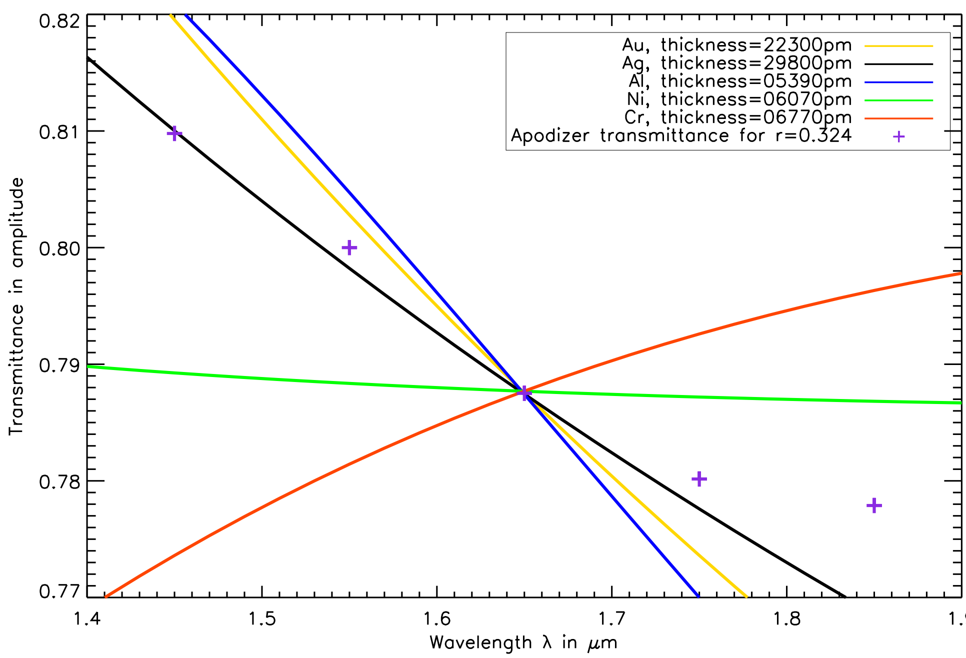

Fig. 1. Amplitude transmission values obtained with the assembly and the 4^{th} model as a function of the wavelength. Different metals with optimized thickness have been considered here for the assembly to obtain transmission values close to those of the 4^{th} model. These results are given for a normalized radial distance $r = 0.324$.

3.3 Results in the image plane

As a first approximation, we have considered the sum of the monochromatic images obtained at each wavelength of our study to simulate polychromatic images reached with each concept. Radial intensity profiles of the polychromatic images obtained in the presence or not of the DZPM have been calculated for all of our models, see Figure 2 left plot. The non coronagraphic profiles achieved with the different models are almost identical one to each other since the amplitude apodizations used for each concept present very similar transmission functions and throughput T of about 58%, see Figure 2 right plot. A summary of the performance for all of our models is given in Table 1. For each concept, we have calculated the intensity level reached at three different angular separations from the star: $2\,\lambda_0/D$, $5\,\lambda_0/D$ and $8\,\lambda_0/D$. Model 3 is our best possible design using an optimization of the apodizer chromaticity. The contrast at $5\,\lambda/D$ is improved by a factor 4-5 or more compared the gray apodizer design. Model 4 & 5, represent a practical implementation using color filter glass and a silver deposit for the apodization resp. Contrast performance is within a factor 2 of the theoretical optimal solution from model 3 (at $5\,\lambda/D$).

Table 1. Comparison of the contrast levels theoretically achieved with the different models of DZPM coronagraph.

Model	**Level at**		
	$2\,\lambda_0/D$	$5\,\lambda_0/D$	$8\,\lambda_0/D$
1	1.39×10^{-5}	5.33×10^{-7}	1.03×10^{-7}
2	1.11×10^{-5}	4.56×10^{-7}	9.59×10^{-8}
3	5.02×10^{-6}	1.10×10^{-7}	1.70×10^{-8}
4	5.55×10^{-6}	1.61×10^{-7}	2.79×10^{-8}
5	5.10×10^{-6}	1.96×10^{-7}	3.69×10^{-8}

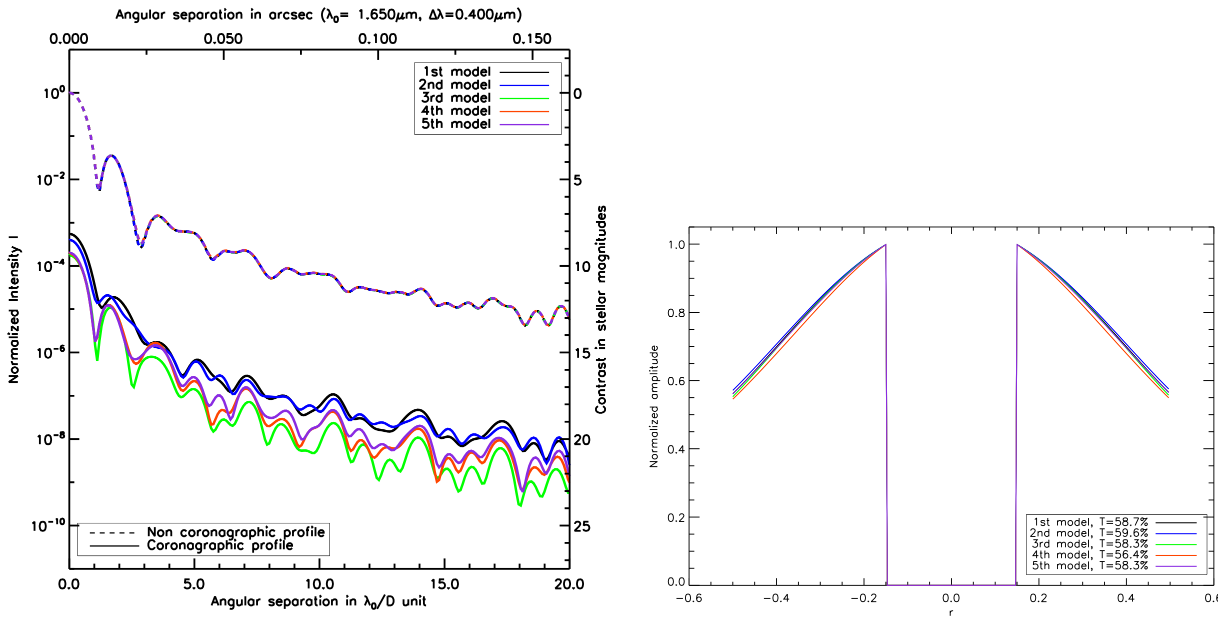

Fig. 2. Left: radial profiles of the images achieved in the presence or not of the DZPM for the different models of our study. **Right**: radial profiles of the amplitude apodization at $\lambda = 1.65\,\mu$m for each of our models. Values of the throughput T is given for each model.

4 Manufacturing aspects

In the following, we analyze manufacturing aspects related to the 5^{th} model. Concerning the phase masks, DZPM prototypes with good quality profiles have been manufactured by SILIOS Technologies. They will soon be tested in our laboratory in Marseilles. To manufacture the apodizer of the 5^{th} model and obtain the required amplitude transmission function for it, we consider the utilization of a typical silver ion exchange process (Findakly 1985) in a glass substrate through an aluminum mask which thickness gradually increases from outside the center of the substrate. Experiments are currently performed at the CCADET of UNAM. Finally, colored phase apodization is also used with the 5^{th} model and expressed as a radially symmetric aberration of the first order. This can be obtained physically by using a powerless lens doublet combined with a mask at the focus. The doublet characteristics are: an infinite focal length at λ_0, glasses with the same refractive index, the same Abbe number and very different partial dispersion.

5 Conclusion

In the context of high contrast imaging, the Dual Zone phase mask (DZPM) stellar coronagraph is a promising concept to remove starlight efficiently over a large spectral bandwidth. The focal plane mask, phase and amplitude apodizations constitute the characteristic elements of this coronagraph. The objective of this paper has consisted in reporting the last improvements made to optimize the performance of the DZPM coronagraph. We have replaced the grey by a colored apodization to increase the starlight attenuation within the search area of substellar mass companions. Afterwards, a physical model of this DZPM coronagraph with colored apodization, based on silver thin film deposited on a fused silica substrate, has been proposed. Encouraging performances have been reached numerically with this concept; some contrast levels of $5.10{\times}10^{-6}$ at $2\,\lambda_0/D$ and $1.96{\times}10^{-7}$ at $5\,\lambda_0/D$ can theoretically be achieved. This represents a mean gain in contrast of 1.23 mag with respect to the DZPM coronagraph using a grey apodizer and proposed by Soummer et al. (2003b). This result has been obtained considering a 25.4% spectral bandwidth (H-band case) and a centrally obstructed circular aperture (E-ELT case). Manufacturing aspects have also been analyzed here and prove to be very encouraging for the fabrication of the DZPM coronagraph.
These advanced studies are the prelude of experiments on the optical bench that we are currently mounting in our laboratory to test the DZPM coronagraph. Results are expected to be presented in a forthcoming paper.

References

Findakly, T. 1985, Opt. Eng., 24, 244

Lloyd, J. P., Gavel, D. T., Graham, J. R., et al. 2003, in Society of Photo-Optical Instrumentation Engineers (SPIE) Conference Series, Vol. 4860, Society of Photo-Optical Instrumentation Engineers (SPIE) Conference Series, ed. A. B. Schultz, 171–181

Roddier, F. & Roddier, C. 1997, PASP, 109, 815

Soummer, R., Aime, C., & Falloon, P. E. 2003a, A&A, 397, 1161

Soummer, R., Dohlen, K., & Aime, C. 2003b, A&A, 403, 369

SF2A 2010
S. Boissier, M. Heydari-Malayeri, R. Samadi and D. Valls-Gabaud (eds)

EXOPLANET CHARACTERIZATION USING ANGULAR AND SPECTRAL DIFFERENTIAL IMAGING

A. Vigan[1], C. Moutou[1], M. Langlois[2], F. Allard[3], A. Boccaletti[4], M. Carbillet[5], D. Mouillet[6] and I. Smith[5]

Abstract. In the near future, new high-contrast imaging instruments dedicated to the direct detection of exoplanets at large orbital separations will be installed at the focus of large ground-based telescopes. Data obtained with these instruments optimized for very high contrast are strongly limited by the speckle noise. Specific observing strategies and data analysis methods, such as angular and spectral differential imaging, are required to attenuate the noise level and possibly detect the faint planet flux. Even though these methods are very efficient at suppressing the speckles, the photometry of the faint planets is dominated by the speckle residuals and it has a direct impact on the determination of the physical parameters of the detected planets. We present here the simulations that have been performed in the context of IRDIS, the dual-band imager of VLT-SPHERE, to estimate the influence of the photometric error on exoplanet characterization. In particular we show that the expected photometric performances will allow the detection and characterization of exoplanets down to the Jupiter mass at angular separations of 1.0" and 0.2" respectively around high mass and low mass stars with 2 observations in different filter pairs. We also show that the determination of the planets physical parameters from photometric measurements in different filter pairs is essentially limited by the error on the determination of the surface gravity.

Keywords: exoplanet, high-contrast imaging, instrument: VLT-SPHERE, IRDIS

1 Introduction

Most of the exoplanets currently known have been detected with indirect methods such as radial velocities or transits. Although these methods are mainly sensitive to planets at small orbital separations ($\lesssim$ 5 AU), some stars are showing long-term trends that may indicate the presence of distant planetary companions. The wide use of adaptive optics systems on large ground-based telescopes has recently allowed to start probing for low mass companions at large orbital distances from nearby stars, leading to the image of the first exoplanet in 2005 around the young brown dwarf 2MASSW-J1207334-393254. In the following years, a handful of these objects have been imaged with existing instruments.

SPHERE (Spectro-Polarimetric High-conrast Exoplanet REsearch; Beuzit et al. 2006) is a second generation instrument for the VLT (Very Large Telescope) at ESO-Paranal Observatory which will be dedicated to the direct detection of exoplanets and low mass companions around nearby stars. Similar instruments are currently being built for other telescopes, such as GPI for Gemini South and HiCIAO for Subaru. This next generation of instruments aims at detecting young exoplanets down to the Jupiter mass ($M_{\rm Jup}$) by reaching contrast values of 10^{-6} to 10^{-7} at angular separations as small as $\sim$0.1$''$ with extreme adaptive optics systems and coronagraphy. SPHERE will have two scientific instruments working in the near-infrared: a diffraction-limited integral field spectrograph, and a differential spectro-imager (Dohlen et al. 2008), IRDIS. IRDIS will support several observing modes including Dual-Band Imaging (DBI) which will provide simultaneous images at two close wavelengths in

[1] LAM, UMR 6110, CNRS, Université de Provence, 38 rue Frédéric Joliot-Curie, 13388 Marseille Cedex 13, France
[2] CRAL, UMR 5574, CNRS, Université Lyon 1, 9 avenue Charles André, 69561 Saint Genis Laval Cedex, France
[3] CRAL, UMR 5574, CNRS, Université Lyon 1, ENS Lyon, 46 allée d'Italie, 69364 Lyon Cedex 07, France
[4] LESIA, UMR 8109, Obs. de Paris, CNRS, Université Paris-Diderot, 5 place Jules Janssen, 92195 Meudon Cedex, France
[5] Laboratoire Fizeau, UMR 6525, CNRS, Université de Nice, Obs. de la Côte d'Azur, Parc Valrose, 06108 Nice Cedex 2, France
[6] LAOG, UMR 5571, CNRS, Université Joseph-Fourier, BP 53, 38041 Grenoble Cedex 9, France

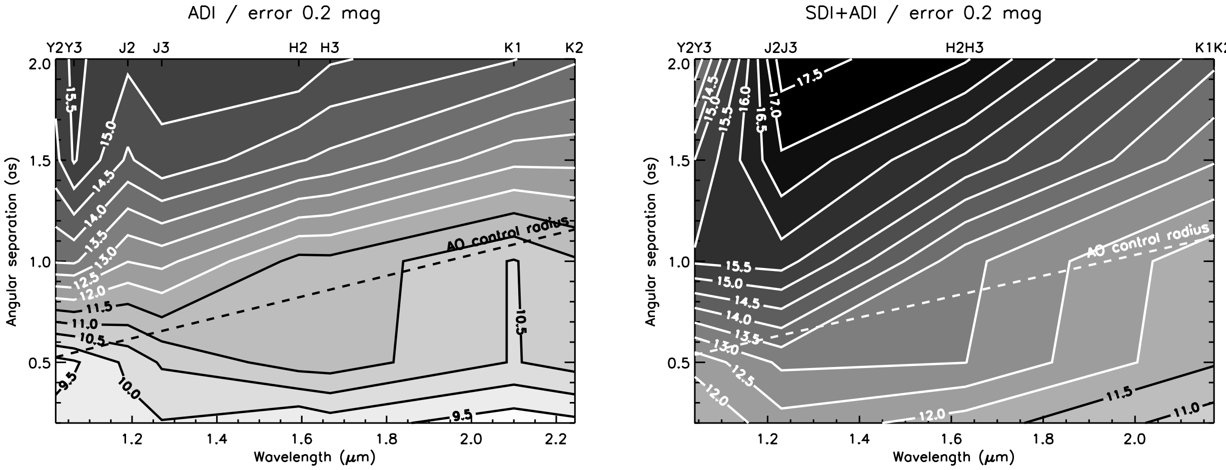

Fig. 1. Star-planet contrast at which a photometric precision of 0.2 mag is reached as a function of wavelength and angular separation for data analyzed with ADI (left) and SDI+ADI (right). Figures from Vigan et al. (2010).

one of its 5 different filter pairs covering Y to Ks bands. The IFS will be diffraction-limited in the near-infrared and will provide spectra from Y to H bands.

An end-to-end model of the SPHERE instrument has been developed to test the performances of the instrument (Carbillet et al. 2008). This code, written in IDL, includes a large number of effects at different spatial and temporal scales. It allowed us to simulate a realistic 4 hours observation sequence with IRDIS of a star at a declination $\delta = -45°$ covering hour angles of -2 hr to +2 hr with an anodized pupil Lyot coronagraph. Fake planets have been introduced into the data cubes, and photometry was calculated to represent different planetary systems with contrast values from $\sim$15 to $\sim$17.5 mag. These data cubes have been used to study the photometric accuracy, which can be expected after using different data analysis methods, and the consequences in terms of mass estimation of the detected objects.

2 Photometric accuracy

Data analysis methods are necessary to attenuate the quasi-static speckle noise, which is an intrinsic limit in high-contrast images (Soummer et al. 2007). We used three different methods: Spectral Differential Imaging (SDI; Racine et al. 1999), Angular Differential Imaging (ADI; Marois et al. 2006) and their combination (SDI+ADI). The flux of the detected objects in the different data cubes analyzed with these methods has been estimated with aperture photometry an compared to the original value to measure the photometric error.

Figure 1 presents the photometric performance which can be expected for 5-σ detections: It shows the star-planet contrast at which a 0.2 mag precision is reached as a function of wavelength and angular separation, for ADI and SDI+ADI data analysis methods. Two interesting effects are visible: (1) the photometric performance clearly depends on wavelength, and (ii) there are two different regimes depending on the position compared to the AO control radius. The first effect is directly related to the chromaticity of the PSF: in speckle-limited regime the noise attenuation is almost constant with angular separation compared to the corona graphic profile, and the level of the coronagraphic profile linearly depends on wavelength. The second effect is related to the AO correction inside the control radius. Inside that region we see a stabilization of the performance, while outside, the photometric performance increases almost linearly with angular separation at all wavelengths. These effects are more visible with ADI because in the case of SDI+ADI, a large part of the chromatic effects have been removed by the SDI part of the analysis.

3 Characterization performances

These empirical photometric performances have then been used to estimate the characterization capabilities of IRDIS in DBI mode. We have created a new simulation in which we have tested for a large number of planetary atmosphere models our ability to determine the physical parameters T_{eff} (effective temperature) and log g (surface gravity) of the objects. The principle of this simulation was to create a planetary system defined

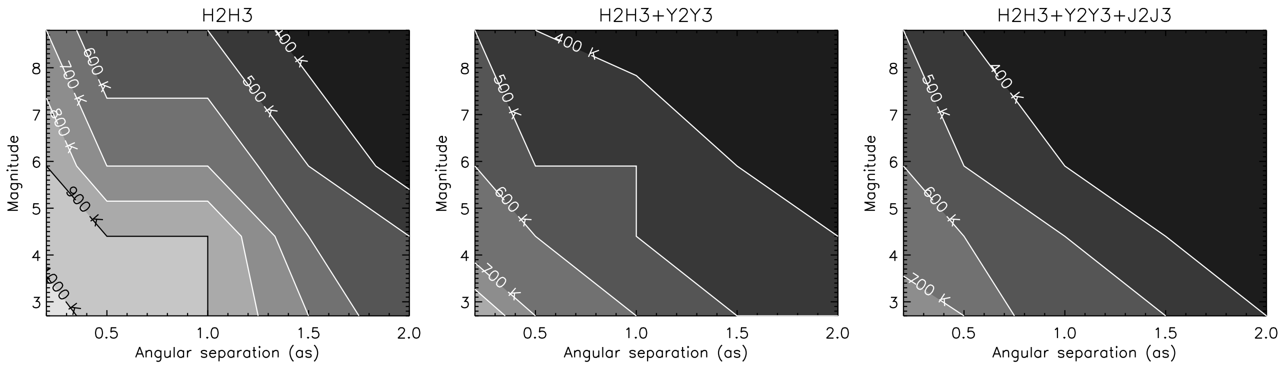

Fig. 2. Lowest T_{eff} which can be estimated as a function of angular separation and star V magnitude for observations with different filter pairs: H2H2 (left), H2H3+Y2Y3 (center) and H2H3+Y2Y3+J2J3 (right). Figure based on Vigan et al. (2010).

by the star magnitude (spectral type) and the planet $T_{eff}/\log g$, simulate an observation with different filter pairs, introduce a photometric error, and try to find out which planet model was used at the beginning of the simulation. All the possible filter pair combinations of IRDIS have been tested with a large sample of planetary atmosphere models (Allard et al. 2001, 2003, 2010 in preparation; Burrows et al. 2006).

This simulation allowed us to set priorities on the different filter pairs of IRDIS for faint objects characterization. H2H3 has the highest priority, followed by Y2Y3/J2J3 and H3H4/K1K2. These priorities are defined for characterization with no *a priori* information. For example, K1K2 or H3H4 filter pairs may reveal to be more interesting when the object is known to be warm. We have studied the lowest planet T_{eff}, which can be estimated using observations with different filter pairs. The results are showed in Fig. 2 where the lowest T_{eff} estimable is given as a function of angular separation and star V magnitude for filter pairs H2H3, H2H3+Y2Y3 and H2H3+Y2Y3+J2J3. We clearly see that using two or three filter pairs brings a large improvement. When using only H2H3, planets with T_{eff} down to 900 K should be characterized at an angular separation of $0.2''$ from bright stars and 700 K from fainter stars. Adding a second filter pair considerably improves these results by 200 K, while adding a third pair confirms these limiting values.

With the considered data analysis methods and according to the evolutionary models from Baraffe et al. (2003) for the COND atmosphere models, we can estimate that in a very young system of 10 Myr, we should be able to characterize a planet of 1 M_{Jup} with H2H3 at separations larger than $0.5''$ around a low mass star (M0 at 10 pc) where the star-planet contrast is favorable, but only further than $2.0''$ around a bright star (F0 at 10 pc) where the contrast difference is larger. With two filter pairs, the limit would be $0.2''$ around a faint star and $1.0''$ around bright star. For older systems, only planets of a few masses of Jupiter could be characterized. At 100 Myr, a Jupiter mass planet would remain out of reach for characterization with H2H3 filters around a bright star, and only at separations larger than $1.5''$ around fainter stars.

Finally, we have studied the impact of errors on the determination of T_{eff} and $\log g$ for hypothetical 2 M_{Jup} planets orbiting at 5 A.U. from M0 and F0 stars at 10 pc aged of 44 ± 30 Myr (average age and errors for young stars in the preliminary SPHERE target sample). According to the evolutionary models from Baraffe et al. (2003), such planets should have $T_{eff} = 516$ K and $\log g = 3.54$ dex, resulting in a contrast of 11.9 mag and 15.6 mag in H band respectively around the M0 and F0 stars. Around a faint star, the parameters T_{eff} and $\log g$ are estimated with an accuracy close to the one given by the atmosphere model grid ($1.9^{+1.3}_{-0.7}$ M_{Jup}), leading to an estimation of $1.9^{+1.2}_{-1.0}$ M_{Jup}. Around a high mass star, the planet is very close to the detection limit at $0.5''$, resulting in a poor estimation of both T_{eff} and $\log g$: the important photometric error in H2H3 leads to a very large uncertainty on $\log g$ (4.33 ± 1.23). The mass of the planet is then estimated to $1.1^{+2.6}_{-0.5}$ M_{Jup}.

4 Conclusion

We have studied the performances of IRDIS, the dual-band imager and spectrograph of SPHERE, for the characterization of faint planetary companions. We have performed detailed end-to-end numerical simulation to obtain realistic data cube representing various planetary systems, which we have used to study the photometric accuracy when using ADI and SDI+ADI data analysis methods. Using the best possible filter pairs sequence, we

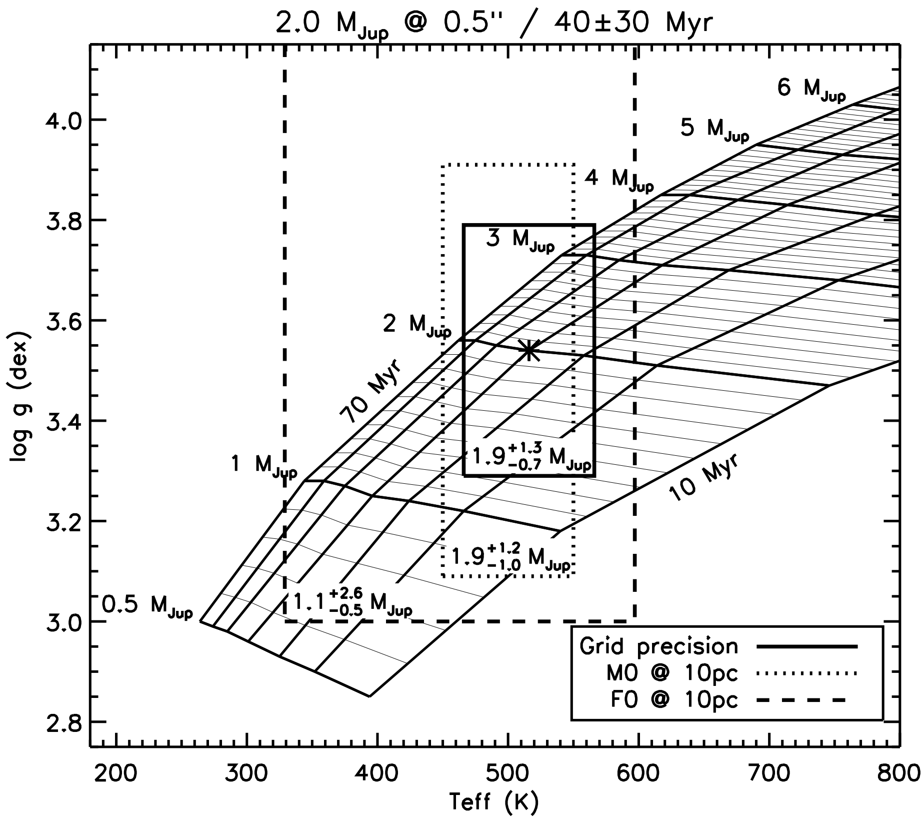

Fig. 3. Isochrones for the COND planetary atmosphere models covering an age of 40 ± 30 Myr used for the determination of the mass of hypothetical 2 M_{Jup} planets orbiting at 5 A.U. from M0 and F0 stars at 10 pc. The error boxes defined by the possible values for T_{eff} and log g of both planets are respectively represented by dotted and dashed rectangles. The position of the planet predicted by the evolutionary models is represented by the star symbol, and the error box defined by the atmosphere models grid precision is given by a plain rectangle. Figure from Vigan et al. (2010).

have studied the lowest T_{eff} of planet which can be estimated, concluding that we should be able to characterize a planet of 1 M_{Jup} with H2H3+Y2Y3 pairs at separations larger than 0.2″ around a low mass star (M0 at 10 pc) where the star-planet contrast is favorable, but only further than 1.0″ around a bright star (F0 at 10 pc). Finally, we have studied the impact of errors on T_{eff} and log g on the estimation of the planet mass. Around faint low mass stars, we should be able to almost reach the precision of the model grids, while around bright stars the large photometric error is a significant limitation to the accurate determination of the planet mass.

References

Allard, F., Guillot, T., Ludwig, H.-G., et al. 2003, in IAU Symposium, Vol. 211, Brown Dwarfs, ed. E. Martín, p. 325

Allard, F., Hauschildt, P. H., Alexander, D. R., Tamanai, A., & Schweitzer, A. 2001, ApJ, 556, 357

Baraffe, I., Chabrier, G., Barman, T. S., Allard, F., & Hauschildt, P. H. 2003, A&A, 402, 701

Beuzit, J.-L., Feldt, M., & Dohlen, K. e. a. 2006, The Messenger, 125, 29

Burrows, A., Sudarsky, D., & Hubeny, I. 2006, ApJ, 640, 1063

Carbillet, M., Boccaletti, A., & Thalmann, C. e. a. 2008, in SPIE Conference Series, Vol. 7015

Dohlen, K., Langlois, M., & Saisse, M. e. a. 2008, in SPIE Conference Series, Vol. 7014

Marois, C., Lafrenière, D., Doyon, R., Macintosh, B., & Nadeau, D. 2006, ApJ, 641, 556

Racine, R., Walker, G. A. H., Nadeau, D., Doyon, R., & Marois, C. 1999, PASP, 111, 587

Soummer, R., Ferrari, A., Aime, C., & Jolissaint, L. 2007, ApJ, 669, 642

Vigan, A., Moutou, C., Langlois, M., et al. 2010, MNRAS, 407, 71

APPROXIMATE ANALYTICAL EXPRESSION FOR AO-CORRECTED CORONAGRAPHIC IMAGING IN PREPARATION OF EXOPLANET SIGNAL EXTRACTION

M. Ygouf[1], L. Mugnier[1], J-F. Sauvage[1], T. Fusco[1], D. Mouillet[2] and J-L. Beuzit[2]

Abstract. The next step in the field of extrasolar planets imaging is on the verge of being reached with instruments such as SPHERE (Spectro Polarimetric High contrast Exoplanet REsearch), which will be capable of performing at the same time direct detection and spectral characterization thanks to integral field spectrograph (IFS) images.

In these multispectral images, the star is not completely cancelled by the AO-corrected coronagraphic system because of residual aberrations of the latter. In particular, the star image comprises quasi-static speckles that must be disentangled from the planet signal in order to get the sought information: is there a planet, where is it and what is its spectrum?

We are developing a specific image post-processing method using a Bayesian inverse problem approach. The essential required building block of such a method is a data model (often called "direct model") with a minimal number of unknown parameters. In the framework of the SPHERE project for the VLT, we propose an approximate analytical direct model of a long-exposure star image for an AO-corrected coronagraphic imaging system and we present some preliminary numerical simulations to validate this model.

Keywords: exoplanets, direct detection, multispectral deconvolution, inverse problems, instrumentation, SPHERE, IFS

1 Introduction

Ground-based instruments have now demonstrated the capability to detect planetary mass companions (Chauvin et al. 2004; Lagrange et al. 2009; Marois et al. 2008; Kalas et al. 2008). First detections have been possible in favourable cases, at large separations and in young systems when low mass companion are still warm ($>=$ 1000 K) and therefore not too faint. There is a very strong astrophysical case to improve the high contrast detection capability very close to stars.

Thus, several instruments combining adaptive optics (AO) and coronagraphs are currently under construction. It is the case of SPHERE (Beuzit et al. 2010), GPI (Graham et al. 2007) and several others that will follow such as EPICS (Kasper et al. 2008). All these instruments will be capable of performing multispectral imaging and will allow characterizing the planets by measuring their spectra.

One of the main limitations for high contrast imaging is the presence of speckles in the focal plane (Racine et al. 1999). They find their origin in wave front imperfections and evolves on various time scale. In order to distinguish a planet from these speckles, it is important to modelize the speckle pattern in function of the aberrations in presence of a coronagraph and adaptive optics.

2 Envisaged post-processing method

In the case of multispectral imaging, some post-processing methods have already been proposed in order to overcome the problem of detection limitation caused by the non-static speckles. Thus, Sparks and Ford (2002) were the first to describe the so-called “spectral deconvolution” method in the framework of space-based observations for an instrument combining a coronagraph and an integral-field spectrograph. The goal of this method

[1] Office National d'Études et de Recherches Aérospatiales, Optics Department, BP 72, F-92322 Châtillon Cedex, France
[2] Laboratoire d'Astrophysique de l'Observatoire de Grenoble, BP53X, 414 Rue de la Piscine, 38041 Grenoble, France

is to take advantage of the wavelength dependence of the PSF in order to remove the speckles while preserving both the flux and spectrum of the planet. The method is entirely based on the fit of a low-order polynomial. Latter, Thatte et al. (2007) presented an extension of the spectral deconvolution method to achieve very high contrast at small inner working radii for AO-corrected ground-based observations but without a coronagraph.

Nevertheless, the current spectral deconvolution method presents some limitations. It is an empirical method where no physical model is made explicit. Moreover, if some planets are present, they perturb the fit. That is why we propose an alternative approach, the Bayesian inverse problem (Idier 2008), which could estimate simultaneously the speckle field and the planet position by taking into account both the prior information we have on the speckles and the one we have on the possible planets.

3 Direct model

3.1 Model of coronagraphic imaging

In order to carry out the Bayesian inverse problem method, we need to derive a parametric direct model of coronagraphic imaging. We assume that, for an AO-corrected coronagraphic image, the direct model is the following sum of three terms, separating the coronagraphic stellar halo, the circumstellar source (for which the impact of coronagraph is neglected) and noise n_λ:

$$i_\lambda(x,y) = h_\lambda^c(x,y) + o_\lambda(x,y) \star h_\lambda^{nc}(x,y) + n_\lambda(x,y), \tag{3.1}$$

where the data are: $i_\lambda(x,y)$, the image we have access to and $h_\lambda^{nc}(x,y)$, the non-coronagraphic PSF which can be calibrated separately. Solving the inverse problem is finding the unknowns: the object $o_\lambda(x,y)$ and the speckle field $h_\lambda^c(x,y)$ which is the coronagraphic "point spread function".

A model description of $h_\lambda^c(x,y)$ directly depends on the turbulence residuals and optical wave front errors. In case of coronagraphic imaging, it is important to distinguish pre-coronagraphic aberrations from post-coronagraphic aberrations. After previous works to model non coronagraphic PSFs (Perrin et al. 2003) and coronagraphic PSFs (Cavarroc et al. 2006; Soummer et al. 2007), Sauvage et al. (2010) proposed an analytical expression for coronagraphic image with a distinction between upstream and downstream aberrations. In the perspective of using such an expression as a basis for inversion, we derive and discuss the merits of an approximation of the Sauvage et al. (2010) expression.

3.2 Model of a non-perfectly corrected approximate coronagraphic PSF

We consider the optical system of Figure 1 of Sauvage et al. (2010) composed of a telescope, a perfect coronagraph and a detector plane. Some residual turbulent aberrations $\phi_r(\rho,t)$ are introduced in the telescope pupil plane. $\phi_r(\rho,t)$ is assumed to be temporally zero-mean, stationary, ergodic and with a power spectral density $S_{\phi_r}(\alpha)$. The static aberrations are separated into two contributions: the aberrations upstream of the coronagraph $\phi_u(\rho)$, in the telescope pupil plane $\mathcal{P}_u(\rho)$ and the aberrations downstream of the coronagraph $\phi_d(\rho)$ in the Lyot Stop pupil plane $\mathcal{P}_d(\rho)$. The perfect coronagraph is defined as an optical device that subtracts a centered Airy pattern to the electromagnetic field.

Assuming that all the phases are small and that the spatial mean of $\phi_u(\rho)$ and $\phi_d(\rho)$ are equal to zero on aperture, we derive a second-order Taylor expansion of expression 24 of Sauvage et al. (2010)'s paper:

$$h_c(\alpha) \quad = \quad \left|\widetilde{\mathcal{P}}_d(\alpha) \star \widetilde{\phi}_u(\alpha)\right|^2 + \left|\widetilde{\mathcal{P}}_d(\alpha)\right|^2 \star S_{\phi_r}(\alpha) - \left\langle \left|P\left[\phi_r\right](t)\right|^2 \right\rangle_t \cdot \left|\widetilde{\mathcal{P}}_d(\alpha)\right|^2 + o\left(\phi^2\right), \tag{3.2}$$

where $\tilde{\mathcal{P}_d}(\alpha)$ and $\tilde{\phi_u}(\alpha)$ are the Fourier transforms of the downstream pupil and upstream aberrations respectively and $P\left[\phi_r\right](t)$ denotes the piston of phase $\phi_r(\rho,t)$. $\left\{ \left\langle \left|P\left[\phi_r(\alpha,t)\right]\right|^2 \right\rangle_t \cdot \left|\widetilde{\mathcal{P}}_d(\alpha)\right|^2 \right\}$ is a corrective term that compensates for the fact that $\phi_r(\rho,t)$ is stationary and thus non-piston-free on the aperture at every instant. Note that $\left|\widetilde{\mathcal{P}}_d(\alpha)\right|^2$ is the Airy pattern formed by the pupil $\mathcal{P}_d(\alpha)$.

4 First results of validation

Qualitative validation This expression is far more intuitive than Equation (24) of Sauvage et al. (2010) and brings physical insight to it:

- firstly, the downstream aberrations do not appear in this expression. While the exact expression depends on three parameters ($\phi_u(\rho)$, $\phi_d(\rho)$ and $D_{\phi_r}(\rho)$), the approximate expression depends on only two parameters which are the Fourier transform of the static upstream phase aberrations $\widetilde{\phi}_u(\alpha)$ and the PSD of the residual turbulent aberrations $S_{\phi_r}(\alpha)$. Cavarroc et al. (2006) had already showed that the main limitation comes from the static aberrations, now we have analytical confirmation that the static upstream aberrations are predominant with respect to the static downstream aberrations;
- secondly, we can separate our expression into two terms: one static term and one turbulent term which is coherent with the Soummer et al. (2007)'s paper and makes a connection between this paper and the physical parameters of interest $\widetilde{\phi}_u(\alpha)$ and $S_{\phi_r}(\alpha)$;
- thirdly, we can show that if we rewrite Equation (3.2) as a function of wavelength we can validate theoretically the spectral deconvolution method.

Quantitative validation We want to compare the approximate expression of Equation (3.2) to the exact expression of Equation (24) in Sauvage et al. (2010) to determine the error due to the Taylor expansion. The simulated instrumental conditions are typical of a SPHERE-like instrument (Fusco et al. 2006) and the same as these of Sauvage et al. (2010). Three simulation programs were used:

- the first simulates an empirical long exposure PSF by adding one hundred short-exposure coronagraphic PSF's;
- the second simulates the analytical long exposure coronagraphic image model;
- the third simulates the approximate analytical long exposure coronagraphic image model.

In order to test the approximate expression for each kind of aberration and to quantify the errors due to the Taylor expansion, we compared it with the exact expression. The results of this comparison are shown in Figure 1. We plotted the circularly averaged intensity profiles of the exact model, the approximate model and the circularly averaged root mean square residual of the difference between them in different configurations to quantify the influence of each kind of aberration:

- in presence of all kinds of aberrations, the corresponding error is about twenty-nine percent (Figure 1, left);
- because the approximate model do not take the downstream aberrations into account, it is interesting to compute the same results without downstream aberrations for the exact model. The corresponding error is about seventeen percent. That means that the contribution of the downstream aberrations is about less than a third of the total error (Figure 1, right);
- if we do the same, without residual turbulent aberrations, the corresponding error is about seven percent. Here again, we can deduce the contribution of the residual turbulent aberrations and upstream aberrations which are approximately equal for these simulation conditions representative of SPHERE (Figure 1, right).

It is interesting to see that the three kinds of aberrations have approximately the same non-negligible error. We must be careful with this result which is right for the SPHERE instrument where the downstream aberrations are three times more important than the upstream aberrations. Thus, it does not call the fact that the upstream aberrations are predominant besides the downstream aberration into question.

These results raise some interesting questions as for example: What happens if we consider a non perfect coronagraph? How do these errors propagate and how do they affect the detection and characterization performances if we use our approximate expression in an inversion process?

5 Conclusion and prospects

We have obtained an approximate expression for AO coronagraphic image that is much simpler than the exact expression of Sauvage et al. (2010). Because it has one less parameter, it would be easier to implement in an inversion process. Qualitatively, the result is consistent with the previous works on coronagraphic and non-coronagraphic imaging. We also have discussed quantitatively the error level with respect to the exact expression due to the approximation in SPHERE-like conditions.

We are currently finalizing the numerical validation of the approximate expression by comparing the results obtained with a perfect 4-quadrant coronagraph and by propagating the aberrations errors into the inversion process. This will allow us to decide if we will use this approximate expression or the exact expression to perform the inversion. Then, we shall implement a first inversion on simulated images before adapting our inversion to real images from the SPHERE instrument.

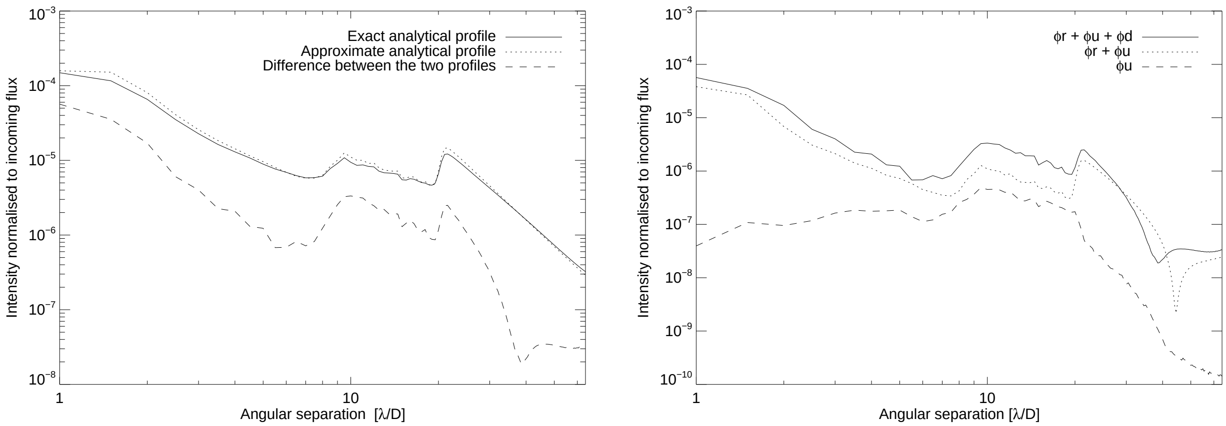

Figure 1. Circularly averaged profiles. [Left] Exact analytical model versus Taylor expansion and error between the two models. [Right] Evolution of the error between the two models in function of the kind of aberrations introduced.

References

Beuzit, J.-L., et al. 2010, In Telescopes and Systems. Proc. Soc. Photo-Opt. Instrum. Eng.

Cavarroc, C., et al. 2006, A&A, 447, 397

Chauvin, G. et al. 2004, A&A, 425, L29

Fusco, T. et al. 2006, Opt. Express, 14(17), 7515

Graham, J. R. et al. 2007, ArXiv e-prints.

Idier, J. 2008, ISTE Ltd and John Wiley & Sons Inc

Kalas, P. et al. 2008, Science, 322, 1345

Kasper, M. et al. 2008, In Society of Photo-Optical Instrumentation Engineers (SPIE) Conference Series, volume 7015 of Society of Photo-Optical Instrumentation Engineers (SPIE) Conference Series

Lagrange, A.-M. et al. 2009, A&A, 493:L21–L25.

Marois, C. et al. 2008, Science, 322, 1348

Perrin, M. D. et al. 2003, ApJ, 596, 702

Racine, R. et al. 1999, PASP, 112, 587

Sauvage, J.-F. et al. in press, J. Opt. Soc. Am.

Soummer, R. et al. 2007, ApJ, 669, 642

Sparks, W. B. and Ford, H. C. 2002, ApJ, 578, 543

Thatte, N. et al. 2007 MNRAS, 378, 1229

ENS

Teaching session

ORIGINS: AN OUTREACH PROJECT TOWARDS CHILDREN

C. Moutou[1] and Association Kaléidoscope[2]

Abstract. We have developed and realised an outreach project about Origins, from the universe formation to the present epoch, in the context of the International Year of Astronomy. The aimed public is primary school, from 8 years age. Various media have been used, from the creation of a theater play to a pedagogical exhibition. The project was shown as a whole ten times during 2009, and the pedagogical elements are still used for school events.

Keywords: outreach, origins, art-science

1 Conception

The original idea came from a gathering of artistic views and scientific views about the question of origins. We wanted to show and discuss in parallel the myths of origins in all cultures, the scientific description of the universe, and a modern myth of origins, as expressed in a creative text and theatral play. Not a pure philosophical discussion, but also a way of communicating scientific questions to the young public. The initial project was made of various elements, in order to transmit emotions and thoughts, and to reach the largest number of individuals:

- A live show made of a theatral creation about the origins, introduced by a short conference on the myths of creation and modern astrophysics
- A portable exhibition with little text, and a chronological reference to events in the universe's history: big bang, first galaxies, star formation, earth formation, apparition of life, evolution
- An artistic mockup of a sun and a planet, used as a pedagogical element lent to schools, and a decorative element during the conference and play

The objective is to trigger the universal questioning on the origins, especially in the mind of young children and in link with their families. We also chose to enhance its multi-cultural and multi-temporal characteristics, showing the diversity and similarity of various myths and legends about the creation of the universe and apparition of life. Into this human context, we introduced the scientific way of thinking, the multiple revolutions based on astronomical discoveries. Finally we presented the modern concept of origins and evolution with its scientific evidence and remaining mysteries, as a contemporaneous "myth". Simple concepts and analogies were used in the conference to help the young public finding its place within time, within space, and in the modern culture where it grows.

2 Realisation and feedback

The project has been prepared during 2008 and first half of 2009. The most intense epoch of realisation and encounters with the public took place from June to October 2009, in about ten places including astronomy festivals and schools.

[1] LAM, 38 rue Frédéric Joliot-Curie, 13388 Marseille
[2] `http://www.kaleidoscopasso.net`

The feedback from the public was very encouraging and positive, on the pedagogical part and on the thematic choice: the Origins are still a lively question in everybody's mind in the present epoch! The public is anxious and in demand about images representing the universe, and references for the difficult temporal scales. The feedback was somehow less enthousiastic on the merging of artistic and scientific material from the adults, but the young public reacted much more positively, which comforted our initial view.

Finally, the exhibition "once upon a time, the universe... 1 second=500 years", was considered accessible to all publics, clear and easily installed, and it is the element of the project with the most living existence after the International Year of Astronomy. It is still circulating from school to school, supporting the teachers and introducing some science in primary schools where it is too much absent! It is quite superficial in its content (little text) but covers many scientific domains, as cosmology, astronomy, geophysics, biology, and thus the teachers can choose to develop the most relevant parts for their pupils, while having a global context exposed in the panels. The mockup is a playful and decorative object, and much appreciated by the children. It is simple and robust enough so that they can manipulate by themselves. It may be used to explain all motions in the planetary systems, eclipses, seasons,...

Fig. 1. Top left: the mockup of a star and planets, a pedagogical and decorative element; top right: children facing the solar system; bottom left: myths and legends of creation told to families, at Centre d'Astronomie (Haute Provence) in August 2009; bottom right: the exhibition "once upon a time, the universe... 1 second=500 years", shown in southern France in July 2009.

Thanks to all entities which supported this project!

GRAAPH

Gravitation and reference systems

NEAR-EARTH ASTEROIDS ASTROMETRY WITH GAIA AND BEYOND

D. Bancelin[1], D. Hestroffer[1] and W. Thuillot[1]

Abstract. Potentially Hazardous Asteroids (PHAs) are Near-Earth Asteroids (NEAs) caraterised by a Minimum Orbital Intersection Distance (MOID) with Earth less than 0,05 A.U and an absolute magnitude H <22. Those objects have sometimes a so significant close approach with Earth that they can be put on a chaotic orbit. This kind of orbit is very sensitive for exemple to the initial conditions, to the planetary theory used (for instance JPL's model versus IMCCE's model) or even to the numerical integrator used (Lie Series, Bulirsch-Stoer or Radau). New observations (optical, radar, fly-by or satellite mission) can improve those orbits and reduce the uncertainties on the Keplerian elements. We investigate here, the impact of the Gaia astrometric observations on the asteroid Apophis's orbit.

Keywords: Gaia mission, NEAs, Apophis, close approach, b-plane

1 Introduction

Gaia is an astrometric mission that will be launched in 2012 and will observe a large number of Solar System Objets down to magnitude 20. The Solar System Science goal is to map thousand of Main Belt Asteroids (MBAs), Near Earth Objects (NEOs) (including comets) and also planetary satellites with the principal purpuse of orbital determination (better than 5 mas astrometric precision), determination of asteroid mass, spin properties and taxonomy. Besides, Gaia will be able to discover a few objects, in particular NEOs in the region down the solar elongation (45°) which are harder to detect with current ground-based surveys.
In the first section, we detailled the nominal scanning law of Gaia and its impact on the number of observations of NEAs. Then we focus our study on asteroid Apophis were we analyse the effect of Gaia observations on the actual position uncertainty, and on the 2029-target b-plane. In the last section, dedicated to the astrometry of newly discovered objects by Gaia, we analyse the combination of ground-based and space-based data, on the short-term ephemerides.

2 Nominal Scanning Law of satellite Gaia

During the 5-years mission, Gaia will continously scan the sky with a specific strategy (Fig. 1): objects will be observed from two lines of sight separated with a constant basic angle. Five constants already fixed determinate the nominal scanning law but two others are still free parameters: the initial spin phase and the initial precession angle. These latter will be fixed at the start of the nominal scientific outcome (possibility of performing test of fundamental physics) together with operational requirements (downlink to Earth windows).

Several sets of observations of NEOs will hence be provided according to the initial precession angle. We used a Java rendez-vous simulator which provided us 35 sets of Gaia observations. Fig. 2 shows the number of NEAs and PHAs that could be observed by Gaia. The number of asteroids does not really change according to the value of the initial precession angle. The mean values of possible observed asteroid are $\sim$ 1650 NEAs and $\sim$ 405 PHAs.

[1] IMCCE, Paris Observatory, 77 Avenue Denfert-Rochereau, 75014 Paris, France

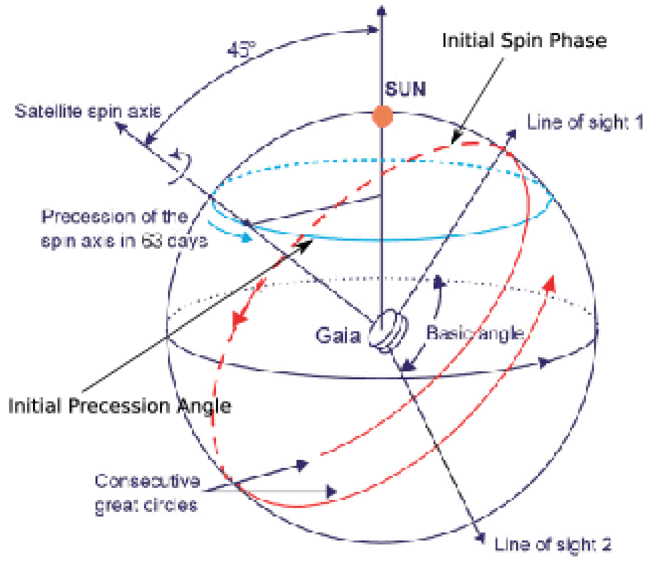

Fig. 1. Nominal Scanning Law of Gaia. (Source: ESA)

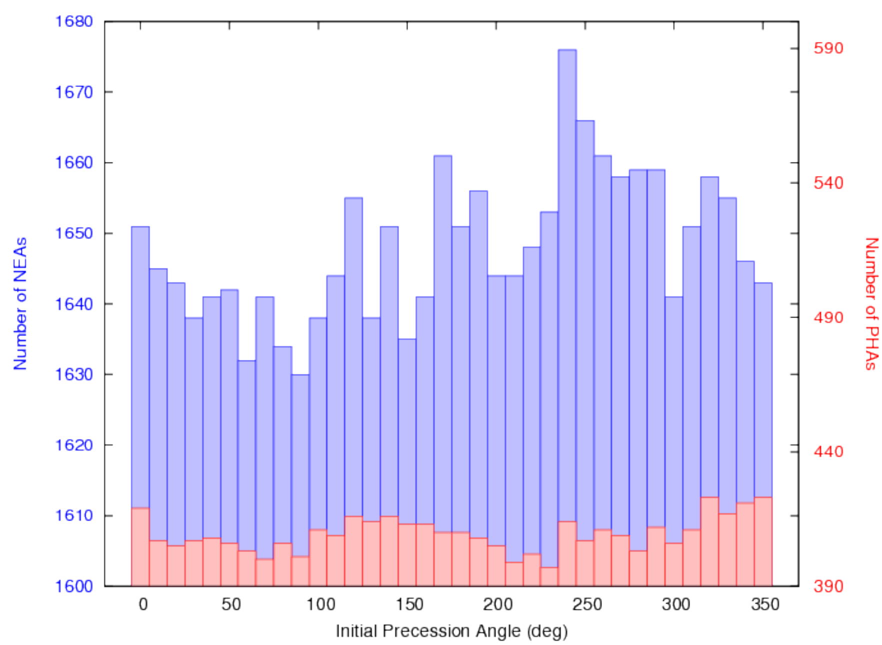

Fig. 2. Number of NEAs and PHAs observed by Gaia with respect to the initial precession angle.

3 Study case of asteroid 99942 Apophis (previously 2004MN4)

We study here the effect of Gaia observations on Apophis orbit. This asteroid has a so deep close-approach with the Eart on April 2029 that its post close-approach orbit becomes chaotic. Thus, the uncertainty on the geocentric position and distance becomes large. From a linear propagation of the covariance matrix, Fig. 3 shows the impact of Gaia astrometry done in 2014 (date of last Gaia observations) on the position uncertainty of Apophis. To this purpose, we considered only one of the sets provided by Gaia.

The position uncertainty is reduced to less than 2 km with Gaia observations. This value remains almost constant until the 2029 close approach (at distance 38000 km to Earth) where the uncertainty will start increasing. We can also analyse the impact of Gaia observations on the geocentric coordinates (ξ, ζ) of the 2029-target b-plane (Valsecchi et al. 2003). The b-plane passes through Earth's center and is perpendicular to the geocentric velocity of the asteroid. The initial covariance of the (ξ, ζ) elements are propagated to this date.

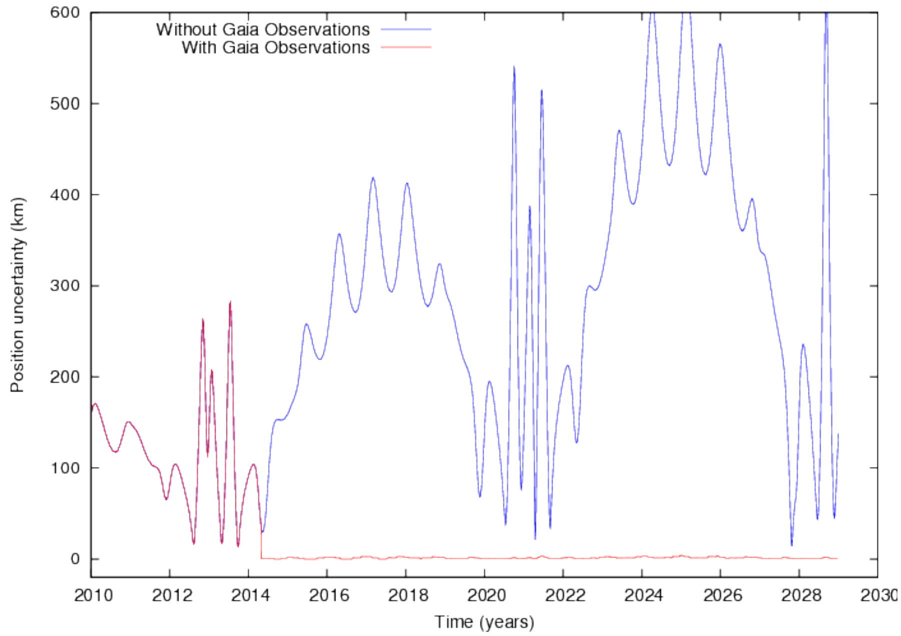

Fig. 3. Position uncertainty of Apophis considering Gaia observations.

Fig. 4 represents the 3σ scattering ellipse where the semiminor axis is defined by $3\sigma_\xi$, the semimajor axis by $3\sigma_\zeta$ and its center by the values of (ξ, ζ) on the nominal solution.

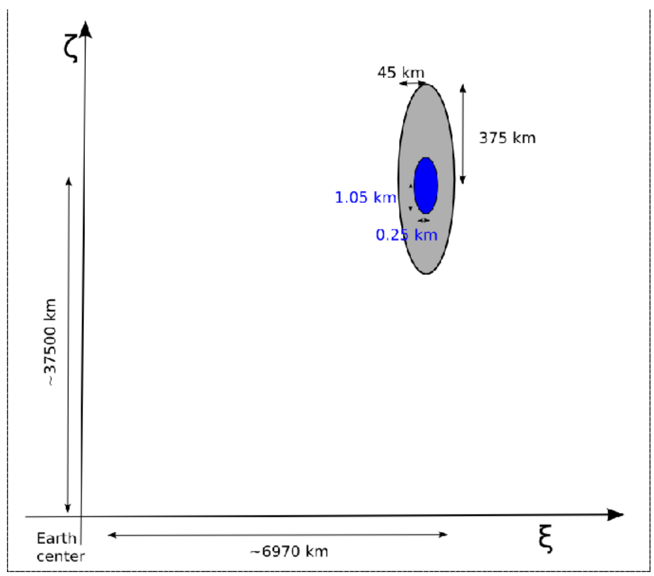

Fig. 4. Scattering ellipse on the target plane on date of close approach (2029/01/13.907) with (blue) and without (grey) Gaia observations.

The uncertainty ellipse size is strongly reduced and the geocentric position of Apophis, at the date of closest approach, is better determinated, considering Gaia observations.

4 Astrometry for newly discovered objets

By combining, in real-time, ground-based to space-based data, it is possible to drastically improve the short-term ephemerides. Fig. 5 shows an illustration of this improvement for the prediction of a newly discovered object by combinig the two kind of data. For our simulation, we considered an hypothetic Apophis that would be discovered by Gaia. When observing a new object, the satellite will send to Earth, as an alert, the coordinates of the unknown object. Thus, it is possible to make a prediction of the position of the hypothetic Apophis on the sky-plane by computing a preliminary orbit (using Statistical Ranging method (Virtanen et al. 2001)). This prediction was made three days after its discovery by Gaia and the 1σ distribution is large (1 degree) and quite far from the expected value (triangle). If we make a geocentric observation on the 4th day after its discovery and combine it with the late Gaia observations, the (α, δ) uncertainty is reduced by a factor 30 and the ephemeris is well improved (note that here the 10 σ distribution is given).

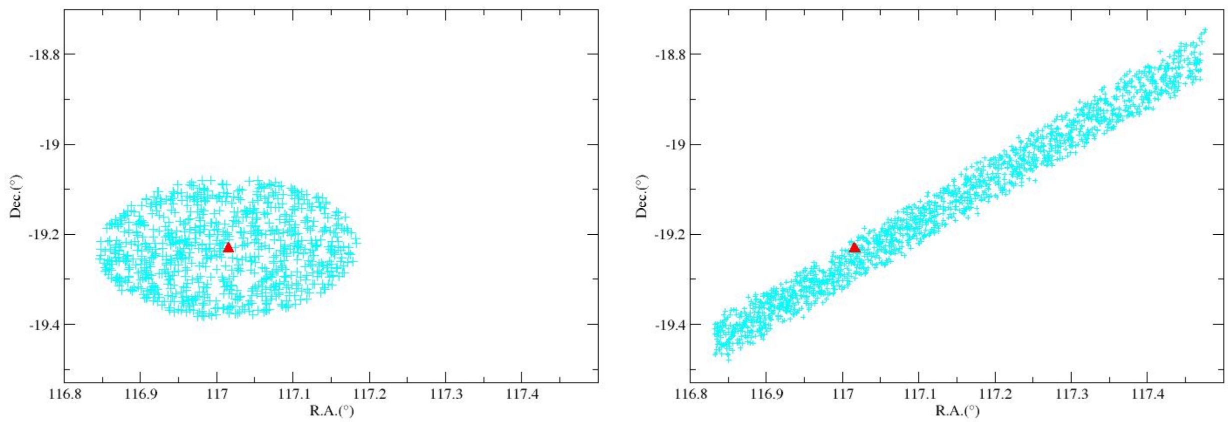

Fig. 5. Example of geocentric distributions (α, δ) for the predicted positions on the 3th day after discovery with only Gaia observations (left 1σ uncertainty) and on the 4th day with an additionnal geocentric observation (right 10σ uncertainty). The triangle represents the expected value

5 Conclusions

Even if Gaia will not be a big NEAs discoverer, it will provide unprecedented accuracy for NEAs orbit's improvement. Besides, this study can be continued considering the astrometric reduction due to the stellar catalogue provided by Gaia. As a matter of fact, this catalogue will be more precise and dense and almost free of zonal errors. Thus, classical ground-based astrometry (and concerning hence more object down to fainter magnitude) will be improved.

References

Valsecchi, G. B., Milani, A., Gronchi, G. F., & Chesley, S. R. 2003, A&A, 408, 1179

Virtanen, J., Muinonen, K., & Bowell, E. 2001, Icarus, 154, 412

SF2A 2010
S. Boissier, M. Heydari-Malayeri, R. Samadi and D. Valls-Gabaud (eds)

DENSIFICATION OF CELESTIAL REFERENCE FRAMES: TOWARDS NEW VLBI OBSERVING STRATEGIES

L. Chemin[1,2] and P. Charlot[1,2]

Abstract. Building celestial reference frames such as the International Celestial Reference Frame (ICRF) from Very Long Baseline Interferometry (VLBI) observations is very important for geodesy, astrometry and astrophysics. We have started a project whose objective is to develop new VLBI analysis methods and observational strategies to densify such reference frames. Our strategy takes advantage of the phase referencing VLBI technique, which allows one to detect radio sources weaker than those traditionally observed with the standard wide-angle VLBI technique used to construct the ICRF. The combination of wide-angle and phase referencing VLBI observations should provide a denser and unified reference grid comprising both strong and weak radio sources. Actual data as well as simulated data will be used to test the method.

Keywords: astrometry, reference frames, VLBI, quasars

1 VLBI astrometric techniques

Celestial reference frames are aimed at measuring positions and motions of objects in the sky with the highest possible accuracy. They are essential for a number of astronomical and astrophysical studies such as Solar System dynamics, kinematics of the Galaxy or physics of distant active galaxies. Since the generation of the International Celestial Reference Frame (ICRF) and its subsequent adoption by the International Astronomical Union (IAU) in 1997 (Ma et al. 1998), the fundamental celestial frame has been defined based on extragalactic sources. The current IAU frame, the ICRF2, in use since 1 January 2010, comprises positions for 3414 sources (corresponding to an average of one source every $\sim 3^{\circ}$ on the sky), with a noise floor of 40 μas in the source coordinates (Fey et al. 2009). The ICRF2 was generated from nearly 30 years of Very Long Baseline Interferometry (VLBI) data (1979–2009) acquired with the standard wide-angle astrometric technique based on group delay measurements. Further densification of the frame with this technique requires sensitive instrumentation (large radiotelescopes, high recording rates,...) along with large amounts of observing time since weaker sources have to be observed.

Such weak sources may be observed more easily by using the differential phase-referencing VLBI technique (Lestrade et al. 1990; Beasley & Conway 1995). The principle of this technique is to calibrate the data of a (weak) target source from a bright angularly-close (a few degrees at most) calibrator, e.g. from the ICRF2 grid. Observations alternate between the target and the calibrator and the phase of the target is estimated relative to that of the calibrator after interpolation over successive calibrators scans. In this way, the data may be integrated over several hours, thereby permitting the detection of weak sources, unlike the standard VLBI technique which is limited to a few minutes integration time. The position of the target relative to that of the calibrator is then derived to an exquisite accuracy of a few tens of μas (Lestrade et al. 1990; Pradel et al. 2006).

2 New observing strategies

Our goal is to investigate the potential densification of the current reference grid by combining the two VLBI techniques described above (global astrometry and phase-referencing). With this scheme, we expect to bring many weak sources into the celestial frame and fill the interspace between the current grid of ICRF2 calibrators, as illustrated in Figure 1. More specifically, we aim at processing jointly VLBI group delay and phase data in

[1] Université de Bordeaux, Observatoire Aquitain des Sciences de l'Univers, BP 89, 33271 Floirac Cedex, France
[2] CNRS/INSU, Laboratoire d'Astrophysique de Bordeaux, UMR 5804, BP 89, 33271 Floirac Cedex, France

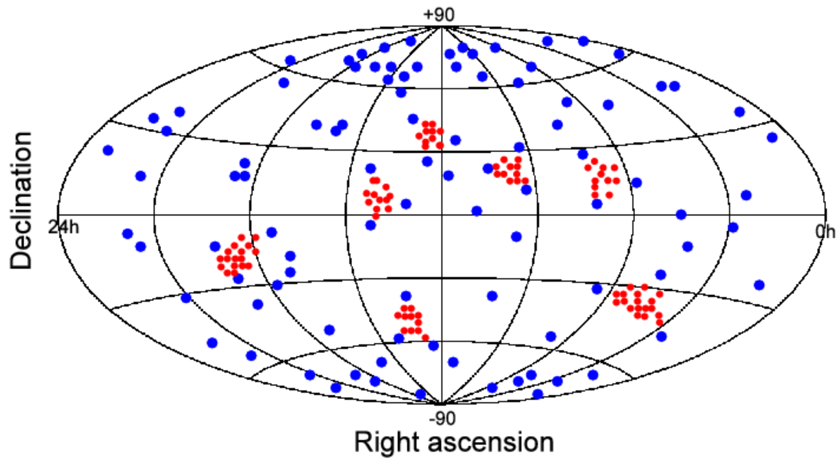

Fig. 1. Schematic representation of the anticipated densification of the current celestial reference frame (blue dots) by adding many weak radio sources observed by phase referencing VLBI (red dots).

Table 1. VLBI software packages used for global astrometry (GA) and phase referencing (PR)

GA	References	GA	References	PR	References
Calc/Solve	Ryan et al. (1993)	OCCAM	Titov et al. (2004)	AIPS	Greisen (2003)
GINS	Bourda et al. (2007)	QUASAR	Kurdubov (2007)	SPRINT	Lestrade et al. (1990)
MODEST	Sovers & Jacobs (1996)	SteelBreeze	Bolotin (2001)	UVPAP	Martí-Vidal et al. (2008)

a consistent and unified way. Table 1 lists the VLBI software packages used for global and phase-referencing VLBI astrometry. Among these, the JPL VLBI software package MODEST appears to be unique as it has the capability of processing both data types (group delays and phases) along with the potential for simulating artificial VLBI data sets. Simulations are likely to play a crucial role here for identifying the observing strategy that provides the highest astrometric accuracy and the most efficient VLBI scheduling. Actual data from the VLBA (Very Long Baseline Array) and EVN (European VLBI Network) archives will also be used for this work.

This project is developed in the framework of the ALBiUS (Advanced Long Baseline interoperable User Software) Joint Research Activity within FP7-RadioNet. It is funded by FP7-RadioNet and the Conseil Régional d'Aquitaine.

References

Beasley, A. J., Conway J. E., 1995, Astronomical Society of the Pacific Conference Series, 82, 328

Bolotin S., 2001, in *Journées Systèmes de Référence Spatio-Temporels 2000*, N. Capitaine (ed) (Paris: Observatoire de Paris), 102

Bourda G., Charlot, P., Biancale, R. 2007, in *18th European VLBI for Geodesy and Astrometry Working Meeting*, J. Böhm, A. Pany and H. Schuh (eds), (Wien:Technische Universität), Heft Nr. 79, 59

Fey, A.L., Gordon D., Jacobs C.S. (eds.), 2009, IERS Technical Note No. 35, Verlag des Bundesamts für Kartographie und Geodäsie (Frankfurt am Main)

Greisen, E.W. 2003, Astrophysics and Space Science Library, Vol. 285, 109

Kurdubov, G. 2007, in *18th European VLBI for Geodesy and Astrometry Working Meeting*, J. Böhm, A. Pany and H. Schuh (eds), (Wien: Technische Universität), Heft Nr. 79, 79

Lestrade, J.-F., Rogers, A.E.E., Whitney, A.R., et al. 1990, AJ, 99, 1663

Ma, C., Arias E.F., Eubanks T.M., et al. 1998, AJ, 116, 516

Martí-Vidal, I., Marcaide J.M., Guirado J.C., et al. 2008, A&A, 478, 267

Pradel, N., Charlot, P., Lestrade, J.-F. 2006, A&A, 452, 1099

Ryan, J.W., Ma, C., Caprette, D.S. 1993, NASA Technical Memorandum 104572

Sovers, O.J., Jacobs, C.S. 1996, JPL Publication 83–89, Rev. 6

Titov, O., Tesmer, V., Boehm, J. 2004, IVS 2004 General Meeting Proceedings, NASA-CP-2004-212255, 267

SF2A 2010
S. Boissier, M. Heydari-Malayeri, R. Samadi and D. Valls-Gabaud (eds)

IN-ORBIT DATA VERIFICATION OF THE ACCELEROMETERS OF THE ESA GOCE MISSION

B. Christophe[1], J.-P. Marque[1] and B. Foulon[1]

Abstract. The ESA GOCE mission aims to map Earth gravity field in unprecedented detail. The Gradiometer is the instrument which makes possible the high resolution restitution of the gravity field to the science communities. The tri-axes Gradiometer of the GOCE Mission is conceived around six electrostatic accelerometers developed by ONERA. The satellite was launched on March 17th, 2009 and the gradiometer was switched on in Science mode on April 7th. Since, the accelerometers are continuously feeding the science channel with data, first during the commissioning and calibration phases, then during the first measurement phase started in September 2009. The paper will illustrate the in-flight behaviour of the six accelerometers as deduced from the analysis of their output signals.

Keywords: GOCE, gravity, gradiometry, accelerometer, noise

1 Introduction

The ESA GOCE mission aims to map Earth gravity field in unprecedented detail. The Gradiometer is the instrument which makes possible the high resolution restitution of the gravity field to the scientific communities to advance our understanding of global ocean circulation patterns and climate change.

The tri-axes Gradiometer of the GOCE Mission is conceived around six electrostatic accelerometers developed by ONERA. Servo-controlled electrostatic suspension provides the control of the sensing proof mass of each accelerometers in terms of linear and rotational motion. Three pairs of identical accelerometers, which form three gradiometer arms, are mounted on an ultra-stable structure. From the difference between accelerations measured by each pair of accelerometers, it is possible to derive the gravity gradient components as well as the perturbing angular accelerations. GOCE is the first mission to access directly to the of Gravity Gradient Tensor (GGT) components in orbit.

The satellite was launched on March 17th, 2009 and the gradiometer was switched on in Science mode on April 7th. Since, the accelerometers are continuously feeding the science channel with data, first during the commissioning and calibration phases.

2 GOCE accelerometer

The main functions of the accelerometric chains are to provide:

- The time-stamped voltages corresponding to the 3D linear accelerations at the position of each accelerometer sensor, delivered at 1 Hz, they are used to retrieve the final components of the GGT.
- The real time 3D linear accelerations of the satellite at the centre of the gradiometer, close to the spacecraft centre of gravity. They are delivered to the Drag Free and Attitude Control System (DFACS) at 10 Hz.

The schematic of the control loop for the ultra-sensitive Y and Z axes is shown on Fig. 1.

2×2 pairs of electrodes control 3 degrees of freedom (dof): the Y and Z translation and the ϕ rotation (roll angle). Going from the 4 electrode voltages at the position detector output to the three dof to be processed by the controller needs a digital combination matrix at the position detector output and a recombination matrix for the inverse operation at the controller output. Main functions inside the loop are provided by the proof-mass position sensor, the digital controller and the action which applies the needed control voltages back to electrodes.

[1] ONERA/DMPH, 29 av. Division Leclerc, 92322 Chatillon, France

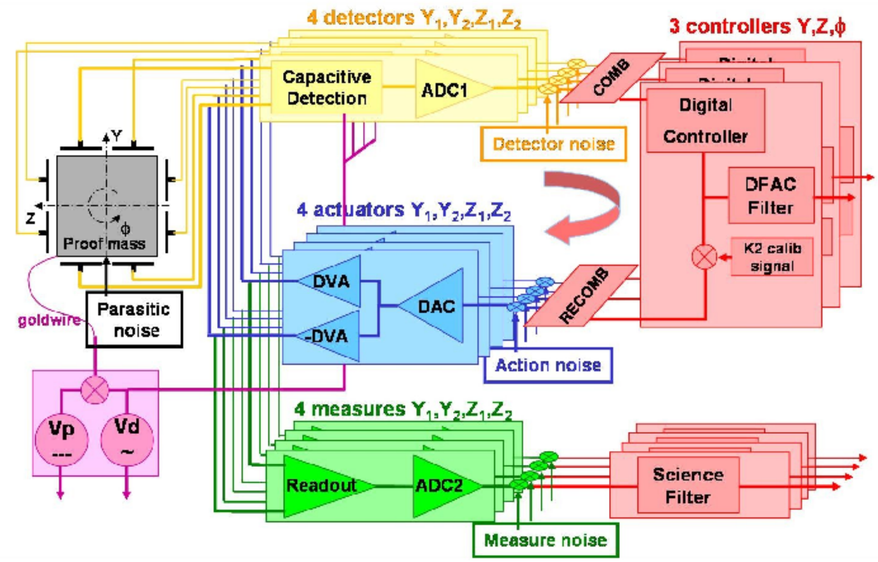

Fig. 1. Schematics of the Y/Z axes control loop

3 Drag-Free Performance

The performance drag free was evaluated for the first time during the commissioning phase in fine drag free mode. On Fig. 2 the red spectrum represents the spectral density of the residual satellite acceleration along the track, with a mean value of $10^{-9}\ m/s^2/\sqrt{Hz}$ below 100 mHz, to be compared with the specified value (the green line) of 2.5 $10^{-8}\ m/s^2/\sqrt{Hz}$. The drag free control system of the satellite, in which the accelerometers are involved as the detectors, was found to be working perfectly providing an excellent rejection of the common mode acceleration. As the 6 accelerometers have a ultra-sensitive measurement axis along the X, in track, direction, the noise figure of the accelerometer DFACS channel can be computed from the combination of the 6 signals. The spectral density of the noise is shown on Fig. 2 by the blue spectrum.

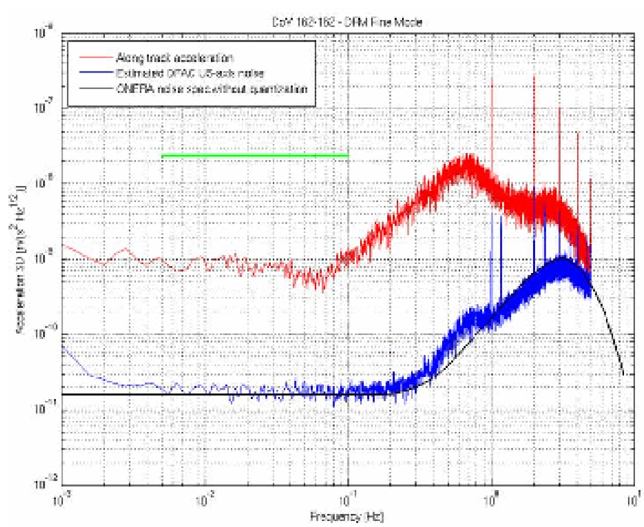

Fig. 2. Drag Free performance: residual satellite acceleration and accelerometer DFACS channel noise (Thales Alenia Space Italy)

The spectrum perfectly matches the predicted noise (black line), leading to the conclusion that the position detection noise and the actuation noise (DVA + DAC), which are the main contributors in the respective frequency bandwidth, have been correctly modeled and suffered no modification during the launch phase.

4 In-orbit verification

As the accelerometer is nominally the main contributor of the GOCE performance in the Upper Measurement Bandwidth (UMBW), several tests were performed for an in-flight evaluation of the accelerometer noise contributor, in the science channel. Some of these verifications are detailed hereafter.

4.1 Stiffness verification

Parasitic stiffness, preventing the proof-mass to move as freely as expected, can be present within the sensor cage. High cleanliness integration conditions and dedicated on ground test allowed to check the correct behaviour of the proof-mass under levitation. However, as parasitic stiffness can occur in space after launch, it is checked in flight with a still better accuracy than on ground test. Such a test is performed by moving the proof-mass inside the cage and recording the corresponding variation of the accelerometer bias. The measured value shall be compared to the value of the nominal stiffness including the negative electrostatic stiffness about $-510^{-2}m/s^2/m$ and the gold wire contribution at a level of $10^{-4}m/s^2/m$.

The stiffness was estimated along the in-line axis of each arm. The results for the 6 accelerometers are in agreement with the expected values, within the accuracy of the estimation of the accelerometer bias. Fig. 3 presents the results of such verification for the three gradiometer arm.

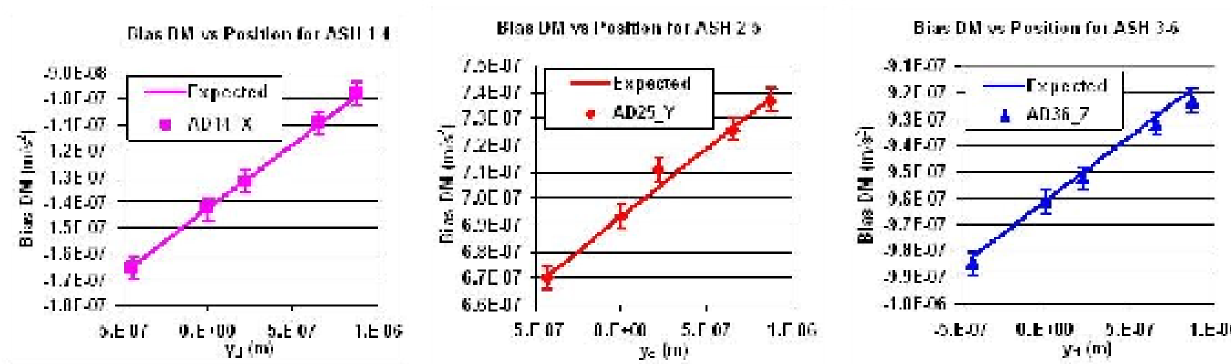

Fig. 3. Verification of the theoretical stiffness of the first (left) the second (center) and the third (right) one-axis gradiometer.

4.2 Action and Science noise

Thanks to the digital control loop, it is possible to check the science noise by opening the control loop (PM no more in levitation) and by recording the science output. In this approach, the science noise is added to the action noise.

- Case 1: $V_{in} = 0$: A first verification is done with a null input at DAC level. In that case, the output noise is the sum of the action and science channel noise. Fig. 4a presents the results for the in-line axis of the OAGX arm. The measured noise is perfectly in agreement with the expected one from on-ground measurement. The same results are found for the 2 other arms.

- Case 2: $V_{in} \neq 0$: Due to the non-null input, there is an additional noise contribution due to the reference voltage stability of the ADC2. This test allows verifying this major contributor to the differential scale factor noise. Fig. 4b presents the results for the in-line axis of the OAGX arm. The measured noise is perfectly in agreement with the expected one as deduced from on-ground measurement. The same results are found for the 2 other arms.

5 Overall performance

The mission overall performance is evaluated by the amplitude spectral density (ASD) of the Gravity Gradient Trace, $(U_{XX} + U_{YY} + U_{ZZ})$. It is determined after the full calibration of the Gradiometer for the coupling and misalignments of the instrument axes, for the Scale factor and the quadratic factor of the accelerometers.

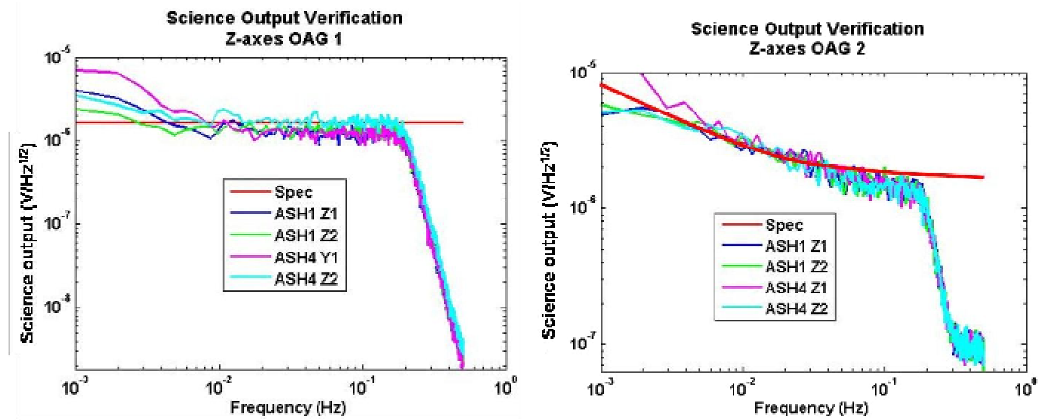

Fig. 4. In-flight verification of the action-science chain noise for in-line electrode of OAGX, (a)with null DAC input (left), (b) with non null DAC input (right)

The result deduced by Thalès Alenia Space Italy from the in-flight measurements shows that the in-flight trace value is 24 $mE/\sqrt{Hz}$ in the Upper MBW [40-100 mHz] (Floberghagen et al. 2010).

Although it is larger than expected, the performance of the gradiometer is very high and a gravity field model with high resolution and accuracy has already been obtained. The first GOCE Geoid, based on 2 months data, was presented in June 2010 by ESA at the ESA Living Planet Symposium in Bergen (Norway) (ESA 2010). Significant improvements were already observed in high resolution areas of the geoid and the gravity field model will be constantly improved with the continuous arrival of datas.

The origin of the performance deviation has not been yet elucidated. The in-flight tests of accelerometers, as described above, did not allow putting into evidence any unexpected behaviour of the accelerometers. A direct in flight evaluation of the accelerometer performance is not possible. Assuming a worst case estimation from the overall performance, the accelerometer noise performance would be within the range 3.1 10^{-12} $m/s^2/\sqrt{Hz}$ to 6.7 10^{-12} $m/s^2/\sqrt{Hz}$ (Marque et al. 2010).

This is the best performance never achieved in orbit by an accelerometer, 15 to 30 times better than the SuperSTAR accelerometer of the GRACE mission.

6 Conclusions

The 6 accelerometers are fully operational in orbit since 18 months as Drag-Free Sensors and as Science Instruments. From an operational point of view the return of experience after more than one year in orbit is a full success.

The verification of the in-flight electronic noise and accelerometer stiffness confirms the on-ground predictions. An identical behaviour is observed for the 6 accelerometers.

The level of 3 10^{-12} $m/s^2/\sqrt{Hz}$ verified in orbit, 15 to 30 times better than GRACE accelerometers, is the target performance required for the future generation of gravity mission. It is best performance never achieved in orbit by an accelerometer. The GOCE type accelerometers are today the best candidate for these future missions, with a high level of technological maturity.

References

ESA 2010, GOCE giving new insights into Earth's gravity, `www.esa.int/SPECIALS/GOCE`

Floberghagen, R., Fehringer, M., Lamarre, D., Muzi, D., Frommknecht, B. & Kern, M. 2010, EGU Conference Vienna (Austria), April 2010

Marque, J.P., Christophe, B. & Foulon, B. 2010, Accelerometers of the GOCE mission: return of experience from one year in orbit, Bergen (Norway), 28 June – 2 July 2010.

GRGS EVALUATION OF THE ITRF2008P SOLUTION, FROM SLR DATA

F. Deleflie[1] and D. Coulot[2]

Abstract. Following Deleflie and Coulot (2009), this paper aims to analyse the preliminary version of the new realization of the International Terrestrial Reference System called ITRF2008p. We compare the quality of the products that we regularly provide as an official ILRS Analysis Center (AC) with the ones obtained using ITRF2008p instead of the ILRS Analysis Working Group rescaled version of ITRF2005. We also compare our results to those obtained by other ACs, in terms of Space Station Coordinates (SSC), Earth Orientation Parameters (EOP), translations and scale factors, following our operational analysis scheme of SLR data, that we performed over the period 1995-2010.

Keywords: SLR data, International Terrestrial Reference Frame, GRGS, space geodesy

1 Introduction

The International Terrestrial Reference System (ITRS) realizations are established and maintained with the global space geodetic networks. The network measurements must be precise, continuous, worlwide, and interconnected by co-locations of different observing techniques. The requirements to be followed in the framework of the GGOS project are to perform a global Terrestrial Reference Frame (TRF) with an accuracy of 1.0 mm, and a stability of 0.1 mm/yr, ensuring a sea level rise measurement coherent with the altimetric data precision. IGN has released during March 2010 the ITRF2008P preliminary version of the next ITRF for evaluation by the technique services. An enormous effort has been achieved by these services (IVS, ILRS, IGS, IDS) and their Analysis and Combination Centers, to provide reprocessed solutions. The quality of the ITRF2008 is certainly benefiting from these technique improved solutions. The Satellite Laser Ranging (SLR) technique is one of these techniques, organized through the International Laser Ranging Service (ILRS) (Pearlman et al., 2002). Each Analysis Center (AC) solution contains Space Station Coordinates (SSC) and daily EOP, using Lageos and Etalon data, according to ILRS/ Analysis Working Group (AWG) guidelines.

The AWG of the ILRS worked on the ITRF2008 submission during the first part of 2009. The combined solution was based on the contribution of seven Analysis Centers (ASI, DGFI, GA, GFZ, our own contribution for GRGS, JCET, and NSGF). After a few dedidated AWG meetings during spring 2009, the final contribution of ILRS for ITRF2008 was sent to IERS during August 2009.

2 Orbit computation

Two geodetic satellites, Lageos-1 and Lageos-2, were used in this study, with an orbital modelling following the AWG guidelines. In particular, we accounted for the last release of the file containing all the data corrections to be applied to SLR data. These data came from about 30 tracking stations (most of them located in the northern hemisphere, due to a well-known heterogeneity of the ILRS network), gathering up a total of 2000 to 3000 normal points per week and per satellite.
Two computations were carried out, the first one using the ILRS AWG rescaled version of ITRF2005 (SLRF2005) for a priori SSC, the second using ITRF2008p. The levels of magnitude of weekly residuals are very similar (for Lageos-1, a mean of 1.27cm ± 2.47mm for SLFR2005, and 1.18cm ± 2.02mm for ITRF2008p ; for Lageos-2, a mean of 1.26cm ± 2.47mm for SLRF2005, and 1.17cm ± 2.16mm for ITRF2008p), even if a slight difference

[1] IMCCE-Observatoire de Paris / GRGS, 77 Avenue Denfert Rochereau, F-75014 Paris
[2] Institut Géographique National, LAREG / GRGS, ENSG, 6-8 Avenue Blaise Pascal, 77455 Champs-sur-Marne, France

can be seen over the period 2007-2009. Figure 1 shows the level of weekly residuals for Lageos-2. There are no significant differences between the time series of orbital parameters deduced from the post-fit analysis with SLRF2005 or ITRF2008p (by the way, it should be worth studying to what extent such expected differences can be absorbed or not through the set of empirical parameters used to compensate the lack of non gravitational forces modelling).

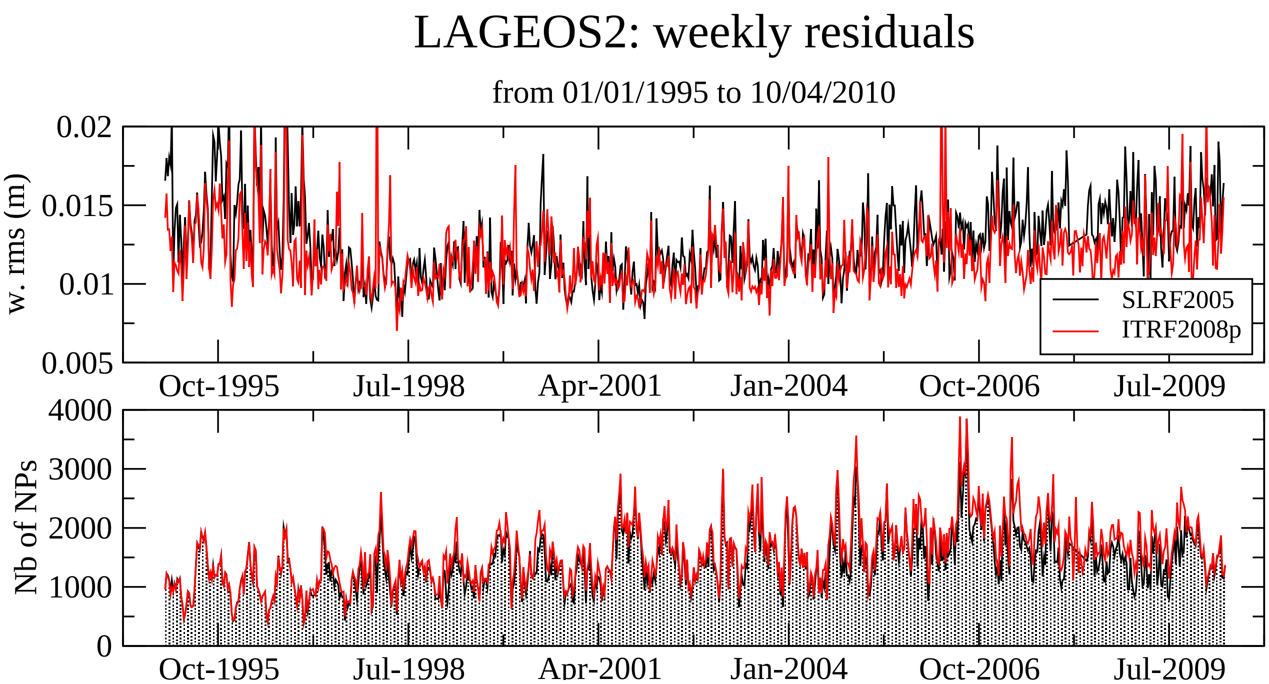

Fig. 1. Residuals of weekly arcs of Lageos-2, from 01/01/1995 to 10/04/2010, and numbers of normal points per week

3 Helmert transformation

To compare various terrestrial frames, realized as sets of SSC, a 7-parameter transformation is estimated, and described by translations (T_x, T_y, T_z), rotations (R_x, R_y, R_z), and a scale factor (D). The transformations are, for the station i, provided though two sets of coordinates (X_i^0, Y_i^0, Z_i^0) and (X_i^1, Y_i^1, Z_i^1),

$$\begin{pmatrix} X_i^1 \\ Y_i^1 \\ Z_i^1 \end{pmatrix} = \begin{pmatrix} X_i^0 \\ Y_i^0 \\ Z_i^0 \end{pmatrix} + \begin{pmatrix} 1 & 0 & 0 & X_i^0 & 0 & -Z_i^0 & Y_i^0 \\ 0 & 1 & 0 & Y_i^0 & Z_i^0 & 0 & -X_i^0 \\ 0 & 0 & 1 & Z_i^0 & -Y_i^0 & X_i^0 & 0 \end{pmatrix} \begin{pmatrix} T_x \\ T_y \\ T_z \\ D \\ R_x \\ R_y \\ R_z \end{pmatrix}$$

and for the corresponding EOP (x_p^1, y_p^1, UT^1) and (x_p^0, y_p^0, UT^0), with $f = 1.002737909350795$,

$$\begin{pmatrix} x_p^1 \\ y_p^1 \\ UT \end{pmatrix} = \begin{pmatrix} x_p^0 \\ y_p^0 \\ UT^0 \end{pmatrix} + \begin{pmatrix} 0 & -1 & 0 \\ -1 & 0 & 0 \\ 0 & 0 & \frac{1}{f} \end{pmatrix} \begin{pmatrix} R_x \\ R_y \\ R_z \end{pmatrix}$$

		ITRF2005	ITRF2008p
T_x	weighted mean	−0.83	−0.05
(mm)	weighted std. dev.	3.97	3.50
	WRMS	4.05	3.50
T_y	weighted mean	−0.13	0.05
(mm)	weighted std. dev.	3.76	3.35
	WRMS	3.76	3.35
T_z	weighted mean	1.29	0.76
(mm)	weighted std. dev.	7.35	7.03
	WRMS	7.46	7.07
scale	weighted mean	−1.91	−0.45
(ppb)	weighted std. dev.	0.69	0.42
	WRMS	2.03	0.62

Table 1. Helmert parameters between (i) ilrsa-v24 solution and ITRF2005, (ii) ilrsa-v24 solution and ITRF2008p

		ITRF2005	ITRF2008p
X_p	weighted mean	40	−2
(μas)	weighted std. dev.	228	203
	WRMS	232	203
Y_p	weighted mean	43	−5
(μas)	weighted std. dev.	222	204
	WRMS	226	204

Table 2. Differences between the pole coordinates from ilrsa-v24 solution consistent with (i) ITRF2005, (ii) ITRF2008p, and the IERS 05 C04 reference time series

4 Results and comparisons between SLRF2005, ITRF2005 and ITRF2008p

4.1 A priori values

We had a look at the differences between the observations (range) and the theoretical corresponding values (distances between the tracking stations and the satellites), computed from (i) the orbit and (ii) the SSC provided in SLRF2005 or ITRF2008p. These differences were reported before adjusting any parameter. When using ITRF2008p, we show that there is an improvement of the RMS of the a priori residuals for the great majority of the stations (for Lageos-1, improvement for 82 % of the stations, with a median improvement of 1.5 mm ; for Lageos-2, improvement for 87 % of the stations, with a median improvement of 2.0 mm). The coordinates of the station number 7810 (Zimmerwald, Switzerland), which is one of the most stable stations in the ILRS network, have ever been improved at the level of 5.7 mm for Lageos-1, and 7.8 mm for Lageos-2 (and we can as well mention the improvement for 7403 (Arequipa, Peru), at the levels of 53.1 mm and 32.4 mm respectively).

4.2 Helmert parameters between (i) ilrsa-v24 combined solution, (ii) SLRF2005, and (iii) ITRF2008p

Figure 2, Tables 1 and 2 show the comparison, for the main parameters defining a TRF and Earth's rotation, between the ilrsa-v24 ILRS combined solution and ITRF2005 and ITRF2008p. It appears that for all parameters, the differences are lower when using ITRF2008p, and that there is a better stability of time series achieved with ITRF2008p. Let us notice, moreover, that the difference for the scale of the ilrsa-v24 solution is much lower with ITRF2008p than with ITRF2005, as shown Figure 2, and Table 1.

5 Short analysis of the contribution of each ILRS AC

Table 3 shows the WRMS of Helmert parameters and of EOP and station position residuals for each individual solution contributing to the combined solution ilrsa-v24 w.r.t. this latter. These values can be seen as quality indicators of each ILRS AC contribution w.r.t. the combined solution.

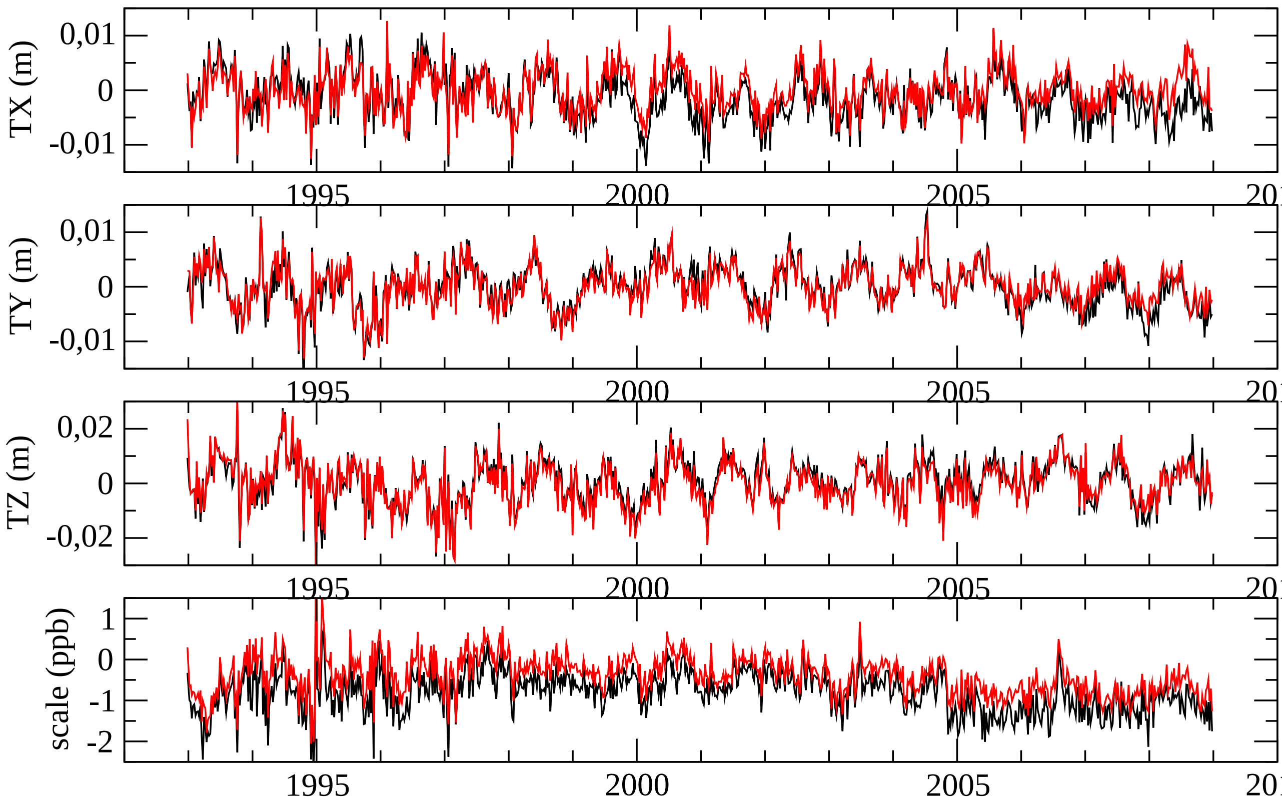

Fig. 2. Translations and scale factors (in mm) between the ilrsa-v24 solution and (i) ITRF2005 and (ii) ITRF2008p

Solution	TX(mm)	TY(mm)	TZ(mm)	D (ppb)	E (mm)	N (mm)	U (mm)	Xp (μas)	Yp(μas)
	WRMS over 1993.0-2009.0				Median WRMS of residuals all stations (20 core stations)			WRMS	
ASI-v23/ilrsa-v24	1.6	1.5	4.9	0.33	5.97 (4.41)	6.54 (5.31)	4.10 (2.97)	164	156
DGFI-v24/ilrsa-v24	4.42	3.43	7.17	0.47	12.63 (8.26)	13.07 (10.11)	8.28 (5.98)	333	310
GA-v22/ilrsa-v24	1.27	1.07	4.41	0.16	9.46 (5.59)	10.25 (5.76)	7.29 (3.97)	208	178
GFZ-v23/ilrsa-v24	2.59	2.77	6.21	0.49	8.56 (6.32)	9.53 (7.55)	6.17 (4.86)	332	316
GRGS-v24/ilrsa-v24	1.62	1.47	1.72	0.2	6.87 (4.29)	7.28 (4.51)	5.10 (3.42)	176	166
JCET-v23/ilrsa-v24	1.20	1.09	3.77	0.26	9.13 (5.79)	9.56 (6.82)	18.60 (12.66)	242	218
NSGF-v24/ilrsa-v24	4.54	5.08	9.76	0.63	14.34 (10.53)	16.76 (12.49)	11.74 (7.43)	554	466
ilrsa v24 / ITRF2008p	*3.50*	*3.35*	*7.07*	*0.62*	*10.91*	*10.63*	*8.8*	*201*	*199*

Table 3. Helmert parameters and station positions and EOP residuals for AC individual contributions w.r.t. the ILRS combined solution, and for ilrsa-v24 solution w.r.t. ITRF2008p and the IERS 05 C04 series

6 Conclusion

We analysed the SLR part of the preliminary version of ITRF2008p. Based on an evaluation in terms of Helmert parameters and 3D WRMS of the coordinate residuals, it seems that the new ITRF is performing better. Station position series WRMS have a better stability in the three components, and we noticed big improvements for SLR stations 7810 and 7403. Let us note that since ITRF retrieves coordinates and velocities from coordinate time series, under the asumption of linear station motion, all the realizations, including ITRF2008, are potentially affected by earthquakes, - as the one that occured near Concepcion, Chili, during spring 2010-: new realizations of the ITRF will still be required by the next few years. By the next few months, as an ILRS Analysis center, we will report further the official (final) ITRF2008[1] reference frame delivered by the ITRS Product Center, as well as the reference frame provided by the DGFI Combination Center, following the same protocol as in this paper.

[1]The final ITRF2008 solution can now be downloaded at the dedicated web site: `http://itrf.ign.fr/ITRF\_solutions/2008/ITRF2008.php` .

The authors thank the staff working at OCA, and that help them managing the French ILRS Analysis Center.

References

Deleflie, F., & Coulot, D., 2009, in *SF2A-2009: Proceedings of the Annual meeting of the French Society of Astronomy and Astrophysics*, M. Heydari-Malayeri, C. Reylé and R. Samadi (eds), p.97

Pearlman, M.R., Degnan, J.J., & Bosworth, J.M. 2002, in Advances in Space Research, 30, 135

SF2A 2010
S. Boissier, M. Heydari-Malayeri, R. Samadi and D. Valls-Gabaud (eds)

THE MICROSCOPE SPACE MISSION AND THE INFLIGHT CALIBRATION APPROACH FOR ITS INSTRUMENT

A. Levy[1], P. Touboul[1], M. Rodrigues[1], G. Métris[2] and A. Robert[3]

Abstract. MICROSCOPE is a fundamental physics space mission which aims at testing the Equivalence Principle (EP) with an accuracy of 10^{-15}. The gravitational signal is measured precisely by a differential electrostatic accelerometer which includes two cylindrical test masses made of different materials. The accelerometer is on-board a drag-free micro-satellite which is controlled either Earth pointing or rotating about the normal to the orbital plane with a very stable angular velocity. The expected accuracy of the EP test could be limited by the inaccurate *a priori* knowledge of the instrument physical parameters associated to the instrument environment on-board the satellite. These parameters are partially measured or estimated by means of ground tests or during the integration of the instrument on the satellite. However, these evaluations are not sufficient and an in-orbit calibration is therefore needed to finely characterize the instrument and to correct the measurements. After the overall presentation of the MICROSCOPE mission and its scientific goal, this paper will focus on the accelerometer and will describe the specific procedures proposed for the in-flight instrument calibration.

Keywords: equivalence principle, gravity, MICROSCOPE, space fundamental physics, accelerometer, calibration

1 Introduction

The Equivalence Principle (EP) expressed by Einstein as a basis of its theory of General Relativity states the universality of free fall. It has been tested throughout the years by ground-based experiments with an increasing accuracy which reaches a few 10^{-13} (Schlamminger et al. 2008). The accuracy is limited by the noisy environment in the laboratory and by the strong local gravity. However, the unification theories which try to merge General Relativity and Quantum Mechanics expect a violation of the EP below this value (Damour et al. 2002). To go beyond this limit, it has been proposed to perform the experiment in space where noise is minimized and the duration of the free fall is not limited. This is the objective of the MICROSCOPE space mission which aims at testing the EP with an accuracy of 10^{-15} (Touboul et al. 2001). To achieve this goal, the payload of the MICROSCOPE satellite is a differential electrostatic accelerometer composed of two test masses made of different material. The accelerometer measures the difference between the gravitational accelerations of the two masses while their inertial motions are controlled identical and thus indicates whether there is violation of the EP or not. The accuracy of the experiment is limited by the inaccurate *a priori* knowledge of the instrument parameters. These parameters have to be better evaluated in orbit. A first estimation is in fact obtained by means of ground tests and during the integration of the instrument in the satellite. An in-orbit calibration is nevertheless necessary to correct finely the measurement and reach the objective of the mission.

After a general presentation of the MICROSCOPE space mission, the instrument is described. The interest of an in-flight calibration is highlighted and quantified. The calibration approach is then presented with its preliminary results.

[1] Onera, F-92322 Châtillon, France
[2] Observatoire de la Côte d'Azur, 06130 Grasse, France
[3] CNES, 31401 Toulouse, France

2 The MICROSCOPE space mission

For the MICROSCOPE space mission, a 200 kg dedicated satellite is developed by CNES within its MYRIAD program of micro-satellite. The Earth is the gravitational source of the EP test and the satellite will be injected on a quasi circular (eccentricity $< 5 \times 10^{-3}$) and heliosynchronous orbit, at an altitude around 810 km. The characteristics of the orbit ensure thermal stability and a reduced correlation between the EP signal and the gravity gradient. The duration of the mission is planned to be one year while the orbit period is about 6000 s. The time span of the measurement, not limited by the free fall, will be superior to 20 orbits.

The payload of the satellite is composed of two independent electrostatic differential accelerometers developed in our laboratory at Onera. Each differential accelerometer includes two test masses and measures the difference between the inertial accelerations of the two masses. One accelerometer is composed of two different masses (platinum/titanium) to perform the EP test and one is composed of two identical masses (platinum/platinum) to be used as a reference. The mass and power budgets of the payload lead to 35 kg and 40 W. The instrument thermal control is passive in order to respect the constraints of the micro-satellite.

The mass motions of the accelerometer are servo-controlled to follow the same orbit with a precision better than 10^{-11} m. This is made possible by the electrostatic actuation which forces the masses to remain concentric. Thus, the two masses undergo the same gravity field and a difference between the electrostatic accelerations applied to the masses will indicate a violation of the Equivalence Principle. The environment is maintained very steady limiting any perturbation and the System of Control of Attitude and Acceleration (SCAA) exploits the measurement of the accelerometer in order to make the satellite drag free along the three degrees of freedom: the surface forces and torques applied on the satellite are countered continuously by the thrust of the propulsion system. To this extent, MICROSCOPE represents a technical challenge.

Another advantage of performing the experiment in space is that the phase and the frequency of the signal to be detected are very well defined. The satellite pointing can be either inertial or spinning, each mode having its advantage. For example when the satellite is spinning, the signal frequency is increased and thus closer to the minimum of the noise of the instrument. The considered spin frequency is 1 mHz and therefore the signal frequency f_{ep}, sum of spin and orbital frequency, will be 1.2 mHz. In inertial mode, the satellite angular velocity is controlled null, limiting the effects of the centrifugal acceleration perturbations.

3 The payload of the mission

A differential electrostatic accelerometer is composed of two cylindrical and co-axial masses, each of them surrounded by cylindrical electrode parts. The two test masses have identical moment of inertia along their three axes in order to minimize the gravity gradient effect. The electrode parts are in gold plated silica in order to ensure the thermal stability. The sensor unit core is maintained under a vacuum better than 10^{-5} Pa thanks to an Invar tight housing and a getter material on top of the sensor unit. The only physical contact on the levitated proof mass is one 5 μm gold wire. The purpose of this wire is to control the electrical potential of the mass. This potential is composed of a constant part used to apply the actuation force and a sinusoid part used to detect the position of the proof mass. Control loops maintain the mass centered and motionless. The same electrodes are in charge of the measurement of the position of the mass through variation of capacitance and of the control of the six degrees of freedom of the mass with electrostatic forces.

The mechanical heart of the sensor is connected to the front end electronic unit linked to the interface control unit. The first unit corresponds to the analog functions such as the position detection while the second one corresponds to the digital control laws and the satellite interface. The satellite payload is operated in a finely stabilized temperature environment and protected from perturbations by a magnetic shield.

The operation of the accelerometer is similar along the six axes and hereafter detailed along the measurement axis which is the cylinder axis (X axis): when the mass moves along this axis, a variation of the recovering surface appears leading to a difference of capacitance between the mass and each electrode corresponding to an analog signal provided by the position detector. This signal is numerized and processed by the control loop laws in order to generate a voltage proportional to the acceleration of the sensor. This voltage is amplified and applied to the electrodes in order to keep the mass at the centre. The output of the control laws is used by the drag free system. The scientific measurement must have a better accuracy so it is picked up on the electrodes at the end of the loop in order to get a lower noise.

4 The in-orbit instrument calibration

4.1 The accelerometer measurement

In the case of a perfect instrument, the accelerometer measurement would be the acceleration applied on the proof mass to maintain it at the centre of the electrostatic cage, $\vec{\Gamma}_{App,k}$ (proof mass k) expressed by:

$$\vec{\Gamma}_{App,k} = \left(\frac{M_{gsat}}{M_{Isat}} - \frac{m_{gk}}{m_{Ik}}\right)\vec{g}(O_{sat}) + (T - I)O_k\vec{O}_{sat} + \frac{\vec{F}_{NGsat}}{M_{Isat}} - \frac{\vec{F}_{NGk}}{m_{Ik}} \tag{4.1}$$

Where M_{gsat} and M_{Isat} are respectively the gravitational and inertial masses of the satellite, m_{gk} and m_{Ik} are respectively the gravitational and inertial masses of the proof mass, O_{sat} is the centre of mass of the satellite, O_k the centre of the proof mass, T is the gravity gradient tensor, I is the gradient of inertia tensor, $\vec{F}_{NGsat}$ and $\vec{F}_{NGk}$ are the non gravitational forces applied respectively on the satellite and the proof mass. The semi differential quantity $\Gamma_{App,d} = \frac{\Gamma_{App,1} - \Gamma_{App,2}}{2}$ thus provides the EP violation signal defined as $\frac{1}{2}(\delta g(O_{sat}))$, with $\delta = \frac{m_{g2}}{m_{I2}} - \frac{m_{g1}}{m_{I1}}$. We define also $\Gamma_{app,d}$ such that $\Gamma_{App,d} = \Gamma_{app,d} + b_{1d}$, with the index "d" meaning differential and with b_{1d} the opposite of the differential non gravitationnal acceleration applied on the proof mass.

But the actual semi differential measurement in the measurement bandwidth along the X axis depends also on the instrument following parameters:

$$\Gamma_{mes,d} = \frac{1}{2}K_{1cx}\delta g_x(O_{sat}) + \frac{1}{2}\begin{bmatrix} K_{1cx} \\ \eta_{cz} + \theta_{cz} \\ \eta_{cy} - \theta_{cy} \end{bmatrix}^t \cdot [T - I] \cdot \begin{bmatrix} \Delta_x \\ \Delta_y \\ \Delta_z \end{bmatrix} + \begin{bmatrix} K_{1dx} \\ \eta_{dz} + \theta_{dz} \\ \eta_{dy} - \theta_{dy} \end{bmatrix}^t \cdot (\vec{\Gamma}_{res_{df}} + \vec{C}) \tag{4.2}$$
$$+ 2K_{2cxx}(\Gamma_{app,d} + b_{1dx}) \cdot (\Gamma_{res_{df,x}} + C_x - b_{0cx}) + K_{2dxx}((\Gamma_{app,d} + b_{1dx})^2 + (\Gamma_{res_{df,x}} + C_x - b_{0cx})^2)$$

Where K_{1cx} and K_{1dx} are the common and differential scale factors along the X instrument axis, θ_{cz} and θ_{dz} (respectively θ_{cy} and θ_{dy}) are the common and differential misalignment parameters along Z (resp. along Y), η_{cz} and η_{dz} (respectively η_{cy} and η_{dy}) are the common and differential coupling parameters along Z (resp. along Y), Δ is the test mass relative off-centring in the satellite frame and K_{2cxx} and K_{2dxx} are the common and differential quadratic factors along X, b_{0cx} is the common read-out bias along X. $\vec{C}$ is the drag free command, C_x its component along X. $\vec{\Gamma}_{res_{df}}$ is the drag free loop residue, $\Gamma_{res_{df,x}}$ its component along X. $\Gamma_{res_{df,x}} + C_x - b_{0cx}$ is in first approximation equal to the common applied acceleration ($\Gamma_{App,c} = \frac{\Gamma_{App,1} + \Gamma_{App,2}}{2}$) used by the SCAA to make the satellite drag free.

4.2 The calibration process

The EP parameter must be detected with a resolution of $8 \times 10^{-15}\,\mathrm{ms}^{-2}$ to reach the objective of 10^{-15}. Tens of group of errors sources including mechanical defects, thermal and magnetic effects have been identified. For each of them, specifications have been associated in order to reach the measurement accuracy. In equation 4.2, three groups of errors explicitly appear depending on: integration of the instrument in the satellite which refers to all the common mode parameters, differences between the two sensors characteristics which refer to all the differential mode parameters and the quadratic non linearities. The values by construction of these parameters are such that they lead to an error by far too large compared to the specified accuracy (Guiu 2007). That is why it is necessary to estimate some parameters in order to correct the measurement and thus reach the specified accuracy. The idea is to amplify the parameter effect using both the capability of the SCAA to force the motion of the satellite through its thrusters and the sensor servo-control to force the motion of the test masses (Guiu 2007). A specific process is proposed to calibrate each parameter:

- $K_{1cx}\Delta_x$ and $K_{1cx}\Delta_z$ by using the Earth's gravity gradient at $2f_{ep}$ as the calibration signal; $K_{1cx}\Delta_y$ by forcing (through the drag-free command) the oscillation of the satellite around its Z axis ($K_{1cx}\Delta_x$ and $K_{1cx}\Delta_z$ can also be calibrated in similar way),
- $\eta_{cz} + \theta_{cz}$ and $\eta_{cy} - \theta_{cy}$ by simultaneously forcing the oscillation of the satellite around the X axis of the instrument and the test mass respectively along its Z axis and Y axis, thus creating a Coriolis effect,
- $K'_{dx}/K_{cx} = (K_{dx} + 2K_{2cxx}b_{1dx} + K_{2dxx}(C_x - b_{0cx}))/K_{cx}$, $(\eta_{dz} + \theta_{dz})/K_{cy}$ and $(\eta_{dy} - \theta_{dy})/K_{cz}$ by forcing the oscillation of the satellite along the instrument X, Y, Z axis. We chose to estimate K'_{dx}/K_{cx} instead of only K_{dx}/K_{cx}, in order to include the biases in the parameter to be estimated and this way to correct the scientific measurement of their effect through the quadratic terms.

- K_{2dxx}/K_{cx}^2 by forcing (through the drag-free command) the oscillation of the satellite along the X axis of the instrument and by analysing the measurement at the double of the oscillation frequency,
- K_{2cxx}/K_{cx}^2 by estimating separately K_{21xx}/K_{11x}^2 and K_{22xx}/K_{12x}^2. To calibrate K_{21xx}/K_{11x}^2 (respectively K_{22xx}/K_{12x}^2) the drag compensation shall be locked on the sensor 2 (resp. 1) and the proof mass 1 (resp. 2) forced to oscillate along its X axis; the measurement 1 (resp. 2) is analyzed at the double of the oscillation frequency.

A standard duration of 10 orbits is selected for each calibration process. After one single round of calibration the data are reprocessed; each iteration improves the global accuracy as the assessment of all individual parameters benefits from the refinement of the other parameters that take part in the measurement equation. The performance of the calibration has been evaluated analytically. We see (table 1) that the calibration process satisfies the requirements for all parameters.

Parameters to be calibrated	Specification	Performance after calibration
$K_{1cx}\Delta_x$	$0.1\,\mu$m	$0.07\,\mu$m
$K_{1cx}\Delta_z$	$0.1\,\mu$m	$0.07\,\mu$m
$K_{1cx}\Delta_y$	$2\,\mu$m	$1.3\,\mu$m
$\eta_{cz}+\theta_{cz}$	1×10^{-3} rad	1.1×10^{-3} rad
$\eta_{cy}-\theta_{cy}$	1×10^{-3} rad	1.0×10^{-3} rad
K'_{dx}/K_{cx}	1.5×10^{-4}	3.5×10^{-5}
$(\eta_{dz}+\theta_{dz})/K_{cy}$	5×10^{-5} rad	1.5×10^{-5} rad
$(\eta_{dy}-\theta_{dy})/K_{cz}$	5×10^{-5} rad	1.5×10^{-5} rad
K_{2dxx}/K_{cx}^2	$250\,\mathrm{s}^2/\mathrm{m}$	$55.9\,\mathrm{s}^2/\mathrm{m}$
K_{2cxx}/K_{cx}^2	$14000\,\mathrm{s}^2/\mathrm{m}$	$581.5\,\mathrm{s}^2/\mathrm{m}$

Table 1. Analytical evaluation of the performance of the calibration process

5 Conclusion

The scientific data of the MICROSCOPE mission have to be corrected in order to reject inaccuracies of the instrument. Therefore, an in-flight calibration has to be performed. The relevant parameters to be calibrated have been determined and an appropriate calibration method has been proposed for each of them. The analytical simulation of the errors of the calibration process shows that the needed parameters of the instrument can be estimated with an accuracy that complies with the objective of MICROSCOPE. The next step of this evaluation is the development of a software which will include the satellite attitude and the drag free system. Such a calibration approach could be considered for other space missions exploiting ultra sensitive accelerometers.

Concerning the development of the instrument, the qualification phase has started as well as the procurements for the flight models. In parallel, the satellite definition that had suffered from difficulties in the propulsion system development is now being completed by considering thrusters similar to the GAIA satellite. And a launch in 2014 is expected.

The authors wish to thank the MICROSCOPE teams at CNES, OCA and ZARM for the technical exchanges. This activity has received the financial support of Onera.

References

Damour, T., Piazza, F., & Venezziano, G. 2002, Phys. Rev. D, 046007

Guiu, E. 2007, Étalonnage de la mission spatiale MICROSCOPE : optimisation des performances, 220. PhD Thesis, University of Nantes

Schlamminger, S., Choi, K., Wagner, T.A. et al. 2008, Phys. Rev. Letter, 100, 041101

Touboul, P., Rodrigues, M., Métris, G. et al. 2001, CRAS, Paris, 2, IV, 9, pp. 1271-1286

THE EVECTION RESONANCE: SOLAR AND OBLATENESS PERTURBATIONS

J. Frouard[1], M. Fouchard[2] and A. Vienne[2]

Abstract. Among resonances commonly influential to the dynamics of satellites, the evection resonance introduces an important correction to the precession frequency of the satellite, as it is well known for the Moon's problem. However, the dynamic of the resonance itself, which is important for satellites stability and capture topics, including its libration and circulation regions, and its elliptic and hyperbolic points, has not been extensively studied. Here we investigate its dynamic with an improved analytic model, making comparisons with previous works, and resort to numerical methods and integrations to study and localize the different features of the resonance. This resonance is found in the outer orbital region near the orbital stability limit. However we also study and localize an other libration region that can be found much more closer to the parent planet when its oblateness is taken into account in the model.

Keywords: celestial mechanics, planets and satellites: general

1 Introduction

The dynamics of the evection resonance $\alpha = \lambda' - \varpi$ (λ' being the longitude of the perturbing body and ϖ being the longitude of pericenter of the satellite) has been studied using an expansion of the solar disturbing function for the first time by Yokoyama et al. (2008). Their results detailled the shape of the resonance for the prograde and retrograde cases, and the apparition in semi-major axis of its elliptic and hyperbolic points.

However, numerical simulations show that resonant orbits can be found closer to the planet and seem to follow different dynamics that the ones predicted by the analytical model. We have thus extended the model of Yokoyama et al. (2008) to upper orders and use a numerical method to precisely determine the dynamics of the resonance (Frouard et al. 2010). In addition, we found that the resonance can be found closer to the planet by taking into account its oblateness.

2 Solar perturbations

We show in Fig.1 the dynamical portrait of the resonance applied to a prograde satellite of Jupiter using the analytical model. This model is developed in Legendre polynomials ; the upper panels of the figure show the dynamics as given by the 2^{nd} polynomial (Yokoyama et al. 2008), while the bottom panels show the modification due to the inclusion of the 3^{nd} polynomial. This term has an important impact on the dynamics and makes the resonance assymetric. This dynamic is closer to the real one but is displaced in semi-major axis. The real locations of the elliptic and hyperbolic points of the resonance as given by the numerical method are shown on Fig.2 (left).

3 Oblateness of the parent planet

Resonant orbits can be found closer to the planet when its oblateness (here we use the $J2$ approximation) is taken into account. An example is shown on Fig.2 (right).

[1] IMCCE/LAL, Observatoire de Paris, UMR 8028, Avenue Denfert-Rochereau, 75014 Paris, France
[2] Université de Lille 1, IMCCE/LAL, UMR 8028, 59000 Lille, France

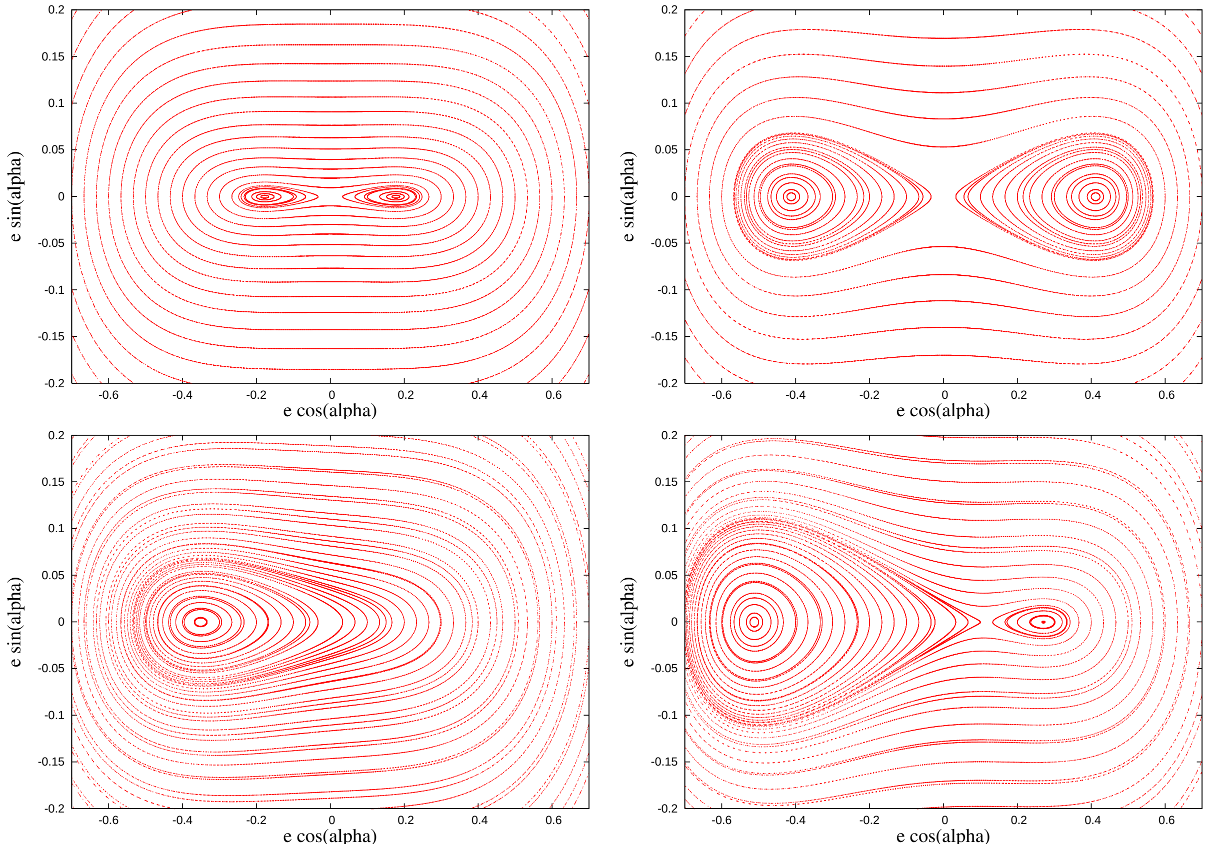

Fig. 1. Analytical averaged model. Dynamics of the evection resonance for a prograde satellite using a model up to the 2^{nd} order polynomial for $a = 0.19$ AU (**top left**) and $a = 0.2$ AU (**top Right**), and up to the 3^{rd} order polynomial for $a = 0.19$ AU (**bottom left**) and $a = 0.2$ AU (**bottom right**).

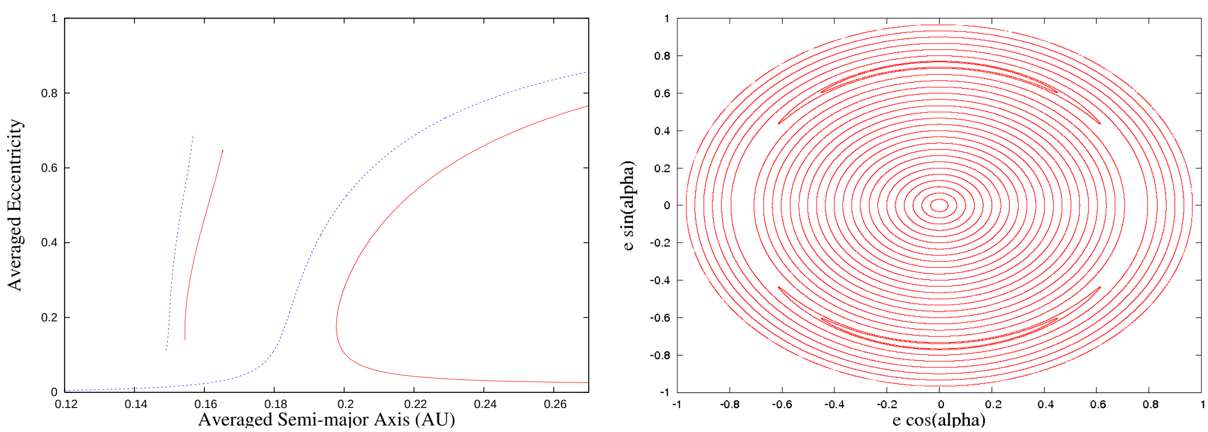

Fig. 2. Left : Location of the evection resonance for prograde satellites with the numerical method (in averaged elements) (the two left curves) and with the analytical model (the two right curves). The island $\alpha = \pi$ is indicated by the dot line, the island $\alpha = 0$ by the solid one. **Right** : Dynamical portrait of the evection resonance for a Jovian satellite with semi-major axis $a = 0.00515$ AU, taking into account the Jupiter's J_2

4 Conclusions

We have investigated the dynamics of the evection resonance and have shown with analytical and numerical methods its location. We also report the presence of the resonance closer to the planet due to its oblateness.

References

Frouard, J., Fouchard, M., & Vienne, A. 2010, A&A, 515, 54

Yokoyama, T., Vieira Neto, E., Winter, O. C., Sanchez, D. M., de Oliveira Brasil, P. I. 2008, Mathematical Problems in Engineering, vol. 2008, doi:10.1155/2008/251978

PCHE

High energy cosmic phenomena

OBSERVATIONS WITH THE HIGH ALTITUDE GAMMA RAY (HAGAR) TELESCOPE ARRAY IN THE INDIAN HIMALAYAS

R.J. Britto[1], B.S. Acharya[1], G.C. Anupama[2], N. Bhatt[3], P. Bhattacharjee[4], S.S. Bhattacharya[3], V.R. Chitnis[1,2], R. Cowsik[2,5], N. Dorji[1], S.K. Duhan[1], K.S. Gothe[1], P.U. Kamath[2], R. Koul[3], P.K. Mahesh[2], A. Mitra[3], B.K. Nagesh[1], N.K. Parmar[1], T.P. Prabhu[2], R.C. Rannot[3], S.K. Rao[1], L. Saha[4], F. Saleem[2], A.K. Saxena[2], S.K. Sharma[1], A. Shukla[2], B.B. Singh[1], R. Srinivasan[2], G. Srinivasulu[2], P.V. Sudersanan[1], A.K. Tickoo[3], D. Tsewang[2], S. Upadhya[1], P.R. Vishwanath[2] and K.K. Yadav[3]

Abstract. For several decades, it was thought that astrophysical sources emit high energy photons within the energy range of the gamma-ray region of the electromagnetic spectrum also. These photons originate from interactions of high energy particles from sources involving violent phenomena in the Universe (supernovae, pulsars, Active Galactic Nuclei, etc.) with gas and radiation fields. Since the first reliable detections of cosmic gamma rays in the 1970's, improvements in instrumentation have led gamma-ray astronomy to an established branch of modern Astrophysics, with a constant increase in the number of detected sources. But the 30-300 GeV energy range remained sparsely explored until the launch of the Fermi space telescope in June 2008. The ground-based gamma-ray telescope array HAGAR is the first array of atmospheric Cherenkov telescopes established at a so high altitude (4270 m a.s.l.), and was designed to reach a relatively low energy threshold with quite a low mirror area (31 m^2). It is located at Hanle in India, in the Ladakh region of the Himalayas. Regular source observations have begun with the complete setup of 7 telescopes on Sept. 2008. We report and discuss our estimation of the systematics through dark region studies, and present preliminary results from gamma-ray sources in this paper.

Keywords: gamma rays: atmospheric Cherenkov technique, methods: data analysis, telescopes: HAGAR

1 The HImalayan Gamma-Ray Observatory (HIGRO)

Located at 4270 m a.s.l. in the Ladakh region of the Himalayas, in North India (Latitude: 32°46'47" N, Longitude: 78°59'35"E), the HImalayan Gamma-Ray Observatory (HIGRO) is a collaboration between four Indian Institutes: Bhabha Atomic Research Centre (BARC) and Tata Institute of Fundamental Research (TIFR) in Mumbai (Bombay), Indian Institute of Astrophysics (IIA) in Bangalore, and Saha Institute of Nuclear Physics (SINP) in Kolkata (Calcutta). It consists of two experiments using the Atmospheric Cherenkov Technique (Koul et al (2005) & Fig. 1). Operating with the full array of telescopes since 2008, the HAGAR experiment is a sampling array of 7 telescopes built with 7 para-axially mounted 0.9 m diameter mirrors each one, giving a total reflective area of ~ 31 m^2 (Chitnis et al. 2009a). The phase 2 of HIGRO will be the installation of an imaging 21 m diameter telescope, MACE (Major Atmosperic Cherenkov Experiment), whose first light is expected in 2012 (Yadav et al. 2009). Other characteristics of this new instrument are a total reflective area of ~ 330 m^2 from 356 mirror pannels, f/1.2 m, FOV of $4° \times 4°$, 1088 pixels. In 2016, MACE should be completed by three additional similar telescopes. The location in longitude of HIGRO will allow uninterupted observations along with other major gamma-ray observatories of the Northern Hemisphere: MAGIC in Canary Islands and VERITAS in the USA. This is particurlary convenient to monitor sources such as AGNs, with flux variabilities in sub-hour time scales.

[1] Tata Institute of Fundamental Research, Homi Bhabha Road, Mumbai 400 005, India
[2] Indian Institute of Astrophysics, Sarjapur Road, 2nd Block, Koramangala, Bangalore 560034, India
[3] Bhabha Atomic Research Centre, Trombay, Mumbai 400 085, India
[4] Saha Institute of Nuclear Physics, 1/AF, Bidhannagar, Kolkata 700 064, India
[5] Now at Washington University, St Louis, MO 63130, USA

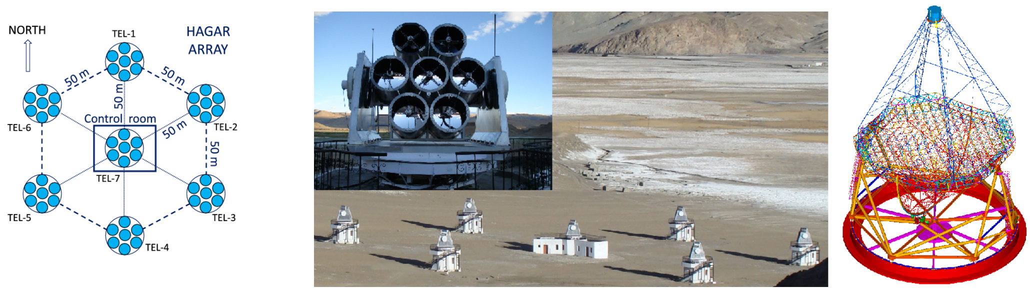

Fig. 1. *Left and middle:* the HAGAR telescope array. *Right:* MACE design

HAGAR operates with a trigger logic designed to significantly reject random triggers due to night sky background light, as well as some of the cosmic ray events. Thus, a coincidence of any 4 telescope pulses above a preset threshold out of 7 telescope pulses, within a resolving time of 150 to 300 ns, is required to generate a trigger pulse. Preliminary simulations yield an estimation of the HAGAR energy threshold to be around 200 GeV before performing analysis cuts on data, for a total experimental trigger rate around 14 Hz. Investigations and tests are currently undergoing to approch the 100 GeV energy threshold.

2 Preliminary analysis of HAGAR data

In order to remove isotropic emission due to cosmic rays, source observation region (ON) is compared with OFF-source region at same local coordinates on the sky, but at a different time (before or after tracking the source region). The Crab nebula, standard candle of the γ-ray astronomy, is used to calibrate the instrument and optimize hadronic rejection. However, signal extraction can be confirmed if background fluctuation between ON and OFF-axis source is not dominant, so an important step in the validation of the analysis method is to observe and analyse data by comparing two sets of OFF-source regions (called dark regions), located at a similar declination of Crab nebula ($\simeq 22°$). A statistical significance less than 3 σ was obtained from 6.6 hours of dark region data (13 pairs) in our preliminary analysis, which is an indication that systematic effects due to sky and time differences during observations are not dominant in our data/analysis. The analysis of 9.1 hours of Crab nebula data (13 pairs) from the period Sept-Dec 2008 gives an excess from the source direction at 6.0 σ significance, corresponding to 4.1 ± 0.7 counts min^{-1} above $\sim$ 250 GeV (Britto et al. 2009).

Several other sources are observed with HAGAR. We give in brackets the duration in hours of the ON-source observations up to September 2010: Galactic sources: Crab Nebula and pulsar (83), Geminga pulsar (59), X-ray binary LSI +61 303 (8), MGRO 2019+37 (13); and extragalactic sources (blazars): Markarian 421 (75) and 501 (49), 1es2344+514 (52), and 3C454.3 (13). Preliminary results from Mkn421 (Chitnis et al. 2009b) and pulsars (Acharya et al. 2009) were reported as upper limits on the fluxes of the gamma rays.

Further improvements in the On/Off pair selection, as well as development of hadronic rejection methods based on simulations and flash ADCs, are expected to improve these preliminary results (Britto et al. 2010). From 2012, MACE is expected to be operational, next to the HAGAR array. MACE was design to reach an energy threshold as low as $\sim$20 GeV, which is good for the studies of pulsars and high redshift AGNs where spectral energy distribution cutoffs are expected.

R.J. Britto would like to thank the organisers of the SF2A conference and the PCHE group for providing financial support to attend the conference. We thanks all members of our institutes and visiting students who have contributed towards the design, fabrication and testing of telescope, and data acquisition systems of HAGAR.

References

Acharya, B.S. et al, 2009, Paper # icrc0669, Proc. of the 31^{st} ICRC

Britto, R.J. et al, 2009, Proc. of SF2A-2009, Annual meeting of the French Society of Astronomy and Astrophysics, M. Heydari-Malayeri, C. Reylé and R. Samadi (eds), p. 131

Britto, R.J. et al, 2010, this volume, p. 139 (`http://proc.sf2a.asso.fr/2010/2010sf2a.conf..0139B.pdf`)

Chitnis, V.R. et al, 2009a, Paper # icrc0696, Proc. of the 31^{st} ICRC

Chitnis, V.R. et al, 2009b, Paper #icrc0697, Proc. of the 31^{st} ICRC

Koul, R. et al. 2005, Proc. of the 29^{st} ICRC, Vol. 5, p. 243
Yadav, K.K. et al. 2009, Proc. of the 44^{th} Rencontres de Moriond (`arXiv.org/abs/0904.3647`)

SF2A 2010
S. Boissier, M. Heydari-Malayeri, R. Samadi and D. Valls-Gabaud (eds)

TOWARDS NEW ANALYSIS OF GAMMA-RAY SOURCES AT HIMALAYAN GAMMA-RAY OBSERVATORY (HIGRO) IN NORTHERN INDIA

R.J. Britto[1], B.S. Acharya[1], G.C. Anupama[2], N. Bhatt[3], P. Bhattacharjee[4], S. Bhattacharya[3], V.R. Chitnis[1,2], R. Cowsik[2,5], N. Dorji[1], S.K. Duhan[1], K.S. Gothe[1], P.U. Kamath[2], R. Koul[3], P.K. Mahesh[2], A. Mitra[3], B.K. Nagesh[1], N.K. Parmar[1], T.P. Prabhu[2], R.C. Rannot[3], S.K. Rao[1], L. Saha[4], F. Saleem[2], A.K. Saxena[2], S.K. Sharma[1], A. Shukla[2], B.B. Singh[1], R. Srinivasan[2], G. Srinivasulu[2], P.V. Sudersanan[1], A.K. Tickoo[3], D. Tsewang[2], S.S. Upadhya[1], P.R. Vishwanath[2] and K.K. Yadav[3]

Abstract. The High Altitude GAmma-Ray (HAGAR) array is a wavefront sampling array of 7 telescopes, set-up at Hanle, at 4270 m a.s.l., in the Ladakh region of the Himalayas (North India). It constitutes the first phase of the HImalayan Gamma-Ray Observatory (HIGRO) project. HAGAR is the first array of atmospheric Cherenkov telescopes established at a so high altitude, and was designed to reach a relatively low threshold (currently around 200 GeV) with quite a low mirror area (31 m^2). Data are acquired using the On-source/Off-source tracking mode, and by comparing these sky regions the strength of the gamma-ray signal is estimated. Regular source observations are running since Sept. 2008 and preliminary results on Crab nebula were reported by 2009. Improvements of our analysis method are still going on, like estimation of arrival direction and estimation of night sky background. New softwares are under development for analysis of flash ADC modules, which provide more information from the incoming Cherenkov light wavefront. We report and discuss our new estimation of the systematics through dark region studies, and present new perspectives in the analysis of gamma-ray sources in this paper.

Keywords: gamma rays: atmospheric Cherenkov technique, methods: data analysis, telescopes: HAGAR

1 The HAGAR experiment

Located at 4270 m a.s.l. in the Ladakh region of the Himalayas, in North India (Latitude: 32°46'47" N, Longitude: 78°59'35"E), the HImalayan Gamma-Ray Observatory (HIGRO) was designed to conduct experiments using the Atmospheric Cherenkov Technique (Britto et al. 2010). Operating with the full array of telescopes since 2008, the HAGAR experiment is a the first phase of HIGRO. It is a sampling array of 7 telescopes, each one built with 7 para-axially mounted 0.9 m diameter mirrors. Other characteristics are: f/D $\sim$ 1; fast Photonis UV sensitive PMTs XP 2268B at the focus of each mirror and with a field of view of $3°17'$; data recorded for each event: relative arrival time of shower front at each mirror accurate to 0.25 ns using TDCs; total charge at each mirror recorded using 12 bit QDCs (ADCs); absolute event arrival time accurate to μs; for trigger generation, the 7 pulses of PMTs of a given telescope are linearly added to form telescope pulse, called *royal sum* pulse. HAGAR operates with a trigger logic designed to significantly reject random triggers due to night sky background (NSB), as well as some of the cosmic ray events. Thus, a coincidence of any 4 telescope pulses above a preset threshold out of 7 royal sum pulses within a resolving time of 150 to 300 ns generates a trigger pulse (Chitnis et al. 2009a). Preliminary simulations yield an estimation of the HAGAR energy threshold to be around 200 GeV from vertical showers, before performing analysis cuts on data, for a total experimental trigger rate around 14 Hz. The phase 2 of HIGRO will be the installation of an imaging 21 m diameter telescope MACE (Major Atmosperic Cherenkov Experiment), whose first light is expected in 2012 (Yadav et al. 2009).

[1] Tata Institute of Fundamental Research, Homi Bhabha Road, Mumbai 400 005, India
[2] Indian Institute of Astrophysics, Sarjapur Road, 2nd Block, Koramangala, Bangalore 560034, India
[3] Bhabha Atomic Research Centre, Trombay, Mumbai 400 085, India
[4] Saha Institute of Nuclear Physics, 1/AF, Bidhannagar, Kolkata 700 064, India
[5] Now at Washington University, St Louis, MO 63130, USA

2 Signal extraction procedure

The analysis of HAGAR data is based on the arrival angle estimation of the incident atmospheric shower w.r.t. the source direction. This angle—called space angle—is obtained for each event by measuring relative arrival times of the showers at each telescope. Precise time calibration of the optoelectronic chain is then required, as well as an accurate pointing of telescopes (Chitnis et al. 2009a). The former is achieved first by computing TDC differences between telescopes from fix angle runs where the theoretical time-offsets are computed, using information on the pointing direction, coordinates of telescopes, and on the transit time of each channel through the electronic chain. The TDC differences between telescopes from fix angle runs yield the calculation of what we call "T_0's" (say "t-zeros"), which are the relative time offsets for all telescope to be used in the analysis to ensure a valid estimation of the relative timing differences in the arrival of the Cherenkov signal on the telescopes. Space angle is then computed by fitting the arriving spherical Cherenkov wavefront, using plane front approximation. For each event, the value of the χ^2 of the fit and other fit parameters are given, and the number of telescopes with valid TDC information, *i.e.* participating in the trigger, is written. Thus are defined four types of events, based on the *Number of Triggered Telescopes* (NTT), viz. events with NTT=4, NTT=5, NTT=6 and NTT=7.

In order to remove isotropic emission due to cosmic rays, source observation region (ON) is compared with OFF-source region at same local coordinates on the sky, but at a different time (before or after tracking the source region for about 30-50 mins). Atmospheric conditions change during observation time, reflected by variations on the trigger rate readings. This add systematics in our analysis. Normalisation of background events of both the ON and OFF source data sets is done by comparing number of events at large space angles, where no gamma-ray signal is expected. This yield a ratio, called normalisation constant, which allows to calculate the ON-OFF excess below one specific cut on the space angle distribution. More on the descrition of the analysis method and data selection can be found in Britto et al. (2009b).

3 Preliminary analysis of HAGAR data

Crab nebula, standard candle of the γ-ray astronomy, is used to calibrate the instrument and optimize hadronic rejection. However, signal extraction can be confirmed if background fluctuation between ON and OFF-axis source is not dominant, so an important step in the validation of the analysis method is to observe and analyse data by comparing two sets of OFF-source regions (called dark regions), located at a similar declination as of Crab nebula ($\simeq 22°$). A statistical significance less than 3 σ was obtained from 6.6 hours of dark region data (13 pairs) in our preliminary analysis, which indicates that systematic effects due to sky and time differences during observations are not dominant in our data/analysis. The analysis of 9.1 hour of Crab nebula data (13 pairs) from the period Sept-Dec 2008 gives about 6.0 σ, corresponding to 4.1 ± 0.7 *counts* min^{-1} above ~ 250 GeV (Britto et al. 2009a,b).

In our earlier analysis, T_0's were computed by using all triggering events, *i.e.* events with $NTT \geq 4$. However, the more telescopes we used in reconstructing the Cherenkov wavefront, the more accurate should be the space angle estimation, as the impact parameter of the shower will be smaller. In the same way, estimation of T_0's is expected to be more accurate when we keep only events with NTT=7 to compute TDC differences, as the curvature of the Cherenkow wavefront is smaller (the impact parameter is smaller, so the plane front approximation of the spherical front whose impact parameter is unknown will be more accurate). We show in Fig. 1 the count rates of dark regions using T_0's computed with all events versus T_0's computed using only 7 fold events. We notice less fluctuation in the count rates while using the new set of T_0's: the standard deviation is equal to 3.8 in the latter case, but 6.7 in the former one.

4 Development of a new analysis for HAGAR

Recent developments in our analysis as well as the upgrade of our hardware setup provide us with additional tools to improve our signal extraction methods.

4.1 Improvement of the timing analysis using T_0's

The T_0 value of Telescope 7 (central telescope) is set at 0 as the reference (Fig. 2 *(bottom left)*). The difference between two extremes T_0 values can be as large as 20 ns. As we require a timing precision of 1 ns, the accuracy of the calculation of T_0's is fundamental. In the process of establishing an accurate analysis method, we have

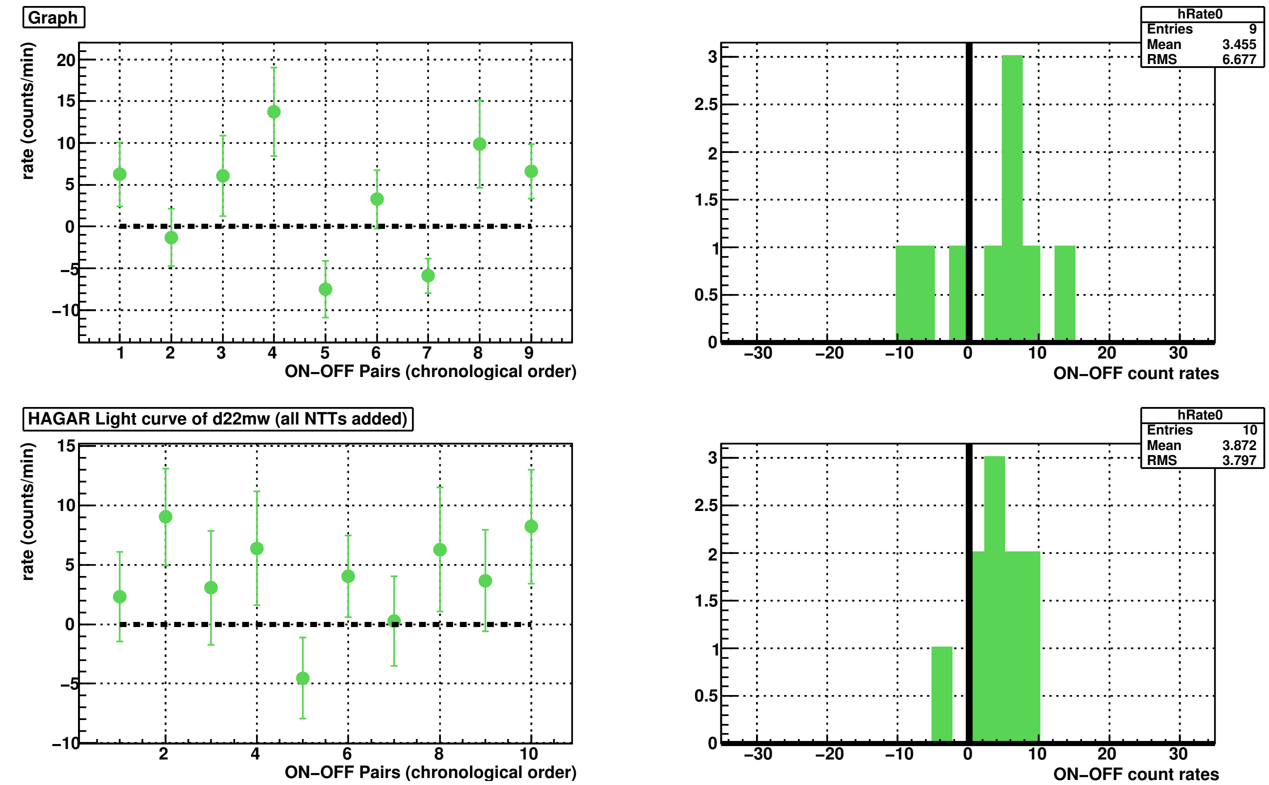

Fig. 1. Count rates from dark regions and distribution of these count rates. *Top:* Analysis with T_0's computed using all events. *Bottom:* Analysis with T_0's computed using events with NTT=7 only.

investigated several ways of computing T_0's. As a dedicated calibration system which would flash same amount of light simultaneously at each PMT is not yet implemented, we compute T_0's using real cosmic-ray events from fix angle runs, as already mentionned above. We need to perform fix angle runs for a long enough duration (typically 40 to 60 mins), so that our statistics is relevant to fit the mean values of the TDC differences.

We have recently found out that the result of the computation of a set of T_0's is dependant of the geometry of the telescope location in the array. As we require that at least 4 telescopes out of 7 get a signal above a preset threshold, we have 64 possible combinations: events which trigger Tel. 1,2,3,4, events which trigger Tel. 1,2,3,5, etc, until events which trigger the combination 1,2,3,4,5,6,7. Through every 64 trigger combination, HAGAR samples the Cherenkov front with a bias which is inherent to the geometric combination of telescopes. The 7-Fold configuration will sample a larger part of the Cherenkov wavefront (which corresponds in average to a smaller impact parameter of the shower, as described above), the combination 1,2,6,7 will sample a smaller part, the combination 1,5,6,7 will sample another smaller part of the wavefront (Fig. 2 *(bottom left)*). Preliminary tests showed us relevance of analysing source data using the 64 combinations of T_0's. We show in Fig. 2 the comparison of space angle distributions displayed for each NTT, when computed by two different methods. The *bottom left* figure contains the space angle distributions computed by applying only one value of T_0 per telescope (computed with 7 fold events only). The *bottom right* figure is after application of the 64 T_0 sets of values (one set per trigger combination). A sharper shape, as well as a smaller mean value of the space angle of NTT=4, 5 and 6, is observed. We expect this new method to allow a more accurate hadronic rejection through the space angle analysis cut.

4.2 Flash ADCs

Since April 2009, we collect data using a parallel acquisition system of Flash ADC in addition to the regular CAMAC-based data acquisition system (TDCs and QDCs). We use two 4-channel modules of Acqiris flash ADC (FADC) digitizer model DC271A. This is a 8 bit compact PCI digitizer with 1 GHz bandwidth with 50 Ω resistance and sampling rate of 1 GS/s. Seven telescope pulses are input to this module. This will enable

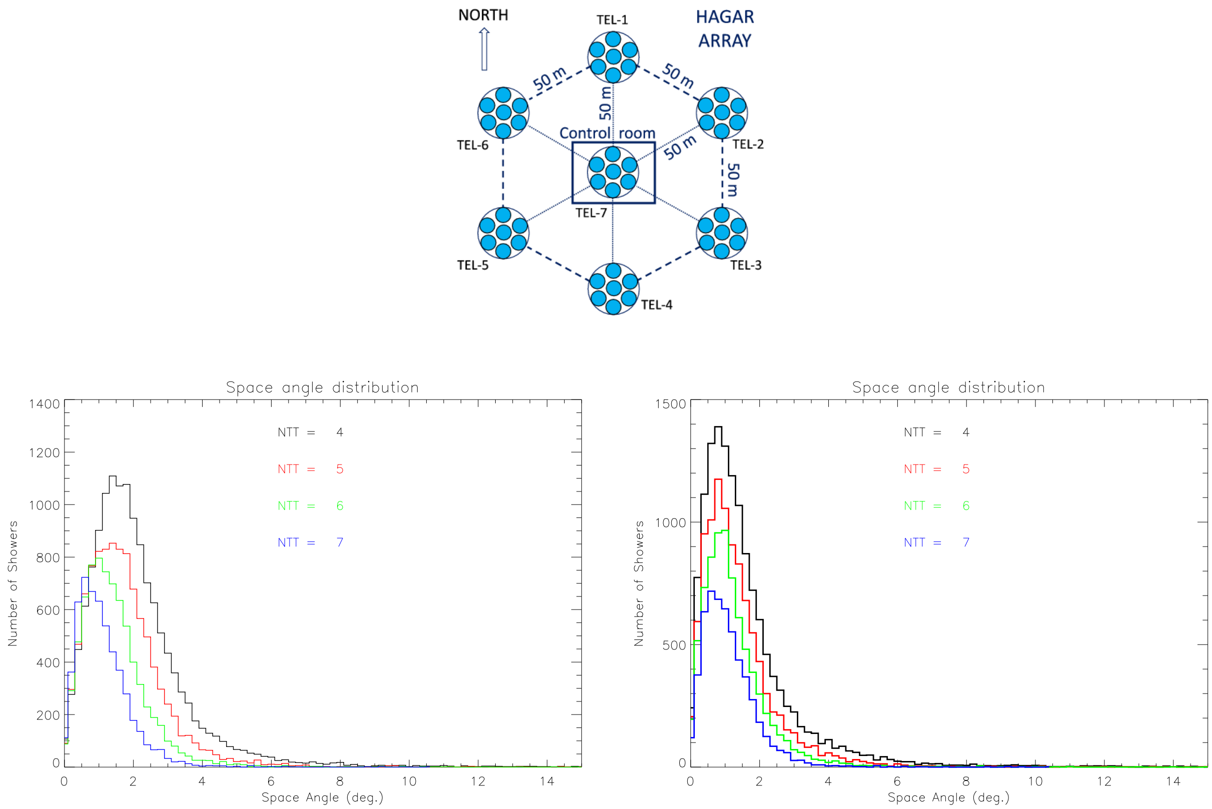

Fig. 2. *Top:* HAGAR layout of the 7 telescopes. *Bottom left and right:* Space angles for the four NTTs of a fix angle run. *Bottom left:* a single value of T_0 per telescope; *Bottom right:* 64 sets of T_0's.

us to study pulse shape, use gamma-hadron separation parameters based on pulse shape, reduce night sky background contribution by restricting window around Cherenkov pulse and also incorporate a technique for a software padding, as applied for the CELESTE experiment (Naurois et al. 2002). We show in Fig. 3 *(left)* a typical saturated FADC event, with a typical pulse fit by a log-normal function (enclosed). We see, on the *right* figure, a zoom on the first 40 nanoseconds, whose counts correspond to a typical night sky background light on FADCs. These 40 ns are used to plot the pedestal of the night sky background for each telescope channel. By comparing NSB in the ON versus OFF data acquisition, we can evaluate the NSB difference and we can expect to balance this difference by an offline addition of noise on the channel with less noise, through the procedure of software padding.

4.3 Hardware upgrade

In July 2010 several upgrades have been implemented in our hardware setup: a meter for monitoring the night sky brightness, and a home made programmable discriminator unit where threshold level could be remotely controled. Also, the trigger circuit was modified and upgraded in order to reduce the width of the coincidence window (to reduce chance triggers). Further upgradation is also planned to linearly add all telescope pulses through what we call "Grand Sum pulse", which could reduce the HAGAR energy threshold. This *Grand Sum* logic will demand the installation of programmable analog delays. Lastly, a new data format for additional house keeping information has been implemented.

5 Conclusion

Observation with the HAGAR telescope array are regular since September 2008. Several Galactic and extra-galactic sources are observed. After reporting preliminary results on the Crab nebula and dark regions, we have implemented new developments in our analysis method. Improvement of the method and development of new

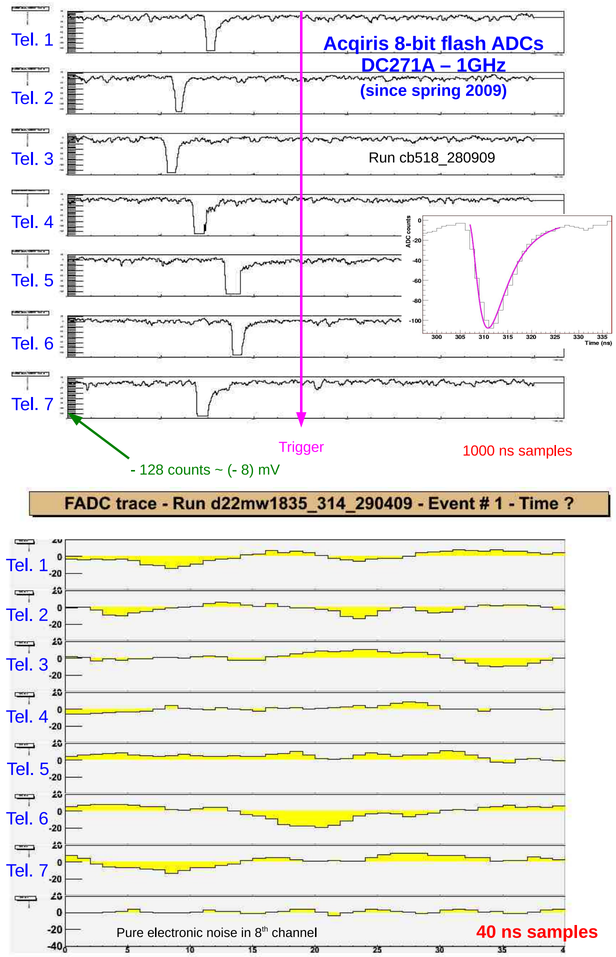

Fig. 3. *Left:* One FADC event, saturated for the seven telescope pulses. Enclosed is a typical event fit with a gamma function. *Right:* Zoom on the 40 first nanoseconds of the FADC windows, for each royal sum, for a typical event (only night sky and electronic noise. The 8^{th} channel is not connected to any telescope.

analysis softwares are still under going. Upgrade of the hardware also give us good expectation in controlling more systematics and decreasing the energy threshold.

R. J. Britto would like to thank the organisers of the SF2A conference and the PCHE group for providing financial support to attend the conference. We thanks all members of our institutes and visiting students who have contributed towards the design, fabrication and testing of telescope, and data acquisition systems of HAGAR.

References

Acharya, B. S. et al, 2009, Paper # icrc0669, Proc. of the 31^{st} ICRC

Britto, R. J. et al, 2009a, Proc. of SF2A-2009, Annual meeting of the French Society of Astronomy and Astrophysics, M. Heydari-Malayeri, C. Reylé and R. Samadi (eds), p. 131

Britto, R. J. et al, 2009b, Paper # icrc0669, Proc. of the 31^{st} ICRC

Britto, R. J. et al, 2010, this volume, p. 135 (`http://proc.sf2a.asso.fr/2010/2010sf2a.conf..0135B.pdf`)

Chitnis, V. R. et al, 2009a, Paper # icrc0696, Proc. of the 31^{st} ICRC

Chitnis, V. R. et al, 2009b, Paper # icrc0697, Proc. of the 31^{st} ICRC

De Naurois, M. et al. 2002, ApJ, 566, 343

Yadav, K. K. et al, 2009, Proc. of the 44^{th} *Rencontres de Moriond*, `arXiv.org/abs/0904.3647`

SF2A 2010
S. Boissier, M. Heydari-Malayeri, R. Samadi and D. Valls-Gabaud (eds)

HIGH-ENERGY RADIATION FROM THE RELATIVISTIC JET OF CYGNUS X-3

B. Cerutti[1], G. Dubus[1] and G. Henri[1]

Abstract. Cygnus X−3 is an accreting high-mass X-ray binary composed of a Wolf-Rayet star and an unknown compact object, possibly a black hole. The gamma-ray space telescope *Fermi* found definitive evidence that high-energy emission is produced in this system. We propose a scenario to explain the GeV gamma-ray emission in Cygnus X−3. In this model, energetic electron-positron pairs are accelerated at a specific location in the relativistic jet, possibly related to a recollimation shock, and upscatter the stellar photons to high energies. The comparison with *Fermi* observations shows that the jet should be inclined close to the line of sight and pairs should not be located within the system. Energetically speaking, a massive compact object is favored. We report also on our investigations of the gamma-ray absorption of GeV photons with the radiation emitted by a standard accretion disk in Cygnus X−3. This study shows that the gamma-ray source should not lie too close to the compact object.

Keywords: radiation mechanisms: non-thermal, stars: individual: Cygnus X−3, gamma rays: theory, X-rays: binaries

1 Introduction

Cygnus X−3 is an accreting high-mass X-ray binary with relativistic jets, *i.e.* a microquasar. This system is composed of a Wolf-Rayet star (see *e.g.* van Kerkwijk et al. 1996) and an unknown compact object, probably a black-hole, in a tight 4.8 hours orbit situated at about 7 kpc from Earth (Ling et al. 2009). The gamma-ray space Telescopes *AGILE* (Tavani et al. 2009) and *Fermi* (Abdo et al. 2009) have detected gamma-ray flares at GeV energies in the direction of Cygnus X−3 (a new gamma-ray flare was recently reported, see Corbel & Hays 2010). This identification is firmly established since the orbital period of the system was found in the *Fermi* dataset. This is the first unambigous detection of a microquasar in high-energy gamma rays. The gamma-ray emission in Cygnus X−3 is transient and correlated with powerful radio flares, associated with the presence of a relativistic jet and episodes of major ejections in the system. This feature suggests that the gamma-ray emission originates from the jet. In this proceeding, we present a model for the gamma-ray modulation in Cygnus X−3 (Sect. 2, see Dubus et al. 2010a for more details). GeV photons could be absorbed by the soft X-rays emitted by an accretion disk around the compact object. We report also on our studies of the gamma-ray opacity in Cygnus X−3 and put constraints on the location of the gamma-ray source in the system (Sect. 3).

2 Gamma-ray modulation

2.1 *The model*

The model relies on simple assumptions. Energetic electron-positron pairs are located at a specific altitude H along the jet and symmetrically (with respect to the compact object) in the counter-jet. These acceleration sites could be related to recollimation shocks as observed in some AGN such as M87 (Stawarz et al. 1996), possibly produced by the interaction of the dense Wolf-Rayet star wind and the jet. This possibility seems to be corroborated by recent MHD simulations (see Perucho et al. 2010). Pairs are isotropic in the comoving frame and follow a power-law energy distribution. The total power injected into pairs is P_e. The jet is relativistic (with a bulk velocity $\beta = v/c > 0$) and inclined in an arbitrary direction parameterized by the spherical angles ϕ_j (polar angle) and θ_j (azimuth angle). The orbit of the compact object is circular with a radius $d = 3\times10^{11}$ cm.

[1] Laboratoire d'Astrophysique de Grenoble, UMR 5571 CNRS, Université Joseph Fourier, BP 53, 38041 Grenoble, France

We define here the orbital phase ϕ such as $\phi \equiv 0.25$ at superior conjunction and $\phi \equiv 0.75$ at inferior conjunction. The Wolf-Rayet star (effective temperature $T_\star \sim 10^5$ K, stellar radius $R_\star \sim R_\odot$) provides a high density of seed photons for inverse Compton scattering on the relativistic pairs injected in the jet ($n_\star \approx 10^{14}$ ph cm^{-3} at the compact object location). Because of the relative position of the star with respect to the energetic pairs and the observer, the inverse Compton flux is orbital modulated. This is a natural explanation for the orbital modulation of the gamma-ray flux observed in Cygnus X−3. Other sources of soft radiation (*e.g.* accretion disk, CMB) can be excluded to account for the modulation, and could instead contribute to the DC component. In addition to anisotropic effects, the relativistic motion of the flow should be considered in the calculation of the Compton emissivity (Doppler-boosting effects, see Dubus et al. 2010b for technical details).

2.2 Results

We applied this model to Cygnus X−3 for two extreme orbital solutions as given in Szostek & Zdziarski (2008). In the first solution (orbit inclination $i = 30^o$), the compact object is a 20 $M_\odot$ black hole orbiting a 50 $M_\odot$ Wolf-Rayet star. In the second solution ($i = 70^o$), the system is composed of a 1.4 $M_\odot$ neutron star and a 5 $M_\odot$ star.

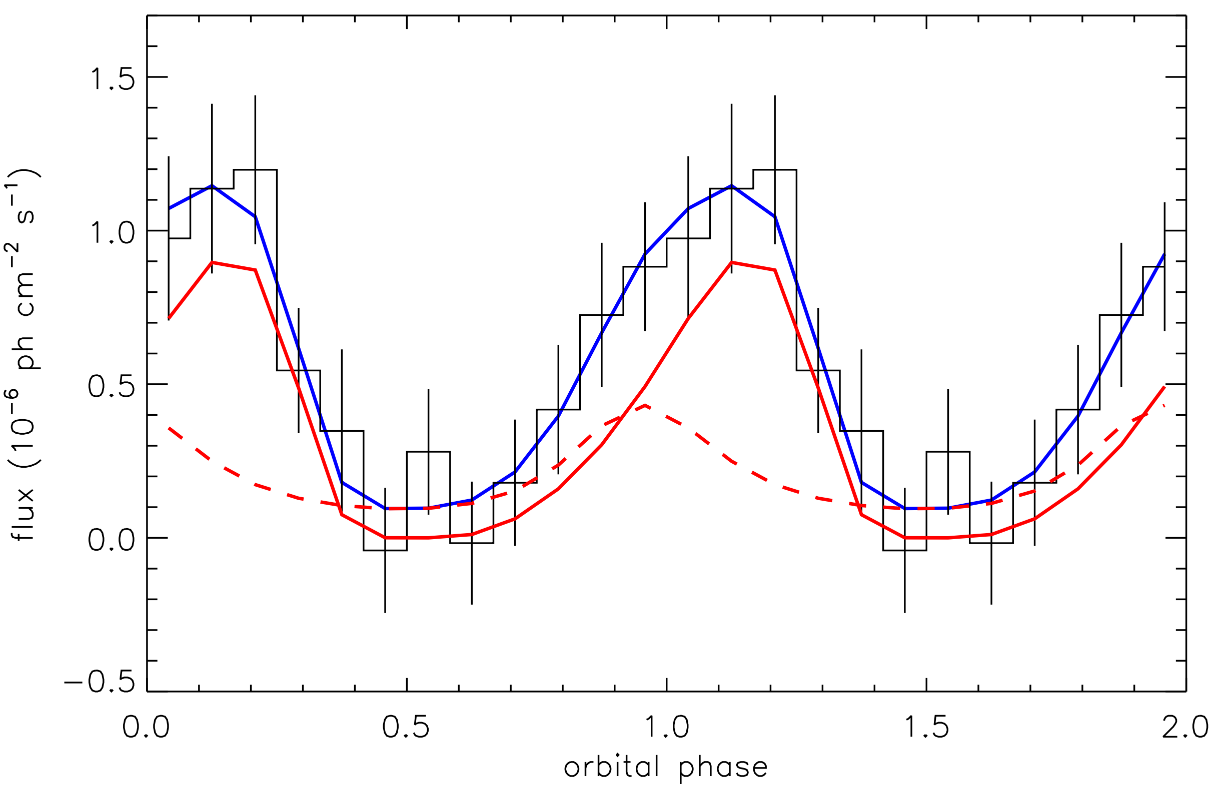

Fig. 1. High-energy gamma-ray flux (> 100 MeV) as a function of the orbital phase (two full orbits) for the black hole solution in Cygnus X−3. Example of a good fit solution of the theoretical model (blue solid line) to the folded *Fermi* lightcurve (data points). The contribution from the jet (red solid line) and the counter-jet (red dashed line) are shown for comparison. Set of parameters: $\beta = 0.45$, $H = 3d$, $\phi_j = 12^o$, $\theta_j = 106^o$ and $P_e = 10^{38}$ erg s^{-1}.

In order to constrain the orientation of the jet, we carried out an exhaustive exploration of the space parameter. The theoretical solutions are compared with the *Fermi* lightcurve using a χ^2 test. The best fit solutions to observations are given by those minimizing the χ^2. Many sets of parameters reproduce correctly the observed gamma-ray modulation. Fig. 1 shows one possible solution. Fig. 2 presents the full distribution of models leading to a good fit, *i.e.* contained in the 90% confidence region*.

It appears from this study that the jet should be inclined close to the line of sight. The jet is mildly relativistic ($\beta < 0.9$) and pairs should not be located within the system ($0.5d < H < 10d$). We favor a massive compact object in the system (*i.e.* a black hole) as the energy budget required to reproduce the GeV flux can be only a small fraction of the Eddington luminosity. This work reveals also that the gamma-ray modulation (amplitude and shape) is very sensitive to the polar angle θ_j, *i.e.* if the jet precesses. The non-detection by *COS B* (Hermsen et al. 1987) and EGRET (Mori et al. 1997) may be the consequence of a non favorable orientation of the jet. The controversial results by *SAS-2* (Lamb et al. 1977) might actually be a real detection.

3 Gamma-ray absorption

3.1 The model

High-energy photons of 100 MeV-1 GeV can be absorbed by ∼0.1-1 keV photons. In Cygnus X−3, the main source of soft X-rays could be provided by an accretion disk around the compact object. Following Zhang & Cheng (1997), we compute the gamma-ray opacity in the thermal radiation field emitted by a standard accretion disk (optically thick, geometrically thin) in Cygnus X−3. The inner radius of the disk R_{in} is set at the last stable orbit. Assuming that the total luminosity of the disk is radiated in X-rays $L_{disk} \approx L_X \approx 10^{38}$ erg s^{-1}, the accretion rate is $\dot{M} \approx 10^{-8}\ M_\odot$ yr^{-1} for the black hole solution. The source of gamma rays is assumed point-like and located above the disk at an altitude z. The disk is inclined at an angle ψ with respect to the observer.

3.2 Results

Fig. 3 presents the gamma-ray opacity map of a 1 GeV photon in the radiation field of the accretion disk in Cygnus X−3. Photons are injected on the revolution axis of the disk. Gamma-ray photons are highly absorbed if the source lies in a compact region around the compact object ($z < 10-1000R_{in}$). Similar maps were obtained by Sitarek & Bednarek (2010) in the context of AGN with an application to Centaurus A. In addition to the thermal component in soft X-rays, the spectrum of Cygnus X−3 exhibits also a non-thermal tail in hard X-rays (see *e.g.* Szostek et al. 2008). This component might be related to the emission from a hot corona of electrons above the accretion disk (see *e.g.* Coppi 1999). These photons could also contribute significantly to increase the gamma-ray opacity in the system at MeV and GeV energies. More theoretical endeavors are required in this direction.

4 Conclusion

Doppler-boosted Compton emission from energetic pairs accelerated at a specific location far from the compact object, in an inclined and mildly relativistic jet explains convincingly the gamma-ray modulation in Cygnus X−3. The lack of absorption signature in the GeV emission implies the source is at least $10^8 - 10^{10}$ cm above the accretion disk. Microquasars provide a nearby and well constrained environment to study accretion-ejection mechanisms and acceleration processes in relativistic jets.

Acknowledgements: This work was supported by the *European Community* via contract ERC-StG-200911.

References

Abdo, A. A., et al. (*Fermi* LAT Collaboration) 2009, Science, 326, 1512

Coppi, P. S. 1999, Astronomical Society of the Pacific Conference Series, 161, 375

Corbel, S., and Hays, E. 2010, ATel #2646

---

*In Dubus et al. (2010a), we implicitly assumed fast cooling such that $P_e \approx \int_{\gamma_{min}}^{+\infty} K_e \gamma_e^{-p} d\gamma_e / t_{ic}$ where $t_{ic} \approx 0.5(\gamma_e/10^3)^{-1}(R/d)^2$ s is the inverse Compton cooling timescale at $\gamma_{min} = 10^3$ (see §4). Unfortunately, the term $(R/d)^2$ was not properly taken into account in our calculation of the distribution of acceptable parameters. The corrected distribution allows for a greater range of solutions with electrons injected at a large distance from the compact object. The corrected Figure 3 is shown here on the left panel in Fig. 2. The parameters of the best fit model and our conclusions are unchanged.

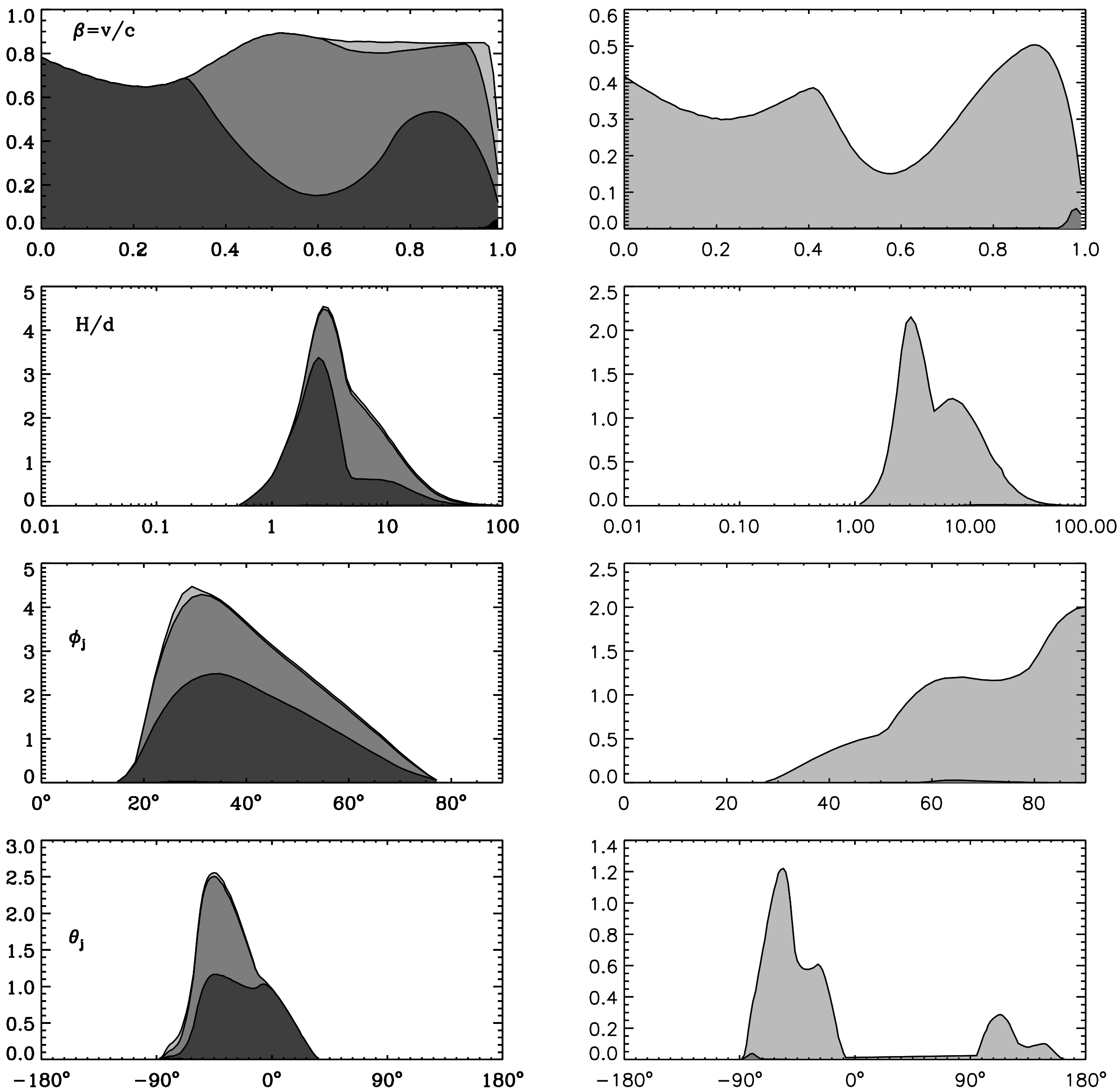

Fig. 2. Distribution of good fit models contained in the 90% confidence region of the χ^2 statistics for the black hole (left panel) and the neutron star orbital solutions (right panel), for the parameters of the jet β (*top* panels), H, ϕ_j, and θ_j (*bottom* panels). Filled regions correspond to a total power injected into pairs $P_e < L_{edd}$ (light gray), $< 0.1\ L_{edd}$ (gray) and $< 0.01\ L_{edd}$ (dark gray), where L_{edd} is the Eddington luminosity.

Dubus, G., Cerutti, B., and Henri, G. 2010a, MNRAS, 404, L55
Dubus, G., Cerutti, B., and Henri, G. 2010b, A&A, 516, A18
Hermsen, W., et al. 1987, A&A, 175, 141
Lamb, R. C., Fichtel, C. E., Hartman, R. C., Kniffen, D. A., and Thompson, D. J. 1977, ApJL, 212, L63
Ling, Z., Zhang, S. N., and Tang, S. 2009, ApJ, 695, 1111
Mori, M., et al. 1997, ApJ, 476, 842
Perucho, M., Bosch-Ramon, V., and Khangulyan, D. 2010, A&A, 512, L4
Sitarek, J., and Bednarek, W. 2010, MNRAS, 401, 1983
Stawarz, Ł., et al. 2006, MNRAS, 370, 981
Szostek, A., and Zdziarski, A. A. 2008, MNRAS, 386, 593

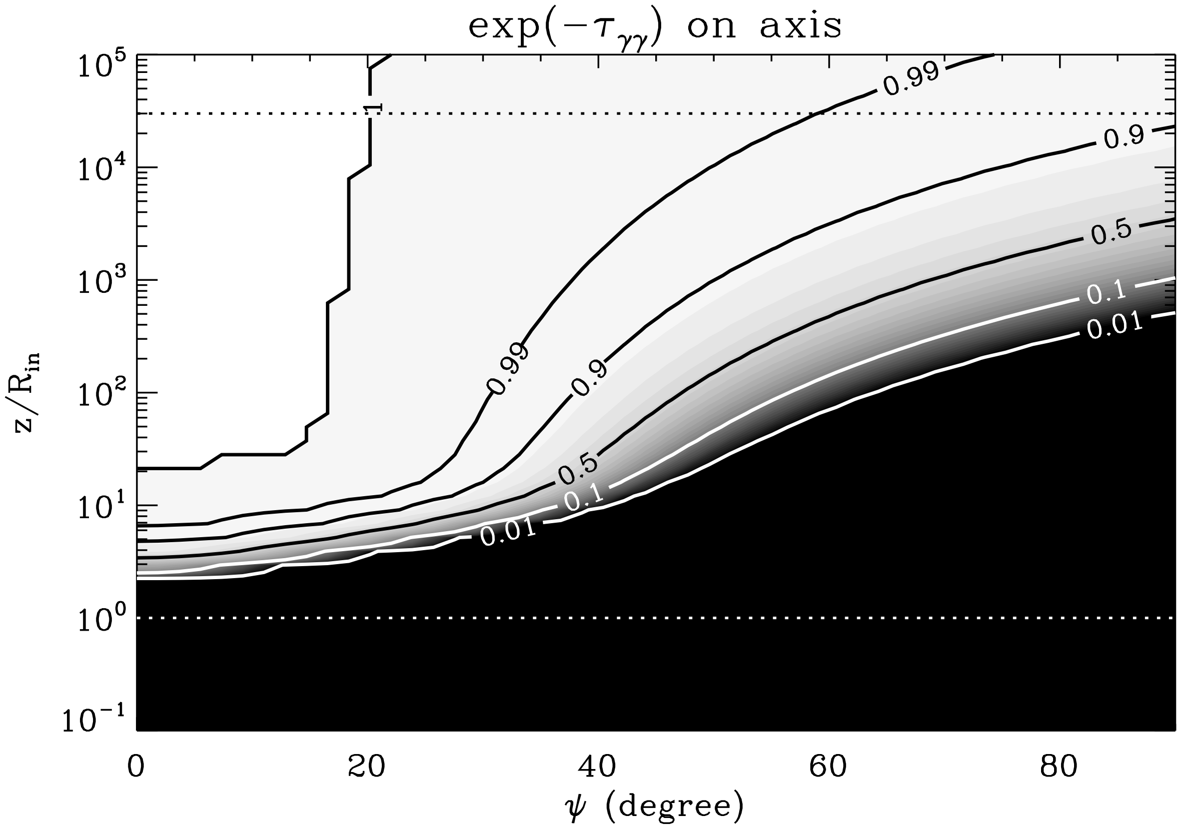

Fig. 3. This map gives the gamma-ray opacity $exp\,(-\tau_{\gamma\gamma})$ as a function of the viewing angle ψ and the altitude of the source above a standard accretion disk z for a 1 GeV gamma-ray photon. The calculation is applied here to Cygnus X−3, for the black hole solution. The source is assumed to be along the axis of the disk. Black regions correspond to high opacity ($\tau_{\gamma\gamma} \gg 1$) and bright regions to low opacity ($\tau_{\gamma\gamma} \ll 1$). The inner and external radius of the accretion disk taken here are $R_{in} = 10^7$ cm and $R_{ext} = 10^{11}$ cm. The white dashed line indicates $z \equiv R_{in}$ and the black dotted line $z \equiv d$.

Szostek, A., Zdziarski, A. A., and McCollough, M. L. 2008, MNRAS, 388, 1001
Tavani, M., et al. (AGILE Collaboration) 2009, Nature, 462, 620
van Kerkwijk, M. H., Geballe, T. R., King, D. L., van der Klis, M., and van Paradijs, J. 1996, A&A, 314, 521
Zhang, L., and Cheng, K. S. 1997, ApJ, 475, 534

MAGNETIC FIELD DRAGGING IN ACCRETION DISCS

R. de Guiran[1] and J. Ferreira[1]

Abstract. Accretion discs are composed of ionized gas in motion around a central object. Sometimes, the disc is the source of powerful bipolar jets along its rotation axis. Theoretical models invoke the existence of a bipolar magnetic field crossing the disc and require two conditions to produce powerful jets: field lines need to be bent enough at the disc surface and the magnetic field needs to be close to equipartition. The work of Petrucci et al (2008) on the variability of X-ray binaries supposes that transitions between pure accretion phases and accretion-ejection phases are due to some variations of the disc magnetization. This rises the problem of the magnetic field dragging in accretion discs. We revisit the method developed by Lubow et al (1994) by including momentum and mass conservation equations in a time-dependent 1D MHD code.

Keywords: accretion discs, MHD, X-ray:binaries, magnetic fields

1 Introduction

First works on magnetic field dragging in accretion discs have focused on the Blandford & Payne (1982) necessary condition for cold jet launching, namely: $tan^{-1}(B_r/B_z) \geq 30°$. Thus, van Ballegooijen (1989) , Lubow et al. (1994), Reyes-Ruiz & Stepinski (1996) developed different methods to address this question in a standard accretion disc (here after SAD). They all conclude that a large effective Magnetic Prandtl number (here after $P_m = \nu_v/\nu_m$ as the ratio of the turbulent viscosity to the magnetic diffusivity) is necessary to reach a sufficient magnetic flux accumulation that satisfy the Blandford & Payne (1982) criterion. Indeed, in a SAD, bent field lines requires a magnetic Reynolds number $R_m = rU_r/\nu_m = R_e P_m \sim r/h$ (with R_e the Reynolds number), whereas in a SAD, $R_e \sim 1$. This is problematic as it tends not to be satisfied according to 3D MRI simulations (Lesur & Longaretti 2009). More recent works, by Lovelace et al. (2009), showed that significant advection of magnetic field could be possible even with $P_m \sim 1$.
On the other hand, the existence of jets do require the presence of a large scale vertical field (McKinney & Blandford 2009). It has been shown that this field must be close to equipartition in order to drive powerful jets (Ferreira & Pelletier 1995).
In this work, we revisit the standing problem of field advection in accretion discs, by introducing new physical input from modern works.

2 Analytical description

The full MHD equations could be written in axisymetry in the in the (r, ϕ, z) cylindrical coordinates. Writting: $a = rA_\phi$ with $\vec{\nabla} \times \vec{A} = \vec{B}$ and $b = rB_\phi$, we have:

$$\frac{\partial \rho}{\partial t} + \nabla \cdot \rho \vec{u} = 0 \tag{2.1}$$

$$\frac{\partial \rho \Omega r^2}{\partial t} + \nabla \cdot \left(\rho \vec{u}_p \Omega r^2 - \frac{b}{\mu_o} \vec{B}_p \right) = \frac{1}{r} \frac{\partial}{\partial r} \rho \nu_v r^3 \frac{\partial \Omega}{\partial r} \tag{2.2}$$

$$\frac{\partial a}{\partial t} + \vec{u}_p \cdot \nabla a = \eta_m J_\phi \tag{2.3}$$

---

[1] Laboratoire dAstrophysique de Grenoble, UMR 5571 CNRS, Universite Joseph Fourier, BP 53, 38041 Grenoble, France

Where $\eta_m = \mu_0 \nu_m$

We focus on the magnetic flux transport coupled with mass and momentum conservation. We assume a thin keplerian disc with $\varepsilon = h/r$ constant with radius (h the height of the disc at a given radius). We also assume that only the turbulent viscosity plays a role in the angular momentum transfer.

2.1 Induction equation

We start with the induction equation, by setting $\Psi = \frac{1}{2h}\int a dz$, we rewrite equation 2.3 integrated over the thickness of the disc:

$$\frac{\partial \Psi}{\partial t} = U_0 \frac{\partial \Psi}{\partial r} - \frac{\eta_m}{2\varepsilon} J_{\phi S} \tag{2.4}$$

With $U_0 = \dot{M}_a/(2\pi r \Sigma)$ with Σ the surface density, $\dot{M}_a$ the accretion rate and $J_{\phi S}$ the surface current density. All the question is determining $J_{\phi S}$ in term of the radial distribution of Ψ. Approximating the disc as rings of toroidal current, an equivalence between $\Psi(r)$ and $J_{\phi S}$ can be found when assuming a potential magnetosphere (Lubow et al. 1994).

2.2 Momentum conservation

By considering a quasi Keplerian motion, one can deduce the accretion rate from equation 2.2

$$\dot{M}_a = \frac{6\pi}{\Omega_K r} \frac{\partial}{\partial r} \left(\Sigma \nu_v \Omega_K r^2 \right) \tag{2.5}$$

2.3 Mass conservation

We then use the mass conservation (equation 2.1) integrated over the thickness of the disc:

$$\frac{\partial \Sigma}{\partial t} = \frac{1}{2\pi r} \frac{\partial \dot{M}_a}{\partial r} \tag{2.6}$$

2.4 Turbulent prescription

At last, we need to do an assumption on the transports parameters:

$$\alpha_v \equiv \frac{\nu_v}{\Omega_K h^2} \tag{2.7}$$

$$\mathcal{P}_m \equiv \frac{\nu_v}{\nu_m} \tag{2.8}$$

Magnetic fields in accretion discs are known as a potential source of turbulence via the Magneto-Rotational Instability (here after MRI). This is expected to lead to anomalous transport coefficients ν_v and ν_m. Recent results by Lesur & Longaretti (2009) show that $P_m \sim 2$ and a behaviour of alpha in $\mu^{0.5}$ for low μ (with μ the magnetization: ratio of the magnetic pressure on the thermal pressure). As we know that MRI is suppressed around equipartition, we use the prescription:

$$\alpha_v(\mu) = 2(\mu(1-\mu))^{1/2} \tag{2.9}$$

Where the local disc magnetization is computed as:

$$\mu = \frac{B_z^2}{\mu_o P} = \frac{2B_z^2}{\mu_o \varepsilon \Sigma \Omega_K^2 r} \tag{2.10}$$

One can study the evolution of the magnetic field and the density in the disc, by solving equations 2.4, 2.6, using 2.5 and the equivalence between $J_{\phi S}$ and $\Psi(r)$.

3 Results

We study the behaviour of a SAD with $P_m = 1$ initially thread by a magnetic flux very compressed in the inner zone of the disc. This field is chosen to have a uniform magnetization at $t = 0$. This initial condition could model the high soft state (labelled C in Petrucci et al. (2008)), right after the jet quenching of X-ray binaries. We use the $\alpha_v(\mu)$ prescription (equation 2.9). The results are shown on Figure 1. At the beginning, of the simulation, the magnetic field diffuse outward as expected in a SAD. Leading to an increasing of μ in the outer zone of the disc, and so a noticeable positive variation of the accretion rate at the outer edge of the disc. We can notice that at the end of the simulation, the disc is approaching a stationary state with an accretion rate quite uniform at the outer radii of the disc. But as the magnetization is very weak in the inner zone, so is α_v, and then the dynamics are very slow.
One can also see that a strong magnetization is reached in the outer disc ($\mu \sim 1$). This is very interesting because the condition for a powerful jet launching is satisfied at these radii.Then, the dynamic of the disc becomes considerably different (which is not taken into account in the code). If we consider the magnetic torque induced by the jet, we would assist to a new advection of the field from the outer edge of the disc.

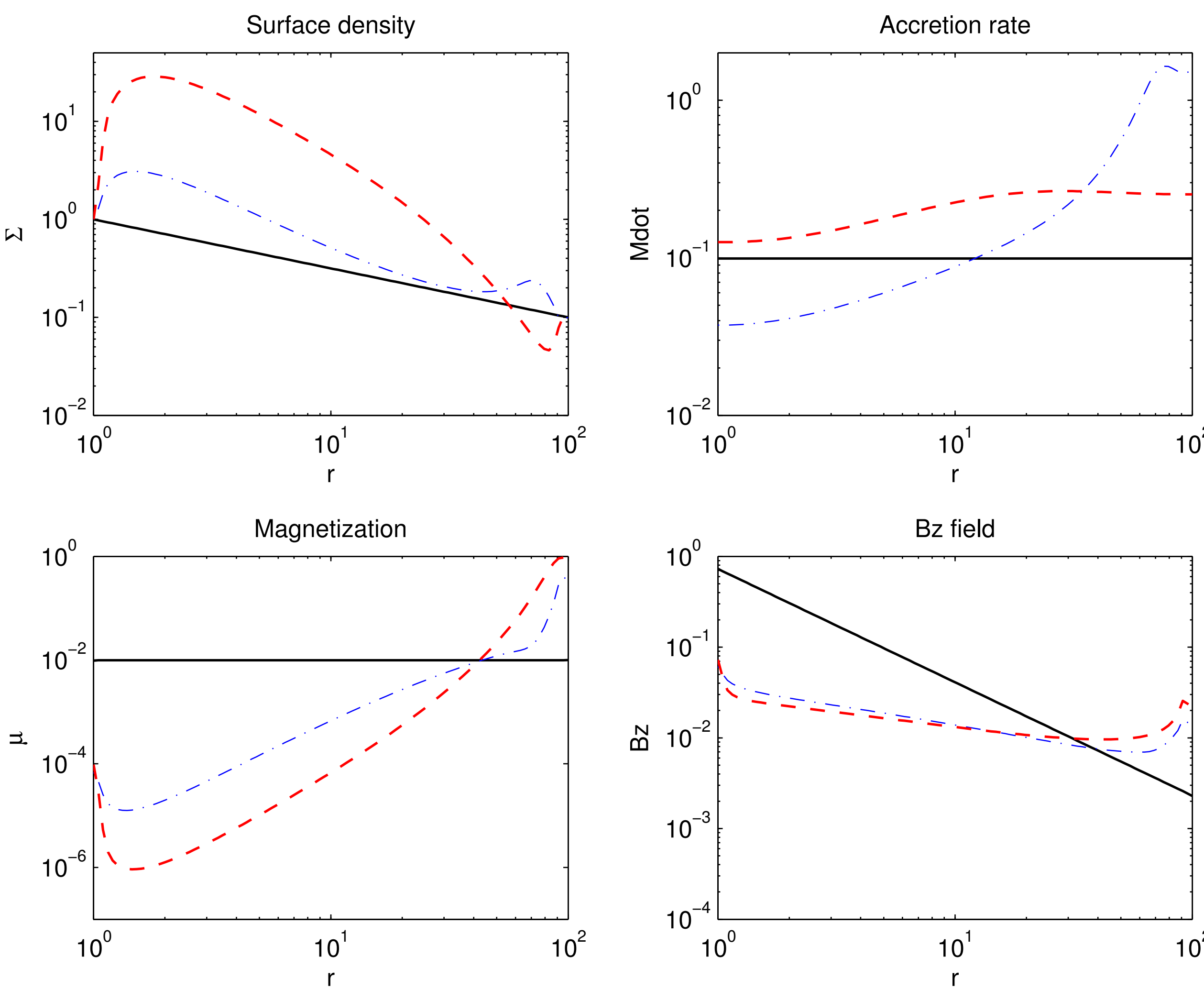

Fig. 1. Density, accretion rate, magnetization and magnetic field in the disc at 3 different times. All the quantities are normalized. The solid line correspond to initial state, the dash-doted line correspond to 10 keplarian time at the outer radius, and the dashed line to 100 keplerian times at the outer radius.

4 Conclusions

The new advection of magnetic field supposed to occur at the end of the simulation would make a transition with the diffusion of the magnetic field observed in the simulation. Thus, we could assist to a phenomenon of magnetic tide. In this sense, this result is very encouraging for the study of transition from high soft to low hard state in X-ray binaries. However here, the accretion rate remains roughly constant during the simulation. But if we work by imposing the accretion rate at the outer radius, a decreasing of it would enhance the magnetization at the outer radii, which is compatible with a transition between high soft to low hard state.

Thank you to all the team from the Laboratoire d'Astrophysique de Marseille for the organisation of this conference.

References

Blandford, R. D. & Payne, D. G. 1982, MNRAS, 199, 883

Ferreira, J. & Pelletier, G. 1995, A&A, 295, 807

Lesur, G. & Longaretti, P. 2009, ArXiv e-prints

Lovelace, R. V. E., Rothstein, D. M., & Bisnovatyi-Kogan, G. S. 2009, ApJ, 701, 885

Lubow, S. H., Papaloizou, J. C. B., & Pringle, J. E. 1994, MNRAS, 267, 235

McKinney, J. C. & Blandford, R. D. 2009, MNRAS, 394, L126

Petrucci, P., Ferreira, J., Henri, G., & Pelletier, G. 2008, MNRAS, 385, L88

Reyes-Ruiz, M. & Stepinski, T. F. 1996, ApJ, 459, 653

van Ballegooijen, A. A. 1989, in *Accretion Disks and Magnetic Fields in Astrophysics*, G. Belvedere (ed) Astrophysics and Space Science Library, Vol. 156, 99

PROPERTIES OF PHONONS IN THE NEUTRON STAR CRUST

L. Di Gallo[1] and M. Oertel[1]

Abstract. Neutron stars are compact objects, created in supernova explosions at the end of the life of massive stars. They contain matter under extreme conditions, in particular concerning the density : starting from a lattice of (neutron rich) nuclei in the crust one reaches nuclear matter at several times the density of atomic nuclei in the center. One way to understand this object is to confront theoretical modelisation with observations. Among observations of pulsars there is the thermal emission of its surface. This observable, which depend on the heat transport properties, is very sensitive to the superfluid and superconducting character of the different sutructures inside the star. The presentation is focussed on the inner crust, where we can find an interesting nuclear structure called the "Pasta Phase". Its excitation spectrum within a superfluid hydrodynamics approach will be discussed in view of calculating the contribution to the heat capacity.

Keywords: neutron star crust, nuclear matter, superfluidity, hydrodynamic modes

1 Introduction

Neutron stars are fascinating objects, containing matter under extreme conditions of temperature, density and magnetic field. In order to study these celestial bodies, theoretical modelisation has to be confronted with observations. A prominent observable is the thermal evolution of isolated neutron stars. The surface temperature can be deduced from the thermal emission. The age, if the neutron star cannot be associated to a known supernova event, can be obtained measuring the ratio $P/2\dot{P}$, where P is the pulse period. From this ratio, assumming the pulsar to be a rotating magnetic dipole, the age can be estimated. The observation of the thermal evolution puts stringent constraints on cooling models. Since the surface temperature is the result of the interplay between thermal radiation and heat transport from inside the star, it is sensitive to the microscopic processes occuring in the different parts of the star at different evolution stages determining heat transport properties of neutron star matter. These are, as neutrinos play an important role for neutron star cooling, neutrino emissivities, and in addition heat capacity and thermal conductivity. Here, we will concentrate on the heat capacity. There are contributions to the heat capacity from all the different possible excitations at the given temperature, such that it is important to consider the entire excitation spectrum. More details about the evaluation of the specific heat and a discussion of the usually considered contributions can be found in Gnedin (2001). In what follows, we will concentrate on the inner crust.

The inner crust of neutron stars is characterised by a transition from homogeneous matter in the core to a lattice of atomic nuclei in the outer crust. Ravenhall & al. (1983) predicted that this transition passes via more and more deformed nuclei. Starting from an almost spherical shape, they could form tubes or slabs immersed in homogeneous neutron rich matter at the different densities. These phases are commonly called the nuclear pasta.

In neutron stars older than several minutes, matter becomes superfluid with energy gaps of the order of 1 MeV in the inner crust, see Chamel (2008). This means, that individual nuclei cannot easily be excited and that their contribution to the specific heat is thus strongly suppressed. The main contributions to the heat capacity considered so far in the crust are electrons and lattice vibrations as well as collective excitations of nuclei. However, the superfluid character of neutron star matter induces collective excitations, not considered before, which can give an important contribution to the heat capacity in certain regions, see Aguilera (2009). The aim of this paper is to study these collective excitations in the inner crust employing a superfluid hydrodynamics approach.

[1] Laboratoire Univers et Théories, Observatoire de Paris, CNRS, Université Paris Diderot, 5 place Jules Janssen, 92190 Meudon, France

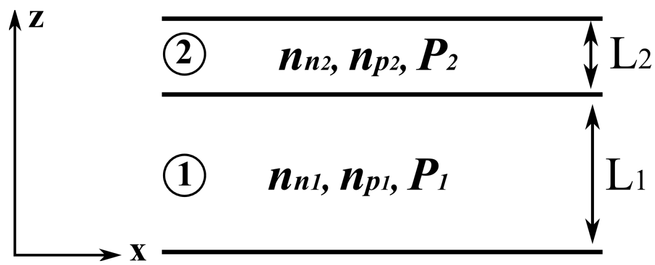

Fig. 1. Representation of "lasagna" structure

2 Superfluid hydrodynamics for the "Lasagna" phase

2.1 Characteristics of "Lasagna"

As mentioned above, the geometrical structure of the different phases in the inner crust can be very different. For the moment we limit our approach to one-dimensional inhomogeneities, i.e. to the phase called "Lasagna". It appears close to the core and it is characterised by a periodic alternance of slabs with different proton and neutron densities as illustrated in Fig. 1. As can be explained from the origin of this phase as deformed nuclei immersed in neutron rich matter, one slab contains nuclear matter with proton and neutron densities of the same order, whereas the other one, having a lower total baryon density, is largely dominated by neutrons. The latter will be labelled by an index "1", the former by "2". The width of a slab (L_1, L_2 in Fig. 1) is typically of the order of 5 fm and the overall baryon density is approximately half nuclear matter saturation density, i.e. 0.08 fm^{-3}.

2.2 Superfluid hydrodynamics approach

We consider a model with two (super)-fluids, one for protons and one for neutrons. Since the considered temperatures are much lower than the pairing gap, we are working in the zero temperature approximation. We are studying local microscopic effects, and the fluid velocities involved are low, such that relativistic effects are probably very small and we can use the non-relativstic approximation. In order to derive the superfluid hydrodynamics equations, we start from energy-momentum conservation and particle number conservation for each species*. We then expand the equations to first order in density perturbations around stationary equilibrium leading to wave equations for the sound waves. Since superfluids have no viscosity, naively we would end up with two sets of independent equations per fluid. There is, however, a non-dissipative interaction between the two fluids called entrainement. The entrainement effect coupling the two superfluids has been first discussed by Andreev & al. (1975) and is nowadays a well known ingredient for superfluid hydrodynamics in homogeneous neutron star matter, see e.g. Prix (2004). Because of entrainement, the two resulting sound modes with corresponding sound speeds are not pure proton or neutron modes, but they are coupled. The parameters of our model are calculated within a Landau-Fermi liquid approach using a relativistic mean field type effective nuclear interaction, see Avancini (2009).

In order to describe the propagation of waves through the slabs, we have to specify boundary conditions at each interface. Our basic assumption is here that contact between the fluids is maintained at all times. This is a standard assumption in problems of wave propagation in inviscid fluids. This assumption implies continuity of fluid velocities perpendicular to the interface and continuity of chemical potentials across the interface. The periodicity is taken into account using the Floquet-Bloch theorem. This means that the wave function $U(z)$ has to satisfy the following condition:

$$U(z+L) = e^{iqL}\ U(z)\ , \tag{2.1}$$

where $L = L_1 + L_2$ is the periodicity (see Fig. 1) and q the Bloch momentum. The Bloch condition, Eq. (2.1) closes our system of equations such that we can now proceed in computing the dispersion relation of propagating waves in the "Lasagna" phase.

*Stricly speaking it is baryon number and charge conservation

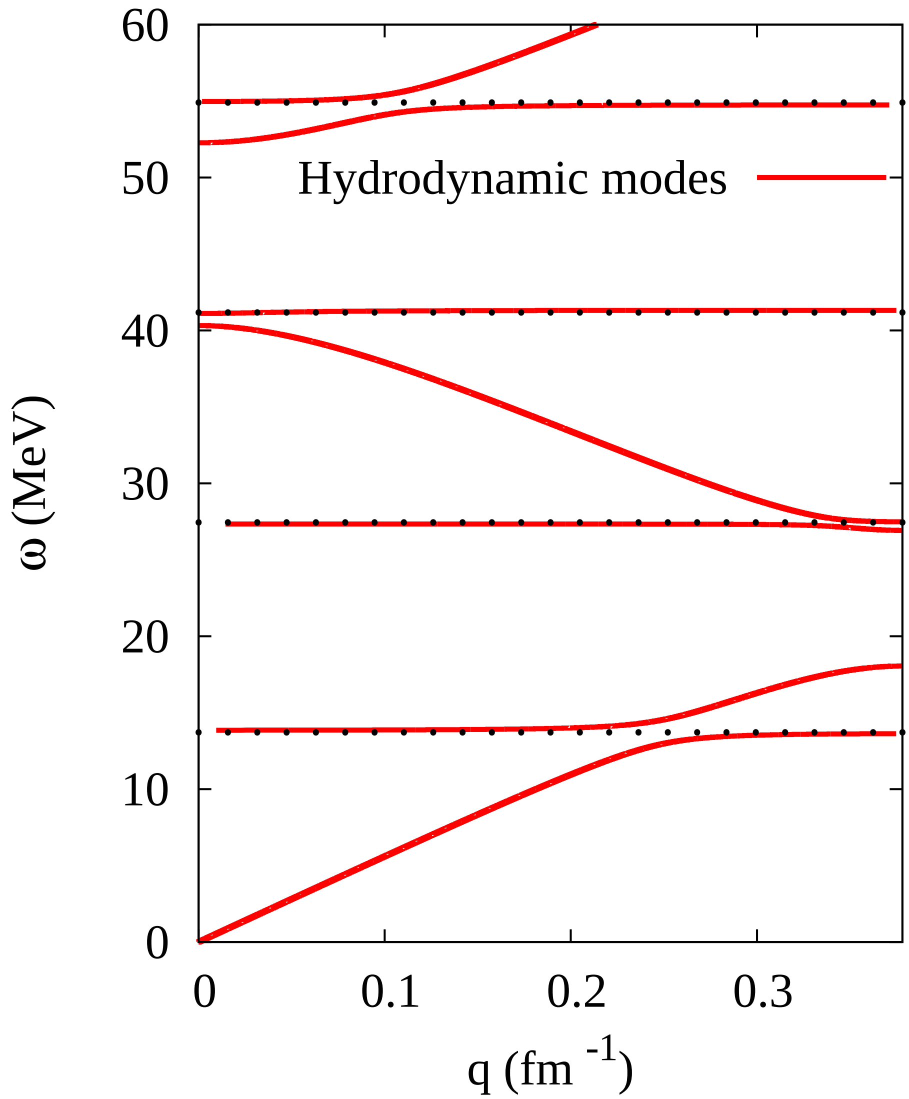

Fig. 2. Dispersion relation (energy as a function of the momentum) for the "Lasagna" phase at baryonic density $n_b = 0.0804\ \text{fm}^{-3}$.

3 Excitation spectrum of the "Lasagna"

At the present stage we consider only waves propagating perpendicularly to the interfaces, i.e. in z-direction (see Fig. 1). Then, for a typical baryonic density $n_b = 0.0804\ \text{fm}^{-3}$ appearing in the model of Avancini (2009) for the "Lasagna" phase, we obtain the dispersion relation shown in Fig. 2. For that baryon density $L_1 = 4.535$ fm and $n_1 = 0.0705\ \text{fm}^{-3}$. For this example, phase 1 contains only neutrons. Phase 2 is smaller in size $L_2 = 3.770$ fm with a density of $n_2 = 0.0923\ \text{fm}^{-3}$ and a proton fraction $Y_p = n_p/n_b = 0.0436$.

The lowest branch is an "acoustic branch". It is called acoustic because it follows a linear dispersion law, $\omega = c_s\, q$ at low momenta, with c_s being the sound speed. For the example at hand, $c_s = 0.2852\, c$, where c denotes the speed of light. We are mostly interested in energies of the same order as the temperature, i.e. below

~ 1 MeV, since these give the main contribution to the thermal energy,

$$E_{th} = \int d^3q\, n(\vec{q})\, \omega(\vec{q}) \ , \tag{3.1}$$

and thus to the specific heat. $n(\vec{q})$ represents here the (bosonic) occupation number. We therefore conclude that for the present example, the only relevant contribution arises from the low momentum part of the acoustic branch with a linear dispersion law.

The other, higher lying branches are called "optical branches", known to appear in periodic structures like the "Lasagna" phase. At the density discussed for the present example, these branches play no role at temperatures below 1 MeV. It is, however, interesting to analyse their structure. The dotted lines in Fig. 2 represent a frequency

$$\omega_j = \frac{u_2}{L_2} j\pi \tag{3.2}$$

with an integer j. u_2 is the sound speed corresponding to the proton dominated mode in phase 2. Many of the optical branches follow well these frequencies. Remembering that phase 1 only contains neutrons, this suggest that these modes could be interpreted as (mainly) protons oscillating in a cavity given by the extension of phase 2. In less dense parts, where the sound speeds are smaller, these optical branches could well give a non-negligible contribution to the thermal properties, too.

4 Summary and outlook

We have presented a first calculation of wave propagation in the "Lasagna" phase in the inner crust of neutron stars. This phase is characterised by alternating slabs of nuclear matter with different densities and proton fractions. We have discussed the resolution of the superfluid hydrodynamics equations taking into account the periodic structure of the medium. The dispersion relation shows one acoustic and several optical branches. We have motivated that these modes, not considered before, can have an influence on the thermal properties of the matter, in particular the specific heat. For the example presented, the main contribution comes from the acoustic branch at low momenta, where the dispersion law is almost perfectly linear. For lower overall baryon densities, other branches could contribute, too.

These rather qualitative arguments should be confirmed by a computation of the contribution to the specific heat. For that purpose, wave propagation has to considered in all directions, not only perpendicular to the interfaces. Work in this direction is in progress.

It would in addition be interesting to extend the work to other geometrical structures like rods, tubes and spheres, as the contributions to the specific heat are expected to be more important for these less dense phases. Finally, the contributions of these collective excitations have to be added to that from electrons and lattice phonons as well as the nuclei in order to examine the influence on the overall cooling behavior of the star.

It is to be expected that the excitations considered here have an effect on neutrino propagation in matter, too, since they are susceptible to couple to neutrinos. It could therefore be interesting to investigate the influence on neutrinos, too.

We thank C. Da Providencia for providing us with the data for densities and sizes within the Lasagna phase in the model of Avancini (2009).

References

Aguilera, D. N., Cirigliano, V.,Pons, J. A., Reddy, S., and Sharma, R. 2009, Phys. Rev. Lett. , 102, 091101

Andreev, A. F. and Bashkin, E. P. 1975, JETP, 42, 164

Avancini, S. S., Brito, L., Marinelli, J. R. et al. 2009, Phys. Rev. C, 79, 035804

Chamel, N., and Haensel, P. 2008, Living Reviews in Relativity, 11, 10

Gnedin, O. Y., Yakovlev, D. G. and Potekhin, A. Y. 2001, MNRAS, 324, 725

Prix, R. 2004, Phys. Rev. D, 69, 043001

Ravenhall, D. G., Pethick, C. J. and Wilson, J. R. 1983, Phys. Rev. Lett., 50, 2066

SF2A 2010
S. Boissier, M. Heydari-Malayeri, R. Samadi and D. Valls-Gabaud (eds)

NEUTRINO DETECTION OF TRANSIENT SOURCES WITH OPTICAL FOLLOW-UP OBSERVATIONS

D. Dornic[1], M. Ageron[2], I. Al Samarai[2], S. Basa[3], V. Bertin[2], J. Brunner[2], J. Busto[2], S. Escoffier[2], F. Schussler[4], B. Vallage[4] and M. Vecchi[2]

Abstract. The ANTARES telescope has the opportunity to detect transient neutrino sources,such as gamma-ray bursts,core-collapse supernovae,flares of active galactic nuclei. To enhance the sensitivity to these sources, a new detection method based on coincident observations of neutrinos and optical signals has been developed. For this purpose the ANTARES Collaboration has implemented a fast on-line muon track reconstruction with a good angular resolution. These characteristics allow to trigger a network of optical telescopes in order to identify the nature of the neutrino sources. An optical follow-up of special events, such as neutrino doublets, coincident in time and direction, or single neutrinos with a very high energy, would not only give access to the nature of their sources but also improve the sensitivity for neutrino detection. The alert system is operational since early 2009, and as of September 2010, 22 alerts have been sent to the TAROT and ROTSE telescopes.

Keywords: Antares, neutrino astronomy, transient sources, optical follow-up

1 Introduction

The ANTARES neutrino telescope (Aslanides et al. 1999) is located in the Mediterranean sea, 40 km south of the french coast of Toulon, at a depth of about 2500 m below sea level. The detector is an array of photomultipliers tubes (PMTs) arranged on 12 slender vertical detection lines. Each string comprises up to 25 floors, i.e. triplets of optical modules (OMs) housing each one PMT. Data taking started in 2006 with the operation of the first line of the detector. The construction of the 12 line detector was completed in May 2008. The main goal of the experiment is to detect high energy muons induced by neutrinos of astrophysical origin interacting in the vicinity of the detector.

The detection of high energy cosmic neutrinos would be the only direct proof of hadronic acceleration processes in astrophysical objects,implying the identification of the sources of ultra high energy cosmic rays without ambiguity. Among the possible astrophysical sites, those that have transient nature such as gamma ray bursts (GRB) or core collapse supernovae (ccSNe), offer one of the most promising perspectives for the detection of cosmic neutrinos thanks to the almost background free search. The emission of neutrinos is predicted by several authors in correlation with other multi-wavelength signals. Their detection could help for example to constrain GRB models, such as the fireball model (Piran 1999). This model tells us how the GRBs operate but important questions still remain such as which processes generate the energetic ultra-relativistic flows or how the shock acceleration is realized.

In contrary to the current gamma-ray observatories, a neutrino telescope can survey at any time a full hemisphere if only up-going events are analyzed and even 4π sr if down-going events are considered. More importantly no assumption is made on the nature of the source and the mechanisms occurring inside.

In this paper, we discuss the implementation of a strategy for the detection of transient sources (Kowalski and Mohr 2007; Dornic et al. 2011; Basa et al. 2009). This method is based on the optical follow-up of selected neutrino events.

[1] IFIC, Edificios Investigacìon de Paterna, CSIC-Universitat de Valencia, Apdo. de correos 22085 Valencia, Spain
[2] CPPM, Faculte des Sciences de Luminy, 163 avenue de Luminy, 13288 Marseille Cedex09, France
[3] LAM, BP8, Traverse du Siphon, 133376 Marseille Cedex 12, France
[4] CEA-IRFU, centre de Saclay, 91191 Gif-Sur-Yvette, France

2 ANTARES neutrino alerts

In order to allow a successful detection, the neutrino trigger has to be set according to the expected neutrino signal emitted from the considered sources. Several models predict the production of high energy neutrinos (10-100 TeV) from GRBs (Waxman and Bahcall 1997; Meszaros and Waxman 2001; Dermer and Atoyan 2003; Razzaque et al. 2003) as well as 1-10 TeV neutrinos from Core Collapse Supernovae (Ando and Beacom 2005). If such sources are close enough, bursts of neutrinos can be expected as discussed in (Razzaque et al. 2005).

Two on-line neutrino trigger criteria are currently implemented in the alert system: the detection of at least 2 neutrino-induced muons coming from similar directions within a predefined time window, or the detection of a single high energy neutrino-induced muon.

To select the events which might trigger an alert, a fast and robust algorithm is used to reconstruct the raw data. This algorithm uses an idealized detector geometry and is independent of the dynamical positioning calibration. The principle is to minimize a χ^2 which compares the times of selected hits with the expectation from a Cherenkov signal of a muon track. A detailed description of this algorithm and its performances can be found in Antares (2010). The resulting direction of the reconstructed muon track is available within about 5 ms and the obtained minimal χ^2 is used as fit quality parameter to remove miss-reconstructed tracks.

To select the alert candidates, first the atmospheric muon background is suppressed. In a second step, a selection of neutrino candidates having a high probability to be of cosmic origin is performed.

In order to set the cuts used for our neutrino selection, we have analyzed the data registered by ANTARES in 2008 corresponding to 173 active days of data taking. During this period, around 600 up-going neutrino candidates were recorded. In order to obtain a good angular resolution*, we only select reconstructed events which trigger several hits on at least 3 lines. The curve labeled "on-line algorithm" of figure 1 shows the median angular resolution as a function the neutrino energy for events selected by the high energy criteria. For the mean energy given by the selection cuts, the angular resolution is around 0.95°. The asymptotic resolution of 0.6° can be achieved when considering the highest energetic events.

An estimation of the energy in the on-line reconstruction is indirectly determined by using the number of hits of the event and the total amplitude of these hits. In order to select events with an energy above around 5 TeV, a minimum of about 20 storeys and about 180 photoelectrons per track are required. These two different trigger logics applied on the 2008 data period select around twenty events (Dornic et al. 2009).

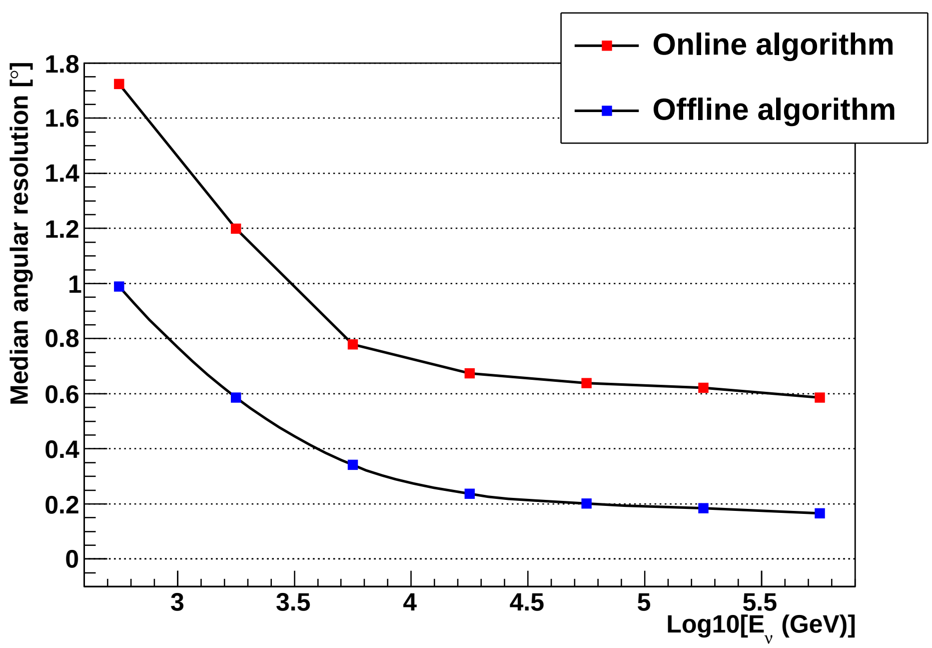

Fig. 1. Angular resolution obtained for both on-line and offline reconstructions as a function of the neutrino energy.

*The angular resolution is defined as the median of the space angular difference between the incoming neutrino and the reconstructed neutrino-induced muon.

Figure 2 shows the estimation of the point spread function for a typical high energy neutrino alerts. Around 70% of the events are contained in the field of view of a typical robotical telescope ($\approx 2°x2°$). With a larger delay (few tens of minutes after the time of the burst), we are able to run the standard reconstruction tool which provides a much better angular resolution using the dynamical positioning of the detector lines. Simulations indicate that, with this algorithm, ANTARES reaches an angular resolution smaller than about 0.3-0.4° for neutrino energies above 10 TeV.

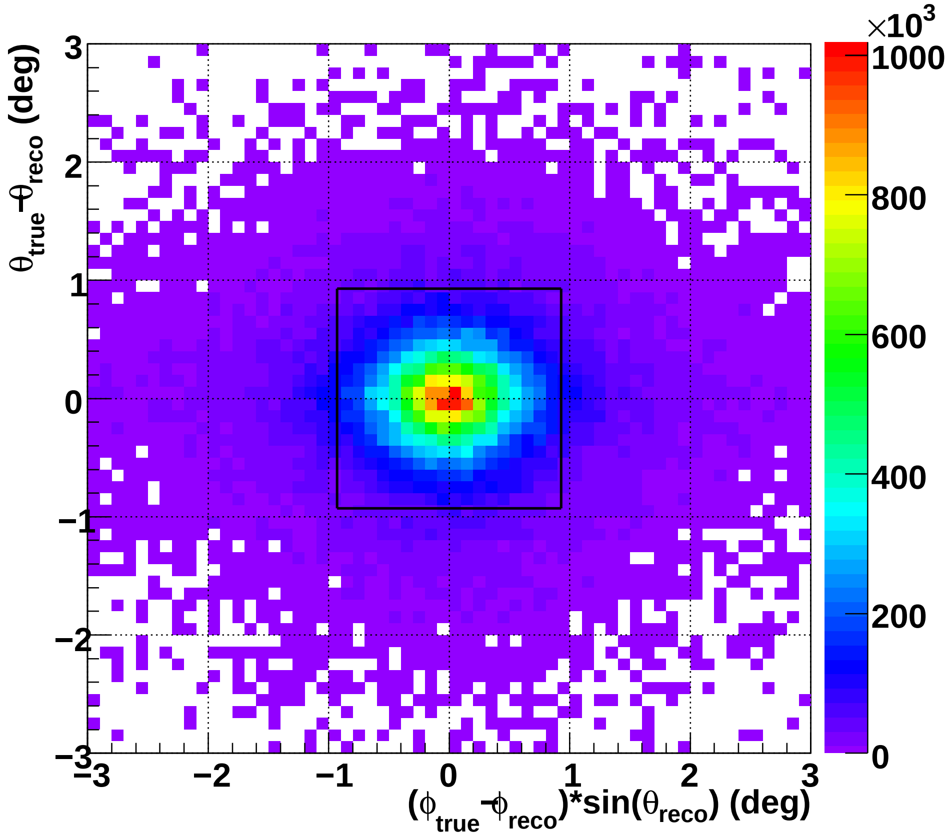

Fig. 2. Bi-dimensional angular resolution. The black square corresponds to the TAROT telescope field of view.

3 Observation strategy of the robotical telescopes

ANTARES is organizing a follow-up program in collaboration with the TAROT and ROTSE telescopes The TAROT (Boer et al. 1999) network is composed of two 25 cm optical robotic telescopes located at Calern (France) and La Silla (Chile). The ROTSE (Akerlof et al. 2003) network is composed of four 45 cm optical robotic telescopes located at Coonabarabran (Australia), Fort Davis (USA), Windhoek (Namibia) and Antalya (turkey).The main advantages of these instruments are the large field of view of about 2 x 2 square degrees and their very fast positioning time (less than 10s). These telescopes are perfectly tailored for such a program. Thanks to the location of the ANTARES telescope in the Northern hemishpere (42.79 degres latitude), all the six telescopes are used for the optical follow-up program. Depending on the neutrino trigger settings, the alert are sent at a rate of abour one or two times per month. With the current settings, the connected telescopes can start taking images with a latency of the order of one minute.

As it was said before, the rolling search method is sensitive to all transient sources producing high energy neutrinos. For example, a GRB afterglow requires a very fast observation strategy in contrary to a core collapse supernovae for which the optical signal will appear several days after the neutrino signal. To be sensitive to all these astrophysical sources, the observational strategy is composed of a real time observation followed by few observations uring the following month. For the real time observation (at T0), 6 images with an exposure of 3 minutes and 30 images with an exposure of 1 min are taken respectively by the first available TAROT and ROTSE telescopes. The integrated time has been defined in order to reach an average magnitude of around 19. For each delayed observation, six images are taken at T0+1,+2, +3, +4, +5, +6, +7, +9, +15, +27 days after the trigger for TAROT (8 images for ROTSE the same days more T0+16 and T0+28 days).

4 Optical image analysis

Once the images are taken, they are automatically processed (flat and dark subtraction) at the telescope site. Once the data is copied from the telescopes, a second analysis is performed off-line, combining the images from all sites. This off-line program is composed by three main steps: absolute astrometric and photometric calibration of the image, subtraction between each image and a reference one and light curve determination for each variable candidates. This program, originally developped for the supernovae search in the SuperNova Legacy Survey (SNLS) project has been adapted in order to look for transient objects in the large field of view taken into account the image quality of the TAROT and ROTSE telescopes. Cases like variable PSF due to the atmospheric conditions or the lower quality images on the CCD edges have to be optimized in order not to lose any optical information. Image subtraction is performed according the methods presented in Alard and Lupton (1998). Here, the image with the best seeing during the first night in case of GRB search or during the whole observations in case of SN search serves as reference. It is also planned that the image analysis step will be included at the end of the automatic detection chain.

5 Conclusions

The follow-up of golden events would improve significantly the perspective for neutrino detection from transient sources. The most important point of the rolling search method is that it is sensitive to any transient source. A confirmation by an optical telescope of a neutrino alert will not only give the nature of the source but also allow to increase the precision of the source direction determination in order to trigger other observatories (for example very large telescopes for the redshift measurement). The alert system is operational since early 2009, and as of September 2010, 22 alerts have been recorded. After a commissioning phase in 2009, all alerts had an optical follow-up in 2010. These numbers are conform to the rate of one or two alerts per months, as it is required by the optical telescope network. The program for the follow-up of ANTARES neutrino events is already operational with the TAROT and ROTSE telescopes. It would be also interesting to extend this technique to other wavelength observation such as X-ray or radio.

This work has been financially supported by the GdR PCHE in France. We want to thank M. Kowalski for discussions on the neutrino triggers and the organization of the optical follow-up.

References

Alard, C. and Lupton, R. 1998, ApJ, 503, 325
Akerlof, C.W. et al. 2001, PASP, 115, 132
Ando, S. and Beacom, J. 2005, Phys. Rev. Lett., 95, 061103
Aslanides, E. et al. (ANTARES collaboration), eprint IFIC/99-42 and `arxiv.org/9907432`
ANTARES collaboration, 2010, submitted
Basa, S. et al, 2009, Nucl. Instrum. Meth. A, 602, 275
Boer, M. et al. 1999, A&AS, 138, 581
Dermer, C. and Atoyan, A. 2003, Phys. Rev. Lett., 91, 071102
Dornic, D. et al. 2009, `arxiv.org/0908.0818`
Dornic D. et al, 2011, Nucl. Instrum. Meth. A, in press
Kowalski, M. and Mohr, A. 2007, Astroparticle Physics, 27, 533
Meszaros, P. and Waxman, E. 2001, Phys. Rev. Lett., 87, 171102
Piran, T. 1999, Phys. Rep., 314, 575
Razzaque, S., Meszaros, P. and Waxman, E. 2003, Phys. Rev. Lett., 90, 241103
Razzaque, S., Meszaros, P., and Waxman, E. 2005, Phys. Rev. Lett., 94, 109903
Waxman, E. and Bahcall, J. 1997, Phys. Rev. Lett., 78, 2292

SF2A 2010
S. Boissier, M. Heydari-Malayeri, R. Samadi and D. Valls-Gabaud (eds)

FERMI GAMMA-RAY SPACE TELESCOPE OBSERVATIONS OF GAMMA-RAY OUTBURSTS FROM 3C 454.3 IN DECEMBER 2009 AND APRIL 2010

L. Escande[1], B. Lott[2], C. D. Dermer[3], Y. Tanaka[4] and on behalf of the Fermi-LAT Collaboration

Abstract. The flat-spectrum-radio-quasar 3C 454.3 underwent an extraordinary outburst in December 2009 when it became the brightest gamma-ray source in the sky for over one week. Its daily flux measured with the *Fermi* Large Area Telescope at photon energies $E > 100$ MeV reached $F_{E>100\ \mathrm{MeV}} = 22 \pm 1 \times 10^{-6}$ ph cm^{-2} s^{-1}, representing the highest daily flux of any blazar ever recorded in high-energy γ rays. It again became the brightest source in the sky in April 2010, triggering a pointed-mode observation by *Fermi*. The γ-ray temporal and spectral properties during these exceptional events are presented and discussed.

Keywords: Galaxies: active, quasars: individual: 3C 454.3, gamma rays: observations

1 Introduction

The radio source 3C 454.3 is a well-known flat spectrum radio quasar (FSRQ) at redshift $z = 0.859$. It entered a bright phase starting in 2000, and has shown remarkable activity in the past decade.

First observations of 3C 454.3 with the *Fermi* Large Area Telescope (LAT) began in July 2008 during *Fermi*'s commissioning period, when the source was found at a high flux state with $F_{E>100\ \mathrm{MeV}} \cong 10 \times 10^{-6}$ ph cm^{-2} s^{-1} Abdo et al. (2009). Observations revealed a timescale less than 2 days for the flux to decline by a factor of 2. The spectrum showed a spectral break around 2 GeV with a spectral steepening from $\Gamma_1 = 2.3$ to $\Gamma_2 = 3.5$. Such a break has now been found to be a common feature in bright FSRQs and in some low-synchrotron peaked BL Lacs as well (Abdo et al. 2010c). Based on weekly light curves, a very moderate "harder when brighter" effect has also been observed, with the photon index obtained with a single power-law fit varying by less than 0.3 for flux ratios varying by >7 (Abdo et al. 2010c).

The continuous monitoring by the *Fermi* LAT showed that the source activity faded continuously in early 2009 and then rose back up from June onwards. It underwent an exceptional outburst in November 2009 - January 2010 when it became the brightest gamma-ray source in the sky for over a week, reaching a record daily flux level in the GeV band (Escande & Tanaka 2009). At the same time it also showed strong activity at several other frequencies. The source remained active afterwards with a slowly decaying flux around 2×10^{-6} ph cm^{-2} s^{-1} until early April 2010 when it brightened up again to a flux level of 16×10^{-6} ph cm^{-2} s^{-1}, prompting the first *Fermi*-LAT target-of-opportunity (ToO) pointed observation beginning on 2010 April 5 lasting for 200 ks.

These two major events offer a unique opportunity to probe intraday variability and the associated spectral changes in the gamma-ray band.More details can be found in Ackermann et al. (2010).

2 Observations and analysis

The *Fermi*-LAT is a pair-conversion gamma-ray telescope sensitive to photon energies greater than 20 MeV. It is particularly suited to blazars observation since it scans the sky constantly: with its field of view of about 2.4 sr, it covers 20% of the sky at any time and permits an all-sky coverage in 3 hours. The data presented here

[1] Universite Bordeaux 1, CNRS/IN2P3, Centre d'Etudes Nucleaires de Bordeaux Gradignan, 33175 Gradignan, France
[2] Universite Bordeaux 1, CNRS/IN2P3, Centre d'Etudes Nucleaires de Bordeaux Gradignan, 33175 Gradignan, France
[3] Space Science Division, Naval Research Laboratory, Washington, DC 20375, USA
[4] Institute of Space and Aeronautical Science, JAXA, 3-1-1 Yoshinodai, Sagamihara, Kanagawa 229-8510, Japan

were collected from 2009 August 27 to 2010 April 5 in survey mode, except for a 200 ks period starting on April 5 at 19:38 UT where the pointed mode was used, resulting in a gain of accumulation of exposure by about a factor of 3.5 over survey mode. Standard cuts were applied to the data. More details concerning the analysis can be found in Ackermann et al. (2010).

3 Results

Figure 1 displays the daily light curves (red points) from MJD 55070 to 55307 (27 August 2009 to 21 April 2010) for fluxes above 100 MeV. The periods showing the fastest flux variations during the December flare, with fluxes changing by more than a factor of 2 in amplitude, are enlarged in the insets, with the $E > 100$ MeV fluxes averaged over a daily, 6-hour, and 3-hour binning shown by the red, open blue and green data points, respectively. The error bars are statistical only. Three flares displaying a flux variation greater than a factor of 2 over less than a day (MJD 55167, 55170 and 55195) have been studied extensively during this period. It is the first time that, in the gamma-ray band, we can study a source over such short periods. The flares were fitted with the function (Abdo et al. 2010a):

$$F = 2F_0(e^{(t_0-t)/T_r} + e^{(t-t_0)/T_f})^{-1} + F_{bgd}(t), \tag{3.1}$$

where T_r and T_f are the rising and falling times, F_0 is the flare flux amplitude and $F_{bgd}(t)$ is a (slowly varying) background flux. The shortest variability time scale is found to be shorter than 3 hours. The lightcurve of the

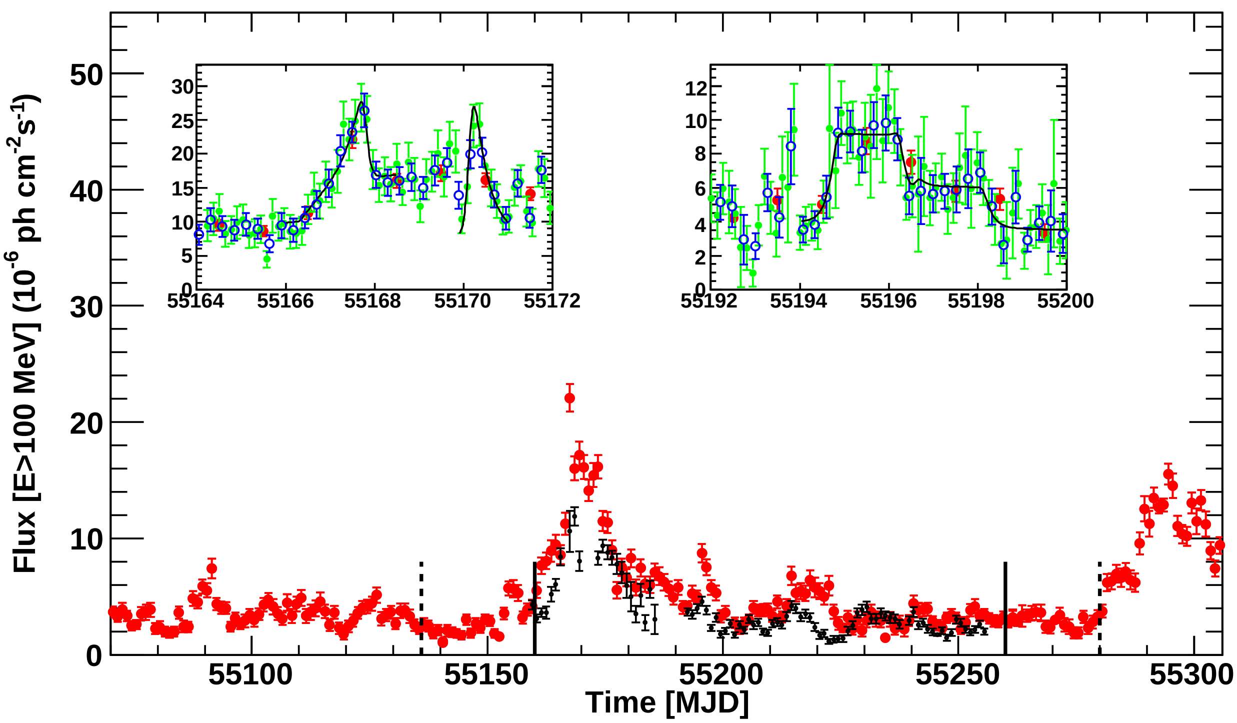

Fig. 1. Lightcurve of 3C 454.3 in the 100MeV-200GeV band (red). The lightcurve of the July-August 2008 flare, shifted by 511 days, is shown for comparison. The insets show blow-ups of the two periods when the largest relative flux increases took place. The red, blue, and green data points in the insets correspond to daily, 6hr, and 3hr averaged fluxes respectively. The fit results discussed in the text are displayed as solid curves.

July-August 2008 flare, shifted by 511 days, is shown for comparison.These two lightcurves exhibit a similar profile : a major outburst which lasts for about 10 days then followed by a long tail of fairly high activity upon which are superimposed minor flares lasting for a few days.

The 1 GeV daily lightcurve (not shown here) closely resembles the 100 MeV one, hinting a little spectral variability. This behavior is confirmed by the very limited variation of the photon spectral index measured for this source. The near constancy of the spectrum is in accord with the results found from the July 2008 flare and the first 6-months of LAT data (Abdo et al. 2009, 2010c). The variation of the amplitude of the weekly photon indices is only $\Delta\Gamma$=0.35 (varying between 2.35 and 2.7) during the period under consideration, but the variation is statistically significant. There is a suggestion that a progressive hardening over several weeks precedes a major outburst, but more such events will be needed to establish whether this behavior is typical. The correlation between index and flux provides insight into acceleration and cooling processes. Loop patterns were looked for during the most rapid flares to reveal a possible universal behavior. Indeed, what is expected after a flare is a softening of the source (cooling effect). But instead of a well-defined, universal pattern, a variety of patterns is found such as a weak hardening during the flux decrease which constitutes an indication of a "hard-lag", linked to acceleration processes. Figure 2 shows the flux and photon spectral index as a function of time in the period around (blue) and during (red) the time of the ToO when the *Fermi*-LAT was in pointed mode (MJD 55291.82-55294.13). The binning is 6 hour and 3 hour for the survey and pointed modes respectively. As expected by the 3.5 fold increase in exposure per unit time during the ToO, the statistical accuracy in the measurement of both parameters improves significantly. Although in a high state, the source was unfortunately fairly steady during this period. No indication for variability more rapid than that observed during the giant outburst is found during the ToO period, as already noted by Foschini et al. (2010). The reduced χ^2 for a constant fit of the photon index is 18.52/16, indicating that the data are consistent with a constant value.

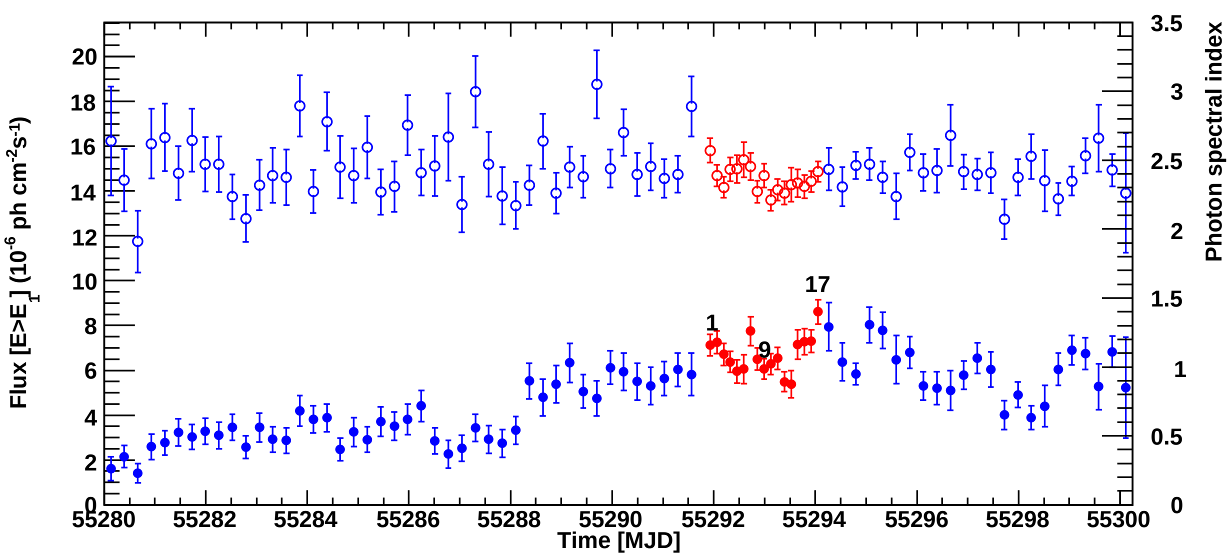

Fig. 2. Flux (filled data points; left-hand axis) and photon index (open data points; right-hand axis) as a function of time in the period surrounding the ToO pointing. Data collected in survey mode (6-hr binning) are in blue, those collected in pointed mode are in red (3-hr binning).

In order to study the evolution of the position of the spectral break of 3C 454.3, integrated spectra were computed over four periods : Period 1, MJD 55121-55165, Period 2, MJD 55166-55173 (week of the giant outburst), Period 3, MJD 55174-55262 and Period 4 MJD 55280-55300. It is the first time that the position of the break can be determined with such a short period of time integration (one week for the giant outburst). The distributions were fitted with a broken power law and a power law with exponential cutoff functions, which are difficult to discriminate for these periods. The variation of break energy (cutoff energy) with flux is displayed in the left (right) panel in Figure 3 for different observing periods. No strong evolution of either the break energy or the cutoff energy is found, but there is some indication of a slight hardening with flux.

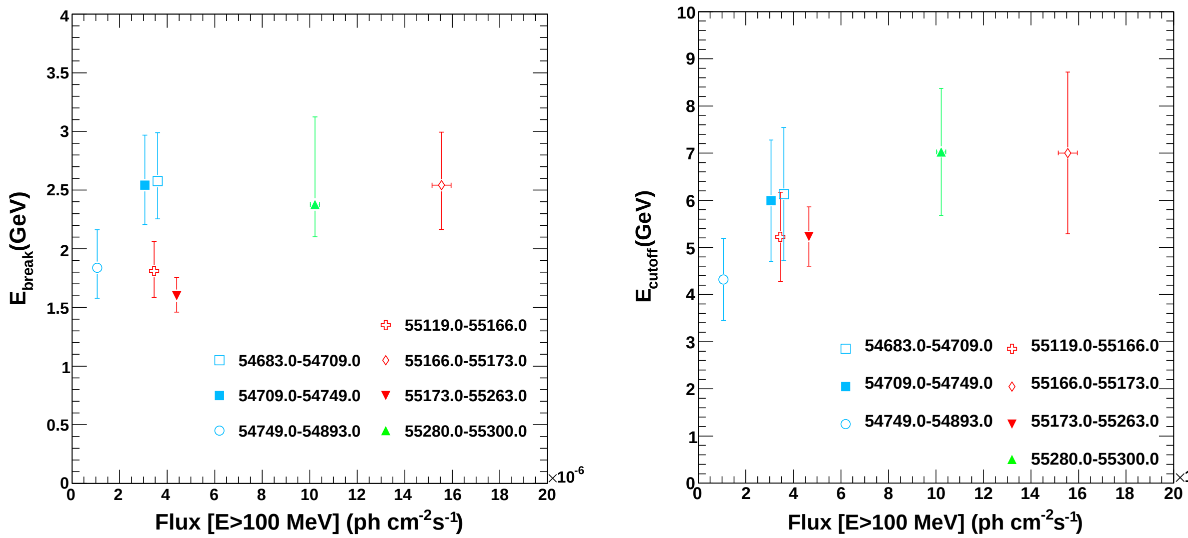

Fig. 3. Evolution of E_{break} and E_{cutoff} with flux.

4 Discussion

Thanks to this series of outbursts observed with the *Fermi*-LAT, a much more accurate picture of the behavior of 3C 454.3 in flaring states has been obtained. A photon flux of $F_{E>100\ \mathrm{MeV}} = 22 \pm 1 \times 10^{-6}$ ph cm^{-2} s^{-1} from 3C 454.3 at $z = 0.859$ implies an apparent isotropic γ-ray luminosity above 100 MeV of $L_\gamma \cong 3.8 \pm 0.2 \times 10^{49}$ erg s^{-1}. This is ~ 3 times larger than the luminosity of the $z = 1.839$ blazar PKS 1502+106 during its August 2008 flare (Abdo et al. 2010b), but still lower than the luminosity of PKS 1622-297 ($\sim 5.1 \times 10^{49}$ erg s^{-1} with the current cosmological model) during the 1995 flare (Mattox et al. 1997). Several parameters of the source can be constrained from these data. The first one is the minimum Doppler factor δ_{min}, defined by the condition that the optical depth $\tau_{\gamma\gamma}(\epsilon_1)$ of a photon with energy $E_1 = \epsilon_1 m_e c^2$ to the $\gamma\gamma$ pair-production process is $\tau_{\gamma\gamma}(\epsilon_1) = 1$. It can be estimate thanks to the expression

$$\delta_{min} \cong \left[\frac{\sigma_T d_L^2 (1+z)^2 f_{\hat{\epsilon}} \epsilon_1}{4 t_{var} m_e c^4}\right]^{1/6} \tag{4.1}$$

Here f_ϵ is the νF_ν spectrum of 3C 454.3 measured at frequency $\nu = m_e c^2 \epsilon / h$. To estimate $\delta_{\rm min}$, the photon with maximum energy E_1 is used during the period in which f_ϵ and variability time $t_{\rm var} = t_{\rm var,d}$ day are measured. The νF_ν flux f_ϵ in eq. (4.1) is evaluated at $\epsilon = \hat{\epsilon} = 2\delta^2/(1+z)^2\epsilon_1$ from the pair-production threshold condition. Swift XRT observations contemporaneous with the time that the 20 GeV photon was detected lead to $\delta_{\rm min} \approx 13$. The location of the emission region compared to the black hole can also been constrained. For a conical geometry of opening angle 2 $\theta_j > R/r \sim 1/\Gamma_b$, the location of the emitting region for the December flare is constrained to be at distance $r < 2c\Gamma_b^2 t_{\rm var}/(1+z) \approx 0.2\Gamma_{15}^2 t_{\rm var,d}$ pc; i.e., towards the outer parts of the BLR. This conclusion tends to disfavor the models in which the Inverse Compton is made on photons from the torus or further in the jet. Several hypotheses can be made concerning the near constancy of the position of the break observed in the spectrum of 3C 454.3 despite very different flux level exhibited by the source. One possibility is related to scattering of a target photon field in the Klein-Nishina regime. Compton scattering takes place in the Thomson limit when the energy of the photon to be scattered is (in $m_e c^2$ units) $\epsilon'' < 1/4$ in the electron rest-frame, denoted by the double primes on quantities. The scattering is in the Thomson regime occurs for $E_C(\mathrm{GeV}) < 12/E_\star(\mathrm{eV})$, independent of the Doppler factor. If the break energy observed in 3C 454.3 at ≈ 2 GeV is due to the transition to scattering in the KN regime, then the underlying target photon energy $E_\star \approx 6$ eV is close to the energy of the Ly α photon at 10.2 eV. We have tested this possibility by comparing the Compton-scattered spectrum from a power-law electron distribution with a monochromatic Ly α photon source with the *Fermi* LAT data. The spectrum we obtained (not shown here) is too hard to fit the data, and treatment of KN effects on cooling (Dermer & Atoyan 2002) or the addition of other soft photon sources will reduce the sharpness of the break.

The difficulty to fit the sharp spectral break with a single power-law electron distribution is in accord with the conclusion of Abdo et al. (2009) that this break reflects a complex electron spectrum.

5 Summary

The correlated spectral and temporal properties of 3C 454.3 during two very strong flaring episodes, when the source was the brightest object in the γ-ray sky, have been studied. An important result of the present work is that the significant spectral break between $\approx 2-3$ GeV in γ-ray spectrum of 3C 454.3 is very weakly dependent on the flux state, even when the flux changes by an order of magnitude. Flux variations of a factor of 2 have been observed over time scales as short as three hours, though only weak variability was observed during the time of the Target of Opportunity pointing of the *Fermi* Telescope towards 3C 454.3.

References

Abdo, A. A., Ackermann, M., Ajello, M., et al. 2010a, ArXiv e-prints 1004.0348

Abdo, A. A., Ackermann, M., Ajello, M., et al. 2010b, ApJ, 710, 810

Abdo, A. A., Ackermann, M., Ajello, M., et al. 2010c, ApJ, 710, 1271

Abdo, A. A., Ajello, M., Atwood, W. B., et al. 2009, ApJ, 699, 817

Ackermann, M., Ajello, M., Baldini, L., et al. 2010, ApJ, 721, 1383

Dermer, C. D. & Atoyan, A. M. 2002, ApJ, 568, L81

Escande, L. & Tanaka, Y. T. 2009, The Astronomer's Telegram, 2328, 1

Mattox, J. R., Wagner, S. J., Malkan, M., et al. 1997, ApJ, 476, 692

SF2A 2010
S. Boissier, M. Heydari-Malayeri, R. Samadi and D. Valls-Gabaud (eds)

RECENT RESULTS OF THE FIGARO COLLABORATION

B. Gendre[1], A. Corsi[2], G. Stratta[1], A. Klotz[3], J.L. Atteia[4], M. Boër[5], S. Cutini[1], F. Daigne[6], R. Mochkovitch[6] and L. Piro[7]

Abstract. The FIGARO collaboration aims are to study the early phase of the gamma ray burst afterglows and the prompt-to-afterglow transition phase, using multi-wavelength observations (mostly from Swift and TAROT). Here, we review the recent results of the collaboration, including the discovery of a rising part of the optical light curve and its theoretical interpretation.

Keywords: gamma-ray: bursts

1 Introduction

Gamma-Ray Bursts (GRBs, see e.g. Piran 2005, for a review) were discovered in the late 1960's (Klebesadel et al. 1973). For about three decades, their exact nature remained elusive. The effort to provide a fast re-pointing of the BeppoSAX satellite allowed for the first detection of their afterglows at all wavelengths (e.g. Costa et al. 1997; van Paradijs et al. 1997). Since then, the specification of each generation of instrumentation devoted to GRB studies included the need to point to the GRB afterglows quickly. Now, with Swift, we have reached the point where we can collect data from X-rays to optical within seconds after the start of the event, thanks to fast moving telescopes triggered by GCN notices (Barthelmy 1998). This run toward fast re-pointing has allowed for prompt optical emission observations by small autonomous telescopes for several GRBs (e.g. Klotz et al. 2009b), and produced a huge set of data available to study the prompt, the prompt-to-afterglow transition, and the early afterglow phases. Here we present the FIGARO collaboration and the results this collaboration has obtained within the last years.

2 The FIGARO collaboration

The France-Italy GAmma Ray burst afterglow Observation collaboration (FIGARO) has been set in 2005 in order to increase the scientific return of the huge set of data made available by this observational strategy. It consists of several experts in data reduction and analysis, experts in the field of GRB theories, and experts in data modelization. The data are provided by the instruments available to the collaboration (the two TAROT robotic telescopes, the public data of Fermi and Swift) and by several observation on competitive facilities (such as XMM-Newton). The collaboration works either on a burst-by-burst basis (when data are important enough to deserve a specific publication) or on a sample basis for statistical studies of the GRB properties. The burst selection main criterion is an observation by one of the TAROT telescopes during the Swift era. As such, we used bursts listed in Klotz et al. (2009b), and reported in Fig. 1. In brief, we have a sample of 13 burst detections, and of 59 observations of GRB field (with a good constraint on the position). About one third of the sample was observed/detected during the prompt phase.

[1] ASI Science Data Center, Frascati, Italy
[2] California institute for Technology, Passadena, USA
[3] Centre d'Etude Spatiale des Rayonnements, Toulouse, France
[4] Laboratoire d'Astrsophysique de Toulouse Tarbes, Toulouse, France
[5] Observatoire de Haute Provence, St Michel l'Observatoire, France
[6] Institut d'Astrophysique de Paris, Paris, France
[7] IASF-Roma, Roma, Italy

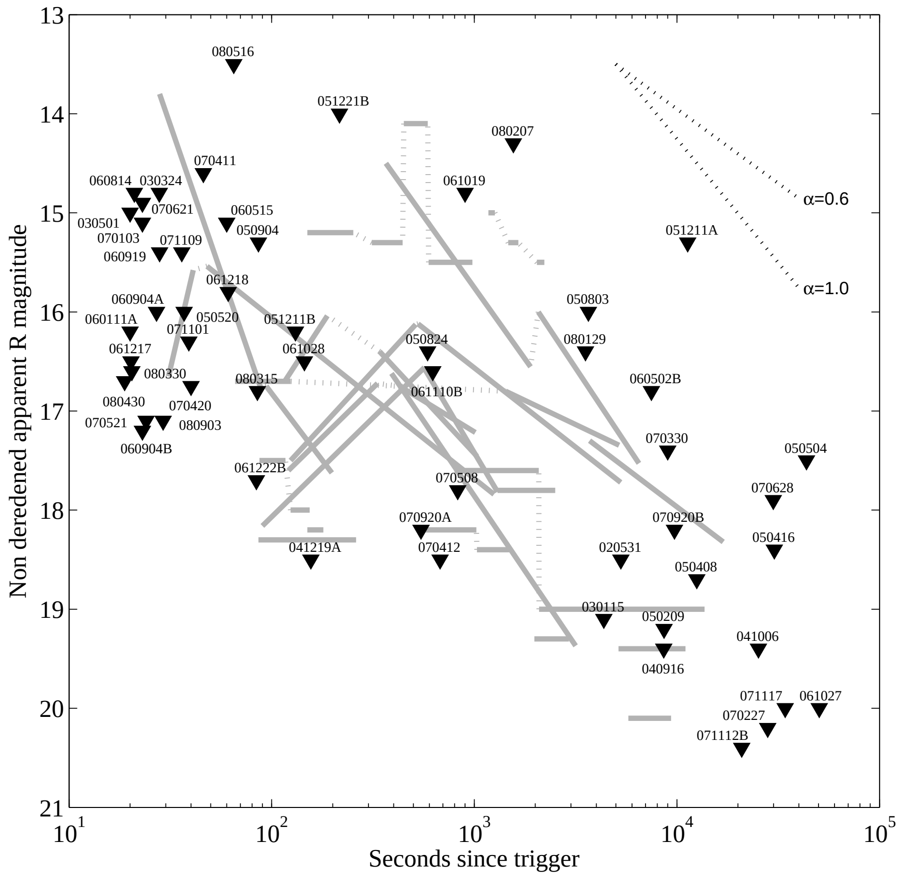

Fig. 1. Light curves of bursts used by the FIGARO collaboration. Triangle are upper limits. Figure extracted from Klotz et al. (2009b).

3 Rising afterglows

An optical rising has been observed for several GRBs (GRB 060904B, GRB 070420, GRB 080330, 080430, see Fig. 1). A similar rise was observed in the near infrared light curves of GRB 060418 and GRB 060607A (Molinari et al. 2007), together with a simultaneous X-ray emission characterized by the presence of various flares. As already noticed, in the Swift era, GRB optical light curves are complex and rarely track the X-ray flux behavior, suggesting a possible different origin. We thus aim at testing whether the global properties of the TAROT GRB sample do favor the hypothesis that we observe a reverse shock signature in optical, without considering the X-ray properties.

We first worked under the hypothesis that, for each GRB in the sample, the optical emission was due to the internal shock model. As this emission is not correlated with the high energy one, this can be ruled out (Klotz et al. 2008). An external shock has been proposed by (Molinari et al. 2007) for those bursts observed by REM (GRB 060418 and GRB 060607A). However, in the TAROT cases the increase and decay indexes are not consistent with the expected values (Klotz et al. 2008).

We then worked under the hypothesis that, for each GRB in the sample, the emissions observed before and after the first temporal break by TAROT both originate from the same physical region (i.e. forward or reverse shocks) (see Corsi et al. 2010, for more details). In this hypothesis, the observed breaks could be due to the RS crossing, i.e. to the onset of the afterglow deceleration phase, or else to the passage of the synchrotron peak frequency into the observed band.

In Corsi et al. (2010), we derived and/or recalled the temporal laws of the reverse shock in various cases: relativistic vs non-relativistic ejecta, thin vs thick shock, constant density profile vs variable density profile (to account for a possible stellar wind from the progenitor), and slow vs fast cooling mode. We then tested these laws on the observed light curves.

Our preliminary results seem to indicate that the best agreement between data and model predictions (allowing for a 3σ scatter of the data) is obtained for the case in which the emission is dominated by a slow cooling forward shock, the optical band is above the synchrotron peak frequency ν_m, and the temporal break is associated with the reverse shock crossing. Else, comparable level of agreement is found for the case in which the emission comes from a slow cooling FS after the RS crossing, with the temporal break being associated to the passage of ν_m in the optical band. The TAROT data alone do not allow us to distinguish between the relativistic and Newtonian hypotheses (Corsi et al. 2010).

As for GRB 060904B, TAROT found the presence of a plateau following the first break. This break in the optical light curve may be explained as forward shock emission in the slow cooling phase from a reverse shock, with the break possibly due to the reverse shock crossing or to the passage of ν_m in the optical band. Under this hypothesis, the observed plateau could be associated with an episode of energy injection into the forward shock, as discussed in more detail in Klotz et al. (2008).

Last, despite all the hypotheses tested, GRB 090102 data cannot be explained with the reverse shock model, and in this case an alternative model needs to be tested.

4 The peculiar GRB 090102

GRB 090102 triggered *Swift*-BAT (trigger 338895, Mangano et al. 2009a) on Jan. 2009, 2^{nd} at 02:55:45 UT (hereafter, T_0). It was also recorded by Konus Wind (Golenetskii et al. 2009), and by INTEGRAL/SPI-ACS (Mangano et al. 2009b). The duration of this event, as observed by *Swift* was $T_{90} = 27.0 \pm 2.2$ s. Due to an observational constraint (Earth limb too close), *Swift* slewed to the position of the afterglow with a delay, and XRT and UVOT observations began only at $T_0 + 395$ s, observing a bright fading source in both the XRT and the UVOT fields of view (Mangano et al. 2009a). The earliest ground search of the optical afterglow was performed by TAROT, starting at T_0+40.8 s (Klotz et al. 2009a).

The X-ray light curve can be adequately fit using a single power law with a decay index $\alpha_X = 1.34 \pm 0.02$. On the other hand, the fit of the optical light curve implies the use of a broken power law model, with a break time on the order of 1000 s. Using other data from GROND, REM and other facilities, it was possible to show that the multi-wavelength observations of this burst cannot be explained by the standard model, and that an alternative model (such as the cannonbal model) should be preferred (Gendre et al. 2010).

The FIGARO collaboration is funded by the GDR PCHE.

References

Barthelmy, S., 1998, in AIP Conf. Proc. 428, Gamma–Ray bursts, ed. C. Meegan & R. Preece (Berlin: Springer), 99

Corsi, A., et al., 2010, in preparation

Costa, E., Frontera, F., Heise, J., et al., 1997, Nature, 387, 783

Gendre, B., Klotz, A., Palazzi, E., Krühler, T., Covino, S., et al., 2010, MNRAS, 405, 2372

Golenetskii, S., Aptekar, R., Mazets, E., et al., 2009, GCN # 8776

Klebesadel, R., Strong, I., & Olson, R., 1973, ApJ 182, L85

Klotz, A., Gendre, B., Stratta, G., et al., 2008, A&A, 483, 847

Klotz, A., Gendre, B., Boër, M., & Atteia, J.L., 2009a, GCN # 8761

Klotz, A., Boër, M., Atteia, J.L., & Gendre, B., 2009b, AJ 137, 4100

Mangano, V., Barthelmy, S.D., Burrows, D.N., et al., 2009a, GCN # 8762

Mangano, V., Markwardt, C.B., Barthelmy, S.D., et al., 2009b, GCN Report 192.1

Molinari, E., Vergani, S.D., Malesani, D., et al., 2007, A&A, 469, L13

Piran, T, 2005, RvMP, 76, 1143

van Paradijs, J., et al., 1997, Nature, 386, 686

THE ASI SCIENCE DATA CENTER

B. Gendre[1], P. Giommi[1] and the ASDC team

Abstract. The ASI Science Data Center (ASDC, www.asdc.asi.it), a facility of the Italian Space Agency (ASI) is a multi-mission science operations, data processing and data archiving center that provides support to several scientific space missions. At the moment the ASDC has significant responsibilities for a number of high-energy astronomy/astroparticle satellites (e.g. Swift, AGILE, Fermi, NuSTAR and AMS) and supports at different level other missions like, Herschel and Planck. The ASDC was established in 2000 based on the experience built with the management of the BeppoSAX Science Data Center. It is located at the ESA site of ESRIN in Frascati, near Rome (Italy).

Keywords: data center

1 Introduction

The ASI Science Data Center (ASDC, www.asdc.asi.it), a facility of the Italian Space Agency (ASI) is a multi-mission science operations, data processing and data archiving center that provides support to several scientific space missions. The ASDC was established in 2000 based on the experience built with the management of the BeppoSAX Science Data Center. It is located at the ESA site of ESRIN in Frascati, near Rome (Italy). Our main responsibilities are to:

- Provide support to ASI funded missions in the field of the observation of the Universe
- Maintain a permanent data archive (including data, software calibration and scientific expertise) of ASI funded scientific missions.
- Act as the interface between ASIs supported scientific missions and the users' community
- Provide on-line access to archival data, analysis software, calibration files and documentation
- Host a copy of the data archive of international missions where Italy is involved
- Develop and maintain software for the efficient access, analysis and comparison of data.
- Collaborate with other data centers and scientific institutions for the exchange of data, software and expertise.

The ASDC is involved in the missions where Italy participates. These include Swift, Fermi, AGILE, Herschel, Gaia, AMS, and NuSTAR. We provide our extensive expertise in software preparation, data archives and user support. As an example, we developed and maintain the analysis software of the Swift XRT, we are involved in the development of the NuSTAR data reduction system, and we hosts the AGILE Data Center, the scientific component of the ground segment of the completely Italian AGILE ASI mission, in charge of all activities related to scientific data processing, archiving and distribution. From an user point of view, the center is organized around archives and catalogs in one side, and around tools available from the web in the other side.

[1] ASI Science Data Center, Frascati, Italy

2 Data side: the ASDC archives and catalogs

The ASDC is the main archive repository or an archive mirror of most missions with Italian involvement. These archives can be accessed through the Multi-Mission Archive portal (`http://www.asdc.asi.it/mmia`), that allows a query for position (or object name) within the archive of the selected mission. Once displayed, the results are linked to various tools that allows for example the online data processing for users not expert in high energy data analysis (see Stratta et al. 2010).

The ASDC also compiles and provides catalogs of refined data, such as, among others, an on-line version of the AGILE First Catalog (Pittori et al. 2009), the 1st Fermi LAT Catalog (Abdo et al. 2010), and the BZCAT Blazar Catalog (Massaro et al. 2010). These interactive on-line catalogs allow refined queries and filtering options.

All of the above databases are progressively inserted into the Virtual Observatory using the dedicated methods and standards.

3 Tool side: the ASDC webtools

The ASDC has developed several tools aimed to help the use of its catalogs and database. Among them, the Swift/XRT Online Data Analysis, the Data Explorer and the SED builder are the most used.

The On-line Analysis tool enables to run the Swift/XRT software task "xrtpipeline" directly on the web, using the latest softaware and calibration files. The user can set specific (and customizable) filter options (such as extraction region taking into account effect of pile-up) in order to obtain accurate science-ready end-products (spectra, light curves and event files). It is also possible to directly fit the spectra and light curves using an online version of XSPEC.

The Data Explorer is a tool which allows the user to navigate through the ASDC and external catalogs and provides an easy way to access data. It can be accessed through several places within the ASDC web pages (such as the multi-mission archive or the tool menu). With this tool, it is possible to browse the internal catalogs (grouped by energy band) and/or selected external databases for sources around the current coordinates, in a user defined search radius, plotting the results within a sky map.

The SED builder is a tool which allows the user to construct a Spectral Energy Distribution for any source presents in the ASDC catalogs, querying both internal and external databases. The SED obtained can automatically cover (depending on the available observations) up to 19 orders of magnitudes, and can be enriched by the insertion of user data.

All tools presented here are provided by the ASI Science Data Centre. For any bug or request please refer to: `http://www.asdc.asi.it/feedback_all`. If you need assistance: `http://swift.asdc.asi.it/helpdesk/login.php?cat=generic`.

The ASDC is funded and managed by the Italian Space Agency (ASI), with the participation of the National Institute of Astrophysics (INAF), the National Institute of Nuclear Physics (INFN) and a number of Universities in Italy.

References

Abdo, A. A., Ackermann, M., Ajello, M., Allafort, A., Antolini, E., et al., 2010, ApJS 188, 405

D'Elia, V., Capalbi, M., Verrecchia, F., Gendre, B., & Giommi, P., 2010, to appear in the AIP "Deciphering the Ancient Universe with GRBs" conference proceedings

Massaro, E., Giommi, P., Leto, C., Marchegiani, P., Maselli, A., et al., 2010, astro-ph/1006.0922

Pittori, C., Verrecchia, F., Chen, A. W., Bulgarelli, A., Pellizzoni, A., et al., 2009, A&A 506, 1563

Stratta, G., et al. 2010, to appear in the AIP "Deciphering the Ancient Universe with GRBs" conference proceedings

SF2A 2010
S. Boissier, M. Heydari-Malayeri, R. Samadi and D. Valls-Gabaud (eds)

EFFECTS OF A MODERATELY STRONG MAGNETIC FIELD IN CORE COLLAPSE SUPERNOVAE

J. Guilet[1], T. Foglizzo [1] and S. Fromang [1]

Abstract. Most studies of core collapse supernovae either neglect any magnetic effect, or assume a very rapid rotation that can amplify the magnetic field enough to produce a magnetically driven explosion (the magnetic pressure is then comparable to the thermal pressure). The effects of a moderate magnetic field that would not be capable of driving an explosion by itself are thus mostly unknown. We suggest that the fluid dynamics could be significantly affected by a magnetic field, which energy is comparable to the kinetic energy. In a very subsonic flow, this condition can be fulfilled even if the magnetic pressure remains small. We study the effect of such a moderately strong magnetic field on the standing accretion shock instability (SASI), using a simplified model of this instability. SASI can be stabilized or strengthened depending on the geometry of the magnetic field. We then describe the dynamics of the singular Alfvén surface where the Alfvén velocity equals the advection velocity (which is equivalent to the magnetic energy being comparable to the kinetic energy). Alfvén waves created by SASI are amplified near this surface. This amplification sends a positive pressure feedback toward the shock, which could be significant to the shock dynamics.

Keywords: supernovae: general, magnetic fields, magnetohydrodynamics, instabilities, shock waves

1 Introduction

The combined effects of rotation and magnetic fields might be able to produce a core collapse supernova explosion exhibiting magnetic jets (Bisnovatyi-Kogan et al. 1976; Shibata et al. 2006). In this scenario the magnetic field is supposed to be amplified via the MRI (Akiyama et al. 2003; Obergaulinger et al. 2009) to a strength such that the magnetic pressure becomes as high as the thermal one, thus enabling the launch of the jets (Burrows et al. 2007). However this requires a very fast rotation, corresponding to the formation of a neutron star rotating typically with a millisecond period. In order to explain the explosion of more slowly or non rotating stars, several hydrodynamical mechanisms have been proposed: the delayed neutrino-driven mechanism (Bethe & Wilson 1985; Marek & Janka 2009), as well as the recently proposed acoustic explosions (Burrows et al. 2006). The work presented here aims at filling the gap between the studies neglecting the magnetic field, and those assuming a fast enough rotation for violent magnetic effects to take place.

We suggest that the multidimensional fluid dynamics can be affected by a magnetic field when the magnetic energy is comparable to the kinetic energy, or equivalently when the Alfvén speed v_A is comparable to the fluid velocity v. This criterion is related to the one comparing the magnetic and thermal pressure through the Mach number $\mathcal{M}$:

$$\frac{P_{\rm mag}}{P_{\rm th}} = \frac{\gamma}{2}\mathcal{M}^2 \left(\frac{v_{\rm A}}{v}\right)^2 . \tag{1.1}$$

In the subsonic flow below the standing accretion shock the pressure ratio is thus smaller than $(v_{\rm A}/v)^2$, by a factor ~ 0.06 at the shock if $\mathcal{M}_{\rm sh} \sim 0.3$, and as low as 10^{-3} if $\mathcal{M} \sim 0.05$ closer to the proto-neutron star. A moderate magnetic field with $v_{\rm A} \sim v$ thus has a modest or negligible pressure, and does not contain enough energy to trigger an explosion. It could however affect the fluid dynamics through the magnetic tension. In the following, we describe two such effects: the influence of the magnetic field on the standing accretion shock instability in Section 2 (following Guilet & Foglizzo (2010)), and the dynamics of an Alfvén surface in Section 3 (following Guilet et al. (2010)).

[1] CEA, Irfu, SAp, Centre de Saclay, F-91191 Gif-sur-Yvette, France.
UMR AIM, CEA-CNRS-Univ. Paris VII, Centre de Saclay, F-91191 Gif-sur-Yvette, France.

2 SASI in a magnetized flow

The Standing Accretion Shock Instability (SASI, e.g. Blondin et al. (2003); Foglizzo et al. (2007); Scheck et al. (2008); Iwakami et al. (2009); Guilet et al. (2010b)) produces large scale non radial shock oscillations. These induce a global asymmetry that could be of crucial importance to the explosion mechanism (in both the acoustic and the neutrino-driven mechanisms) and to accelerate the forming neutron star to a high velocity (Scheck et al. 2006). Endeve et al. (2010) have shown that SASI can also amplify the magnetic field, highlighting the importance of understanding SASI in a MHD context.

For this purpose, we performed a linear analysis of a magnetized variant of the simplified toy model of SASI described by Foglizzo (2009). This planar and adiabatic flow comprises a shock and a potential step that decelerates the fluid at a distance below the shock, thus mimicking the deceleration of accreting material close to the proto-neutron star. We study the effect of a magnetic field that is either horizontal (parallel to the shock) or vertical (perpendicular to the shock).

In the presence of a magnetic field, the advective-acoustic cycle responsible for the hydrodynamical instability (Foglizzo et al. 2007) splits in up to five cycles. This stems from the separation of the advected entropy-vorticity wave into one entropy, two slow magnetosonic, and two Alfvén waves. The propagation of the Alfvén and slow waves at or close to the Alfvén speed causes a phase shift between the different cycles that is proportional to the magnetic field intensity. As a result the different cycles interfere, leading to oscillations of the growth rate as a function of the magnetic field strength (Fig. 1). Furthermore, a horizontal magnetic field increases significantly the efficiency of the cycles containing the vorticity (in the form of slow and Alfvén waves). This leads to an overall increase of the growth rate superposed to the oscillations due to the interferences (Fig. 1, right panel). By contrast a vertical magnetic field (which would correspond to a radial field in spherical geometry) does not affect each individual cycle efficiency, thus only the rather stabilizing effect of the interferences is present (Fig. 1, left panel).

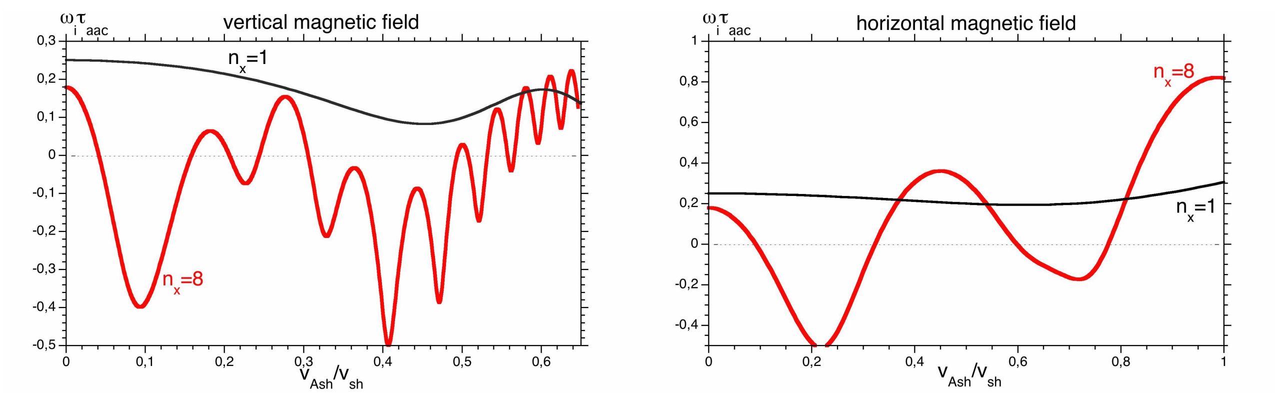

Fig. 1. The growth rate of SASI as a function of the magnetic field strength, parameterized by the ratio of Alfvén and advection speeds below the shock (from Guilet & Foglizzo (2010)). Black and red curves represent respectively the mode with one and eight wavelengths in the width of the box ($n_x = 1$ and $n_x = 8$). The left panel corresponds to a vertical magnetic field, while the right panel corresponds to a horizontal magnetic field (parallel to the shock). In both geometries, the interference between the vorticity and entropy cycles causes oscillations of the growth rate, which tend to stabilize SASI. In the case of a horizontal magnetic field, the vorticity cycle is amplified, which induces an increase of the growth rate.

3 Dynamics of an Alfvén surface

An Alfvén surface is defined as a surface where the flow velocity equals the Alfvén velocity. In core collapse supernovae, such a surface exists during the phase of accretion onto the proto-neutron star even for a weak magnetic field, because the infall velocity vanishes at the center of the star. An interesting property of this Alfvén surface is that Alfvén waves propagating against the flow accumulate, and are amplified as they approach it in the sense that their energy flux increases (Williams (1975), and see Fig. 2 of this proceeding). The amplification

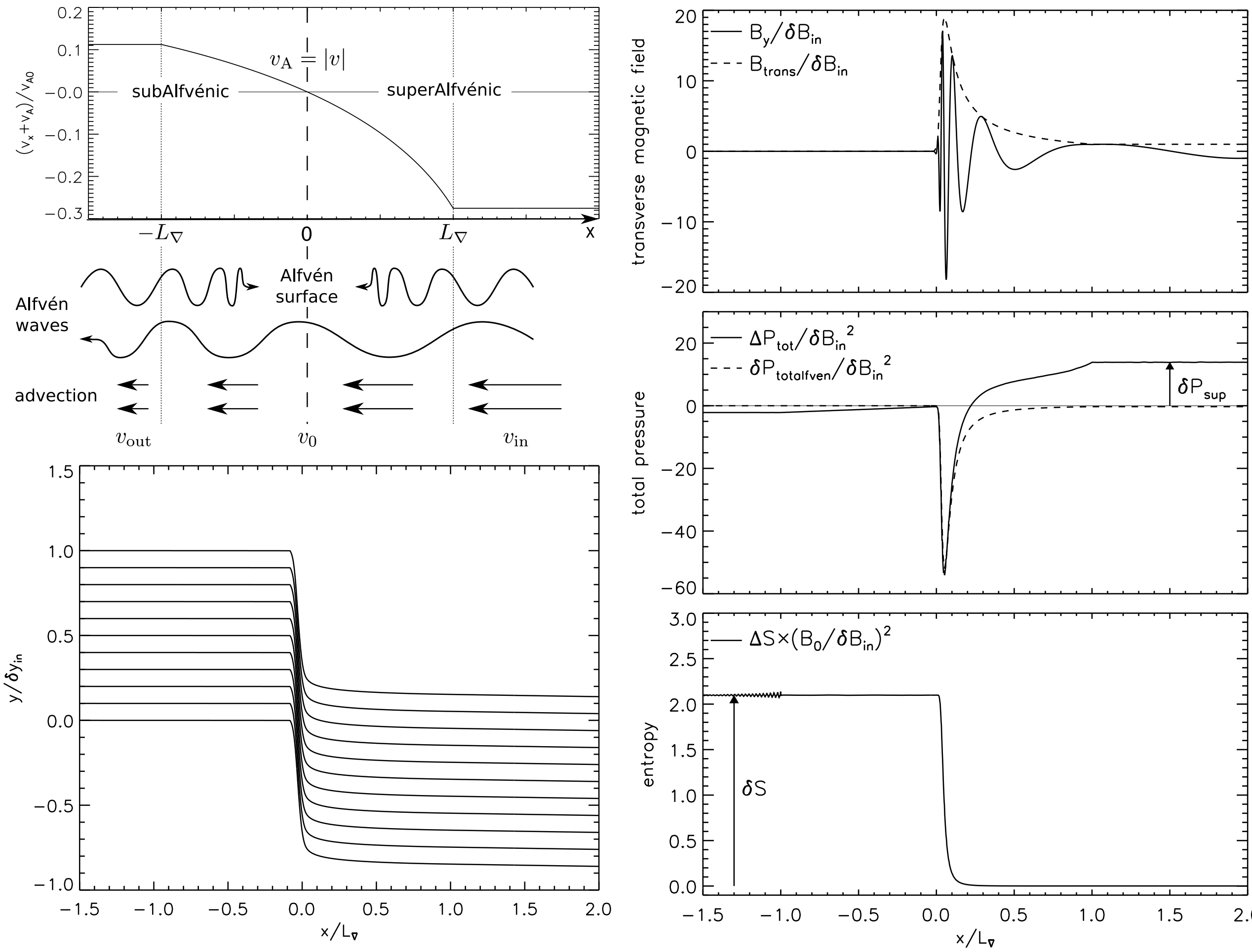

Fig. 2. Upper left panel: Schematic view of the setup of the Alfvén surface simulations. An external potential step located in $-L_\nabla < x < L_\nabla$ decelerates the flow from a superAlfvénic to a subAlfvénic velocity. An Alfvén wave propagating against the flow is sent from either the lower or the upper boundary, and accumulates at the Alfvén surface. The upper part of the figure represents the propagation speed of this wave ($v + v_A$), which vanishes at the Alfvén surface located in $x = 0$. On the contrary, Alfvén waves propagating in the same direction as the flow are not affected by the Alfvén surface as their propagation velocity $v - v_A$ does not vanish. **Bottom left panel:** Magnetic field lines for a small amplitude Alfvén wave in the low frequency regime. The scale in the y direction has been normalized by the displacement of the incident wave $\delta y_{in} = \delta B_{in}/(k_{in} B_0)$. **Right panel:** Profiles of the perturbed transverse magnetic field (upper plot), total pressure (middle plot), and entropy (bottom plot) for a small amplitude high frequency Alfvén wave. The pressure and entropy have been normalized by δB_{in}^2 and $\delta B_{in}^2/B_0^2$ in order to define dimensionless quantities that are independent of the incident wave amplitude in the linear regime.

timescale is controlled by the strength of the gradients, whose lengthscale is noted L_∇:

$$\tau = \left(\frac{\partial(v + v_A)}{\partial x}\right)^{-1} \sim \left(\frac{\mathrm{d}v}{\mathrm{d}r}\right)^{-1} \sim \frac{L_\nabla}{v}. \tag{3.1}$$

The amplification is fast enough to take place before the explosion if the Alfvén surface lies in the strong gradients slightly above the proto-neutron star surface, which requires a magnetic field strength of $B \sim 3.10^{13}$ G. While substantially lower than the magnetic field needed for a magnetic explosion, this remains a rather large value and should lead to a magnetar strength magnetic field once compressed to the size of a cold neutron star.

To study the consequences of the Alfvén wave amplification, we performed 1D simulations of a simplified model of Alfvén surface, which are summarized in Fig. 2. We find that the amplification stops either by non linear effects (for large enough amplitudes of the incident wave), or when the wavelength becomes as small as the resistive or viscous scale (for incident waves of small amplitude). The amount of entropy created by this dissipation corresponds to an energy flux that can be much larger than that of the incident Alfvén wave if the flow is weakly dissipative. We also find that the amplification of the Alfvén wave creates an acoustic signal that increases the upstream pressure (Fig. 2, middle plot of the right panel). Using analytical estimates, Guilet et al. (2010) concluded that the Alfvén wave created by SASI could be amplified to a large amplitude ($\delta B \sim 10^{15}\,$G) and create a significant pressure increase below the shock.

4 Conclusions

We have described two magnetic effects that become important when the magnetic energy is comparable to the kinetic energy, or equivalently when the Alfvén speed is comparable to the fluid velocity. Interestingly this condition can be fulfilled in the very subsonic part of the accretion flow (close to the proto-neutron star) even if the magnetic pressure remains modest. The propagation of vorticity through Alfvén and slow waves can alter the growth of SASI in a way that depends on the magnetic field geometry. A vertical magnetic field has a rather stabilizing influence due to the interference between the different cycles. On the other hand a horizontal magnetic field favors the growth of SASI by amplifying the vorticity cycles. We also studied the amplification of Alfvén waves in the vicinity of an Alfvén surface, where the Alfvén and advection velocity coincide. This amplification creates an acoustic feedback that increases the upstream pressure. This pressure increase might affect significantly the shock dynamics if the magnetic field is strong enough for the Alfvén surface to lie above the proto-neutron star surface. One should note that an important caveat of the studies described above is that they assume a given magnetic field strength without explaining its origin. Strictly speaking the results thus apply only for a magnetic field already present in the progenitor star. If the field is created in situ the results might not directly apply as they could be affected by the turbulent character of such a field.

This work has been partially funded by the Vortexplosion project ANR-06-JCJC-0119.

References

Akiyama, S., Wheeler, J. C., Meier, D. L., & Lichtenstadt, I. 2003, ApJ, 584, 954
Bethe, H. A. & Wilson, J. R. 1985, ApJ, 295, 14
Bisnovatyi-Kogan, G. S., Popov, I. P., & Samokhin, A. A. 1976, Ap&SS, 41, 287
Blondin, J. M., Mezzacappa, A., & DeMarino, C. 2003, ApJ, 584, 971
Burrows, A., Livne, E., Dessart, L., Ott, C. D., & Murphy, J. 2006, ApJ, 640, 878
Burrows, A., Dessart, L., Livne, E., Ott, C. D., & Murphy, J. 2007, ApJ, 664, 416
Endeve, E., Cardall, C. Y., Budiardja, R. D., & Mezzacappa, A. 2010, ApJ, 713, 1219
Foglizzo, T., Galletti, P., Scheck, L., & Janka, H.-T. 2007, ApJ, 654, 1006
Foglizzo, T. 2009, ApJ, 694, 820
Guilet, J. & Foglizzo, T. 2010, ApJ, 711, 99
Guilet, J., Sato, J., & Foglizzo, T. 2010b, ApJ, 713, 1350
Guilet, J., Foglizzo, T., & Fromang, S. 2010, ArXiv e-prints
Iwakami, W., Kotake, K., Ohnishi, N., Yamada, S., & Sawada, K. 2009, ApJ, 700, 232
Marek, A. & Janka, H.-T. 2009, ApJ, 694, 664
Obergaulinger, M., Cerdá-Durán, P., Müller, E., & Aloy, M. A. 2009, A&A, 498, 241
Scheck, L., Kifonidis, K., Janka, H.-T., & Müller, E. 2006, A&A, 457, 963
Scheck, L., Janka, H.-T., Foglizzo, T., & Kifonidis, K. 2008, A&A, 477, 931
Shibata, M., Liu, Y. T., Shapiro, S. L., & Stephens, B. C. 2006, Phys. Rev. D, 74, 104026
Williams, D. J. 1975, MNRAS, 171, 537

THE COSMIC-RAY POPULATION OF NEARBY GALAXIES

P. Martin[1]

Abstract. Every star-forming galaxy is thought to host a large-scale population of cosmic rays accelerated in the various astrophysical shocks that accompany the evolution of massive stars from the main sequence to the compact remnant. As they propagate in the interstellar medium, these non-thermal particles radiate in the radio and gamma-ray bands through interactions with matter and radiation fields. The resulting diffuse glow bears the marks of the cosmic-ray acceleration and transport processes, and the comparison of the emissions from different galactic systems thus can provide insights into both aspects of the cosmic-ray phenomenon. Such a study was however not possible before the LAT gamma-ray telescope onboard the *Fermi* satellite came into operation about two years ago. In this paper, we review the detections of some external star-forming systems achieved by the *Fermi*/LAT so far, and we emphasise how these observations hold potential for improving our understanding of galactic cosmic rays.

Keywords: cosmic rays, galaxies: Milky Way, LMC, SMC, M82, NGC253, gamma rays: galaxies

1 Introduction

Cosmic rays (CRs) with energies $< 10^{15}$ eV are very likely energised by the powerful outflows that accompany massive star evolution, from main-sequence stellar winds to supernova explosions and even beyond with the fast rotation/accretion-driven plasma ejections from compact objects. Yet, CRs are not simply a side-product confined to these phenomena. They actually diffuse out from their sources to eventually form an essential component of the entire Milky Way (MW) and as such, they have observational consequences on quite large scales. The sky in gamma rays with energies >100 MeV is dominated at the 80-90% level by diffuse emission from CRs illuminating the interstellar medium (ISM) of our Galaxy through the processes of Bremsstrahlung and inverse-Compton scattering for CR leptons, and neutral pion production and decay for CR nuclei. In the same time, at the other end of the electromagnetic spectrum, the <1 GHz radio flux is dominated by synchrotron emission from CR leptons spiralling in the Galactic magnetic field.

Extended radio emission of that nature has been observed in countless galaxies and the relation to the massive-star-forming activity seems to be evidenced by the so-called FIR-radio correlation, at least to first order (Helou et al. 1985; Yun et al. 2001; Murphy et al. 2006). Conversely, the gamma-ray sky has remained nearly devoid of external galaxies whose emission in the >100 MeV range result primarily from stellar activity and the associated CR-ISM interactions. At the end of the 1990s, the LMC was the only such source of high-energy gamma-rays detected by the EGRET telescope onboard the CGRO satellite (Sreekumar et al. 1992).

This was regrettable since the characteristics of the diffuse gamma-ray emission from a given galaxy can inform us about its CR population and particularly about its hadronic component, which cannot be directly inferred from the radio observations, and so comparing the emission from galactic systems with different geometries, contents, and physical conditions provide the possibility to make further progress understanding the origin and propagation of CRs. In addition, studying externally-viewed systems allows to get rid from the complications inherent to line-of-sight accumulation in the Milky Way and from the possible bias due to our particular position in the Galactic disk and in the local bubble especially (Grenier 2004; Putze et al. 2010).

The higher sensitivity of the LAT telescope onboard the *Fermi* satellite launched in 2008 was predicted to

[1] Max-Planck Institut für extraterrestrische Physik, 85748 Garching, Germany

extend the sample of star-forming gamma-ray-emitting galaxies to several nearby objects, thus allowing for the first time a population study. In this paper, we review some of the detections achieved by the *Fermi*/LAT over its first two years of operation and we emphasise how these observations hold potential for challenging and/or improving our understanding of galactic cosmic rays.

2 Star-forming galaxies detected in high-energy gamma-rays

External galaxies actually are a major source class in the >100 MeV sky, as they account for about half of the entries in the 1FGL catalog, the rest being unassociated objects (Abdo et al. 2010a). Yet, the vast majority of these galaxies emit in gamma-rays through the activity of an accreting central black hole or so-called galactic nucleus. In this work, we are interested only in galaxies that emit in gamma-rays through CR-ISM interactions resulting from stellar activity and in the following we will therefore refer to these systems as star-forming galaxies.

After slightly less than two years of operation, the *Fermi*/LAT observations have allowed the detection of 4 external star-forming galaxies. Among these are the Small and Large Magellanic Clouds (hereafter SMC and LMC), on which we will focus for the most part of this paper (Abdo et al. 2009, 2010b). The two other objects detected so far are the starburst galaxies M82 and NGC253 (Abdo et al. 2010d).

3 Morphological information

The proximity of the Magellanic Clouds (hereafter MCs) and their relatively large angular sizes (about 6-8° and 8-10° in optical for the SMC and LMC respectively) allowed to unambiguously resolve their gamma-ray emission using the *Fermi*/LAT. From only 11 months of data, the LMC was already spatially resolved at a level enabling to correlate the gamma-ray emission with known structures in the galaxy, while 17 months of data did not provide enough statistics for such correlations to be conclusively established in the SMC. The emission from M82 and NGC253 is consistent with point-source emission, so the morphological information on the gamma-ray diffuse emission from external star-forming galaxies comes from the MCs only.

In the LMC, the distribution of the gamma-rays reveals a strong emission from the 30 Doradus direction. An estimated ∼25% of the total >100 MeV flux indeed come from a rather compact region ∼ 200 pc in size coincident with this very active star-forming region, one of the most active of the Local Group of galaxies. On a larger scale, the gamma-ray emission is poorly correlated with the gas distribution but instead strongly correlates with tracers of massive stars like ionised gas or WR stars. These observations therefore establish an unambiguous connection between CR acceleration sites and massive-star-forming regions. They also suggest a short diffusion length for 1-10 GeV protons, which apparently remain confined close to their production sites. Related to that, it is also interesting to note that the gas ridge south of 30 Doradus, which hosts ∼20% of the total gas mass of the galaxy, is definitely not a bright source of high-energy emission, thereby suggesting that 1-10 GeV protons do not so easily diffuse through the gas.

In the SMC, the situation is less clear-cut because of the more limited statistics. The emission is not clearly correlated with the gas distribution or with the active star-forming regions or known pulsars and supernova remnants, but a certain correlation with supergiant shells is observed, as in the case of the LMC. The maximum of the emission does not correspond to the highest gas column density in the galaxy or to the most active star-forming region NGC602, but more *Fermi*/LAT data are needed here to firmly establish the morphology of the gamma-ray emission from the SMC.

4 Spectrometric information

The spectra derived for the MCs look quite similar and are actually rather flat, with a spectral index $\sim$2. A dedicated spectral modelling was done from a one-zone model, taking into account the specificities of the MCs in terms of gas mass, size...etc, but assuming a electron-to-proton ratio and CR spectrum similar to the local MW. The modelled spectra fit the data quite well (with an underdensity of CRs compared to locally, see further down) and the distribution of the different spectral component is similar to what is obtained for the MW. In both cases, the assumptions of electron-to-proton ratio and CR spectrum similar to the local MW do not conflict with the radio synchrotron measurements, but the uncertainties are large.

The spectra, however, are not really constraining above $\sim$10 GeV because of limited statistics and so the slope of the spectrum up to TeV energies remains rather ill-defined from *Fermi* measurements. We emphasise here the importance of the spectral slope over the GeV-TeV range for constraining the transport processes (see for instance Lacki et al. 2010, about M82 and NGC253, which were detected at TeV energies by VERITAS and HESS, respectively).

5 Photometric information

From the observed > 100 MeV photon fluxes, it is possible to estimate the average CR density in the galaxies under consideration. Under the assumption that the gas content of a galaxy is uniformly irradiated by CRs, the > 100 MeV emissivity can be derived. Then, a comparison to the locally measured value gives an upper-limit on the average CR nuclei density in the galaxy, under the implicit assumption that the CR nuclei spectrum is similar (which appears to be the case from the spectral measurements, see above).

The inferred average CR densities for the SMC and LMC are smaller than the value measured locally in the MW by factors of 6-7 and 2-4 respectively. In the case of the SMC, such a lower CR density is likely to be due to a smaller CR confinement volume because the CR injection rate per unit volume in the SMC does not appear to be lower than in the MW (as inferred for instance from the average temperature of the dust, which is observed to be higher in the SMC than in the MW, hence indicating that the star formation rate per unit volume is at least similar to the MW). The same conclusion can probably be reached for the LMC. In contrast, M82 and NGC253 have average CR densities that are larger than the local one by factors of $\sim$100-1000.

Yet, the resolved emission from the LMC seems to show a more complicated picture than these average estimates. In the Fig. 10 of Abdo et al. (2010b), which shows the emissivity (or equivalently CR density) distribution across the LMC, it can be seen that, although the emissivity in the LMC is on average 2-4 times smaller than the local value, it can reach values twice as high over a significant fraction of the galaxy. This naturally comes from the poor correlation of the gamma-ray emission with the gas distribution, which means that in places the emissivity should be pushed to high values to compensate for the low gas column density.

6 Conclusions

After less than two years of operation, the LAT instrument onboard the *Fermi* satellite has allowed the detection of 4 star-forming galaxies emitting in high-energy, GeV gamma-rays as a result of their stellar activity and the associated CR-ISM interactions. The current sample of such objects includes the SMC, the LMC, M82, and NGC253, with the Magellanic Clouds being spatially resolved at GeV energies. These observations allow for the first time to compare the emission from CR-ISM interactions in galactic systems with different geometries, contents, and physical conditions, hence providing the possibility to make further progress in our understanding of the origin and propagation of CRs.

The LMC displays a gamma-ray emission that is poorly correlated with the gas distribution but instead strongly correlates with massive stars, and in particular with the very active 30 Doradus region. This confirms the role of massive stars in CR acceleration and suggest a short diffusion length of $\sim$1-10 GeV CR protons around their injection sites. The emission from the SMC does not seem to be correlated with neither the gas or the massive star forming regions, but the current photon statistics are too limited to conclusively relate the gamma-ray emission with particular features in the galaxy. The spectra of the galaxies in our sample are quite similar in the GeV range and consistent with that of our Galaxy in terms of underlying CR spectrum, electron-to-proton ratio, and relative contribution of the various spectral components. The average CR densities in the Magellanic Clouds objects are lower than the local Galactic value, but the resolved emission from the LMC shows that such average estimates may not be representative.

The ongoing survey of the sky by *Fermi*/LAT will probably lead to the detection of other nearby objects like M31 or M33, and very likely allow defining upper limits on others. A real population study will then be possible, which will inform us about how CR populations are affected by the global galactic properties. Beyond constraining the CR production and transport processes, the outcomes of such a study may be relevant to the FIR-radio correlation, the extragalactic gamma-ray background, or the prospects for neutrino astronomy.

Most of the work presented here was done within the *Fermi*/LAT Collaboration. The author wishes to particularly thank Jürgen Knödlseder, Andrew Strong, and Pierre Jean for their contribution.

References

Abdo, A. A., Ackermann, M., Ajello, M., et al., 2010, ApJl, 709, L152

Abdo, A. A., Ackermann, M., Ajello, M., et al., 2010, ApJS, 188, 405

Abdo, A. A., Ackermann, M., Ajello, M., et al., 2010, A&A, 512, A7

Abdo, A. A., Ackermann, M., Ajello, M., et al., 2010, ApJ, 710, 133

Abdo, A. A., Ackermann, M., Ajello, M., et al., 2010, *accepted by A&A*

Abdo, A. A., Ackermann, M., Ajello, M., et al., 2010, *submitted to A&A*

Grenier, I. A., 2004, *ArXiv Astrophysics e-prints.*

Helou, G., Soifer, B. T., and Rowan-Robinson, M., 1985, ApJl, 298, L7

Lacki, B. C., Thompson, T. A., Quataert, E., et al., 2010, *ArXiv e-prints*

Murphy, E. J., Helou, G., Braun, R., et al., 2006, ApJl, 651, L111

Putze, A., Derome, L., and Maurin, D., 2010, A&A, 516, A66

Sreekumar, P., Bertsch, D. L., Dingus, B. L., et al., 1992, ApJl, 400, L67

Yun, M. S., Reddy, N. A., and Condon, J. J., 2001, ApJ, 554, 803

SF2A 2010
S. Boissier, M. Heydari-Malayeri, R. Samadi and D. Valls-Gabaud (eds)

SIMULATION OF BLACK HOLE FORMATION IN STELLAR COLLAPSE

J. Novak[1], M. Oertel[1] and B. Péres[1]

Abstract. The collapse of massive stars leads in principle to the formation of a black hole with possible observables, from gamma-rays to neutrinos and gravitational waves. The complex physics involved in this phenomenon require the use of numerical models. We here present a starting project, based on the code CoCoNuT, to perform realistic studies in full general relativity and with detailed microphysics, of the collapse of a rotating stellar core to a black hole.

Keywords: supernovae: general, methods: numerical, black hole physics

1 Introduction

In the last years many efforts have been devoted to the simulations of gravitational supernova (stellar core collapse) and, in particular, to the mechanism which leads to the explosion of the outer layers of the star (Buras et al. 2003). In connection with these simulations, much insight has been gained on the neutron star formation process, with important informations on their rotation frequencies and kick velocities at birth. On the other hand, much fewer investigations have been undertaken concerning the birth of black holes from the collapse of massive main-sequence stars. However, there are several highly interesting questions that are still unanswered at present time: what is the threshold mass of the main-sequence progenitor star that differentiates between the formation of a neutron star and a black hole? What is the general scenario: direct or delayed collapse? In particular, what happened to SN87A? How can long-gamma-ray-bursts be explained by the collapsar model? What are the neutrinos and gravitational wave signals coming from the stellar collapse to a black hole? What can be the kick velocity and spin of a newly born stellar-mass black hole? This short presentation is not intended to answer these questions, but to report on an emerging project, which aim is to study some of these aspects. Nevertheless, let us here mention that recent studies (e.g. O'Connor & Ott 2010) seem to point toward a global picture where the collapse would always first form a proto-neutron star, which would in turn collapse to a black hole when cooling down and accreting more mass from outer stellar layers.

Difficulties of such models reside in the complexity of involved physics and the many ingredients one must take into account to build a realistic model. First, initial data of massive main-sequence stars at the end of their evolution are poorly known (in particular their rotation state and magnetic field). Then models require relativistic approaches: for the hydrodynamics (during the collapse typical velocities can reach up to $0.3c$) and for the gravitation (a black hole is a general-relativistic object). More elaborated magneto-hydrodynamic studies show that there can be several instabilities occurring: the magneto-rotational instability (MRI) or the standing accretion shock instability (SASI), see (Foglizzo 2009). Finally, microphysical aspects are very important, with the appearance of additional particles (to standard neutrons, protons, electrons an neutrinos) which must be taken into account in the equation of state (EOS) and the neutrino transfer which implies the solution of the Boltzmann equation, which is in $6 + 1$ dimensions.

2 Numerical approach

The building-up of so complex models requires numerical tools. In our project, we use the `CoCoNuT`* code (Dimmelmeier et al. 2005) which solves relativistic magneto-hydrodynamic equations with Godunov-type methods

[1] Laboratoire Univers et Théories, Observatoire de Paris, CNRS, Université Paris Diderot, 5 place Jules Janssen, 92190 Meudon, France
*`http://www.mpa-garching.mpg.de/hydro/COCONUT`

and Einstein equations in conformally-flat condition or in the fully-constrained scheme (see Sec. 3) with spectral methods (Grandclément & Novak 2009). This conformal-flatness condition (CFC) has been introduced by Isenberg (2008), as an approximation to general relativity, where gravitational waves are discarded. It is a very good approximation for the case of stellar-core collapse because it is an exact formulation of Einstein equations in the case of spherical symmetry; therefore, the Schwarzschild black hole solution can be properly described within CFC. As gravitational waves are not present in CFC computational spacetimes, they are extracted from the `CoCoNuT` simulation with the standard quadrupole formula, using thus only information coming from the hydrodynamic quantities.

The equations for the gravitational potential are solved using the LORENE[†] library developed at LUTh since several years, and the transmission of informations from the hydrodynamic grid (finite volume methods) to the gravitational field one (spectral methods) is performed through the "*mariage des maillages*" technique, as described by Dimmelmeier et al. (2005). The system of equations for this relativistic model is closed by an EOS from Lattimer & Swesty (1991). Electron capture and neutrino escape during the collapse phase are modeled with a simple parameterized scheme defined by Liebendörfer (2005). Finally, the appearance of the black hole is tracked with an apparent horizon finder, as described by Lin & Novak (2007). This code is fully three-dimensional and uses spherical coordinate system and grid in order to better describe the geometry of the collapse.

3 General relativity issues

One of the main recent features of our models is the use of original and efficient formulation of Einstein equations. Indeed, within standard approach to general relativity (so-called "3+1 formalism"), equations for the relativistic gravitational field are cast into evolution equations and constraints, as it is the case for Maxwell equations. Thus, there are two possibilities to solve for the Einstein equations. *Free schemes*: one does not solve the constraints as they are in principle satisfied during the integration, if they were satisfied initially. *Constrained schemes*: one solves all the constraints at every time-step, but only some of the evolution equations. On the one hand, free schemes can suffer from the appearance of constraint-violating modes, on the other hand the constrained scheme used in `CoCoNuT`, as devised by Bonazzola et al. (2004) exhibits problems of non-uniqueness of the solution of the system of non-linear elliptic equations, when approaching the formation of the black hole.

This non-uniqueness problem has been cured making use of local stability theorems for non-linear elliptic partial differential equations (PDE). Technically, the extrinsic curvature needs to be rescaled, together with a hierarchical integration of the PDE system, as explained in Cordero-Carrión et al. (2009). In this study, the authors also used the code `CoCoNuT`, with the new constrained formulation of the Einstein equation and showed that the code was then able to follow the collapse of a rotating neutron star to a black hole, with no more uniqueness problems for the system of elliptic PDEs arising from the constraints. Initial data are that of a rotating neutron star in Dirac gauge (Lin & Novak 2006), situated on the unstable branch (with the gravitational mass decreasing with increasing central density), for which pressure is initially lowered by about 1%. The collapse has been studied even after the formation of an apparent horizon and the numerical solution has been compared to other studies, in particular that of Baiotti et al. (2005) who used completely different settings: free evolution scheme, Cartesian grid, finite volume and difference numerical techniques . . . Among other points, the gauges used in each study are different and it is therefore quite difficult to compare directly gauge-dependent quantities. However, all qualitative behaviors are the same, as well as some of gauge-independent quantities. This is a good indication that both codes actually give reasonable results and that the new constrained scheme used in `CoCoNuT` works well.

The simulations leading to a black hole are stopped rather shortly after the apparent horizon forms. This is due to the stretching of the coordinate system, which is defined to avoid the singularity which is forming at a finite time inside the apparent horizon. The stretching induces strong gradients on various quantities and the collapse itself make central density grow to very high values. This gives very severe limitations on the time-step. From all these problems, one must deal with the black hole using some particular setting. In the last years, the simulations of black holes have made great progress using two techniques: so-called "punctures" or "excision". In our project, we plan to use excision technique, where a neighborhood of the central singularity is removed from the computational domain and replaced by boundary conditions, particularly for elliptic PDEs. In most common approaches, it is the apparent horizon that is chosen to be the excision surface. In particular it is

[†] `http://www.lorene.obspm.fr`

much better behaved than the event horizon, because it is a quasi-local concept, which makes the black hole to be described as a causal object. Recently, with this approach Vasset et al. (2009) were able to recover the rotating black hole (Kerr) spacetime only from such boundary conditions and Einstein equations. This results gives good hope that excision techniques can be implemented within the `CoCoNuT` code to simulate a rotating black hole in a stable and accurate manner. The goal here is also to be able to follow the interaction between the black hole and its surrounding (mass accretion, spin-up) on longer timescales.

4 Microphysics

Many of the improvements in the `CoCoNuT` code reside in the implementation of better matter models –or *microphysics*– as neutrino transport or better EOS (Oertel & Fantina 2010). As mentioned in the introduction, the treatment of the neutrino transport is a very demanding task. Approximate schemes are, of course, possible to model the impact of neutrinos onto the collapse. Among very simplified approaches one has the *leakage scheme* (Ruffert et al. 1995), where the neutrino mean free path is computed to determine the time decrease of neutrino density. The energy taken away by neutrinos gives a cooling term in hydrodynamic equations, but there is little possibility to obtain an energy spectrum, nor to use the escaping neutrinos to deposit energy behind the shock (neutrino heating). This leakage scheme is currently being implemented in `CoCoNuT`. More elaborated approximate schemes include *flux-limited diffusion scheme*, where the neutrino distribution function obeys a diffusion equation, for each energy group; isotropic diffusion source approximation (IDSA), where the distribution function is split into trapped and streaming neutrino parts and finally, full Boltzmann transport, with approximations on the dimensionality (e.g. "ray-by-ray" method).

Many numerical studies that use general relativity to model the gravitational field take into account over-simplified microphysics: polytropic EOS, or Γ-law in which the adiabatic index depends in a piecewise linear way on the density to mimic the stiffening of matter around nuclear density. There are therefore many vital improvements to be made on our models. First, the computation of a realistic EOS, based on the Lattimer & Swesty (1991) one, but taking into account the appearance of additional particles as muons, pions or hyperons, see Oertel & Fantina (2010). This is a particular feature of the core-collapse scenario forming black holes because, contrary to usual core-collapse supernovae giving birth to neutron stars, the temperatures reached in the central regions of the collapsing star are much higher and therefore, new particles can be formed. Another important point is the computation of neutrino-nucleon interaction terms that are made in a way that is consistent with the EOS. This point is a collaborative effort with the Institut de Physique Nucléaire (IPN) at Orsay, to build-up complete tables of all the interaction terms, from same principles as the EOS.

Finally, a crucial physical reaction for the core-collapse are the electron capture rates, which are responsible for the sudden decrease of pressure and neutrino production through inverse β-decay. Electrons are captured on free protons and heavy nuclei, but these capture rates can be rather sensitive to temperature effects, which have not been taken into account in any supernova simulation. The study of Fantina et al. (2009) looks at this temperature influence on capture rates and shows, using a one-zone, Newtonian code, that deleptonization is reduced when temperature effects are taken into account, which influences the overall dynamics, with an increase of the shock energy of about 0.4 FOE. As this is not negligible, it is of highest importance to incorporate such effects in the numerical model. Although this effect alone cannot solve the supernova puzzle (Buras et al. 2003), it can contribute, together with other realistic physical ingredients, to the modeling of successful explosions of core-collapse supernovae. It also shows the potential importance of microphysical realistic models for the simulation of stellar core-collapses.

5 Conclusions

At present time, the code `CoCoNuT` is able to successfully model the three-dimensional collapse of a rotating neutron star to a black hole. Nevertheless, much more effort is to be put in these models in order to get very interesting astrophysical informations on the birth of stellar-mass black holes. Most of all, initial data remain the main uncertainty in such models. In particular, the lack of reliable two-dimensional models of massive star evolution prevents us from having good models for rotation and magnetic field in evolved massive stars. Another issue with initial models is the little number of groups working on the subject: almost all the numerical simulations of stellar core-collapse rely on the models by Heger & Woosley. It is quite important to have some alternative computations of these very important models and we have now been in contact with Limongi & Chieffi who are developing such models.

As about 99% of the energy in a supernova is released via neutrino emission, it is vital to be able to correctly model this phenomenon. The incorporation of neutrino transport is just starting in `CoCoNuT`, but we already consider the necessity of having a neutrino-nucleon interaction, which is coherent with the EOS, in particular as we devise an EOS which is really adapted to the case of the collapse to a black hole (higher temperatures). The `CoCoNuT` code is able to take into account also the magnetic field, through ideal MHD equations, but because of too low resolution, it seems for the moment very difficult to look at the most interesting phenomenon, which is the magneto-rotational instability. On the other hand it may be possible, once the modeling of black hole is improved with excision techniques, to look on highly interesting phenomenon of SASI in the presence of black hole, and its influence on black hole kicks and spins.

Finally, gravitational waves should be extracted in a clean manner from our simulations thanks to the use of general relativistic models, using a fully constrained scheme, which is now accurate and stable. However, a major issue in the future for our project is the development of efficient parallel version of LORENE and `CoCoNuT`, to be able to combine all the above mentioned features with sufficient resolution. Since this a only a starting project, and since many important expertise is present, we have good hopes for the future.

References

Baiotti, L., Hawke, I., Montero, P.J et al. 2005, Phys. Rev. D, 71, 024035

Bonazzola, S., Gourgoulhon, E., Grandclément, P. & Novak, J. 2004, Phys. Rev. D, 70, 104007

Buras, R., Rampp, M., Janka, H.-T. & Kifonidis, K. 2003, Phys. Rev. Lett., 90, 241101

Cordero-Carrión, I., Cerdá-Durán, P., Dimmelmeier, H. et al. 2009, Phys. Rev. D, 79, 024017

Dimmelmeier, H., Novak, J., Font, J.A., Ibàñez, J.M. & Müller, E. 2005, Phys. Rev. D, 71, 064023

Fantina, A., Donati, P. & Pizzochero, P.M. 2009, Phys. Lett. B, 676, 140

Folglizzo, T. 2009, ApJ, 694, 820

Grandclément, P. & Novak, J. 2009, Living Rev. Relativity, 12, 1

Isenberg, J. 2008, Int. J. Mod. Phys. D, 17, 265 (*following a first unpublished version of 1978*)

Lattimer, J.M. & Swesty F.D. 1991, Nucl. Phys. A, 535, 331

Liebendörfer, M. 2005, Astrophys. J., 633, 1042

Lin, L.M. & Novak, J. 2006, Class. Quantum Grav., 23, 4545

Lin, L.M. & Novak, J. 2007, Class. Quantum Grav., 24, 2665

O'Connor, E. & Ott, C. 2010, Class. Quantum Grav., 27, 114103

Oertel, M. & Fantina, A. this volume, p. 155 (http://proc.sf2a.asso.fr/2010/2010sf2a.conf..0155D.pdf)

Ruffert, M., Janka, H.T. & Schäfer, G. 1995, Astrophys. & Space Sci., 231, 423

Vasset, N., Novak, J. & Jaramillo, J.L. 2009, Phys. Rev. D, 79, 124010

SF2A 2010
S. Boissier, M. Heydari-Malayeri, R. Samadi and D. Valls-Gabaud (eds)

AN EXTENDED EQUATION OF STATE FOR SIMULATIONS OF STELLAR COLLAPSE

M. Oertel[1] and A. Fantina[2]

Abstract. In core-collapse events matter is heated and compressed to densities above nuclear matter saturation density. For progenitors with masses above about 25 solar masses, which eventually form a black hole, the temperatures and densities reached during the collapse are so high that a traditional description in terms of electrons, nuclei, and nucleons is no longer adequate. We will present here an improved equation of state which contains in addition pions and hyperons. They become abundant in the high temperature and density regime, and we will discuss the effect on the thermodynamic properties.

Keywords: core collapse, equation of state, dense matter

1 Introduction

Supernovae and hypernovae figure among the most spectacular events observed in the universe because of the immense amount of energy involved. In general, one can distinguish between thermonuclear and core-collapse events. Here we will be interested in the latter. These occur at the end of the life of massive ($M \gtrsim 8M_{\odot}$) stars: if the iron core exceeds the Chandrasekar mass a gravitational collapse is induced. At the center a compact star is formed, which is a neutron star in the classical gravitational supernova. Depending among others on the progenitor mass, its metallicity, and rotation, as well a black hole can be formed. These events are known as hypernovae or collapsars. For about thirty years, simulations are performed in order to explore these events and to answer related questions, for example on the precise conditions for forming a neutron star or a black hole. The simulations are extremely complex, since they involve many different ingredients: multi-dimensional hydrodynamics, neutrino transport, general relativity and complicated microphysics. Despite all the effort, many unknowns remain in the simulations, in particular on the engine driving a successful supernova explosion. Apart from the observations via electromagnetic radiation, the neutrino and gravitational wave signal could give interesting information on the models. More details about the state-of-the-art of the simulations and in particular on neutrino transport can be found in Novak et al. (2010).

The microphysics input for the simulations concerns essentially two domains, the interaction rates for neutrino-matter interaction and deleptonization, i.e. electron capture, and the equation of state (EOS). In this talk we will discuss the latter. It is not an obvious task to construct an EOS. The main difficulty arises from the fact that a very large range of (baryon number) densities ($10^{-10}\text{fm}^{-3} \lesssim n_B \lesssim 1\text{fm}^{-3}$), temperatures ($0 < T \lesssim 150$ MeV) and proton fractions ($0 < Y_p = n_p/n_B < 0.6$) has to be covered. Within this range the characteristics of nuclear matter change dramatically, from an ideal gas of different nuclei up to uniform strongly interacting matter, containing in the most simple case just free nucleons but potentially more exotic components such as hyperons or mesons. Even a transition to deconfined quark matter cannot be excluded. Although there is a large variety of EOSs available for cold dense matter relevant for the description of neutron stars, at present, only two hadronic EOSs exist which are commonly used in core collapse simulations, where temperature effects play a crucial role, that by Lattimer and Swesty (1991) and by Shen et al. (1998). These two equations of state use different nuclear interactions, but are based on the same limiting assumptions: they take into account non-interacting α-particles, a single heavy nucleus and free nucleons in addition to the electron, positron and photon gas. In particular at low densities the composition of matter is much more complicated,

[1] LUTH, Observatoire de Paris/CNRS/Université Paris Diderot, 5 place Jules Janssen, 92195 Meudon, France
[2] IPN Orsay, Université Paris Sud/CNRS-IN2P3, 15 rue Georges Clemenceau, 91406 Orsay

with a large number of different nuclei. Although this should not have a large impact on the purely thermodynamical properties, it is important to correctly describe the composition of matter in order to determine the electron capture rates and neutrino interactions. Therefore, in the last years, several groups have started to build EOSs using mainly statistical approaches to improve the low density part of the EOS (see e.g. Hempel and Schaffner-Bielich (2010)). This part of the EOS of state can be confronted with the knowledge obtained from multi-fragmentation models used to analyze data from low energy heavy-ion collisions. Up to know, there are less attempts to improve the high energy part of the EOS, although there are many indications that probably the physics of the standard EOS is too poor in this regime, too. First of all, our knowledge about the QCD phase diagram suggests a transition to the QGP plasma within the range of densities and temperatures reachable in core collapse events, i.e. within the range of our tables. Of course, there are lots of uncertainties about this phase transition, such that its occurence cannot be affirmed, but the possibility has to be kept in mind when employing a purely nuclear EOS such as the Lattimer and Swesty (1991) or Shen et al. (1998) one up to densities well above nuclear matter saturation density and temperatures as high as several tens of MeV. There is some first work including this phase transition, see Sagert et al. (2009). Secondly, even without thinking about a QCD phase transition, other forms of (exotic) matter could appear at high densities and temperatures. Already for a long time for cold EOS used for neutron star models, hyperons, pions and kaons have been considered. At temperatures above about 20 MeV, this point becomes even more crucial. This has been confirmed by the first attempts including hyperons and pions in the EOS by Shen et al. (1998) for simulations, see Sumiyoshi et al. (2009). We will discuss here the construction of a new EOS including hyperons, pions and muons based on the Lattimer and Swesty (1991) one and the effects on some thermodynamic quantities important for the simulations.

2 The model for the equation of state

Let us start the description of our model for the extended EOS with a description of the original EOS by Lattimer and Swesty (1991). As mentioned above, it contains electrons, positrons, photons, nucleons, α-particles, and one (average) heavy nucleus. Electrons and positrons are treated as noninteracting free Fermi gas in pair equilibrium, and the α-particles as free Boltzmann gas. The nuclear interaction is based on a liquid drop model. The phase transition between the phase containing nuclei and the nuclear matter phase is built via a Maxwell construction. More details about the underlying theory can be found in Lattimer and Swesty (1991) or under `http://www.astro.sunysb.edu/dswesty/lseos.html`. On the same web page, the original tables as well as the source code can be found. To obtain our EOS, we have corrected a small error for the value of the α-particle binding energy, which has to be measured with respect to the neutron mass, too, as all other energies.

We have added to the Lattimer and Swesty (1991) pions, muons and hyperons. For the first two, no interaction has been assumed and they have just been added as a free gas, satisfying the overall constraint on charge neutrality. Concerning the muons we have to mention the following point. Traditionally, the electron fraction $Y_e = (n_{e^-} - n_{e^+})/n_B$ is used in addition to the temperature and baryon number density n_B as parameter for the EOS. If the muon lepton number was conserved independently of the electron lepton number we should introduce an additional variable, the muon fraction and the simulation codes should evolve muon number, too. For the moment we have assumed that muons and electrons have the same chemical potential and have thus generalized the definition of the electron fraction to include muons as $Y_e = (n_{e^-} - n_{e^+} + n_{\mu^-} - n_{\mu^+})/n_B$. Hyperons are added by extending the model by Balberg and Gal (1997) to finite temperature. We have slightly adapted the parameters for the hyperon-nucleon (YN) and hyperon-hyperon (YY) interaction in order to be compatible with current experimental data on hypernuclei. This approach has the great advantage that hyperons are added on a nuclear interaction which is exactly the same as in the original EOS by Lattimer and Swesty (1991), such that an “artificial phase transition”, induced only by matching one nuclear model to another and thus completely unphysical, is avoided.

For comparison, we have kept for the nuclear part the three different parameter sets provided by the original code by Lattimer and Swesty (1991), characterised by the value of the compression modulus K of symmetric nuclear matter at saturation density. The values available are $K = 180, 220, 375$ MeV. Today, the preferred value for K from nuclear experiments is 240 ± 10 MeV Piekarewicz (2010). The obvious error is rather small, such that the two extreme values for K used in the Lattimer and Swesty (1991) EOS are in principle disfavored and the preferred parameter set for simulations should be that with $K = 220$ MeV. We will, however, keep the two other sets for two reasons. The first one is purely historical: in many simulations the parameter set with $K = 180$ MeV has been used, such that for comparison with the existing literature it is interesting to have this value at hand. The second one is that the experimental result of 240 ± 10MeV is not uncontested. In particular, the extraction of this value from data on isoscalar giant monopole resonances depends on the density dependence of the nuclear symmetry energy, a quantity under intensive debate in recent years. We therefore think that a wider range of values should be considered. In that sense, the range of values of the EOS represents an extreme variation of the nuclear parameter sets, i.e. it can give an indication about the uncertainties in the simulations coming from the uncertainties on the EOS.

There are even more uncertainties on the YY and YN interaction. In order to give an indication about these uncertainties, we compare the results using the model by Balberg and Gal (1997) with a completely different model, the G-matrix parametrization by Vidaña et al. (2010). Apart from the question of matching the latter model to another subsaturation EOS, its weak point is that it becomes very soft at high densities and low temperatures such that the predicted maximum mass for neutron stars is not easily compatible with observational data. We are using it here mainly for comparison to give an indication on the uncertainties coming from the underlying baryonic models. In any case, we are mainly interested in the high temperature region, where the interaction should become less important because the kinetic energy gains in importance with respect to the interaction energy.

3 Some thermodynamics

Within this section we will discuss the effects of our extension of the EOS on matter composition and thermodynamical quantities relevant for the simulations. Let us look as an example on the fractions of Λ and Σ^- hyperons at $T = 60$ MeV and $n_B = 0.32\text{fm}^{-3}$ which are shown in Fig. 1. Λ and Σ^- are the first hyperons to appear and at that density, which corresponds to roughly two times nuclear matter saturation density, and temperature they are the most abundant ones. Different simulations have shown that these conditions can well be reached in core-collapse events for progenitor masses above roughly 25 $M_\odot$. "LS+" thereby indicates our

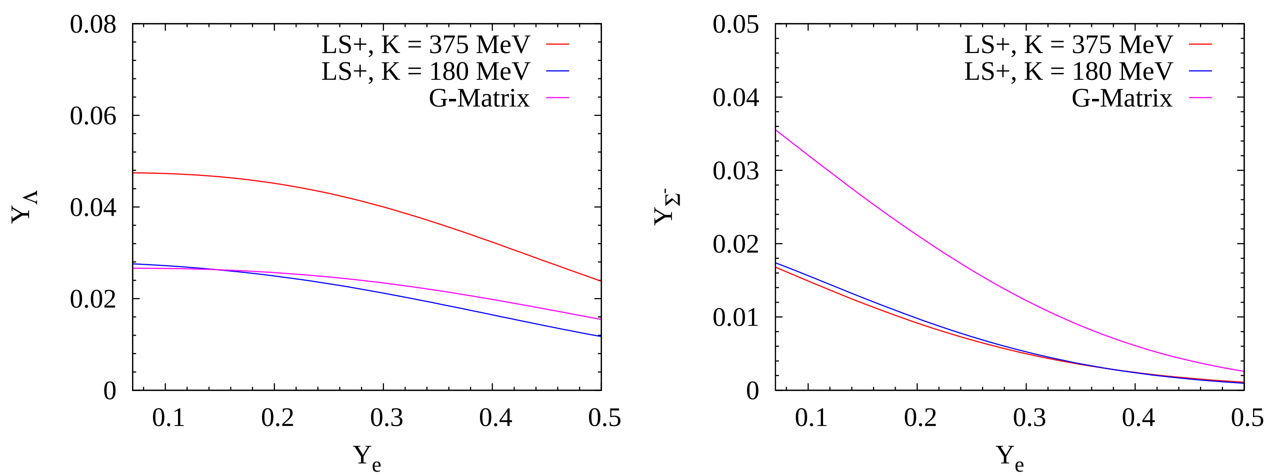

Fig. 1. The fraction of Λ and Σ^- hyperons at a baryon number density of $n_B = 0.32\text{fm}^{-3}$ and a temperature of $T = 60MeV$ as a function of the electron fraction.

new EOS of state with the model by Balberg and Gal (1997) for the hyperons and "G-matrix" the hyperonic model by Vidaña et al. (2010). It can be seen that in both cases the abundancies of the additional particles in the EOS are of the order of 5%. This means that they can have a non-negligible influence on the thermodynamic properties. This can be seen from the results for pressure and sound speed displayed in Fig. 2. They are shown for the same density and temperature as the abundancies in Fig. 1. For comparison we have shown here the original EOS by Lattimer and Swesty (1991) with the $K = 180$ MeV parameter set. The results with the G-matrix approach differ considerably from the others, such that one remark is that it seems important to test a variety of baryonic models in order to get an idea on the uncertainties induced in the simulations. Only two different models, Lattimer and Swesty (1991) and Shen et al. (1998), are much too restrictive. The other remark is that including additional particles on the Lattimer and Swesty (1991) EOS induces a difference of the order of the difference between the three parameter sets. That means that those particles should be included at high density and temperature.

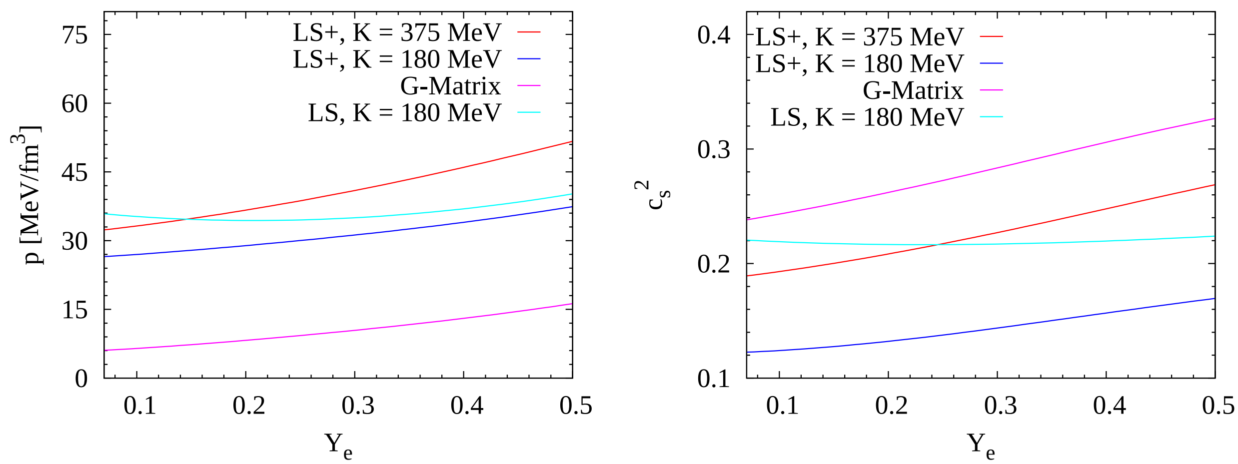

Fig. 2. Pressure and sound speed as a function of the electron fraction at the same density and temparture as in Fig 1.

4 Outlook

The ultimate answer on the importance of the additional particles can only come from realistic simulations. We have shown that at high density and temperature they become important, but a priori this does not preclude anything on the relevance for the core-collapse events. We expect that, since in classical supernova events, temperatures and density stay relatively low compared with those discussed above, that our extended EOS will be more relevant in events forming a black hole. This would be in agreement with the first studies by Sumiyoshi et al. (2009). It has to be seen whether the EOS dependence shows up in the neutrino and gravitational wave signal of those events. Of course, for a full simulation, the deleptonization and neutrino-matter interaction rates have to be evaluated coherently. This will be kept for future work.

References

Balberg, S. & Gal, A. 1997, Nucl. Phys. A, 625, 435.

Hempel, M. & Schaffner-Bielich, J. 2010, Nucl. Phys. A, 837, 210

Lattimer, J.M., & Swesty, F.D. 1991, Nucl. Phys. A, 535, 331

Novak, J., Oertel, M. & Peres, B. 2010, this volume, p. 183 (`http://proc.sf2a.asso.fr/2010/2010sf2a.conf..0183N.pdf`)

Piekarewicz, J. 2010, J. Phys. G, 37, 064038

Sagert, I. et al. 2009, Phys. Rev. Lett., 102, 081101

Shen, H., Toki, H., Oyamatsu, K. & Sumiyoshi, K. 1998, Nucl. Phys. A, 637, 435

Sumiyoshi, K., Ishizuka, C., Ohnishi, A. & Suzuki, H. 2009, Astrophys. J. Lett., 690, L43

Vidaña, I., Logoteta, D., Providência, C., Polls, A. Bombaci, I. 2010, `arXiv.org/abs/1004.3958`

SF2A 2010
S. Boissier, M. Heydari-Malayeri, R. Samadi and D. Valls-Gabaud (eds)

FUNDAMENTAL PHYSICS IN OBSERVATIONAL COSMOLOGY

P. Peter[1]

Abstract. I discuss, through a few examples, how observational cosmology can provide insights on hypothetical fundamental physics phenomena or mechanisms, such as Grand Unified Theory, Superstring alternatives to the inflation paradigm, and inflation itself.

Keywords: grand unified theory, superstring theory, inflation, bouncing cosmological models

1 Introduction

Cosmology has definitely entered a phase of precision measurements: Cosmic Microwave Background (CMB) anisotropies (Komatsu 2010), Large Scale Structure (LSS) observations (Abazajian et al. 2009) and the magnitude-redshift distribution of Supernovæ Ia (Amanullah et al. 2009) to name the most prominent, have radically transformed the field. Forthcoming experiments (e.g. Planck) and new data such as Baryonic Acoustic Oscillations (Percival et al. 2009) or those based on the 21 cm transition (Furlanetto et al. 2006) will further change our view of primordial cosmology (Peter and Uzan 2009). It is no longer enough to try and roughly understand cosmological observations: time has come to use these data in a new way instead of merely gather them.

One such way is to test inflationary predictions in greater details to decide which version is the most satisfactory, and hence to known how it should be implemented in a high energy physics scheme, in particular in a string theory framework; I present in Sec. 2 a specific example based on the reheating temperature (Martin & Ringeval 2010). Another way consists in evaluating directly some consequences of high energy models such as Grand Unified Theories (GUT); for this, I concentrate (Sec. 3) on the still possible fraction of topological defects as active seeds for CMB fluctuations (Bouchet et al. 2002; Fraisse et al. 2008; Pogosian et al. 2009). Finally, taking the special case of bouncing cosmology (Sec. 4), I argue that challengers to inflation may still be worth investigating, both at the theoretical and observational levels (Peter & Pinto-Neto 2008).

2 Inflation

Inflation (Martin 2008) is nowadays the most widely accepted solution to the old puzzles of standard cosmology. Its basic predictions concern the background itself (e.g., the ratio of the total density $\rho_{\rm tot}$ to the critical density $\rho_{\rm crit}$, Ω that is expected to be unity to an amazing precision, leading to a vanishing curvature $\Omega = 1 \Longleftrightarrow \mathcal{K} = 0$) as well as its perturbations that have acted as primordial seeds for the formation of the now observed LSS. These perturbations imprinted the CMB in a way that must be correlated with LSS: a consistent model should explain both sets of data.

Inflation is modeled by a scalar field slowly rolling in a potential. A few parameters of this potential allow for an almost complete fit of the whole available set of data; in fact, it is often argued that only the slow-roll phase is probed by astrophysical observations; this phase requires the scalar field to be far from its equilibrium value. In itself, this is already quite an achievement, and a way to discriminate between various models.

The degree of accuracy of the most recent data has now increased to a such a level that it has become possible to probe the different part of the potential corresponding to reheating, i.e. the transition between the end of inflation itself and the radiation dominated era, at a time for which the scalar field is therefore close to its true minimum. The reheating phase duration affects the observational range of scales at which one observes

[1] $\mathcal{G}\mathbb{R}\varepsilon\mathbb{C}\mathcal{O}$ – Institut d'Astrophysique de Paris, UMR7095 CNRS, Université Pierre & Marie Curie,
98 bis boulevard Arago, 75014 Paris, France

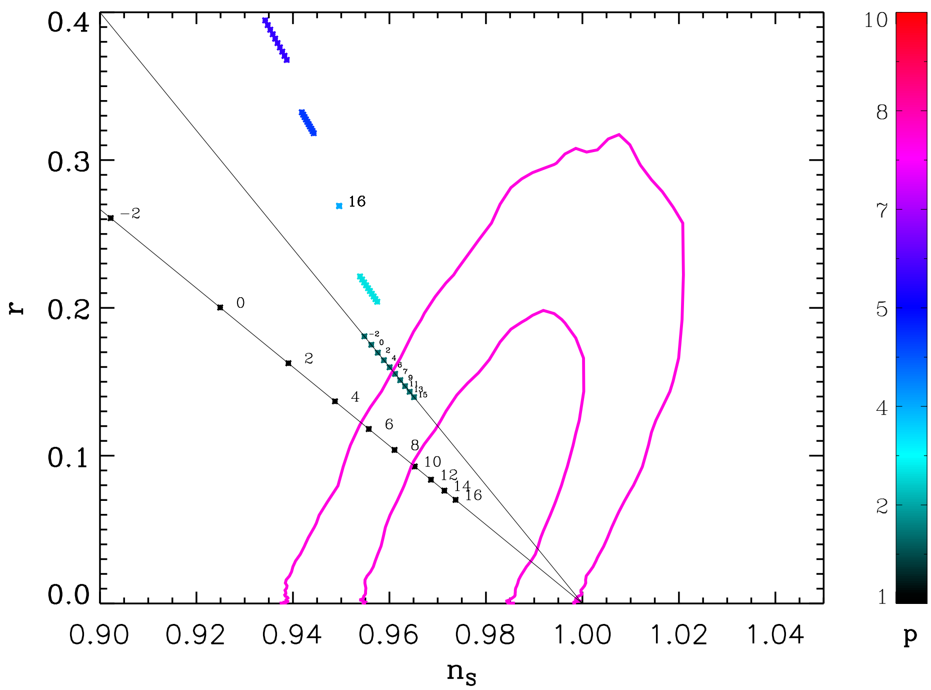

Fig. 1. One and two-σ WMAP confidence intervals in the $(n_{\rm S}, r)$ plane. Quoted numbers indicate the reheating temperature in the form $T_{\rm reh} = 10^{\#} g_*^{-1/4}$GeV) for various values of the scalar field power p in the potential (lines are for $p \gtrsim 1$ and $p = 2$). See Martin & Ringeval (2010), from which this figure is taken, for details.

the end of the slow-roll phase. Measurements of the spectral index $n_{\rm S}$ and the tensor-to-scalar ratio r thus constrain this phase characteristics (equation of state, duration and hence temperature). Fig. 1, taken from Martin & Ringeval (2010), illustrates this point in the case of large field models, for which the potential takes the form $V \propto \varphi^p$.

3 GUT and cosmic defects

Another direct consequence of high energy theories comes straight from GUT, and those are topological defects (Vilenkin & Shellard 2000) and cosmic strings in particular, whose formation is almost inevitable in most cosmologically consistent models (Jeannerot et al. 2003).

If one considers cosmic string contribution to the CMB as a viable source of cosmological perturbations, one rapidely finds that it cannot be made, by itself, to fit the currently available data; this is due, in particular, to the fact that defects are active seeds, and hence cannot produce a coherent spectrum. In other words, the observed acoustic oscillations in the resulting spectrum would be damped. Fig. 2 shows a typical spectrum due to cosmic strings, as calculated e.g. by Ringeval (2010): those can merely be part of the final spectrum, although for some values of the parameters, it is seen that there exists a (small) multipole window for which they might actually dominate the signal.

As a source of cosmological perturbations, strings would also produce non gaussianities in a way that is sufficiently different from the inflation case to be distinguished (Ringeval 2010). It can be argued that forthcoming data have a large potential to exhibit such a string signal: that would be a direct measurement of the GUT symmetry breaking energy scale!

4 Bounces

As we have seen, the now standard inflationary paradigm can be modified by inclusion of topological defects. However, the fact that this mechanism is the best currently available to fit all the data doesn't mean it is unique.

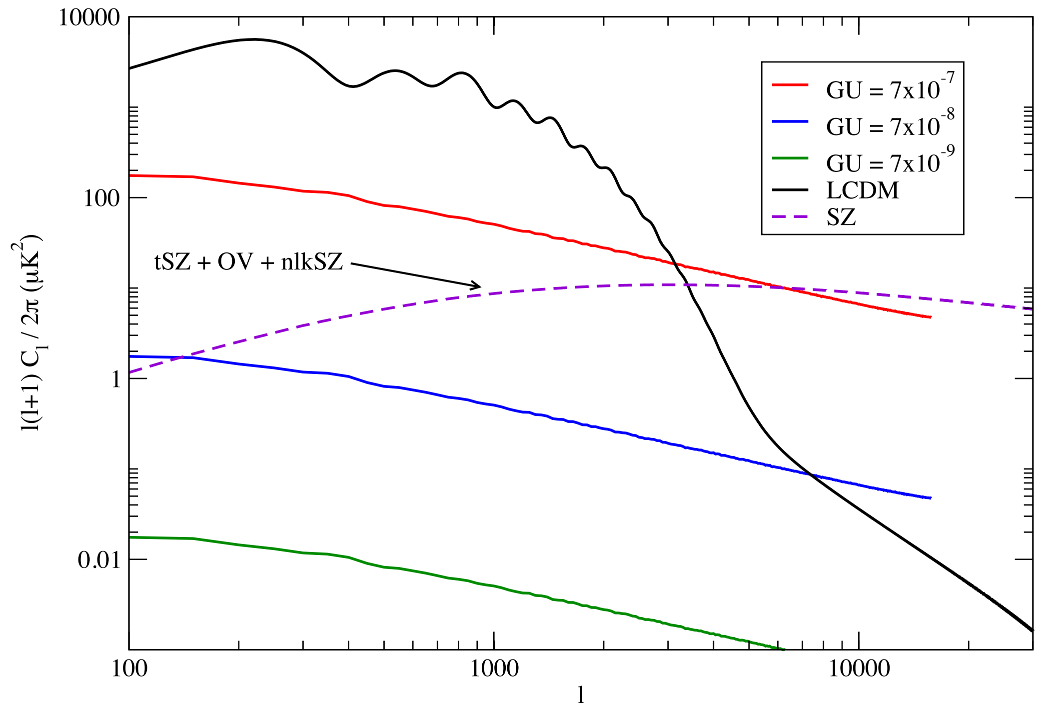

Fig. 2. Multipole spectrum for the standard ΛCDM model – best fit to the currently available data (Komatsu 2010) – and for a network of cosmic strings for different values of the energy per unit length U in units of the Planck mass squared. The dashed curve represents the contribution from the Sunyaev-Zeldovitch effects, namely thermal (tSZ), Ostriker-Vichniak (OV) and nonlinear kinetic (nlkSZ). From Ringeval (2010)

.

In fact, a reasonnable way to test its effectiveness would be to find a challenger, and possibly confirm or rule it out. This is what happened to cosmic strings, so the question can be asked as to whether there does exist any plausible contender? It turns out there can be: the bouncing scenario.

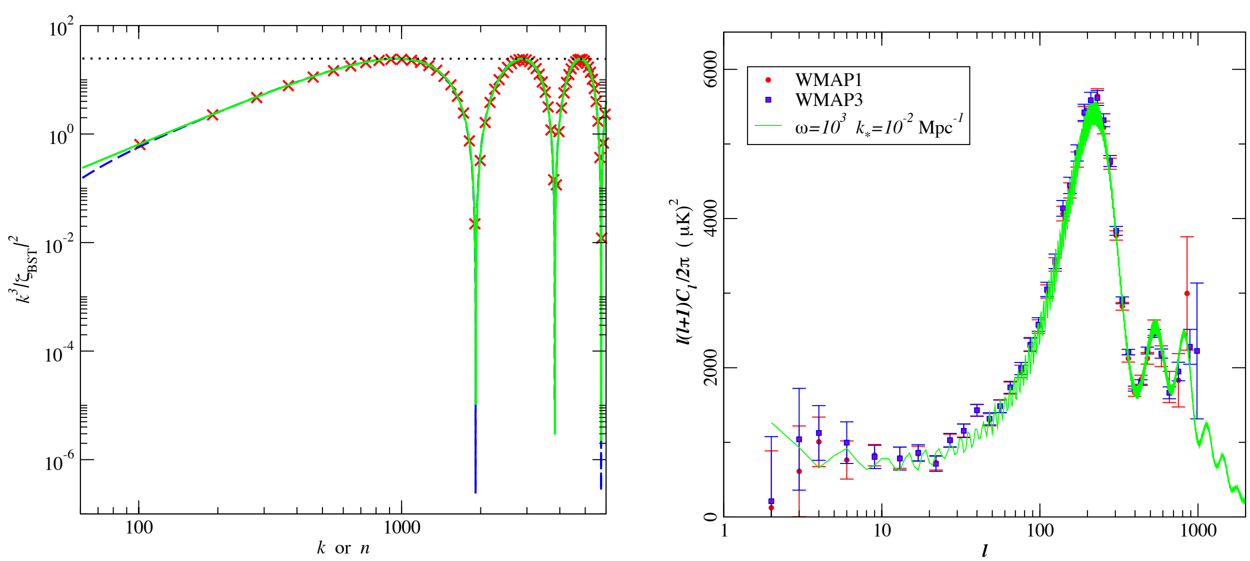

Fig. 3. The primordial spectrum $k^3|\zeta_{\rm BST}|^2$ (right) and subsequent multipoles C_ℓ (left) for a typical bouncing model. From Falciano et al. (2008)

.

Instead of using a phase of accelerated ($\ddot{a} > 0$) expansion ($\dot{a} > 0$) as inflation does, having a bounce supposes a phase of decelerated ($\ddot{a} < 0$) contraction ($\dot{a} < 0$). As a result, just before the bounce itself, the total density can be as close to critical as one wishes. With a contraction dynamics dominated by a regular, matter or radiation, fluid, the horizon, being an integral quantity over time (Martin & Peter 2004), can be made to diverge, hence solving this puzzle as well. The remaining usual issues such as homogeneity can be addressed under reasonnable additional assumptions (Peter & Pinto-Neto 2008).

Crucial to any cosmologically relevant model is the existence of primordial perturbations which will seed the LSS formation; these can be rather problematic in a bounce model (Peter & Pinto-Neto 2002). It is often said that this category of models faces the difficulty of being very much model dependent which, it is argued, is not the case of inflation. Not only is this last assertion erroneous, each inflationary model leading to different observational prediction*, but it is also misleading since most bouncing models do also share generic prediction features.

The most important difficulty faced by bouncing models is that classical General Relativity (GR) is very reluctant, under general energy conditions, to let the Hubble rate vanish! Options however can be considered. In the framework of GR, one needs at least a positive spatial curvature and a scalar field (Martin & Peter 2003; Falciano et al. 2008). Still in the classical domain, one can either modify gravity in order to render it non singular (Fabris et al. 2003; Abramo et al. 2010) or consider a fluid that does not satisfy the usual energy conditions (Abramo & Peter 2007; Finelli et al. 2008). Finally, one can use some version of quantum gravity that would apply to the Universe as a whole: these would lead to quantum cosmology models (Peter et al. 2005, 2006, 2007), allowing for a bounce independently of the curvature. In almost all of these models, it turns out that the spectrum of primordial perturbations is modified to include an oscillatory part, that can be compared to observations as examplified on Fig. 3.

5 Conclusions

Precision cosmology is opening new windows of observations: future data will constrain high energy theories!

I should like to thank J. Martin and C. Ringeval for many enlightning discussions and for providing the relevant figures coming from their works.

References

Abramo, L., R.& Peter, P., 2007, JCAP 09, 001.

Abramo, L., R., Peter, P. & Yasuda, I., 2010, Phys. Rev. D81, 023511.

Abazajian, K., et al. 2009, Ap. J. S., 182, 543.

Amanullah, R. et al., 2010, Ap. J. 716, 712.

Bouchet, F. R., Peter, P., Riazuelo, A. & Sakellariadou, M., 2001, Phys. Rev. D65, 021301.

Fabris, J. C., Furtado, R. G., Peter, P. & Pinto-Neto, N., 2003, Phys. Rev. D67, 124003.

Falciano, F. T., Lilley, M. & Peter, P. Phys. Rev. D77, 083513.

Finelli, F., Peter, P. & Pinto-Neto, N., 2008, Phys. Rev. D77, 103508.

Fraisse, A. A., Ringeval, C., Spergel D. N. & Bouchet, F. R., 2008, Phys. Rev. D78, 043535.

Furlanetto, S. R., Peng Oh, S. & Briggs, F. H., 2006, Phys. Rep. 433, 181.

Jeannerot, R., Rocher, J. & Sakellariadou, M., 2003, Phys. Rev. D68, 103514

Komatsu, E. et al., 2010, arXiv:1001.4538.

Martin, J., 2008, Lect. Notes Phys. 738, 193.

Martin, J., & Peter, P., 2003, Phys. Rev. D68, 103517.

Martin, J., & Peter, P., 2004, Phys. Rev. Lett. 92, 061301.

Martin, J. & Ringeval, C., 2001, Phys. Rev. D82, 023511.

Martin, J., Ringeval, C., Trotta, R., 2010 arXiv:1009.4157

Percival, W. J. et al., 2010, MNRAS 401, 2148.

Peter, P. & Pinto-Neto, N., 2002, Phys. Rev. D66, 063509.

*The fact that it is possible to identify a generic "slow-roll" category of inflationary models does not mean these models produce undistinguishable predictions (Martin et al. 2010).

Peter, P. & Pinto-Neto, N., 2008, Phys. Rev. D78, 063506.
Peter, P. Pinho, E., & Pinto-Neto, 2005, JCAP 07, 014.
Peter, P. Pinho, E., & Pinto-Neto, 2006, Phys. Rev. D73, 104017.
Peter, P. Pinho, E., & Pinto-Neto, 2007, Phys. Rev. D75, 023516 (2007).
Peter, P. & Uzan, J.-P., 2009, Primordial Cosmology (Oxford University Press).
Pogosian, L., Henry Tye, S.-H., Wasserman, I. & Wyman, M., 2009, JCAP 0902, 013.
Ringeval, C., 2010, arXiv:1005.4842
Vilenkin, A. & Shellard, E. P. S., 2000, Cosmic Strings and Other Topological Defects (CUP).

SF2A 2010
S. Boissier, M. Heydari-Malayeri, R. Samadi and D. Valls-Gabaud (eds)

THE PERTINENCE OF JET EMITTING DISCS IN MICROQUASARS THEORY AND COMPARISON TO OBSERVATIONS

P.-O. Petrucci[1], J. Ferreira[1], G. Henri[1], J. Malzac[2] and C. Foellmi[1]

Abstract. Jet Emitting Disc (JED) has dynamical properties quite different from both the standard and advection dominated discs. It also exhibits three different thermal equilibrium branches at a given radius: two stable (cold and hot) and one intermediate unstable. The hot solution has all the characteristics of the so-called "hot corona" generally invoked in XrB sytems in the Low/Hard states. We detail the energetics and radiative expectations of our model and show their good agreement with those observed in Cygnus X-1 in terms of jet power, jet velocity and spectral emission.

Keywords: X-rays: binaries, accretion, accretion disks, magnetic fields: MHD

1 Introduction

Jet emitting discs (JED herafter) were originaly studied by Ferreira & Pelletier (1993) in their magnetized accretion ejection structures model (MAES herafter). This model was developed so as to treat both the accretion disc and the jet it generates consistently. The idea is the same as in earlier studies of magneto-centrifugally launched disc winds (Blandford & Payne 1982). However, in the MAES, the solution starts from the midplane of the resistive MHD disc and evolves outwards in the ideal MHD wind/jet. This differs drastically from other studies where the disc was only treated as a boundary condition, hence forbidding any precise quantication of the effect of the MHD wind on the disc.

The resolution of the thermal equilibrium of a JED gives three branches, a cold and hot ones, both thermally and viscously stable and an intermediate unstable one. The hot branch, that would be observationally very similar to ADAFs, corresponds to the JED solution discussed in this paper and applied to Cyg. X-1 (Petrucci et al. 2010, hereafter P10). Thus JEDs could account for most of the successes of the ADAFs, while explaining jet formation (see Ferreira's talk, this proceeding).

1.1 JED Physical properties and global energy budget

Since a JED undergoes mass loss, the disc accretion rate is written as

$$\dot{M}_a(R) = \dot{M}_{a,out}\left(\frac{R}{R_{out}}\right)^{\xi} = \dot{m}\dot{M}_{Edd} \tag{1.1}$$

where ξ measures the local disc ejection efficiency (Ferreira & Pelletier 1993), $\dot{M}_{out}$ the accretion rate at the disc outer radius R_{out} and $\dot{M}_{Edd} = L_{Edd}/c^2$ the Eddington accretion rate. The ejection efficiency ξ is equivalent to the p exponent used in ADIOS models (Blandford & Begelman 1999). But, in strong contrast to the latter, it is not *assumed* but computed as a function of the disc parameters as a trans-Alfvénic regularity condition (see Ferreira 1997 for more details).

[1] Laboratoire d'Astrophysique de Grenoble, Université Joseph Fourier - Grenoble 1 / CNRS, UMR 5571, BP 53, 38041 Grenoble Cedex 09, France
[2] Centre d'Etude Spatial des Rayonnement, UMR 5187, 9, av du Colonel Roche BP 44346 31028 Toulouse Cedex 4 France

The disc's aspect ratio in a gas supported disc is $\varepsilon = H/R = c_s/v_K$, namely the ratio of the isothermal sound speed to the Keplerian speed $v_K = \Omega_K R$. The radial profiles of the accretion velocity u_o, particle density $n = \rho_o/m_p$, gas pressure P_{gas}, and vertical magnetic field B_z in the JED midplane are given by

$$u_o = -u_r = m_s c_s = m_s\,\varepsilon\,\Omega_K R \tag{1.2}$$

$$n = \frac{\dot{M}_a(R)}{4\pi m_p \Omega_K R^3 m_s \varepsilon^2} \tag{1.3}$$

$$P_{gas} = \rho_o c_s^2 = \frac{\dot{M}_a(R)\Omega_K}{4\pi R m_s} \tag{1.4}$$

$$B_z = \left(\frac{\mu}{m_s}\right)^{1/2} \sqrt{\frac{\mu_o \dot{M}_a(R)\Omega_K}{4\pi R}} \tag{1.5}$$

where we have introduced two dimensionless parameters, the sonic Mach number $m_s = u_o/c_s$ and the disc magnetization $\mu = \mu_o^{-1} B_z^2/P$.

The global energy budget in an accretion-ejection structure is

$$P_{acc} = P_{JED} + P_{jets} = P_{rad} + P_{adv} + P_{jets} \tag{1.6}$$

The total accretion power P_{acc} released in a quasi-Keplerian accretion disc writes as

$$\begin{aligned} P_{acc} &= \frac{GM\dot{M}_a(R_{in})}{2R_{in}} - \frac{GM\dot{M}_a(R_{out})}{2R_{out}} \\ &= \frac{GM\dot{M}_{a,out}}{2R_{in}} \left[\left(\frac{R_{in}}{R_{out}}\right)^{\xi} - \frac{R_{in}}{R_{out}}\right] \end{aligned} \tag{1.7}$$

The power P_{adv} is advected onto the central object along with the accreting material scales. P_{jets} is the sum of the total (kinetic, potential, and internal) energy flux advected by the outflowing plasma and the MHD Poynting flux leaving the disc surfaces. Since we are mainly interested in powerful jets, the latter contribution dominates, and it can be shown that (see P10):

$$P_{jets} \simeq b P_{acc} \tag{1.8}$$

Consequently, given the above expressions, the total JED power P_{JED} and JED luminosity P_{rad} are given by

$$P_{JED} = P_{acc} - P_{jets} = (1-b)P_{acc} \tag{1.9}$$

$$P_{rad} = P_{JED} - P_{adv} = (1-b)P_{acc} - P_{adv}. \tag{1.10}$$

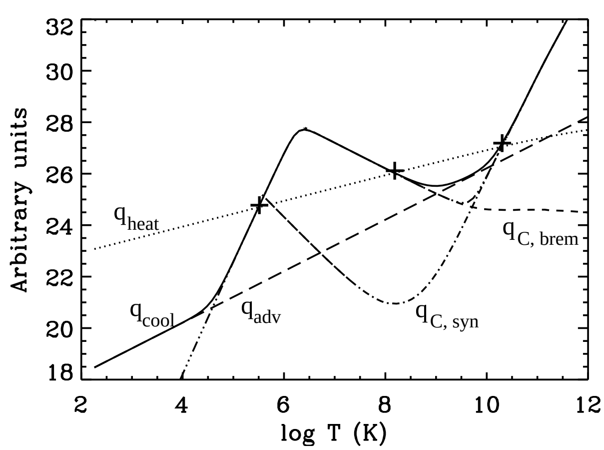

Fig. 1. Thermal balance of a jet emitting disc (JED) at $r = 6$ for $\dot{m}$ =0.001 and $m = 10$. The underlying JED structure has a jet power parameter $b = 0.5$ and an ejection efficiency $\xi = 0.1$. The dotted line is the heating term q_{heat}, the dot-dot-dot-dashed line the radiative cooling term q_{rad}, and the long dashed line is the advective term q_{adv}. The Comptonized bremsstrahlung $q_{C,brem}$ (short dashed) and the Comptonized synchrotron $q_{C,sync}$ (dot-dashed) radiative terms are also shown. The solid line corresponds to $q_{rad} + q_{adv}$ and the solutions of Eq. (2.1) are indicated by crosses.

The jet power parameter b is thus a crucial parameter as it controls the power sharing between the jet and the disc. Since it is generally found in the range 0.5-0.99 (see P10), JEDs considered here are engines converting accretion power into ejection power with high efficiency. To get the fraction of the power P_{rad} that is actually radiated away, however we need to compute the JED thermal balance. This is explained in the next section.

2 JED thermal balance

The equation governing the internal energy of the accretion flow writes as

$$q_{heat} = q_{rad} + \underbrace{P\nabla.\mathbf{u} \ + \nabla U.\mathbf{u}}_{q_{adv}} \tag{2.1}$$

where q_{heat} is the heating power density, q_{rad} the sum of all radiative cooling terms, P the total plasma pressure, $\mathbf{u}$ the flow velocity, U its internal energy and q_{adv} the advection term. Equation (1.9) directly provides the radial JED volumetric heating rate in a disc ring of height $2H$, radius R and extent dR i.e. $q_{heat}(R) = \dfrac{1}{4\pi RH}\dfrac{dP_{JED}}{dR}$.

Figure (1) shows the different heating, cooling, and advection terms as functions of the temperature for a given black hole mass, JED radius, and accretion rate. The resolution of the thermal equilibrium gives three branches of solutions, indicated by crosses on the figure. The hottest one corresponds to the JED solution discussed in this paper (a more detailed discussion of the other solutions is postponed to a future work). It is a hot, optically thin, thermally and viscously stable disc solution that behaves radiatively in the same way as the LHAF solutions studied by Yuan (2001) (see also Yuan et al. 2006 for a discussion on hot one-temprature accretion flows). The major difference concerns the underlying dynamics of our JED solutions, which self-consistently include the presence of powerful self-collimated jets.

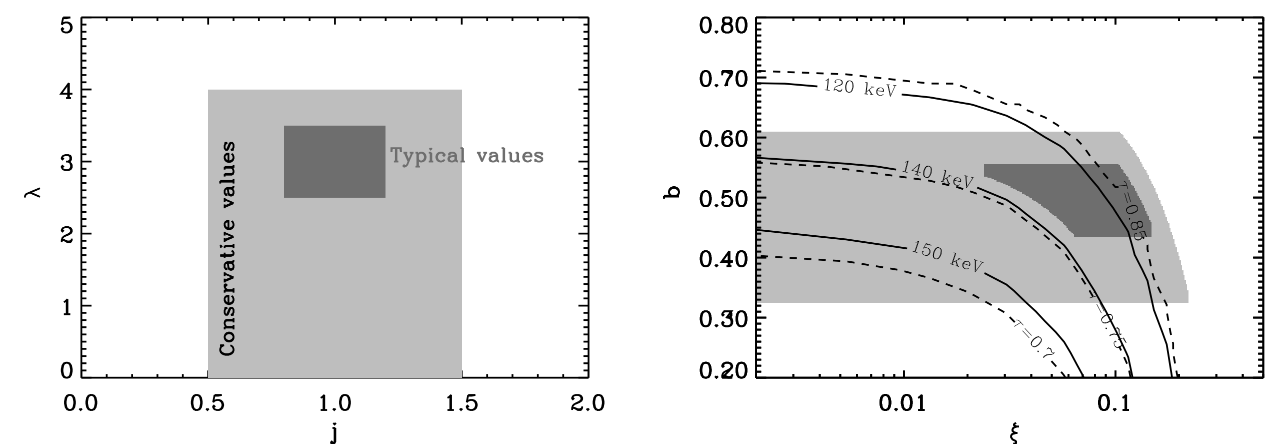

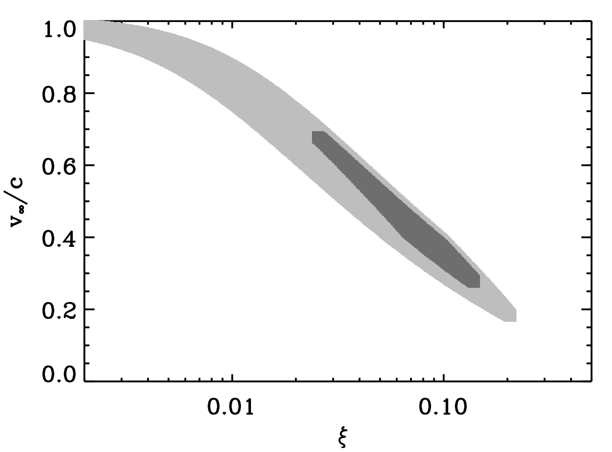

Fig. 2. Top-left: the parameter space $j - \lambda$ allowed by the observations. **Top right**: Observational constraints translated into our JED parameter space $\xi - b$. Overplotted are the contours of temperature (solid lines) and optical depth (dashed lines) for an accretion rate of 1-2% Edd., typical of Cyg X-1. **Bottom-left**: terminal jet velocity V_∞/c as function of the disc ejection efficiency ξ

3 Comparison to Cygnus X-1

The energetics of the jets and the X-ray corona of Cygnus X-1 have been investigated recently by Malzac et al. (2009 herafter M09). Observations constraint the ratio $j = P_{jets}/L_h$ of the total jet kinetic power to the typical X-ray luminosity in the hard state as well as the ratio λ of the soft to hard radiative efficiencies to be in the ranges (M09):

$$0.45 \leq j = \frac{P_{jets}}{L_h} \leq 1.5 \text{ and } \lambda = \frac{L_s}{\dot{M}_s}\frac{\dot{M}_h}{L_h} \leq 4 \tag{3.1}$$

These observational constraints on j and λ can be easily translated into constraints on our JED parameters b and ξ, where $P_{jets} \simeq bP_{acc}$ and $\dot{M}_a(R) \propto R^{\xi}$.

The top left panel of Fig. (2) displays the domain in the observed parameter space $j - \lambda$ allowed by the observations. The top right panel shows the same constraints but translated into our JED parameter space $\xi - b$. Our treatment of the disc thermal balance allows us to estimate the expected temperature and optical depth within a JED. Contours of these two quantities at a radius of 10 R_G are overplotted in the top-left panel of Fig. (2), the solid lines representing the temperature while the dashed lines the optical depth. The black hole mass is taken equal to 10 $M_{\odot}$ and the total luminosity is about 1% of the Eddington luminosity. This corresponds to the typical luminosity of Cyg X-1 close to the hard-to-soft state transition. The ratio of the outer to inner JED radii is fixed to 100 but our results do not strongly depend on this parameter. Interestingly, the temperature ranges between 120 and 140 keV and the optical depth $\tau \simeq 0.7 - 0.9$, which are not so far, given the simplicity of our thermal balance computation, from the values deduced from sophisticated fits of Cyg X-1 in the hard state

Finally the bottom-left panel of Fig. (2) shows V_∞/c as a function of b and ξ. The generally accepted values (i.e. the dark grey area in Fig. 2) provide a range in V_∞/c between 0.3 and 0.6 in good agreement with observations. This is remarkable as it arises from another independent observational constraint.

The accretion and ejection properties of JEDs agree with the observations of the prototypical black hole binary Cygnus X-1. The JED solutions are likely to be relevant to the whole class of microquasars.

The authors acknowledge financial support from the SF2A.

References

Blandford, R. D. & Begelman, M. C. 1999, MNRAS, 303, L1
Blandford, R. D. & Payne, D. G. 1982, MNRAS, 199, 883
Ferreira, J. 1997, A&A, 319, 340
Ferreira, J. & Pelletier, G. 1993, A&A, 276, 625
Malzac, J., Belmont, R., & Fabian, A. C. 2009, MNRAS, 400, 1512
Petrucci, P.-O., Ferreira, J., Henri, G., Malzac, J., & Foellmi, C. 2010, A&A, 477
Yuan, F. 2001, MNRAS, 324, 119
Yuan, F., Taam, R. E., Xue, Y., & Cui, W. 2006, ApJ, 636, 46

JOINT SEARCHES FOR GRAVITATIONAL WAVES AND HIGH-ENERGY NEUTRINOS WITH THE ANTARES, LIGO AND VIRGO DETECTORS

V. Van Elewyck[1] and the ANTARES and VIRGO Collaborations and the LIGO Scientific Collaboration

Abstract. Cataclysmic cosmic events can be plausible sources of both gravitational waves (GW) and high-energy neutrinos (HEN). Both GW and HEN are alternative cosmic messengers that may escape very dense media and travel unaffected over cosmological distances. For this reason, they could also reveal new or hidden sources that were not observed by conventional photon astronomy, such as the putative failed GRBs.

After a brief discussion on the plausible common sources of GW and HEN, this constribution presents the strategies for coincident searches of GW and HEN that are currently developed by the ANTARES and VIRGO/LIGO collaborations within the GWHEN working group.

Keywords: multi-messenger astronomy, high-energy neutrinos, gravitational waves

1 Introduction

Astroparticle physics has entered an exciting period with the recent development of experimental techniques that have opened new windows of observation of the cosmic radiation in all its components. In this context, and despite their elusive nature, both high-energy neutrinos (HENs) and gravitational waves (GWs) are now considered as candidate cosmic messengers. Contrarily to high-energy photons (which are absorbed through interactions in the source and with the extragalactic background light) and cosmic rays (which are deflected by ambient magnetic fields, except at the highest energies), both HENs and GWs may indeed escape from dense astrophysical regions and travel over large distances without being absorbed, pointing back to their emitter.

It is expected that many astrophysical sources produce both GWs, originating from the cataclysmic event responsible for the onset of the source, and HENs, as a byproduct of the interactions of accelerated protons (and heavier nuclei) with ambient matter and radiation in the source. Moreover, some classes of astrophysical objects might be completely opaque to hadrons and photons, and observable only through their GW and/or HEN emissions. The detection of coincident signals in both these channels would then be a landmark event and sign the first observational evidence that GW and HEN originate from a common source. GW and HEN astronomies will then provide important information on the processes at work in the astrophysical accelerators. The most plausible GW/HEN sources are presented in Section 2, along with relevant references*.

Common HEN and GW astronomies are also motivated by the advent of a new generation of dedicated experiments. This contribution concentrates on the feasibility of joint GW+HEN searches between the ANTARES neutrino telescope (and its future, km^3-sized, successor KM3NeT) and the GW detectors VIRGO and LIGO (which now form one single experimental collaboration). The detection principle and performances of the instruments are presented in Section 3, while Section 4 proposes some hints at the analysis strategies that will be set up to optimize coincident GW+HEN detection among the three experiments.

The joint search activities described here are performed in the framework of a dedicated GWHEN working group which gathers collaborators from ANTARES, VIRGO and LIGO, with a data-exchange policy regulated by a specific Memorandum of Understanding (signed February, 2010).

[1] Laboratoire Astroparticule et Cosmologie & Université Paris Diderot-Paris 7, Case 7020, F-75205 Paris Cedex 13, France

*More information can also be obtained on the website of the first Workshop on Gravitational Waves and High-Energy Neutrinos, held in May 2009 in Paris: `http://www.gwhen-2009.org` .

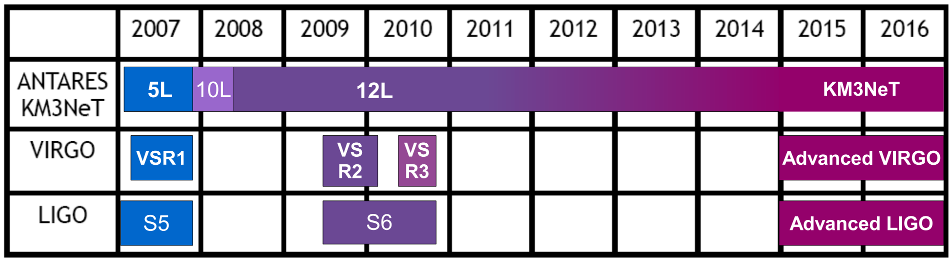

Fig. 1. Time chart of the data-taking periods for the ANTARES, VIRGO and LIGO experiments, indicating the respective upgrades of the detectors (as described in the text). The deployment of the KM3NeT neutrino telescope is expected to last three to four years, during which the detector will be taking data with an increasing number of PMTs before reaching its final configuration (see the KM3NeT TDR 2010).

2 Potential common sources of GW and HEN

Potential sources of GWs and HENs are likely to be very energetic and to exhibit bursting activity. Plausible GW+HEN emission mechanisms include two classes of galactic sources which could be accessible to the present generation of GW interferometers and HEN telescopes. **Microquasars** are believed to be X-ray binaries involving a compact object that accretes matter from a companion star and re-emits it in relativistic jets associated with intense radio (and IR) flares. Such objects could emit GWs during both accretion and ejection phases; and the latter phase could be correlated with a HEN emission provided the jet has a hadronic component (Migliari et al. 2002; Distefano et al. 2002; Pradier 2008). **Soft Gamma Repeaters (SGRs)** are X-ray pulsars with a soft γ-ray bursting activity which, according to the magnetar model (Thompson and Duncan 1995), can be associated with star-quakes. The deformation of the star during the outburst could produce GWs, while HENs could again emerge from hadron-loaded flares (Ioka 2001; Ioka et al. 2005).

Gamma-Ray Bursts (GRBs) are a promising class of extragalactic sources. In the prompt and afterglow phases, HENs ($10^5 - 10^{10}$ GeV) are expected to be produced by accelerated protons in relativistic shocks and several models predict detectable fluxes in km^3-scale detectors (Waxman and Bahcall 1997; Alvarez-Muniz et al. 2000; Rachen and Mészáros 2008). **Short-hard GRBs** are thought to originate from coalescing binaries involving black holes and/or neutron stars; such mergers could emit GWs detectable from relatively large distances, with significant associated HEN fluxes (Nakar 2007). As for the **long-soft GRBs**, the collapsar model is compatible with the emission of a strong burst of GWs during the gravitational collapse of the (rapidly rotating) progenitor star and in the pre-GRB phase; however this population is distributed over cosmological distances so that the associated HEN signal is expected to be faint (Kotake 2006; Ott 2009; Vietri 2008). The subclass of **low-luminosity GRBs**, with γ-ray luminosities a few orders of magnitude smaller, are believed to originate from a particularly energetic, possibly rapidly-rotating and jet-driven population of core-collapse supernovae. They could produce stronger GW signals together with significant high- and low-energy neutrino emission; moreover they are often discovered at shorter distances (Gupta and Zhang 2007). Finally, the **failed GRBs** are thought to be associated with supernovae driven by mildly relativistic, baryon-rich and optically thick jets, so that no γ-rays escape. Such "hidden sources" could be among the most promising emitters of GWs and HENs, as current estimations predict a relatively high occurrence rate in the volume probed by current GW and HEN detectors (Ando and Beacom 2005).

3 The detectors

The **ANTARES** detector (see e.g. Coyle et al. 2010) is the first undersea neutrino telescope; its deployment at a depth of 2475m in the Mediterranean Sea near Toulon was completed in May 2008. It consists in a three-dimensional array of 884 photomultiplier tubes (PMTs) distributed on 12 lines anchored to the sea bed and connected to the shore through an electro-optical cable. Before reaching this final (12L) setup, ANTARES has been operating in various configurations with increasing number of lines, from one to five (5L) and ten (10L); the respective periods are indicated on the time chart of Fig. 1.

ANTARES detects the Cherenkov radiation emitted by charged leptons (mainly muons, but also electrons

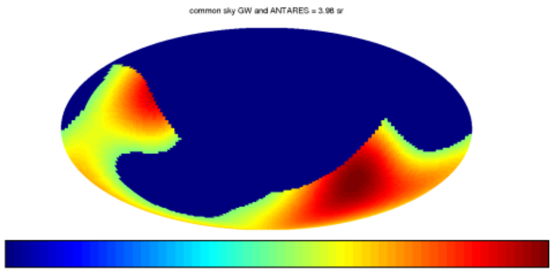

Fig. 2. Instantaneous common sky coverage for VIRGO + LIGO + ANTARES in geocentric coordinates. This map shows the combined antenna pattern for the gravitational wave detector network (above half-maximum), with the simplifying assumption that ANTARES has 100% visibility in its antipodal hemisphere and 0% elsewhere. The colour scale is from 0% (left, blue) to 100% (right, red).

and taus) induced by cosmic neutrino interactions with matter inside or near the instrumented volume. The knowledge of the timing and amplitude of the light pulses recorded by the PMTs allows to reconstruct the trajectory of the muon and to infer the arrival direction of the incident neutrino, as well as to estimate its energy. ANTARES is expected to achieve an unprecedented angular resolution (about 0.3° for neutrinos above 10 TeV) as a result of the good optical properties of sea water (Aguilar et al. 2005).

The data acquisition system of ANTARES is based on the "all-data-to-shore" concept, which allows to operate different physics triggers to the same data in parallel. Satellites looking for GRBs can also trigger the detector in real time via the GCN (Gamma-Ray Burst Coordinate Network) alert system. About 60s of buffered raw data are then written on disk and kept for offline analysis (Bouwhuis et al. 2009). Since last year, ANTARES has also implemented the possibility to trigger an optical telescope network on the basis of "golden" neutrino events selected by a fast, online reconstruction procedure. This program is described by D. Dornic (for the ANTARES Coll.) elsewhere in these Proceedings. The possibility to extend it to other instruments in different wavelength domains (such as the gamma-ray telescope FERMI) is also under study. All these characteristics make the ANTARES detector especially suited for the search of astrophysical point sources, and transients in particular. ANTARES is intended as the first step towards a km^3-sized neutrino telescope in the Mediterranean Sea, currently under R&D in the framework of the KM3NeT Consortium (see the KM3NeT TDR 2010).

The GW detectors **VIRGO** (see e.g. Acernese et al. 2008), with one site in Italy, and **LIGO** (e.g. Sigg et al. 2008), with two sites in the United States, are Michelson-type laser interferometers. They consist of two light storage arms enclosed in vacuum tubes oriented at 90° from each other. Suspended, highly reflective mirrors play the role of test masses. Current detectors are sensitive to relative displacements (hence GW amplitude) of the order of 10^{20} to 10^{22} Hz$^{-1/2}$. Their current detection horizon is about 15 Mpc for standard binary sources.

Early in 2007, both experiments joined their efforts and agreed on full data exchange starting from the concomitant data-taking phase during 2007 (VSR1/S5), which partially coincided with the ANTARES 5L configuration. A second data-taking phase has started mid-2009 with upgraded detectors VIRGO+ and eLIGO, corresponding to a gain of a factor 2 (at least) in sensitivity (Accadia et al. 2010), and in coincidence with the operation of ANTARES 12L. The current LIGO and Virgo science runs (L6/VSR3) will stop by the end of 2010 to open the way to the development of the next generation of detectors: Advanced VIRGO and Advanced LIGO, to be operational by 2015 with an expected sensitivity ∼10 times better than the current instruments (Harry et al. 2010). As can be seen from Figure 2, the VIRGO/LIGO network monitors a good fraction of the sky in common with ANTARES: the instantaneous overlap of visibility maps is about 4 sr (∼ 30% of the sky).

4 Outlook on the analysis strategies

GW interferometers and HEN telescopes share the challenge to look for faint and rare signals on top of abundant noise or background events. The GW+HEN search methodology involves the combination of GW/HEN candidate event lists, with the advantage of significantly lowering the rate of accidental coincidences.

Two strategies are currently under study. The first one consists in an event-per-event search for a GW signal correlating in space and time with a given neutrino event considered as an external trigger; it makes use of existing analysis pipelines developed e.g. for GRB searches. Alternatively, comprehensive searches for time-coincidences between independent lists of neutrino and GW events can also be performed, followed by a test of spatial correlation using the combined GW/HEN likelihood skymap. This second, more symmetrical, option requires the existence of two independent analysis chains scanning the whole phase space in search for interesting events. In both cases an astrophysically motivated (and possibly source- or model-dependent), time interval is used to define the coincidence window. If a coincident event is found, its significance is obtained by comparing to the distribution of accidental events obtained with Monte-Carlo simulations using time-shifted data streams (and scrambled real neutrino event lists when needed).

Preliminary investigations of the feasibility of such searches have already been performed (Aso et al. 2008; Pradier 2009) and indicate that, even if the constituent observatories provide several triggers a day, the false alarm rate for the combined detector network can be maintained at a very low level (1/600 yr). A major issue for the analysis lies in the combined optimisation of the selection criteria for the different detection techniques.

5 Conclusions

A joint GW+HEN analysis program could significantly expand the scientific reach of both GW interferometers and HEN telescopes. The robust background rejection arising from the combination of two totally independent sets of data results in an increased sensitivity and the possible recovery of cosmic signals. The observation of coincident triggers would provide strong evidence for the existence of common sources. Beyond the benefit of a potential high-confidence discovery, coincident GW/HEN (non-)observation shall play a critical role in our understanding of the most energetic sources of cosmic radiation and in constraining existing models. They could also reveal new, “hidden” sources unobserved so far by conventional photon astronomy.

References

Accadia, T. et al. [VIRGO Collaboration] 2010, J. Phys. Conf. Ser., 203, 012074

Acernese, F. et al. [VIRGO Collaboration] 2008, Class. Quant. Grav., 25, 184001; see also `http://www.virgo.infn.it/`

Aguilar, J.A. et al. [ANTARES Collaboration] 2005, Astropart. Phys, 23, 131

Alvarez-Muniz, J., Halzen, F. & Hooper, D. W. 2000, Phys. Rev., D62, 093015

Ando, S. & Beacom, J. 2005, Phys. Rev. Lett., 95(6), 061103

Aso, Y. et al. 2008, Class. Quant. Grav., 25, 114039

Bouwhuis, M. [ANTARES Collaboration] 2009, Procs. 31^{st} ICRC, Lodz, Poland

Coyle, P. et al. [ANTARES Collaboration] 2010, arXiv:1002.0754; see also `http://antares.in2p3.fr`

Dessart, L. et al. 2008, Astrophys. J. Lett., 673, L43

Distefano, C. et al. 2002, Astrophys. J. 575, 378

Gupta, N. & Zhang, B. 2007, Astropart. Phys., 27, 386

Harry G.M. [LIGO collaboration] 2010, Class. Quant. Grav., 27, 084006

Ioka, K. 2001, MNRAS, 327, 639

Ioka, K. et al. 2005, Astrophys. J., 633, 1013

KM3NeT Consortium 2010, Technical Design Report - to be downloaded at `http://www.km3net.org/`

Kotake, K. et al. 2006, Repts. Prog. Phys., 69, 971

Migliari, S. et al. 2002, Science, 297, 1673

Murase, K. et al. 2006, Astrophys. J., 651, L5

Nakar, E. 2007, Physics Reports, 442, 166 (and references therein)

Ott, C. D. 2009, Class. Quant. Grav., 26, 063001

Pradier, T. 2008, arXiv:0807.2567

Pradier, T. 2009, Nucl. Instrum. Meth. A, 602, 268

Rachen, J.P. & Meszaros, P. 2008, Phys. Rev. D, 58, 123005

Sigg, D. et al. [LIGO Collaboration] 2008, Class. Quant. Grav., 25, 114041; see also `http://www.ligo.caltech.edu/`

Thompson, C. & Duncan, R. C. 1995, MNRAS, 275, 255

Vietri, M. 2008, Phys. Rev. Lett., 80, 3690

Wang X.-Y. et al. 2007, Phys. Rev. D, 76(8), 083009

Waxman, E. & Bahcall, J.N. 1997, Phys. Rev. Lett. 78, 2292

PCMI-PNPS-PNP

Gas and dust spectroscopy with Herschel

DUST SILICATE EMISSION IN FIR/SUBMM

A. Coupeaud[1], K. Demyk[1], C. Mény[1] and C. Nayral[2]

Abstract. The far-infrared to millimeter wavelength (FIR-mm) range in astronomical observations is dominated by the thermal emission from large (10-100 nm) and cold (10-20 K) dust grains, which are in thermal equilibrium with the interstellar radiation field. However, the physics of the FIR-mm emission from such cold matter is not well understood as shown by the observed dependence with the temperature of the spectral index of the dust emissivity β and by the observed far infrared excess. Interestingly, a similar behaviour is observed in experiments of characterization of the spectral properties of dust analogues. We present a study of the optical properties of analogues of interstellar silicate grains at low temperature in the FIR/submm range aiming to understand their peculiar behaviour. Such studies are essential for the interpretation of the Herschel and Planck data.

Keywords: analogues interstellar grains, emissivity spectral index, temperature, anticorrelation, submillimeter wavelength range, Herschel, Planck

1 Introduction

The Interstellar Medium (ISM) is composed of 99 % of gas and 1 % of dust. Interstellar dust has the property to absorb and scatter UV-visible photons produced by stars and is thus the dominant source of opacity in our galaxy. Among the three major components invoked in the model of Désert et al. (1990), the big grains are large enough (10-100 nm) to be at the thermal equilibrium with the interstellar radiation field, at temperatures of a few tens of K and thus emit in the far infrared (FIR). An important component of these grains is silicates. They explain in particular the bands observed at 9.7 and 18 μm and are predominantly in the amorphous state in the ISM. Thanks to ISO and the discovery of emission bands from crystallized silicate in various environments, we now know that these silicates are mostly magnesium and iron rich silicates such as pyroxene ($Mg_xFe_{1-x}SiO_3$) and olivine ($Mg_xFe_{2-2x}SiO_4$). These silicate grains dominate the dust emission in the far-infrared/submillimeter range which is usually expressed as follow: $I_\lambda = M_d \kappa_{\lambda_0} (\frac{\lambda}{\lambda_0})^{-\beta} B_\lambda(T)$, where I_λ is the spectral intensity, $B_\lambda(T)$ is the Planck function at the dust temperature, M_d is the column density of grains along the line of sight, κ is the mass absorption coefficient and β is the emissivity spectral index. Simple semi-classical models of absorption, such as the Lorentz model for damping oscillators and the Drude model for free charge carriers, provide a temperature independent asymptotic value β=2 for 3D solids. However, this value of the spectral index is not in agreement with the observations of the FIR/submm SED of interstellar dust emission (Dupac et al. 2003; Désert et al. 2008; Reach et al. 1995).

Indeed, over various sites of the ISM, PRONAOS observations revealed an anticorrelation between the dust grain mean temperature T and the emissivity spectral index β, with β values go down to $\sim$ 1 at 80 K and up to 2.4 at 11 K (Dupac et al. 2003). Désert et al. (2008) confirmed this inverse relationship found by PRONAOS, with β values decrease to 1.3 at 25 K and increase to 4 below 10 K. In addition, the data of the FIRAS instrument on board the COBE (Cosmic Background Explorer) satellite revealed the existence of a significant millimeter excess of the dust emission with respect to a single greybody law. This has been interpreted as due to the presence of very cold dust (5-7 K) in the ISM (Finkbeiner et al. 1999) in addition to a warmer component responsible for the emission maximum near 100 μm. However, the millimeter excess appeared to be extremely

[1] Université de Toulouse, UPS, CESR, 9 avenue du colonel Roche, F-31028 Toulouse cedex 4, France and CNRS, UMR5187, F-31028 Toulouse, France
[2] Université de Toulouse, INSA, UPS, LPCNO, 135 avenue de Rangueil, F-31077 Toulouse France and CNRS, LPCNO, F-31077 Toulouse France

well correlated with the FIR dust emission. This could be indicative of a situation in which the excess could also be produced by unidentified processes intrinsic to the grain component radiating at thermal equilibrium, without requiring an additional colder component. The first results of the Herschel mission show the observed submm excess previously observed by Reach et al. (1995) in many different sources in our Galaxy (Anderson et al. 2010; Rodon et al. 2010) and in external galaxies such as the Magellanic Clouds (Bot et al. 2010).
At the same time, different laboratory studies of the spectral properties of astronomical dust analogues in the FIR/submm spectral range at low temperature have been performed. Agladze et al. (1996) found that the absorption coefficient of $2MgO.SiO_2$ and $MgO.2SiO_2$ grains decreases with increasing temperature up to 20 K and then increases again at higher temperature in the 700μm-3mm range. Mennella et al. (1998) reported a significant temperature dependence of the emissivity spectral index for the amorphous iron rich silicate $FeSiO_4$ (β =2.1 at 24 K down to 1.4 at 294 K) in the 200μm-2mm range. Boudet et al. (2005) performed measurements on different types of amorphous silicates as $MgSiO_3$ for temperature between 10 and 300 K and wavelengths from 100 μm to 1mm. They confirmed a strong temperature and frequency dependency of the absorption coefficient.

Despite all these observational and experimental evidence, the phenomenological origin of this β-T anticorrelation remains unclear. More experimental studies are required in order to progress in the understanding of the physical and chemical grain properties responsible for the temperature-dependent optical behavior observed in the ISM. It appears crucial to perform new measurements on other amorphous materials in a more extended wavelength range for the data analysis of the Herschel and Planck missions.

2 Experiments

A better understanding of optical properties does not necessarily require working on realistic interstellar analogues; one way is to work first on the expected simplest solids showing these properties. We have thus chosen to study silica, SiO_2 and three amorphous Mg-rich silicates which are classical astronomical dust analogues: one olivine-type Mg_2SiO_4 and two pyroxenes-type $MgSiO_3$ and $CaMgSi_2O_6$. The silica samples were synthesised with a sol-gel method, according to the published procedure (El Hawi et al. 2009), which allow us to control some essential parameters like the size, the morphology and the porosity of the nanoparticles. These parameters are characterized by Transmission Electronic Microscopy (TEM) to measure the size and specify the shape of the nanoparticles; by X Rays Diffraction (XRD) to define if the material is amorphous or crystalline and by Nuclear Magnetic Resonance (NMR) to characterize the environment around the silicon and hydrogen atoms in the material. This last method is very important because of the hydrophilic character of the silica which leads to water adsorption and silanols (SiOH groups) formation. This hydrophilic character depends on the state of the surface and on the synthesis process (dry or wet processes) and thus varies from sample to sample. We have studied different amorphous silica samples having different size, synthesis method, water and SiOH content, porosity. We synthesised spheroidal and non porous SiO_2 nanoparticles of 37$\pm$14 nm and 154$\pm$30 nm diameter, a specific area about 30$\pm$15 m^2/g and a density of $\sim$ 1.7$\pm$15 g/cm^3. Commercially SiO_2 samples consist of non porous spherical particles with 500 nm diameter (Lancaster) and silica-fumed agglomerates (Aldrich). The silica fumed is composed of 7 nm spherical particles linked together to form micrometer chains, very highly branched with a high surface area (390$\pm$40 m^2/g). The silicate were synthesised by sol-gel method according to the procedures described in Mitchell et al. (1998) and Gillot et al. (2009). To remove the organic residual from the synthesis, all the silicate samples were heated up to 400°C or 500°C depending on the synthesis procedure. TEM characterization shows that the grains are micrometer-sized grains for the Mg_2SiO_4 sample and have an average grains size of $\sim$100 nm for the $MgSiO_3$ and $CaMgSi_2O_6$ samples. These silicates presented specific area comprised between 80 and 130 m^2/g.

For the FIR spectroscopic measurements all these silica and silicate powder samples were mixed with polyethylene powder at 120°C and we applied on this homogeneous mixture a pressure of 7 tons during 5 min to obtained 10 mm diameter pellets. The FIR/submm optical properties of the samples were measured with the experimental set-up ESPOIRS. It is composed of a spectrometer Bruker IFS113V Fourier Transform InfraRed (FTIR) coupled with a cryostat which allows us to cool down our samples from 300 K to 4 K. The spectrometer is equipped with a Hg lamp source, different Mylar beam splitters with thickness of 3.5, 12, 23, 50, 100 μm and a 4 K-bolometer detector. This configuration allows to perform measurements in the 2 - 800 μm wavelength range (5000 - 12.5 cm^{-1}). The transmittance spectra were calculated by dividing the spectrum of the sample pellet by the one of a blank polyethylene pellet. The transmission spectra of each sample were recorded during a cooling cycle from room temperature (300 K) to 10 K. To complete our wavelength range from 800 to 1000 μm we performed some experiments on the AILES (Advanced Infrared Line Exploited for Spectroscopy) beamline at the synchrotron SOLEIL (Brubach et al. 2010). The mass absorption coefficient of the measured sample is derived from the transmission spectrum according to : $\kappa = \kappa_{\lambda_0} (\lambda/\lambda_0)^{-\beta}$

3 Results : evolution of the optical properties

The complete study about the four silica samples is detailed in Coupeaud et al. (in preparation). We only discuss here the results for the silica fumed and the 30 nm silica samples (Fig. 1. a) and b)). First, we observe for both samples the decrease of κ with decreasing temperature. This decrease of opacity with temperature is greatly enhanced for long wavelengths. Furthermore, we report a break in the absorption curves around 350 μm especially obvious for silica sample of 30 nm. The spectral index, measured between 350 and 600 μm, increases when the temperature decreases for both silica samples: $\beta \sim 1$ and $\beta \sim 2$ at 300 K and $\beta \sim 2$; $\beta \sim 3$ at 10 K, for the fumed and the 30 nm silica samples, respectively. We thus observe experimentally an anticorrelation β-T. Similar results are found for all the four silica samples (Coupeaud et al., in preparation).

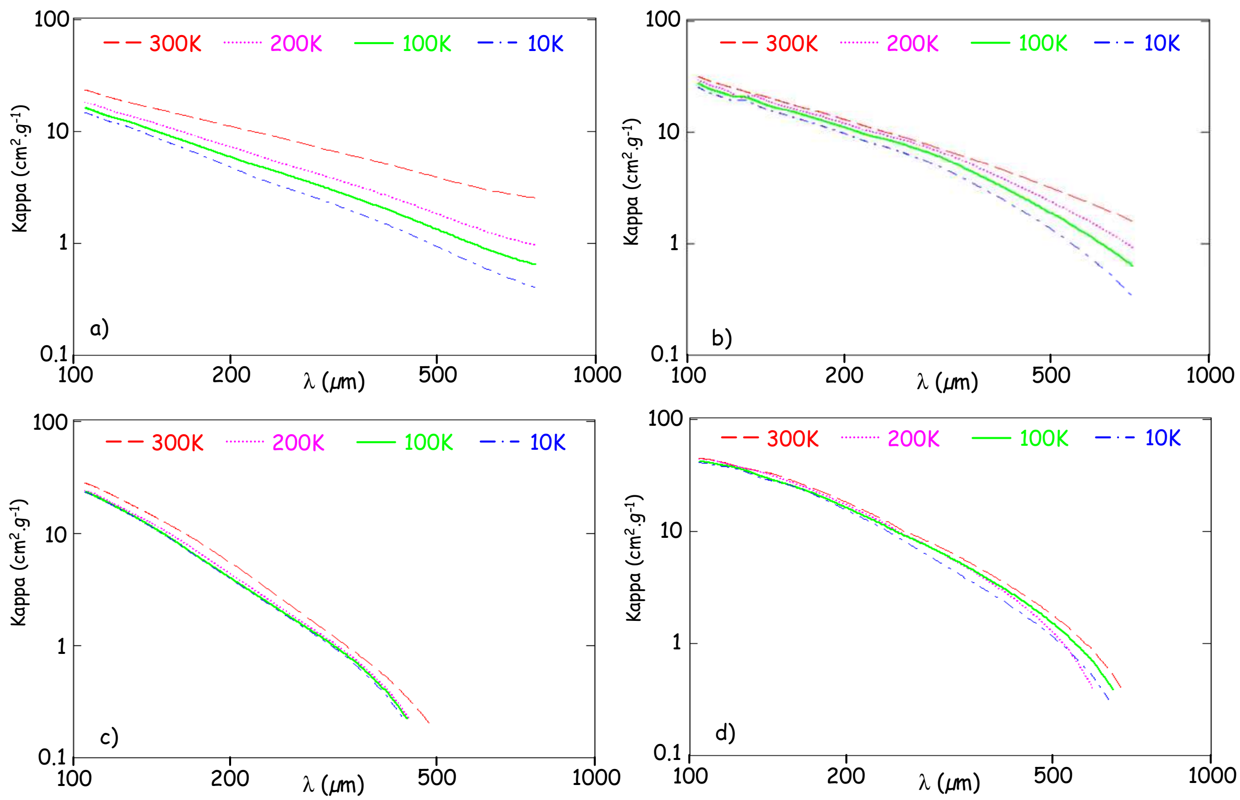

Fig. 1. Evolution of the mass absorption coefficient κ ($cm^2\,g^{-1}$) as a function of the wavelength λ (μm) at 300 K, 200 K, 100 K and 10 K for a) the amorphous (non annealed) silica fumed, b) the amorphous (non annealed) silica 30 nm diameter, c) the crystalline (annealed at 1300°C) silica fumed and d) the crystalline (annealed at 1100°C) silica 30 nm diameter.

To investigate the hypothesis that OH groups present in silica are responsible for the anticorrelation, the silica powders were heated at different temperatures. Indeed, a thermal treatment at the appropriate temperature leads to the dehydration (the removal of physically adsorbed water) and dehydroxylation (the removal of silanol groups from the silica surface). Annealing at 200°C remove physisorbed water (Serp et al. 2002; Ek et al. 2001) while the dehydroxylation processes occur slowly from 200°C up to 1200°C. The temperatures at which physisorbed water and silanol groups were assumed to be totally released were dependent on the silica (Zhuravlev 2000; Ek et al. 2001). For the crystallized silica fumed and 30nm silica samples, we observe no variation of κ and β with the temperature (Fig. 1. c) and d)) and these observations are the same for the four silica samples. This shows that the β-T anticorrelation observed is related to the defects in the amorphous structure of the material (eg. SiOH content). For more details see Coupeaud et al. (in preparation).

Then, we report the evolution of κ as a function of λ in logarithmic scale at different temperatures for the amorphous and crystallized Mg_2SiO_4 sample (Fig. 2. a) and b)). For the amorphous sample, as for silica, κ decreases with decreasing temperature and this decrease of opacity with the temperature is more pronounced at long wavelengths. Furthermore, we report a break around 650 μm especially obvious for low temperatures $\leq$ 100 K. The spectral index measured between 650 and 1000 μm is equal to $\beta \sim 2.6$ at 300 K, it increases to $\beta \sim 4$ at 10 K. Unlike silica, the OH content cannot be responsible for this behaviour because of the thermal treatment at 500 °C which eliminates the silanol groups in this silicate sample. In this case, the defects involved could be created by the Mg^{2+} ions present in the material. To test this hypothesis, we have annealed the samples until the crystallization of forsterite. We observe no variation of κ and β with temperature for the cristallized sample(Fig. 2. b)). This indicates that the β-T anticorrelation observed is related to the defects in the amorphous structure of the material (eg. Mg^{2+} ions content, porosity). For more details see Coupeaud et al. (in preparation).

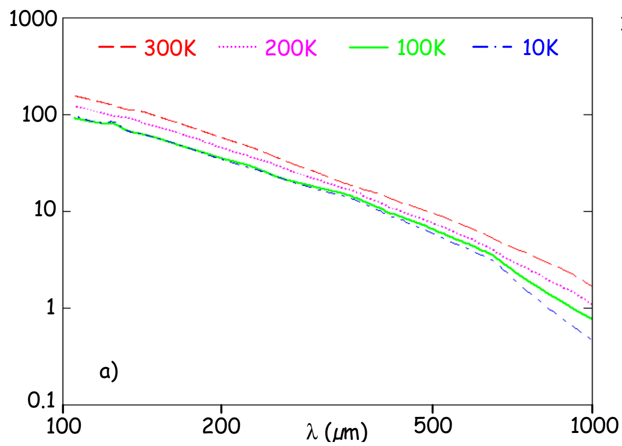

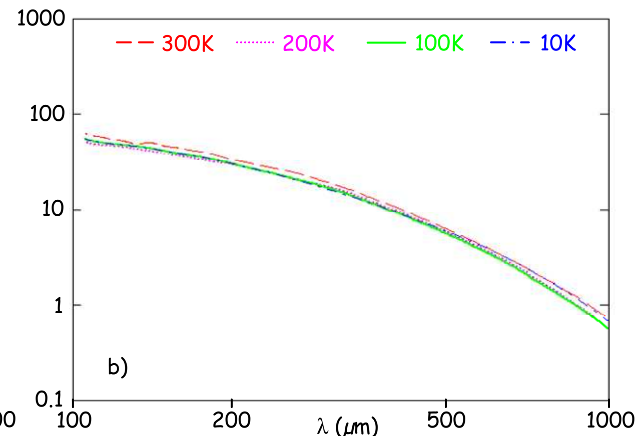

Fig. 2. Evolution of the mass absorption coefficient κ ($cm^2\,g^{-1}$) as a function of the wavelength λ (μm) at 300 K, 200 K, 100 K and 10 K for a) the amorphous (annealed at 500°C) Mg_2SiO_4 and b) the crystalline (annealed at 1100 °C) forsterite

4 Conclusions

In all amorphous samples, the absorption shows an anticorrelation between the temperature and the spectral index, in qualitative agreement with astrophysical data. The temperature dependent absorption is related to the amorphous state of the material. It can be modified with various annealing of the amorphous sample, and suppressed when annealing leads to crystallization of the samples. In the amorphous materials and at a given temperature, the spectral index cannot anymore be considered as a constant over the whole submillimeter spectral range. This, and the decrease of the opacity with the temperature must be taken into account for the analysis of Herschel/Planck data.

We acknowledge SOLEIL for provision of synchrotron radiation facilities and we would like to thank Pascale Roy, Jean-Blaise Brubach and Gaelle Creff for their assistance in using beamline AILES. Support by the French National Agency (ANR-07-BLAN-0364-02) and the PPF (Plan Pluri-Formation) from the OMP/UPS "Molécules et grains" are acknowledged.

References

Agladze, N. I., Sievers, A. J., Jones, S. A., Burlitch, J. M., & Beckwith, S. V. W. 1996, ApJ., 462, 1026

Anderson L.D, Zavagno, A., Rodon, J., et al. 2010, A&A 518, L99

Bot, C., Ysard, N., Paradis, D., et al. accepted in A&A

Boudet, N., Mutschke, H., Nayral, C., et al. 2005, ApJ., 633, 272

Brubach, J.B., Manceron, L., Rouzière, M., et al. 2010, AIP Conference Proceedings, 1214, 81

Désert, F.-X., Boulanger, F., & Puget, J. L. 1990, A&A, 237, 215

Désert F.-X., Macías-Pérez J. F., Mayet F., et al. 2008, A&A, 481, 411

Dupac, X., Bernard, J.-P., Boudet, N., et al. 2003, A&A, 404, L11

Ek, S., Root, A., Peussa, M., & Niinisto, L. 2001, Thermochimica Acta, 379, 201

El Hawi, N., Nayral, C., Delpech, F., et al. 2009, Langmuir, 25, 7540

Finkbeiner, D.P., Davis, M., & Schlegel, D.J., 1999, ApJ., 524, 867

Gillot, J., Roskosz, M., Depecker, C., Roussel, P., & Leroux, H. 2009, 40^{th} Lunar and Planetary Science Conference, 1763

Mennella, V., Brucato, J. R., Colangeli, L., et al. 1998, ApJ., 462, 1026

Mitchell, M.B.D., Jackson, D., & James, P.F. 1998, J. of Sol-Gel Science and Technology, 13, 359

Reach, W. T., Dwek, E., Fixsen, D. J., et al. 1995, ApJ., 451, 188

Rodon, J.A., Zavagno, A., Baluteau, j,-P., et al. 2010, A&A 518, L80

Serp, P., Kalck, P., & Feurer, R. 2002, Chem. Rev., 102, 3085

Zhuravlev, L.T. 2000, Colloids and Surfaces A, 173, 1

SF2A 2010
S. Boissier, M. Heydari-Malayeri, R. Samadi and D. Valls-Gabaud (eds)

THE FIRST STEP OF INTERSTELLAR CHEMISTRY REVEALED BY HERSCHEL/HIFI

E. Falgarone[1], M. Gerin[1], B. Godard[2] and M. De Luca[1]

Abstract. Absorption spectroscopy performed with Herschel/HIFI in the direction of bright star-forming regions of the inner Galaxy provides a new probe of the interstellar medium. The ground-state transition of several light hydrides are found to have large optical depths and are therefore sensitive tracers of gas components that are poorly known such as gas of low density containing only a small fraction of molecular hydrogen. The large observed abundances of HF, CH^+, OH^+, H_2O^+ among others, provide new clues on the processes leading to the incorporation of heavy elements into interstellar chemistry.

Keywords: astrochemistry, diffuse interstellar medium, hydrides, absorption spectroscopy, submillimeter and far infrared

1 Absorption spectroscopy with HIFI and the unique properties of light hydrides

The HIFI instrument aboard the Herschel satellite is an heterodyne instrument in the submillimeter range. The ground-state rotational transitions of light hydrides fall in this wavelength range because of the low reduced mass of these species. Their dipole moment is in general large, so the critical densities of these transitions are very high ($n_{\rm H} > 10^7$ cm^{-3}) and only the lowest level of the rotational ladder (J=0) is significantly populated in the low density, weakly irradiated, diffuse interstellar medium (ISM): the light hydrides are therefore expected to be detected via absorption lines against the strong dust continuum emission of massive star-forming regions. Absorption spectroscopy is very sensitive and reaches in the far-infrared the same range of column densities as in the visible or UV range for species that are accessible in the two wavelength ranges. The spectral resolution is high: HIFI observations reach 0.1 km s^{-1}. Last, hydrides form from reactions with molecular hydrogen and, depending on the species, they provide clues on the first steps of interstellar chemistry in gas containing only a low fraction of H_2. In absorption, they are valuable tracers of the diffuse gas (in space and velocity), independently of other tracers, such as CO or dust emission.

Figure 1 displays seven of the lines detected so far in absorption against the dust continuum emission of the remote star-forming region W31C (or G10.6-0.34). It shows the line-to-continuum ratio as a function of the LSR velocity, so that absorption ranges between 1 (continuum level) and 0 (saturated absorption). The different spectra are shifted for clarity but the scales remain the same (except for SH^+ that is scaled by a factor 10). Two main results are immediately noticeable: (1) some of the lines are heavily saturated over most of the velocity range sampled by the line of sight, such as CH^+(1-0), others such as water or HF are saturated over only restricted velocity intervals, while SH^+ or H_2O^+ have an optical depth clearly smaller than unity at all velocities, and (2) the similarity between the velocity profiles of HF and H_2O for instance is striking.

Several papers have already been published in the A&A Herschel and Herschel/HIFI Special Issues. Some of the most salient results obtained so far are summarized here. Additional results include CH (Gerin et al. 2010), H_2Cl^+ (Lis et al. 2010), C_3 (Mookerjea et al. 2010) and nitrogen hydrides (Persson et al. 2010).

[1] Ecole Normale Supérieure & Observatoire de Paris, France
[2] Centro de Astrobiologica, CSIC-INTA, Madrid, Spain

1.1 HF

Although fluor is not an abundant element, the HF(1-0) transition is saturated because most of fluor available in the gas phase is in the form of HF that has a larger binding energy than H_2. The H_2 + F reaction is highly exothermic with a small activation energy barrier of 500 K. The comparison of the spectra of HF with para-water shows that in spite of the abundance ratio, $[O]/[F] \sim 10^4$, the optical depth of HF(1-0) is larger than that of para-H_2O (Neufeld et al. 2010). The analysis of the optical depth of the different velocity components shows that at least 1/3 of gas-phase fluor is in the form of HF. HF is therefore a new tracer of H_2 since it is present as soon as H_2 is present (Neufeld et al. 2010, Sonnentrucker et al. 2010).

1.2 OH^+ and H_2O^+

The direct comparison of the absorption profiles of OH^+ and H_2O^+ (Figure 1) is not straightforward because of the hyperfine structure of the transitions (Gerin et al. 2010). Nevertheless, it is visible that the OH^+ spectrum is more saturated than that of H_2O^+. The ratios of the column densities inferred are significantly larger than unity. This is unexpected because the two species are closely linked: the oxygen chemistry in the ISM is initiated by cosmic-ray (or X-ray) ionization of hydrogen. Then the slightly endothermic charge exchange reaction H^+ + O produces O^+ which reacts rapidly with H_2 to form OH^+. Subsequent rapid H-atom abstraction produces H_2O^+ and H_3O^+, opening the gas-phase route to H_2O. The large ratio of OH^+ to H_2O^+ column densities implies that the absorbing gas is weakly shielded from the ambient radiation field with only a low fraction of hydrogen in the molecular form (less than 10%). The large column densities in turn imply a large ionization rate, up to $\zeta = 2.4 \times 10^{-16}$ s^{-1}, a result similar to that inferred from the abundances of H_3^+ observed in the diffuse ISM.

1.3 CH^+ and SH^+

These two radicals are different from all others because their formation proceeds via highly endothermic reactions of either C^+ or S^+ with H_2. It has been known since its first detection, four decades ago, that UV-driven chemistry in diffuse gas cannot reproduce the large abundances of CH^+ that have been found in the Solar neighborhood. Since the CH^+(1-0) line is so saturated, column densities are inferred from absorption lines of $^{13}CH^+$(1-0) (Falgarone et al. 2010). The large abundances are confirmed along sight-lines crossing the Galaxy, with however a large scatter. A specific warm non-equilibrium chemistry activated by short bursts of turbulent dissipation (the so-called TDR model, for Turbulent Dissipation Regions, Godard et al. 2009, 2010) is able to reproduce the observed CH^+ abundances in the diffuse medium. Interestingly, the CH^+ abundance is proportional to the dissipation rate, which makes this radical a specific tracer of the dissipation of suprathermal energy in the ISM. SH^+ is much less abundant than CH^+ but they form a very unique couple for the study of turbulent dissipation in the diffuse ISM. The endothermicities of their formation pathways differ by a factor larger than 2, hence their abundance ratio is a unique tracer of the probability distribution of dissipated energy.

2 Perspectives

Absorption spectroscopy of light hydrides provides unique and versatile informations on a variety of processes in the ISM, as well as the first steps of interstellar chemistry. They specifically probe the least molecular regions of the diffuse ISM. The large opacites of the ground-state lines make them anticipated tracers of yet unseen gas components in external and high-z galaxies.

The results presented here have been (and are still being) obtained in the framework of the guaranteed time key-project PRISMAS (Probing interestellar molecules with absorption line spectroscopy, PI M. Gerin) of the Herschel/HIFI instrument.

References

Falgarone E., Godard B., Cernicharo J. et al. 2010 A&A 521 L15

Gerin M., De Luca M., Black J. et al. 2010 A&A 518 L110

Gerin M., De Luca M., Goicoechea J. et al. 2010 A&A 521 L16

Godard B., Falgarone E., Gerin M. et al. 2010 A&A 520 20

Godard B., Falgarone E., Pineau des Forêts 2009 A&A 495 847

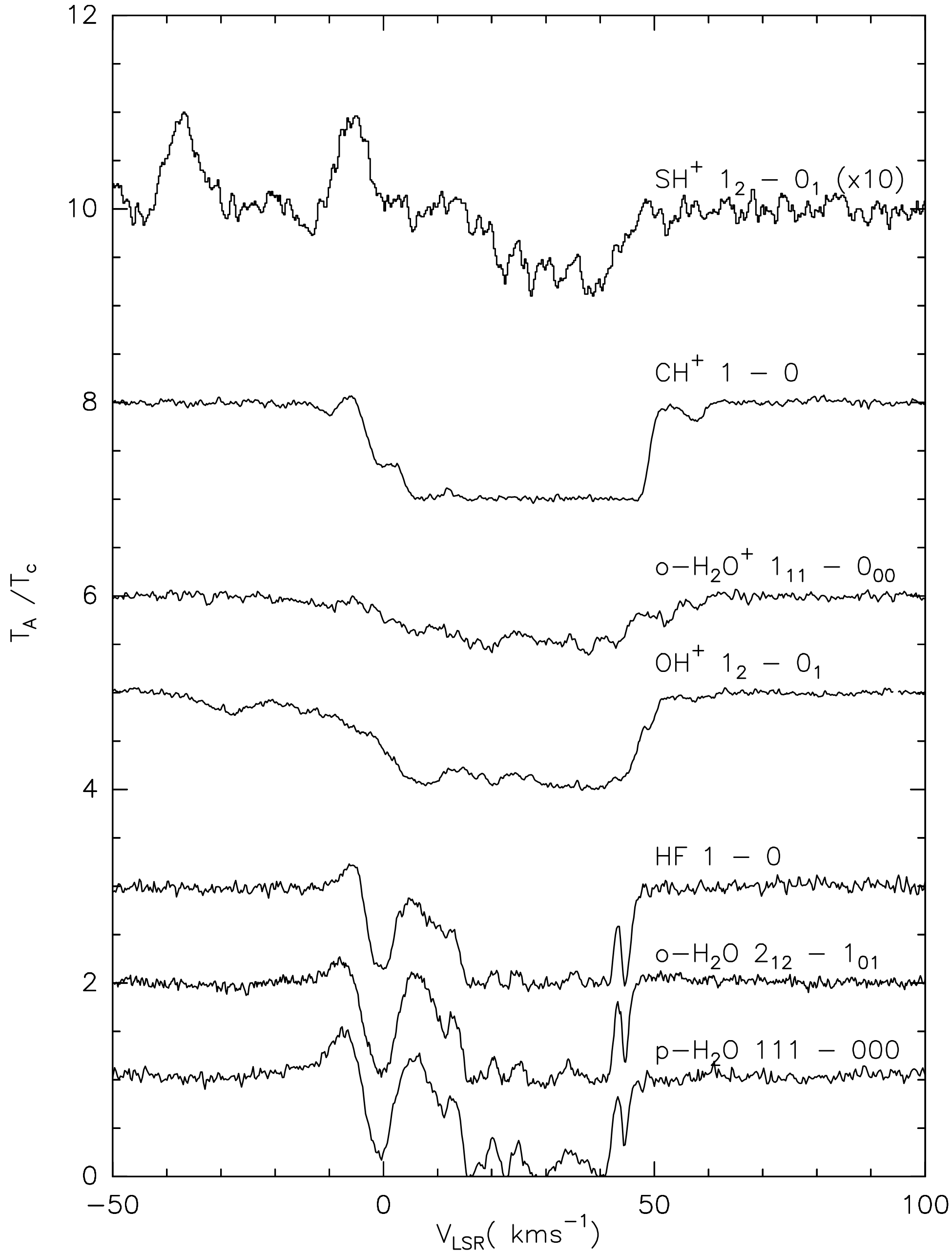

Fig. 1. Absorption of the ground-state rotational transitions of six light hydrides observed against the dust continuum emission of the bright star-forming region W31C (or G10.6-0.34) by Herschel/HIFI. The emission lines in the SH^+ spectrum are methanol lines from the star-forming region.

Lis D.C., Pearson J.C., Neufeld D.A. et al. 2010 A&A 521 L9

Mookerjea B.,, Giesen T., Stutzki J. et al. 2010 A&A 521 L13

Neufeld D.A., Sonnentrucker P., Phillips T.G. et al. 2010 A&A 518 L108

Neufeld D.A., Goicoechea J., Sonnentrucker P. et al. 2010 A&A 521 L10

Persson C., Black J., cernicharo J. et al. 2010 A&A 521 L45

Sonnentrucker P., Neufeld D.A., Phillips T.G. et al. 2010 A&A 521 L12

SF2A 2010
S. Boissier, M. Heydari-Malayeri, R. Samadi and D. Valls-Gabaud (eds)

SPIRE SPECTROSCOPY OF THE INTERSTELLAR MEDIUM

E. Habart[1], E. Dartois[1], A. Abergel[1], J.-P. Baluteau[2], D. Naylor[3], E. Polehampton[3,4], C. Joblin[5] and SAG 4 consortium

Abstract. The SPIRE Fourier Transform Spectrometer on-board Herschel allows us, for the first time, to simultaneously measure the complete far-infrared spectrum from 194 to 671 μm. A wealth of rotational lines of CO (and its isotopologues), fine structure lines of C^0 and N^+, and emission lines from radicals and molecules has been observed towards several galactic regions and nearby galaxies. The strengths of the atomic and molecular lines place fundamental constraints on the physical conditions but also the chemistry of the interstellar medium. FTS mapping capabilities are also extremely powerful in characterizing the spatial morphology of the extended region and understand how the gas properties vary within the studied region. Here, we present a first analysis of SPIRE spectroscopic observations of the prototypical Orion Bar photodissociation region.

Keywords: infrared: ISM, submillimeter: ISM, ISM: lines and bands, ISM: molecules, ISM: clouds, ISM: evolution, ISM: general

1 Introduction

The Orion Bar located between the Orion molecular cloud and the HII region surrounding the Trapezium stars is one of the best-studied photodissociation regions (PDRs) in the Galaxy. Much of the emission from massive star-forming regions will originate from these interfaces, which are responsible for reprocessing the energy output from stars and reemitting this energy at infrared-millimetre wavelengths including a rich mixture of gas lines (i.e., Hollenbach & Tielens 1999). Visible-ultraviolet stellar radiation governs the chemical and thermal state of the gas in these regions. The impinging radiation field on the Bar is χ=(0.5–2.5)$\times 10^4$ χ_0 (Tielens & Hollenbach 1985; Marconi et al. 1998), where χ_0 is the Solar neighbourhood far-UV interstellar radiation field as given by Draine (1978). The UV field varies as a function of depth within the cloud, providing a unique opportunity to study how the dust populations and the molecular content evolve with the excitation and physical conditions. This is important for the evolution of the cloud and its associated star formation.

2 Observations with the FTS

The SPIRE FTS simultaneously measures the source spectrum across two wavebands: Spectrometer Long Wavelength (SLW), covering 14.9 - 33.0 cm^{-1} (303-671 μm) and Spectrometer Short Wavelength (SSW) covering 32.0 - 51.5 cm^{-1} (194-313 μm). Each band is imaged with a hexagonal bolometer array with pixel spacing of approximately twice the beam-width. The Full Width at Half Maximum (FWHM) beam-widths of the SLW and SSW arrays vary between 29 - 42" and 17-21" respectively. The source spectrum, including the continuum, is obtained by taking the inverse transform of the observed interferogram. For more details on the SPIRE FTS instrument, calibration and data reduction procedures, the reader is referred to the articles by Griffin et al. (2010); Swinyard et al. (2010). Our observations are part of the "Evolution of Interstellar dust" key program

[1] Institut d'Astrophysique Spatiale, UMR 8617, CNRS/Université Paris-Sud 11, 91405 Orsay, France
[2] Laboratoire d'Astrophysique de Marseille, UMR6110, CNRS/Université de Provence, 13388 Marseille Cedex 13, France
[3] Institute for Space Imaging Science, University of Lethbridge, Lethbridge, Canada
[4] The Rutherford Appleton Laboratory, Chilton, Didcot OX11 0QX, UK
[5] CESR, UMR5187, CNRS/Université de Toulouse, 31028 Toulouse cedex 4, France

of the SPIRE consortium (Abergel et al. 2010). The Orion Bar was observed with a single pointing in the high-resolution mode of the SPIRE FTS on 2009 September 13 (*Herschel* observation ID, 1342183819). Two scan repetitions were observed which gave an on-source integration time of 266.4 seconds. The unapodized spectral resolution was 0.04 cm^{-1} (1.2 GHz). After apodization (using extended Norton-Beer function 1.5; Naylor & Tahic 2007) the FWHM of the resulting instrument line shape is 0.0724 cm^{-1} (2.17 GHz). While unapodized FTS spectra provide the highest spectral resolution, the instrument line shape, which for an ideal FTS is the classical sinc function, is characterized by relatively large secondary oscillations with negative lobes. An iterative spectral-line fitting routine was developed to extract line parameters from unapodized FTS spectra (Jones et al. 2009).

3 Results

3.1 Detected gas lines

The averaged apodized FTS spectra over the three SLW/SSW detectors aligned on the Bar and corrected for obliquity effects* are presented in Fig. 1. The FTS wavelength coverage allows us to detect a wealth of rotational lines of CO (and its isotopologues), fine structure lines of C and N^+, and emission lines from several radicals and molecules. The expected line positions for detected species are marked in Fig. 1. The ^{12}CO transitions, which appear as the bright narrow lines, are here seen for the first time together from J=4-3 to 13-12 in a single spectrum. The ^{13}CO lines are clearly detected from J=5-4 to 13-12. Most of the $C^{18}O$ lines are visible but blended with the ^{13}CO lines; some $C^{17}O$ lines are detected. One emission line at about 359 μm lies at the position of the fundamental rotational transition of CH^+ (Naylor et al. 2010). This detection can be related to the observation of the CH lambda doublet transitions at about 556.5 μm and 560.7 μm, although it is possibly blended with an HCO^+ $J = 6 \rightarrow 5$ line. The ortho-H_2O $1_{10} \rightarrow 1_{01}$ line at $\sim$538 and para-H_2 $2_{11} \rightarrow 2_{02}$ at 398 μm are clearly detected. The $\sim$269 μm para-H_2O $1_{11} \rightarrow 0_{00}$ line was also detected, but the signal-to-noise ratio is low. Some other H_2O lines may be blended. The H_2S $2_{12} \rightarrow 1_{01}$ line at $\sim$407 μm is detected, while other fainter H_2S lines at shorter wavelengths are only marginally detected. Some features related to the emission of HCO^+, HCN, CN and C_2H are observed as expected (e.g., Hogerheijde et al. 1995; Simon et al. 1997; Young Owl et al. 2000; Teyssier et al. 2004; van Der Wiel et al. 2009), but to help distinguish the spectral confusion for fainter lines or unresolved k-ladder transitions from species such as methanol, the actual signal-to-noise ratio will be improved as the SPIRE FTS response is better understood and, scheduled deeper observations will also help.

3.2 Mapping gas lines

Fig. 1 presents sparse sampled† maps of nearly the complete CO and ^{13}CO band measured. Off-axis calibrations are not guaranteed because both detector arrays have not yet been fully characterised. The comparison between these maps shows the effects of optical depth and excitation in the molecular cloud particularly well. The emission of the less abundant ^{13}CO isotopologue probes the denser shielded regions, while the ^{12}CO optically thick emission likely comes from the less dense surface layers (Lis et al. 1998). The highest rotational lines, which are very sensitive to both gas densities and temperatures, show strong and peaked emission on the Bar, while they are not visible in the off Bar positions. Emission lines of species such as C, N^+ or CH^+ show spatially extended emission.

3.3 Molecular column densities

We used the observed line intensities and the CASSIS software‡ to estimate the beam-averaged molecular column densities. We list in Table 1 column densities estimated for a volume density of 10^5 cm^{-3} as applicable to the extended molecular gas in the Bar (Hogerheijde et al. 1995) and in the high-density limit, because some of

*The obliquity effect is important at the highest frequencies, where a significant error in the line position is introduced.

†The present FTS science demonstration phase observations sparsely samples the field of view and do not allow us to present fully sampled maps.

‡Based on analysis carried out with the CASSIS software and CDMS, JPL spectroscopic databases and RADEX (van Der Tak et al. 2007) molecular databases. CASSIS has been developed by CESR-UPS/CNRS (`http://cassis.cesr.fr`).

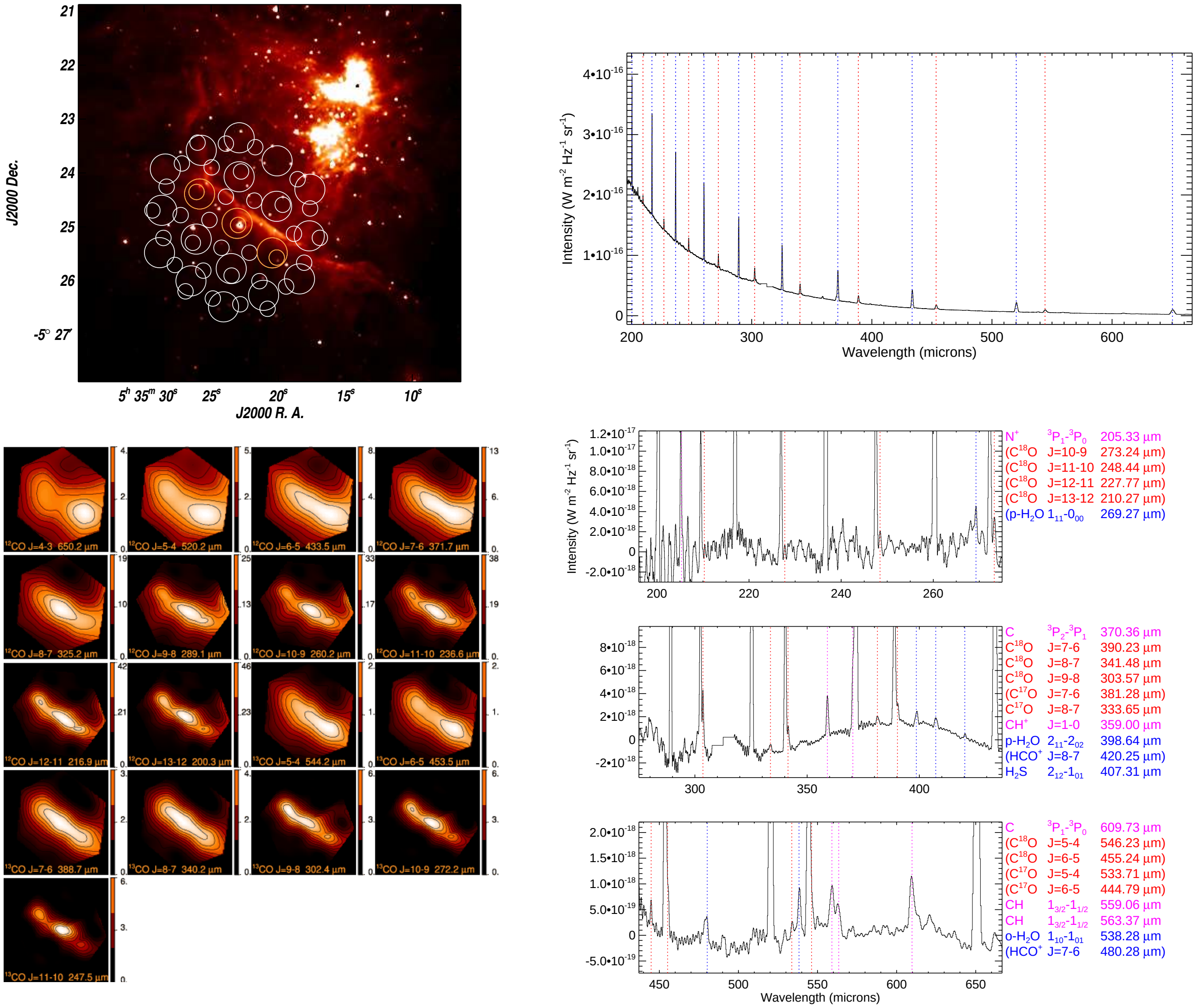

Fig. 1. Upper left : Map of the Orion Bar obtained with Spitzer (IRAC at 3.8 μm) with the SPIRE SLW (large circle) and SSW (small circle) array positions marked. The three arrays on the Bar are marked by yellow large and small circles. The PDR is wrapped around the HII region created by the Trapezium stars (right corner) and changes from a face-on to an edge-on geometry where the emission peaks. Upper right : Averaged apodized FTS spectra over the three arrays on the Bar. The blue and red dotted lines delinate the ^{12}CO and ^{13}CO lines position respectively. Lower right : Zoom of the averaged apodized FTS spectra continuum substracted. Dotted lines show the positions where specific gas lines are expected, excluding the ^{12}CO and ^{13}CO lines. The corresponding lines and wavelengths are marked on the right. Lines between brackets are only possibly detected at this level of analysis. Lower left : Sparse sampled maps in the ^{12}CO and ^{13}CO lines measured, except for the ^{13}CO $J = 12-11$ at $\sim$227 and $J = 13-12$ at 209 μm lines. Scales are in 10^5 erg s^{-1} cm^{-2} sr^{-1}. Contour levels are drawn at 10, 20,..., 90 % of the maximum intensity.

the line emission may originate from dense clumps§. We adopt the mean molecular gas temperature towards the Bar of $\sim$85 K for kinetic temperatures as determined from the ground Hogerheijde et al. (1995), and the more extreme 50 to 150 K range values that probe different zones of the PDR (Lis & Schilke 2003; Batrla & Wilson 2003). The line widths were taken equal to 3 km s^{-1}, following previous higher resolution observations

§The clumpiness of the PDR inferred by Hogerheijde et al. (1995) was confirmed by interferometric data of Young Owl et al. (2000); Lis & Schilke (2003). Clump densities up to 10^7 cm^{-3} were derived by Lis & Schilke (2003), while the density of the interclump medium should fall between a few 10^4 cm^{-3} (Young Owl et al. 2000) and 2 10^5 cm^{-3} (Simon et al. 1997).

(Hogerheijde et al. 1995; Johnstone et al. 2003). Our values for the column densities agree for species detected from the ground with previously published values to within a factor of $2-3$: Hogerheijde et al. (1995) for $C^{18}O$ and HCO^+; Johnstone et al. (2003) for $C^{17}O$; and Leurini et al. (2006) for H_2S. Beam dilution effects could introduce a significant factor. To convert the observed $C^{18}O$ J=8-7 and $C^{17}O$ J=8-7 line intensities to a total H_2 column density, we assume isotopic ratios $^{16}O/^{18}O\sim560$, $^{16}O/^{17}O\sim1800$ (Wilson & Rood 1994) and a relative CO abundance to H_2 of 1.1×10^{-4} as applicable for the Orion Bar PDR (Johnstone et al. 2003). We find $N(H_2)\sim9\ 10^{22}$ cm^{-2} assuming $T\sim85$ K, which implies the following molecular abundances on the Bar: x(ortho-H_2O)$\leq3.3^{+3.3}_{-1.7}\ 10^{-7}$; x(para-$H_2O$)$\leq5^{+11.7}_{-3.1}\ 10^{-7}$; x($HCO^+$)$\leq3.9^{+8.3}_{-2.1}\ 10^{-9}$; x($CH^+$)$=7.2^{+2.6}_{-0.7}\ 10^{-11}$; x($H_2S$)$=3.4^{+2.3}_{-1}\ 10^{-10}$. H_2O is extremely sensitive to the local physical conditions in molecular clouds: close to the surface, molecules are photodissociated, while deeper into the cloud molecules freeze onto grain surfaces (i.e., Hollenbach et al. 2009). Desorption of ices (Westley et al. 1995; Seperuelo Duarte et al. 2009) could supply gas-phase species. The high abundances of sulphur species remain an interesting puzzle for interstellar chemistry (i.e., Goicoechea et al. 2006). The observed abundance of species such as H_2S are difficult to interpret in models. H_2S results from a mixed chemistry involving gas-phase reactions and grain-related processes.

Table 1. Beam-averaged molecular column densities.

Species	Transition	Wavelength (microns)	E_u (K)	Intensity[a] (10^{-6} erg s^{-1} cm^{-2} sr^{-1})	Column density (10^{15} cm^{-2})
$C^{18}O$	$J=7\rightarrow6$	390.2	147.5	2.6[1.1]	7.7[24,3.8][b]
$C^{18}O$	$J=8\rightarrow7$	341.5	189.6	3.3[1.1]	15[72,5.5][b]
$C^{18}O$	$J=9\rightarrow8$	303.6	237.0	11[3.9]	96[720,25][b] - 10[43,5.4][c]
$C^{17}O$	$J=8\rightarrow7$	333.7	194.1	1.4[1.1]	6.6[33,2.3][b]
CH^+	$J=1\rightarrow0$	359.0	40.1	6.7[1.1]	0.0065[0.0058,0.0088][c]
ortho-H_2O	$1_{10}\rightarrow1_{01}$	538.3	61.0	2.6[1.1]	$\leq$30[60,15][b,d]
para-H_2O	$2_{11}\rightarrow2_{02}$	398.6	136.9	2.0[1.1]	$\leq$45[150,17][b,d]
HCO^+	$J=8\rightarrow7$	420.3	154.1	$\leq$0.7[e]	$\leq$0.35[1.1,0.16][b,e]
H_2S	$2_{12}\rightarrow1_{01}$	407.3	55.1	1.4[1.1]	0.031[0.023,0.052][c]

(a): Intensities with uncertainty in between brackets. (b): Beam-averaged column densities using RADEX with $n=10^5$ cm^{-3} and T=85 K, with estimations for 50 and 150 K in between brackets. (c): Beam-averaged column densities in the high-density (LTE) limit for 85 K, with estimations for 50 and 150 K in between brackets. (d): Note that the density (or temperature) could be higher than assumed, which would decrease the column density, and the para-H_2O $2_{11}\rightarrow2_{02}$ line could be affected by IR pumping. (e): We used the HCO^+ $J=8\rightarrow7$ line because the HCO^+ $J=7\rightarrow6$ line is possibly blended with an HCl $J=1\rightarrow0$ line. Column densities from ^{12}CO and ^{13}CO lines are uncertain due to high optical depth and are not listed.

4 Conclusions

We have analysed the first spectral survey taken in the Orion Bar by the FTS of SPIRE. A wealth of rotational lines of CO (and its isotopologues), fine structure lines of C and N^+, and emission lines from radicals and molecules such as CH^+, CH, H_2O or H_2S were found. For species detected from the ground, our estimates of the column densities agree with previously published values. The comparison between ^{12}CO and ^{13}CO maps shows particularly the effects of optical depth and excitation in the molecular cloud. The distribution of the ^{12}CO and ^{13}CO lines with upper energy levels is discussed in Habart et al. (2010). Fully sampled map will be investigated in the near future. SPIRE/FTS data should be associated to PACS and HIFI data. In particular, observations of gas cooling lines at high spectral resolution with HIFI will allow us to assign some lines that could be merged in the lower resolution SPIRE spectra and provide missing information about the gas velocity within the PDR.

References

Abergel, A, Arab, H, Compiègne, M, et al. 2010, *A&A*, 518:L96.

Batrla, W & Wilson, T. L. 2003, *A&A*, 408:231.

Draine, B. T. 1978, *Astrophysical Journal Supplement Series*, 36:595.

Goicoechea, J. R, Pety, J, Gerin, M, Teyssier, D, Roueff, E, Hily-Blant, P, & Baek, S. 2006, *A&A*, 456:565.

Griffin, M. J, Abergel, A, Abreu, A, et al. 2010, *A&A*, 518:L3.

Habart, E, Dartois, E, Abergel, A, et al. 2010, *A&A*, 518:L116.

Hogerheijde, M. R, Jansen, D. J, & Van Dishoeck, E. F. 1995, *A&A*, 294:792.

Hollenbach, D. J & Tielens, A. G. G. M. 1999, *Reviews of Modern Physics*, 71:173.

Hollenbach, D, Kaufman, M. J, Bergin, E. A, & Melnick, G. J. 2009, *ApJ*, 690:1497.

Johnstone, D, Boonman, A. M. S, & van Dishoeck, E. F. 2003, *A&A*, 412:157.

Jones, S, Naylor, D, Gom, B, & Spencer, L. 2009, *Proc. 30th Canadian Symposium on Remote Sensing.*

Leurini, S, Rolffs, R, Thorwirth, S, Parise, B, Schilke, P, Comito, C, Wyrowski, F, Güsten, R, Bergman, P, Menten, K. M, & Nyman, L. A. 2006, *A&A*, 454:L47.

Lis, D. C & Schilke, P. 2003, *ApJ*, 597:L145.

Lis, D. C, Serabyn, E, Keene, J, Dowell, C. D, Benford, D. J, Phill, T. G, Hunter, T. R, & Wang, N. 1998, *ApJ*, 509:299.

Marconi, A, Testi, L, Natta, A, & Walmsley, C. M. 1998, *A&A*, 330:696.

Naylor, D & Tahic, M. 2007, *J. Opt. Soc. Am. A 24, 3644-3648.*

Naylor, D, Dartois, E, Habart, E, et al. 2010, *A&A*, 518:L117.

Seperuelo Duarte, E, Boduch, P, Rothard, H, Been, T, Dartois, E, Farenzena, L. S, & Da Silveira, E. F. 2009, *A&A*, 502:599.

Simon, R, Stutzki, J, Sternberg, A, & Winnewisser, G. 1997, *A&A*, 327:L9.

Swinyard, B, Ade, P, Baluteau, J, et al. 2010, *this issue.*

Teyssier, D, Fossé, D, Gerin, M, Pety, J, Abergel, A, & Roueff, E. 2004, *A&A*, 417:135.

Tielens, A. G. G. M & Hollenbach, D. 1985, *ApJ*, 291:722.

van Der Tak, F. F. S, Black, J. H, Schoeier, F. L, Jansen, D. J, & van Dishoeck, E. F. 2007, *A&A*, 468:627.

van Der Wiel, M. H. D, van Der Tak, F. F. S, Ossenkopf, V, Spaans, M, Roberts, H, Fuller, G. A, & Plume, R. 2009, *A&A*, 498:161.

Westley, M. S, Baragiola, R. A, Johnson, R. E, & Baratta, G. A. 1995, *Nature*, 373:405.

White, G. J & Sandell, G. 1995, *A&A*, 299:179.

Wilson, T. L & Rood, R. 1994, *ARA&A*, 32:191.

Young Owl, R. C, Meixner, M. M, Wolfire, M, Tielens, A. G. G. M, & Tauber, J. 2000, *ApJ*, 540:886.

SF2A 2010
S. Boissier, M. Heydari-Malayeri, R. Samadi and D. Valls-Gabaud (eds)

HERSCHEL/HIFI REVEALS THE FIRST STAGES OF STELLAR FORMATION

F. Herpin[1], S. Bontemps[1], L. Chavarria[1], F. van der Tak[2], F. Wyrowski[3] and E. van Dishoeck[4]

Abstract. The understanding of the star formation is still on progress. Especially, the formation of high-mass stars is much less understood than the low-mass case: even the time order of observational phenomena is uncertain. Water, one of the most important molecules in the Universe, might elucidate key episodes in the process of stellar birth, and especially could be a major role in the formation of high-mass stars. For both types of stars, the source chemical composition is not well known and even less known is the chemical evolution of the interstellar matter throughout the various phases of star formation. This talk presents the first results of the various Herschel Space Observatory star formation key-programs. One of the instruments on-board HSO, HIFI, is the most powerful spectrometer never built, covering a huge frequency range, most of them unaccessible from ground. In particular, one of the KP, WISH, aims at following the process of star formation during the various stages and at using the water as a physical diagnostic throughout the evolution.

Keywords: ISM: molecules, abundances, stars: formation, protostars, early-type, line: profiles

1 Introduction

In the deeply embedded phase of star formation, it is often only possible to trace the dynamics of gas in a young stellar object (YSO) through resolved emission-line profiles. The various dynamical processes include infall from the surrounding envelope towards the central protostar, molecular outflows, and strong turbulence. One of the goals of the Herschel Space Observatory (HSO) and of its spectrometer HIFI is to probe these processes and determine the abundance of the chemical species as a function of evolution (van Dishoeck et al., submitted to PASP).

Three instruments are on board the HSO, launched on May 14th, 2009: the Photodetector Array Camera and Spectrometer PACS, the Spectral and Photometric Imaging Receiver SPIRE, and the Heterodyne Instrument for the Far-IR HIFI. HIFI is composed of the Wide Band Spectrometer WBS and of the High Resolution Spectrometer (built by the CESR and the LAB). HIFI allows to observe between 250 and 625 microns (bands 1-5), and between 157 and 213 microns (bands 6-7). HIFI is a major step forward compared to other space facilities because of higher spatial resolution (3-5 w.r.t. SWAS/ODIN, 8 with ISO-LWS), higher sensitivity (10 w.r.t. SWAS/ODIN), higher spectral resolution (up to 125 kHz), and larger colder aperture, and more observing time than balloon and airborne instruments.

The OB stars are the main contributors to the evolution and energy budget of galaxies. Their formation, however, has not been understood yet and the classical scheme for low-mass star formation (Andre 2000) cannot be applied as such to OB stars. Indeed, young OB stars and protostars strongly interact with the surrounding massive clouds and cores, leading to a complex and still not clearly defined sequence of objects from pre-stellar cores that are often believed to be hosted in the so-called IR dark clouds, to high-mass protostellar objects (HMPOs), to hot molecular cores (HMC) and uItra compact HII regions (e.g. Beuther 2007; Menten 2005).

[1] Université de Bordeaux , Laboratoire d'Astrophysique de Bordeaux, CNRS/INSU, UMR5804, Floirac, France
[2] SRON Netherlands Institute for Space Research, PO Box 800, 9700 AV, Groningen, The Netherlands
[3] Max-Planck-Institut für Radioastronomie, Auf dem Hügel 69, 53121 Bonn, Germany
[4] Leiden Observatory, Leiden University, PO Box 9513, 2300 RA Leiden, The Netherlands

2 Spectral surveys of protostars

Spectral surveys are essential to study the chemical content of the star forming regions (SFRs) because different molecules are produced in different regions with different physical conditions and because different molecular transitions are excited in regions with different temperatures and densities. They aim at answering to the following questions: 1) what is the degree of complexity of the molecules in SFRs ? ; 2)When and how do they form and evolve ?
Two Guaranteed Time Key-Programs (GT-KP) are dedicated to the study of star formation through spectral surveys: HEXOS (Herschel observations of EXtra-Ordinary Sources, Bergin et al.) towards Orion KL, and CHESS (Chemical HErschel Surveys of Star- forming regions, Ceccarelli et al.) towards a sample of protostars, from low- to high-mass. First results about deuteration (Vastel 2010) and the detection of the new species H_2O^+ and H_2Cl^+ (Lis 2010).

3 Water in Star forming regions

The WISH GT-KP (Water In Star forming regions with Herschel, PI: E. van Dishoeck) aims at probing the stellar formation through water observations with HIFI and PACS towards a large sample of low-, intermediate- and high-mass protostellar objects and circumstellar disks. The large variations of water abundance (e.g. evaporation from dust grains for T$>$ 100K) depending on the physical conditions allow to test different regions, and, hence, to characterize different evolutionnary stages. Also, water is a very good probe of gas flows (infall, outflow). But maybe more important, water plays a crucial role in the energy balance and, as an efficient cooling agent, could help to understand how massive stars can form. Finally, water molecules are the main oxygen reservoir.

3.1 *Low-mass prestellar cores and protostars*

First Herschel results show the first observation of water in low-mass protostellar cores. Caselli (2010) have made the first detection of water ($1_{10} - 1_{01}$) in pre-stellar core, L1544 (Taurus) and derive an upper limit for its abundance of 10^{-9} (density of 10^5 cm-3).

The first water maps of outflows/jets have been performed by Nisini (2010) and show large variations of water abundance depending on the importance of the shocks and on the evolutionary stage of the object.

Kristensen (2010) have studied NGC 1333 (L$\sim$ 20L$_\odot$, d$\sim$250 pc) and derived water abundance of $10^{-5} - 10^{-4}$ in the outflow while water is less abundant in the envelope (10^{-9}). IRAS4A clearly exhibits an infall signature. The bulk of the emission comes from shocks in the molecular jets, both at small scale (a few 100 AU) and at large scale; emission from the passively heated envelope is also seen.

From Benz (2010), Bruderer (2010), the origin of the water emission is now clearly established:
- a passively heated envelope with a hot core (compact region of $\sim$200 AU) where H_2O evaporates.
- along outflows where the water emission extends from, and where the water abundance increases within the shocks.

3.2 *Intermediate-mass protostars*

WISH observations towards intermediate-mass protostars (Johnstone 2010) revealed powerful outflows. The water emission comes from the hot part of the envelope (T$>$ 100K) where its abundance is $\sim 10^{-5}$. Self-absorption from the external envelope is observed.

3.3 *High-mass protostellar objects*

The study of the high-mass protostar formation represents a large fraction of the WISH KP. This part is led by F. Herpin, F. van der Tak and F. Wyrowski. It consists of HIFI pointed observations of 14 water lines, including rare isotopic lines ($H_2{}^{18}O$, $H_2{}^{17}O$) in 19 sources (more deep H_2O $1_{10} - 1_{01}$ observation of four infrared-dark cloud cores) at different evolutionary stages (mid-IR-quiet and mid-IR-bright massive dense cores, hot molecular cores and UCHII regions). Maps of water emission with HIFI ($1_{10} - 1_{01}$, $2_{02} - 1_{11}$, $1_{11} - 0_{00}$) and PACS maps in 4 lines of 6 proto-clusters are also performed. The goal is to determine the abundance and distribution of water in the envelopes, massive outflows, and to precise the filling, cooling and chemistry of intra-cluster gas.

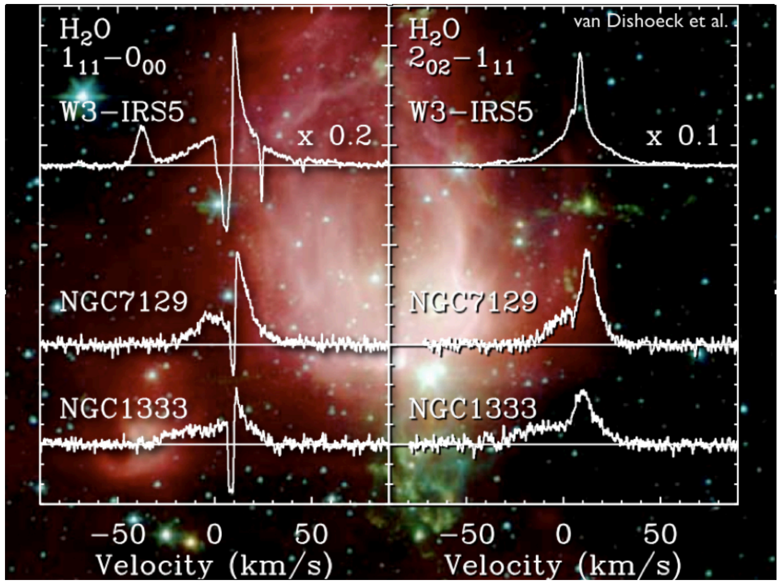

Fig. 1. Comparison of the HIFI water $1_{11} - 0_{00}$ and $2_{02} - 1_{11}$ line profiles between a low-mass (NGC 1333, Kristensen et al. 2010), intermediate-mass (NGC 7129, Johnstone et al. 2010) and high-mass (W3-IRS5, Chavarria et al. 2010) protostellar object.

The observations include chemically related species (O, OH, H_3O^+), radiation diagnostics of UV and X-rays, and a few key high-J CO lines too. The interpretation of the data is made through the line profile analysis and a line modelling using MC3D (Wolf 2003) for the continuum and RATRAN (Hogerheijde 2000) for the lines.

A first look to the water line profiles towards objects with different mass shows that water lines are stronger and more complex in high-mass protostellar objects (see Fig.1). The DR21(Main), in Cygnus X (L=45000 $L_\odot$, d=1.7 kpc) region, a relatively evolved object, was observed by the HSO (VanderTak 2010) in the ^{13}CO 10-9 and H_2O $1_{11} - 0_{00}$ (1113 GHz) lines. The profiles exhibit different components coming from the outflow, the protostellar envelope itself, and a foreground cloud. The high water abundance ($7{\times}10^{-7}$) in the warm outflow is probably due to the evaporation of water-rich icy grain mantles, while the H_2O abundance is kept down by freeze-out in the dense core ($1.6{\times}10^{-10}$) and by photodissociation in the foreground cloud (4×10^{-9}).

Marseille (2010) published the first comparison of water spectra (H_2O and $H_2{}^{18}O$ $1_{11} - 0_{00}$, H_2O $2_{02} - 1_{11}$) obtained in W43-MM1 (mid-IR quiet HMPO), W33A (mid-IR bright HMPO) and G31.41+0.31 and G29.96-0.02 (HMC). The higher abundance ($> 10^{-8}$) derived for G31.41+0.31 and W43-MM1 is not clearly linked to luminosity, mass and temperature or assumed evolutionary stage of the source.

The mid-IR bright massive dense core W3-IRS5 (Perseus region, d=2.0 kpc) was studied by Chavarria (2010). Several water lines have been observed and modelled. Emission in the rare isotopologue lines is only reproduced in the models by including a jump in the water abundance in the inner envelope. The emission in the rare species comes from the inner envelope where the water abundance is greatly enhanced (evaporation from dust grains). Emission from this region could be the expected contribution from the passively radiatively heated inner envelope. The signature of outflow (high-velocity emission of 33-40 km/s) is seen, but no infall is observed. Profiles reveal absorption from the cold molecular cloud ($T \leq 10$ K) in which the proto-stellar envelope is embedded. From the model interpretation, we conclude that the water emission is coming from the 2 sources first observed by Rodon (2008). The water abundance is 10^{-4} in the inner protostellar envelope ($T > 100$K) while it is $10^{-8,9}$ in the outer envelope (see Fig.2).

Finally, a large study of the demistry has been made by Benz (2010) for W3-IRS5 and Bruderer (2010) for AFGL2591 within the WISH KP. Through the observations of various hydrides, a radiation diagnostics in the systems protostar-disk-outflow is possible. Actually, hydrides are produced at high temperatures via reactions with atomic ions within strong UV or X fields. The following species have been detected: OH, CH ($2\ 10^{-8}$ in AFGL2591), NH (10^{-9}), SH, OH^+ ($3\ 10^{-10}$), CH^+ (10^{-8}), NH^+, SH^+, H_2O, H_2O^+($7\ 10^{-10}$), H_3O^+. The first detection of OH^+ and H_2O^+ reveals the gas phase path to produce water, and, hence, complete the water chemical puzzle. They conclude that FUV radiation from central protostar irradiates and heats the walls of the outflow cavity making the abundance of CH^+, OH^+ and NH^+ to increase by several orders of magnitude in the

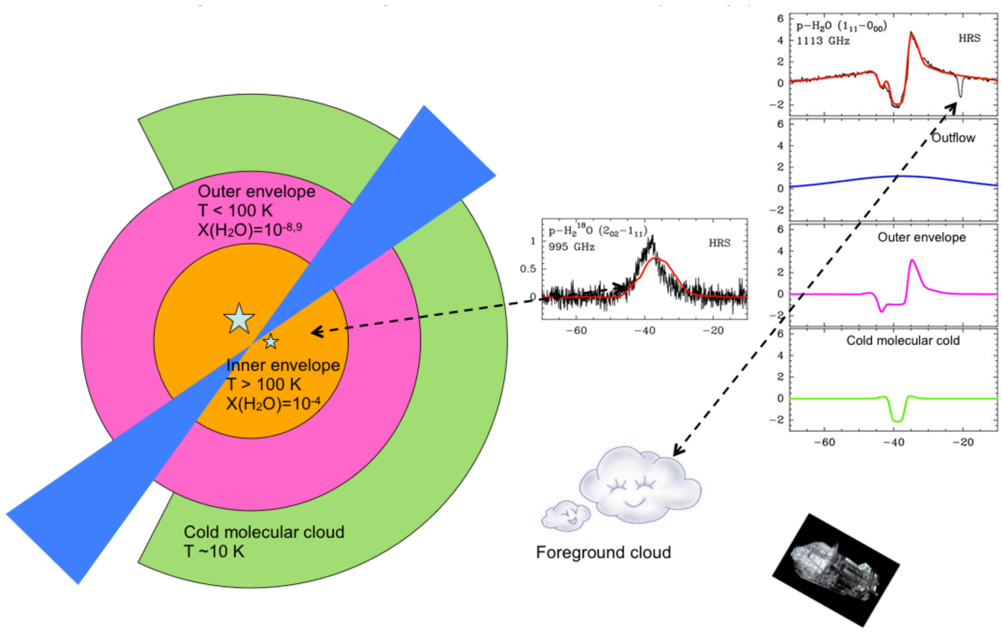

Fig. 2. Schematic view of W3-IRS5 high-mass massive dense core and of the different components of the water line profiles (Chavarria et al. 2010).

walls of the outflow.

We would like to thank the CNES for its financial suppport.

References

André, P., Ward-Thompson, D. & Barsony, M. 2000, *Protostars and Planets IV*, 59

Beuther, H., Churchwell, E.B., McKee, et al. 2007, *Protostars and Planets V*, 165

Menten, K.M., Pillai, T. & Wyrowski, F. 2005, Massive Star Birth: A Crossroads of Astrophysics, IAU Symposium 227 proceeding, 23

Benz, A., Bruderer, S., van Dishoeck, E. et al. 2010, A&A in press

Bergin, E.A., Phillips, T.G., Comito, C. et al. 2010, A&A in press

Bruderer, S., Benz, A., van Dishoeck, E. et al. 2010, A&A in press

Caselli, P., Keto, E., Pagani, L. et al. 2010, A&A in press

Ceccarelli, C. et al. 2010, A&A in press

Chavarria, L., Herpin F., Jacq, T. et al. 2010, A&A in press

Hogerheijde, M.R., van der Tak, F.F.S. 2000, A&A, 362, 697

Johnstone, D., Boonman, A.M.S., van Dishoeck, E.F. et al. 2010, A&A in press

Kristensen, L., Visser, R., van Dishoeck, E.F. et al. 2010, A&A in press

Lis, D.C, Pearson, J., Neufeld, D.A. et al. 2010, A&A in press

Marseille, D., van der Tak, F.F.S., Herpin, F. et al. 2010, A&A in press

Nisini, B., Benedettini, M., Codella, C. et al. 2010, A&A in press

Rodon, J., Beuther, H., Megeath, T. et al. 2008, A&A, 490, 213

van der Tak, F.F.S., Marseille, M., Herpin, F. 2000, A&A, 518, 107

Vastel, C., Ceccarelli, C. Caux, E. et al. 2000, 2010, A&A in press

Wolf, S. 2003, ApJ, 582, 859

SF2A 2010
S. Boissier, M. Heydari-Malayeri, R. Samadi and D. Valls-Gabaud (eds)

INITIAL HIGHLIGHTS OF THE HERSCHEL IMAGING SURVEY OF OB YOUNG STELLAR OBJECTS (HOBYS)

T. Hill[1], F. Motte[1], S. Bontemps[1,2], A. Zavagno[3], N. Schneider[1], M. Hennemann[1], J. di Francesco[4] and The HOBYS consortium

Abstract. We present initial Herschel HOBYS highlights of the Rosette molecular complex. The five Herschel wavebands of SPIRE (250/350/500 μm) and PACS (70 and 160 μm) allows HOBYS to provide an unbiased and complete census of intermediate- to high-mass young stellar objects, some of which are not detected by Spitzer. Key core properties, derived from spectral energy distributions, such as bolometric luminosity and mass, are used to constrain their evolutionary status.

Keywords: stars: formation, stars: early-type, submillimetre continuum, Herschel, protostars, ISM: individual (Rosette)

1 High-mass star formation and HOBYS

Our knowledge of high-mass star formation ($> 8\,\mathrm{M}_\odot$) is still rather schematic, though an evolutionary sequence of their earliest phases is staring to emerge. Bright IRAS sources embedded within massive envelopes have been recognised as high-mass protostellar objects (e.g. Beuther et al. 2002). Cold massive dense cores associated with weak mid-infrared emission, but with clear signposts of OB-type protostars, have been qualified as IR-quiet and are observed to host high-mass Class-0 protostars (Motte et al. 2007; Bontemps et al. 2010). Controversy remains regarding the existence and lifetime of high-mass analogues of prestellar cores, since infrared dark clouds are numerous (Simon et al. 2006) but only a few harbour starless, massive, and dense enough cores (e.g. Motte et al. 2007).

The Herschel imaging survey of OB Young Stellar objects (HOBYS, see `http://hobys-herschel.cea.fr`) is a guaranteed time key program which aims to identify and characterise the precursors of OB stars, measure the core/envelope mass and bolometric luminosity and assess the importance of triggering in high-mass star forming regions. Using the SPIRE/PACS instruments, HOBYS will image all of the molecular complexes forming OB-type stars at distances less than 3 kpc from the Sun. These 70–500 μm observations provide an unbiased census of massive young stellar objects (YSOs) and trace the large-scale emission of the surrounding clouds. This survey will yield, for the first time, accurate bolometric luminosity and envelope mass estimates for homogeneous and complete samples of OB-type YSOs, allowing us to estimate the evolutionary state of each source, and the lifetime of each evolutionary state.

We present here some of the first results from HOBYS focusing on the Rosette molecular cloud (Motte et al. 2010; Schneider et al. 2010; Hennemann et al. 2010). For a review of the Rosette see Schneider et al. (2010).

2 Observations

The Rosette molecular cloud was observed on October 20, 2009, during the science demonstration phase, using the parallel PACS/SPIRE mode at 70/160μm and 250/350/500μm, respectively, and a scan speed of 20"/s. The data reduction for the PACS and SPIRE observations are as described in Hennemann et al. (2010) and Schneider et al. (2010), respectively.

[1] Laboratoire AIM, CEA/IRFU - CNRS/INSU - Universit Paris Diderot,CEA-Saclay, 91191 Gif-sur-Yvette Cedex, France
[2] Laboratoire d'Astrophysique de Bordeaux, CNRS/INSU - Universit de Bordeaux,BP 89, 33271 Floirac Cedex, France
[3] Laboratoire d'Astrophysique de Marseille (UMR 6110 CNRS & Universit de Provence), 38 rue F. Joliot-Curie, 13388 Marseille Cedex 13, France
[4] National Research Council of Canada, Herzberg Institute of Astrophysics, University of Victoria, Department of Physics and Astronomy, Victoria, Canada

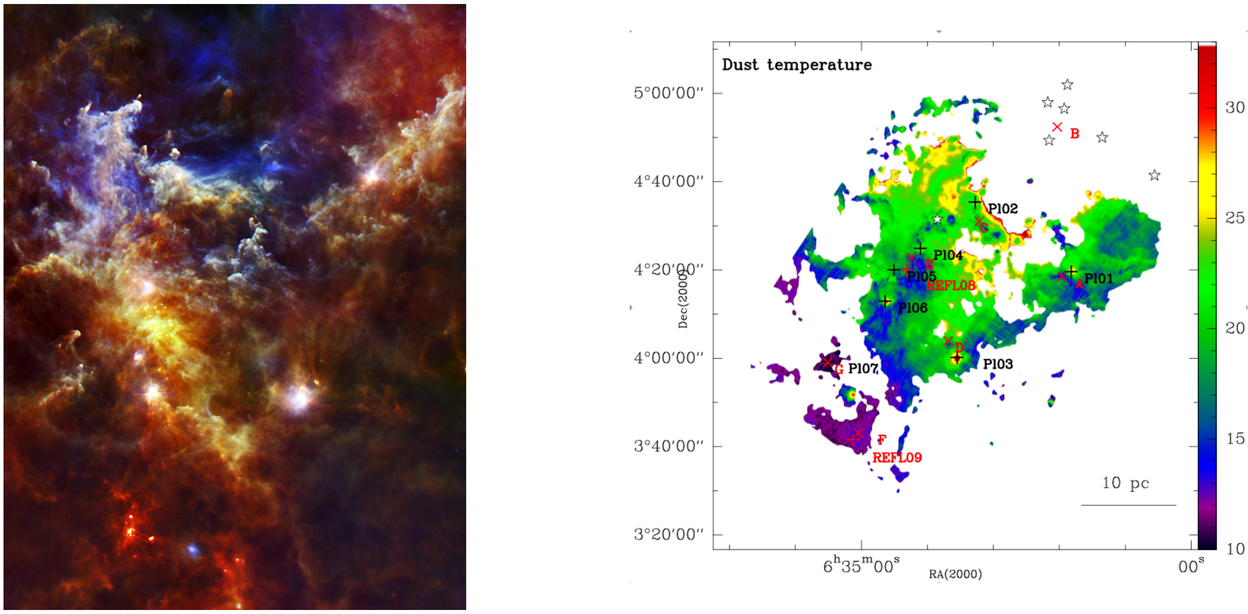

Fig. 1. bf Left: Composite 3-colour Herschel image of the Rosette molecular complex. PACS 70μm (blue), PACS 160μm (green), and SPIRE 250μm (red) (Motte et al. 2010). **Right**: Dust-temperature map obtained from a pixel-by-pixel SED fit to the five Herschel wavebands. Black crosses, and 'PL' indicate clusters identified by Phe & Lada (1997) while red crosses and labels are clusters from Poulton et al. (2008), and label REFL the clusters from Román-Zúñiga et al. (2008) (see Schneider et al. 2010, for more detail).

3 Results

Figure 1 (left), presents a three-colour image of the Rosette molecular complex. The sensitivity achieved in this image allows detection of compact YSOs down to 5-$\sigma \simeq 0.3\,M_\odot$ at 160 μm. In Rosette, this corresponds to spatial scales ranging from ∼0.05–0.2 pc to ∼40 pc.

The HII-region/molecular cloud interface, where the UV radiation has the largest impact is the most prominent in the blue and shows the most complex and filamentary structure (see Fig, 1, left). The dust temperature map, obtained from a pixel-to-pixel SED fit to the five Herschel wavebands (Fig. 1, right), shows that the highest temperatures in this complex (30 K) are found at this interface. At this point, the UV radiation from the NGC 2244 cluster has erased the low-density gas, leaving only the densest gas as 'pillars'. Schneider et al. (2010) show that the penetration depth of this radiation is ∼ 10 pc, which is approximately the border between the warm and colder gas phase. At larger depths, the cold, dense molecular ridge is less influenced by the UV radiation and appears to be less structured. The dust temperature map shows a decreasing temperature with increasing distance from the interface, such that the coldest region is in the remote part of the cloud. The total mass of the Rosette complex mapped by Herschel is ∼105 $M_\odot$. The column density map (Fig. 5 Schneider et al. 2010) indicates a clear increasing gradient in average density from the HII-region into the molecular cloud. In the 'compression' zone of the molecular cloud/HII-region interface, the densities are around 0.5×10^3 cm^3, whilst the remote regions have a higher densities of 1.8×10^3 cm^3 and 3.9×10^3 cm^3, respectively.

Source extraction was performed using a multi-resolution analysis (Motte et al. 2007), which filters out large spatial scales (>0.5 pc) in order to focus on compact sources. Above 5-σ, we extract 4000 − 900 sources at 70 and 500 μm, respectively (see Motte et al. 2010, for more detail). Analysis of Rosette yields a catalogue of dense cores with sizes 0.02-0.3 pc at 160 μm.

Simple grey-body spectral energy distributions (SEDs) were drawn for the 46 most massive cores, by combining these Herschel observations with Spitzer MIPS and IRAC fluxes where possible. For each core, the dust temperature and the mass were obtained, which vary from 12-40 K and 0.8-39 $M_\odot$, for the sample (Motte et al. 2010). The bolometric luminosity of each massive dense core was estimated from integration of the SED over the 3.6-500 μm range. The protostellar or starless nature of the dense cores was drawn from associations with or without 24μm Spitzer emission, respectively.

Six protostellar and three prestellar cores with radii ∼0.18 pc and masses between ∼20-40 $M_\odot$ were identified from SED fitting (Motte et al. 2010). Four of the six protostars are cooler and have lower luminosities which makes them good candidates for hosting early stage, high-mass protostars. The three massive starless cores are slightly larger and more massive than the protostellar sample ($\sim$0.22 pc, $\sim$30 $M_\odot$) and are also cooler (13 K). They are likely gravitationally bound and are possible examples of high-mass analogues of low mass prestellar cores (Motte et al. 2010).

A handful of starless dense cores were also discovered to have warm temperatures: $\sim$19 $M_\odot$, $\sim$0.14 pc, $\sim$27 K (see Fig. 5a Motte et al. 2010). The nature of these objects is as yet unclear, but they do not seem to correspond to remnant cloud surrounding an already formed cluster. If gravitationally bound, these warm, massive, but not centrally peaked, dense cores could concentrate their mass, cool down, and then form the next generation of intermediate- to high-mass stars in Rosette. They have high luminosities ($\sim$100 $L_\odot$) and are part of the $>10^3$ $L_\odot$ IRAS point sources associated with the PL1, PL3, and PL4 embedded clusters (see Fig. 1, right).

Herschel traces younger, colder objects (cf. Fig. 3, core 3) compared with Spitzer (core 1). In the submillimetre, i.e. 250μm, the sources are blended together preventing a dust temperature measurement on the protostar scale. Thus, in order to profile early-stage protostars it is necessary to concentrate on the 70 and 160 μm Herschel data (Hennemann et al. 2010).

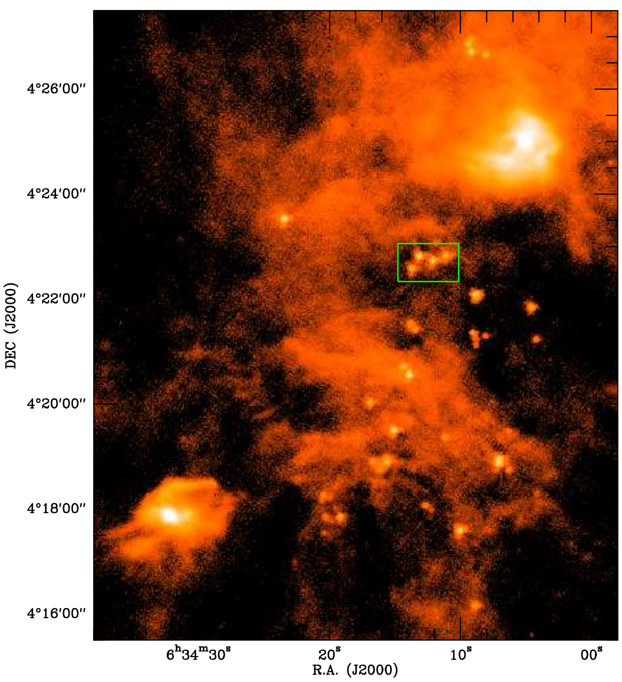

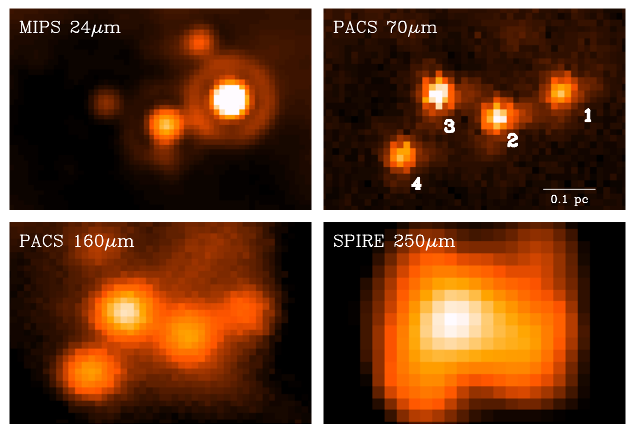

Fig. 2. Left: PACS 70μm of the Rosette molecular cloud centre. The region harbours the embedded clusters PL4 (northwest), PL5 (southeast), and a concentration of compact Herschel sources. **Right**: Four protostars in the central cluster at 24, 70, 160 and 250μm. The region represents the box highlighted on the left image. (Hennemann et al. 2010).

Hennemann et al. (2010) extracted a sample of 88 protostars from the aforementioned Motte et al. (2010) catalogue which were clearly detected at 70μm with FWHM <15". 17 of these sources are devoid of 2MASS and Spitzer associations. Using 70 and 160μm fluxes derived from aperture photometry, in addition to Spitzer data when available, and assuming the same dust temperatures as derived from Motte et al. (2010), SEDs were drawn to estimate the bolometric luminosity and envelope masses of these 88 protostellar objects.

Figure 3 plots the bolometric luminosity as a function of the envelope mass. This relation is often used as a proxy for stellar mass and evolution (cf André et al. 2000; Bonte et al. 1996). Evolutionary tracks are displayed for stars of different masses (cf. André et al. 2008; Bontemps et al. 2010). The Rosette protostellar sample of occupies the low- to high-mass regimes in the diagram. The diagonal lines in Fig. 3 indicate an approximate border zone between envelope-dominated class 0 and star-dominated class I objects based on the comparison of M_{env} to M_* (cf. Andre & Montmerle 1994).

A surprisingly large fraction of the protostellar sample ($\sim$2/3) falls within the candidate Class 0 regime (top left part of the diagram). A practical criterion inferred from this diagram is $L_\lambda > 350\,\mu m/L_{bol} > 1\%$ for Class 0 sources (André et al. 2000). Applying this relation to this protostellar sample results in more intermediate-mass objects classified as Class I, i.e., a more conservative Class 0 assignment, i.e, 'Candidate Class 0'. The central cluster harbours a significant number of sources in the Class 0 regime between 2–10 $M_\odot$ and 4–30 $L_\odot$, whilst the PL7 region (see Fig. 1) contains 3 sources with relatively low luminosities, indicating that both regions are younger compared with the remaining protostars in the sample.

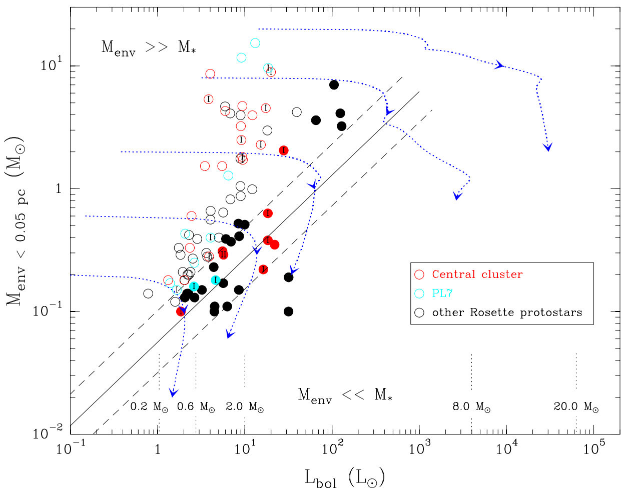

Fig. 3. Envelope mass versus bolometric luminosity diagram for the sample of Herschel protostars in Rosette. The central cluster and PL7 subsamples are emphasised by coloured symbols. Evolutionary tracks for stellar masses between 0.2 and 20 $M_{\odot}$ are included. The solid line corresponds to 50% of the mass accreted; the dashed lines account for the estimated uncertainties of M_{env} and L_{bol}. Open symbols: candidate Class 0 protostars with $L_{\lambda} > 350\,\mu m/L_{bol} > 1\%$; filled symbols: Class I protostars with $L_{\lambda} > 350\,\mu m L_{bol} \leq 1\%$ (Hennemann et al. 2010).

4 Conclusions

The initial results from the HOBYS key program are promising as Herschel provides detailed insight into the workings of the Rosette molecular cloud. In particular, there is: a clear dust tempereature and tentative age gradient running from the HII-region/cloud interface into the cloud (Schneider et al. 2010); three massive prestellar dense cores and a few warm starless cores that could represent the highly-sough precursors of high mass protostars (Motte et al. 2010); and rich protoclusters forming low- to high-mass protostars, among which there are a large number of Class 0 protostars (Hennemann et al. 2010).

T. Hill acknowledges support from the CEA/Marie Curie Eurotalents program. The SPIRE and PACS instruments were developed by a consortium of institutes which are as recognised in the aforementioned Herschel papers.

References

André P., Montmerle T., 1994, ApJ, 420, 837

André P., Ward-Thompson D., Barsony M., 2000, Protostars and Planets IV, p. 59

André et al. P., 2008, A&A, 490, L27

Beuther H., Schilke P., Menten K. M., Motte F., Sridharan T. K., Wyrowski F., 2002, ApJ, 566, 945

Bonte S., Andre P., Terebey S., Cabrit S., 1996, A&A, 311, 858

Bonte S. et al., 2010, A&A, 518, L85

Hennemann M. et al., 2010, A&A, 518, L84

Motte F., Bonte S., Schilke P., Schneider N., Menten K. M., Broguière D., 2007, A&A, 476, 1243

Motte F. et al., 2010, A&A, 518, L77

Phe R. L., Lada E. A., 1997, ApJ, 477, 176

Poulton C. J., Robitaille T. P., Greaves J. S., Bonnell I. A., Williams J. P., Heyer M. H., 2008, MNRAS, 384, 1249

Román-Zúñiga C. G., Elston R., Ferreira B., Lada E. A., 2008, ApJ, 672, 861

Schneider N. et al., 2010, A&A, 518, L83

Simon R., Rathborne J. M., Shah R. Y., Jackson J. M., Chambers E. T., 2006, ApJ, 653, 1325

PRELIMINARY WORK TO ALMA, HERSCHEL, SOFIA: SUBMILLIMETER WAVE SPECTROSCOPY OF COMPLEX ORGANIC MOLECULES

L. Margulès[1], M. Goubet[1], R. Motiyenko[1], S. Bailleux[1], T.R. Huet[1] and G. Wlodarczak[1]

Abstract. Laboratory analysis of the microwave and millimeter-wave spectra of potential interstellar molecules is a prerequisite for their subsequent identification by radioastronomical techniques. The spectral analysis is used to obtain spectroscopic parameters that are used in the assignment procedure of the laboratory spectra, as well as to predict with a high degree of precision the frequencies of transitions not measured in the laboratory.

Keywords: identification, data analysis, laboratory, observational, molecules, submillimeter

1 Isotopic species of a major weed : Methyl Formate

1.1 Introduction

This huge effort of gathering spectroscopic data is nowadays still pursued in order to prepare the future large sub-millimeter facilities like the ground-based ALMA (Atacama Large Millimeter Array) and the Herschel space observatory. It is expected that the high sensitivity and angular resolution reached by the instruments in these facilities combined with very precise spectroscopic analysis will provide accurate information about the formation of stars in the interstellar molecular clouds.

The astrophysical study of other molecular isotopologues of methyl formate is important for several reasons. First it gives access to the isotopic abundance in astronomical environments. Second it allows the astronomers to discriminate in their surveys the transition lines due to the isotopologues and eventually eliminate them to be able to discover new species. Indeed the upcoming ALMA and Herschel sub-mm facilities will provide large amounts of high precision ($\Delta\nu \leq$ 1MHz) spectroscopic data in the wavelength range down to 150μm (corresponding to 2 THz in frequency). The interferometric operation of ALMA, in addition, will provide a so far unprecedented spatial resolution and a sensitivity which reaches the limit of line confusion. Both HIFI/Herschel and ALMA focus on dense clouds with young stars and surrounding material that contain molecular species with numerous and strong transitions throughout the whole sub-mm region. Much of the line emission comes from known species, such as methyl formate and similarly complex molecules. Without spectral identifications, however, the resulting forest of spectral lines will seriously hinder the detection and analysis of new molecular and radical species. This problem is known as the 'Weeds and Grass problem'. For an optimal science exploitation of ALMA and Herschel it is necessary to cut down the weeds and to recognize the grass. Methyl formate and its isotopologues are classified as "weed, class I" species due to their abundance in observations. Third, the observation of isotopologues transitions is needed to derive correct column densities for abundant molecules exhibiting optically thick lines, which could be the case for methyl formate in some hot cores.

This is why we decided in Lille, to do the systematic studies of all the mono-istopic species of methy formate.

1.2 Experiment

All the isotopic species were measured from 2 to 660 GHz using different spectrometers. These new measurements were fitted together with those from the litterature. Rotational spectra in the 4-20 GHz spectral range

[1] Laboratoire PhLAM, CNRS UMR 8523, Université de Lille1, 59655 Villeneuve d'Ascq Cedex, France

were recorded using a molecular beam microwave Fourier transform spectrometer in Lille. The accuracy of frequency measurements is estimated to be better than 3 kHz. The rotational spectrum was studied in the range 8-80 GHz using the Oslo Stark spectrometer, the accuracy of the spectral measurements is about 0.1 MHz for isolated lines.

Concerning the millimeter-submilimeter wave measurements: in the frequency range 580-660 GHz a Russian Istok backward wave oscillator (BWO) is used. It is phase locked to a harmonic of Agilent E8257D synthesizer which provides in our design large-step (~30MHz) frequency control. High-resolution frequency scan is provided by tuning a reference source of BWOs PLL: HP 3325 synthesizer. In the lower frequency range (150-525 GHz), solid state frequency multipliers are used as a source of radiation. The frequency of the Agilent E8257D synthesizer is first multiplied by six and amplified with a Spacek active sextupler. Then we used passive Schottky multiplier (x2, x3, x5) from Virginia Diodes Inc. In order to minimize frequency determination errors, all the reference synthesizers are locked on a GPS signal. The detector is an InSb liquid He-cooled bolometer from Queen Mary College. In order to improve the sensitivity of the spectrometer the sources are frequency modulated at 10 kHz and lock-in detection with the second harmonic is used. The absorption cell is a stainless steel tube (6 cm diameter, 220 cm length), the pressure used during measurements is 2.6 Pa (26 bar).

We are replacing our old BWO's sources with a multiplier chain based on solid state sources. As shown in Fig. 1, these sources are more compact, easier to use, and we have a larger frequency coverage. We could increased the number of measured lines. The spectroscopic parameters are better determined, so the prediction we make are more reliable. The tests we did are very positive in the lower part of the range (150-525 GHz). Our project is now to increase the frequency of the chain up to 1 Thz.

1.3 Theoretical model

Like many others complex organic molecules, methyl format exhibits large amplitude motion. The assigment and analysis of the spectra is not obvious. Here, it is the internal rotation of the methyl group around the rest of the molecule. As the molecule is light and as the barrier to internal rotation is not so high ($V_3 \approx 389$ cm^{-1} for the normal species), the internal rotation splittings are relatively large, reach values up to a few MHz in the torsional ground state, and the transition frequencies are thus difficult to calculate with accuracy, especially at high J values, without appropriate theory.

We will not go too much into details about the theory in this paper. The description of the theory used could be find in (Carvajal et al. 2009; Margulès et al. 2009) respectively for the symmetric and asymmetric methyl rotor. The need of different theories could be seen in the Fig. 2. The potential energy function is a three fold potential in the case of symmetric CH_3 rotor. With a partial deuteration of the methyl group (CH_2D or CHD_2) this leads to an effective potential energy function which no longer displays threefold. The spectra observed will also be different.

Concerning the symmetric case, each rotational line is split into a doublet (characterized by the symmetry labels A and E). Concerning the asymmetric rotor, there are three lines: one due to the in-plane conformer, and two others due to the internal rotation splitting for the two equivalent out of plane conformers

1.4 Results

The studies about the isotopic species are finished. The results are publised for $H^{13}COOCH_3$, $HCOO^{13}CH_3$ (Carvajal et al. 2009), $DCOOCH_3$ (Margulès et al. 2010), and $HCOOCH_2D$ (Margulès et al. 2009) species. About the $HC^{18}OOCH_3$, $HCO^{18}OCH_3$ and $HCOOCHD_2$, the manuscript are in preparation. The theoretical models used reproduce very efficiently the measurements. Despite the fact that we could reach high quantum numbers values (J up to 70). The $H^{13}COOCH_3$, $HCOO^{13}CH_3$, and $DCOOCH_3$ were detected without ambiguity in ORION (B. Tercero, N. Marcelino and J. Cernicharo, CSIC-INTA, Madrid, SPain).

1.5 Conclusion

All the mono-subtitued isotopic species of a major weed were studied. Due to these new studies more than 500 lines were identified in Orion.

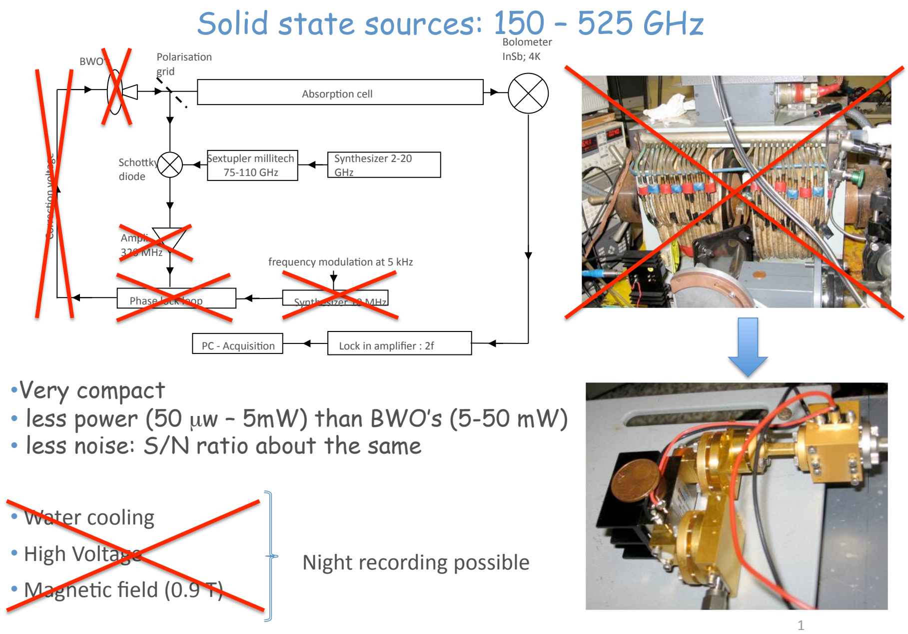

Fig. 1. Potential energy function of methyl formate

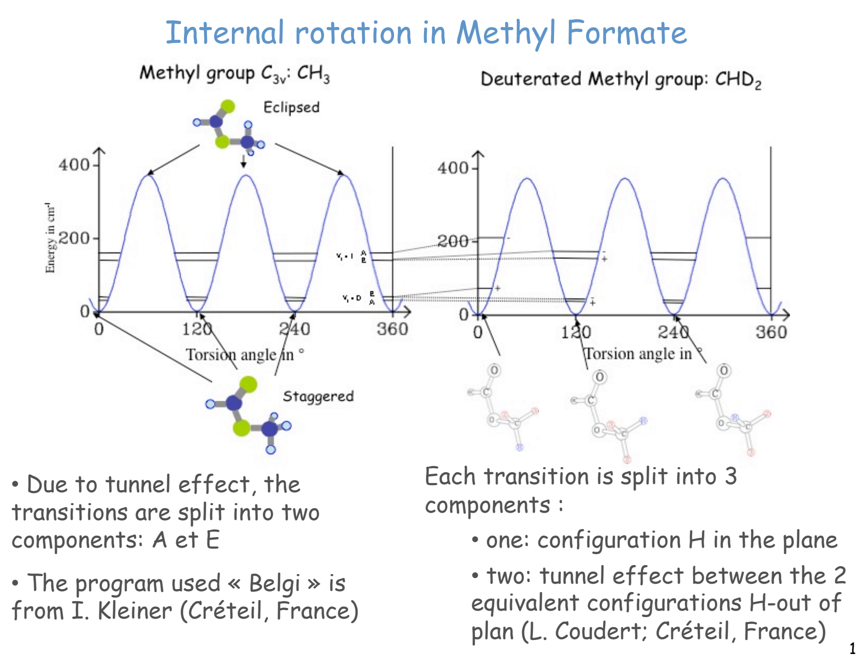

Fig. 2. New solid state submillimeter wave spectromter in Lille

2 Jet-Ailes

”Jet-AILES” is a consortium including researchers from the PhLAM at Lille 1 University (T. Huet and M. Goubet), the IPR at Rennes 1 University (R. Georges), the LADIR at Paris VI University (P. Asselin and P. Soulard) and the AILES beamline at the SOLEIL synchrotron (O. Pirali and P. Roy). The objective is to take advantage of the brightness of the synchrotron radiation source in the FIR region (Roy et al. 2006) to probe a supersonic expansion. There are two main interests of such a set-up. Firstly, molecules and molecular complexes prepared in a supersonic jet are observed in the gas phase at very low temperature (few tenths of Kelvin) in a very low density environment (of the order of 10^{-10} cm^{-3}). Secondly, Signals of large amplitude motions and typical signatures of COMs and hydrogen bond complexes lie in the FIR region. Technically the synchrotron radiation coming from the high resolution spectrometer of the AILES beamline (Bruker IFS125-HR) is transferred to the expansion chamber by bare gold mirrors. Then, a planar expansion is probed by a multi-reflections optical device called SORM (acronym for ”Systme Optique Rflexions Multiples”) (Gross et al. 1989). Finally, the IR beam is redirected to various detectors depending on the studied region (a Si bolometer in the FIR, a MCT photovoltaic detector in the MIR and a InSb detector in the NIR). To our knowledge, it is the unique supersonic jet device successfully coupled to a synchrotron radiation source in the FIR region. Although the set-up is still under optimization, some encouraging results have already been obtained. The Q branch of the out-of-plane bending mode of methylformate, centered at 331 cm^{-1}, has been observed. This detection highlights the good sensitivity of the experiment since the vaporization conditions were not optimal and its calculated intensity is only of about 20 km.mol^{-1}. A high resolution (2.5.10^{-3} cm^{-1}) spectrum of $(CO_2)_m$ ($m \leq 5$) complexes as well as a medium resolution (10^{-2} cm^{-1}) spectrum of CO_2–$(H_2O)_n$ ($n \leq 4$) complexes has been recorded for the first time in the ν_3 of CO_2 spectral range (2350-2360 cm^{-1}). Bands of the perturbed OH stretching mode (around 3550 cm^{-1}) of ether–H_2O complexes, ethers being $(CH_2)_2O$ and $(CH_3)_2O$, have been observed. According to the difficulty in forming small hydrated aggregates, these results show the good efficiency of the adiabatic expansion. Forthcoming runs of experiments will focused on the study of the FIR spectrum of glycolaldehyde and its hydrated complex as well as acetic acid and its dimer. Both molecules are stable isomers of methylformate and are also astrophysically relevant.

This work was supported by the Centre National dEtudes Spatiales (CNES) and the Programme National ”Physique et Chimie du Milieu Interstellaire”. This work was also done under the ANR-08-BLAN-0054 and ANR-08-BLAN-0225.

References

Carvajal, M., Margulès, L., Tercero, B. et al. 2009, A&A, 500, 1109

Margulès, L., Coudert, L.H., Møllendal, H. et al. 2009, J. Mol. Spectrosc., 254, 55

Margulès, L., Huet, T.R., Demaison, J. et al. 2010, ApJ, 714, 1120

Roy, P., Rouzires, M., Qi, & Z., Chubar, O. 2006, Infrared Physics & Technology, 49, 139

Gross, M., et al. 1989, Spectrochim. Acta, B44, 597

DUST IN MOLECULAR CLUMPS FROM THE HI-GAL SURVEY

D.J. Marshall[1], L.A. Montier[1], I. Ristorcelli[1], L. Anderson[2], J.P. Bernard[1] , C. Brunt[3], P. Martin[4], J. Mottram[3], D. Paradis[5] and J. Rodon[2]

Abstract. Dust properties in molecular clouds may give clues to the star formation process. By using recent observations of dust and gas emission, we seek to constrain the dust properties in discrete molecular clumps in the plane of the Milky Way. Using observations of the interstellar gas, we separate observed dust emission from the Hi-GAL survey, using the Herschel Space Observatory, into discrete line of sight components. A new dust spectral inversion technique is used where the dust emission is assumed to be a linear sum of a finite number of components, where the emission from each component follows a modified blackbody emission law. We are able to obtain the dust properties in over 60 molecular clumps in a 4 square degree zone centred on l=30º, b=0º. The dust in a few of the molecular clumps is found to be warmer than the dust associated with the atomic phase of the gas. This suggests that these clumps are not heated solely by the interstellar radiation field, but also contain an internal heating source suggesting the onset of an initial stage of star formation.

Keywords: ISM: clouds, galaxy: disk, infrared: ISM

1 Introduction

Hi-GAL (Molinari et al. 2010a) is a Key-Project of the Herschel Space Observatory that is using 343 hours observing time to carry out a 5 band photometric imaging survey at 70, 160, 250, 350 and 500 μm of a 2 degree wide strip of the Milky Way Galactic Plane in the longitude range $-60^o \leq l \leq 60^o$. The dust properties inferred from the dust emission provides us with crucial information on the physical state of the ISM. The conditions within molecular clouds are particularly interesting as these are the future sites of star formation. However, the derivation of dust properties within molecular clouds is not trivial as many line of sight components contribute to the dust emission. We present a new method to obtain the dust properties within individual molecular cores.

2 Data

We use Herschel SDP observations at l=30 and b=59 from the Hi-GAL survey (Molinari et al. 2010b), HI data from the VGPS (Stil et al. 2006) and ^{12}CO from the GRS (Jackson et al. 2006) along with a CO clump catalogue (Rathborne et al. 2009). All observations have been degraded to a common angular resolution of 1'.

3 Three dimensional inversion

3.1 Classic inversion methods

The dust emission associated with a molecular core can be difficult to identify in the Hi-GAL data. We use a catalogue of CO cores and proceed with an inversion technique to extract the dust properties of the cores.

Classical inversion methods (Giard et al. 1994; Sodroski et al. 1997; Paladini et al. 2007) seek to invert the full sky dust emission into a number of Galactocentric radii in order to study dust properties as a function of Galactic position and

[1] Universit de Toulouse, UPS, CESR, CNRS, UMR5187, 9 avenue du colonel Roche, F-31028 Toulouse cedex 4, France
[2] Laboratoire d'Astrophysique de Marseille (UMR 6110 CNRS & Universit de Provence), 38 rue F. Joliot-Curie, 13388 Marseille, Cedex 13, France
[3] University of Exeter, Physics Building, Stocker Road, Exeter EX4 4QL, UK
[4] Canadian Institute for Theoretical Astrophysics, University of Toronto, 60 St. George Street, Toronto, ON M5S 3H8, Canada
[5] Spitzer Science Center, California Institute of Technology, CALTECH, 1200 East California Boulevard, MC 220-6, Pasadena, CA 91125, USA

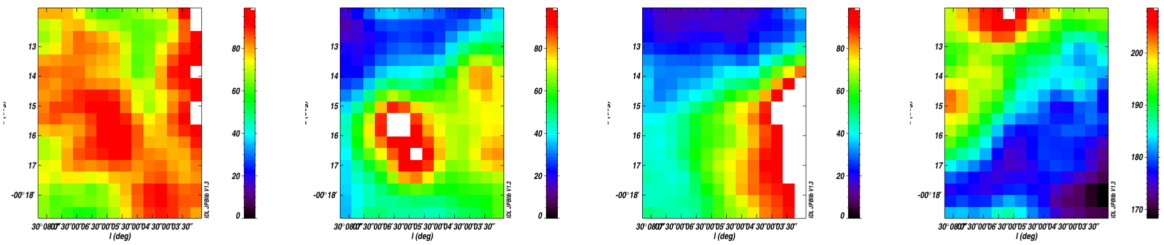

Fig. 1. Components used in the inversion for the CO core G029.89-00.26_c4. From left to right are: CO_{before}, CO_{clump}, CO_{after} and HI. Before and after refer to the radial velocity with respect to the clump and are not necessarily physically before and after the CO clump.

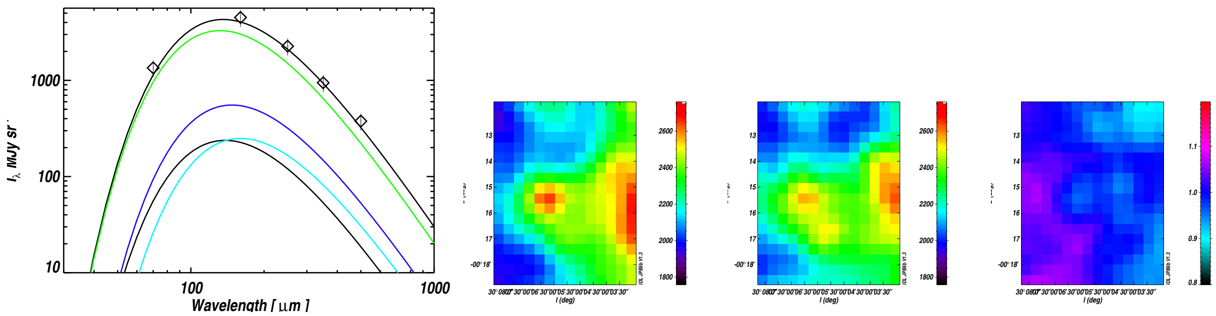

Fig. 2. Left: SEDs for the components presented in Fig.1 : HI(green), CO_{before}(black), CO_{clump}(dark blue) and CO_{before}(light blue). The total of all components (solid line) is compared to the average observed spectrum by Herschel (diamonds). **Right**: Original Hi-GAL 250 μm image, modelled observations and ratio of model/observations. It can be seen that the model accounts very well for the dust emission throughout the selected region.

in each phase of the interstellar gas (atomic, molecular and ionised). The radial velocity of the gas is used to separate the Galactic gas emission into a number of Galactocentric rings and then the dust emissivity for each ring in each gas phase is calculated. The problem being solved can be written, for any dust observation I_λ, as:

$$I_\lambda = \Sigma_{i=1}^{n} \left(\epsilon_{H_I}(R_i, \lambda) N_{H_I}^i + \epsilon_{H_2}(R_i, \lambda) N_{H_2}^i + \epsilon_{H_{II}}(R_i, \lambda) N_{H_{II}}^i \right) \tag{3.1}$$

where the sum is over a number (n) of Galactocentric rings (denoted by the index i) and where N_{H_I}, N_{H_2} and $N_{H_{II}}$ are the total gas column density of the gas observations in each ring i for the atomic, molecular and ionised components, respectively. The result of this inversion is the dust emissivity ϵ per ring and per phase of the gas.

3.2 Dust spectral inversion

For the problem at hand, namely to isolate the dust properties within individual molecular clumps, classic inversion methods are not adequate. Indeed there are a number of free parameters which require a large number of pixels in order to have more equations than unknowns. Using higher resolution data which is now becoming available in the plane of the Galaxy does help a great deal in reducing the minimum size of the regions which can be inverted. However when the inversion is applied band by band to small zones it is not uncommon for the inversion technique to provide mathematically good solutions which are not physical. A simple example would be negative emissivities which provide a good solution to Eq.3.1 but which obviously provides an unsatisfactory solution.

As such, we have proceeded with a slight twist on the classic inversion methods by assuming, apriori, that the spectral energy distribution (SED) of the different components are all dominated by dust in thermal equilibrium. We model such dust by a modified blackbody, where at a frequency ν and for a dust temperature T, the observed flux I_ν is given by:

$$I_\nu = B(\nu, T)\nu^{-\beta} \tag{3.2}$$

where β is the spectral index.

The inversion equation thus becomes:

$$I_{\nu_1..\nu_n} = \Sigma_{i=1}^{n} \epsilon_{H_I}(i) B(\nu_1..\nu_n, T_i)\nu^{-\beta_i} + \epsilon_{H_2}(i) B(\nu_1..\nu_n, T_i)\nu^{-\beta_i} \tag{3.3}$$

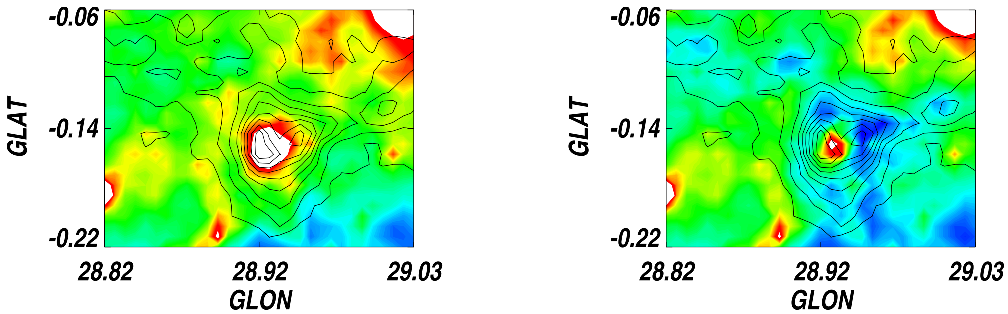

Fig. 3. Residue in the fitting procedure for clump G029.14-00.16_c3. **LEFT**: Original Hi-GAL 250 μm image with CO clump contours. **RIGHT**: Observed Hi-GAL image with CO clump contribution removed. Note that only the dust emission associated to the clump has been removed and not the dust associated with all CO.

thus there are three parameters per component and all frequencies are adjusted simultaneously. This reduces the degrees of freedom of the problem and ensures that the spectra obtained for the components is indeed a modified blackbody.

As an example, a set of components is shown in Fig.1. The second component from the left is the CO emission integrated over the FWHM velocity range of the CO clump from Rathborne et al. (2009). The component on either side of the clump are the CO emission integrated up to the clump and after the clump, respectively. The fourth component is the total line of sight HI gas.

The appropriate ϵ and T are solved for each component via the above inversion method, while keeping $\beta = 2$. The resulting SEDs from this inversion are shown on the left side of Fig.2, and where the total SED is compared to the observed average SED. It should be stressed that the SEDs for each pixel are being solved for simultaneously. Using the derived parameters it is possible to reconstruct the observed image using the gaseous templates. This is shown on the right side of Fig.2. The modelled dust emission (middle) is obtained by using each of the gaseous components and applying the appropriate derived ϵ, T pair and then summing all of the components. Any one of the bands can be recreated - here the SPIRE 250 μm band is reconstructed. The result is directly comparable to the original observations (left). On the right is the ratio between model and observations. It can be seen that in this case, the dust emission has been well accounted for.

4 Results and discussion

4.1 *Missing gas*

After having inverted the dust emission and reconstructed the modelled emission (e.g. Fig.2), there may be a significant fraction of the dust emission which is not accounted for. This may be due to dust associated with ionised gas, as we do not include components of this gas phase. Another possibility is that the CO being used is no longer tracing all the molecular gas as it has become optically thick, or the CO molecules are freezing out onto the dust grains. An interesting example of this excess residue is shown for the 250 μm band in Fig.3. A central core is left behind after the inversion.

4.2 *Hot cores*

The temperature of the dust in the clumps with respect to the diffuse component associated with the HI is an interesting point. One might suppose that the dust in the clump should be colder as it will be more shielded from the interstellar radiation field. However, when comparing the dust temperature in the clumps to the dust temperature associated with the HI (displayed in Fig.4), a number of the molecular cores are found to have significantly warmer dust than the HI component. This would seem to suggest an internal source of heating in the clumps, which may indicate that some stage of star formation has begun.

Interestingly, the 'hot' cores are not distributed randomly across the field, but are clustered near l=30.5, b=0.5. In Fig4 the CO clumps have been plotted on top of the dust temperature map of Bernard et al. (2010). The clumps with a higher temperature than the HI are represented by a circle and the rest are represented by squares. Many of the hotter cores are associated with colder spots in the temperature map. This is because the temperature map is a mean temperature of the entire line of sight whereas here we are separating the different line of sight contributions.

There are many candidate MYSO (from the RMSX survey, Mottram et al. 2010), plotted as red stars, surrounding the 'hot' cores. None of these coincide with a hot core so this may be the sign of triggered star formation. Follow up observations of the 'hot' cores will help to reveal their true identity.

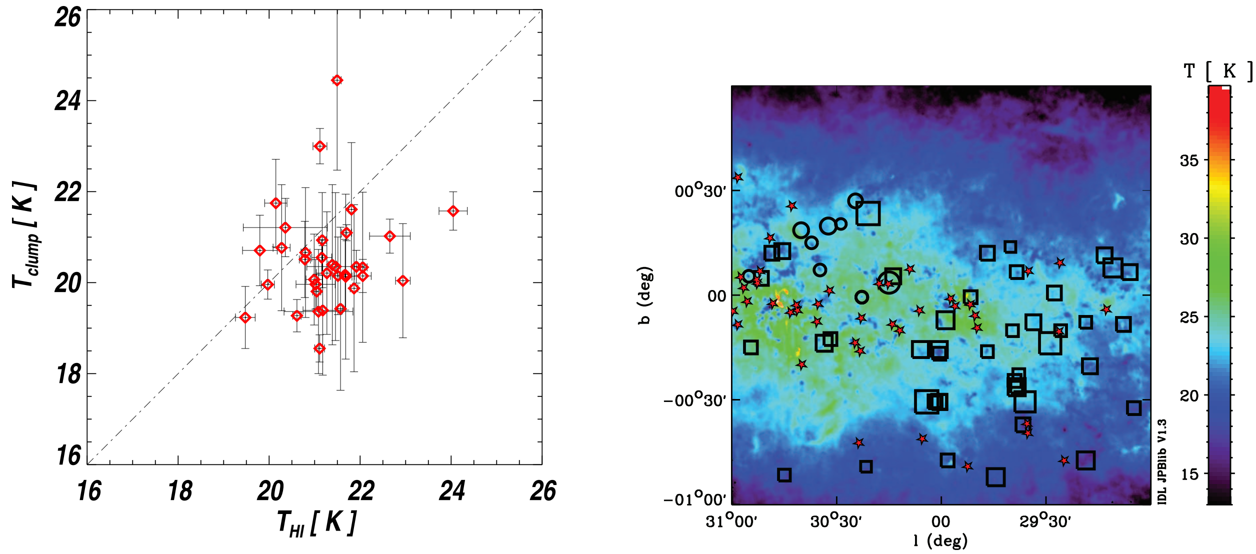

Fig. 4. Left: Dust temperature in the CO clumps vs the dust temperature in the HI gas. A number of the CO clumps show dust which is significantly hotter than the dust in the HI gas. Right: Distribution of the clumps with respect to a dust temperature map of the l=30 SDP field. The clumps with dust hotter than the HI are plotted as circles, the others as squares. Candidate MYSO from the Red MSX survey are plotted as red stars.

5 Conclusions

This new method for dust emission inversion can be applied to the entire Hi-GAL survey, where molecular and atomic observations exist. It will be possible to explore the dust properties in an unprecedented number of cores. Furthermore, this inversion singles out interesting cores for follow up study. A number of candidate hot molecular cores have already been identified as well as cores where the dust emissivity may be enhanced in their cores.

References

Bernard, J., Paradis, D., Marshall, D. J., et al. 2010, A&A, 518, L88

Giard, M., Lamarre, J. M., Pajot, F., & Serra, G. 1994, A&A, 286, 203

Jackson, J. M., Rathborne, J. M., Shah, R. Y., et al. 2006, ApJS, 163, 145

Molinari, S., Swinyard, B., Bally, J., et al. 2010a, A&A, 518, L100

Molinari, S., Swinyard, B., Bally, J., et al. 2010b, PASP, 122, 314

Mottram, J. C., Hoare, M. G., Lumsden, S. L., et al. 2010, A&A, 510, A89

Paladini, R., Montier, L., Giard, M., et al. 2007, A&A, 465, 839

Rathborne, J.M., Johnson, A.M., Jackson, J.M., Shah, R. Y., & Simon, R. 2009,ApJS, 182, 131

Roman-Duval, J., Jackson, J. M., Heyer, M., et al. 2009, ApJ, 699, 1153

Sodroski, T. J., Odegard, N., Arendt, R. G., et al. 1997, ApJ, 480, 173

Stepnik, B., Abergel, A., Bernard, J.-P., et al. 2003, A&A, 398, 551

Stil, J. M., Taylor, A. R., Dickey, J. M., et al. 2006, AJ, 132, 1158

DETECTION OF ATOMIC IRON AND OTHER METALS IN THE CIRCUMSTELLAR ENVELOPE OF IRC+10216

N. Mauron[1] and P.J. Huggins[2]

Abstract. We report the detection of several metals in atomic form in the gas phase of the envelope of IRC+10216, the archetype of evolved carbon-rich AGB stars. By observing with VLT-UVES a background star located behind the envelope at 35 arcsec from center, optical absorption lines of Na, K, Ca, Fe and Cr are revealed. It is the first time that circumstellar Fe is detected in a dusty envelope. The column densities of the circumstellar metals are derived. Then, the abundances of these metals are obtained with a model treating the photoionization of these elements in the outer envelope. The fraction of these metals present in the gas phase can be obtained, and a strong depletion of Fe and Ca onto grains is derived. The atomic abundances can also be compared to the abundance of metals carried by molecules. Our observations suggest that in the gas phase, the metals are much more abundant in atomic form than in molecular form. Our results are also consistent with metal depletions in planetary nebulae.

Keywords: AGB stars, mass-loss, circumstellar matter

1 Introduction

This research grew out of several earlier investigations on the colors and the structure of the envelope of IRC+10216 (Mauron et al. 2003; Mauron & Huggins 1999). UBV imaging of the envelope had been carried out to study the reflection of the Galactic light by the dust. A by-product of the photometry of field stars was the realization that a background star, located at about 1400 pc behind IRC+10216, could be used as a target for optical absorption line investigations. Its angular offset with respect to IRC+10216 is 35 arcsec, and it is a G-type star with V=16.0. The first investigations of this star were done with a VLT-UVES 2-hour exposure to search for diffuse bands (Kendall et al. 2002). No such bands were found, but we detected remarkable absorption lines of NaI and KI. Because IRC+10216 is at high galactic latitude, there is little interstellar matter on the line of sight, and in view of the central wavelength and characteristic profiles, these lines are of circumstellar origin. Then, it was realized that in principle, one could search for other elements in absorption in this spectrum, like CaII 3933-3968, CaI 4226, FeI 3820, and other resonance lines. In practice, the difficulty is that the star spectrum is not flat like for an OB star, but is solar-like with many photospheric absorption lines. We could resolve this problem because: 1) the spectrum of the target is very similar to the solar spectrum; and 2) its radial velocity is favourable: the circumstellar resonance lines are centered at -19.3 km s^{-1} (heliocentric center of mass velocity of IRC+10216), while the corresponding photospheric lines of the target are at +52 km/s. Therefore, the template spectrum of the Sun can be used and, after a small velocity shift, fitted on the target spectrum to search for any circumstellar feature. Eventually, we detected lines of KI 7665-7699, NaI 5890-5896 and 3300, CaI 4226, CaII 3933-3968, FeI 3860-3720 and several weak lines CrI in the blue, and measured their equivalent widths. We also searched for lines of AlI, TiI, TiII, MnI, and SrII, and put limits on their strengths.

2 Results and conclusions

From the profiles and equivalent widths, we determined the column densities of each element. It is then possible to interpret them quantitatively with the model of Glassgold & Huggins (1986) which includes photoionization

[1] CNRS & University of Montpellier, France
[2] New-York University, USA

and recombination of metal atoms and ions in an expanding envelope. The gas temperature and electronic density were taken from Cordiner et al. (2007). This model allows us to determine ratios like N(FeI) / N(FeII) on the line of sight, and correct our column densities for ionization to obtain abundances of each element, or upper limits.

The results are the following: Ca and Fe are depleted in the circumstellar gas phase, i.e. only about 5/1000 of Fe is in gas, and only 3/1000 of Ca. For Na, K, and Cr, the fractions in gas are 20 percent, 4 percent and 2.5 percent respectively. These results suggest that most of the metallic elements are in dust, either through condensation or through adsorption. However, some of the elements, like Na, are only slightly depleted. We could also put useful limits to Ti and Mn: we find that their fractions in the gas phase are lower than 3.5 percent and 1.6 percent.

The abundances of these metals in atomic form can be compared to their abundances in molecular form. It appears that the latter are smaller by an order of magnitude. For example, NaCl and NaCN have been observed, and their summed relative abundance (with respect to the total number of Na nuclei) is 4/1000. This is much lower than the 20 percent mentioned above for atomic Na. The same is true for K (3/1000 in KCN, 4 percent in atoms and ions). Therefore, it is unlikely that the metallic atoms and ions that we observe have their origins in the photodissociation of metal-bearing molecules. More probably, the metal-bearing molecule formation is not complete.

It is also possible to compare the depletions in IRC+10216 to those found in the ionized region of NGC 7027, a carbon-rich planetary nebula. We find that iron and calcium are more depleted in the AGB envelope (5/1000 and 3/1000, for Fe and Ca resp.) than in NGC7027 (2 percent and 18 percent, respectively). In contrast, Na and K are more volatile elements with low depletions: 20 percent of Na and 4 percent of K are in the 10216 gas phase, while these elements are essentially not depleted in NGC 7027. This suggests the following evolutionary effects in the transition from AGB to PN: nearly complete evaporation of the volatile species Na and K, and partial erosion of more refractory species Ca, and possibly Fe.

3 Conclusions

In conclusion, our results directly constrain the condensation efficiency of metals in a carbon-rich circumstellar envelope and the mix of solid and gas phase metals returned by the star to the interstellar medium. The abundances of the uncondensed metal atoms that we observe are typically larger than the abundances of the metal-bearing molecules detected in the envelope. The metal atoms are therefore the major species in the gas phase and likely play a key role in the metal chemistry. More details can be found in Mauron & Huggins (2010).

References

Cordiner, M.A., et al. 2007, Molecules in Space and Laboratory, ed. J.L. Lemaire, and F. Combes

Glassgold A.E., Huggins, P.J. 1986, ApJ, 306, 605

Kendall, T.R., Mauron, N., McCombie, J., & Sarre, P.J. 2002, AA, 387, 624

Mauron, N., de Laverny, P., Lopez, B. 2003, AA, 401, 985

Mauron, N., Huggins, P.J. 1999, AA, 349, 203

Mauron, N., Huggins, P.J. 2010, AA, 513, A31

THE KINETIC DATABASE FOR ASTROCHEMISTRY

V. Wakelam[1] and The KIDA Team

Abstract. KIDA (for KInetic Database for Astrochemistry) is a project initiated by different communities in order to 1) improve the interaction between astrochemists and physico-chemists and 2) simplify the work of modeling the chemistry of astrophysical environments. Here astrophysical environments stand for the interstellar medium and planetary atmospheres. Both types of environments use similar chemical networks and the physico-chemists who work on the determination of reaction rate coefficients for both types of environment are the same.

Keywords: astrochemistry, interstellar medium, planetary atmospheres, kinetic data

1 Introduction

Modeling of chemical processes in the interstellar medium and in planetary atmospheres (hereafter referred to as astrophysical environments) share common difficulties, namely a lack of reference data for many processes and large uncertainty for those data which have been measured in the laboratory, in physical conditions generally not representative of the target environment. A permanent link between modelers and physicochemists appears therefore as a necessity for modelers to publicize their most urgent data needs and for physico-chemists to advertise new data. This is the best way to maintain prevent the use of inappropriate or obsolete data/extrapolations in chemical networks. KIDA is a project initiated by different communities in order to i) improve the interaction between astrochemists and physico-chemists and ii) simplify the work of modeling the chemistry of astrophysical environments.

2 Kinetic data

KIDA is designed to gather all the kinetic data that can be of interest for the chemical modeling of the interstellar medium and planetary atmospheres. At the moment, KIDA records nine types of reaction: direct cosmic-ray processes; photo-processes induced by cosmic-rays; photo-processes; bimolecular reactions and dissociative neutral attachment; charge exchange reactions; radiative associations; associative detachment; electronic (dissociative) recombination and attachment; third-body assisted association. The database provides the user with extensive information about the data (references, details on the methods to obtain the data, validity range of temperature, etc). Users inputs. KIDA is by design a collaborative project. The interface enables users to attach comments or new information to data already stored in KIDA, or to populate the database with new data. The reviewing of new data by a group of experts prior to publication in the database is a strong asset of KIDA. The experts. The role of the KIDA experts is to validate the addition of data from data providers and give recommendation about the rate coefficients to use in specific physical conditions. In most cases, when a recommendation is given, the details of the expertise can be seen in a data sheet provided on the reaction page. Recommendations can be of four types: (1) not recommended; (2) not rated; (3) valid; and (4) recommended value. Data outputs. Modelers can extract lists of reactions from KIDA, based on different search criteria. The lists are automatically commented to alert the user on reactions that might be problematic. Output formats should enable insertion in various chemistry codes without further processing by the user.

[1] Université de Bordeaux, Observatoire Aquitain des Sciences de l'Univers, 2 rue de l'Observatoire, BP 89, F-33271 Floirac Cedex, France - CNRS, UMR 5804, Laboratoire d'Astrophysique de Bordeaux, 2 rue de l'Observatoire, BP 89, F-33271 Floirac Cedex, France

3 Chemical networks

A second section of the database is an archive of chemical networks published by modelers. This feature should enable the sharing and intercomparison of models and ensure the traceability and reproducibility of models outputs.

4 Links with other projects

As an interdisciplinary project, KIDA is linked with other projects (Fig.1): Europlanet is a European network for planetary science, funded by the FP7. KIDA is part of the new databases constructed in this context. VAMDC is a Virtual Atomic and Molecular Data Centre, which aims at interfacing several databases. This project is funded by the FP7 and lead by M-L. Dubernet (Observatoire de Paris, France). E3ARTHs is a project funded by the European Research Council (Starting Grant), lead by F. Selsis (Bordeaux University, France) to build modeling tools for exo-planetary atmospheres. Simulations of the chemical composition of habitable planets will be done with KIDA. CATS is a set of tools in development for the optimized analysis of the future ALMA data. CATS is funded by Astronet and lead by P. Schilke (Max Plank Institute, Bonn). KIDA will be directly interfaced with the chemical models of CATS.

5 Conclusions

KIDA was built by and for astrochemists and physico-chemists. The KIDA website is online since may 2010 (`http://kida.obs.u-bordeaux1.fr`). Anyone can register to KIDA, submit and download data. More details about the kinetic data and the spirit of KIDA can be found in a publication recently accepted to Space Science Reviews Wakelam (2011) (`http://kida.obs.u-bordeaux1.fr/uploads/documents/issi-database.pdf`).

Fig. 1. KIDA logo

We acknowledges the sources of funding: the Agence Nationale de la Recherche from France, the European Research Council, Astronet, the Seven Framework Program of the European Commission FP7, the Centre National de la Recherche Scientifique from France (french programs PCMI and PNP) and the french University of Bordeaux. The KIDA team also thanks the International Space Science Institute from Switzerland for financing the meetings of some of the team members.

References

Wakelam, V., Smith I.W.M., Herbst, E., Troe, J., Geppert, W., Linnartz, H., Oberg, K., Roueff, E., Aguùndez, M., Pernot, P., Cuppen, H. M., Loison, J. C., Talbi, D. 2011, accepted in Space Science Reviews

PNPS

Stellar physics

SF2A 2010
S. Boissier, M. Heydari-Malayeri, R. Samadi and D. Valls-Gabaud (eds)

STELLAR ROTATION IN THE HYADES AND PRAESEPE: GYROCHRONOLOGY AND BRAKING TIMESCALE

P. Delorme[1], A. Collier Cameron[2], L. Hebb[3], J. Rostron[4], T.A. Lister[5], A.J. Norton[6], D. Pollacco[7] and R.G. West[8]

Abstract. We present the results of photometric surveys for stellar rotation in the Hyades and in Praesepe, using data obtained as part of the SuperWASP exoplanetary transit-search programme. We determined accurate rotation periods for more than 120 sources whose cluster membership was confirmed by common proper motion and colour-magnitude fits to the clusters' isochrones. This allowed us to determine the effect of magnetic braking on a wide range of spectral types for expected ages of $\sim$ 600 Myr for the Hyades and Praesepe. Both clusters show a tight and nearly linear relation between $J - Ks$ colour and rotation period in the F,G and K spectral range. This confirms that loss of angular momentum was significant enough that stars with strongly different initial rotation rates have converged to the same rotation period for a given mass, by the age of Hyades and Praesepe. In the case of the Hyades our colour-period sequence extends well into the M dwarf regime and shows a steep increase in the scatter of the colour-period relation, with identification of numerous rapid rotators from $\sim$0.5 $M_\odot$ down to the lowest masses probed by our survey ($\sim$0.25 $M_\odot$). This provides crucial constraints on the rotational braking timescales and further clears the way to use gyrochronology as an accurate age measurement tool for main-sequence stars.

Keywords: stars: rotation; stars: open clusters; Hyades, Praesepe

1 Candidate selection

1.1 Observations

We determined stellar rotation rates using data from the SuperWASP camera array, located at the Observatorio del Roque de los Muchachos on La Palma, Canary Islands. With its 8 cameras, SuperWASP (described in detail in Pollacco et al. 2006) has a total field of view of 640 deg^2. This extremely wide field of view provides the ability to make repeated observations of areas of the sky as large as the full Hyades cluster, providing densely sampled photometric data. The corresponding fields were observed between 25 and 100 times per night on average, with typically 5 to 10 minutes between each 30s exposure. The data was reduced by the standard WASP pipeline, described in detail by Pollacco et al. (2006); Collier Cameron et al. (2009, hereafter CC09). Each SuperWASP source is matched with NOMAD and Hipparcos data, providing high signal to noise photometry in the standard $BVJHK$ bands, proper motion as well as parallax when available. SuperWASP photometric data itself is only used to derive the rotation period from the photometric rotational modulation of the signal due to stellar spots.

[1] Laboratoire d'Astrophysique de Grenoble, Observatoire de Grenoble, BP 53, 38041 Grenoble Cedex 9, France. e-mail: `philippe.delorme@obs.ujf-grenoble.fr`
[2] University of St Andrews
[3] Vanderbilt University
[4] University of St Andrews
[5] Las Cumbres Observatory
[6] The Open University
[7] Queen's University
[8] University of Leicester

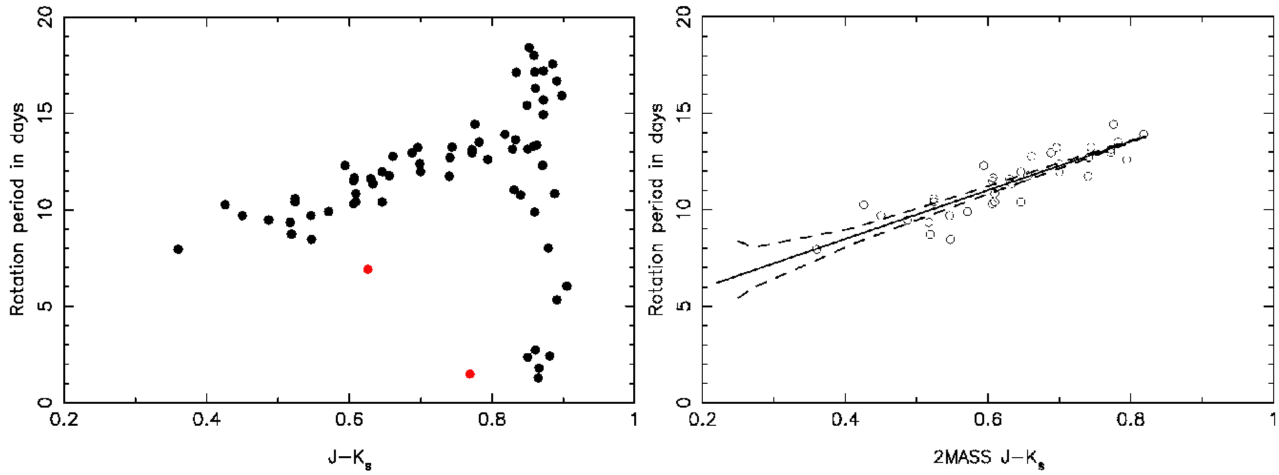

Fig. 1. *Left:* $J - K_s$ colour-period plot of all selected Hyades members. The 2 outliers highlighted in red are known spectroscopic binaries. *Right :* $J - K_s$ colour-period plot of Hyades members that are used to derive the colour-period relation (black line). The dashed lines represent the expected spread in periods caused by differential rotation (see CC09 for details).

1.2 Light curve analysis

We used the generalised Lomb-Scargle periodogram formulation of Zechmeister & Kürster (2009) to look for quasi-sinusoidal light curve modulation in all stars in the fields. The details of the frequency analysis and the optimised False Alarm Probability (FAP) calculation we used are described by CC09. We looked for signal modulation due to rotation periods between 1.1 days and 20 days and selected only signals with a FAP<0.05.

1.3 Cluster membership

Each source with a detected period was examinated to determine whether or not it was a cluster member. A cluster membership probability was derived by comparing the proper motion and the apparent magnitudes of each candidate to those expected for Hyades or Praesepe members. This was carried out assuming Gaussian distribution of both population and weighted by the relative number of stars in the field and in the cluster to take into account that there are many more field stars than cluster stars in our sample. As in CC09, we extended this definition of cluster membership to include information on the apparent magnitude and the same rationale was applied to determine whether the colour and apparent magnitude of each source was closer to the field distribution or to the colour magnitude relation expected for each cluster. After a visual examination of all selected variable cluster members, we retained 70 Hyades members and 52 Praesepe members with a reliable measured rotation period.

1.4 Period-colour relation

To derive a clean period-colour relation, we selected the reliable candidates which sit in the $0.2 < J - K_s < 0.82$ colour range, where Hyades and Praesepe members appear to follow a smooth colour-relation. Since higher order fits did not improve the correlation, we used a simple linear fit to find the period-colour relation.

The relations derived are the following :

$$P_{Hyades} = 11.401 + 12.652\,(J - K_s - 0.631) \quad (1.1)$$

$$P_{Praesepe} = 9.648 + 12.124\,(J - K_s - 0.528) \quad (1.2)$$

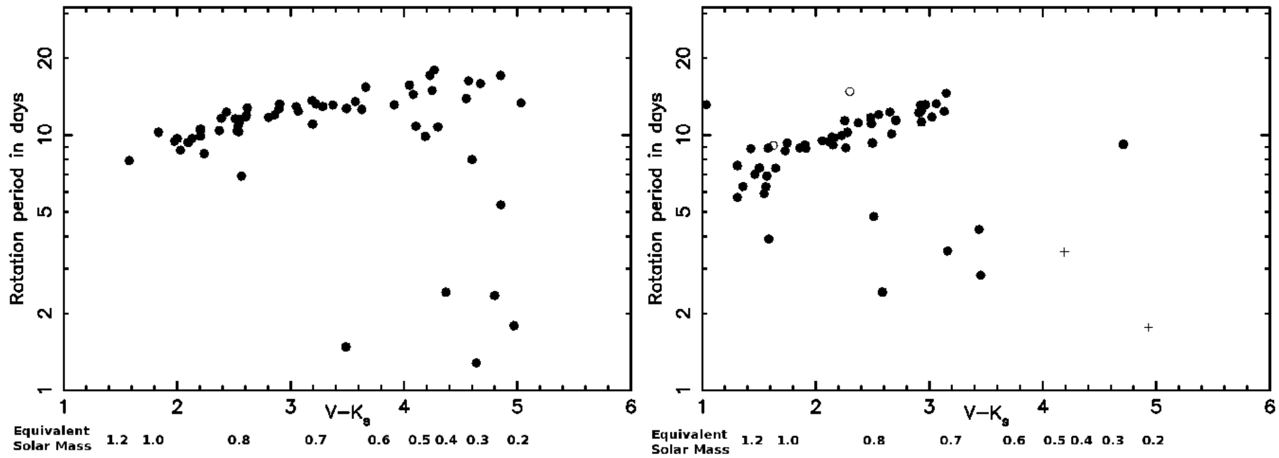

Fig. 2. *Left:* Log of rotation period-$V - K_s$ colour plot of objects identified as Hyades members. *Right:* Same for Praesepe members. The crosses are 2 Praesepe objects from Scholz & Eislöffel (2007). Full circles are objects with a membership probability above 0.85, hollow circles are objects with a membership probability above 0.5.

2 Comparison between the Hyades and Praesepe: age and braking.

2.1 Braking timescales

Deriving stellar rotation braking timescales over a wide range of stellar masses, and especially in the M-dwarf regime where stars become entirely convective, puts strong constraints on theoretical models of magnetic field/rotational braking. As seen in Fig. 1, our survey determined rotation periods of M-dwarf stars both in the Hyades and Praesepe. However, these figures use the $J - K_s$ colour that tend to saturate for the reddest stars ($J - K_s$ only varies from 0.82 to 0.86 when the stellar mass varies from 0.6 $M_\odot$ to 0.25 $M_\odot$) that are the most interesting to explore rotational braking timescales. Fig. 2, shows the logarithmic rotation period as a function of the $V - K_s$ colour.

For the Hyades this breakdown is obvious because we have a good sampling at low masses: the cluster is nearby and its M-dwarfs are bright enough to derive reliable rotation periods. It seems to occur for $V - K_s >$ 4.0 (i.e. masses $\lesssim 0.5 M_\odot$), with the apparition of numerous fast rotators as well as a significant increase of the slow rotators scattering around the colour-period relation. The Hyades data therefore demonstrate that FGK and M stars above 0.5 $M_\odot$ have converged toward a simple colour-period relation by Hyades age, about 625 Myr.

The breakdown of the period-colour relation is less clear-cut for Praesepe because this cluster is farther away and the survey detection limit is in the late K/early M-dwarf range. It is however clear that objects redder than $V - K_s$=3.2 (or below 0.65 $M_\odot$) have converged toward a the colour-period relation by Praesepe age and it appears that Praesepe stars rotation rate have clearly converged for masses higher than 0.65 $M_\odot$ and have not converged in the mid/late M dwarf range (see Scholz & Eislöffel 2007). The colour-period relation breakdown in Praesepe must then occur in between, in the 0.65–0.4 $M_\odot$ mass range.

2.2 Relative age of Praesepe compared to the Hyades

Barnes (2003) coined the word "gyrochronology" to describe the technique that permits us to derive the age of a star when its rotation period is known. This assumes, following the early study of Skumanich (1972), that the rotation period of stars of given mass converges after a certain time to the same value independently of the initial conditions and that their rotation period then evolves following a simple $t^{-1/2}$ spindown law. The data presented here confirms that Hyades and Praesepe stars with $0.2 < J - K_s < 0.82$ have already converged toward a well defined colour-rotation period relation.

Any star in this colour range can have its period, and thus its age, derived with respect to an age/rotation

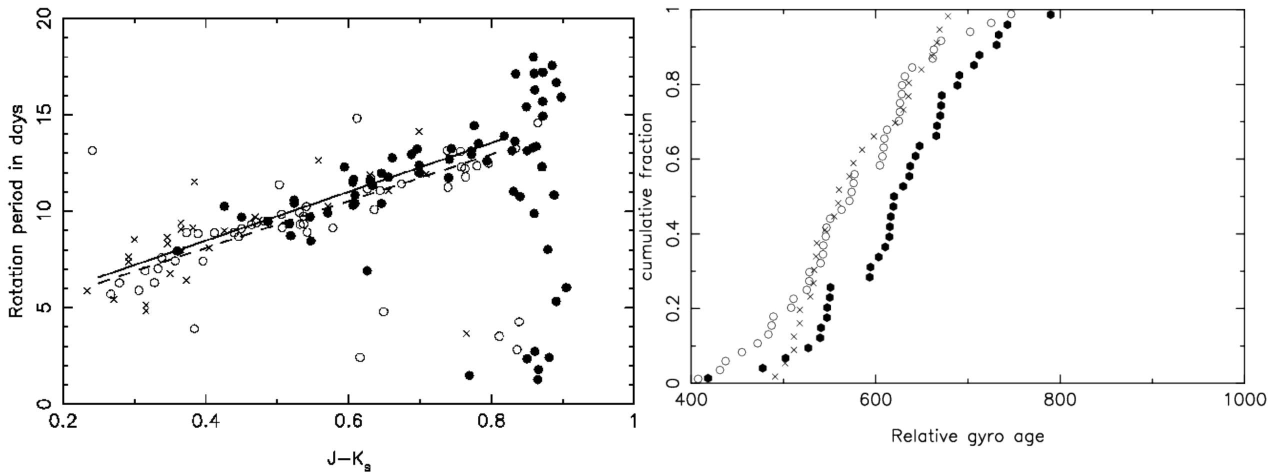

Fig. 3. *Left:* $J - K_s$ colour-period plot of Hyades (black circles for SWASP objects and crosses for R87-95 objects) and Praesepe members (hollow circle). The period-colour relation are also shown, black line for the Hyades and dashed line for Praesepe. *Right:* Cumulative fraction plot of Hyades members ages (black circles), Praesepe members ages (hollow circles) and Coma members ages (crosses)

reference. To derive Praesepe's age relatively to the Hyades, we anchored the age-period relation assuming a mean Hyades age of 625 Myr (P98). We derived the age of Praesepe stars by computing the rotation period they would have if they had the age of Hyades and comparing this hypothetical period to the measured one we were able to compute an age for each slow rotator in Praesepe as follows:

$$t \ = \ 625 \left(\frac{P}{11.401 \ + \ 12.652\,(J - K - 0.631)} \right)^2 \ . \tag{2.1}$$

The age of Praesepe was derived from the averaged ages of these 43 stars, and stands at 578±12 Myr. This absolute value needs to be taken with caution since the uncertainties on the actual Hyades age, that we use to anchor the relation, are much bigger (± 50 Myr Perryman et al. 1998) than our errors. However, the relative measurements are much more reliable and a Student T-test on these $0.2 < J - K_s < 0.82$ samples showed that there is only 1.5% likelihood they derive from the same age distribution. Using our new SWASP data for the Hyades and CC09 data for the Coma cluster, we also derived an improved estimation of Coma's age: 584±10 Myr.

2.3 *Individual stars age distribution relative to Hyades age*

Fig. 3 shows the ages of individual stars in our sample for each of these 3 clusters. The large scatter in ages observed on this figure is likely not real but most of it is probably due to the scatter of the colour-period-age relation at about 600 Myr. This scatter is 85 Myr for the Hyades, 85 Myr for Praesepe and 61 Myr for Coma (respectively 76 Myr, 77 Myr and 55 Myr with the improved gyrochronological relation), showing that at these ages the simple gyrochronology spin-down law from Skumanich (1972) enables age measurements for individual stars with a better than 15% accuracy, improving as the square root of the number of cluster members when measuring the age of a cluster. If this relation is properly calibrated for field stars, gyrochronology should provide even more accurate age measurements for individual field stars because the scatter of the colour-period-age relation is expected to decrease with age.

3 Conclusion

We presented an analysis of SWASP data that found more than 120 rotational variables that we identified as Hyades and Praesepe cluster members. This allowed us to put strong constraints on the rotational braking time by showing that the periods of all FGK and M single stars down to $\sim$0.5 M$_\odot$ in our sample have converged toward a relatively tight period-colour relation by Hyades age. We used gyrochronological relations and the period-colour relations derived for each cluster to accurately measure their relative ages, assuming the Hyades are 625

Myr old. This yields ages of 578±12 Myr for Praesepe and 584±10 Myr for Coma and gives a statistically strong statement that Praesepe and the Hyades are not exactly co-eval and that the former is 47±17 Myr younger than the latter.

References

Barnes, S. A. 2003, ApJ, 586, 464

Collier Cameron, A., Davidson, V. A., Hebb, L., et al. 2009, MNRAS, 400, 451

Perryman, M. A. C., Brown, A. G. A., Lebreton, Y., et al. 1998, A&A, 331, 81

Pollacco, D., Skillen, I., Cameron, A., et al. 2006, ApSS, 304, 253

Scholz, A. & Eislöffel, J. 2007, MNRAS, 381, 1638

Skumanich, A. 1972, ApJ, 171, 565

Zechmeister, M. & Kürster, M. 2009, A&A, 496, 577

SF2A 2010
S. Boissier, M. Heydari-Malayeri, R. Samadi and D. Valls-Gabaud (eds)

SHOCK INDUCED POLARIZED HYDROGEN EMISSION LINES IN OMICRON CETI

N. Fabas[1], A. Lèbre[1] and D. Gillet[2]

Abstract. We have performed a spectropolarimetric survey of the variable Mira star omicron Ceti along three pulsation cycles. We present those new data collected with the Narval instrument mounted on the Télescope Bernard Lyot in Pic du Midi, France. We have detected time variable polarimetric signatures (on QUV Stokes spectra) associated with Balmer hydrogen emission lines supposed to be formed behind the front of a shock wave propagating throughout the stellar atmosphere. We associate the linear polarization of Balmer emission lines in Mira stars to the presence and the structure of the radiative shock wave.

Keywords: shocks, Mira, AGB, spectropolarimetry, line: formation

1 Introduction

Mira stars are cool, evolved (AGB) and late-type variable stars. They are radially pulsating stars with a long period of brightness variation (from 150 to 1000 days), time during which the luminosity might change up to 2.5 visual magnitudes on average. A cool and very extended stellar atmosphere is present, surrounded with a circumstellar envelope. Their low surface temperature ($< 3000K$) allows the existence of molecules inducing a strong absorption on the stellar spectrum.
Another interesting feature is the presence of strong emissions on the Balmer hydrogen lines. These lines are observed during about 80% of the luminosity period. Radiative hypersonic shock waves propagating periodically throughout the atmosphere are believed to be at the origin of those emissions. The structure of those shocks ar complex (Fadeyev & Gillet 2004). The front of the shock is a region where strong gradients of temperature, pressure and velocity are formed due to the strength of the shock. Just behind the front, there is a region of strong ionization and, further behind, the gas gets cooler and recombines. The radiation thus produced propagates and may interact with the region before the front, called the precursor.
Omicron Ceti (also known as Mira) is the prototype of the Mira stars. It is an oxygen-rich (M type) star with a period of 332 days and a visual magnitude varying from 3 to 10. It is also a binary star.

2 Observations with Narval

With the Narval spectropolarimeter mounted on the TBL at the Pic du Midi, we did a survey of omicron Ceti during three pulsation cycles (from 2007 to 2010, see Fig.1). The wavelength coverage runs from 369 to 1048 nm in a single exposure, with a resolving power of about 65000. The outputs are the four Stokes parameters (intensity I, linear polarization Q and U, circular polarization V). We have detected a strong polarization in hydrogen Balmer lines at maximum light. Hereafter, we present two spectropolarimetric observations, one around minimum light ($\phi = 1.67$) and one around maximum light ($\phi = 3.05$) in Hδ (Fig.2).

Around the minimum light, the shock wave is high in the stellar atmosphere and weakening. It is therefore not strong enough to produce the emission lines as illustrated in our observation at $\phi = 1.67$. There is no signature in any of the Stokes parameter. Around the maximum light, the shock wave is just emerging from the photosphere and accelerating. The hydrogen Balmer emission is very intense as we can see in our observation at phase $\phi = 3.05$ and this emission seems to be polarized because of the signatures detected on the other Stokes parameters (especially U). On the Q-U graph, the linear polarization is all along the U-axis.

[1] GRAAL - UMR 5024 - Université Montpellier II/CNRS France
[2] Observatoire de Haute-Provence - USR 2207 - OAMP/CNRS France

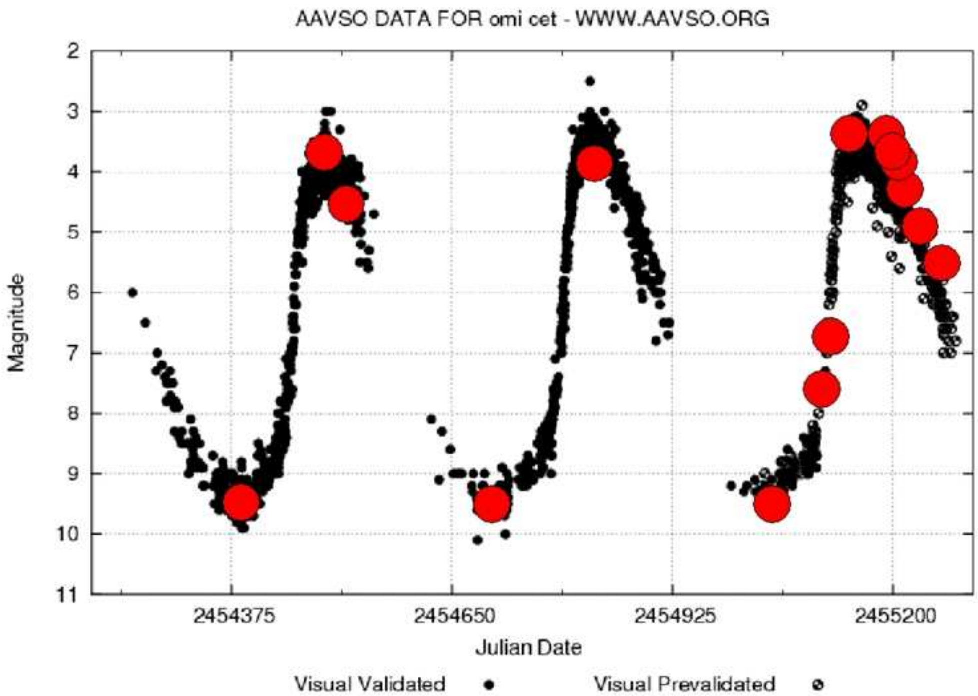

Fig. 1. Light curve of omicron Ceti (from AAVSO) on the three cycles of the survey. Each red circle is one spectropolarimetric observation. The three maxima are set at phases $\phi = 1.00$, $\phi = 2.00$ and $\phi = 3.00$ consecutively

3 Main results

We confirm, in the Hδ line, the high linear polarization already reported by McLean & Coyne (1978) in Hβ for o Cet at its 1977 maximum of luminosity. Besides, our work on the aforementioned survey allowed us to see that the linear polarization in the Balmer lines appears to be time variable and null at the minimum light. We think that this emission, supposedly formed in the recombination part of the shock wave, is also locally polarized in this shock. Behind its front, hydrogen atoms are ionized. Turbulence generated by the shock into these charged particles might create a magnetic field and therefore polarization.

We acknowledge with thanks the variable stars observations of the AAVSO International Database contributed by observers worldwide and used in this research. We also acknowledge financial support from the "Programme National de Physique Stellaire" (PNPS) of CNRS/INSU, France.

References

Fadeyev, Y. & Gillet, D. 2004, A&A, 420, 423

McLean, I.S. & Coyne, G.V. 1978, ApJ, 226, 145

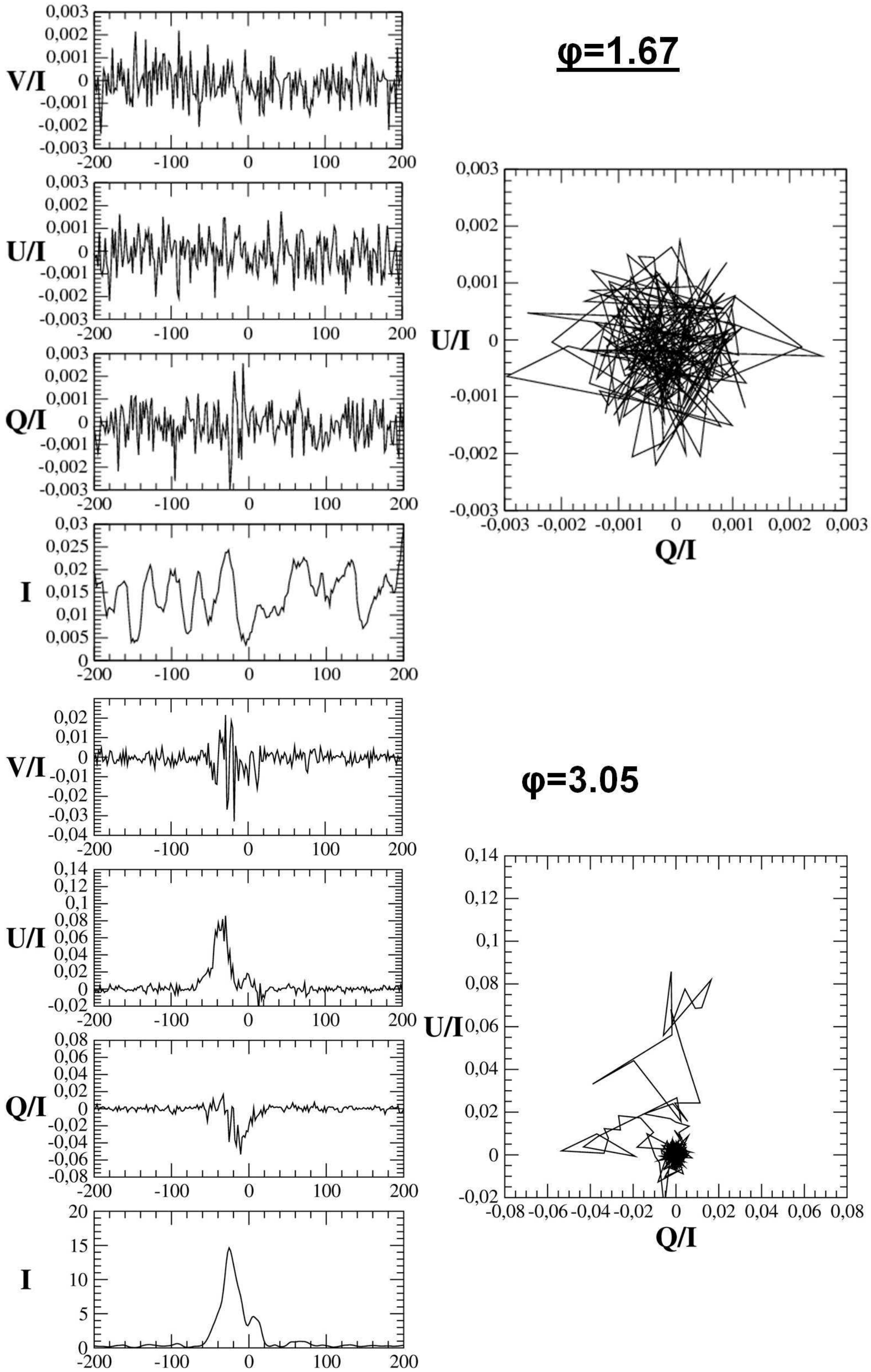

Fig. 2. Two spectropolarimetric observations of o Ceti around minimum light ($\phi = 1.67$) and maximum light ($\phi = 3.05$). For each phase, we have a series of spectra for the 4 Stokes parameters (abscissa is stellar rest frame velocity in km s^{-1}) and also a graph showing U against Q in order to visualise the direction of linear polarization.

THERMOHALINE INSTABILITY AND ROTATION-INDUCED MIXING IN LOW- AND INTERMEDIATE-MASS STARS

N. Lagarde[1] and C. Charbonnel [1, 2]

Abstract. Thermohaline mixing was recently identified as the dominating process that governs the photospheric composition of low-mass bright giant stars (Charbonnel & Zahn 2007a). Here we present the predictions of our stellar models computed with the code STAREVOL, taking into account this mechanism together with rotational mixing. We compare the predictions for the surface abundances with recent observations in evolved stars, and discuss the corresponding ^{3}He yields in the context of Galactic chemical evolution.

Keywords: hydrodynamics, instabilities, stars: abundances, evolution, rotation, Galaxy: abundances

1 Introduction

At all stages of their evolution, low- and intermediate-mass stars (LIMS) exhibit the signatures of complex physical processes that require challenging modelling beyond canonical (or standard) stellar theory (by canonical we refer to the modelling of non-rotating, non-magnetic stars, in which convection is the only mechanism that drives mixing in stellar interiors). Charbonnel & Zahn (2007, hereafter CZ07) identified thermohaline mixing as the process that governs the surface abundances of LIMS evolving on the upper end of the red giant branch (RGB). In these stars, this double-diffusive instability is induced by the mean molecular weight inversion created by the $^3He(^3He, 2p)^4He$ reaction in the radiative layers between the convective envelope and the hydrogen burning shell (Eggleton et al. 2006). Here we focuss on the case of LIMS of solar-metallicity. We discuss the cumulated impact of thermohaline and rotation-induced mixings on the surface abundances, based on models computed with the code STAREVOL (see e.g. Decressin et al. 2009). Details on the assumptions and computations can be found in Charbonnel & Lagarde (2010), together with a more complete comparison with observations in Galactic open clusters.

2 Models and results

In order to quantify precisely the impact of each transport process at the various evolutionary phases, we have computed models with the following assumptions: (1) Standard models (no mixing mechanism other than convection); (2) Models including thermohaline mixing only (rotation velocity V=0); (3) Models including thermohaline mixing and rotation-induced processes for different initial rotation velocities.

For the turbulent diffusivity produced by the thermohaline instablity, we use the prescription advocated by CZ07 based on Ulrich (1972) arguments for the aspect ratio α (length/width) of the salt fingers as supported by laboratory experiments (Krishnamurti 2003) and including Kippenhahn et al. (1980) extended expression for the case of a non-perfect gas. For the treatment of rotation-induced mixing we proceed as follows. Solid-body rotation is assumed when the star arrives on the zero age main sequence (ZAMS). Typical initial (i.e., ZAMS) rotation velocities are chosen depending on the stellar mass based on observed rotation distributions in young open clusters (Gaigé 1993). Surface braking by a magnetic torque is applied for stars with an effective temperature on the ZAMS lower than 6900 K that have relatively a thick convective envelope as discussed in Talon & Charbonnel (1998); the adopted braking law follows the description of Kawaler (1988). From the ZAMS on, the evolution of the internal angular momentum profile is accounted for with the complete formalism developed by Zahn (1992) and Maeder & Zahn (1998) that takes into account advection by meridional circulation and diffusion by shear turbulence.

[1] Geneva Observatory, University of Geneva, Chemin des Maillettes 51, 1290 Versoix, Switzerland
[2] LATT, CNRS UMR 5572, Toulouse University, 14, av. E.Belin, 31400 Toulouse, France

2.1 Models predictions for $^{12}C/^{13}C$

In figure 1, we present observations of carbon isotopic ratio in evolved stars belonging to different Galactic open clusters, as a function of cluster's turn off mass. The data are compared with our theoritical predictions at solar metallicity. For low-mass stars ($M < 1.7M_{\odot}$), thermohaline mixing on the RGB appears to be the main mecanism explaining the low-carbon isotopic ratios observed. On the other hand, rotation-induced mixing is found to change the stellar structure so that in the mass range between $\sim$ 1.5 and 2.2 $M_{\odot}$ the thermohaline instability occurs earlier on the red giant branch than in non-rotating models. Finally, rotation accounts for the observed star-to-star abundance variations at a given evolutionary status, and is necessary to explain the features of CN-processed material in intermediate-mass stars.

2.2 Models predictions for Lithium on TP-AGB

In all the models that we have computed along the TP-AGB, thermohaline transport leads to non negligible fresh lithium production, as shown in figure 2. There we present the evolution of the surface lithium abundance N(Li) as a function of effective temperature and bolometric magnitude for TP-AGB models of 1.25 and 2.0$M_{\odot}$ stars. Theoritical predictions are compared with observations in the sample of low-mass oxygen-rich AGB variables belonging to the Galactic disk studied by Uttenthaler & Lebzelter (2010). Let us note that despite this strong Li production at that phase, the total stellar Li yields remain negative.

2.3 Models predictions for ^{3}He

In figure 3, we present the evolution of ^{3}He mass fraction at the surface of 1$M_{\odot}$ model at solar metallicity in the standard case and in the case with thermohaline mixing (black solid and red dotted lines respectively). Thermohaline mixing induces a strong decrease of ^{3}He at the bump luminosity, and the mass fraction of ^{3}He at the AGB tip is strongly reduced when thermohaline mixing is accounted for compared to the standard predictions. As a consequence, the overal ^{3}He yields are also strongly affected, as shown in 4. As will be discussed elsewhere (Lagarde et al., in preparation), this helps reconciling the theoretical Galactic evolution of ^{3}He with observations of this element in Galactic HII regions (i.e Balser et al. 1994, 1999; Bania et al. 1997, 2002).

3 Conclusions

An inversion of molecular weight created by the $^{3}He(^{3}He, 2p)^{4}He$ reaction is at the origin of thermohaline mixing in low- and intermediate-mass stars brighter than the luminosity of the bump on the RGB (see e.g. CZ07). Models including the transport of chemical induced by this double-diffusive instability explain very well the observations of ^{12}C/^{13}C in low-mass stars in Galactic open clusters. Rotation-induced mixing allows us to explain the ^{12}C/^{13}C anomalies in giant stars with a mass higher than $1.7M_{\odot}$. Thermohaline mixing has also an effect during TP-AGB, where it allows the production of lithium, in agreement with observations in oxygen-rich variables. Finaly, it can help reconciling the theoretical ^{3}He yields with the behaviour of this primordial element in the Galaxy.

References

Balser, D. S., Bania, T. M., Brockway, C. J., Rood, R. T., & Wilson, T. L. 1994, ApJ, 430, 667

Balser, D. S., Bania, T. M., Rood, R. T., & Wilson, T. L. 1999, ApJ, 510, 759

Bania, T. M., Balser, D. S., Rood, R. T., Wilson, T. L., & Wilson, T. J. 1997, ApJS, 113, 353

Bania, T. M., Rood, R. T., & Balser, D. S. 2002, Nature, 415, 54

Charbonnel, C. & Lagarde, N. 2010, ArXiv e-prints

Charbonnel, C. & Zahn, J.-P. 2007, A&A, 467, L15

Decressin, T., Mathis, S., Palacios, A., et al. 2009, A&A , 495, 271

Eggleton, P. P., Dearborn, D. S. P., & Lattanzio, J. C. 2006, Science, 314, 1580

Gaigé, Y. 1993, A&A, 269, 267

Gilroy, K. K. 1989, ApJ, 347, 835

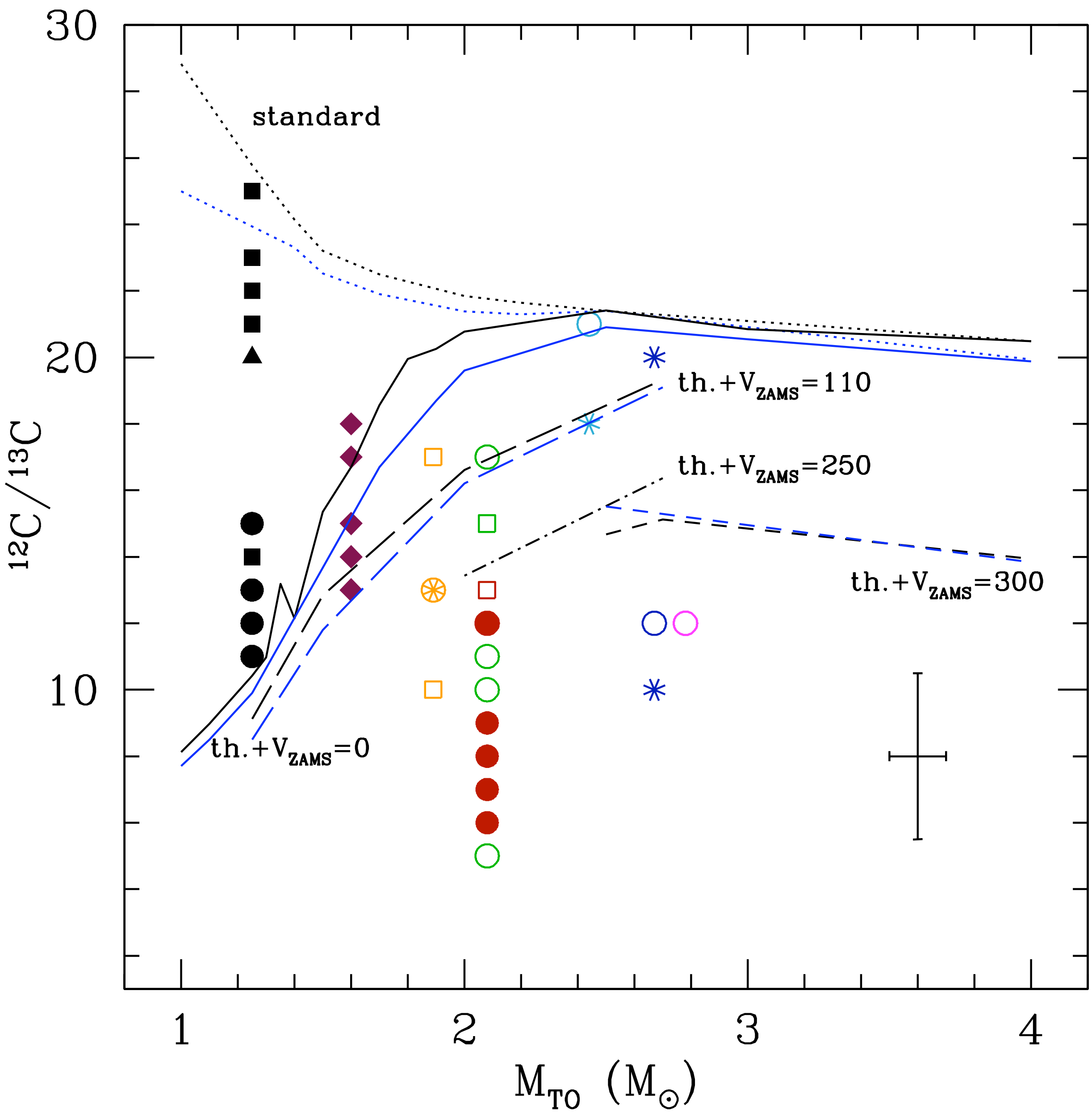

Fig. 1. Observations of $^{12}C/^{13}C$ in evolved stars of Galactic open clusters by Smiljanic et al. (2009, open cluster), Gilroy (1989), Gilroy & Brown (1991), and Mikolaitis et al. (2010) as a function of the turnoff mass of the corresponding host cluster. Squares, circles, and asteriscs are for RGB, clump, and early-AGB stars respectively, while diamonds are for stars from Gilroy (1989) sample with doubtful evolutionary status; triangles are for lower limits. A typical error bar is indicated. Theoretical predictions are shown at the tip of the RGB and after completion of the second dredge-up (black and blue lines respectively). Standard models (no thermohaline nor rotation-induced mixing) are shown as dotted lines, models with thermohaline mixing only (V_{ZAMS}=0) as solid lines, and models with thermohaline and rotation-induced mixing for different initial rotation velocities as indicated as long-dashed, dot-dashed, and dashed lines. Figure from Charbonnel & Lagarde (2010).

Gilroy, K. K. & Brown, J. A. 1991, ApJ, 371, 578

Kawaler, S. D. 1988, ApJ, 333, 236

Kippenhahn, R., Ruschenplatt, G., & Thomas, H.-C. 1980, A&A, 91, 175

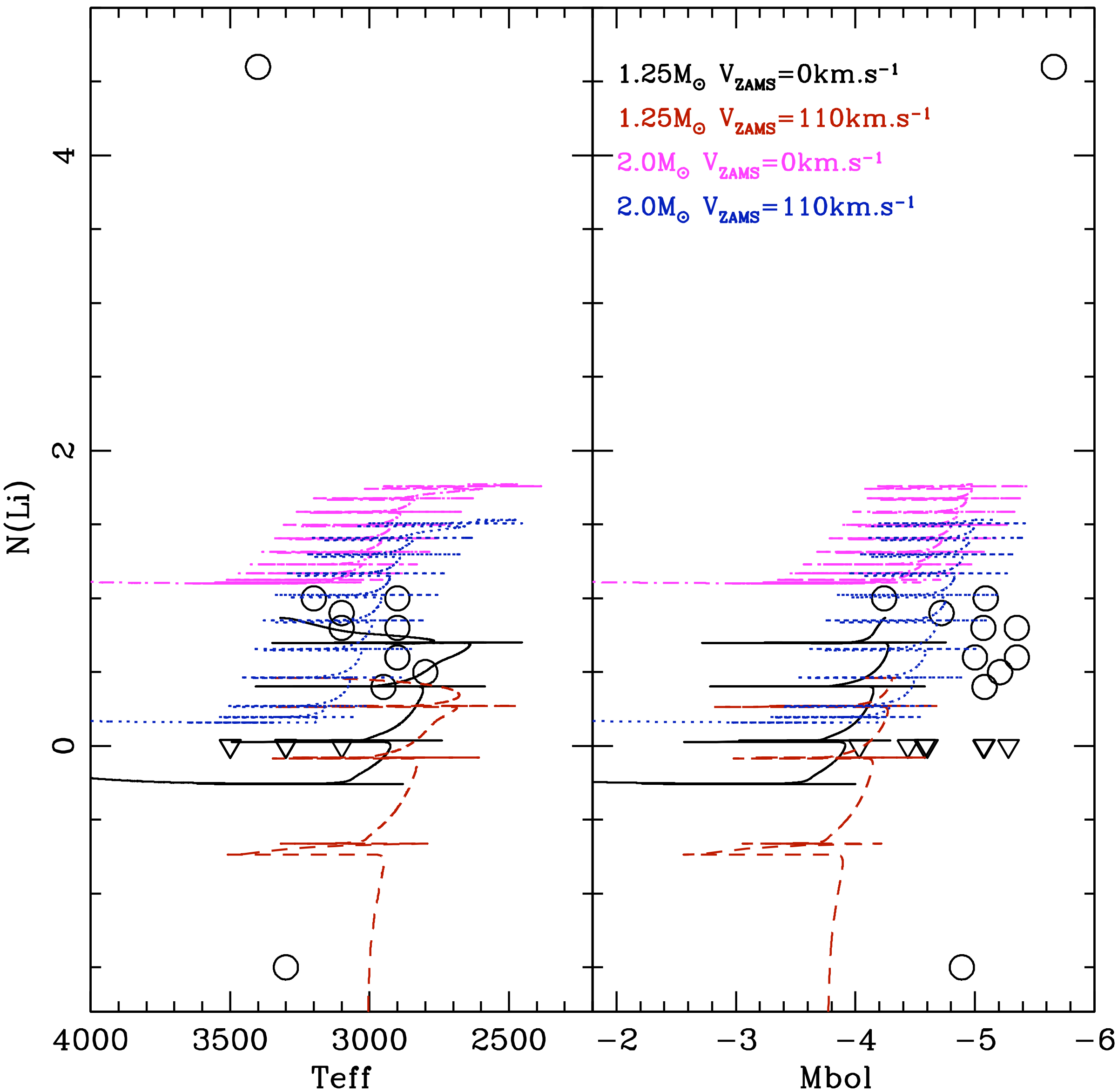

Fig. 2. Lithium observations in oxygen-rich variables belonging to the Galactic disk (Uttenthaler & Lebzelter 2010); circles and triangles are for abundance determinations and upper limits respectively) as a function of effective temperature and bolometric magnitude. Theoretical lithium evolution is shown from the early-AGB up to the end of the TP-AGB. Various lines correspond to predictions for stellar models of different masses computed without or with rotation as indicated, and with thermohaline mixing in all cases. Figure from Charbonnel & Lagarde (2010).

Krishnamurti, R. 2003, Journal of Fluid Mechanics, 483, 287

Maeder, A. & Zahn, J.-P. 1998, A&A, 334, 1000

Mikolaitis, Š., Tautvaišienė, G., Gratton, R., Bragaglia, A., & Carretta, E. 2010, MNRAS, 407, 1866

Smiljanic, R., Gauderon, R., North, P., et al. 2009, A&A, 502, 267

Talon, S. & Charbonnel, C. 1998, A&A, 335, 959

Ulrich, R. K. 1972, ApJ, 172, 165

Uttenthaler, S. & Lebzelter, T. 2010, A&A, 510, A62+

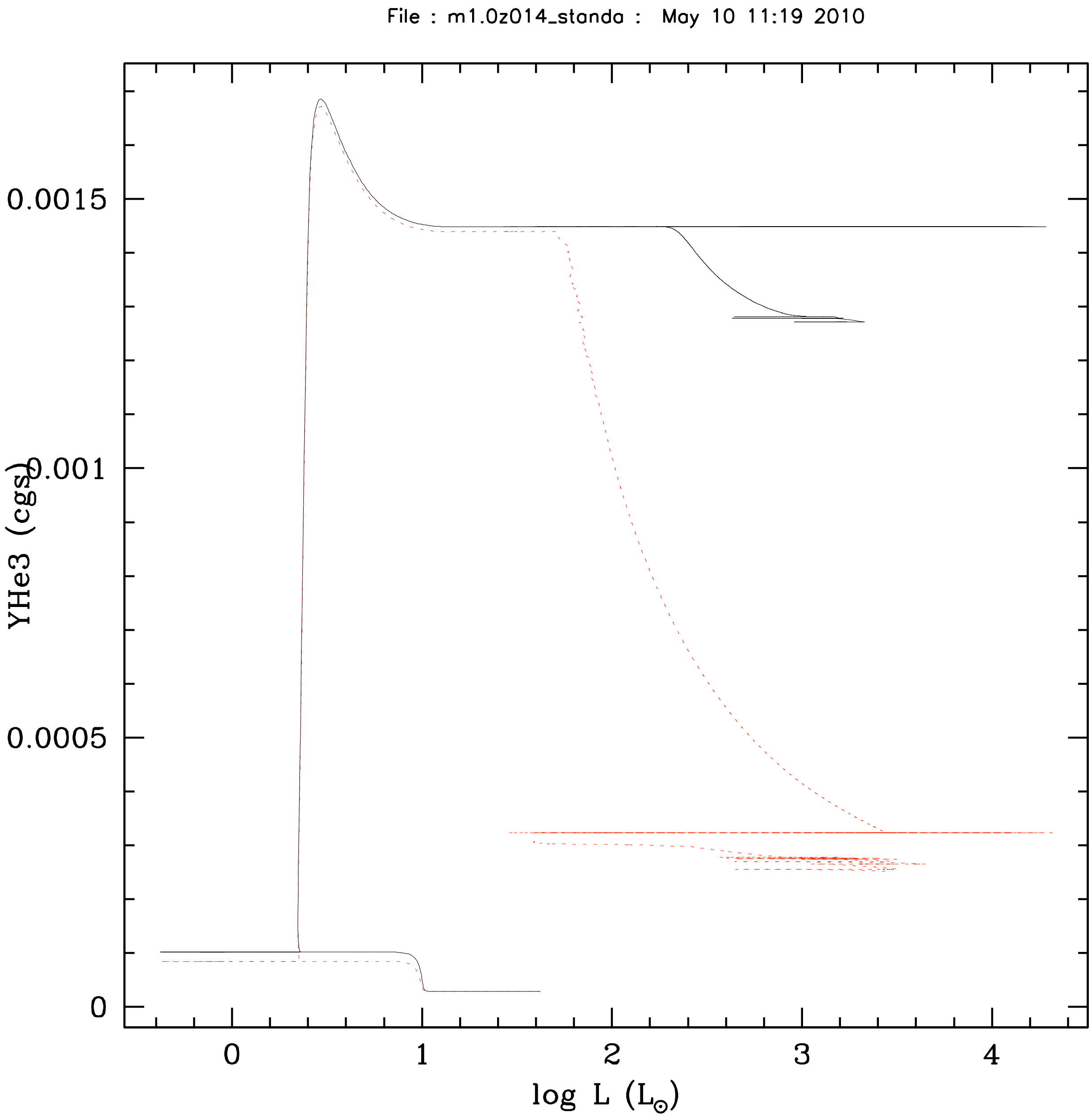

Fig. 3. Evolution of the surface abundance of ^{3}He (in mass fraction) from the pre-main sequence up to the AGB tip for $1M_\odot$ models at solar metallicity. The black solid line and the red dotted-line correspond to the standard and thermohaline cases respectively.

Zahn, J.-P. 1992, A&A, 265, 115

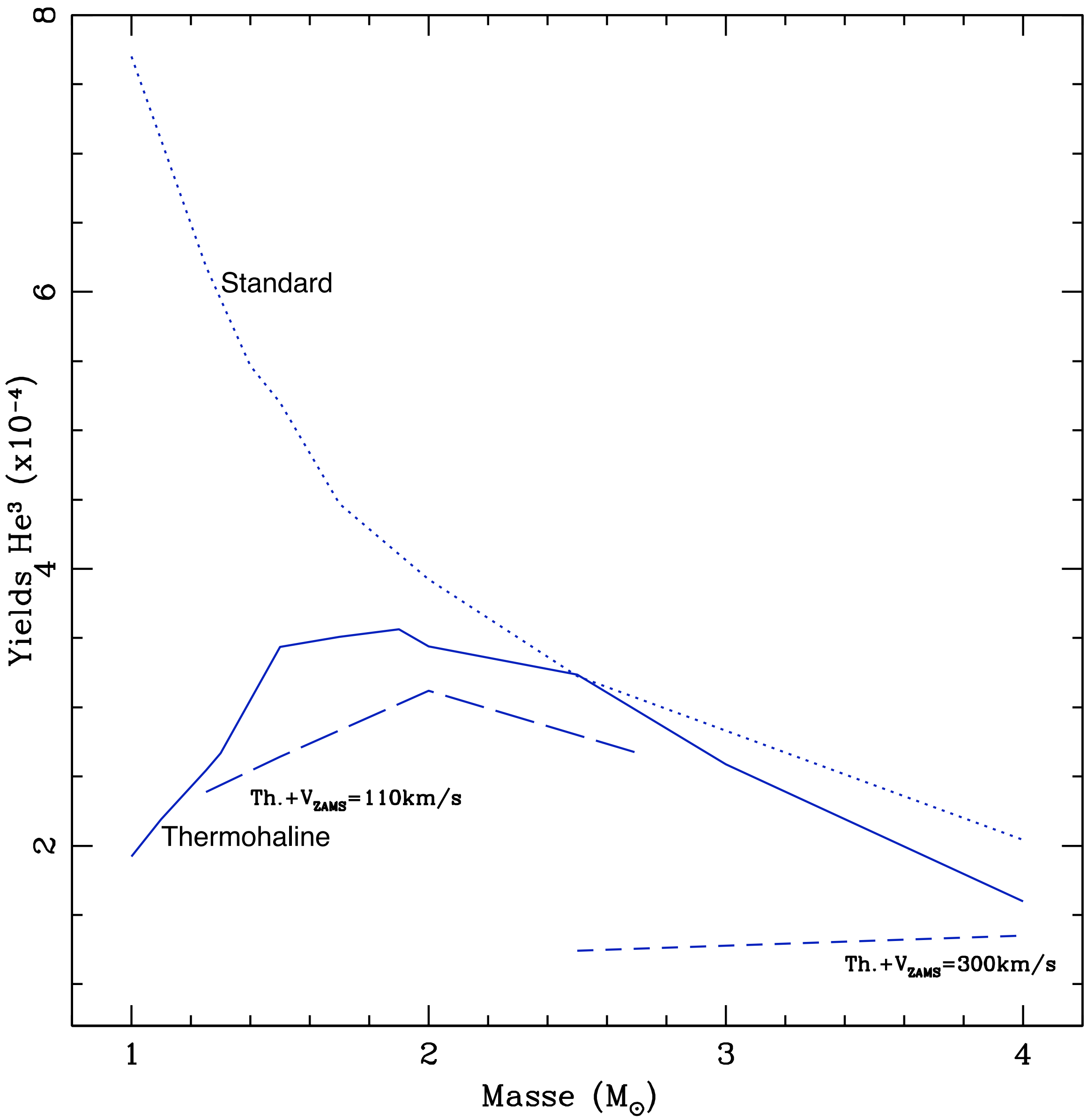

Fig. 4. Theoretical ^{3}He yields at solar metallicity as a function of initial stellar mass. The standard predictitions are shown by the dotted line; the thermohaline predictions are shown by the solid line; and the rotation+thermohaline models are shown as a long dashed lines for $V_{ZAMS} = 110km/s$ and as a short dashed lines for $V_{ZAMS} = 300km/s$. Figure from Lagarde et al. (in prep.)

SF2A 2010
S. Boissier, M. Heydari-Malayeri, R. Samadi and D. Valls-Gabaud (eds)

HYDRODYNAMICAL SIMULATIONS OF PINWHEEL NEBULA WR 104

A. Lamberts[1], S. Fromang[2] and G. Dubus[1]

Abstract. The interaction of stellar winds from two companion stars leads to the formation of a shocked structure. Several analytic solutions have been developpped to model this phenomenon. We compare our 2D and 3D hydrodynamical simulations to these results and highlight their shortcomings. Analytic solutions do not take orbital motion into account although this drastically changes the structure at large distances, turning it into a spiral. This is observed in Pinwheel Nebulae, binaries composed of a Wolf-Rayet star and an early-type star. Their infrared emission is due to dust whose origin is stil poorly constrained. We perform large scale 2D simulations of one particular system, WR 104. Including the orbital motion, we follow the flow up to a few steps of the spiral. This is made possible using adaptive mesh refinement. We determine the properties of the gas in the winds and confirm the flow in the spiral has a ballistic motion.

Keywords: stars: individual (WR104), stars: binaries, winds, circumstellar matter, hydrodynamics, methods: numerical

1 Introduction

Massive stars possess line-driven radiative winds. These winds are highly supersonic, with terminal velocities reaching more than 1000 km.s^{-1}. Their mass loss rates range from $10^{-8} M_{\odot}\mathrm{yr}^{-1}$ for O stars to $10^{-5} M_{\odot}$ yr^{-1} for Wolf-Rayet (WR) stars. Many massive stars belong to binary systems (Van der Hucht 2001) and form colliding wind binaries (CWB). The interaction of two winds from companion stars creates a double-shocked structure. For each wind there is a free unshocked component upstream of the shock and a dense, hot shocked wind downstream (Stevens et al. 1992). The shocked winds of both stars are separated by a contact discontinuity, where the normal velocity components equalize while pressure is continuous. If the two winds are identical, this surface is equidistant to both stars. If the winds have different momenta the shocks are bent towards the star with the weaker wind. The momentum ratio is given by

$$\eta = \frac{\dot{M}_1 v_{\infty 1}}{\dot{M}_2 v_{\infty 2}} \tag{1.1}$$

where the subscript 1 stands for the stronger wind, the subscript 2 for the weaker one. For $\eta \gg 1$ the weaker wind is very collimated and the whole structure looks like a cometary tail.

As a prototype of CWB, we consider WR 104, a system composed of an O-B star and a WC9 star. The WR wind is 500 times denser than the OB wind, which is very collimated. The resulting structure is a narrow, spiral structure (Harries et al. 2004). The system has a 245 days period, the separation a =2.34 AU, the orbit is very close to circular and the system is viewed almost pole-on. This system shows a beautiful example of Pinwheel Nebula in infrared (Tuthill et al. 2008). The step of the spiral is determined by the properties of the strong WR wind. Up to now large scale models have assumed ballistic motion of the shocked winds along an Archimedian spiral.

The infrared emission is due to the presence of dust in the WR wind, whose origin is still poorly constrained. The CWB certainly plays a role since dust emission is seen to occur preferentially at periastron in other systems. This suggests dust production (Marchenko & Moffat 2006) seems to be possible only in dense regions. As the

[1] Laboratoire d'Astrophysique de Grenoble, UMR 5571 CNRS, Université Joseph Fourier, BP 53, 38041 Grenoble, France
[2] Laboratoire AIM, CEA/DSM-CNRS-Université Paris Diderot, IRFU/Service dAstrophysique, CEA-Saclay F-91191 Gif-sur-Yvette, France

WR wind is very poor in hydrogen and dust is composed of carbon and hydrogen some mixing of the O-B star wind with the WR star wind probably occurs. Radiative aspects also seem to play a role, as the second step of the spiral seems to be in the shadow of the first one, shielding dust from UV radiation from the star. In this proceeding we report on hydrodynamical simulations of WR 104. We first compare our code to analytic solutions without orbital motions and highlight their limitations. Then we perform large scale 2D simulations of the Pinwheel nebula. This gives us quantitative estimates of the density and velocity structures of the winds.

2 Comparison to analytic models

Several authors have developed analytic solutions for CWB (see *e.g.* Gayley (2009) and references therein.). Almost all are based on the 'thin shell' hypothesis : thermal pressure can be neglected in the shocked winds so both shocks and the contact discontinuity are merged in one single layer. We compared our 2D and 3D adiabatic ($\gamma = 1.67$) simulations to the solution of Canto et al. (1996) assuming conservation of mass, momentum and angular momentum through the shell. We also compared to the solutions of Antokhin et al. (2004), assuming equality of momentum perpendicular to the shell . The results are shown in figure 1 for both the 2D and 3D case. We show the density map and overplot the two analytic solutions. In these simulations $\eta = 8$, the velocity from the stronger wind is 8 times higher than for the weaker wind, both mass loss rates are identical.

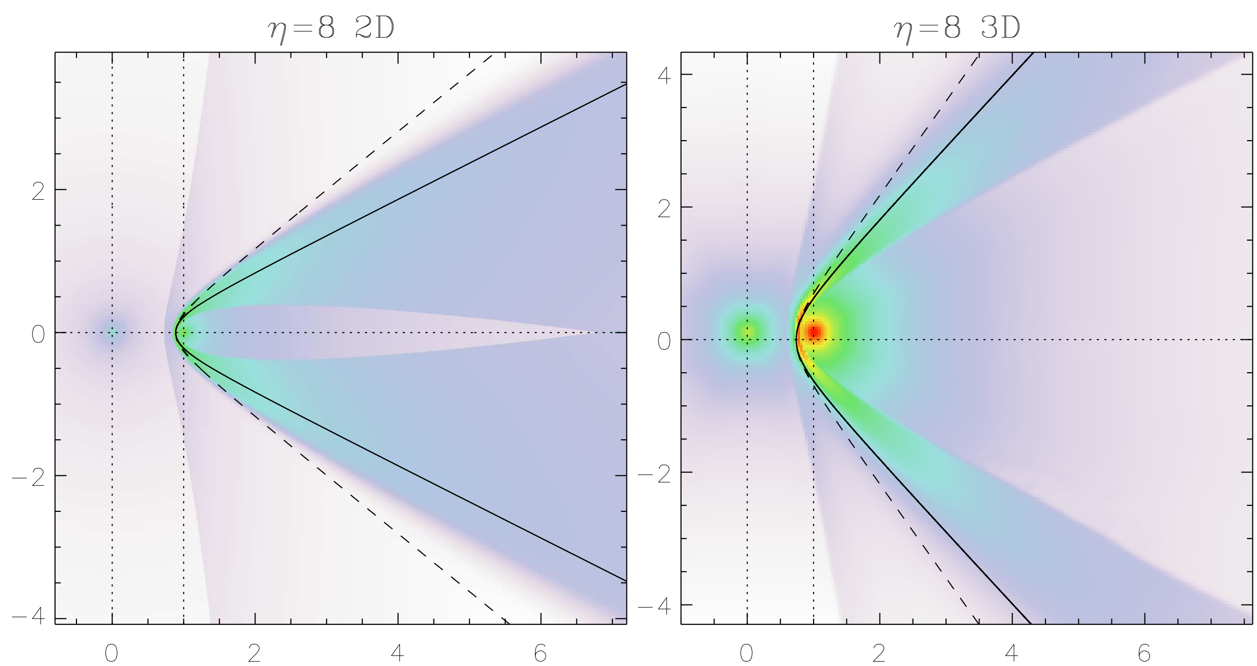

Fig. 1. Density in 2D (left panel) and 3D (right panel) for $\eta = 8$. The stars are located at the intersections of the dotted lines. The dashed line represents the solution from Canto et al. (1996), the solid line the solution from Antokhin et al. (2004). The length scale is the binary separation a.

One can clearly distinguish the two shocks and the contact discontinuity. The location of the contact discontinuity is approximately matched by the analytic solutions. Simulations with an isothermal equation of state ($\gamma = 1$) should yield solutions closer to the 'thin shell approximation'. As the shocked gas is allowed to cool, the two shocks are much closer to each other. In the left panel from figure 2 we can see both shocks and the contact discontinuity have merged in one single layer. The right panel shows the same simulation once the steady state is reached. The structure is dominated by the 'thin shell instability' and the shocks cannot clearly be distinguished anymore (Pittard 2009). High spatial resolution is required to allow its growth. This cannot be modelled with the analytic solutions. Moreover the analytic solutions do not account for the orbital motion and for effect of thermal pressure which pushes away the shocks. These effects can be properly modelled using hydrodynamical simulations.

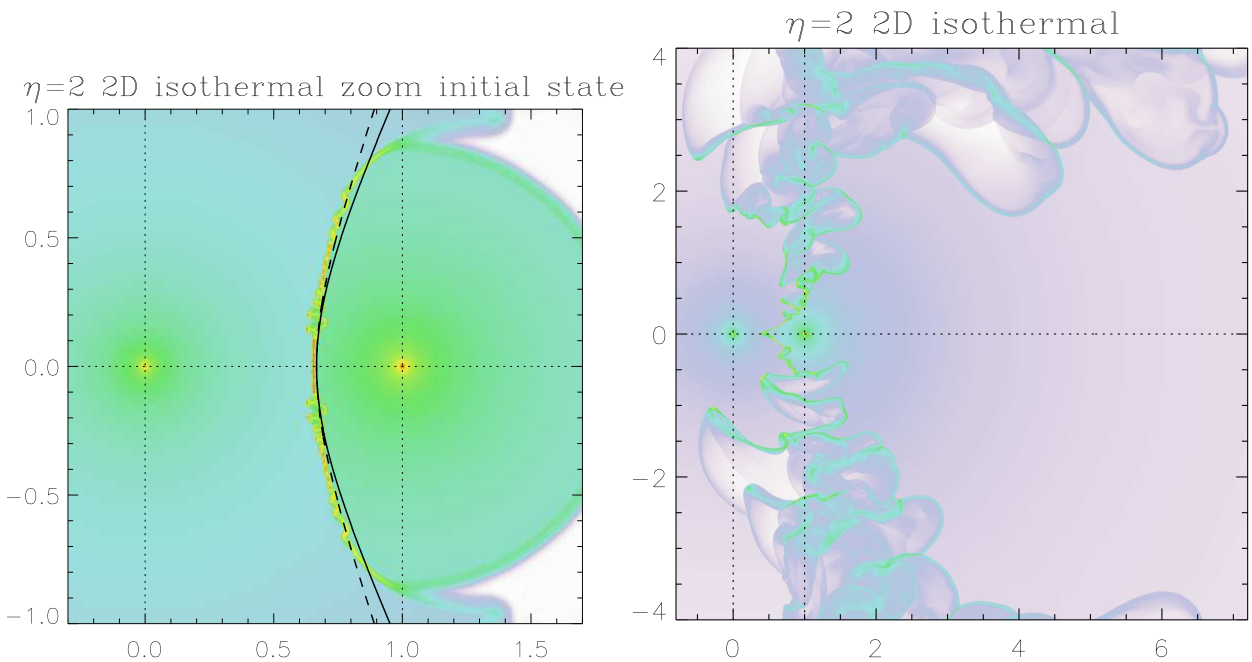

Fig. 2. Density for $\eta = 2$ in the isothermal case. Left panel : zoom on binary at the initial state. The analytic solutions are overplotted. Right panel : Density in the whole box in the steady state

3 The case of WR 104

3.1 Method

We use the code RAMSES (Teyssier 2002; Fromang et al. 2006), to solve the equations of hydrodynamics using a finite volume method. The Adattive Mesh Refinement (AMR) enables us to locally increase the spatial resolution according to the properties of the flow. We can properly resolve the shock formation and determine the large scale structure at reasonable computational cost. Indeed $\eta = 305$ in WR 104 so the shocks are very close to the O-B star. A proper modelling is thus very demanding. We use a method developed by Lemaster et al. (2007) to implement the winds.

We want to see at least one step of the spiral structure. The step S is determined by the velocity of the stronger WR wind and the orbital motion. One has $S/a \simeq 70$ (Harries et al. 2004) so we choose to take a box length of 200 a. We stress this involves a very high resolution close to the binary because we want to properly capture shock formation. Less resolution is needed to compute the large scale structure, so we gradually decrease it towards the edges of the computational domain.

3.2 Results

Here we present some initial investigations of the CWB structure in WR 104. We first made a 2D simulation with adiabatic winds. The density map and profiles are shown in figure 3. The different components of the wind can clearly be seen. Most of the gas is composed of the unshocked WR wind. We can see on the left panel its density decreases $\propto r^{-1}$ as one expects in 2D. The densest zone is the shocked WR wind at both edges of the spiral. It also has a $\propto r^{-1}$ profile. The low density unshocked O-B wind is very collimated and cannot be distinguished ont the density map. The density in the shocked O-B wind at the center of the spiral is constant, confirming the hypothesis of ballistic motion. We overplot the analytic solution for the Archimedian spiral using a black solid line, it perfectly matches the results of the simulation.

While the present simulation uses an adiabatic equation of state, in reality the cooling timescale in the WR wind is much smaller than the dynamical timescale. This suggests an isothermal equation of state is more appropriate. We thus expect the presence of the thin shell instability. Mixing between both winds might be more efficient in this case. This could explain the chemical composition of the dust. To show this instability, high resolution is required throughout the whole simulation zone. The density map is shown on figure 4. The

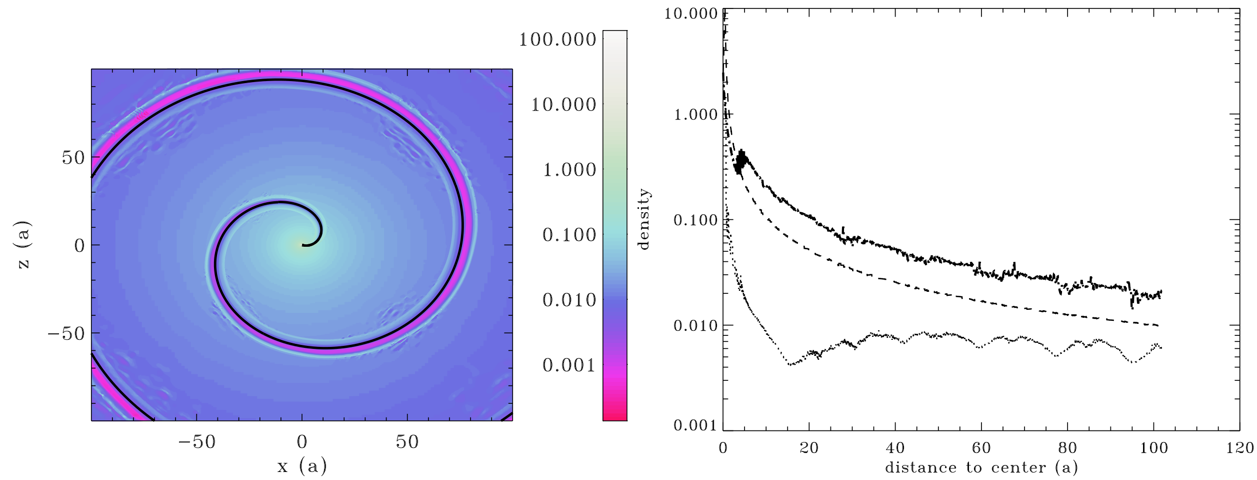

Fig. 3. Left panel: Density map of WR 104. The theoretical Archimedian spiral is overplotted. Left panel : Density profile of WR 104. The dashed line represents the density in the unshocked WR wind, the solid line represents the density in the shocked WR wind and the dotted line represents the density in the shocked O-B wind

structure is similar to the adiabatic case. No instabilities can be seen in the spiral, which is confirmed in the zoomed image on the right panel. This can have a physical or numerical reason. The extreme confinement of the O-B star wind could prevent the developpement of the instability. Orbital motion could also have a stabilizing effect. It also adds more numerical diffusion and an even higher resolution might be needed to correctly model the instability.

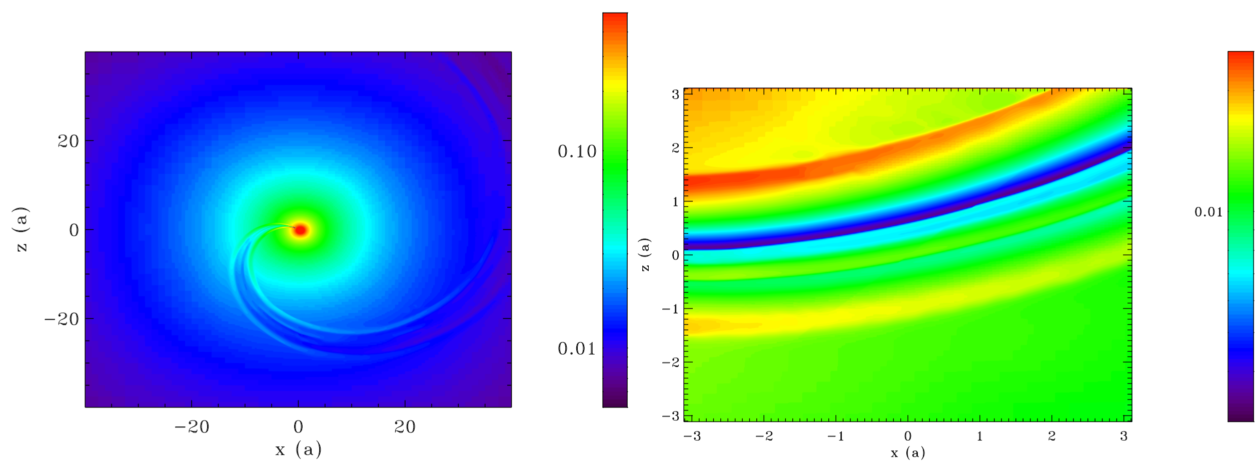

Fig. 4. Density map (left panel)in the isothermal case. Zoom on the spiral (right panel).

4 Summary and conclusions

Properly modelling colliding wind binaries requires numerical simulations. Although analytic solutions are good approximations, only simulations can properly take into account the effects of thermal pressure and orbital motion. They might also capture possible dynamical instabilities in the flow. We presented a preliminary study of WR 104, a dust-producing binary. We performed 2D large scale simulations of the system, completely modeling one step of the spiral structure. This work confirms that motion along the spiral is ballistic. More analysis is necessary to put stronger constrains on dust formation. We will also make a deeper study of the thin shell instability. We want to understand what physical or numerical aspects prevent its developpement in the simulation of WR 104.

This work is supported by the European Community via contract ERC-StG-200911. This work was performed using HPC resources from GENCI- [CINES] (Grant 2010046891)

References

Antokhin, I. I., Owocki, S. P., & Brown, J. C. 2004, ApJ, 611, 434
Canto, J., Raga, A. C., & Wilkin, F. P. 1996, ApJ, 469, 729
Fromang, S., Hennebelle, P., & Teyssier, R. 2006, A&A, 457, 371
Gayley, K. G. 2009, ApJ, 703, 89
Harries, T. J., Monnier, J. D., Symington, N. H., & Kurosawa, R. 2004, MNRAS, 350, 565
Lemaster, M. N., Stone, J. M., & Gardiner, T. A. 2007, ApJ, 662, 582
Marchenko, S. V. & Moffat, A. F. J. 2006, arXiv0610531
Pittard, J. M. 2009, MNRAS, 396, 1743
Stevens, I. R., Blondin, J. M., & Pollock, A. M. T. 1992, ApJ, 386, 265
Teyssier, R. 2002, A&A, 385, 337
Tuthill, P. G., Monnier, J. D., Lawrance, N., et al. 2008, ApJ, 675, 698
Van der Hucht, K. A. 2001, VizieR Online Data Catalog, 3215

SF2A 2010
S. Boissier, M. Heydari-Malayeri, R. Samadi and D. Valls-Gabaud (eds)

THE THREE-DIMENSIONAL STRUCTURE OF VORTICES IN PROTOPLANETARY DISKS AND DUST TRAPPING

H. Meheut[1, 2], P. Varniere[1], F. Casse[1] and M. Tagger[3]

Abstract. Protoplanetary disks vortices are of high interest for planetesimals formation as they can accelerate the growing process of the dust. Indeed previous two dimensional studies have shown that they could concentrate the solid particles in their centre. One mechanism proposed to explain the emergence and survival of a vortex in a differentially rotating disk, is the Rossby Wave Instability (RWI). In this context, we present the structure of a three dimensional RWI vortex and we study the concentration of solid particles in this structure. We show that the dust are effectively concentrated in these vortices, and that the concentration depends on the size of the particles.

Keywords: accretion, accretion disks, protoplanetary disks, hydrodynamics, instabilities, methods: numerical

1 Introduction

The growing of dust of sub-μm size toward planet is achieved through multiple steps. The core accretion scenario explains the growth of grains to centimetre or meter scale thanks to electrostatic interactions, but the growth is then halted since solids of this size decouple from the gas and start feeling the headwind of the sub-Keplerian gas. This force them to spiral onto the central star in a highly too short timescale of a few hundreds years. Large-scale and long-lived vortices have been proposed as an alternative to this scenario, as the anticyclonic streamlines induce a drag toward their centre (Barge & Sommeria 1995). This results in a concentration of grains that can highly accelerate the growing process (Inaba & Barge 2006; Lyra et al. 2009) and this is one of the reason why numerous recent studies focus on vortices (Barranco & Marcus 2005; Lesur & Papaloizou 2009; Heng & Kenyon 2010; Paardekooper et al. 2010). The emergence of such vortices, in a differentially rotating disk, stayed unexplained until recently. Whereas different mechanisms have now been explored, we here concentrate on the Rossby wave instability (Lovelace et al. 1999; Tagger 2001) that was proposed by Varnière & Tagger (2006).

This instability can grow, and therefore sustain vortices, in an extremum of the quantity $\mathcal{L} = \frac{\kappa^2}{2\Omega\Sigma}$ that is usually called vortensity or specific vorticity. Here Ω is the rotation frequency, κ is the epicyclic frequency defined as $\kappa^2 = 4\Omega + 2\Omega\partial_r\Omega$ in (r, ϕ, z) coordinates and Σ is the vertically integrated density, called surface density. This extremum can exist at different radius of the protoplanetary disk, such as the edges of the dead-zone (Varnière & Tagger 2006) or the snow line region (Kretke & Lin 2007), that both create a maximum in the density profile.

2 Numerical setup

We have performed two types of numerical simulations, the first one with only a gas disk, and the other one with a mixed gas and solid disk.

[1] AstroParticule & Cosmologie (APC), UMR7164, Université Paris Diderot, 10 rue Alice Domon et Leonie Duquet, 75205 Paris Cedex 13, France
[2] Physikalisches Institut, Universität Bern, 3012 Bern, Switzerland
[3] Laboratoire de Physique et Chimie de l'Environnement et de l'Espace (LPC2E), Universite d'Orléans/CNRS, France

The first one are simulations of unmagnetised and isentropic gas disks. The hydrodynamical equations are solved with the up to date Versatile Advection Code (Tóth 1996) with a cylindrical grid. The mesh has $150 \times 64 \times 64$ cells, on a non-uniform grid that allows to reach a higher resolution on the region of interest. The initial conditions correspond to a radially decreasing density, on which we added a bump to satisfy the RWI criterion. The computational domain goes from $(r_i, 0, 0)$ to $(6r_i, 2\pi, r_i)$, with r_i the radius of the inner boundary of the simulation. The bump is place at a radius of $3r_i$. All the numerical details concerning these simulations are described in our recent paper (Meheut et al. 2010).

Then a second type simulations have been done, with both gas and solid grains. The gas is treated as before, and the dust is considered as a pressureless fluid. The dust evolution equations are solved with a 4^{th} order Runge-Kutta method. The drag force is calculated in the Epstein regime and no back-reaction of the dust on the gas is considered. Yet this bi-fluid version of VAC is not parallelised, and therefore needs a lot of computational time. For this reason, the gas initial conditions are the one obtained at the end of the previous simulation, whereas the dust is initialized with the azimuthally averaged gas density and with a keplerian rotation velocity. The initial azimuthally averaged gas-to-dust ratio is constant over the disk, and fixed to 10^{-2}.

3 Results

The gas simulation has proven the existence of the RWI in a 3D disk, and has shown the emergence and survival of an anticyclonic vortex due to this instability. The detail study of the 3D RWI and its growth are presented in Meheut et al. (2010), here we focus on the vortex structure and its implication for dust trapping.

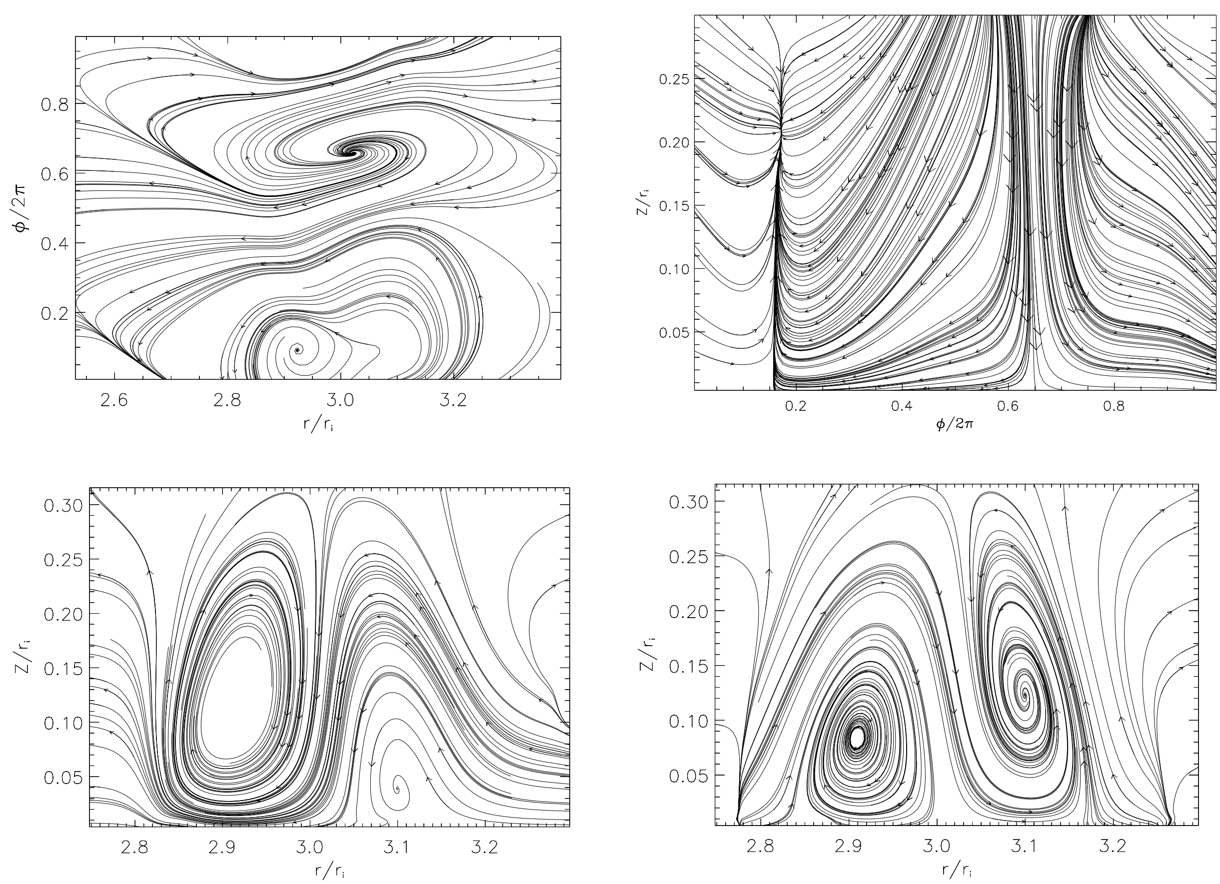

Fig. 1. *Top:* Velocity streamlines in a frame rotating with the disk in the midplane of the disk (*left*) and in the vertical plane at $r = 3r_i$ (*right*). *Bottom:* Velocity streamlines in a vertical frame at $\phi/2\pi = 0.64$ (*left*) and 0.66 (*right*).

The velocity streamlines are presented on Fig. 1. This figure shows the non-axisymetrical part of the velocities. The midplane streamlines confirm the presence of a cyclonic ($\phi/2\pi \sim 0.2$) and anticyclonic ($\phi/2\pi \sim 0.6$) vortex. The converging and diverging streamlines corresponds respectively to upward and downward displacements as can be seen on the vertical cut in the $r = 3r_i$ plane. The vertical structure of the vortex is then more complex than previously thought. This complexity also appears when plotting the radial and vertical velocity streamlines at the centre of the anticyclonic vortex, as shown in the bottom part of the figure. It shows rolls structures on the whole vertical height of the disk, and on each part of the initial density bump that was placed at $r = 3r_i$. The bottom left plot is a vertical cut in the front part of the anticyclonic vortex, it shows accreting streamlines that are vertically modified in the rolls; whereas in the back part of the vortex (bottom right) the streamlines have the opposite direction.

This 3D structure was supposed to modify the dust concentration mechanism: we expected the intermediate size solids to follow the gas in the downward stream but not in the upward stream due to gravity. The bi-fluid simulation confirms this prediction after only approximately one twentieth of an orbit as shown on Fig. 2. One can see that there are two region of dust high density that correspond to the bottom of the upward streamlines. On the other hand, the dust concentration depends on the dust size. The smaller particles follow the gas in its vertical displacement and therefore are less concentrated. The gas drag has a lower effect on the biggest ones that are then less concentrated by the vortex. We then obtained the highest concentration for $500\mu m$ to $1mm$ size dust.

4 Summary and discussion

Here we have presented the first results obtained with our bi-fluid code, allowing to follow gas and dust in a 3D Rossby vortex. The simulation showed that the anticyclonic vortex effectively concentrates the dust and that the highest concentration is obtained for intermediate dust size ($500\mu m$ to $1mm$).

The result presented here only aimed to give a proof of principle of the solid concentration in 3D Rossby vortices but more developments are needed. First, the gas drag should be extended to the Stokes regime to have a better modelisation of the biggest particles. Then the numerical method used to solve the solid evolution equation should be improved with the use of a Riemann solver that will allow to obtain a longer time evolution simulation.

The 3D vortex structure we have obtained also needs to be analyzed analytically as it is only recently that the RWI has started to be analyse in three dimensions. One approach was recently proposed by (Umurhan 2010), but it does not include such 3D vortex structure.

This work was granted access to the HPC resources of IDRIS under the allocation 2009-i2009042125 made by GENCI (Grand Equipement National de Calcul Intensif).

References

Barge, P. & Sommeria, J. 1995, Astronomy and Astrophysics, 295, L1

Barranco, J. A. & Marcus, P. S. 2005, Astrophysical Journal, 623, 1157

Heng, K. & Kenyon, S. J. 2010, ArXiv e-prints

Inaba, S. & Barge, P. 2006, Astrophysical Journal, 649, 415

Kretke, K. A. & Lin, D. N. C. 2007, Astrophysical Journal Letters, 664, L55

Lesur, G. & Papaloizou, J. C. B. 2009, Astronomy and Astrophysics, 498, 1

Lovelace, R. V. E., Li, H., Colgate, S. A., & Nelson, A. F. 1999, Astrophysical Journal, 513, 805

Lyra, W., Johansen, A., Zsom, A., Klahr, H., & Piskunov, N. 2009, Astronomy and Astrophysics, 497, 869

Meheut, H., Casse, F., Varniere, P., & Tagger, M. 2010, Astronomy and Astrophysics, 516, A31+

Paardekooper, S., Lesur, G., & Papaloizou, J. C. B. 2010, Astrophysical Journal

Tagger, M. 2001, Astronomy and Astrophysics, 380, 750

Tóth, G. 1996, Astrophysical Letters Communications, 34, 245

Umurhan, O. M. 2010, ArXiv e-prints

Varnière, P. & Tagger, M. 2006, Astronomy and Astrophysics, 446, L13

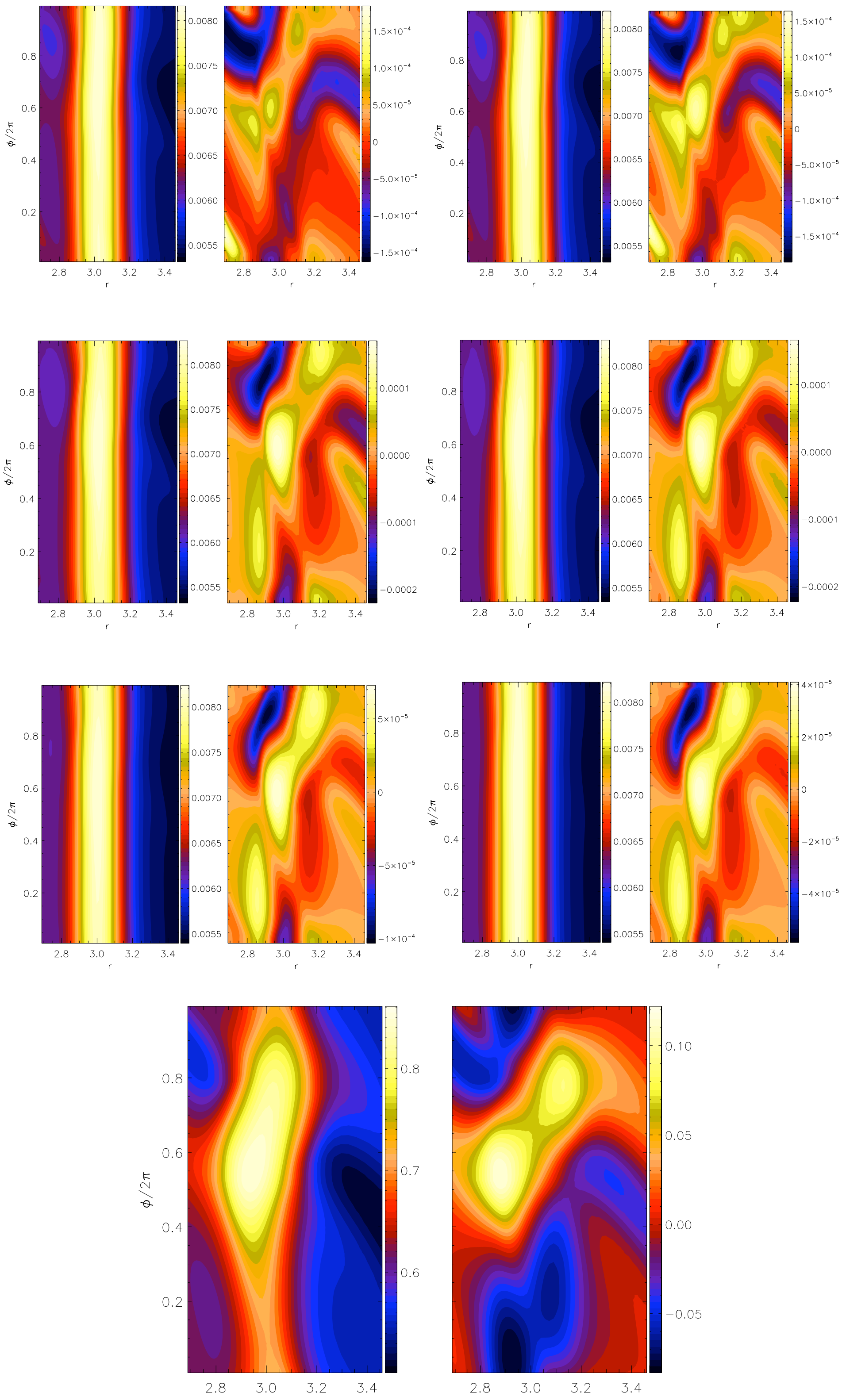

Fig. 2. Density (*left*) and non-axisymetrical part of density (*right*) plotted in the midplane of the disk for different sizes of particles: $10\mu m$, $100\mu m$, $500\mu m$, $1mm$, $5mm$, $1cm$ (from top left to bottom right). The corresponding plot for the gas is also given at the bottom for comparison.

LONG-TERM MAGNETIC FIELD MONITORING OF THE SUN-LIKE STAR ξ BOOTIS A

A. Morgenthaler[1], P. Petit[1], M. Aurière[1], B. Dintrans[1], R. Fares[1], T. Gastine[1], J. Lanoux[2], F. Lignières[1], J. Morin[1,3], J. Ramirez[4], S. Théado[1] and V. Van Grootel[1]

Abstract. Phase-resolved observations of the solar-type star ξ Bootis A were obtained using the Narval spectropolarimeter at Telescope Bernard Lyot (Pic du Midi, France) during years 2007, 2008, 2009 and 2010. The data sets enable us to study both the rotational and the long-term evolution of various activity tracers. Here, we focus on the large-scale photospheric magnetic field (reconstructed by Zeeman-Doppler Imaging), the Zeeman broadening of the FeI 846.84 nm magnetic line, and the chromospheric CaII H and Hα emission.

Keywords: stars: activity, stars: chromospheres, stars: imaging, stars: magnetic field, stars: solar-type, stars: individual: ξ Bootis A

1 Magnetic field m

Using a line-list matching a stellar photospheric model for the spectral type of ξ Bootis A (G8), we calculated from the observed spectrum a single, averaged photospheric line profile using the LSD multi-line technique (Donati et al. (1997)). Thanks to this cross-correlation method, the noise level of the mean Stokes V line profile is reduced by a factor of about 30 with respect to the initial spectrum. The resulting noise levels are in the range 3.10^{-5}-1.6^{-4} I_c (where I_c denotes the intensity of continuum).

Assuming that the observed temporal varaibility of Stokes V profiles is controlled by the stellar rotation, we reconstructed the magnetic geometry of our star by means of Zeeman-Doppler Imaging (ZDI). We employ here the modelling approach of Donati & Brown (1997), including also the spherical harmonics expansion of the surface magnetic field implemented by Donati et al. (2006) in order to easily distinguish between the poloidal and toroidal components of the reconstructed magnetic field distribution.

The global mean field is around 64.4 Gauss in 2007, 19.2 in 2008, 28.8 in 2009 and 16.1 in 2010. The fraction of poloidal field (wrt toroidal field) is 18% in 2007, 56% in 2008, 35% in 2009 and 63% in 2010.

2 Chromospheric activity (CaII H and Hα)

To study the evolution of the chromospheric CaII H emission during a rotation period, we calculated an emission index from our sets of Stokes I spectra with the method described in Wright et al. (2004) (Fig. 1). The index globally decreased between 2007 and 2010 (the mean values for the four years are respectively 0.413, 0.387, 0.390 and 0.366). A rotational modulation is clearly observed in 2008 and 2010. We also reconstructed an index to monitor the evolution of the chromospheric Hα emission using the same passbands as Gizis et al. (2002). A very good correlation (about 0.85) appears between the Hα and the CaII H index.

[1] Laboratoire d'Astrophysique de Toulouse-Tarbes, Université de Toulouse, CNRS, France
[2] Centre d'Etude Spatiale des Rayonnements, Université de Toulouse, CNRS, France
[3] Dublin Institue for Advanced Studies, Dublin, Ireland
[4] Instituto de Astronomia - Universidad Nacional Autonoma de Mexico, Coyoacan, Mexico

3 Zeeman broadening

We computed the Zeeman broadening by determining the width of a FeI magnetic line (λ = 846.84 nm, g = 2.493) for each intensity spectrum and we observed a decrease between each year. Moreover, there is a correlation of 0.86 between the CaII H activity indicator and the widths of the magnetic line for the whole data set (Fig. 1). We note that such correlation does not exist between the chromospheric index and the width of a neighbouring line with a weak Landé factor.

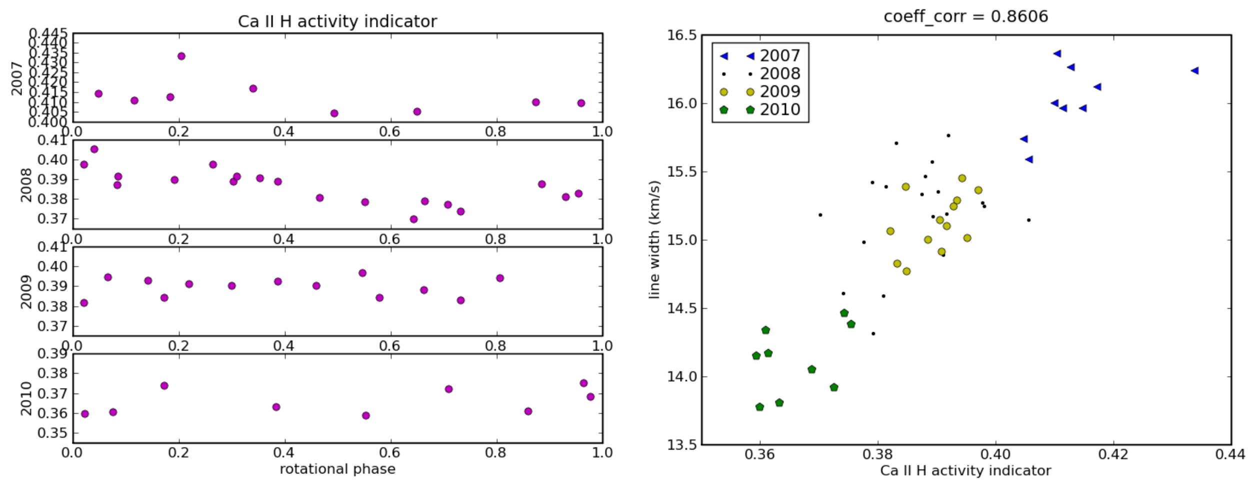

Fig. 1. Left : CaII H activity indicator as a function of the rotational phase for 2007, 2008, 2009 and 2010 (from top to bottom). Right : correlation between the widths of the FeI 846.84 nm magnetic line and the values of the CaII H index.

4 Discussion

An obvious decrease of the global magnetic field is visible between 2007 and 2010. The same kind of variations occurred for the CaII H and Hα index during the same period, as for the width of our magnetic line. In the same time, the fraction of poloidal field increased of 45%, which indicates a significant change in the geometry of the field. ξ Bootis A did not show recent dramatical changes like the magnetic polarity reversals recently reported for HD190771 (Petit et al. (2009)) or τ Bootis (Fares et al. (2009)). Future monitoring of the star will tell us wether its magnetic evolution is associated to some kind of cyclicity, and if its global magnetic field can undergo polarity switches, as observed on more massive solar-type stars up to now.

References

Donati, J.-F., & Brown, S.F., 1997, A&A, 326, 1135

Donati, J.-F., Semel, M., Carter, B.D., Rees, D.E. & Collier Cameron, A., 1997, MNRAS, 291, 658

Donati, J.-F., Howarth, I.D., Jardine, M.M., et al., 2006, MNRAS, 370, 629

Fares, R., Donati, J.-F., Moutou, C., et al., 2009, MNRAS, 398, 1383

Gizis, J.E., Reid, I.N., Hawley, S.L., 2002, ApJ, 123, 3356

Petit, P., Dintrans, B., Morgenthaler, A., et al., A&A, 508, L9

Wright, J.T., Marcy, G.W., Butler, R.P., Vogt, S.S., 2004, ApJS, 152, 261

SF2A 2010
S. Boissier, M. Heydari-Malayeri, R. Samadi and D. Valls-Gabaud (eds)

HOW TO USE AND TO PUBLISH WITH THE FREE AVAILABLE CODE Cesam2k

B. Pichon[1]

Abstract. We present -1- a short description of the stellar structure and evolution code Cesam in its modern version – named Cesam2k – with its main options (physics and numerics) -2- the charter to publish results obtained with Cesam2k.

Keywords: stellar structure, stellar evolution, code

1 Introduction

For astrophysicists using Cesam in their research, we present in section 2, the genesis of this code and its present version – named Cesam2k – which is today the only version to use. In section 3, we summarize the main options (concerning physics or numerics) of this code. In section 4, we outline a user guide for standard or advanced users. Finally, in section 5, we present the charter of Cesam2k which explain the rules of publishing results obtained with Cesam2k.

2 A brief story of Cesam and Cesam2k

The story begins in 1987 with CESAM, an acronym for “Code d'Evolution Stellaire Adaptatif et Modulaire” (in English for an Adapative and Modular Code for Stellar structure and Evolution). This code was designed by Pierre Morel under encouragement of Evry Schatzman and Annie Baglin under the auspices of the GdR131. This first version was written in Fortran 77 and need to be compiled each time the user changes any options. With the help of Bernard Pichon, since 2001, a totally new version was designed and Cesam – renamed (of course) Cesam2k – rewritten in Fortran 90/95 with many important new features. Cesam2k was officially presented to the astrophysical community at Nice meeting in may 2003 (see `http://www.oca.eu/cesam/meeting.html`. Later on, a few colleagues contributed to some improvements : we can quote, for instance, the names of Yveline Lebreton, Sacha Brun, Laurent Piau (in chronological order). Note that Cesam (without 2k) refers to previous versions (cesam4 or cesam5, before 2001) now obsolete (no correction, no maintenance, ...) and not recommended to use.

3 A short description of Cesam2k

Cesam2k is (now) easy to use (see section 4) and is ready to use : it need only one compilation because all options are now included in the executable file. In its new version, Cesam2k remains free available **but**, to publish results obtained with it, need agreement with the authors. Hence, Cesam2k is a collaborative code always under development (see section 5 for details). The current stable version is (at mid-2010) V3.2.12 and the experimental one is V3.3.7. There is also a CoRot dedicated version (V1.1.8) created by Evelyne Lebreton at Meudon.

[1] Université de Nice Sophia-antipolis, Laboratoire Cassiopée (UMR 6202 du CNRS), Observatoire de la Côte dAzur

Here, we present the main available options for the physics :

- Convection : 6 subroutines, plus the over- and the under- shoot and 2 convection criteria (Schwarzschild, Ledoux)
- Diffusion : microscopic, turbulent and, not yet public available, the radiative acceleration
- Rotation : the effects of rotation are treated with the help of the Maeder & Zahn's theory
- Equation of state : 8 subroutines with their associated data
- Opacities : 8 subroutines with their associated data (can be modified)
- Atmosphere : 5 subroutines, plus non-radiative Cayrel atmospheres (5 files of associated date), plus (not yet public available) Marcs atmospheres.
- Nuclear reaction network : 18 subroutines (the subroutine set also the chemical species followed during stellar evolution)
- mass loss : 4 subroutines
- Chemical composition : 7 premixed compositions; the user can modify abundance of any element

Here, we present the main 'user' available options :

- Stop criterion : 15 available
- Output format : 9 available
- Numerics : 13 predefined sets of numerical parameters (also, for very advanced user to modify any of these parameters in the so-called .rg files)

4 How to use Cesam2k

First, if you are interested to use Cesam2k, and as previously stated, the best choice is to contact one of the authors : `mailto:Bernard.Pichon@oca.eu` or `mailto:Pierre.Morel@oca.eu`. Note that, now, Pierre Morel is emeritus.
Only one configuration file need to be edited (the so-called .don files) and we recommend, for simplest models, to keep 'robust' physics. But, for 'advanced' physics, take care in the coherence of choices; some routines are not easy to use. Also, do not use experimental options without contacting one of the authors : as counterexample, Piau et al. (Astron. Astrophys. 506 (2009) 175) misuse an experimental version of Cesam2k (moreover not publicaly available (!)) which leads to erroneous conclusions about the effect of radiative accelerations and therefore a comment shall/should be published soon !!
For advanced users, few (sub-) configuration files are available, for instance, to modify the numerics, the chemical composition, the interactive plot, ... Experimental versions are only available upon request.
The new architecture of the code allows programmers to easily add new routines; the template of any physical subroutine is provided and the new routine is called through a generic call. Hence, Cesam2k is open to collective improvements and its use in the astrophysical community.

5 How to publish with Cesam2k

In brief, a charter is available (in French) since 2008 October 02 (`http://www.oca.eu/cesam/charte_CESAM.txt`) (see the text in annex).
The underlying idea is that the authors of any paper (which use Cesam2k in a significant manner) share the work with the principal authors of Cesam2k in adding their names as co-authors of the paper (as a "free remuneration" of all the previous work : many year-men). Note also, for the CNRS, the first indicator is the publishing rate !
Hence, Cesam2k is *de facto* a collaborative code.

In more details :

- For minor use of Cesam2k (in the sense of the main conclusions of your work would be achieved without it), the best is to inform us. We will answered with the appropriate acknowledgment to add in your paper and we also add your publication in the list of the publications that use Cesam2k.
- For important use of Cesam2k, the authors should contact us before publication. Note that, in this case, upon the basis of co-publishing, we can help you towards the best use of Cesam2k.
- The special case of contributors which improve (significantly) Cesam2k (for example, adding new physics such as rotation, diffusion, models of atmospheres, ...) : The authors must be contacted at least for advices (how to implement these new routines in the framework of Cesam2k). After that, depending on the work done, we guarantee, owing to the charter, that for each paper using these new routines, this new author benefits same returns as us. Remember always that Cesam2k is a collaborative code where authors are paid as co-authoring in your papers !!

For instance, we quote here a paper that violates the Cesam2k charter. Turck-Chieze et al. (Ap.J. 715 (2010) 1539) claims that they use a (new improved ???) version of Cesam2k **but** –1– This work is the comparison of Cesam2k with an another code, therefore this work use clearly Cesam2k with a very significant manner; –2– we are not aware of this (is it really true ? : no other previous paper describing the changes); –3– this paper clearly violates the Cesam2k charter (the Cesam2k web site is quoted in this paper); –4– Some sentences in this paper (for example, the quick description of Cesam2k) are wrong .

6 Conclusions

Our wish : Use Cesam2k with us !!
Improve Cesam2k with us and you will be welcome with us !!

7 Annex

L'utilisateur de Cesam2k (TM), quelle que soit la façon dont il s'est procuré la version qu'il utilise, s'engage *de facto* à suivre les régles suivantes. Afin d'éviter tout malentendu, les éditeurs des différentes revues scientifiques seront également alertés de l'existence de cette charte.

1) Il ne sera en aucun cas "propriétaire" de la version, même modifiée, chaque version du code étant donc publique. Seuls les auteurs primaires du code [PM, BP, YL] se réservent le droit de posséder et d'utiliser des versions "privées".

2) Par conséquent, avant toute publication scientifique, il en informera les auteurs primaires [actuellement] "Bernard.Pichon@oca.eu", "Yveline.Lebreton@univ-rennes1.fr" "Pierre.Morel@oca.eu" (chercheur émérite) en y indiquant clairement la part "dite essentielle" du travail relative à l'emploi de Cesam2k c'est-à-dire la part du travail sans lequel celui-ci n'aurait pas pu être fait s'il n'avait pas disposé de ce code. Cette information inclut obligatoirement l'envoi des sources nouvelles si besoin.

3) Les auteurs ainsi contactés lui signifieront, selon cette part essentielle du travail constaté (d'un commun accord) SOIT les noms des personnes qui devront figurer comme auteurs de la publication [cas le plus probable pour des articles dans des revues] SOIT les références et remerciements à inclure dans la publication [cas le plus probable pour des communications à des congrès, colloques]. Il va de soi que vu le type de partage "collaboratif" (au seul "cout gratuit" de la présence dans la liste des auteurs de 2 ou 3 noms supplémentaires) de ce code, chaque utilisateur "régulier" aura le profit de toutes corrections d'erreur signalées et de toutes les améliorations publiques.

SF2A 2010
S. Boissier, M. Heydari-Malayeri, R. Samadi and D. Valls-Gabaud (eds)

VALIDATION OF M-DWARF ATMOSPHERE MODELS AND EFFECTIVE TEMPERATURE SCALE OF M DWARFS

A.S. Rajpurohit[1], C. Reylé[1], M. Schultheis[1] and F. Allard[2]

Abstract. We present a comparison of low-resolution spectra of 60 stars covering the whole M-dwarf sequence. Using the most recent PHOENIX stellar atmosphere models we do a first quantitative comparison to our observed spectra in the wavelength range 500-900 nm. We perform a first confrontation between models and observations and we assign an effective temperatures to the observed M-dwarfs. Teff-spectral type relations are then compared with the published ones. This comparison also aims at improving the models.

Keywords: M-dwarfs, cool atmosphere models

1 Introduction

Low-mass dwarfs are the dominant stellar component of the Galaxy. Our understanding of the Galaxy therefore relies upon the description of this faint component. Indeed M-dwarfs have been employed in several Galactic studies. Moreover, M dwarfs are now known to host exoplanets, including super-Earth exoplanets (see e.g. Bonfils et al., 2007). The study of M dwarfs has therefore relevant implications for both stellar and Galactic astronomy. Over the last decade, stellar models of very low mass stars have made great progresses, but they still have to use some incomplete or approximate input physics such as uncertain oscillator strengths for some line and molecular bands and missing opacities sources. Descriptions of these stars therefore need a strong empirical basis, or validation.

2 Comparison between atmosphere models and M-dwarf spectra

M-dwarfs remain elusive and enigmatic objects because of their small size and cool surface temperature. M-dwarf spectra are characterized by the presence of strong molecular absorptions such as TiO, VO, H_2O and CaH. A complete understanding of the theoretical description of the stellar atmosphere, temperature, abundances, sizes and luminosities is yet not fully understood. We compared 60 M-dwarfs (from M0 to M9) with optical spectroscopic classification (Reylé et al., 2006), on a large wavelength range, with the most recent PHOENIX stellar atmosphere models, varying the effective temperature. The models used are the most recent version BT-Settl-2010 taking into account the solar abundances from Asplund et al. (2009) and based on 2D hydrodynamic simulations including a description of dust grain formation from Freytag et al. (2010). The models are available on-line.*. Fig. 1 shows the comparison between model (blue line) and observations (red line) for a M0 star (left), a M3.5 star (middle) and a M5.5 star (right). We found some discrepencies probably due to bad opacity assumptions (see e.g. TiO absorption around 6500Å). New constraints on opacities will be drawn from this comparison. For M6 and later dwarfs, the model is not able to fit properly the blue part and the red part of the observed spectra.

[1] Observatoire de Besançon, Institut Utinam, UMR CNRS 6213, BP 1615, 25010 Besançon Cedex, France
[2] C.R.A.L., UMR CNRS 5574, Ecole Normale Supérieure, 69364 Lyon Cedex 07, France
*`http://phoenix.ens-lyon.fr/simulator`

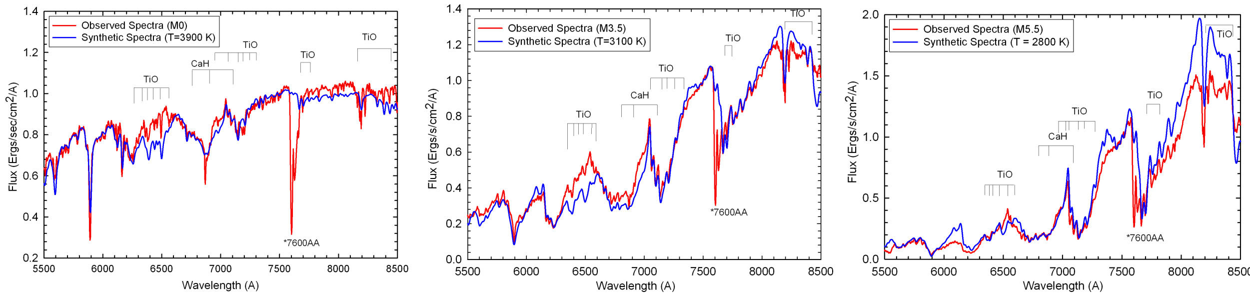

Fig. 1. Comparison between model (blue line) and observations (red line). Left: M0 star and model with Teff=3900K. Middle: M3.5 star and model with Teff=3100K . Right: M5.5 star and model with Teff=2800K.

3 Effective temperature scale of M-dwarfs

We derived the spectral type of the synthetic spectra by computing the spectral indices (TiO_5, CaH_2, CaH_3, PC3) and derived a SpT-Teff relation. This relation is not valid for Teff<2800K or SpT earlier than M6 where we did not find a good fit between observed and synthetic spectra. Thus we do not used the PC3 indices valid for >M6. The adopted SpT (solid lines) is the average from TiO_5, CaH_2 and CaH_3 spectral indices. The relation is compared to others found in the literature (Fig. 2).

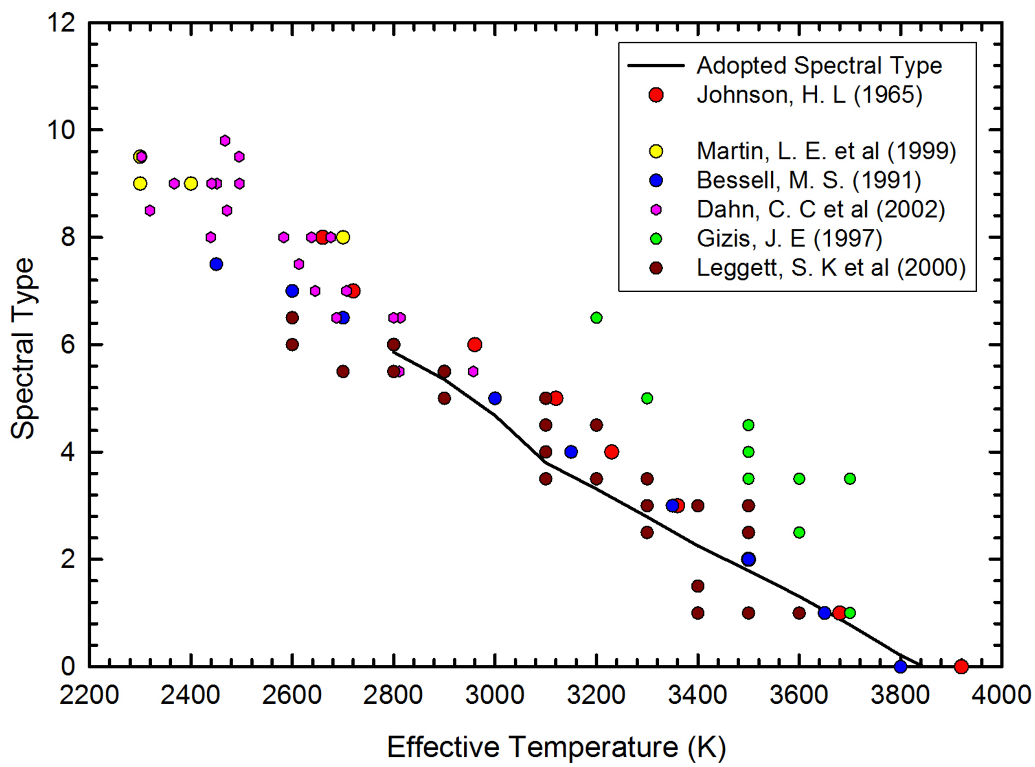

Fig. 2. Our adopted spectral type - Teff relation (solid line) compared to relations from Johnson (1964), Bessel (1991), Gizis (1997), Martín et al. (1999), Leggett et al. (2000), Dahn et al. (2002)

Financial support from the French Programme National de Physique Stellaire (PNPS) is gratefully acknowledged.

References

Asplund et al. 2009, ARA&A, 47, 481
Bessel M. S. 1991 AJ, 101, 662
Bonfils X. et al. 2007, A&A, 474, 293
Dahn C. C. et al. 2002 ApJ, 124, 1170
Freytag B. et al. 2010, A&A, 513, 19
Gizis J. E. 1997 AJ, 113, 806
Johnson H.-L. 1964, Boletin de los Observatorios Tonantzintla y Tacubaya, 3, 305
Leggett S. K. et al. 2000 ApJ, 535, 965
Martín E. et al. 1999, AJ, 118, 2466
Reylé et al. 2006, MNRAS, 373, 705

PNP

Planets

IRRADIATED DISKS AND PLANET POPULATION SYNTHESIS

N. Cabral[1], L. Fouchet[1], Y. Alibert[1], C. Mordasini[2] and W. Benz[1]

Abstract. Recent planet population synthesis models (Alibert et al. 2010, submitted) have emphasized the key role played by the proto-planetary disk properties in determining the overall planet population characteristics. We present a disk model that takes into account viscous heating and irradiation by a central star. We consider the case of an equilibrium flaring angle. We illustrate the consequences of the resulting changes in the disk structure on the planet population by the synthetic populations corresponding to each of the different structures.

Keywords: planetary systems: formation, protoplanetary disks, planets and satellites: formation

1 Introduction

Properties of disks are important for planet formation. To compute planet formation, models are now built together with their disk environnement. Moreover, population synthesis calculations require the determination of the formation path of many planets which are computer time demanding. Therefore, the aim is to improve the disk model taking account irradiation by a central star using a simplified prescription, checking that the resulting midplane temperature and surface density, that are important to the planet formation, are similar to the one obtained using more detailed disk models.

2 Disk Model

We compute the disc structure and its time evolution following the method 1+1D given by Papaloizou and Terquem (1999), see also Alibert et al. (2005).

To compute the vertical structure we consider the equations in the thin-disk approximation : the hydrostatic equilibrium, the energy conservation and the diffusion equation for the radiative flux. These three equations are integrated, at fixed radius, from the disk "surface" H (defined as the height where the optical depth is 10^{-2}) down to the midplane, $z = 0$, with four boundary conditions, three at the surface and one at the center. Only one value of H, allows to simultaneously fulfil all the boundary conditions. Thus, we have the pressure $P(z, r_o)$, the temperature $T(z, r_o)$ and the radiative flux $F(z, r_o)$, for z equal 0 to H, and for each radius r_o. Then, we calculate the viscosity ν using the standard α-parametrization (Shakura and Sunyaev 1973). Subsequently, we compute the time evolution of the disc considering the well-known diffusion equation (Lyndell-Bell and Pringle 1974). To solve the diffusion equation we need to specify two boundary conditions : the inner and outer radius.

In order to explore the effect of irradiation. We assume that all the disk is irradiated, neglecting all possible shadowing effects. The irradiation effect is included by modifing the temperature boundary condition of the vertical structure. The irradiation temperature is derived in Hueso and Guillot (2005) :

$$T_{irr} = T_* \left[\frac{2}{3\pi} \left(\frac{R_*}{r} \right)^3 + \frac{1}{2} \left(\frac{R_*}{r} \right)^2 \left(\frac{H_p}{r} \right) \left(\frac{\mathrm{d} \ln H_p}{\mathrm{d} \ln r} - 1 \right) \right]^{\frac{1}{4}}, \tag{2.1}$$

where R_* is the stellar radius, r is the distance to the star and H_p is the pressure scale height. The flaring angle, $\mathrm{d} \ln H_p / \mathrm{d} \ln r$, is taken at its equilibrium value 9/7 (Chiang and Goldreich 1997).

In Fig. 1 we compare the mid-plane temperature and surface density in a disk of constant accretion rate ($\dot{M} = 10^{-8}\, M_\odot\, yr^{-1}$) with the results of D'Alessio et al. (1998).

[1] Physikalisches Institut, Universität Bern, CH-3012 Bern, Switzerland
[2] Max-Planck Institute for Astronomy, Königstuhl 17, 69117 Heidelberg, Germany

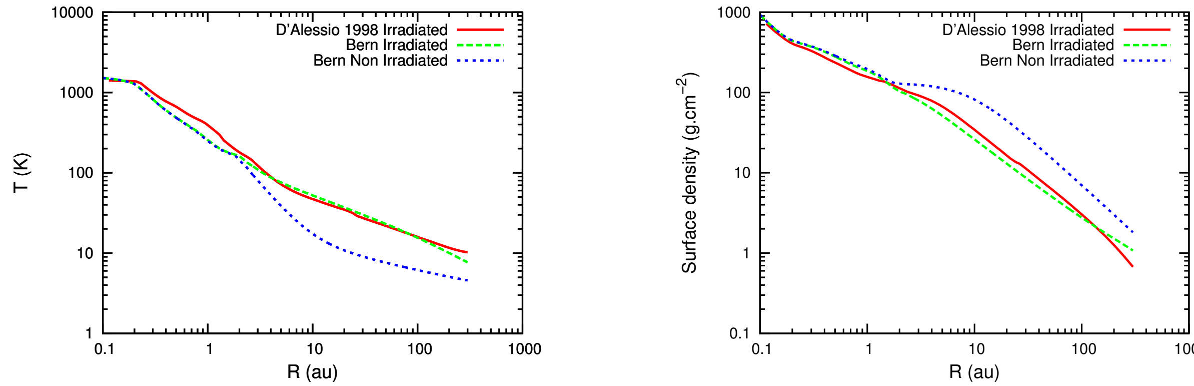

Fig. 1. *Left*: Temperature midplane. *Right*: Surface density. The model of D'Alessio et al. (1998) in red solid line, the model of Bern with irradiation in green long dashed line, and without irradiation in blue short dashed.

We first note that the temperature is substantially higher in the outer parts of the disk when irradiation is included. We obtain a good match for the midplane temperature and surface density.

3 Population Synthesis Model

In Fig. 2 we show the effects of irradiation on the expected planet population. We compute the theoretical planet populations, using the same parameters for irradiated and no-irradiated cases.

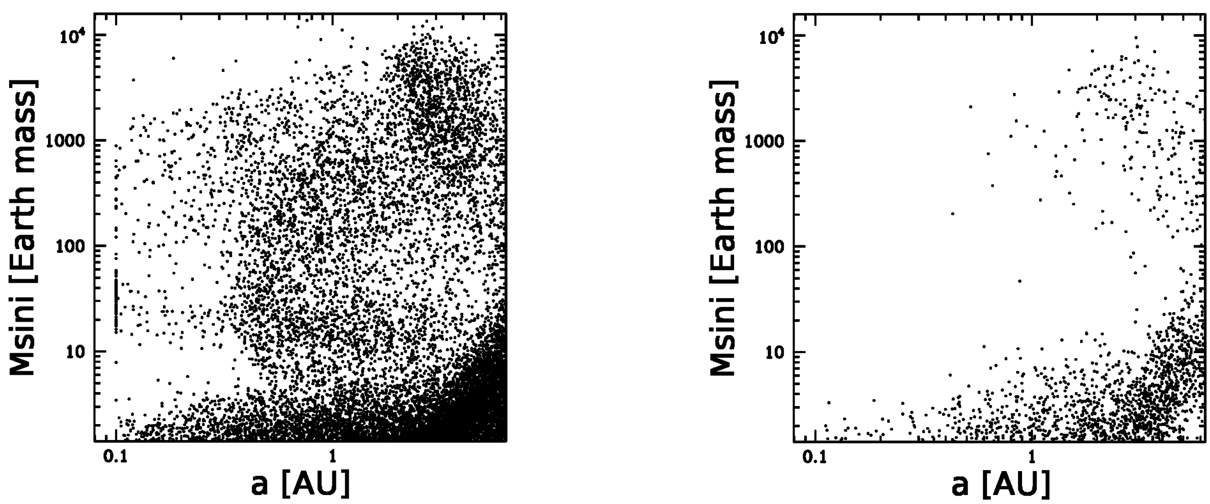

Fig. 2. Mass versus semi-major axis for synthetic planets. *Left* panel: without irradiation effects. *Right* panel : including irradiation effects.

Comparing the two panels, it is obvious that stellar irradiation has a strong effect on the expected planet population : hot planets do not exist anymore. The effect is as big in the nominal model because we use a larger reducing factor for type I migration, $f_I = 10^{-3}$. Therefore, the changes in population are due to assumptions in the model more than in physics. Hence, if we use $f_I = 10^{-1}$ instead 10^{-3}, we retrieve a few hot planets.

References

Alibert, Y., Mordasini, C., Benz, W., & Winisdoerffer, C. 2005, A&A, 434, 343

Chiang, E. I. & Goldreich, P. 1997, ApJ, 427, 987

D'Alessio, P., Canto, J., Calvet, N., & Lizano, S. 1998, ApJ, 500, 411

Hueso, R. & Guillot, T. 2005, A&A, 442, 703

Lyndell-Bell, D., & Pringle, J. E. 1974, MNRAS, 168, 603
Papaloizou, J. C. B. & Terquem, C. 1999, ApJ, 521, 823
Shakura, N. I. & Sunyaev, R. A. 1973, A&A, 24, 337

SF2A 2010
S. Boissier, M. Heydari-Malayeri, R. Samadi and D. Valls-Gabaud (eds)

SEARCH AND CHARACTERIZATION FOR EXTRASOLAR PLANETS WITH THE SOPHIE CONSORTIUM

I. Boisse[1], F. Bouchy[1, 2], G. Hébrard[1,2], S. Udry[3], X. Delfosse[4], A.-M. Lagrange[4], D. Queloz[3], C. Moutou[5], L. Arnold[2], X. Bonfils[3,4], R. Díaz[1,2], A. Eggenberger[4], D. Ehrenreich[4], T. Forveille[4], C. Lovis[3], F. Pepe[3], C. Perrier[4], A. Santerne[5], N. C. Santos[6], D. Ségransan[3] and A. Vidal-Madjar[1]

Abstract. The SOPHIE Consortium started, in November 2006, several programs of exoplanet search and characterization in the Northern hemiphere with the spectrograph SOPHIE based on the 1.93m telescope at the Observatoire de Haute-Provence. We present here the latest SOPHIE results which include new exoplanets, studies of transiting planets through Rossiter-McLaughlin effect, characterizations of stellar activity of planet-host star and observation of the Earth as a transiting planet.

Keywords: planetary systems, techniques: radial velocities and spectroscopic, stars: activity, planets and satellites: atmospheres

1 Introduction

The high-precision SOPHIE spectrograph (Perruchot et al. 2008) has been opened to the community since October 2006 at the 1.93-m telescope at the Observatoire de Haute-Provence (OHP). At the same time, the SOPHIE consortium, composed of researchers from five institutes, initiated a large program to search for and characterize extrasolar planets (Bouchy et al. 2009). This large program is divided in five complementary subprograms with different objectives: a high-precision search for super-Earths, a giant planets survey on a volume-limited sample, a search for exoplanets around M-dwarfs, a search for planets around early-type main sequence stars and a long-term follow-up of ELODIE long period candidates. The consortium benefits almost half of the available night on the telescope that allows a high level of flexibility and reactivity, an involvement in the follow-up and the optimization of the instrument, and a good sharing of the telescope time as a function of weather conditions and observing strategy of the subprograms.

2 Search for planetary systems

SOPHIE has replaced the ELODIE spectrograph (Baranne et al. 1996). Then, surveys of the consortium are both continuation and extension of the planet-search programs carried out with ELODIE (Queloz et al. 1998). They also complement the HARPS programs performed in the southern hemisphere (Mayor et al. 2003). The detection of three exoplanets that were first found from the ELODIE surveys before to be monitored by SOPHIE have been published. Da Silva et al. (2006) reported two intermediate period (40 and 974 days) of, respectively, 2.5 and 5.6 M_{Jup} planets orbiting the metal-rich stars HD43691 and HD132406. Also monitored by CORALIE,

[1] Institut d'Astrophysique de Paris, Université Pierre et Marie Curie, UMR7095 CNRS, 98bis bd. Arago, 75014 Paris, France [iboisse@iap.fr]
[2] Observatoire de Haute Provence, 04870 St Michel l'Observatoire, France
[3] Observatoire de Genève, Université de Genève, 51 Ch. des Maillettes, 1290 Sauverny, Switzerland
[4] Laboratoire d'Astrophysique de Grenoble, Observatoire de Grenoble, Université Joseph Fourier, CNRS, UMR 5571, 38041, Grenoble Cedex 09, France
[5] Laboratoire d'Astrophysique de Marseille, Université de Provence & CNRS, 38 rue Frédéric Joliot-Curie, 13388 Marseille cedex 13, France
[6] Centro de Astrofísica, Universidade do Porto, Rua das Estrelas, 4150-762 Porto, Portugal

a Jupiter-mass (0.47 M_{Jup}) planet HD45652b orbiting a metal-rich star in a 44 days was announced by Santos et al. (2008) (Fig. 1, *right*).

An early F-type star, θ Cygni was observed during five years with ELODIE and SOPHIE. A pseudo-periodic RV variations of about 150 days was detected with a variable semi-amplitude. Desort et al. (2009) showed that the available data are not well explained by a one (or two) planet system, and considered a possible stellar origin.

Three planet-host stars were discovered from SOPHIE observations that were part of the survey for giant planets around bright stars in a volume-limited sample. A massive planet (or light brown dwarf) were characterized by Bouchy et al. (2009) orbiting HD16760 with a period of 465 days. A two planets system HD9446b,c were reported by Hébrard et al. (2010a) with a hierarchical disposition. The SOPHIE RV measurements of HD9446 and the two-planets Keplerian orbits are shown in Fig. 1 (*left*). Boisse et al. (2010b) announced HD109246b, orbiting a G0V star, with a minimum mass of 0.77 M_{Jup} and a orbital period of 68 days (Fig. 1, *right*). We also present a correction method for the so-called seeing effect that affects the SOPHIE RV, and a description of some calibrations that are implemented in the SOPHIE automatic reduction pipeline (derivation of the photon-noise RV uncertainty and some useful stellar properties: $v \sin i$, [Fe/H], $\log R'_{HK}$).

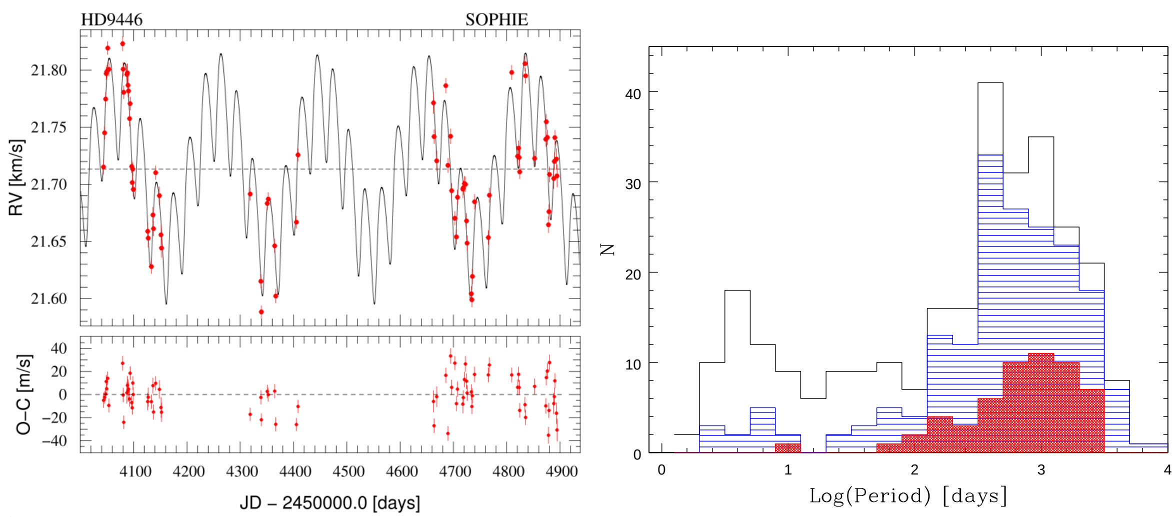

Fig. 1. *Left:* RV from SOPHIE measurements of HD9446 as a function of time and Keplerian fit revealing a two planets system. At the bottom are reported the residuals from the fit (Hébrard et al. 2010a). *Right:* Period distribution of the known extrasolar planet orbiting single dwarf stars via RV surveys. Horizontal stripped illustrates the distribution for planets more massive than 0.8 M_{Jup} and the shaded one for planets more massive than 4 M_{Jup} (Boisse et al. 2010b). With respective periods of 30, 44 and 68 days, HD9446b, HD45652b and HD109246b are placed in a sparsely populated region of the period distribution of extrasolar planet.

3 Characterization of planetary systems during transit observations

Spectroscopic transit of planets have also been observed by SOPHIE allowing refinement of the parameters of the system as well as measurement of the sky-projected angle between the normal of the orbital plane and the stellar spin axis. The detection of the Rossiter-McLaughlin effect of the transiting exoplanet HAT-P-2b when the planet was transiting its parent star by Loeillet et al. (2008), showed that the sky-projected spin-orbit angle is consistent with zero. The spectroscopic transit of XO-3b shown in Fig. 2 was also done with SOPHIE (Hébrard et al. 2008). This planet with a high mass and an eccentric orbit was the first detection of a misaligned spin-orbit system.

The transit of the 111-day period exoplanet was established by Moutou et al. (2009) thanks to spectroscopic observations with SOPHIE and photometric with the 120-cm telescope at OHP. We observed only the egress of the transit because ingress occurred before sunset (full duration of the transit were characterized in the following studies to be close to 12 hours). Pont et al. (2009) presented a combined analysis of photometric and spectroscopic data. With an upper limit on the transit duration, the authors reinforced the hypothesis of spin-orbit misalignment in this system. Finally, new spectroscopic observations with SOPHIE of the first half of the RM effect allowing the measurement of the second known misaligned system (Hébrard et al. 2010b). These misalignment suggest that some close-in planets might result from gravitational interaction between planets and/or stars rather than migration due to interaction with the accretion disk.

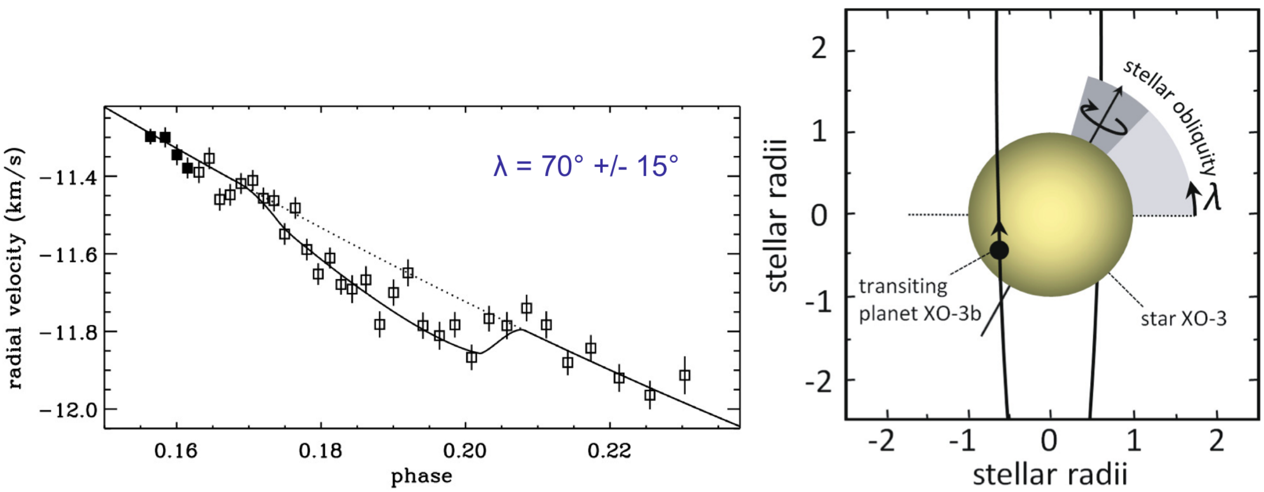

Fig. 2. *Left:* RV from SOPHIE measurements of the Rossiter-McLaughlin effect of XO-3b when the planet transits its parent star (Hébrard et al. 2008). The solid line shows the fitted model. *Right:* Schematic view of the XO-3 system with transverse transit, as seen from the Earth. The stellar spin axis is shown, as well as the planet orbit. The grey area shows the range the $\lambda = 70 \pm 15°$, which is favored by SOPHIE observations (Hébrard et al. 2008).

4 Others studies

4.1 Monitoring stellar activity

The precision of RV search for exoplanets is dependant of the noise induced by photospheric luminosity variations due to activity phenomena. Boisse et al. (2009) presented a study of the stellar activity of the transiting planet host star HD189733. We compared the variability in spectroscopic activity indices in HeI (5875.62 Å), Hα (6562.81 Å) and both of the CaII H& K lines (3968.47 Å and 3933.66 Å) with the evolution in the RV measurements and the shape of spectral lines. We used these correlations to correct from the RV jitter due to activity. This results in achieving high precision in measuring the orbital parameters of the planetary system.

4.2 The Earth as an extrasolar transiting planet

In order to identify the atmospheric gaseous bio-signatures observable in the Earth atmosphere as for an extrasolar planet, we observed the light transmitted through the Earth's atmosphere during Lunar eclipse. At optical wavelengths, we identified in the transmission spectra ozone, molecular oxygen, neutral sodium, molecular nitrogen and oxygen through the Rayleigh signature. This work is a proxy for the characterization and the search from bio-marker signatures from the ground with extremely-large telescope of future transiting Earth-like planets (Fig. 3).

5 Perspectives

Some new results are going to be published. Massive planets and brown dwarfs candidates from the giant planets survey around bright stars will be described in Díaz et al. (2010). Candidates from the follow-up of long-term trends revealed by ELODIE were fully characterized with complementary SOPHIE measurements achieving the discoveries of Jupiter-mass or massive planets on Jupiter or Saturn-like orbits.

The high-precision program permitted to identify some limitations related to the bonnette of the telescope that was designed for ELODIE some 15 years ago. Optimizations were done as the replacement of the guiding camera and its software or the installation of a new cryogenic controller system. Tests on square and octagonal

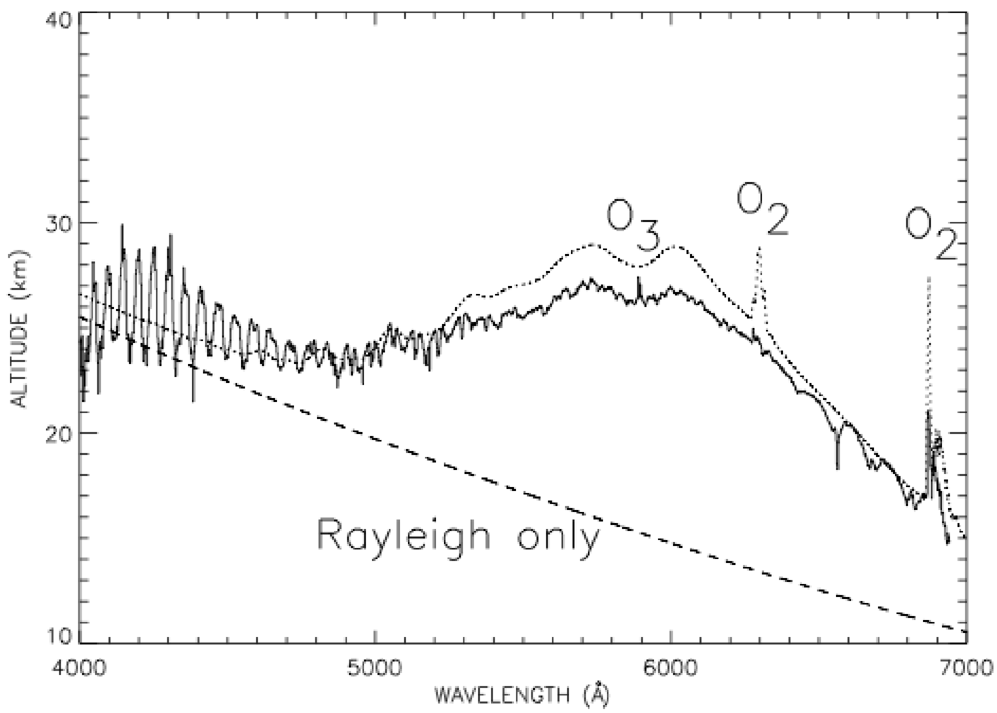

Fig. 3. Absorbing atmosphere thickness of the Earth versus wavelength as it will be observed during the transit of an extrasolar planet (observed with SOPHIE during Lunar eclipse in solid line and atmospheric model in dotted line) (Vidal-Madjar et al. 2010).

section fibers are under development in the aim to improve the stability of the spectrograph illumination (Boisse et al. 2010a). These will allow an improvement of the SOPHIE RV accuracy from now about 4-5 $\mathrm{m\,s^{-1}}$ to 2 $\mathrm{m\,s^{-1}}$. The high-precision search for super-Earths, subprogram stops since several months will then reach its objectives.

The authors thanks all the staff of Haute-Provence Observatory for their contribution to the success of the SOPHIE project and their support at the 1.93-m telescope. We wish to thank the "Programme National de Planétologie" (PNP) of CNRS/INSU, the Swiss National Science Foundation, and the French National Research Agency (ANR-08-JCJC-0102-01 and ANR-NT05-4-44463) for their continuous support to our planet-search programs.

References

Baranne, A., Queloz, D., Mayor, M., et al. 1994, A&AS, 119, 373

Boisse, I., Moutou, C., Vidal-Madjar, A., et al. 2009, A&A, 495, 959

Boisse, I., Bouchy, F., Chazelas, B., Perruchot, S., Pepe, F., Lovis, C., Hébrard, G. 2010a, in *New technologies for probing the diversity of brown dwarfs and exoplanets*, EPJ Web of Conferences, in press, `arXiv.org:1001.0794`

Boisse, I., Eggenberger, A., Santos, N.C. et al. 2010b, A&A, in press, `http://arXiv.org/abs/1006.4984`

Bouchy, F., Hébrard, G., Udry, S. et al. 2009, A&A, 505, 853

Da Silva, R., Udry, S., Bouchy, F. et al. 2006, A&A, 446, 717

Desort, M., Lagrange, A.-M., Galland, F. et al. 2009, A&A, 506, 1469

Hébrard, G., Bouchy, F., Pont, F. et al. 2008, A&A, 481, 52

Hébrard, G., Bonfils, X., Ségransan, D. et al. 2010a, A&A, 513, 69

Hébrard, G., Désert, J.-M., Díaz, R. et al. 2010b, A&A, 516, 95

Loeillet, B., Shporer, A., Bouchy, F. et al. 2008, A&A, 481, 529

Mayor, M., Pepe, F., Queloz, D. et al. 2003, The Messenger, 114, 20

Moutou, C., Hébrard, G., Bouchy, F. et al. 2009, A&A, 498, L5

Perruchot, S., Kohler, D., Bouchy, F. et al. 2008, in *Ground-based and Airborn Instrumentation for Astronomy II*, I.S. McLean and M.M. Casali (eds) Proceedings of the SPIE, vol. 7014, 17

Pont, F., Hébrard, G., Irwin, J.M., et al. 2009, A&A, 509, 695

Queloz, D., Mayor, M., Sivan, J.P. et al. 1998, in *Brown dwarfs and extrasolar planets*, eds. R. Rebolo, E.L. Martin & M.R. Zapatero Osorio, ASP Conf. Ser., 143, 324

Santos, N.C., Udry, S., Bouchy, F. et al. 2008, A&A, 487, 369

Vidal-Madjar, A., Arnold, L., Ehrenreich, D. et al. 2010, A&A, 523, A57

SF2A 2010
S. Boissier, M. Heydari-Malayeri, R. Samadi and D. Valls-Gabaud (eds)

A NEW MODEL OF COMETARY NON-GRAVITATIONAL FORCES

L. Maquet[1], F. Colas[1], J. Crovisier[2] and L. Jorda[3]

Abstract. The gravitational orbit of a comet is affected by the sublimation of water molecules by the nucleus when the comet approaches perihelion. This outgassing triggers a non-gravitational force (NGF) which significantly modifies the orbit of the comet. The amplitude of the perturbation depends on several parameters which can be constrained by visible, infrared and radio observations of the coma and nucleus of the comet. It depends also on the nucleus density, which can in turn be determined by modeling the effect of the NGF on the orbit of a comet. This method is the only method available so far to estimate the density of cometary nuclei. Up to now, the modeling of this effect is mostly based on an empirical model defined in the early 70's which uses a simplified isotropic outgassing model. Attempts have been made to use advanced anisotropic thermal models to calculate the NGF taking into account several observational constraint and to retrieve the nucleus density, but: (i) this approach is restricted to a handful of cometary nuclei which are sufficiently well-known to allow this type of modeling, and (ii) the authors usually don't fit directly the astrometric measurements but rather non-gravitational parameters calculated with the above-mentioned empirical model. We present a new model for non-gravitational forces with the aim of revisiting the problem of NGF calculation and nucleus density determination. The method is based on the separation of the surface of the nucleus in several surface elements located at different latitudes. The contribution of each surface element to the overall NGF is fitted from the astrometric measurements together with the density of the nucleus. This new method will be used to interpret future astrometric measurements of these pristine objects with GAIA.

Keywords: non-gravitational forces, comets, dynamics

1 Introduction

The last empirical model of non-graviational forces mostly used is Marsdens'one (Marsden et al. 1973) which was developped about 37 years ago. This symetrical model considers a global activiy of an half pure ice nucleus.

In this present work, we are revisiting the problem of NGF calculation and nucleus density determination. In the first section, we present the hypothesis of the model and a geometrical aproach. Then we focus our study on the calculation and the fit of the model. Finally, the last section is dedicated to the preliminary results.

2 Hypothesis of the model

The nucleus is modelized as a pseudo-sphere cut into latitudinal bands (Fig. 1). The thermal inertia of the nucleus is neglected and the gas velocity is considered proportional to the thermal gas velocity. These hypotheses are less restrictive than the Marsden's one (Marsden et al. 1973) and allow the seasonal effects.

3 Calculation and fit of the model

After simplification of the calculation, we see that the acceleration due to the outgassing of the water depends on the product of density by the radius of the nucleus ρR and on the coefficients C_i describing the activity of each latitudinal bands :

$$\overrightarrow{A_{NG}}(t) \propto \frac{1}{\rho R} \sum_{i=1}^{k} C_i \left(\frac{d\overrightarrow{F}(t)}{dS} \right)_i \tag{3.1}$$

[1] IMCCE - Observatoire de Paris-Meudon, 75014 Paris, France
[2] LESIA - Observatoire de Paris-Meudon, 92195 Meudon, France
[3] LAM - Observatoire Astronomique de Marseille-Provence, 13388 Marseille, France

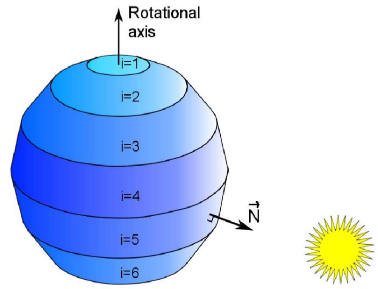

Fig. 1. Geometrical view of a modelized nuclei with seven latitudinal strips.

The surfacic force (Fig. 2) depends on the sublimation rate Z from the incidence of the sun rays and the calculation of the gas velocity V_g from the temperature (Crifo 1987) :

$$\left(\frac{d\overrightarrow{F(t)}}{dS}\right)_i = Z_i(t).V_{g_i}(t).M_{H_2O}.\overrightarrow{N_i} \tag{3.2}$$

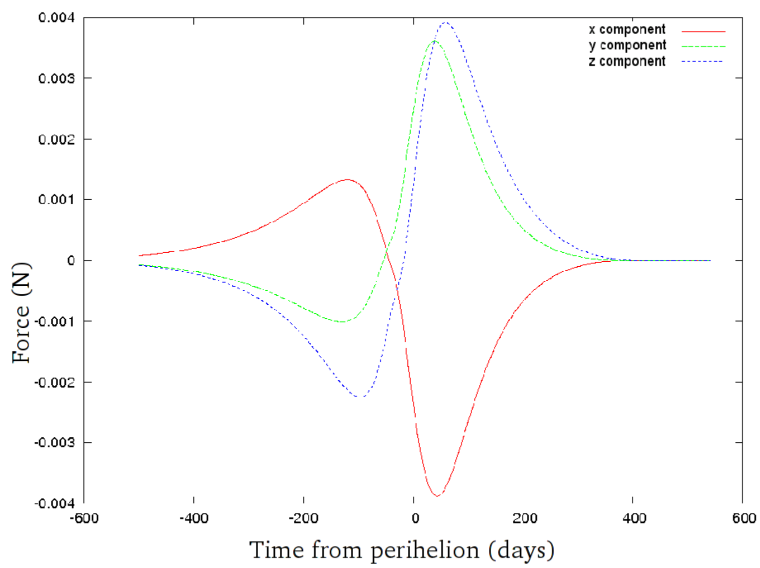

Fig. 2. Example of force components of one of the bands.

The fitting of the model was made by least square method and now the L-BFGS method (a quasi-Newton method for constrained optimisation) is being tested. The fitted parameters are :

- the initial conditions of position and velocity of the comet
- ρR, the density-radius
- coefficients C_i (between 0 and 1)

The fitted data are :

- currently : astrometric positions from the MPC
- In a near future : water production rate (HST, radio measurements in Nancay and also visible observations), gas velocity (radio in Nancay)

4 Preliminary results

4.1 Verification of the calculation of the subsolar point

The latitude of the subsolar point is the starting point for calculating the elevation of the sun, the gas production rate and thus non-gravitational forces. Its position in the cometocentric frame varies over time depending on the rotational axis inclination, and on the nucleus rotation around its axis and around the sun. Figure 3 shows that the calculation of the latitude of the subsolar point gives similar results than Davidsson and Gutiérrez (2004).

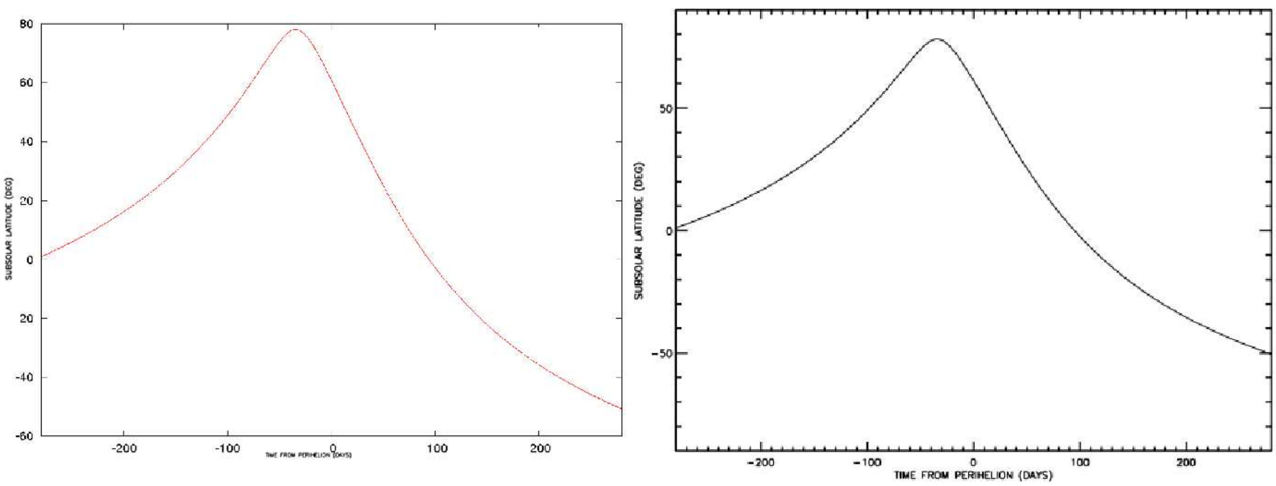

Fig. 3. Latitude of the subsolar point with axis orientation $(\alpha, \delta) = (220^\circ, -10^\circ)$ compared to the calculation of Davidsson and Gutiérrez (2004) on the right for the comet 19P/Borelly

4.2 Calculation of the non-gravitational acceleration

Figure 4 shows the gas production curve. Which is obtained from the following energy balance :

$$(1 - A)\,\frac{F\odot}{R_h^2}\cos z = \epsilon\sigma T^4 + H(T)Z(T)(1-\alpha) \tag{4.1}$$

where A is the Bond's albedo, $F\odot$ the solar constant, R_h the heliocentric distance of the comet, z the elevation of the sun, ϵ the infrared emissivity of the nucleus, σ the Stefan-Boltzmann constant, T the surfacic temperature of the zone, α a water recondensation parameter (Crifo 1987), $H(T)$ the sublimation latent heat and $Z(T)$ the sublimation rate. The displacement of the peak from perihelion is due to the spin axis orientation (,)=(220,-10).

Figure 5 shows the maximal contributions of each latitudinal band to the non-gravitational acceleration for a seven strips model. We can see that all the contributions are relatively distinct hence allowing an adjustement of the coefficients C_i. The total non-gravitational acceleration consists in a linear combination of these contributions.

5 Conclusions

In a near future, the model will be fitted by the Broyden-Fletcher-Goldfarb-Shanno method to constrain the C_i coefficients. We will apply this model to known comets like, 19P/Borelly, 81P/Wild2, 103P/Hartley2 and 1P/Halley. One of the main goal is to determine the density-radius. GAIA astrometric measurements will be very useful as they will allow to measure comet nucleus position.

The next evolutions of the model will be to use an ellipsoidal shape for the nucleus as well as to add the fitting of the production rate using $Af\rho$ measurements and of the gas velocity using radio measurements from Nancay observatory.

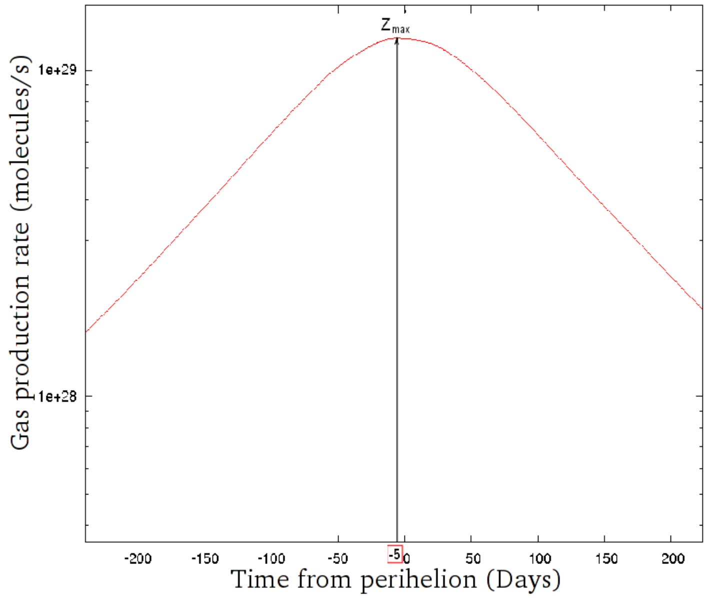

Fig. 4. Gas production rate of a fully active nucleus with spin axis orientation $(\alpha, \delta) = (220^\circ, -10^\circ)$ (Davidsson and Gutiérrez 2004) as function of time for the comet 19P/Borelly

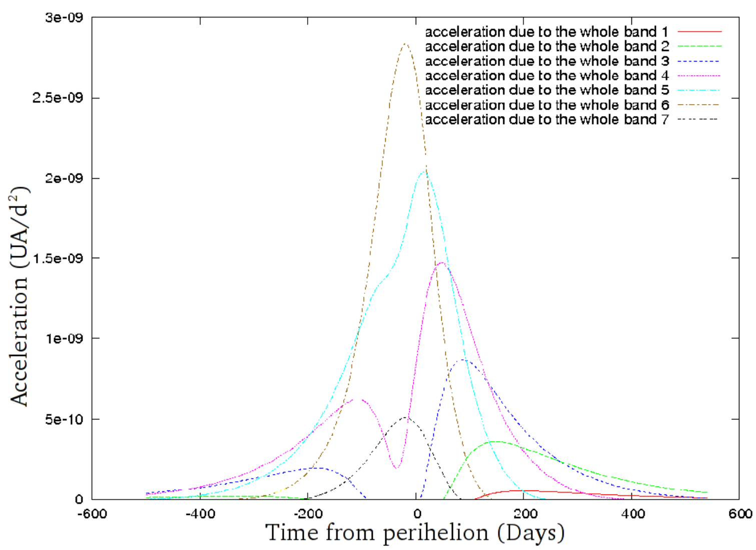

Fig. 5. Non-gravitational accelerations of the whole bands for a seven strips model of the comet 19P/Borelly

References

Crifo J.F. 1987, A&A, 187, 438

Davidsson B.J.R. and Gutiérrez P.J. 2004, Icarus, 168, 392

Marsden B.G. et al. 1973, AJ, 78, 211

PNST - PCHE

Sun and Earth

SF2A 2010
S. Boissier, M. Heydari-Malayeri, R. Samadi and D. Valls-Gabaud (eds)

AUTOMATED DETECTION OF FILAMENTS IN SDO DATA

É. Buchlin[1], C. Mercier[1], S. Engin[1], S. Parenti[1] and J.-C. Vial[1]

Abstract. Solar eruption can eject billions of tons of plasma to the interplanetary space, with geophysical effects and impacts on human activities. The time constraints for space weather application as well as the huge volume of data that needs to be analyzed, especially since the launch of SDO, imply that the detection of solar filaments and their eruptions must be automated. Most current detection codes use Hα data, which are not available frequently enough for these applications. We present a new detection code that we have developed at IAS and that uses the high spatial and temporal-resolution SDO/AIA He II 30.4 nm data.

Keywords: Sun: filaments, Sun: solar-terrestrial relations, techniques: image processing

1 Introduction

Instabilities of the magnetic field can cause the ejection of plasma to the interplanetary space, producing a Coronal Mass Ejection (CME), which can strongly perturb the solar wind. If directed towards the Earth, a CME can put some human activities at risk. However, its effects can be mitigated if it is detected well enough before arriving on the Earth. This is one of the main stakes of space weather.

In this process, filaments (or prominences when seen in emission at the solar limb), which are made of plasma maintained in suspension in the corona by the magnetic field, play a major role, as they provide the material (about 100 times denser and colder than the surrounding corona) that can be ejected to the CME. The detection of a filament and its subsequent disappearance thus provides a signature for the start of a potential CME.

Filament detection is usually performed from images taken in the Hα 656.3nm line (e.g. Bernasconi et al. 2005; Fuller et al. 2005; Gao et al. 2002; Jing et al. 2004; Scholl & Habbal 2007; Zharkova & Schetinin 2005). For example, the Bernasconi et al. (2005) code is based on a threshold, region growing to a second, higher threshold, and a morphological filter for the selection of elongated structures. This code produces a list of filaments (with size, position, and chirality), and it tracks them as a function of time.

The interest of Hα images lies in the fact that in these images filaments are easily seen as dark, elongated structures on a brighter background. However, these data come from ground-based observatories only*, and despite current improvements to the capabilities of these observatories, high-cadence observations during all day, every day, cannot be done. At the moment a few tens of images per day are available at most, and this is not enough to detect filament eruptions in near real-time.

For this reason we developed a new filament detection code that can use data which is continuously available at high cadence. The 30.4nm channel, routinely observed by space instruments like SoHO/EIT, STEREO/SECCHI and now SDO/AIA would be one of the main components of such a detection system. The He II 30.4nm line shares indeed some of its emission properties with the Hα line, and filaments are also visible as dark structures in this channel, although the separation from the background is more difficult than for Hα. In particular, the data from SDO/AIA, with their high resolution (4096^2 pixels at 0.6 arcsec resolution) and high cadence (10s for the 30.4nm channel) offer a new opportunity for such an enterprise.

[1] Univ Paris-Sud, Institut d'Astrophysique Spatiale, UMR8617, CNRS, F-91405 Orsay, France

*For example from the global Hα network: Mauna Loa, Big Bear, Meudon, Kanzelhöhe, Catania, Yunnan, and Huairou solar observatories.

2 Development of a new filament detection code

Methods used to detect filaments in Hα cannot generally be used for the 30.4nm channel, mainly because at 30.4nm the background contains features from the chromospheric network, which have a high contrast. For this reason we rather choose to start with a filtering in curvelets space, in order to select dark elongated structures against this contrasted background. Curvelets (Starck et al. 2002) are orthogonal functions analogous to wavelets in 2D, characterized by a position, scale, and orientation (Fig. 1). Then we use a threshold to obtain clusters of pixels, and we give a score to these clusters according to their size, shape, position, and intensity. The clusters of pixels with the best scores, or scores above some threshold, are considered as filaments. Then their spine is computed and the resulting filaments can be tracked as a function of time.

3 Current status and perspectives

The filament detection is now working, but a proper assessment of its results remains to be done. Improvements are still needed in order to be able to rely on tracking of detected filaments for the near-real-time detection of filament eruptions. Such improvements could come for example from adding to the computation of scores a criterion of proximity to a magnetic field polarity inversion line. We are also currently working on including this code in the SDO/AIA data pipeline, first at MEDOC in IAS, with the aim of producing a catalog of filaments and their eruptions than can be sent to the Heliophysics Events Knowledge Base (`http://www.lmsal.com/hek`).

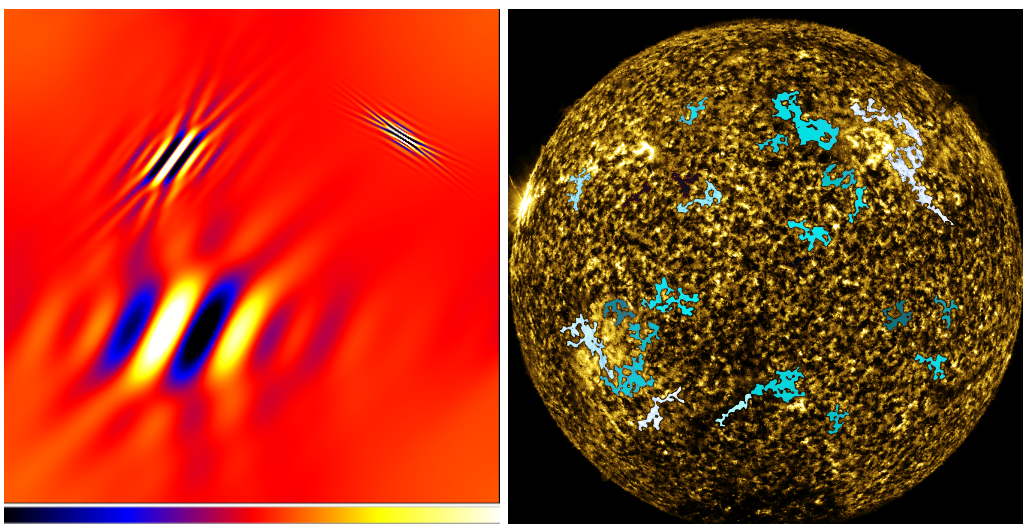

Fig. 1. Example curvelet functions (real part), and detected filaments in a SDO/AIA image (blue/white pixels, brighter blue means better score).

References

Bernasconi, P. N., Rust, D. M., & Hakim, D. 2005, Sol. Phys., 228, 97

Fuller, N., Aboudarham, J., & Bentley, R. D. 2005, Sol. Phys., 227, 61

Gao, J., Wang, H., & Zhou, M. 2002, Sol. Phys., 205, 93

Jing, J., Yurchyshyn, V. B., Yang, G., Xu, Y., & Wang, H. 2004, Astrophys. J., 614, 1054

Scholl, I. F. & Habbal, S. R. 2007, Sol. Phys., 194

Starck, J., Candes, E. J., & Donoho, D. L. 2002, IEEE Transactions on Image Processing, 11, 670

Zharkova, V. V. & Schetinin, V. 2005, Sol. Phys., 228, 137

SF2A 2010
S. Boissier, M. Heydari-Malayeri, R. Samadi and D. Valls-Gabaud (eds)

NONLINEAR DIFFUSION EQUATION FOR ALFVÉN WAVE TURBULENCE

S. Galtier and É. Buchlin[1] [1]

Abstract. We discuss about the possibility to derive rigorously a nonlinear diffusion equation for incompressible MHD turbulence. The background of the analysis is the asymptotic Alfvén wave turbulence equations from which a differential limit is taken. The result is a universal diffusion-type equation in $\mathbf{k}$-space which describes in a simple way and without free parameter the energy transport perpendicular to the external magnetic field $\mathbf{B_0}$ for transverse fluctuations. It is compatible with both the thermodynamic equilibrium and the finite flux spectra derived by Galtier et al. (2000). This new system offers a powerful description of a wide class of astrophysical plasmas.

Keywords: magnetohydrodynamics, turbulence, waves

The measurements made in particular by various spacecrafts have added substantially to our knowledge of astrophysical plasmas. Among the different media widely analyzed we find the interstellar medium, the solar wind or the Sun's atmosphere. In the latter case, it is believed that magnetohydrodynamic (MHD) turbulence plays a central role in the dynamics and the small scale heating. For example, in active region loops spectrometer analyses revealed non-thermal velocities reaching sometimes 50 km/s (Chae et al. 1998); this line broadening is generally interpreted as unresolved turbulent motions with length scales smaller than the diameter of coronal loops which is about one arcsec and timescales shorter than the exposure time of the order of few seconds. Turbulence is evoked in the solar coronal heating problem since it offers a natural process to produce small scale heating (see *e.g.* Heyvaerts & Priest 1992). Weak MHD turbulence is now proposed has a possible regime for some coronal loops since a very small ratio is expected between the fluctuating magnetic field and the axial component (Rappazzo et al. 2007). Inspired by the observations and by recent direct numerical simulations of 3D MHD turbulence (Bigot et al. 2008a), an analytical model of coronal structures has been proposed (Bigot et al. 2008b) where the heating is seen as the end product of a wave turbulent cascade. Surprisingly, the heating rate found is non negligible and may explain the observations.

MHD turbulence modeling is the main tool to investigate the situations previously discussed. Although it cannot be denied that numerical resources have been significantly improved during the last decades, direct numerical simulations of MHD equations are still limited for describing highly turbulent media (see *e.g.* Mininni & Pouquet 2007). For that reason, shell cascade models are currently often used to investigate the small scale coronal heating (Buchlin & Velli 2007) and its impact in terms of spectroscopic emission lines. Transport equations are also used for example in the context of solar wind acceleration in the extended solar corona (Cranmer & van Ballegooijen 2003). The *ad hoc* model is an advection-diffusion equation for the evolution of the energy spectrum whose inspiration is found in the original paper by Leith (1967). It is also a cascade model where the locality of the nonlinear interactions is assumed but where the dynamics is given by a second-order nonlinear partial differential equation whereas we have ordinary differential equations for shell models.

A theoretical understanding of the statistics of turbulence and the origin of the power law energy spectrum, generally postulated from dimensional considerations *à la* Kolmogorov, remains one of the outstanding problems in classical physics which continues to resist modern efforts at solution. The difficulty lies in the strong nonlinearity of the governing equations which leads to an unclosed hierarchy of equations. Faced with that situation different models have been developed like closure models in Fourier space. In the meantime, Leith (1967) and Iroshnikov (1964) proposed a diffusion approximation to inertial energy transfer for respectively isotropic HD and MHD turbulence. This new class of *ad-hoc* models describes the time evolution of the spectral energy density for originally an isotropic 3D incompressible turbulence, in terms of a partial differential equation

[1] Univ Paris-Sud, Institut d'Astrophysique Spatiale, UMR8617, CNRS, F-91405 Orsay, France

by making a diffusion approximation to the energy transport process in the $\mathbf{k}$–space representation. Ignoring forcing and dissipation the Leith's equation for HD turbulence reads in Fourier space

$$\frac{\partial E(k)}{\partial t} = \frac{\partial}{\partial k}\left(k^{11/2}\sqrt{E(k)}\frac{\partial}{\partial k}\left(\frac{E(k)}{k^2}\right)\right) , \tag{0.1}$$

where $E(k)$ is the unidimensional energy spectrum. Beyond its relative simplicity, equation (0.1) exhibits several important properties like the preservation after time integration of a non negative spectral energy and the production of the Kolmogorov spectrum, $k^{-5/3}$, in the inertial range.

The generalization of the Leith's model to 3D isotropic MHD turbulence was first made by Iroshnikov (1964) and then in a different way by Zhou & Matthaeus (1995). In the latter case, the main modification happens in the evaluation of the transfer time for which a combination of the eddy turnover time τ_{eddy} and the Alfvén time τ_A was proposed. The phenomenological evaluation of the transfer time allows the recovering of either the Kolmogorov, $k^{-5/3}$, or the Iroshnikov–Kraichnan, $k^{-3/2}$, spectrum when the ratio τ_{eddy}/τ_A is respectively much less or much larger than one.

The case of Alfvén wave turbulence for which a relatively strong B_0 is required is an important limit for which a rigorous analysis is possible (Galtier et al. 2000). The wave kinetic equations derived are a set of coupled integro-differential equations which are not obvious to handle numerically or analytically. This remark was a motivation for deriving a simpler set of equations by taking the differential limit of the asymptotically exact Alfvén wave equations. The systematic derivation gives in the simplest case (*i.e.* for zero cross-helicity) the following equation for the transverse fluctuations (Galtier & Buchlin 2010)

$$\frac{\partial E_\perp(k_\perp)}{\partial t} = \frac{\partial}{\partial k_\perp}\left(k_\perp^6 E_\perp(k_\perp)\frac{\partial}{\partial k_\perp}\left(\frac{E_\perp(k_\perp)}{k_\perp}\right)\right) , \tag{0.2}$$

where $E_\perp(k_\perp)$ is the energy spectrum and $k_\perp$ is the wavenumber transverse to the uniform magnetic field $\mathbf{B_0}$. This nonlinear diffusion equation reproduces the finite flux solution in $k_\perp^{-2}$ as well as the thermodynamic equilibrium spectrum in $k_\perp$ (see Galtier & Buchlin (2010) for numerical illustrations). It is a simple and therefore useful system for describing a wide class of astrophysical plasmas. Coronal magnetic loops characterized by a strong axial magnetic field are probably a first good example of application of Alfvén wave turbulence.

References

Bigot, B., Galtier, S., & Politano, H. 2008a, Phys. Rev. E, 78, 066301

Bigot, B., Galtier, S., & Politano, H. 2008b, A&A, 490, 325

Buchlin, É., and Velli, M. 2007, ApJ, 662, 701

Chae, J., Schühle, U., & Lemaire, P. 1998, ApJ, 505, 957

Chandran, B.D.G. 2005, Phys. Rev. Lett., 95, 265004

Cranmer, S.R., & van Ballegooijen, A.A. 2003, ApJ, 594, 573

David, C., Gabriel, A.H., Bely-Dubau, F., et al. 1998, A&A, 336, L90

Galtier, S., Nazarenko, S.V., Newell, A.C., & Pouquet, A. 2000, J. Plasma Phys., 63, 447

Galtier, S., & Buchlin, É. 2010, ApJ, in press

Heyvaerts, J., & Priest, E.R. 1992, ApJ, 390, 297

Iroshnikov, P. 1964, Sov. Astron., 7, 566

Leith, C.E. 1967, Phys. Fluids, 10, 1409

Mininni, P.D., & Pouquet, A. 2007, Phys. Rev. Lett., 99, 254502

Rappazzo, A.F., Velli, M., Einaudi, G., & Dahlburg, R.B. 2007, ApJ, 657, L47

Zhou, Y., & Matthaeus, W.H. 1990, J. Geophys. Res., 95, 14881

SF2A 2010
S. Boissier, M. Heydari-Malayeri, R. Samadi and D. Valls-Gabaud (eds)

SCIENCE OUTPUTS OF THE CDPP ON-LINE ANALYSIS TOOL AMDA

V. Génot[1], C. Jacquey[1], E. Budnik[2], M. Bouchemit[1], M. Gangloff[1], A. Fedorov[1], B. Lavraud[1], N. André[1], G. Fruit[1], P. Louarn[1], C. Harvey[1], E. Pallier[1], E. Penou[1], R. Hitier[3], B. Cecconi[4], F. Dériot[5], D. Heulet[5], J.-L. Pinçon[6] and B. Besson[5]

Abstract. According to the Virtual Observatory paradigm the CDPP developed an on-line data mining tool, AMDA (Automated Multi-Dataset Analysis) : it is a web-based facilities for analyzing on-line space physics data coming from its own local database as well as remote ones (CDAWeb, CAA, MAPSKP, THEMIS database). This tool allows the user to perform on-line classical manipulations such as data visualization, parameter computation or data extraction. AMDA also offers innovative functionalities such as event searching using the data from multiple sources in either a visual or an automated way, the generation, exploitation and management of time-tables, or event lists. This presentation will focus on scientific analyses performed by AMDA users in recent years.

Keywords: databases, virtual observatory, analysis tool, space physics

1 Introduction

While the astronomy and astrophysics domain are relatively advanced regarding their implication in the creation of Virtual Observatories (VO), space and planetary physics are just beginning their first steps into this effort (Harvey et al. 2008). At the French and European level, it is one of the goals of CDPP (Centre de Données de Physique des Plasmas) to encourage the space physics community to participate in this project. Recently, the CDPP opened a new web-based service called AMDA (Jacquey et al. (2009)), aimed at being the CDPP contribution to the Virtual Observatory. This poster describes a few scientific use cases of AMDA.

2 AMDA uses cases

To date AMDA has been use for scientific analysis in the diverse fields of magnetosheath, plasma sheet, and turbulence physics, space weather and comparative planetology, as described in the poster which may obtained at the CDPP web site. In the following we detailed a particular use case.

On Figure 1 is displayed two different ways of finding events with AMDA, either by visual inspection (steps 1a and 1b) or by automatic detection of events (steps 2a and 2b). The use case is the detection of magnetopause crossings at geosynchronous orbit using LANL satellites data. In this aim we define the parameter C_{MPX} (see Figure 1) which is expected to present a positive/negative spike for inbound/outbound crossings and the typical time scale of the magnetopause crossing is given by $1/|C_{\mathrm{MPX}}|$. From trial and error we found that $|C_{\mathrm{MPX}}| > 0.05$ is an adequate condition to efficiently select magnetopause traversals.

For the visual inspection method, the user may plot C_{MPX} (top panel of Figure 1b) together with other parameters (here T and N). By mouse click he/she may select periods of time where C_{MPX} peaks which marks magnetopause crossings. This time intervals may be recorded for future use in a time table. Alternatively the user can start a systematical search for events by asking AMDA to look for all interval satisfying the condition $C_{\mathrm{MPX}} > 0.05$ (Figure 2a). This conditional search procedure results also in a time table which is illustrated on Figure 2b.

[1] CESR, Universitté de Toulouse (UPS) & CNRS (UMR5187), 9 av. colonel Roche, 31400 Toulouse, France
[2] Noveltis, 2 av. de l'Europe, 31520 Ramonville Saint-Agne, France
[3] Co-Libri, 11300 Pauligne, France
[4] LESIA, Observatoire de Paris-Meudon, 5 place Janssen, 92190 Meudon, France
[5] CNES, Centre Spatial de Toulouse, 18 avenue E. Belin, 31401 Toulouse, France
[6] LPCE, Laboratoire de Physique et Chimie de l'Environnement, 45071 Orléeans, France

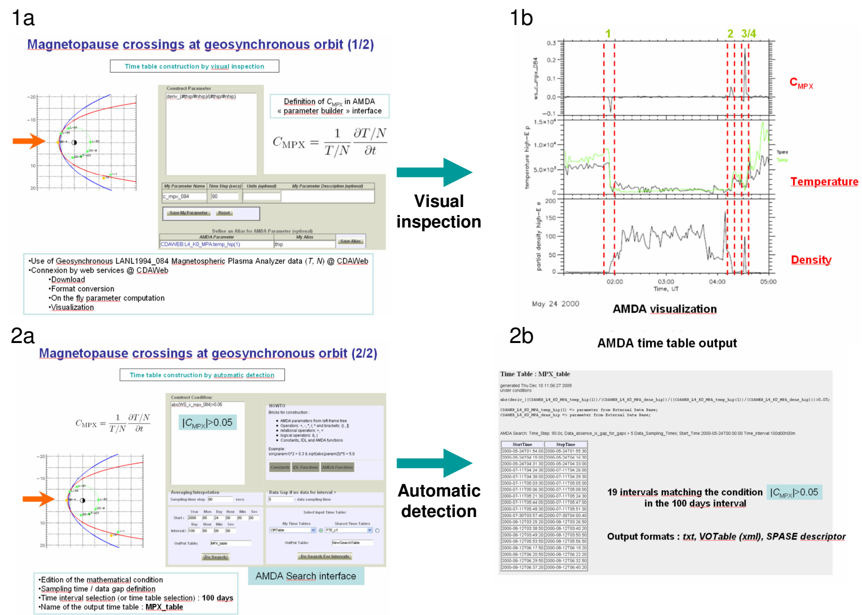

Fig. 1. Two ways for producing time tables in AMDA : visual inspection and automatic detection in the case of magnetopause crossings at geosynchronous orbits.

3 Conclusions

Detailed presentations and uses of AMDA may be found in the literature (see for instance André et al. (2009); Génot et al. (2009); Jacquey et al. (2010)) or directly on the CDPP web site, `http://cdpp.cesr.fr`.

References

André, N., Cecconi, B., Budnik,et al. 2009, SF2A-2009: Proceedings of the Annual meeting of the French Society of Astronomy and Astrophysics, held 29 June - 4 July 2009 in Besançon, France. Eds.: M. Heydari-Malayeri, C. Reylé and R. Samadi, p.231

Génot, V., Jacquey, C., Bouchemit, et al. 2009, Advances in Space Research, Volume 45, Issue 9, p. 1145-1155

Jacquey, C., Génot, V., Budnik, et al. 2010, The Cluster Active Archive, Studying the Earth's Space Plasma Environment. Edited by H. Laakso, M.G.T.T. Taylor, and C. P. Escoubet. Astrophysics and Space Science Proceedings, Berlin: Springer, p.239-247

Harvey, C., Gangloff, M., King, T., et al. 2008, Earth Science Informatics

SF2A 2010
S. Boissier, M. Heydari-Malayeri, R. Samadi and D. Valls-Gabaud (eds)

A NEW TURBULENCE REGIME IN THE SOLAR-WIND AT ELECTRON SCALES

R. Meyrand[1] and S. Galtier[1]

Abstract. Solar wind turbulence is characterized by a Kolmogorovian magnetic fluctuations spectrum at large scales followed by a second inertial range with steeper spectra associated with nonlinear dispersive processes. Recent observations reveal the presence of a third region – called dissipation range – at scales smaller than the electron inertial length and characterized by steeper spectra. We investigate this regime in the electron magnetohydrodynamics approximation and discuss the possibility to derive an exact and universal law for third-order structure functions. This law corresponds to a magnetic fluctuations isotropic spectrum in $k^{-11/3}$ compatible with the observations. We conclude on the possible existence of a third turbulence regime in the solar wind instead of a dissipation range as recently postulated.

Keywords: electron magnetohydrodynamics, solar wind, turbulence

1 Solar wind turbulence

Solar wind turbulence provides an ideal laboratory for studying high Reynolds number plasma turbulence. This unique situation allows us to investigate for example the origin of anisotropy, to evaluate the mean energy dissipation rate, to detect multiscale intermittency, or to analyze different regimes of turbulence characterized by a steepening of the magnetic field fluctuations spectrum with a power law index going from $-5/3$, at frequencies lower than 1Hz, to indices lying around -2.5 at higher frequencies (see *e.g.* Klein et al. 1993; Smith et al. 2006; Alexakis et al. 2007; Bigot et al. 2008; MacBride et al. 2008; Kiyani et al. 2009).

The spectral break near 1Hz has been a subject for intensive studies and controversies in the last decades. It was first interpreted as the onset of dissipation caused for example by kinetic Alfvén wave damping (Leamon et al. 1998). Then, it was demonstrated that the wave damping rate usually increases very strongly with wavenumbers and should lead to a strong cutoff in the power spectra rather than a steepened power law (Li et al. 2001). In the meantime, there are some indications that the fluctuations are accompanied by a bias of the polarization suggesting the presence of right-hand polarized, outward propagating waves (Goldstein et al. 1994). Also it was proposed (Stawicki et al. 2001) that Alfvén – left circularly polarized – fluctuations are suppressed by proton cyclotron damping and that the high frequency power law spectra are likely to consist of whistler fluctuations (Matthaeus et al. 2008). It is currently believed that the steepening of the spectra at 1Hz is mainly due to non-linear dispersive processes that range from kinetic Alfvén waves (Howes et al. 2008), electromagnetic ion-cyclotron Alfvén waves (Gary et al 2008), or/and electron whistler waves (Ghosh et al. 1996; Galtier 2006; Galtier & Buchlin 2007) in the framework of Hall magnetohydrodynamics (MHD) or simply electron MHD.

The most recent solar wind observations made with the high resolution magnetic field data of the Cluster spacecraft (Alexandrova et al. 2009; Sahraoui et al. 2009) reveal the presence of a third region – called dissipation range – at scales smaller than d_e and characterized by even steeper magnetic fluctuations spectra with a power law index around -3.8. These spectra observed only on half a decade are interpreted as either a power law (Sahraoui et al. 2009) or an exponential law (Alexandrova et al. 2009). Although the theoretical interpretation of such a regime is still open (Matthaeus et al. 2008), a recent theoretical analysis shows that a kinetic Alfvén wave cascade subject to collisionless damping cannot reach electron scales in the solar wind at 1 AU (Podesta et al. 2010). The direct consequence is that the spectra observed must be supported by another type of wave modes. It is noteworthy that this new regime at electron scales gives rise to the same controversy as the steepening found two decades ago around 1Hz which brings up naturally the following question: Have we really found the dissipation scale of the solar wind plasma or is it the onset of a new turbulence regime?

[1] Univ Paris-Sud, Institut d'Astrophysique Spatiale, UMR8617, CNRS, F-91405 Orsay, France

2 Universal laws at electron scales $\ell < d_e$

The turbulence regime at scales smaller than the electron inertial length d_e has been recently investigated through the electron MHD approximation (Meyrand & Galtier 2010). The assumptions of homogeneity and isotropy are made to derive an exact and universal law for third-order structure functions. This law takes the form

$$d_i d_e^2 \langle \delta J_L (\delta \mathbf{J})^2 \rangle = \frac{4}{3} \varepsilon^J r \, , \tag{2.1}$$

with d_i the ion inertial length, $\mathbf{J}$ the current density, $\delta\mathbf{J} \equiv \mathbf{J}(\mathbf{x}+\mathbf{r}) - \mathbf{J}(\mathbf{x})$ and ε^J the mean energy dissipation rate per unit mass. By definition L means the longitudinal component of the vector, *i.e.* the one along the direction $\mathbf{r}$. The derivation of this universal law is not straightforward but then one can predict easily the form of the associated magnetic spectrum since one has the relation $\mathbf{J} = \nabla \times \mathbf{B}$; it reads

$$B^2(k) \sim \left(\frac{\varepsilon^J}{d_i d_e^2} \right)^{2/3} k^{-11/3} \, . \tag{2.2}$$

We see that the power law is compatible with the most recent solar wind measurements (-3.8). Although the assumption of isotropy is in apparent contradiction with the observations, it is claimed that the method used is a powerful way to have a first estimate of the anisotropic spectrum. Indeed, the main source of anisotropy is the presence of a large scale magnetic field which reduces the nonlinear transfer along its direction. Then, the most relevant spectral scaling is the transverse one for which the spectral index corresponds to the isotropic case if arguments based on the critical balance condition are used.

3 Conclusion

The turbulence regime at scales smaller than the electron inertial length d_e is discussed through the approximation of electron MHD. A new universal and exact law in terms of structure functions for the current density may be derived (Meyrand & Galtier 2010). This law leads to the prediction of a $k^{-11/3}$ power law spectrum for the magnetic field fluctuations compatible with the most recent observations made with Cluster. This result is the first prediction for the magnetic fluctuations spectrum at these length scales. The possibility to get a turbulence regime at electron scales questions the origin of dissipation in the solar wind and more generally in space plasmas.

References

Alexakis, A., Bigot, B., Politano, H., & Galtier, S. 2007, Phys. Rev. E, 76, 056313
Alexandrova, O., Saur, J., Lacombe, C. et al. 2009, Phys. Rev. Lett., 103, 165003
Bigot, B., Galtier, S., & Politano, H. 2008, Phys. Rev. E, 78, 066301
Galtier, S. 2006, J. Plasma Phys., 72, 721
Galtier, S., & Buchlin, E. 2007, ApJ, 656, 560
Gary, S.P., Saito, S., & Li, H. 2008, Geophys. Res. Lett., 35, L02104
Ghosh, S., Siregar, E., Roberts, D.A., & Goldstein, M.L. 1996, J. Geophys. Res., 101, 2493
Goldstein, M.L., Roberts, D.A., & Fitch, C.A. 1994, J. Geophys. Res., 99, 11519
Howes, G.G. et al. 2008, J. Geophys. Res., 113, A05103
Kiyani, K.H. et al. 2009, Phys. Rev. Lett., 103, 075006
Klein, L., Bruno, R., Bavassano, B., & Rosenbauer, H. 1993, J. Geophys. Res., 98, 17461
Leamon, R.J., Smith, C.W., Ness, N.F., Matthaeus, W.H., & Wong, H.K. 1998, J. Geophys. Res., 103, 4775
Li, H., Gary, S.P., & Stawicki, P. 2001, Geophys. Res. Lett., 28, 1347
MacBride, B.T., Smith, C.W., & Forman, M.A. 2008, ApJ, 679, 1644
Matthaeus, W.H., Servidio, S., & Dmitruk, P. 2008, Phys. Rev. Lett., 101, 149501
Meyrand, R., & Galtier, S. 2010, ApJ, 721, 1421
Podesta, J.J., Borovsky, J.E., & Gary, S.P. 2010, ApJ, 712, 685
Sahraoui, F., Goldstein, M.L., Robert, P., & Khotyaintsev, Yu V. 2009, Phys. Rev. Lett., 102, 231102
Smith, C.W., Hamilton, K., Vasquez, B.J., & Leamon, R.J. 2006, ApJ, 645, L85
Stawicki, O., Gary, P.S., & Li, H. 2001, J. Geoph. Res., 106, 8273

THE SUN AS A PARTICLE ACCELERATOR: HARD X-RAY AND γ-RAY DIAGNOSTICS OF ENERGETIC PARTICLES

N. Vilmer[1]

Abstract. Explosive phenomena of magnetic energy conversion in the solar corona lead to the production of energetic particles at all energies. While some fast particles (electrons and ions) produce high energy radiation when interacting with the solar atmosphere (X-rays,γ-rays), others escape in the corona and interplanetary medium, produce radio emission and may eventually reach the Earth's orbit. I shall illustrate here with some high-energy observations the properties that can be derived on energetic particles. I will concentrate on some of the observations obtained in the last years at high spectral resolution with RHESSI and INTEGRAL/SPI and on the spatially resolved observations provided by RHESSI. I shall present some open questions still being discussed and give a brief overview of future observations in the field of high energy solar physics.

Keywords: Sun, flares, particle acceleration, X-rays, gamma-rays

1 Introduction

The Sun is a powerful particle accelerator. This has been known for years, since the first detection of solar energetic protons by ground-based neutron monitors, the first detection of solar flares in radio and X-rays, the first observations of gamma-ray line flares from energetic protons in 1972 and first detection of >100 MeV solar neutrons aboard SMM/GRS in 1982 (see e.g. Vilmer, MacKinnon and Hurford 2010 for a review).

Solar flares and coronal mass ejections (CMEs) are the most powerful events in the solar system. In several tens of minutes, they can convert up to 10^{32} ergs of magnetic energy into accelerated particles, heated plasma and ejected solar material. An estimate of this energy budget has been performed for some events (see e.g. Emslie et al (2004)). It is found that the energy contained in energetic electrons and ions interacting at the Sun is a large amount of the magnetic energy which can be released in active region during a solar flare. Understanding particle acceleration in flares therefore provides powerful constraints on coronal energy conversion processes.

2 Hard X-ray and gamma-ray diagnostics of flare energetic particles

The most quantitative diagnostics of energetic particles interacting at the Sun are provided by hard X-ray/γ-ray observations which give information on electron and ion energy spectra, numbers and energy contents. Fig. 1 (Left) shows a theoretical HXR/GR spectrum of a solar flare from 1 keV to 100 MeV. Flare accelerated electrons (energies above > 10 keV) produce bremsstrahlung continuum emission by their braking in the Coulomb field of ambient ions, and above 500-700 keV of ambient electrons. This continuum is dominant below 1 MeV and again in the 10-50 MeV range. Energetic ions with energies in the > 1 MeV/nuc to 100 MeV/nuc range produce through interaction in the solar atmosphere a complete γ-ray line (GRL) spectrum which consists of several nuclear de-excitation lines, neutron capture and positron annihilation lines (see e.g. Ramaty, 1986; Share and Murphy, 2006 and Vilmer, MacKinnon, Hurford, 2010 for reviews). When ions over a few hundred MeV/nuc are produced in the flare, nuclear interactions with the ambient medium produce secondary pions whose decay products lead to a broad-band continuum at photon energies above 10 MeV (with a broad peak around 70 Mev from neutral pion radiation) and also secondary neutrons which, if energetic enough, may escape from the Sun

[1] LESIA, Observatoire de Paris, CNRS, UPMC, Universit Paris-Diderot, 5 place Jules Janssen, 92195 Meudon, France

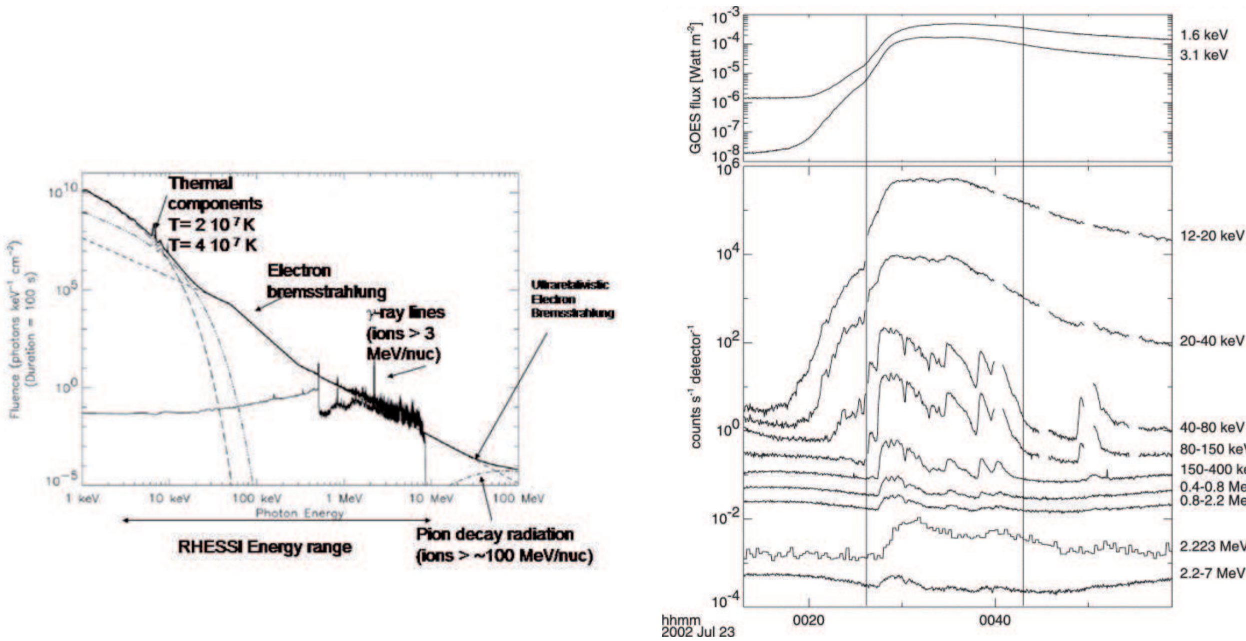

Fig. 1. Left: Theoretical HXR/GR spectrum. Right: RHESSI HXR and γ-ray count rates for the 2002 July 23 flare, scaled to fit: 20-40 keV 0.3; 40-80 keV 0.07; 80-150 keV 0.02; 150-400 keV; 400-800 keV 0.001; 800-2218 keV 0.0005; 2218-2228 keV 0.01; and 2228-7000 keV 2 10-5. The slow variation through the interval is due to the background from cosmic-ray interactions with the atmosphere and spacecraft (from Lin et al., 2003).

and be directly detected in interplanetary space or at ground level (resp > 10 MeV or 200 MeV neutrons) (see e.g. Chupp and Ryan, 2009 for a review).

The temporal and spectral characteristics of HXR/GR and GRL radiations provide strong constraints on acceleration timescales (< 100 ms for electrons, <2s for ions), electron and ion energy spectra, numbers as well as energetic ion abundances. Fig. 1 (Right) shows an example of the temporal evolution of HXR and GR line emissions observed by RHESSI for the 23 July 2002 flare. The 2.223 MeV line from neutron capture radiation is as expected delayed by $\simeq$ 100 s with respect to the prompt γ-ray lines in the 2.2-7 MeV range. This is due to the time needed for the thermalization of the fast neutrons produced in the nuclear reactions before they can be captured by ambient hydrogen to produce deuterium in an excited nuclear state leading to the emission of a 2.223 MeV photon.

High energy observations of solar flares have been observed for three solar cycles. Before the launch of the solar dedicated RHESSI mission (Lin et al., 2002), emission above 100 keV was one of the last domain where no spatially resolved observations were obtained. Before the launch of RHESSI and of INTEGRAL in 2002 (Vedrenne et al., 2003) quantitative constraints from HXR/GRL spectroscopy had been deduced from observations with limited spectral resolution. Since then several flares have been observed in the hard X-ray domain at high spectral resolution with RHESSI and several γ-ray flares have been observed with both RHESSI and INTEGRAL for which a detailed γ-ray line shape analysis could be achieved.

3 Energy release and electron/ion interaction sites

HXR (> 20 keV) images usually show double compact sources ((F) in Figure 2 Left). They are interpreted as the footpoints of magnetic loops in which electrons propagate from the acceleration site before impinging on the chromosphere and produce thick-target X-ray emission. Such double compact sources are observed in most events. However, in a small number of events, compact (LT) above the loop-top sources are observed. They are found to be located at higher altitudes at higher X-ray energies and can be interpreted as the result of the energization of the plasma by shocks originating from the reconnection site in the low corona. In addition to these loop-top sources, coronal (C) sources are also observed with RHESSI at energies up to 20 keV (see Fig. 2 Left from Sui et al., 2003). While the temperature of the loop-top sources increases towards higher altitudes, the temperature of the coronal sources increases towards lower altitudes. These observations could indicate the formation of a current sheet between the loop top and coronal sources in which the magnetic energy conversion takes place. Few events of this kind (< 5) have been observed so far (see e.g. the review by Fletcher et al., 2010), and this is one of the goal of the future hard X-ray imagers to search for such configurations in many more events.

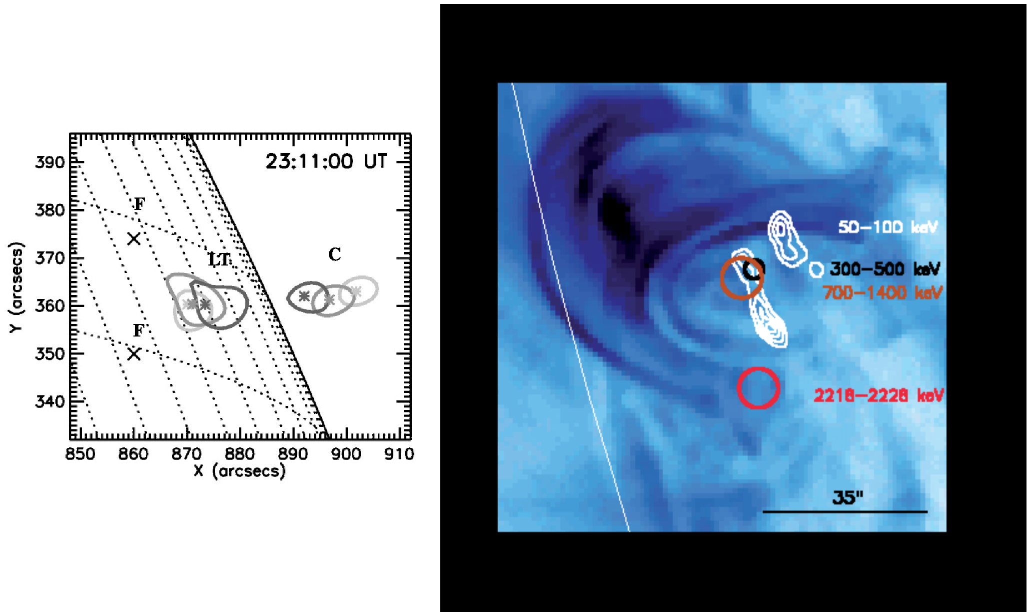

Fig. 2. Left: RHESSI images observed in different energy bands. Loop top sources in the following energy bands: 6-8 keV, 10-12 keV and 16-20 keV (from light to dark contours) are shown. The contours of the coronal sources above the limb are respectively for the 10-12, 12-14 and 14-16 keV energy bands (from light to dark). The crosses mark the two footpoints of the X-ray loop (from Sui and Holman, 2003). Right: Respective location of γ-ray source at 2.2 MeV and of hard X-ray sources observed with RHESSI. The circles represent 1 σ errors for the 300-500 keV , 700-1400 keV and 2218-2228 keV maps made with identical parameters. The white contours show the high resolution 50-100 keV map with 3" resolution. The background is a TRACE image showing the post-flare loops (adapted from Hurford et al.,2003).

One of the most intriguing result from RHESSI imaging comes from the observations of the first GRL event imaged. The 2.2 MeV neutron capture line location was indeed displaced by 20" from the centroid of the HXR sources in the 50-100 keV range imaged in the same conditions (Fig.2 Right) (Hurford et al., 2003). Although the 2.2 MeV line images the neutron interaction site rather than the energetic ion interaction site itself, it was nevertheless shown in Hurford et al. (2003) that the 2.2 MeV line emission locates the energetic ion interaction region within 1", thus still implying a previously unexpected significant displacement between the ion and electron interaction sites. Imaging in the GRL domain with RHESSI has been achieved now for 5 events (see Vilmer, MacKinnon & Hurford, 2010, for a review). For four of the five events, a single unresolved source was observed in the GRL domain but given the constraints of the imaging technique, there is no evidence that the true GRL line sources are predominantly single sources, a result that would be in contrast to typical hard X-ray double sources. Statistically significant displacements between HXR anf GRL sources were observed in three of the five events. Given the limited number of observations, it is difficult to make definite conclusions on the relative locations of electron and ion interaction sites. Improving the imaging in the GRL domain is clearly one of the goals of future instruments.

The different electron and ion interaction sites observed in a few events can be interpreted as revealing either different electron and ion acceleration sites or showing different transport for electrons and ions accelerated in the same site. The explanations of these displacements (clearly NOT instrumental) are however still largely unknown.

4 Constraints on energetic electrons and ions deduced from high resolution X-ray/γ-ray spectrum

HXR/GR observations obtained with high spectral resolution enable detailed analysis of the bremsstrahlung continuum and resolution of individual γ-ray lines. In the HXR domain bremsstrahlung photon spectra at high resolution can be directly inverted to get the effective mean electron flux spectrum in the source (see e.g. Piana et al. 2003) (Fig. 3 Left). This quantity is the electron spectrum that would be required to observe the photon spectrum in a homogeneous source and is the only quantity which can be derived from the photon spectrum without making any assumption on the transport of electrons between acceleration and emitting sites. Fig. 3 (Left) shows the comparison of the values of the electron flux spectrum deduced by forward fitting of a model electron spectrum to the photon spectrum and of the regularized inverted spectrum. The electron flux spectrum is an essential quantity to really constrain acceleration models. Such spectra have been obtained however so far for very few (< 10) events (see e.g. Kontar et al., 2010 for a review).

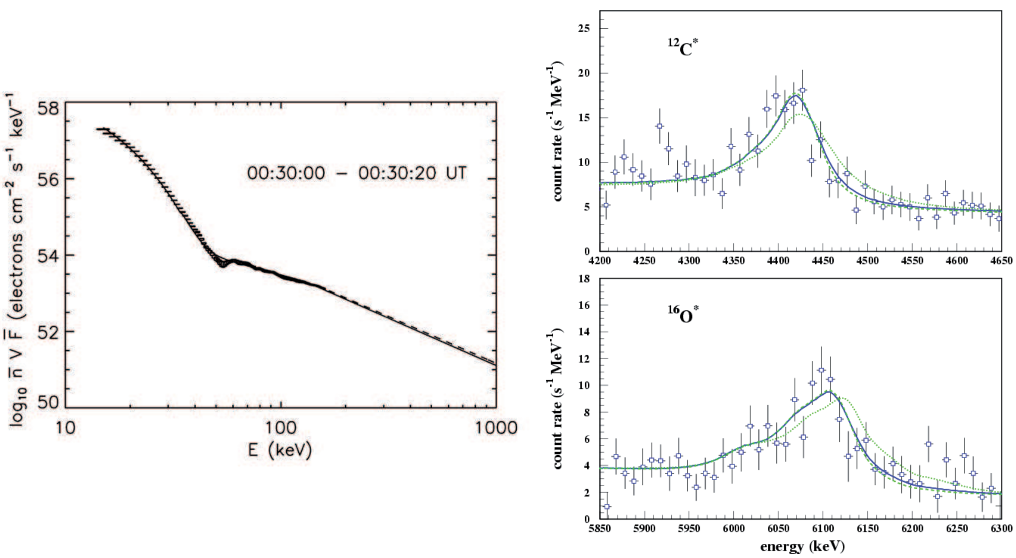

Fig. 3. Left: Regularized mean electron flux spectrum obtained from inversion of the photon spectrum (data points) observed by RHESSI (Piana et al., 2003). The solid line shows the forward fitted electron spectrum necessary to reproduce the same X-ray spectrum (Holman et al, 2003). Right: Observed and calculated line shapes of the 4.44 and 6.13 MeV ambient ^{12}C and ^{16}O deexcitation lines observed by INTEGRAL/SPI for the 28 October 2003. The dashed line represents the calculated line shape for a downward isotropic distribution. The full line and dotted line represent the calculated line shapes for other models (see Kiener et al., 2006 for details) (from Kiener et al., 2006).

Spectral resolution in the γ-ray line domain allows to better constrain the line fluences and to analyse line shapes. This provides information on proton and α-particle energy and angular distributions. Figure 3 right shows an example of the γ-ray line shapes measured for a solar flare at high spectral resolution with INTEGRAL/SPI. The comparison of the results of detailed calculations of line shapes to the observations provide strong constraints on the ratio of accelerated helium with respect to accelerated protons (α/p) in the flare (Kiener et al., 2006). The line shapes depend however on many parameters: angular distribution of interacting ions, spectral index of the energetic ions and α/p so that only the combination of line shapes and line fluences can provide information on regions of allowed parameters: in the case shown in the figure, this leads to the determination of the ion spectral index between -3 and -4, a relatively low value of α/p around 0.1 and a relatively wide angular distribution of emitting ions (Kiener et al., 2006). The number of solar flares for which γ-ray line spectra at high resolution have been obtained is still very small (around 5 combining RHESSI and INTEGRAL/SPI observations) (see Vilmer et al., 2010 for a review) but this is a very promising field to improve the constraint on ion acceleration in solar flares.

5 Conclusions

Two particular advances characterise the HXR/γ-ray observations in the last solar cycle:

-spectral resolution adequate to allow direct inversion of the HXR continuum photon spectrum to derive the energetic electron spectrum produced in flares.

-spectral resolution to reveal γ-ray line shapes to better constrain line fluences and the derived parameters on accelerated ions.

-imaging with a higher dynamic range in the HXR domain allowing to image some coronal HXR sources.

-first γ-ray images, showing for a few events an unexpected behaviour of the electron and ion interaction sites.

Only a few of the observed HXR events are however adequate to be analysed at high spectral resolution or are strong enough to provide images with a high dynamic range in the HXR domain. In the near future, STIX (Spectrometer/Telescope for Imaging X-rays) instrument aboard Solar Orbiter should provide HXR observations at high spectral and spatial resolution with a sensitivity of 15 times the one of RHESSI. In the γ-ray domain where the number of events analysed with high resolution spectroscopy or that can be imaged is still very limited, we look forward to further observations with RHESSI and INTEGRAL in the coming maximum. In the higher energy range not discussed here we expect new results from flares observed with the non-solar dedicated mission FERMI. New instrumentation such as GRIPS should provide observations in the γ-ray domain with improved angular resolution and sensitivity. Finally, several new missions aimed at understanding particle acceleration at the Sun are being studied for the > 2020 timeframe either on the ESA or NASA side. A package of HXR/γ-ray instrumentation is proposed for these missions (e.g. on the ESA side, the SPARK (Solar Particle Acceleration, Radiation and Kinetics) mission proposed by UCL/MSSL as a M3 mission).

References

Chupp, E.L. & Ryan, J.M., 2009 Research in Astronomy and Astrophysics, 9, 11.

Emslie A.G., Kucharek H., Dennis B.R. et al., 2004,JGR,Vol. 109, 104.

Fletcher, L., Dennis, B.R., Hudson, H.S. et al., Space Science Reviews, in press.

Holmann G.D. Sui L Schwartz R.A. and Emslie A.G., 2003, ApJ, Vol. 595, L97-L101.

Hurford G.J. Schwartz R.A. Krucker S. et al., 2003, ApJ, Vol.595, L77-L80.

Kiener,J., Gros, M., Tatischeff, G. et al., 2006, Astronomy and Astrophysics, 445, 725.

Kontar, E.P., Brown, J.C., Emslie, A.G. et al., Space Science Reviews, in press.

Lin R.P. Dennis B.R. Hurford G.J. et al., 2002, Solar Physics,Vol. 210, 3-32.

Lin R.P. Krucker S. Hurford G.J. et al., 2003, ApJ, Vol. 595,L69-L76.

Piana M., Massone A.M., Kontar E.P. et al., 2003, ApJ, Vol.595, L127-L130.

Ramaty R., 1986, Physics of the Sun, Vol. 2, 291-323.

Share,G.H.& Murphy, R., 2006, American Geophysical Union Geophysical Monograph Series, 165,177.

Sui L. & Holman G.D., 2003, ApJ, Vol. 596, L251-L254.

Vedrenne, G., et al., 2003, Astron. Astrophys., 411, L63.

Vilmer,N., MacKinnon, A.L., & Hurford,G., 2010, Space Science Reviews, in press

PNST - PCHE

Sun, Earth and high energy cosmic phenomena

SF2A 2010
S. Boissier, M. Heydari-Malayeri, R. Samadi and D. Valls-Gabaud (eds)

CONSTRAINTS ON THE COSMIC RAY DIFFUSION COEFFICIENT IN THE W28 REGION FROM GAMMA-RAY OBSERVATIONS

S. Gabici[1], S. Casanova[2,3], F. A. Aharonian[2,4] and G. Rowell[5]

Abstract. GeV and TeV gamma rays have been detected from the supernova remnant W28 and its surroundings. Such emission correlates quite well with the position of dense and massive molecular clouds and thus it is often interpreted as the result of hadronic cosmic ray interactions in the dense gas. Constraints on the cosmic ray diffusion coefficient in the region can be obtained, under the assumption that the cosmic rays responsible for the gamma ray emission have been accelerated in the past at the supernova remnant shock, and subsequently escaped in the surrounding medium. In this scenario, gamma ray observations can be explained only if the diffusion coefficient in the region surrounding the supernova remnant is significantly suppressed with respect to the average galactic one.

Keywords: cosmic rays, gamma rays, supernova remnants

1 Introduction

Cosmic ray (CR) spallation measurements allow us to infer the average residence time t_{res} of CRs in the Galaxy. Then, if h is the distance that a CR has to move away from its source before escaping the Galaxy (i.e. the Galaxy's thickness), it is possible to estimate the CR diffusion coefficient as $D \approx h^2/t_{res}$. A thorough comparison between spallation data and CR transport models gives: $D_{gal} \approx 10^{28}(E/10 \text{ GeV})^{\delta} \text{ cm}^2\text{s}^{-1}$, where E is the CR particle energy and $\delta \sim 0.3 \div 0.7$ (Berezinskii et al. 1990). However, this has to be intended as the average CR diffusion coefficient in the Galaxy, and local variations (both in time and space) of the diffusion coefficient might exist.

In particular, the diffusion coefficient might be suppressed close to CR sources. This is because CRs can excite magnetic turbulence while streaming away from their acceleration site. This would enhance the scattering rate of CR themselves and thus reduce the diffusion coefficient (Kulsrud & Pierce 1969). The problem of estimating, on theoretical grounds, the diffusion coefficient around CR sources is far from being solved, mainly because of its intrinsic non-linearity and because various mechanisms might damp the CR–generated waves and thus affect the way in which CRs diffuse (e.g. Farmer & Goldreich 2004; Ptuskin et al. 2008).

Gamma ray observations can provide us with constraints on the diffusion coefficient close to CR sources. After escaping from their sources, CRs undergo hadronic interactions with the surrounding gas and produce gamma rays. The characteristics of such radiation (i.e. its spectrum and intensity as a function of the time elapsed since CRs escaped the source) depend on the value of the diffusion coefficient that can thus be constrained, if a reliable modeling for CR acceleration at the source is available. The presence of massive Molecular Clouds (MCs) close to the source would enhance the gamma ray emission, making its detection more probable.

The study of gamma ray emission from runaway CRs has been studied by Aharonian & Atoyan (1996) for the case of a generic CR source, while the specific (and most popular) situation of CR acceleration at SuperNova Remnants (SNRs) has been described in a series of recent papers (Gabici & Aharonian 2007; Gabici et al. 2009; Casanova et al. 2010). The study of such radiation is of great importance not only in order to reach a better understanding of the way in which CRs diffuse in the interstellar magnetic field, but also because its detection can provide an indirect way to identify the sources of galactic CRs.

[1] Laboratoire APC, 10 rue A Domon et L Duquet, 75205 Paris Cedex 13, France
[2] Max-Planck-Institut für Kernphysik, Heidelberg, Germany
[3] Ruhr-Universitaet Bochum, Fakultaet fuer Physik und Astronomie, Bochum, Germany
[4] Dublin Institute for Advanced Studies, Dublin, Ireland
[5] School of Chemistry and Physics, University of Adelaide, Adelaide, Australia

2 The supernova remnant W28

W28 is an old SNR in its radiative phase of evolution, located in a region rich of dense molecular gas with average density $\gtrsim 5$ cm^{-3}. At an estimated distance of ~ 2 kpc the SNR shock radius is ~ 12 pc and its velocity ~ 80 km/s (e.g. Rho & Borkowski 2002). By using the dynamical model by Cioffi et al. (1988) and assuming that the mass of the supernova ejecta is $\sim 1.4\ M_\odot$, it is possible to infer the supernova explosion energy ($E_{SN} \sim 0.4 \times 10^{51}$erg), initial velocity ($\sim 5500$ km/s), and age ($t_{age} \sim 4.4 \times 10^4$yr).

Gamma ray emission has been detected from the region surrounding W28 both at TeV (Aharonian et al. 2008) and GeV energies (Abdo et al. 2010; Giuliani et al. 2010), by HESS, FERMI, and AGILE, respectively. The TeV emission correlates quite well with the position of three massive molecular clouds, one of which is interacting with the north-eastern part of the shell (and corresponds to the TeV source HESS J1801-233), and the other two being located to the south of the SNR (TeV sources HESS J1800-240 A and B) . The masses of these clouds can be estimated from CO measurements and result in ≈ 5, 6, and $4 \times 10^4 M_\odot$, respectively, and their projected distances from the centre of the SNR are ≈ 12, 20, and 20 pc, respectively (Aharonian et al. 2008). The GeV emission roughly mimics the TeV one, except for the fact that no significant emission is detected at the position of HESS J1800-240 A.

In this paper, we investigate the possibility that the gamma ray emission from the W28 region could be the result of hadronic interactions of CRs that have been accelerated in the past at the SNR shock and then escaped in the surrounding medium *. To do so, we follow the approach described in Gabici et al. (2009) (hereafter GAC2009), which we briefly summarize below.

For each particle energy E we solve the diffusion equation for CRs escaping the SNR. For simplicity we treat the SNR as a point like source of CRs and we consider an isotropic and homogeneous diffusion coefficient $D = \chi D_{gal} \propto E^{0.5}$ (see Eq. 5 in GAC2009). Here, χ represents possible deviations with respect to the average CR diffusion coefficient in the Galaxy. The solution of the diffusion equation gives the spatial distribution of CRs around the source f_{CR}, which is roughly constant up to a distance equal to the diffusion radius $R_d = \sqrt{4\ D\ t_{diff}}$, and given by $f_{CR} \propto \eta E_{SN}/R_d^3$, where η is the fraction of the supernova explosion energy converted into CRs, and t_{diff} is the time elapsed since CRs with energy E escaped the SNR (see eq. 6 in GAC2009). For distances much larger than R_d the CR spatial distribution falls like $f_{CR} \propto \exp(-(R/R_d)^2)$ (see eq. 6 in GAC2009). Following GAC2009, we assume that CRs with energy 5 PeV (1 GeV) escape the SNR at the beginning (end) of the Sedov phase, at a time ~ 250 yr ($\sim 1.2 \times 10^4$ yr) after the explosion, and that the time integrated CR spectrum injected in the interstellar medium is $\propto E^{-2}$. In this scenario, particles with lower and lower energies are released gradually in the interstellar medium (Ptuskin & Zirakashvili 2005), and we parametrize the escape time as: $t_{esc} \propto E^{-\alpha}$ which, during the Sedov phase, can also be written as $R_s \propto E^{-2\alpha/5}$, where R_s is the shock radius at time t_{esc} and $\alpha \sim 4$. From this it follows that the assumption of point like CR source is good for high energy CRs only ($\sim$ TeV or above), when R_s is small, but it becomes a rough approximation at significantly lower energies. This is because low energy particles are believed to be released later in time, when the SNR shock radius is large (i.e. non negligible when compared to R_d).

We now provide a simplified argument to show how we can attempt to constrain the diffusion coefficient by using the TeV gamma ray observations of the MCs in the W28 region. The time elapsed since CRs with a given energy escaped the SNR can be written as: $t_{diff} = t_{age} - t_{esc}$. However, for CRs with energies above 1 TeV (the ones responsible for the emission detected by HESS) we may assume $t_{esc} << t_{age}$ (i.e. high energy CRs are released when the SNR is much younger than it is now) and thus $t_{diff} \sim t_{age}$. Thus, the diffusion radius reduces to $R_d \sim \sqrt{4\ D\ t_{age}}$. We recall that within the diffusion radius the spatial distribution of CRs, f_{CR}, is roughly constant, and proportional to $\eta E_{SN}/R_d^3$. On the other hand, the observed gamma ray flux from each one of the MCs is: $F_\gamma \propto f_{CR} M_{cl}/d^2$, where M_{cl} is the mass of the MC and d is the distance of the system. Note that in this expression F_γ is calculated at a photon energy E_γ, while f_{CR} is calculated at a CR energy $E_{CR} \sim 10 \times E_\gamma$, to account for the inelasticity of proton-proton interactions. By using the definitions of f_{CR} and R_d we can finally write the approximate equation, valid within a distance R_d from the SNR:

$$F_\gamma \propto \frac{\eta\ E_{SN}}{(\chi\ D_{gal}\ t_{age})^{3/2}} \left(\frac{M_{cl}}{d^2} \right).$$

Estimates can be obtained for all the physical quantities in the equation except for the CR acceleration efficiency η and the local diffusion coefficient χD_{gal}. By fitting the TeV data we can thus attempt to constrain,

*This scenario has been described in a number of recent papers (Fujita et al. 2009; Ohira et al. 2010; Li & Chen 2010).

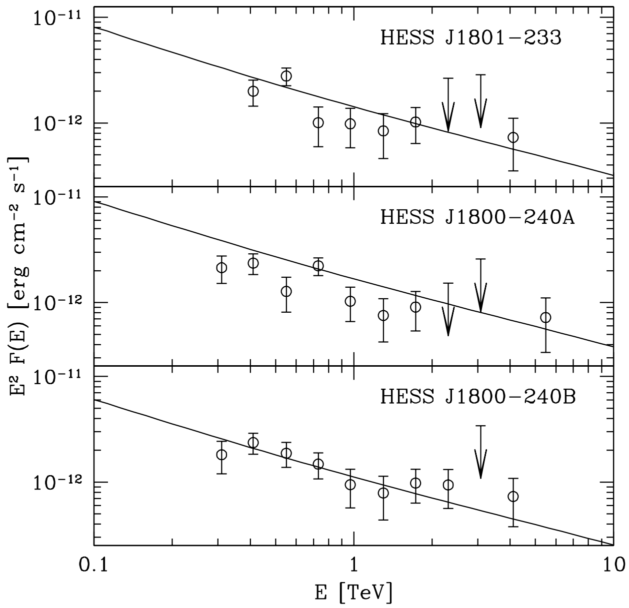

Fig. 1. Simultaneous fit to the three TeV sources detected by HESS in the W28 region. Gamma ray spectra have been calculated by using the parameterizations by Kamae et al. (2006), where a multiplicative factor of 1.5 has been applied to account for the contribution to the emission from nuclei heavier than H both in CRs and in the interstellar medium.

within the uncertainties given by the errors on the other measured quantities (namely, E_{SN}, t_{age}, M_{cl}, and d) and by the assumptions made (e.g. the CR injection spectrum is assumed to be E^{-2}), a combination of these two parameters (namely $\eta/\chi^{3/2}$). The fact that the MCs have to be located within a distance R_d from the SNR can be verified a posteriori. Given all the uncertainties above, our results have to be interpreted as a proof of concept of the fact that gamma ray observations of SNR/MC associations can serve as tools to estimate the CR diffusion coefficient. More detection of SNR/MC associations are needed in order to check whether the scenario described in this paper applies to a whole class of objects and not only to a test-case as W28. Future observations from the Cherenkov Telescope Array will most likely solve this issue.

Fig. 1 shows a fit to the HESS data for the three massive MCs in the W28 region. A simultaneous fit to all the three MCs is obtained by setting $\eta/\chi^{3/2} \approx 20$, which implies that the diffusion coefficient (normalized to the average galactic one) χ has to be much smaller than 1 for any reasonable value of $\eta < 1$. For example, an acceleration efficiency $\eta = 30\%$ corresponds to a CR diffusion coefficient of $\chi = 0.06$, which in turn gives a diffusion distance for TeV particles of $R_d \approx 60$ pc. This means that the results in Fig. 1 are valid if the physical (not projected) distances between the MCs and the SNRs do not significantly exceed R_d. Small values of the diffusion coefficient have been also proposed by Giuliani et al. (2010); Fujita et al. (2009); Li & Chen (2010). Note that, since we are considering gamma rays in a quite narrow (about one order of magnitude) energy band around ≈ 1 TeV, we are actually constraining the diffusion coefficient of CRs with energy ≈ 10 TeV, and we cannot say much about the energy dependence of the diffusion coefficient on a broad energy interval.

In principle, observations by FERMI and AGILE might be used to constrain the diffusion coefficient down to GeV particle energies. However, in this energy band the uncertainties are more severe because of the following reasons: *i)* low energy CRs are believed to be released late in time, when the SNR shock is large, and thus the assumption of point-like source is probably not well justified (see Ohira et al. 2010 for a model that takes into account the finite size of the SNR) ; *ii)* for the same reason, we can no longer assume that $t_{diff} \sim t_{age}$, as we did for high energy CRs. In other words, we need to know the exact time at which CRs with a given energy escape the SNR. Though some promising theoretical studies exist (e.g. Ptuskin & Zirakashvili 2005), our knowledge of the escape time of CRs from SNRs is still quite limited.

Fig. 2 shows a fit to the broad band gamma ray spectrum measured from FERMI and HESS. The three panels refers to (left to right) the sources HESS J1801-233, HESS J1800-240 A and B, respectively. Dashed lines represent the contribution to the emission from CRs that escaped from W28, dotted lines the contribution from background CRs, and solid lines the total emission. Since FERMI data refers to the emission after background

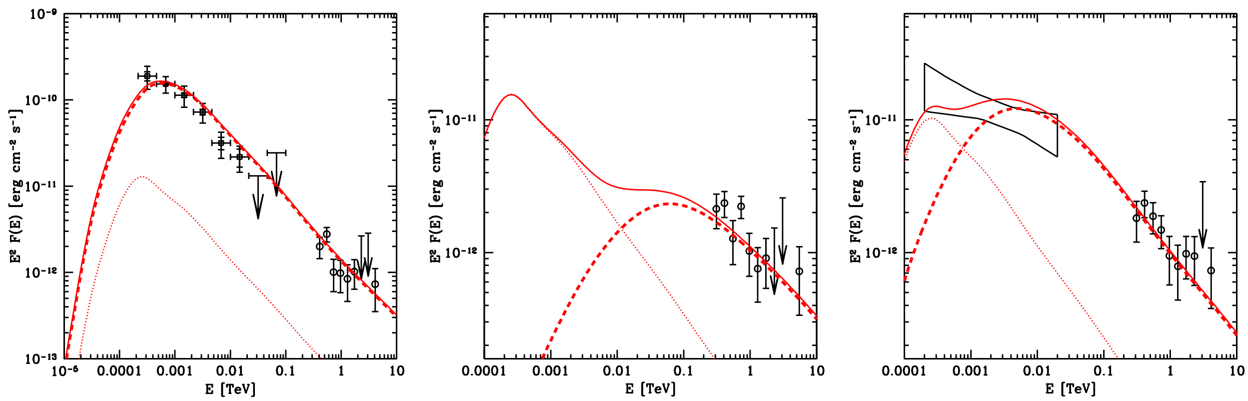

Fig. 2. Broad band fit to the gamma ray emission detected by FERMI and HESS from the sources HESS J1801-233, HESS J1800-240 A and B (left to right). Dashed lines represent the contribution to the gamma ray emission from CRs that escaped W28, dotted lines show the contribution from the CR galactic background, and solid lines the total emission. Distances to the SNR centre are 12, 65, and 32 pc (left to right). FERMI and HESS data points are plotted in black. No GeV emission has been detected from HESS J1800-240 A.

subtraction, dashed lines have to be compared with data points. The (often non-trivial) background subtraction issue might add another source of uncertainty in the comparison between data and predictions. An acceleration efficiency $\eta = 30\%$ and a diffusion coefficient $\chi = 0.06$ have been assumed, while the distance from the SNR centre is assumed to be (left to right) 12, 65, and 32 pc. Keeping in mind all the above mentioned caveats, it is encouraging to see that a qualitative agreement exists between data and predictions also in the GeV band.

3 Conclusions

We investigated the possibility that the gamma ray emission detected from the MCs in the region of the SNR W28 is produced by CRs that escaped the SNR. This interpretation requires the CR diffusion coefficient in that region to be significantly suppressed with respect to the average galactic one. Such suppression might be the result of an enhancement in the magnetic turbulence due to CR streaming away from the SNR.

SG thanks M. Walmsley for many interesting discussions. The research leading to these results has received funding from the European Union [FP7/2007-2013] under grant agreement n^{o} 256464 and 221093.

References

Abdo, A.A., et al. 2010, ApJ, 718, 348

Aharonian, F.A., & Atoyan, A. 1996, A&A, 309, 917

Aharonian, F.A., et al. 2008, A&A, 481, 401

Berezinskii, V.S., Bulanov, V.A., Dogiel, V.L., Ginzburg, V.L., & Ptuskin, V.S. 1990, Astrophysics of Cosmic Rays (Amsterdam: North-Holland)

Casanova, S., et al. 2010, PASJ, in press – arXiv:1003.0379

Cioffi, D.F., McKee, C.F., & Bertschinger, E. 1988, ApJ, 334, 252

Farmer, A.J., & Goldreich, P. 2004, ApJ, 604, 671

Fujita, Y. Ohira, Y., Tanaka, S.J., & Takahara, F. 2009, ApJ, 707, L179

Gabici, S., & Aharonian, F.A. 2007, ApJ, 665, L131

Gabici, S., Aharonian, F.A., & Casanova, S. 2009, MNRAS, 396, 1629 (GAC2009)

Giuliani, A., et al. 2010, A&A, 516, L11

Kamae, T., Karlsson, N., Mizuno, T., Abe, T., & Koi, T. 2006, ApJ, 647, 692

Kulsrud, R., & Pearce, W.P. 1969, ApJ, 156, 445

Li, H., & Chen, Y. 2010, MNRAS, in press – arXiv:1009.0894

Ohira, Y., Murase, K., & Yamazaki, R. 2010, MNRAS, in press – arXiv:1007.4869

Ptuskin, V.S., & Zirakashvili, V.N. 2005, A&A, 429, 755
Ptuskin, V.S., Zirakashvili, V.N., & Plesser, A.A. 2008, Adv. Space Res., 42, 486
Rho, J., & Borkowski, K.J. 2002, ApJ, 575, 201

MULTIPLE STELLAR POPULATIONS IN GALACTIC GLOBULAR CLUSTERS: OBSERVATIONAL EVIDENCE

A.P. Milone[1], G. Piotto[2], L.R. Bedin[3], A. Bellini[4], A.F. Marino[5] and Y. Momany[6]

Abstract. An increasing number of both photometric and spectroscopic observations over the last years have shown the existence of distinct sub-populations in many Galactic globular clusters and shattered the paradigm of globulars hosting single, simple stellar populations. These multiple populations manifest themselves in a split of different evolutionary sequences in the cluster color-magnitude diagrams and in star-to-star abundance variations. In this paper we will summarize the observational scenario.

Keywords: stars: abundances, stars: atmospheres, stars: population II, galaxy: globular clusters

1 Introduction

In recent years an increasing amount of photometric and spectroscopic observational evidence have shattered the paradigm of globulars as the prototype of single, simple stellar populations (see Piotto 2009 for a recent review). Spectroscopic studies have demonstrated that most globular clusters (GC) have no detectable spread in their iron content and also *s*-process elements do not exhibit large star-to-star variations in the majority of globulars (e.g. Carretta et al. 2009a and references therein). On the contrary, every time we have at our disposal a large sample of stars for a given GC, star-to-star variations in the light elements C, N, O, Na, and Al have been clearly detected (e.g. Carretta et al. 2009b, Pancino et al. 2010 and references therein). These variations are related to correlations and anticorrelations, which indicate the occurrence of high temperature hydrogen-burning processes (including CNO, NeNa, MgAl cycles) and cannot occur in presently observed low mass GC stars.

Today it is widely accepted that the observed light-elements variations provide strong support to the presence of multiple stellar populations in GCs with the second generations formed from the material polluted by a first generation of stars. On the contrary the debate on the nature of possible polluters is still open (e.g. D'Antona et al. 2004, Decressin et al. 2007).

While abundance variations are well known since the early sixties, it was only the recent spectacular discovery of multiple sequences in the color-magnitude diagram (CMD) of several GCs that provides an un-controversial prove of the presence of multiple stellar populations in GCs and brought new interest and excitement in GCs research (e.g. Piotto et al. 2007). Photometric clues, often easy to detect simply by the inspection of high-accuracy CMDs, arise in form of multiple main sequences (MS, Bedin et al. 2004, Piotto et al. 2007, Milone et al. 2010), split sub-giant branch (SGB, Milone et al. 2008, Anderson et al. 2009, Piotto 2009), and multiple red-giant branch (RGB, Marino et al. 2008, Yong et al. 2008, Lee et al. 2009).

Many population properties, like the chemical composition, the spatial distribution, the fraction of stars in each population and their location in the CMD apparently differ from cluster to cluster. Multiple stellar populations have been detected for the first time in the Milky Way satellite ω Centauri in form of either multiple MSs (e.g. Anderson 1997, Bedin et al. 2004, Bellini et al. 2010), multiple SGBs (e.g. Sollima et al.

[1] Dipartimento di Astronomia, Università di Padova, Vicolo dell'Osservatorio 3, Padova, I-35122, Italy
[2] Dipartimento di Astronomia, Università di Padova, Vicolo dell'Osservatorio 3, Padova, I-35122, Italy
[3] Space Telescope Science Institute, 3700 San Martin Drive, Baltimore, MD 21218, USA
[4] Dipartimento di Astronomia, Università di Padova, Vicolo dell'Osservatorio 3, Padova, I-35122, Italy
[5] Max Plank Institute for Astrophysics, Postfach 1317, 85741, Garching, Germany
[6] European Southern Observatory, Alonso de Cordova 3107, Vitacura, Santiago, Chile

2005), multiple RGBs (Lee et al. 1999, Pancino et al. 2000) and large star-to-star variation in iron and s-elements (e.g. Johnson et al. 2010, Marino et al. 2010). Due to its large mass this GCs have been always considered as a peculiar stellar system and often associated to the remnant of a dwarf galaxy.

The 'extreme' case of ω Centauri is not analyzed in this work where we focus on 'normal' GCs. The following sections are an attempt to define some groups of 'normal' clusters that share similar properties.

2 Light-elements correlations and spread RGB. The case of NGC 6121.

The Na-O anticorrelation has been observed in all the Galactic GCs studied to date and indicates the presence of multiple stellar populations in GCs. These chemical inhomogeneities revealed themselves a spread or bimodal distribution of stars along the RGB when sensitive colors are used.

In this context the nearby GC NGC 6121 (M4) is one of the most studied cases (e.g. Ivans et al. 1999, Marino et al. 2008). An high resolution spectroscopic study conduced on a sample of more than a hundred RGB stars in this GC, has recently demonstrated that two different stellar populations are present (Marino et al. 2008). These two populations have been identified by means of a strong dichotomy in the sodium abundance, that is related to a bimodality in the CN band strengths. The presence of two different groups of stars is visible also on the Na-O anticorrelation: a bulk of stars with Na and O resembling the halo field content, and likely associated to the first stellar generation, can be easily distinguished from stars enhanced in Na and with lower O abundance, associated with the second generation. The two populations of Na-poor/O-rich/CN-weak and Na-rich/O-poor/CN-strong stars populate two different regions along the RGB, when plotted in a U vs. $(U-B)$ CMD. The Na-rich group defines a narrower sequence on the red side of the mail RGB locus, while the Na-poor one populates a bluer, more spread portion of the RGB. The RGB spread is visible from the base of the RGB to its tip, and it is due to the dichotomy in the CN bands, given that the U filter is highly affected by CN molecular bands.

3 Multimodal MSs. The cases of NGC 2808 and NGC 6752

In few cases the MS morphology strongly supports the presence of stellar generations with different helium content. The most striking evidence comes from the color magnitude diagram (CMD) of NGC 2808 which exhibits two additional MSs that run blueward of the main MS ridge line and have been associated to subsequent episodes of star formation (Piotto et al. 2007).

Apart from the triple MS, NGC 2808 shows observational evidence indicating the presence of multiple stellar populations also in other region of the CMD. Its horizontal branch (HB) is greatly extended bleward and is well populated on both sides of the instability strip. The distribution of stars along the HB is multimodal (Sosin et al. 1997, Bedin et al. 2000) with three significant gaps, one of these gaps being at the color of the RR Lyrae instability strip. In fact, even though the HB is well populated both to the blue and to the red of the instability strip, very few RR Lyrae stars have been identified in NGC 2808. The other two gaps are on the blue extension of the HB and delimit three distinct segments.

Even the RGB is not consistent with a single stellar population. The CMDs shown by Yong et al. (2007) and Lee et al. (2009) revealed a large color spread among RGB stars that cannot be attributed to photometric errors only. Furthermore, an analysis of medium-high-resolution spectra of 122 RGB stars have revealed an extended Na-O anticorrelation in NGC 2808 (Carretta et al. 2006) with the presence of three distinct groups: O-normal (peak at [O/Fe] +0.28), O-poor (peak at [O/Fe] −0.21) and super-O-poor (peak at [O/Fe] −0.73) stars.

On the basis of their relative numbers, Piotto et al. (2007) associated the three MSs with the three HB segments defined by Bedin et al. (2000), and the three groups of stars with different O content found by Carretta et al. (2006). Since cluster stars have around the same iron content (Carretta et al. 2007, 2010), a multimodal distribution of He abundances seems to be the only way to take into account for both the complex HB and the multiple MS (D'Antona et al. 2005) and is consistent with the observed abundance pattern. In this case the population associated to the red MS (rMS) have nearly primordial helium, while stars of the middle (mMS) and blue MS (bMS) are formed from the ejecta produced by an earlier stellar generation through the complete CNO and MgAl cycle and are He-enhanced (Y$\sim$0.33 and Y$\sim$0.38, respectively). This scenario is nicely confirmed by the recent work of Bragaglia et al. (2010) who measured chemical abundances of one star on the rMS and one ond the bMS and found that the latter shows an enhancement of N, Na, and Al and a depletion of C and Mg as expected for material polluted by first-generation massive stars.

A split or a broad MS is not a peculiarity of NGC 2808 but is present also in other GCs like 47 Tucanae and NGC 6752 (Anderson et al. 2009, Milone et al. 2010). In these cases the color spread has been tentatively attributed to small variations in He (Δ Y$\sim$0.02-0.03). As an example in Fig. 1 we show the Hess diagram for MS stars of NGC 2808 and NGC 6752 from Hubble space telescope *HST* ACS/WFC and WFC3/UVIS cameras.

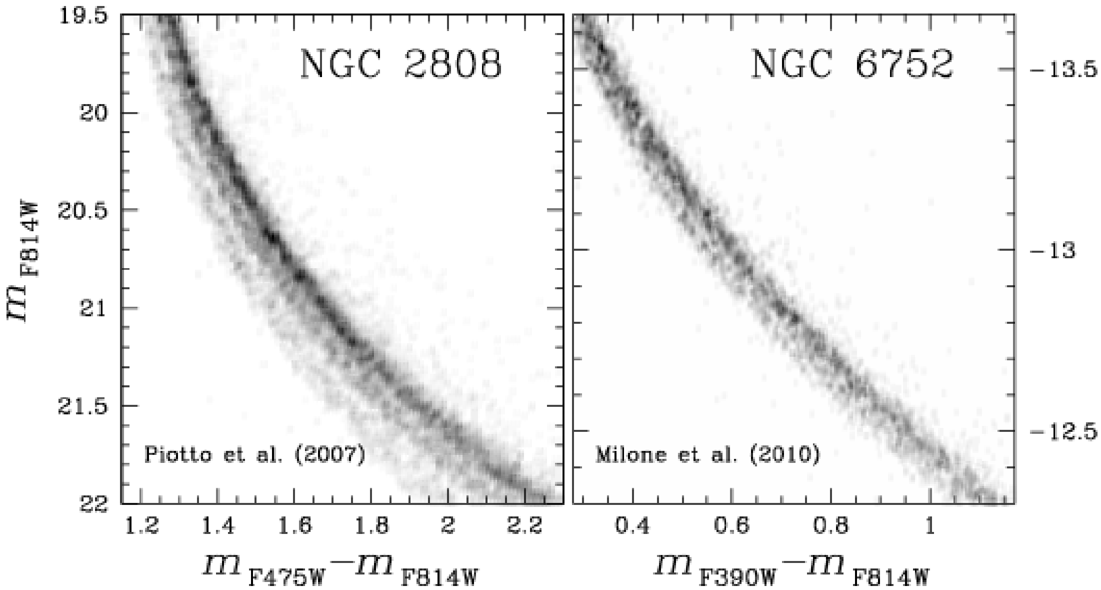

Fig. 1. Hess diagram of NGC 2808 and NGC 6752 zoomed around the MS region.

4 SGB split clusters: NGC 1851 and NGC 6656

High-accuracy photometry obtained with the WFPC2, the WFC/ACS and the WFC3/UVIS cameras on board of the *HST* has revealed that in several clusters there is a broad, split, or multimodal SGB as shown in Fig. 2 for NGC 1851, NGC 6388, NGC 104, NGC 6656, NGC 5286, and NGC 6715 (Milone et al. 2008, Anderson et al. 2009, Piotto et al. 2009, Moretti et al. 2008).

NGC 1851 and NGC 6656 are the most studied clusters of this group and will be analyzed in more detail in the following. We find that the SGB of both NGC 1851 and NGC 6656 is clearly split into two branches with the bright SGB component containing about the 60% of the total number of SGB stars and the remaining 40% of stars belonging to the faint SGB (Milone et al. 2008, Piotto 2009, Marino et al. 2009).

These results have brought new interest on these GCs and a lot of effort have been made to understand their star formation history. Theoretic studies demonstrate that the double SGB can been explained in terms of two stellar groups, only slightly differing in age, with the younger one having an increased C+N+O abundance (Cassisi et al. 2008, Ventura et al. 2009). Indeed, significant star-to-star variations in the overall CNO abundance have been detected among NGC 6656 RGB stars by Marino et al. (2010) and in two out four NGC 1851 giants by Yong et al. (2009). As an alternative possibility, we note that the double SGB is consistent with two stellar populations with constant CNO but differing in age by $\sim$1 Gyr (Milone et al. 2008).

A peculiar property of the cluster pair NGC 1851-NGC 6656 is the large scatter in the abundance of those n-capture elements that are associated to s-process (Marino et al. 2009, 2010, Hesser et al. 1982, Yong et al. 2008). In both clusters n-capture elements are clearly segregated around two distinct values of barium and yttrium in sharp contrast with what found in most GCs, where the abundance of these elements does not exhibit significant star-to-star variations. As an example, Fig. 3a shows the iron abundance as a function of [Y/Fe] for NGC 6656.

These recent results nicely match with previous photometric analysis by Ritcher et al. (1999) and Calamida et al. (2007) who found that NGC 6566 and NGC 1851 exhibit a bimodal distribution in the m_1 index among RGB stars. A similar RGB bimodality has been observed in the hk index by Lee et al. (2009) and in the U vs. ($U-I$) and U vs. ($U-V$) CMD by Han et al. (2009) and Momany et al. (2004). In these cases the RGB components are clearly associated to the two SGBs.

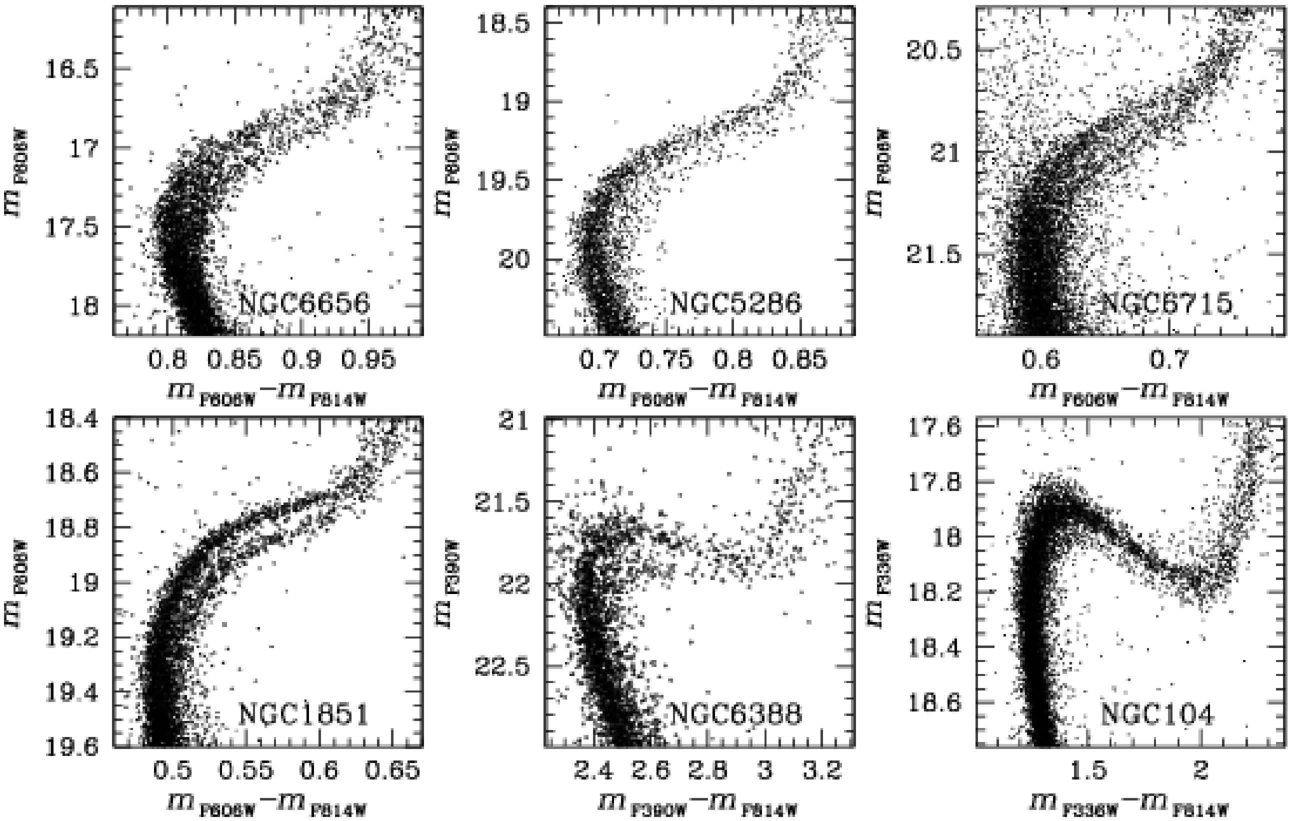

Fig. 2. Collection of CMDs from *HST* ACS/WFC and WFC3/UVIS data for six GCs with spread or split SGB. (Piotto et. 2010, Milone et al. 2008, 2010 Anderson et al. 2009).

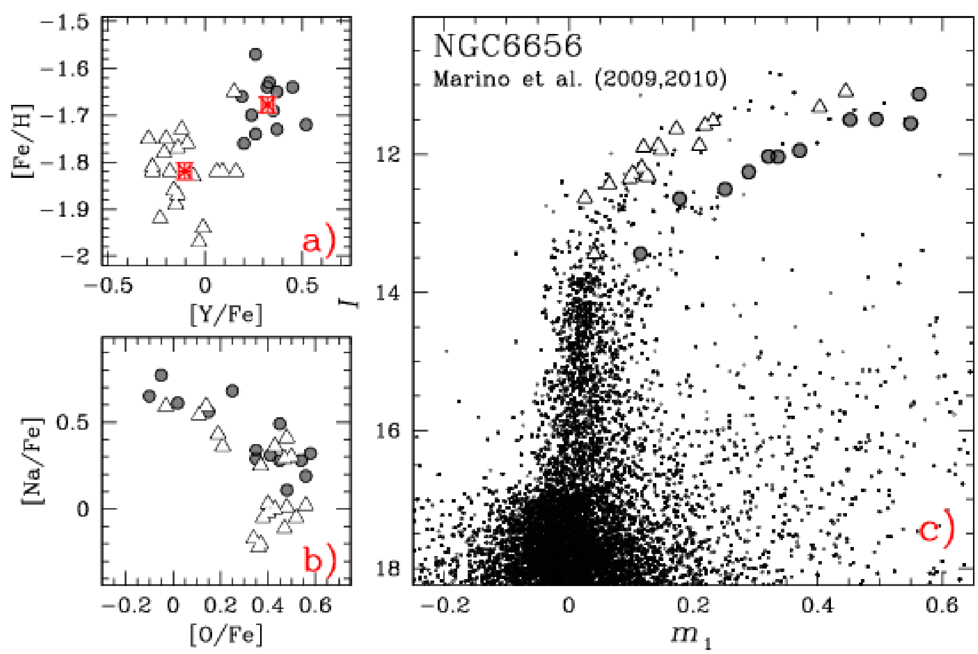

Fig. 3. *Panel a)*: [Fe/H] as a function of [Y/Fe] for RGB stars in NGC 6656. The two groups of *s*-rich and *s*-poor stars are plotted as gray circles and white triangles, respectively. The Na-O anticorrelation for the same stars of NGC 6656 is shown in *Panel b)* while in *Panel c)* we marked them in the I versus m_1 diagram.

In the light of these results we matched spectroscopic data of NGC 6656 from Marino et al. (2009, 2010) with the Strom̈gren photometry by Richter et al. (1999). Results are shown in Fig. 3c where we plotted the m_1 versus I diagram for NGC 6656 corrected for differential reddening and found that s-rich and s-poor stars define two distinct RGBs. As the m_1 index is strongly dependent by the CN bands strength, we expect this bimodality as due to the overabundance in both C and N measured by Marino et al. (2010) in s-rich stars.

A fundamental piece of the puzzle comes from the [Fe/H] measurements. While the presence of a possible iron dispersion among stars in NGC 1851 is still controversial (Yong et al. 2008, Carretta et al. 2010, Villanova et al. 2010), when we compare the iron abundance for NGC 6656 with the s-elements abundance, we find a strong correlation, with s-rich stars having a systematically higher [Fe/H] of δ[Fe/H] $= 0.14 \pm 0.03$ (Marino et al. 2009) as shown in Fig. 3a. This result demonstrates that, at odds with 'normal' monometallic GCs the different stellar populations of NGC 6656 have significant differences in their iron content and that core-collapse supernovae played a prominent role in the star formation history of this cluster.

An intriguing property of this pair of clusters is that both the s-rich and the s-poor group of stars have its own Na-O anticorrelation as shown in Fig 3b for NGC 6656. For the latter a C-N anticorrelation has also been detected in both the s-groups by Marino et al. (2010). Variations in light elements have been considered as the signature of multiple stellar populations, therefore this result may indicate that NGC 1851 and NGC 6656 have experienced a very complex star formation history with the presence of two stellar groups with discrete s-elements abundance, each containing multiple generation of stars with different sodium and oxygen content.

5 Conclusions

For several decades GCs have been considered as the best approximation of simple stellar populations consisting of coeval and chemically homogeneous stars. This picture have been mainly challenged by two two observational facts.

Since the seventies we know that GCs exhibit a peculiar pattern in their chemical abundances with large star-to-star variations in the abundances of C, N, Na, O, Mg, and Al. These variations are primordial since they are observed in stars at all the evolutionary phases and are peculiar to GC stars. Field stars only changes in C and N abundance expected from typical evolution of low-mass stars.

In addition, since the early sixties we know that the HB of some GCs are quite peculiar. The distribution of stars along the RGB can be multimodal with the presence of one or more gaps and in same cases the HB can be extended toward very high temperatures. It is well known metallicity is the first parameter governing the HB morphology there are some GCs with almost the same iron content but different HB morphology demonstrating the metallicity alone is not enough to reproduce the observational scenario. This problem, known as the *second-parameter* problem, still lacks of a comprehensive understanding.

The recent discoveries of multiple stellar populations in GCs have shattered once and for all the long-held paradigm of GCs as simple stellar populations and brought new interest on these stellar systems.

It is very tempting to relate the second parameter HB problem to the complex abundance pattern of GCs as well as to the multiple sequences observed in the CMD of some clusters. As already mentioned the observed variations of light elements indicate the presence of material processed through hot H-burning processes and should be also He-enriched. While small variations in helium content should have a small impact on colors and magnitudes for MS stars a large impact is expected on the colors of HB stars since He-rich stars should be also less massive.

In summary the discovery of multiple stellar populations started a new era on globular cluster research. While the observational scenario is still puzzling and there is a rather incoherent picture of the multipopulation phenomenon, for the first time we might have the key to solve a number of problems, like the abundance anomalies and possibly the second parameter problem, as well as the newly discovered multiple sequences in the CMD.

We gratefully acknowledge M. Hilker, R. Kraft, C. Sneden, and G. Wallerstein for sending us their data.

References

Anderson, J. 1997, PhD thesis, Univ. of California, Berkeley

Anderson, J., Piotto, G., King, I.R., Bedin, L.R., & Guhathakurta, P. 2009, ApJ, 697, L62

Bedin, L.R., Piotto, G., Zoccali, M., Stetson, P. B., Saviane, I., Cassisi, S., & Bono, G. 2000, A&A, 363, 159

Bedin, L.R., Piotto, G., Anderson, J., Cassisi, S., King, I.R., Momany, Y., & Carraro, G. 2004, ApJ Letters, 605, L125

Bellini, A., Bedin, L.R., Piotto, G., et al. 2010 AJ, 140, 631

Bragaglia, A., Carretta, E., Gratton, R., et al. 2010 ApJ, 720, L41

Calamida, A., et al. 2007, ApJ, 670, 400

Carretta, E., et al. 2009, A&A 505, 117

Carretta, E., et al. 2009, A&A 508, 695

Carretta, E., et al. 2010, ApJ, 722, L1

Cassisi, S., Salaris, M., Pietrinferni, A., Piotto, G., Milone, A. P., Bedin, L. R., & Anderson, J. 2008, ApJ, 672, L115

D'Antona, F., Bellazini, M., Caloi, V., Fusi Pecci, F., Galleti. S., & Rood, R. T. 2005, ApJ, 631, 868

Decressin, T., Meynet, G., Charbonnel, C., Prantzos, N., & Ekström, S. 2007, A&A, 464, 1029

Hesser, J. E., Bell, R. A., Harris, G. L. H. & Cannon, R., D. 1982, AJ, 87, 1470

Han, S., Lee, Y., Joo, S. et al. 2010, ApJ, 707, L190

Johnson, C. I., & Pilachowski, C. A., 2010, ApJ, 722, 1373

Lee, Y.-W., Joo, J.-M., Sohn, Y.-J., Rey, S.-C., Lee, H.-C., & Walker, A. R. 1999, Nature, 402, 55

Lee, J.-W., Kang, Y.-W., Lee, J., & Lee, Y.-W. 2009, Nature, 462, 480

Marino, A. F., Villanova, S., Piotto, G., Milone, A. P., Momany, Y., Bedin, L. R., & Medling, A. M., 2008, A&A 490, 625

Marino, A. F., Milone, A. P., Piotto, G., Villanova, S., Bedin, L. R., Bellini, A., & Renzini, A. 2009, A&A, 505, 1099

Marino, A. F., Sneden, C., Wallerstein, G. et al. 2010, in preparation

Marino, A. F., Piotto, G., Gratton, R., Milone, A. P., Zoccali, M., Bedin, L. R., Villanova, S., & Bellini, A. 2010, in IAU Symp. 268, Light Elements in the Universe, ed. C. Charbonnel et al. (Cambridge: Cambridge Univ. Press), 183

Milone, A. P. et al. 2008, ApJ, 673, 241

Milone, A. P., et al. 2010, ApJ, 709, 1183

Momany, Y., Bedin, L., R., Cassisi, S., Piotto, G., Ortolani, S., Recio-Blanco, A., De Angeli, F., & Castelli, F. 2004 A&A, 420, 605

Moretti, A.,Piotto, G.,Arcidiacono, C., et al. 2008, A&A 503, 755

Pancino, E., Ferraro, F. R., Bellazzini, M., Piotto, G., & Zoccali, M. 2000, ApJ, 534, L83

Pancino, E., Rejkuba, M., Zoccali, M., Carrera, R. 2010, in press (arXiv1009.1589)

Piotto, G., Bedin, L. R., Anderson, J., King, I. R., Cassisi, S., Milone, A. P., Villanova, S., Pietrinferni, A., & Renzini, A. 2007, ApJ, 661, L53

Piotto G. 2009, in IAU Symposium No. 258, the Ages of Stars, arXiv0902.1422

Richter, P., Hilker, M., & Richtler, T. A&A, 1999, 350, 476

Sosin, C., et al. 1997, ApJ, 480, L35

Yong, D., & Grundahal, F. 2008, ApJ, 672, L39

Yong, D., Grundahal, F., Johnson, A., & Asplund, M. 2008, ApJ, 684, 1159

Yong, D., Grundahal, F., D'Antona, F., Karacas, A. I., Lattanzio, J. C., & Norris, J., E., 2009 ApJ, 695, L62

Ventura, P., Caloi, V., D'Antona, F., Ferguson, J., Milone, A., Piotto, G., 2009 MNRAS, 399, 934

SAIt - PNCG - PNPS - AS GAIA

Resolved stellar populations

SF2A 2010
S. Boissier, M. Heydari-Malayeri, R. Samadi and D. Valls-Gabaud (eds)

DWARF GALAXIES IN THE LOCAL GROUP: CORNERSTONES FOR STELLAR ASTROPHYSICS AND COSMOLOGY

G. Bono[1, 2, 3], P.B. Stetson[4], M. Monelli[5], M. Fabrizio[1], N. Sanna[6], M. Nonino[7], A.R. Walker[8], F. Bresolin[9], R. Buonanno[1, 10], F. Caputo[2], M. Castellani[2], C.E. Corsi[2], M. Dall'Ora[11], I. Ferraro[2], P. François[12], G. Iannicola[2], M. Matsunaga[13], L. Pulone[2], M. Romaniello[3], J. Storm[14] and F. Thévenin[15]

Abstract. Dwarf galaxies have been the crossroad of significant theoretical and observational efforts, but we still lack firm constraints concerning their formation and evolution. They are also fundamental laboratories to investigate the impact of the environment on star formation and on chemical evolution in stellar systems that are order of magnitudes smaller than giant galaxies. We present some recent results concerning the dwarf spheroidal Carina and the dwarf irregular IC10. In particular, we focus our attention on the evolutionary properties of their stellar populations using accurate and deep color-magnitude diagrams. We also briefly discuss the impact that the transition from old, low-mass (horizontal branch) to intermediate-age (red clump) helium burning stars has in constraining the star formation history of complex stellar systems.

Keywords: galaxies: individual (Carina, IC10), galaxies: stellar content, galaxies: dwarf, local group, galaxies: kinematics and dynamics, stars: evolution, stars: fundamental parameters

1 Introduction

Dwarf galaxies are ubiquitous stellar systems outnumbering giant systems in the Local Group (LG, Mateo 1998), in the Local Volume (up to 25 Mpc, Vaduvescu & McCall (2008)), and in the nearby Universe (Popesso et al. 2006; Gonzalez et al. 2007). According to the most widely accepted cosmological (Λ Cold Dark Matter) model, the density fluctuations typical of dwarf galaxies are the first to undergo dynamical instability and to collapse. However current models and observations do not allow us to satisfactorily constrain the epoch when these systems formed. Yet, according to the simulations, dark matter halos, after their formation, start to merge, thus forming larger structures (Navarro et al. 1997). In addition, it is not yet clear whether primordial dark matter halos already included a baryonic component. It has been suggested (Haardt & Madau 1996) that the accretion of baryons begins after the re-ionization era ($\sim$10 Ga ago). However current cosmological models

[1] Università di Roma "Tor Vergata" - Rome, Italy
[2] INAF–Osservatorio Astronomico di Roma, via Frascati 33, Monte Porzio Catone, Rome, Italy
[3] European Southern Observatory, Karl-Schwarzschild-Str. 2, 85748 Garching bei München Germany
[4] DAO–HIA, NRC, 5071 West Saanich Road, Victoria, BC, V9E 2E7, Canada
[5] IAC, Calle Vía Lactea, 38200 La Laguna, Tenerife, Spain
[6] University of Virginia, 530 McCormick Road, 22903 Charlottesville, VA, USA
[7] INAF–OAT, via G.B. Tiepolo 11, 40131 Trieste, Italy
[8] NOAO–CTIO, Casilla 603, La Serena, Chile
[9] Institute for Astronomy, 2680 Woodlawn Drive, Honolulu, HI 96822, USA
[10] ASI–Science Data Center, ASDC c/o ESRIN, via G. Galilei, 00044 Frascati, Italy
[11] INAF–OACN, via Moiariello 16, 80131 Napoli, Italy
[12] Observatoire de Paris-Meudon, GEPI, 61 avenue de l'Observatoire, 75014 Paris, France
[13] Institute of Astronomy, University of Tokyo, 2-21-1 Osawa, Mitaka, Tokyo 181-0015, Japan
[14] AIP, An der Sternwarte 16, 14482 Potsdam, Germany
[15] Observatoire de la Côte d'Azur, BP 4229, 06304 Nice, France

predict a number of dwarfs significantly larger than that observed near giant spirals like the Milky Way and M31. This discrepancy is called the "missing satellite problem". It has not yet been established whether this discrepancy is due to the limits of theoretical models or to observational bias at the dark matter halos that were able to sustain star formation and chemical self enrichment at some epoch constitute the population of dwarf galaxies we observe today. Dwarfs display a huge variety in their gas content and star formation history, but have very similar structural properties and seems to obey to the same general scaling laws of giant galaxies. It is widely believed, and supported by state-of-the-art chemo/hydro/dynamical models, that gas-rich, star forming dwarf irregulars (dIs) and gas-poor quiescent dwarf spheroidals (dSphs) can simply represent different stages of a unique evolutionary path, driven by several internal and external factors.

However, we still lack firm constraints on galaxy formation and evolution (or transition) among different morphological types. Kormendy (1985, 1987), using high spatial resolution CCD images, found a well defined dichotomy between ellipticals (Es) and spheroidals (Sphs, Kormendy et al. 2009). In particular, early type galaxies are distributed along a sequence moving from cD (bright, low central surface brightness) to dwarf ellipticals (like M32, fainter, high central surface brightness). On the other hand, spheroidals are distributed along a different sequence that overlaps with spiral-galaxy disks and dwarf irregulars in which the faintest systems have a low central surface brightness (see Fig. 1 in Kormendy et al. 2009). On the basis of this clear empirical dichotomy it has been suggested that E and Sph galaxies are stellar systems that underwent different formation and evolution processes. In particular, Sphs might be either Spiral disks or Irregulars that lost their gas or transformed it into stars. The above findings are suggesting a galaxy formation scenario in which ellipticals only form via mergers, while spheroidals are defunct irregulars.

Several physical mechanisms have been suggested to support this scenario. The supernovae-driven energy feedback can remove a large amount of gas (Dekel & Silk 1986; Navarro et al. 1996; Veilleux et al. 2005). Tidal stripping and tidal stirring (Mayer et al. 2006), as well as ram pressure gas stripping (Chung 2007), UV flux from the host galaxy (Mayer et al. 2007) and galaxy harassment (Moore et al. 1998) can also remove both dark matter and baryons from dwarf galaxies and may induce star formation. However, the dichotomy between E and Sph galaxies has been questioned (Jerjen & Binggeli 1997; Gavazzi et al. 2005; Ferrarese et al. 2006). They suggest a smooth transition from Sphs to low-luminosity Es, since their intrinsic parameters are continuous. Moreover, the correlation between the shape of the brightness profile and the galaxy luminosity is continuous when moving from Es to Sphs.

The quoted arguments concerning galaxy formation and evolution are based on the integrated properties of complex systems. We can address the same problems more effectively using more quantitative information concerning the stellar and gas content of these systems. The disruption of dwarf galaxies and the ensuing formation of larger host galaxies can be traced back in time using kinematic properties, the metallicity distribution and the age distribution of their stellar populations (Grebel 2001; Gallart et al. 2005; Tolstoy et al. 2009). However, the details of the story are far from settled.

To address the quoted problems we decided to take into account two LG dwarf galaxies, namely Carina, the prototype of dwarf spheroidal galaxies with well defined multiple star formation episodes, and IC10, the prototype of dwarf irregular galaxies showing evidence of recent/ongoing star formation episodes.

2 The LG dwarf spheroidal Carina

Carina plays a key rôle among the LG dSph galaxies. The reasons are manifold: *i)* It is relatively close, and its central density is modest ($\log \rho = 0.17\ M_\odot\, pc^{-3}$, Mateo 1998). *ii)* Carina shows multiple, star formation episodes separated in time and in the amount of stellar mass involved (Dolphin 2002; Rizzi et al. 2003; Monelli et al. 2003). *iii)* Carina hosts a broad variety of variable stars ranging from low and intermediate-mass hydrogen burning dwarf Cepheids (δ Scuti, SX Phoenicis, Mateo et al. 1998) to low (RR Lyrae, Saha et al. 1986) and intermediate-mass helium burning stars (Anomalous Cepheids, Dall'Ora et al. 2003). *iv)* High-resolution spectra are available for less than a dozen of bright Red Giants (RGs). The mean metallicity is [Fe/H]=-1.69 dex, but the measurements show a spread of half dex (Koch et al. 2008). Independent measurements by Shetrone et al. (2003), using high-resolution spectra for five bright RGs, provided a mean metallicity of [Fe/H]=-1.64 and σ=0.2 dex. *v)* Calcium triplet measurements based on medium resolution spectra are also available for a large sample (437) of RG stars (Koch et al. 2006). Their metallicity distribution shows a peak at [Fe/H]=-1.72 ± 0.01 dex, but the metallicity distribution ranges from roughly -2.5 to -0.5 dex. By using the same spectra, but different selection criteria Helmi et al. (2006) found a metallicity distribution ranging from ~ -2.3 to ~ -1.3 dex.

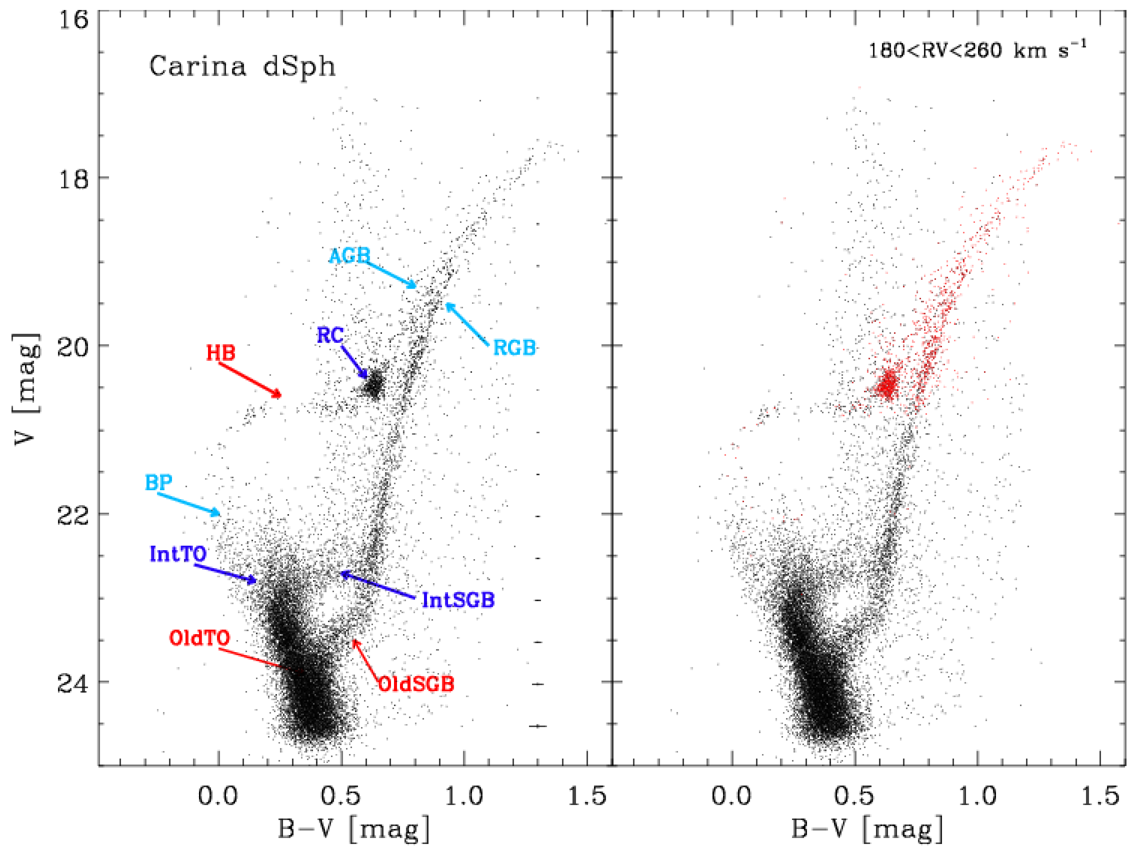

Fig. 1. *Left*: Optical V, $B-V$ Color Magnitude Diagram of the Carina dwarf spheroidal galaxy based on data collected with ground-based telescopes (Bono et al. 2010). Stars plotted are candidate Carina stars. The error bars on the right display intrinsic photometric errors both in magnitude and in color. The most relevant evolutionary phases of old (blue) and intermediate-mass (red) stars are labeled. In particular, MSTO (main sequence turn-off), BP (blue plume), SGB (sub giant branch), RGB (red giant branch), HB (horizontal branch), RC (red clump) and AGB (Asymptotic Giant Branch). *Right*: Same as the left, but the red dots display the distribution of evolved candidate Carina stars (1360 stars) selected using the radial velocity distribution ($180 \leq RV \leq 260$ km s^{-1}, 4σ).

However, we are facing a stark discrepancy between the spread in metallicity suggested by spectroscopic measurements and metallicity indicators such as the width in color of the red giant branch (RGB). Deep and accurate Color-Magnitude Diagrams (CMDs) of Carina indicate that the width in color of the RGB is quite limited (Monelli et al. 2003; Harbeck et al. 2001). This evidence was further supported in a recent investigation by Bono et al. (2010). They adopted more than 4000 multi-band (U,B,V,I) individual CCD images from three different ground-based telescopes covering the entire body of the galaxy. Moreover, to properly separate candidate Carina and field stars they performed an accurate selection using the $U-V$,$B-I$ color-color plane. They performed a detailed comparison with old (Galactic globular clusters) and intermediate-age (Small Magellanic Cloud open clusters) stellar systems and they found that the intrinsic spread in metallicity should be within 0.2 dex.

The left panel of Fig. 1 shows the V, $B-V$ CMD of candidate Carina stars based on the data collected by Bono et al. (2010). A glance at the data plotted in this CMD indicate that the quoted finding is supported by different photometric indicators. The spread in magnitude of old, low-mass helium burning stars (Horizontal Branch, HB) is only of the order of 0.15 mag, while a spread of 1.5 dex in metallicity would imply a spread in magnitude at least a factor of two larger (M_V(RR)≈0.18–0.36 mag/dex, Bono et al. 2003). The same outcome applies if we take into account intermediate-age helium burning stars (red clump, RC). By fitting the $B-V$ color distribution of RC stars, we found that the sigma is 0.12 mag, while a spread of 1.5 dex in metallicity would imply a spread in $B-V$ color that is a least a factor of two larger (see Fig. 6 in Bono et al. 2010). The above findings are minimally affected by the selection of candidate Carina stars, since HB stars are typically bluer than field stars. Moreover, the possible presence of field stars among the RC stars causes an increase in their spread in color.

To further constrain the mismatch between metallicity measurements and photometric indicators we decided to took advantage of an unprecedented sample of spectroscopic data of Carina stars (Fabrizio et al. 2010). We collected low-, medium- and high resolution spectra of evolved (old HB, intermediate-age RC, young blue plume, red giants) Carina stars using two different instruments available at the VLT, namely FORS2 (multi-object slit spectrograph) and GIRAFFE (multi-object fiber spectrograph). We ended up with a sample of ≈21,340 individual spectra of ≈2,000 stars covering the entire body of the galaxy. By using the radial velocity distribution, we selected more than 1,200 candidate Carina stars ($180 \leq RV \leq 260$ km s^{-1}, 4σ). These data were complemented with similar radial velocity measurements provided by Walker et al. (2007) and we ended up with a sample of 1,360 candidate Carina stars that is ≈75% larger than any previous Carina RV sample.

Data plotted in the right panel of Fig. 1 further support the photometric indicators concerning the spread in metallicity. The sample of RG, RC and HB stars kinematically selected cover limited ranges in color (RG, RC) and in magnitude (HB).

3 The LG dwarf irregular IC10

Among the dIs of the LG, IC10 is an interesting system, since it underwent a strong star-formation activity during the last half billion years. It is considered the only LG analog of starburst galaxies and a fundamental laboratory for the analysis of massive young stars and evolved intermediate-mass stars. Even though IC10 has been the cross-road of several investigations, its structural parameters and in particular its radial extent are poorly defined. Massey & Armandroff (1995) found that the major-axis of IC10 is $\sim 7'$. A similar diameter ($\sim 6'$) was found by Jarrett et al. (2003) using the isophotal radii from 2MASS near infra-red (NIR) images. More recently, Tikhonov & Galazutdinova (2009), using both ground-based and space images, suggested that the extent of the thick disk along the minor axis is $\approx 10\farcm5$. By using Asymptotic Giant Branch (AGB) and RGB stars as tracers of intermediate and old age stellar populations, Demers et al. (2004) suggested that IC10 should have a halo of $\sim 30'$diameter. The photometric method they adopted to pinpoint AGB and RGB stars relies on broad (R, I) and intermediate-band filters (TiO, CN). By using the 12k mosaic camera available on Canada-France-Hawaii Telescope (CFHT) they identified more than ≈ 600 AGB and ≈ 15000 RGB stars. The observational scenario becomes even more complicated if we consider the radio measurements by Huchtmeier (1979) indicating that IC10 has a huge envelope of neutral hydrogen extending over more than 1 square degree ($62' \times 80'$) across the galaxy.

The puzzling difference between the radial extent based on optical and on radio data was recently settled by Sanna et al. (2010). By using space (ACS and WFPC2 at HST) and ground-based (SuprimeCam at Subaru, Omega Cam at CFHT) images they found sizable samples of RG stars up to radial distances of $18'$-$23'$from the galactic center. Star counts also indicate the occurrence of IC10 stars at least at 3σ level up to $34'$-$42'$from the center. This evidence further supports the hypothesis that the huge HI cloud covering more than 1° across the galaxy is associated with IC10.

Data plotted in Fig. 2 also suggest that the stellar population characterized by different ages show relevant radial gradients. The CMD plotted in the top left corner shows a well defined blue main sequence of very young main sequence Turn-Off (TO) stars ($t \sim$30–200 Ma, $M(TO)/M_\odot \approx 8 - 3$). The dashed-dotted (30 Ma) and the dashed (200 Ma) isochrone plotted in this figure are based on scaled solar evolutionary models constructed by Pietrinferni et al. (2004)*, at fixed total metallicity ([M/H]=−0.66 dex). The same group of stars is marginally present in the CMD based on the WFPC2 and disappears at larger radial distances. On the other hand, the candidate AGB stars i.e. the tracers of intermediate-age stars with I-band magnitude similar to the stars located across the tip of the RGB ($I \sim$22 mag) and redder colors ($3 \leq V - I \leq 4.5$) are present both in the center and in the external regions. The same outcome applies to RG stars, i.e. to the tracers of old stars. The solid line shows an old α-enhanced isochrone (t=13 Ga) also constructed by (Pietrinferni et al. 2006) at the same fixed total metallicity of the young isochrones. These findings indicate that this galaxy might have experienced an ongoing star formation activity not only during the last few tens of Ma, but also during the last few hundreds of Ma. Current photometry does not allow us to constrain whether IC10 experienced a steady star formation activity on the time scale of Ga, but strongly supports the occurrence of an old stellar population (see Fig. 3 in Sanna et al. 2009).

*See also `http://www.oa-teramo.inaf.it/BASTI`

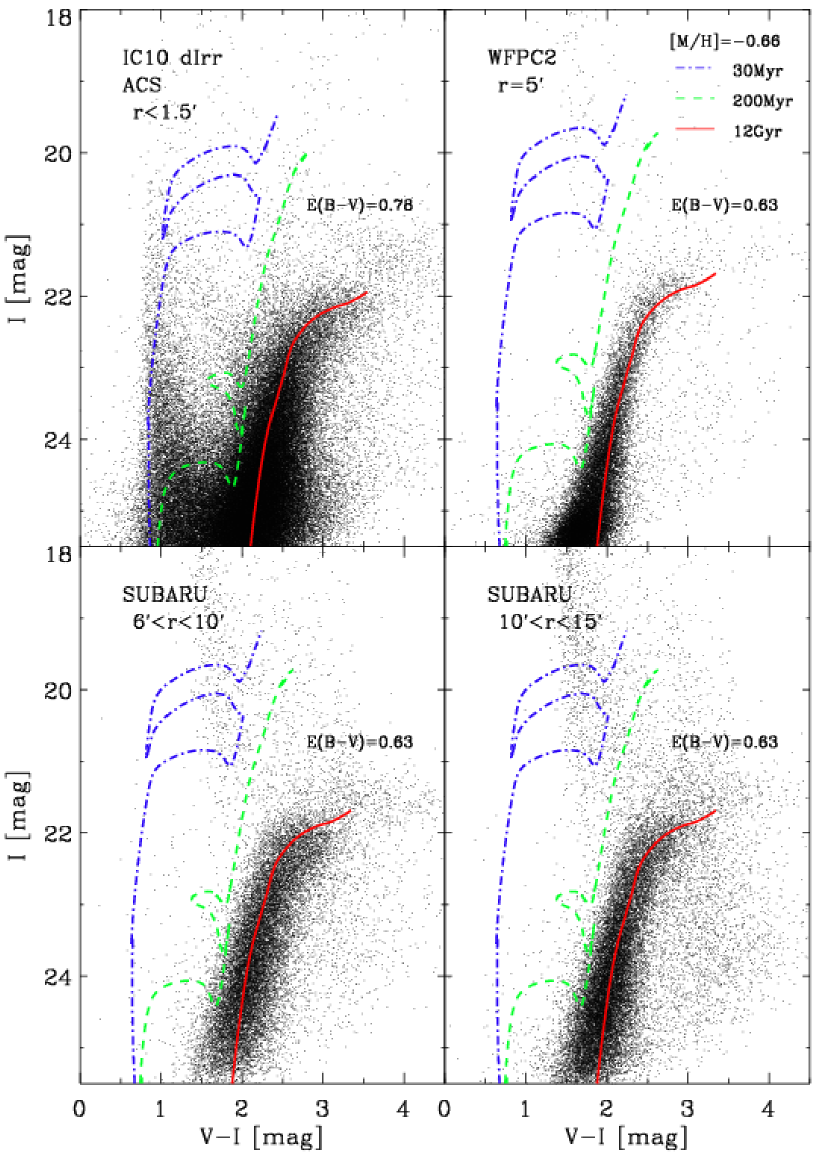

Fig. 2. *Top Left*: Optical I, $V-I$ CMD of the IC10 dwarf irregular galaxy based on data collected with ACS at HST and covering the central regions of galaxy (Sanna et al. 2009). The colored lines show three scaled solar isochrones (Pietrinferni et al. 2004, 2006) at fixed metal content ([M/H]=−0.66 dex) and different ages (see labeled values). The reddening and the distance modulus are also labeled. *Top Right*: Same as the left, but the CMD is based on images collected with the WFPC2 at HST. This pointing is located at 5′from the galaxy center (see Fig. 1 in Sanna et al. 2010). *Bottom Left*: Same as the top, but the CMD is based on images collected with the SuprimeCam at the Subaru telescope. The stars ploted in this CMD are located in an annulus around the galaxy center. *Bottom Right*: same as the left, but for stars in a more external annulus.

4 Conclusions

The scenario emerging from detailed photometric and spectroscopic investigations of Local Group dwarf galaxies is quite complex. A gas-poor system like Carina dSph galaxy according to current estimates is characterized by a large M/L ratio ranging from 30 (Mateo 1998) to 14 (Walker et al. 2009). This value agrees with similar estimates for LG dSphs and supports the view that they should be dark matter dominated. On the other hand, photometric indicators indicate that the chemical enrichment of both the old and the intermediate-age populations is quite limited and within 0.2 dex. This finding once supported by accurate measurements of iron and α-element abundances of RG stars can shed new lights on the chemical history of Carina stellar populations, and in turn firm constraints on the yields retained by this galaxy.

According to a recent estimate the IC10 dI has a M/L ratio that is one order of magnitude larger (Sanna et al. 2010, M/L$\sim$10, []) than previous estimates (M/L$\sim$1, Woo et al. 2008), thus suggesting that dIs might host a similar amount of dark matter than dSphs. The radial distribution of IC10 old- and intermediate-age stellar populations agrees quite well with the size of the huge neutral hydrogen cloud detected by Huchtmeier (1979) and Cohen (1979). This indicate that the stellar halo and the hydrogen cloud have, within the errors, similar radial extents (Tikhonov & Galazutdinova 2009). This evidence further supports numerical simulations suggesting that dwarf galaxies might have tidal radii significantly larger than empirical estimates (Hayashi et al. 2003; Kazantzidis et al. 2004). New and deeper data on this interesting system will allow us to constrain the possible occurrence of an old stellar population across the disc. This is a robust observable to constrain whether the formation of discs in dwarf galaxies follows the so-called down-sizing paradigm, i.e. massive discs formed before the low-mass ones (Cowie et al. 1996).

Finally, we mention that new theoretical and empirical insights are required to understand why dSphs and GCs do not seem to follow the Faber-Jackson relation (Chilingarian et al. 2010). The former systems appear to have, at fixed total luminosity, a radial velocity dispersion smaller than Ultra Compact Dwarfs (UCDs) and dwarf ellipticals. On the other hand, the latter systems show in this plane a steeper slope when compared with the other compact stellar systems. The empirical scenario becomes even more puzzling if we also account for their mean metallicity. The dSphs follow the same metallicity-luminosity relation of dwarf and giant ellipticals. However, the GCs and the UCDs cover a broad range in metallicity and do not show a clear correlation (see Fig. 8 in Chilingarian et al. 2010).

These open problems concerning the formation and evolution of dwarf galaxies, their chemical evolution and their stellar content are an excellent viaticum for those interested in addressing cosmological problems using nearby resolved stellar populations.

It is a real pleasure to thank the SOC of the workshop on Resolved Stellar Populations held in Marseille during the SF2A meeting, for inviting me to give a talk on dwarf galaxies in the Local Group. I would also like to thank young and less young collaborators with whom I am sharing the pleasure to understand the properties of these “fluffy” stellar systems.

References

Bono, G., et al. 2010, PASP, 122, 651

Bono, G., Caputo, F., Castellani, V., Marconi, M., Storm, J., & Degl’Innocenti, S. 2003, MNRAS, 344, 1097

Chilingarian, I., Mieske, S., Hilker, M., & Infante, L. 2010, `http://arXiv.org/abs/1011.1852`

Chung, A. 2007, PhD Thesis, Columbia University

Cohen, R.J. 1979, MNRAS, 187, 839

Cowie, L. L., Songaila, A., Hu, E. M., & Cohen, J. G. 1996, AJ, 112, 839

Dall’Ora, M. et al. 2003, AJ, 126, 197

Dekel, A., & Silk, J. 1986, ApJ, 303, 39

Demers, S., Battinelli, P., Letarte, B. 2004, A&A, 424, 125

Dolphin, A. E. 2002, MNRAS, 332, 91

Fabrizio, M. et al. 2010, PASP, submitted

Ferrarese, L., et al. 2006, ApJS, 164, 334

Gallart, C., Zoccali, M., & Aparicio, A. 2005, ARA&A, 43, 387

Gavazzi, G., Donati, A., Cucciati, O., Sabatini, S., Boselli, A., Davies, J., & Zibetti, S. 2005, A&A, 430, 411

Gonzalez, A. H., Zaritsky, D., & Zabludoff, A. I. 2007, ApJ, 666, 147

Grebel, E. K. 2001, Astrophysics and Space Science, Supplement 1, 277, 231

Haardt, F., & Madau, P. 1996, ApJ, 461, 20

Harbeck, D., et al. 2001, AJ, 122, 3092

Hayashi, E., Navarro, J. F., Taylor, J. E., Stadel, J., Quinn, T. 2003, ApJ, 584, 541

Helmi, A., et al. 2006, ApJ, 651, L121

Huchtmeier, W. K. 1979, A&A , 75, 170

Jarrett, T. H. Chester, T., Cutri, R., Schneider, S. E., Huchra, J. P. 2003, AJ, 125, 525

Jerjen, H., & Binggeli, B. 1997, in *The Nature of Elliptical Galaxies; 2nd Stromlo Symposium*, M. Arnaboldi, G.S. da Costa & P. Saha (eds), ASP Conference Series, Vol. 116, 298

Kazantzidis, S., Mayer, L., Mastopietro, C., Diemand, J., Stadel, J., Moore, B. 2004, ApJ, 608, 663

Klypin, A., Kravtsov, A. V., Valenzuela, O., & Prada, F. 1999, ApJ, 522, 82

Koch, A., Grebel, E. K., Wyse, R. F. G., Kleyna, J. T., Wilkinson, M. I., Harbeck, D. R., Gilmore, G. F., & Evans, N. W. 2006, AJ, 131, 895

Koch, A., Grebel, E. K., Gilmore, G. F., Wyse, R. F. G., Kleyna, J. T., Harbeck, D. R., Wilkinson, M. I., & Evans, N.W. 2008, AJ, 135, 1580

Koposov, S. E., Yoo, J., Rix, H.-W., Weinberg, D. H., Macciò, A. V., & Miralda Escudé, J. 2009, ApJ, 696, 2179

Kormendy, J. 1985, ApJ, 295, 73

Kormendy, J. 1987, in *Dark matter in the universe*, IAU Symposium 117, 139

Kormendy, J., Fisher, D. B., Cornell, M. E., & Bender, R. 2009, ApJS, 182, 216

Kravtsov, A. 2010, Advances in Astronomy, 2010, ID 281913

Massey, P. & Armandroff, T. E. 1995, AJ, 109, 2470

Mateo, M. L. 1998, ARA&A, 36, 435

Mateo, M., Hurley-Keller, D., & Nemec, J. 1998, AJ, 115, 1856

Mayer, L., Mastropietro, C., Wadsley, J., Stadel, J., & Moore, B. 2006, MNRAS, 369, 1021

Mayer, L., Kazantzidis, S., Mastropietro, C., & Wadsley, J. 2007, Nature, 445, 738

Monelli, M. et al. 2003, AJ, 126, 218

Moore, B., Ghigna, S., Governato, F., Lake, G., Quinn, T., & Stadel, J. 1998, in *Galactic Halos*, D. Zaritsky (ed), ASP Conference Series, Vol. 136, 426

Moore, B., Ghigna, S., Governato, F., Lake, G., Quinn, T., Stadel, J., & Tozzi, P. 1999, ApJ, 524, L19

Navarro, J. F., Frenk, C. S., & White, S. D. M. 1996, ApJ, 462, 563

Navarro, J. F., Frenk, C. S., & White, S. D. M. 1997, ApJ, 490, 493

Pietrinferni, A., Cassisi, S., Salaris, M., Castelli, F. 2004, ApJ, 612, 168

Pietrinferni, A., Cassisi, S., Salaris, M., Castelli, F. 2006, ApJ, 642, 797

Popesso, P., Biviano, A., Böhringer, H., & Romaniello, M. 2006, A&A, 445, 29

Rizzi, L., Held, E. V., Bertelli, G., & Saviane, I. 2003, ApJ, 589, L85

Saha, A., Monet, D. G., & Seitzer, P. 1986, AJ, 92, 302

Sanna, N. et al. 2009, ApJ, 699, L84

Sanna, N., et al. 2010, ApJ, 722, L244

Shetrone, M., Venn, K. A., Tolstoy, E., Primas, F., Hill, V., & Kaufer, A. 2003, AJ, 125, 684

Tikhonov, N. A., Galazutdinova, O. A. 2009, AstL, 35, 748

Tolstoy, E., Hill, V., & Tosi, M. 2009, ARA&A, 47, 371

Vaduvescu, O., & McCall, M. L. 2008, A&A, 487, 147

Veilleux, S., Cecil, G., & Bland-Hawthorn, J. 2005, ARA&A, 43, 769

Walker, M. G., Mateo, M., Olszewski, E. W., Gnedin, O. Y., Wang, X., Sen, B., & Woodroofe, M. 2007, ApJ, 667, L53

Walker, M. G., Mateo, M., Olszewski, E. W., Peñarrubia, J., Evans, N.W., & Gilmore, G. 2009, ApJ, 704, 1274

Woo, J., Courteau, S., Dekel, A. 2008, MNRAS, 390, 1453

OPEN CLUSTERS AS TRACERS OF THE GALACTIC DISK

A. Bragaglia[1]

Abstract. Open clusters are good tracers of the properties of the Galactic disk, of its formation, and evolution. There are about 2000 open clusters in catalogues, but we have a measure of age and distance only for about one half of them, and the situation is even worse for metallicity. We are still far from fully exploiting the potentialities of these objects to understand our Galaxy. To this end, the results of the Gaia satellite will be of paramount importance, coupled with complementary and follow-up observations from the ground.

Keywords: Galaxy: disc, Hertzsprung-Russell (HR) diagram, open clusters and associations: general

1 Introduction

Open clusters (OCs) are very useful to describe the properties of the Galactic disk (Friel 1995; Bragaglia & Tosi 2006). Especially in the pre-Gaia* era, their distances and ages are more easily determined than for field stars, except the very near ones. They are useful templates for stellar models at all masses, and are complementary to globular clusters. OCs can be used to describe the metallicity distribution of the disk (e.g., to find gradients and their possible evolution with time). If we wish to use OCs to study the history of the disk we have, of course, to concentrate on the old clusters.

OCs are not the only possibility to study the metallicity distribution. To study the present day distribution we may use H II regions or O/B stars (e.g., Rudolph et al. 2006), or Cepheids, for which the distance is very well defined (e.g., Andrievsky et al. 2004). If we wish to explore the past, we can use samples like the one in the Geneva-Copenhagen survey (Nordström et al. 2004) or planetary nebulae. For the latter there is however controversy on the actual slope of the gradient and on its evolution with time (see e.g., Maciel et al. 2005; Stanghellini & Haywood 2010, for two different views).

A problem, when dealing with field stars, is their migration in the disk (see e.g., Roškar et al. 2008, for a recent paper on the subject): stars may be found at very large distances from their original birth position, and this implies a mixing of the metallicities and a modification/smearing of any gradient. OCs seem more resilient and they generally move much less, so that their present-day Galactocentric distance is a good approximation of the one at birth, as shown in a recent paper by Wu et al. (2009), who calculated the orbits of about 500 OCs.

2 The present situation and the impact of Gaia

There are about 2000 known open clusters (see the catalogue by Dias et al. 2002)†, but information on distance and age is present only for about one half. A measure of metallicity based on several indirect methods is available only for about one tenth of the sample, while metallicity and abundances based on high-resolution spectroscopy for less than about one twentieth. Unfortunately, this wealth of information is not homogeneous, and this has to be kept in mind when studying the properties of the OC sample.

Fig. 1, which uses information from the Dias et al. (2002) catalogue, shows that OCs do not seem to follow an age-metallicity relation: there are old clusters at each metallicity (even if, of course, the sample is small for very old age and very low/high metallicity). It also shows that there is an age dispersion at every Galactocentric

[1] INAF-Osservatorio Astronomico di Bologna, via Ranzani 1, 40127 Bologna, Italy

*The Gaia satellite will derive very high precision parallaxes, proper motions, radial velocities, etc for about 10^9 stars, see `http://www.rssd.esa.int/index.php?project=GAIA&page=index`.

†See web updates at `http://www.astro.iag.usp.br/~wilton`

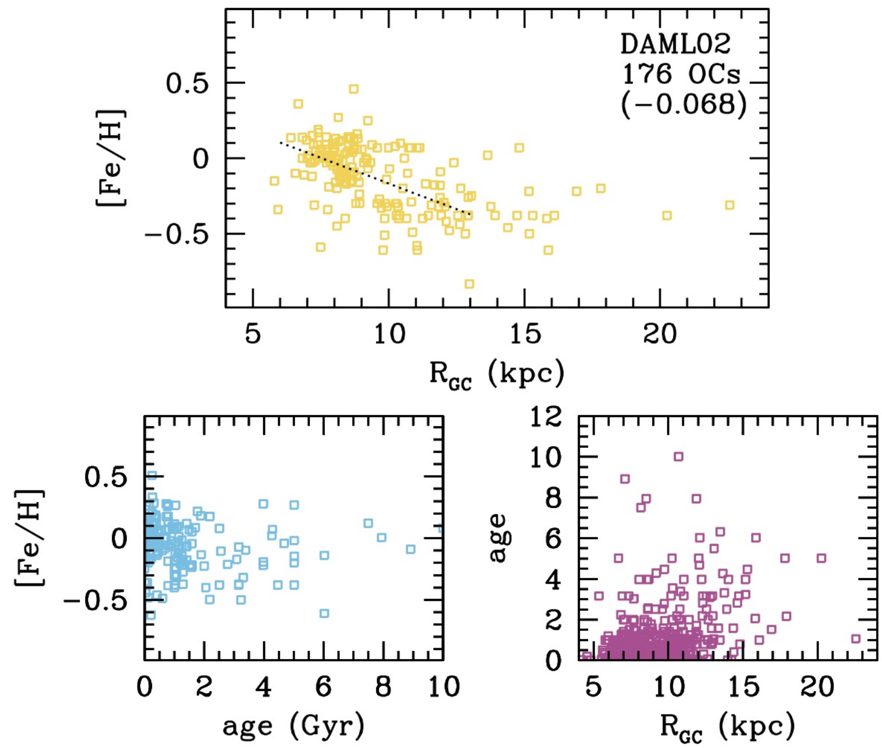

Fig. 1. Using data from Dias et al. (2002), I show here *i*) the metallicity distribution as a function of Galactocentric distance (upper panel), indicating the slope of the metallicity gradient computed in the inner 13 kpc; *ii*) the metallicity distribution as a function of age (lower, left panel), showing that at all ages there is a large spread in metallicity; *iii*) the distribution of age with distance from the Galactic centre (lower, right panel), where we see that old OCs are present in the whole disk.

distance; only old clusters are catalogued at large distances, but this may well be an observational bias. Finally, the figure displays the radial distribution of OC metallicities; there appears to be a decrease in metallicity going towards the outer part of the disk, with a lot of scatter, and maybe a flattening in the outermost region. If we compute a simple linear regression in the 6-13 kpc region, [Fe/H] decreases by about -0.07 dex kpc^{-1}; this interval has been chosen because there seems to be indications that some transition in the metallicity distribution appears near R$_{GC}$ $\sim$ 13 kpc (see e.g., Sestito et al. 2008; Carraro et al. 2007; Friel, Jacobson, & Pilachowski 2010). A separation near 10 kpc had been proposed by Twarog, Ashman, & Anthony-Twarog (1997), who thought that OCs presented a step distribution, with inner clusters with [Fe/H]$\simeq 0$ and outer ones with [Fe/H]$\simeq -0.3$ dex; this picture has however been recently challenged by Sale et al. (2010).

While the Dias et al. (2002) catalogue or the WEBDA database (see `http://www.univie.ac.at/webda`) are very useful, we need to consider (sub)samples of OCs analysed in the most homogeneous way to be sure of not missing any details because of systematics between different studies. An example is the BOCCE (Bologna Open Cluster Chemical Evolution) program (see Bragaglia & Tosi 2006; Carretta et al. 2007, and references therein), where deep, precise photometry and high resolution spectroscopy is being obtained for a sample of about 40 OCs, to determine age, distance, reddening, metallicity, and detailed chemical composition. This will, for instance, give strong constraints to models of Galactic chemical evolution. Fig. 2 illustrates what is already possible to do. There are about 70 old OCs for which the metallicity has been derived using high resolution spectroscopy by many different groups. Using these [Fe/H] values and the most recent and reliable distances and ages, we may build the radial metallicity distribution at different epochs and this can be compared with results of chemical evolution models. But recall that this sample is not homogeneous and that distances (and ages) are still rather poorly constrained.

The Gaia space mission, which will fly in the next years, will produce data of unprecedented precision also for the OC sample, providing in particular individual distances and proper motions for all cluster stars brighter than about V=20. Radial velocities, metallicities and abundances will only be obtained for the brightest objects.

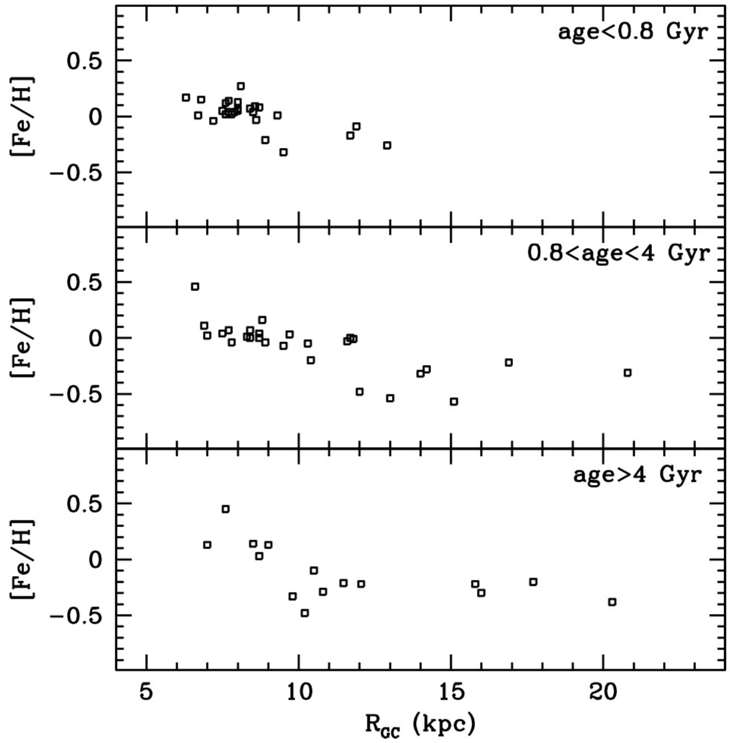

Fig. 2. Radial distribution of metallicity for the about 70 OCs with [Fe/H] derived using high-resolution spectroscopy, divided in three age intervals. The oldest clusters seem to define a steeper slope, especially if we limit to the inner 12-13 kpc.

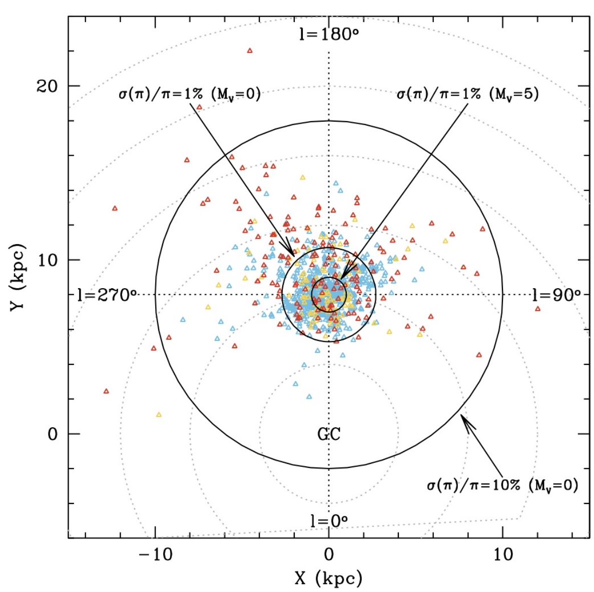

Fig. 3. Distribution of the known OCs in the Galactic plane; the Galactic centre is at (0,0), the Sun at (0,8) kpc. The OCs are indicated with light blue, yellow, and red symbols for young, intermediate-age, and old clusters, respectively. Also indicated are the approximate regions for which the Gaia distances will be more precise than 1% for main sequence and giant stars, and 10% for giants.

Fig. 3 shows what will be the impact of Gaia on the measured distances: for almost the entire OC family, a precision in distance better than 10 % for the individual star, hence much better for the cluster as a whole, will be reached, at least for giant stars (the brightest ones in the old OCs useful to study the history of the disk). An even higher precision will be reached by proper motions, permitting a clear-cut separation of cluster members from field stars, a very difficult task in most instances with the present data.

3 Wish list

To fulfill the promise of understanding the formation and evolution of the Galactic disk using open clusters we need:

- Large samples of OC, with a full coverage in position, age, and metallicity;
- To add undiscovered/unstudied clusters;
- To obtain precise, deep photometry (wide/narrow band and IR) on wide fields;
- Information on membership (from proper motion or radial velocity)
- Information on binary fraction and, possibly, on individual binaries;
- Spectroscopy, at resolution from about 10000 (for radial velocity) to 50000 (abundances) of large, significant samples of stars in each OC;
- Up-to-date stellar models and conversions to the observational plane;
- Using the maximum homogeneity in observations and analysis.

Part of these will be provided by Gaia, but coordinated ground based efforts are required, together with some advances in stellar modeling and precise and homogeneous studies.

I wish to thank the organizers of the "Resolved stellar populations" Workshop for the opportunity to talk about open clusters. Special thanks go to all people collaborating with me on this subject. I have made ample use of the WEBDA, originally created by J.-C. Mermilliod and presently maintained by E. Paunzen.

References

Andrievsky, S.M., Luck, R.E., Martin, P. & Lépine, J.R.D. 2004, A&A, 413, 159
Bragaglia A. & Tosi M. 2006, AJ, 131, 1544
Carraro G., Geisler D., Villanova S., Frinchaboy P.M. & Majewski S.R., 2007, A&A, 476, 217
Carretta, E., Bragaglia, A. & Gratton, R.G. 2007, A&A, 473, 129
Dias W.S., Alessi B.S., Moitinho A. & Lépine J.R.D. 2002, A&A, 389, 871
Friel E.D. 1995, ARA&A, 33, 381
Friel E.D., Jacobson H.R. & Pilachowski C.A. 2010, AJ, 139, 1942
Maciel, W.J., Lago, L.G. & Costa, R.D.D. 2005, A&A, 433, 127
Nordström, B., et al. 2004, A&A, 418, 989
Roškar R., Debattista V. P., Quinn T. R., Stinson G. S. & Wadsley J. 2008, ApJ, 684, L79
Rudolph, A. L., Fich, M., Bell, G. R., Norsen, T., Simpson, J. P., Haas, M. R., & Erickson, E. F. 2006, ApJS, 162, 346
Sale, S. E., et al. 2010, MNRAS, 402, 713
Sestito P., Bragaglia A., Randich S., Pallavicini R., Andriewsky S.M. & Korotin S.A. 2008, A&A, 488, 943
Stanghellini, L. & Haywood, M. 2010, ApJ, 714, 1096
Twarog B. A., Ashman K. M. & Anthony-Twarog B. J. 1997, AJ, 114, 2556
Wu Z.-Y., Zhou X., Ma J. & Du C.-H. 2009, MNRAS, 399, 2146

SF2A 2010
S. Boissier, M. Heydari-Malayeri, R. Samadi and D. Valls-Gabaud (eds)

PHOTOCENTRIC VARIABILITY OF RED SUPERGIANT STARS AND CONSEQUENCES ON GAIA MEASUREMENTS

A. Chiavassa[1], E. Pasquato[2], A. Jorissen[2], S. Sacuto[3], C. Babusiaux[4], B. Freytag[5,6,7], H.-G. Ludwig[8], P. Cruzalèbes[9], Y. Rabbia[9], A. Spang[9] and O. Chesneau[9]

Abstract. Red supergiant stars are characterized by large convection-related surface structures that cause surface inhomogeneities and shock waves. We explore the impact of granulation on the photocentric motion using 3D simulations of convection with CO5BOLD and post-processing radiative transfer code Optim3D to compute spectra and intensity maps in the Gaia G band [325 – 1030 nm]. We found that the Gaia parallax for Betelgeuse-like supergiants are characterized by a systematic error of a few percents.

Keywords: supergiants, astrometry, parallaxes, hydrodynamics

1 Introduction

The aim of the Gaia mission is to determine high-precision astrometric parameters that, together with multi-band and multi-epoch photometric and spectrocopic data, will be used to reconstruct the formation, history and evolution of the Galaxy.
Red supergiant (RSG) stars are characterized by vigorous convection which imprints a pronounced granulation pattern on the stellar surface (Chiavassa et al. 2010). As a consequence, the granulation-related variability must be quantified in order to better characterize any resulting systematic error on the parallax determination.

2 RHD simulations of red supergiant stars

We employed detailed radiation-hydrodynamics (RHD) simulation of RSGs (Freytag et al. 2002; Freytag & Höfner 2008). The model has a mass of 12 $M_\odot$, employs an equidistant numerical mesh with 235^3 grid points with a resolution of 8.6 $R_\odot$ (or 0.040 AU), a luminosity average over time (i.e., over 5 years) of $L = 93\,000 \pm 1300\ L_\odot$, an effective temperature of $T_{\rm eff}$ = 3490±13 K, a radius of $R = 832 \pm 0.7\ R_\odot$, and a surface gravity $\log g = -0.337 \pm 0.001$. This is our most successful RHD simulation so far because it has stellar parameters closest to Betelgeuse (Chiavassa et al. 2009). We computed spectra and intensity maps based on snapshots from the RHD simulations (Fig. 1, left), using the code Optim3D (Chiavassa et al. 2009) and a solar composition (Asplund et al. 2005).

[1] Max-Planck-Institut für Astrophysik, Karl-Schwarzschild-Str. 1, Postfach 1317, D-85741 Garching b. München, Germany
[2] Institut d'Astronomie et d'Astrophysique, Université Libre de Bruxelles, CP. 226, Boulevard du Triomphe, B-1050 Bruxelles, Belgium
[3] Department of Astronomy, University of Vienna, Türkenschanzstrasse 17, A-1180 Wien, Austria
[4] GEPI, Observatoire de Paris, CNRS, Université Paris Diderot, Place Jules Janssen F-92190 Meudon, France
[5] Université de Lyon, F-69003 Lyon, France; Ecole Normale Supérieure de Lyon, 46 allée d'Italie, F-69007 Lyon, France; CNRS, UMR 5574, Centre de Recherche Astrophysique de Lyon; Université Lyon 1, F-69622 Villeurbanne, France
[6] Department of Physics and Astronomy, Division of Astronomy and Space Physics, Uppsala University, Box 515, S-751 20 Uppsala, Sweden
[7] Istituto Nazionale di Astrofisica, Osservatorio Astronomico di Capodimonte, Via Moiariello 16, I-80131 Naples, Italy
[8] Zentrum für Astronomie der Universität Heidelberg, Landessternwarte, Königstuhl 12, D-69117 Heidelberg, Germany
[9] UMR 6525 H. Fizeau, Univ. Nice Sophia Antipolis, CNRS, Observatoire de la Côte d'Azur, Av. Copernic, F-06130 Grasse, France

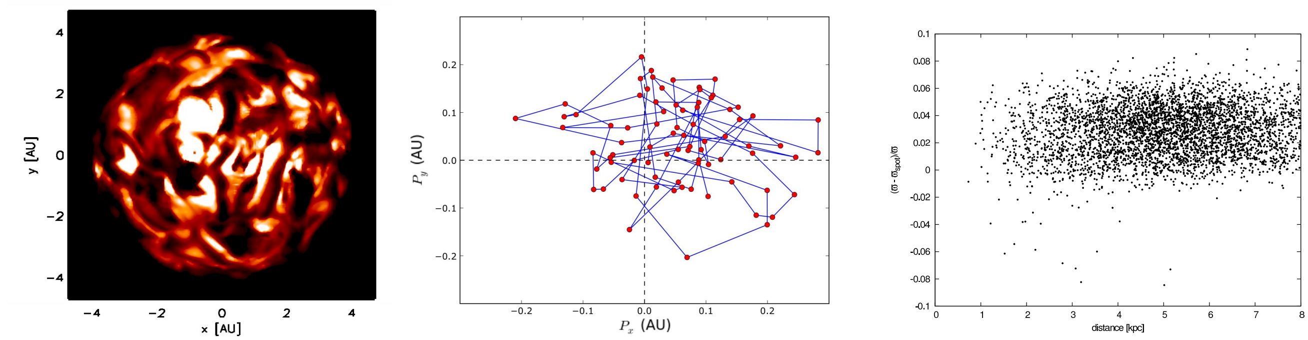

Fig. 1. *Left panel:* map of the linear intensity (the range is [0 – 230000] erg/s/cm^2/Å) in the Gaia G band photometric filter (Jordi & Carrasco 2007). *Central panel:* photocenter displacement as a function of time. Each point is a snapshot 23 days apart for a total of 5 years of simulation (comparable to the duration of the Gaia mission). *Right panel:* Relative difference between the parallaxes computed with and without the photocentric motion of the central panel, as a function of the distance.

3 Predictions

The simulated surface of RSGs (Fig. 1, left) displays high-contrast structures with spots up to 50 times brighter than the dark ones with strong changes over some weeks. This aspect is connected with the underlying granulation pattern, but also with dynamical effects such as shocks and waves which dominate at optical depths smaller than 1. We computed the position of the photocenter for all the synthetic maps (Fig. 1, center) and found that the photocenter excursion goes from 0.005 to 0.3 AU over 5 years of simulation (the stellar radius is $\approx$ 4 AU, left panel of the Figure).

4 Conclusions

We found that the convection-related structures on the surface of RGSs affect the position of the photocenter of Betelgeuse-like supergiants. In fact, Fig. 1 (right) shows that the Gaia parallax computed with ($\varpi_{\rm spot}$, calculated using a photocentric motion deduced from Fig. 1 and using Gaia Object Generator v7.0, GOG* Isasi et al. 2010, central panel) and without (ϖ) surface brightness asymmetries may be affected by a systematic error of a few percents. It might be of interest to monitor the photocentric deviations for a few well selected RSGs during the Gaia mission. Monitoring their phase closure on three different base lines would provide valuable information on the size of the inhomogeneities present on the stellar surface (see Sacuto et al., in preparation). However, there is a little hope to be able to correct the Gaia parallaxes of RSGs from this parallax error, without knowing the run of the photocentric shift for each considered star. More details and predictions can be found in Chiavassa, Pasquato, Jorissen et al. (submitted to A&A).

References

Asplund, M., Grevesse, N., & Sauval, A. J. 2005, ASP Conference Series, 336, 25

Chiavassa, A., Haubois, X., Young, J. S., Plez, B., Josselin, E., Perrin, G., & Freytag, B. 2010, A&A, 515, A12

Chiavassa, A., Plez, B., Josselin, E., & Freytag, B. 2009, A&A, 506, 1351

Freytag, B., Höfner, S. 2008, A&A, 483, 571

Freytag, B., Steffen, M., & Dorch, B. 2002, Astronomische Nachrichten, 323, 213

Isasi, Y., Figueras, F., Luri, X., & Robin, A. C. 2010, Highlights of Spanish Astrophysics V, 415

Jordi, C., & Carrasco, J. M. 2007, The Future of Photometric, Spectrophotometric and Polarimetric Standardization, 364, 215

*`http://gaia-gog.cnes.fr`

THE VIMOS-VLT DEEP SURVEY: THE GROUP CATALOGUE

O. Cucciati[1], C. Marinoni[2], A. Iovino[3], S. Bardelli[4], C. Adami[1], A. Mazure[1] and the VVDS Team

Abstract. We present a homogeneous and complete catalogue of optical galaxy groups identified in the VIMOS-VLT spectroscopic Deep Survey (VVDS). We use mock catalogues extracted from the Millennium simulation to study the potential systematics that might affect the overall distribution of the identified systems, and also to asses how well galaxy redshifts trace the line-of-sight velocity dispersion of the underlying mass overdensity. We train on these mock catalogues the adopted group-finding technique (the Voronoi-Delaunay Method, VDM), to recover in a robust and unbiased way the redshift and velocity dispersion distributions of groups and maximise the level of completeness (C) and purity (P) of the group catalogue. We identify 318(/144) VVDS groups with at least 2(/3) members within $0.2 \leq z \leq 1.0$, globally with C=60% and P=50%. We use the group sample to study the redshift evolution of the fraction f_b of blue galaxies within $0.2 \leq z \leq 1$ in both groups and in the whole ensemble of galaxies irrespectively of their environment.

Keywords: galaxies: clusters, high redshift, evolution, statistics, cosmology: large-scale structure

1 This work

We used the data collected for the VVDS-0226-04 deep field ("VVDS-02h" field, Le Fèvre et al. 2005) to produce a homogeneous and complete optically-selected galaxy group catalogue, with reliable properties like redshift and line of sight velocity dispersions (σ_{los}). The aim is to study galaxy properties in very dense regions, on scales at which the physical processes driven by galaxy interactions are believed to play a major role. This work is extensively described in Cucciati et al. (2010). We refer the reader to Gerke et al. (2005, 2007); Knobel et al. (2009) and Iovino et al. (2010) for similar works based on different data sets.

We used galaxy mock catalogues that mimic the VVDS observational strategy, and that were extracted from the Millennium simulations (Springel et al. 2005), coupled to a semi-analytic model for galaxy formation (De Lucia & Blaizot 2007). Using these mocks, we first verified that the VVDS-02h survey sampling rate allows us to recover at least 50% of the groups (with a virial l.o.s. velocity dispersion $\sigma_{vir} \geq 350$ km/s) that are potentially present in the parent photometric catalogue up to $z = 1$. We also tested how well σ_{vir} of the halo mass particles can be estimated using sparsely sampled galaxy velocities. We verified that with this method, given the characteristics of our survey (flux limit, sampling rate, redshift measurement error) we are able to recover a sensible value of σ_{vir} for $\sigma_{vir} \geq 350$ km/s. Finally, we used these mock catalogues to train our group-finding algorithm, based on the Voronoi-Delaunay Method (VDM).

Applying the optimised algorithm to the VVDS real sample, we obtained a catalogue of 318 groups of galaxies (with at least two members) in the range $0.2 \leq z \leq 1.0$. Among these groups, 63 have a measured l.o.s. velocity dispersion >350 km/s. The group catalogue is characterised by an overall completeness of $\sim 60\%$ and a purity of $\sim 50\%$. Nearly 19% of the total population of galaxies live in these systems. We verified that the number density distribution as a function of both redshift ($n(z)$) and velocity dispersion ($n(\sigma)$) of the VVDS groups with σ >350 km/s scales in qualitative agreement with the analogous statistics recovered from the mocks.

Finally, we studied the fraction f_b of blue galaxies ($U - B \leq 1$) in the range $0.2 \leq z \leq 1$. We used a luminosity-limited subsample of galaxies extracted from our data ($M_B \leq -18.9 - 1.1z$), complete up to $z = 1$.

[1] Laboratoire d'Astrophysique de Marseille, Université de Provence, CNRS, 38 rue F. Joliot-Curie, F-13388 Marseille, France
[2] Centre de Physique Théorique, UMR 6207 CNRS-Université de Provence, F-13288, Marseille
[3] INAF-Osservatorio Astronomico di Brera, Via Brera 28, I-20021, Milan, Italy
[4] INAF-Osservatorio Astronomico di Bologna, Via Ranzani 1, I-40127, Bologna, Italy

We found that f_b is significantly lower in groups than in the global galaxy population. Moreover, f_b increases as a function of redshift irrespective of the environment, with marginal evidence of a higher growth rate in groups. We also analysed how f_b varies as a function of group richness, finding that, at any redshift explored, f_b decreases in systems with increasing richness. Further explorations of the properties of VVDS groups is left to future work. We only note that the cross-correlation studies of our optically-selected catalogue with samples inferred in the same field with independent techniques will help us to gain insights not only into cluster selection biases but also the physics at work within these extreme environments.

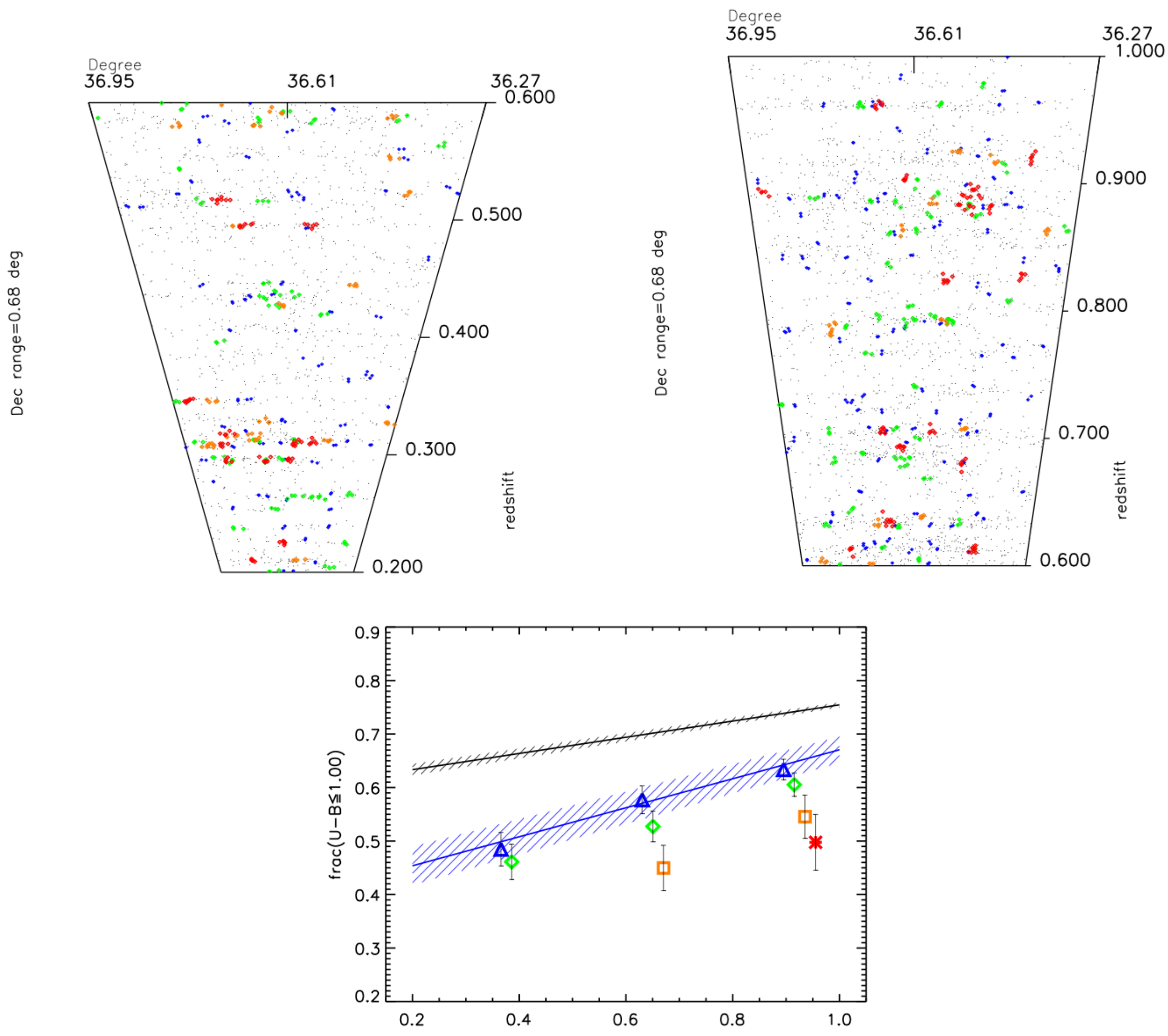

Fig. 1. *Top panels*: Two-dimensional VVDS galaxy distribution as a function of Right Ascension and redshift (points are compressed on the Declination dimension), for two different redshift bins ($0.2 \leq z \leq 0.6$ and $0.6 \leq z \leq 1.0$). Black dots are field galaxies, coloured dots are group members: blue dots are pair members, green are triplet members, orange are quartet members and red dots are members of groups with 5 or more members. *Bottom panel*: Fraction of blue galaxies ($U - B \leq 1$) as a function of redshift for group galaxies (blue empty triangles). The linear fit to these points is over-plotted as a blue line, while the upper black line is the linear fit for f_b computed within the 'total' sample. The dashed areas along the two linear fits show the locus where the linear fits could lie considering their 1-σ error on both intercept and slope. Other symbols are for group galaxies in groups with increasing richness (richness increases from blue triangles to red stars, passing by green diamonds and orange squares).

References

Cucciati, O., Marinoni, C., Iovino, A., et al. 2010, A&A, 520, A42
De Lucia, G. & Blaizot, J. 2007, MNRAS, 375, 2
Gerke, B. F., Newman, J. A., Davis, M., et al. 2005, ApJ, 625, 6
Gerke, B. F., Newman, J. A., Faber, S. M., et al. 2007, MNRAS, 376, 1425
Iovino, A., Cucciati, O., Scodeggio, M., et al. 2010, A&A, 509, A40
Knobel, C., Lilly, S. J., Iovino, A., et al. 2009, ApJ, 697, 1842
Le Fèvre, O., Vettolani, G., Garilli, B., et al. 2005, A&A, 439, 845
Springel, V., White, S. D. M., Jenkins, A., et al. 2005, Nature, 435, 629

SF2A 2010
S. Boissier, M. Heydari-Malayeri, R. Samadi and D. Valls-Gabaud (eds)

MULTIPLE POPULATIONS IN GLOBULAR CLUSTERS: A THEORETICAL POINT OF VIEW

T. Decressin[1]

Abstract. Globular clusters exhibit peculiar chemical patterns where Fe and heavy elements are constant inside a given cluster while light elements (Li to Al) show strong star-to-star variations. Besides precise photometric studies reveal that numerous globular clusters display multiple or broad main sequences, subgiant or giant branches. This peculiar chemical pattern can be explained by self-pollution of the intracluster gas occurring in the early evolution of clusters. Here the possible strong impact of fast rotating massive stars is reviewed. First providing they rotate initially fast enough they can reach the break-up velocity during the main sequence and a mechanical mass-loss will eject matter from the equator at low velocity. Rotation-induced mixing will also bring matter from the convective core to the surface. From this ejected matter loaded in H-burning material a second generation of stars will born. The chemical pattern of these second generation stars are similar to the one observed for stars in globular cluster with abundance anomalies in light elements. Then during the explosion as supernovae the massive stars will also clear the cluster of the remaining gas. If this gas expulsion process acts on short timescale it can strongly modify the dynamical properties of clusters by ejecting preferentially first generation stars.

Keywords: stars: abundances, stars: evolution, stars: mass loss, globular clusters: general, stellar dynamics, methods: N-body simulations

1 Introduction

Globular clusters are self-gravitating aggregates of tens of thousands to millions of stars that have survived over a Hubble time. Many observations show that these objects are composed of multiple stellar populations. The first evidence rests on the chemical analysis that reveals large star-to-star abundance variations in light elements in all individual clusters studied so far, while the iron abundance stays constant (for a review see Gratton et al. 2004). These variations include the well-documented anticorrelations between C-N, O-Na, Mg-Al, Li-Na and F-Na (Kraft 1994; Carretta et al. 2007; Gratton et al. 2007; Pasquini et al. 2007; Carretta et al. 2010; Lind et al. 2009). H-burning at high temperature around 75×10^6 K is required to explain this global chemical pattern (Arnould et al. 1999; Prantzos et al. 2007). As the observed chemical pattern is present in low-mass stars both on the red giant branch (RGB) and at the turn-off that do not reach such high internal temperatures, the abundance anomalies must have been inherited at the time of formation of these stars.

Besides, deep photometric studies provide another indications for multiple populations in individual GCs with the discoveries of multiple giant and sub-giant branches or main sequences. In ω Cen a blue main sequence has been discovered (Bedin et al. 2004) that is presumably related to a high content in He (Piotto et al. 2005; Villanova et al. 2007). A triple main sequence has been discovered in NGC 2808 (Piotto et al. 2007). The additional blue sequences are explainable by a higher He content of the corresponding stars which shifts the effective temperatures towards hotter values. He-rich stars have also been proposed to explained the morphology of extended horizontal branch (hereafter HB) seen in many globular clusters (see e.g., Caloi & D'Antona 2005). Whereas no direct observational link between abundance anomalies and He-rich sequences has been found, this link is easily understood theoretically as abundance anomalies are the main result of H burning to He.

These observed properties lead to the conclusion that globular clusters born from giant gas clouds first form a generation of stars with the same abundance pattern as field stars. Then a polluting source enriches

[1] Argelander Institute for Astronomy (AIfA), Auf dem Hügel 71, D-53121 Bonn, Germany
Present address: Observatoire Astronomique de l'Université de Genève, 51, chemin des Maillettes, CH-1290 Sauverny, Switzerland

the intracluster-medium with H-burning material out of which a chemically-different second stellar generation forms. This scheme can explain at the same time the abundance anomalies in light elements and He-enrichment.

Two main candidates that reach the right temperature for H-burning have been proposed to be at the origin of the abundance anomalies (Prantzos & Charbonnel 2006): (a) intermediate mass stars evolving on the thermal pulses along the asymptotic giant branch (hereafter TP-AGB), and (b) main sequence massive stars. After being first proposed by Cottrell & Da Costa (1981) the AGB scenario has been extensively studied (see e.g., Ventura & D'Antona 2008a,b, 2009, see Ventura, this volume) and has been seriously challenged by rotating AGB models that predict unobserved CNO enrichment in low-metallicity globular clusters (Decressin et al. 2009).

On the other hand, as being suggested by Brown & Wallerstein (1993) and Wallerstein et al. (1987), massive stars can also pollute the interstellar medium (ISM) of a forming cluster (see Smith 2006; Prantzos & Charbonnel 2006). In particular Decressin et al. (2007b) show that fast rotating massive stars (with a mass higher than $\sim 25\ M_\odot$) are good candidates for the self-enrichment of globular clusters. An alternative suggestion has been proposed by de Mink et al. (2009) to considered non-conservative mass-transfer from binaries stars. In the following we will only considered the consequences of the pollution by rotating massive stars.

In the wind of fast rotating massive stars (WFRMS) scenario, rotationally-induced mixing transports H-burning products (and hence matter with correct abundance signatures) from the convective core to the stellar surface. Providing initial rotation is high enough, the stars reach the break-up on the main sequence evolution. As a result a mechanical wind is launched from the equator that generates a disk around the star similar to that of Be stars (e.g. Townsend et al. 2004). Later, when He-burning products are brought to the surface, the star has already lost a high fraction of its initial mass and angular momentum, so that it no longer rotates at the break-up velocity. Matter is then ejected through a classical fast isotropic radiative wind. From the matter ejected in the disk, a second generation of stars may be created with chemical pattern in agreement with observations. Latter on when the He-burning products reach the surface the star do not rotate any longer at the critical velocity and this matter is ejected in fast radiative winds which will escape the cluster (see Decressin et al. 2007a).

2 Dynamical consequences for globular clusters

Based on the determination of the composition of giant stars in 19 globular clusters by Carretta et al. (2009b) the stars with abundance anomalies populated between 50 to 80% of the cluster stars. How to produce such a high fraction of chemically peculiar stars? The main problem is that assuming a Salpeter (1955) IMF for the polluters, the accumulated mass of the slow winds ejected by the fast rotating massive stars would only provide 10% of the total number of low-mass stars. To match the observations thus requires either (a) a flat IMF with a slope of 0.55 instead of 1.35 (Salpeter's value), or (b) that 95% of the first generation stars have escaped the cluster (Decressin et al. 2007a). Here we first verify whether such a high loss of stars is possible, and which are the main processes that could drive it.

The viability of a self-enrichment scenario by fast-rotating massive stars has been explored by Decressin et al. (2008). They have shown that first-generation low-mass stars are mainly lost from the cluster, which is assumed to initially be in dynamical equilibrium and mass-segregated, before two-body relaxation induces a spread of second generation stars and a full mixing of the cluster.* Afterwards, the evolution is smoother and the variation in the fraction of second-generation stars takes longer. Any radial difference between first and second generation stars is erased after 10-12 Gyr of evolution because the cluster relaxation time (a few Gyr) is much shorter than the age of the clusters. Even if the relaxation-driven evaporation increases the fraction of second generation (which harbour abundance anomalies) to about 25%, this ratio remains too low to fully explain the observations (between 50–80%, Carretta et al. 2009a). The increase in the fraction of second-generation stars mainly occurs in the early times and points towards the high sensitivity of the fraction of second-generation stars on cluster dynamics.

As it operates early in the cluster history (a few million years after cluster formation at the latest), initial gas expulsion by supernovae is an ideal candidate for such a process. As the gas still present after the star formation is quickly removed, it ensues a strong lowering of the potential well of the cluster so that the outer parts of the cluster can become unbound.

Baumgardt & Kroupa (2007) computed a grid of N-body models to study this process and its influence on cluster evolution by varying the free parameters: star formation efficiency, SFE, ratio between the half-mass

*D'Ercole et al. (2008) find similar results with the AGB scenario.

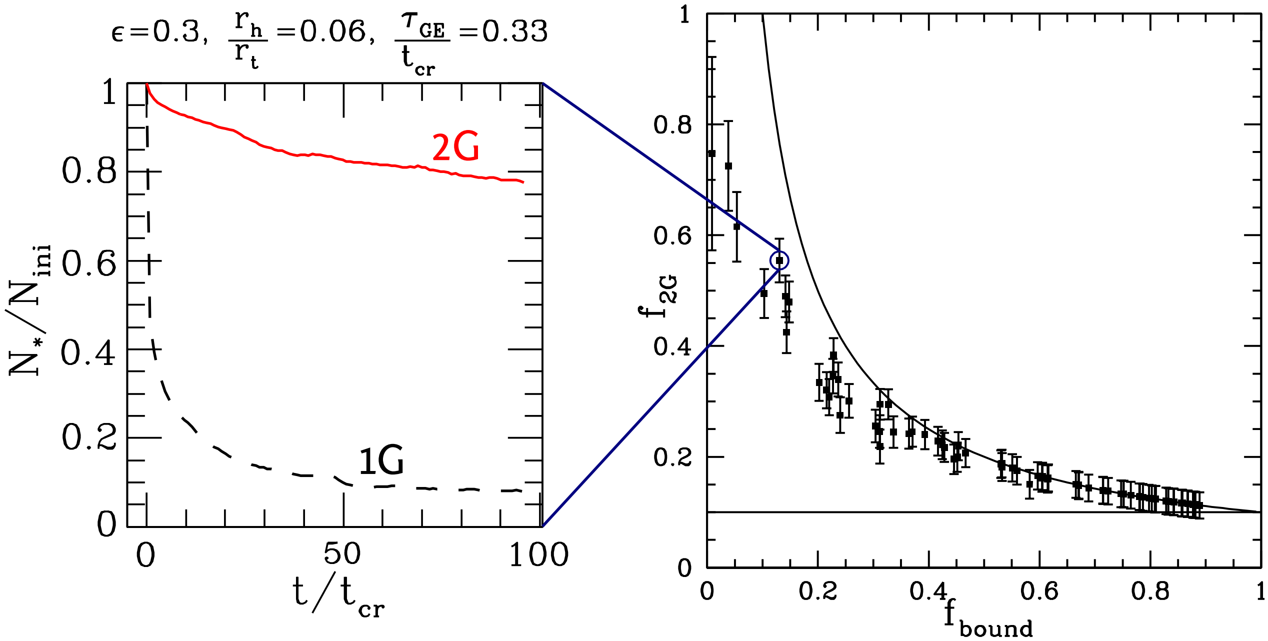

Fig. 1. *Left:* Number of first (dotted line) and second (full line) generation stars relative to their initial number as a function of time for a cluster with the following initial properties: $\epsilon = 0.3$, $r_\mathrm{h}/r_\mathrm{t} = 0.06$ and $\tau_{GE}/t_\mathrm{cr} = 0.33$. *Right:* Fraction of second-generation stars as a function of the final fraction of bound stars at the end of the computations of Baumgardt & Kroupa (2007), i.e., after about 100 initial crossing times. Dashed lines indicate limiting cases where no second-generation stars are lost (upper) and no preferential loss of first-generation stars occurs (lower). Estimates of the statistical errors are also included based on the number of first, N_1, and second, N_2, generation stars bound to the cluster.

and tidal radius, r_h/r_t, and the ratio between the timescale for gas expulsion to the crossing time, τ_M/t_Cross. They show in particular that, in some extreme cases, the complete disruption of the cluster can be induced by gas expulsion. This process has also been used successfully by Marks et al. (2008) to explain the challenging correlation between the central concentration and the mass function of globular clusters as found by De Marchi et al. (2007).

To explore the evolution of two distinct generation of stars, the N-body models of Baumgardt & Kroupa (2007) have been artificially divided into two populations: about 10% of the stars with initially low specific energy (i.e., low velocity stars orbiting near the cluster centre) mimic second generation stars while the others stars represent the first generation. Fig. 1 (left panel) shows that in the case of a cluster which loses around 90% of its stars, the ejection of stars from the cluster mostly concerns first generation ones. At the end of the computation only 7% of first generation stars remain bound to the cluster along with most of second generation stars. Therefore the number ratio between the second to first generation stars increases by a factor of 10: half of the population of low-mass stars still populating the cluster are second generation stars. The final fraction of second generation stars is strongly dependent of the initial properties of the cluster as shown in Fig. 1 (right panel) where this number is shown as a function of the fraction of star still bound to the cluster for the whole set of computation done by Baumgardt & Kroupa (2007) (see Decressin et al. 2010 for more details).

Thus if globular clusters are born mass segregated, dynamical processes (gas expulsion, tidal stripping and two-body relaxation) can explain the number fraction of second generation stars with abundance anomalies.

T.D. acknowledges support from the Swiss National Science Foundation (FNS) and from the “Programme National de Physique Stellaire” of CNRS/INSU, France.

References

Arnould, M., Goriely, S., & Jorissen, A. 1999, A&A, 347, 572

Baumgardt, H. & Kroupa, P. 2007, MNRAS, 380, 1589

Bedin, L. R., Piotto, G., Anderson, J., et al. 2004, ApJ, 605, L125
Brown, J. A. & Wallerstein, G. 1993, AJ, 106, 133
Caloi, V. & D'Antona, F. 2005, A&A, 435, 987
Carretta, E., Bragaglia, A., Gratton, R., & Lucatello, S. 2009a, A&A, 505, 139
Carretta, E., Bragaglia, A., Gratton, R., et al. 2010, A&A, 516, A55
Carretta, E., Bragaglia, A., Gratton, R. G., et al. 2009b, A&A, 505, 117
Carretta, E., Bragaglia, A., Gratton, R. G., Lucatello, S., & Momany, Y. 2007, A&A, 464, 927
Cottrell, P. L. & Da Costa, G. S. 1981, ApJ, 245, L79
De Marchi, G., Paresce, F., & Pulone, L. 2007, ApJ, 656, L65
de Mink, S. E., Pols, O. R., Langer, N., & Izzard, R. G. 2009, A&A, 507, L1
Decressin, T., Baumgardt, H., Charbonnel, C., & Kroupa, P. 2010, A&A, 516, A73
Decressin, T., Baumgardt, H., & Kroupa, P. 2008, A&A, 492, 101
Decressin, T., Charbonnel, C., & Meynet, G. 2007a, A&A, 475, 859
Decressin, T., Charbonnel, C., Siess, L., et al. 2009, A&A, 505, 727
Decressin, T., Meynet, G., Charbonnel, C., Prantzos, N., & Ekström, S. 2007b, A&A, 464, 1029
D'Ercole, A., Vesperini, E., D'Antona, F., McMillan, S. L. W., & Recchi, S. 2008, MNRAS, 1228
D'Orazi, V., Lucatello, S., Gratton, R., et al. 2010, ApJ, 713, L1
D'Orazi, V. & Marino, A. F. 2010, ApJ, 716, L166
Gratton, R., Sneden, C., & Carretta, E. 2004, ARAA, 42, 385
Gratton, R. G., Lucatello, S., Bragaglia, A., et al. 2007, A&A, 464, 953
Kraft, R. P. 1994, PASP, 106, 553
Lind, K., Primas, F., Charbonnel, C., Grundahl, F., & Asplund, M. 2009, A&A, 503, 545
Marks, M., Kroupa, P., & Baumgardt, H. 2008, MNRAS, 386, 2047
Pasquini, L., Bonifacio, P., Molaro, P., et al. 2005, A&A, 441, 549
Pasquini, L., Bonifacio, P., Randich, S., et al. 2007, A&A, 464, 601
Piotto, G., Bedin, L. R., Anderson, J., et al. 2007, ApJ, 661, L53
Piotto, G., Villanova, S., Bedin, L. R., et al. 2005, ApJ, 621, 777
Prantzos, N. & Charbonnel, C. 2006, A&A, 458, 135
Prantzos, N., Charbonnel, C., & Iliadis, C. 2007, A&A, 470, 179
Salpeter, E. E. 1955, ApJ, 121, 161
Smith, G. H. 2006, PASP, 118, 1225
Townsend, R. H. D., Owocki, S. P., & Howarth, I. D. 2004, MNRAS, 350, 189
Ventura, P. & D'Antona, F. 2008a, A&A, 479, 805
Ventura, P. & D'Antona, F. 2008b, MNRAS, 385, 2034
Ventura, P. & D'Antona, F. 2009, A&A, 499, 835
Villanova, S., Piotto, G., King, I. R., et al. 2007, ApJ, 663, 296
Wallerstein, G., Leep, E. M., & Oke, J. B. 1987, AJ, 93, 1137

SF2A 2010
S. Boissier, M. Heydari-Malayeri, R. Samadi and D. Valls-Gabaud (eds)

MASSIVE SPECTROSCOPIC ANALYSIS OF THE STELLAR POPULATIONS IN THREE OF THE COROT/EXOPLANET FIELDS

J.-C. Gazzano[1,2], M. Deleuil[1], P. de Laverny[2], G. Kordopatis[2], C. Moutou[1], A. Recio-Blanco[2], A. Bijaoui[2], F. Bouchy[3,4] and C. Ordenovic[2]

Abstract. We derived the atmospheric parameters ($T_{\rm eff}$, log g, [M/H], [α/Fe]), $V_{\rm rad}$, and $V \sin i$ for 1227 *CoRoT*/Exoplanet targets in three of the fields observed by *CoRoT*. We derived the corresponding absolute magnitude using evolutionary models. We combined 2MASS colours with a new implementation of the infrared flux method, and the $T_{\rm eff}$ from *MATISSE* to constrain the interstellar extinction. These steps allowed us to measure the stellar distances, hence deriving kinematics information. This opened the path to the study of the stellar populations found in these *CoRoT* fields. These studies showed the potential of combining a multi-fiber instrument like *FLAMES/GIRAFFE*, with an automatic tool to determine efficiently atmospheric stellar parameters, as *MATISSE*.

Keywords: techniques: spectroscopy, stars: fundamental parameters, planetary systems, general, CoRoT, galaxy: structure, kinematics, chemistry

1 Introduction

CoRoT space mission has been gathering thousands of light-curves since early 2007 (Baglin et al. 2006). The goals are to detect planetary transits and measure stellar oscillations. To support this mission, we observed with the *FLAMES/GIRAFFE* spectrometer 1914 *CoRoT* targets in three of the *CoRoT* fields, the *Long Run Anticenter 01*, *Long Run Center 01*, and *Short Run Center 01* (strategy described in Baglin et al. 2007). The objectives of these observations were to follow-up the planetary candidates detected in *CoRoT* data and to characterise the stellar populations in the *CoRoT* fields. We could perform a spectroscopic analysis on 75% of the spectra (1227 stars, Gazzano et al. 2010a). The properties of the fields observed can be found in table 1. The atmospheric parameters of the stars in these fields are mandatory for characterising the stellar populations in these Galactic directions, and could also be linked to the *CoRoT* lightcurves. Getting to know the Galactic structure and kinematics of these fields is a serious asset for understanding the planet detections in the CoRoT fields and the diametrically opposed pointing directions offers the possibility to explore different Galactic regions, with different properties.

2 Automatic spectroscopic analysis

The obvious preliminary step is to correct the spectra from the stellar radial motion. We cross correlated the spectra with a weighted mask (Baranne et al. 1996; Pepe et al. 2002) to measure the radial velocity ($V_{\rm rad}$) and an estimate of the rotational velocity ($V \sin i$). The $V_{\rm rad}$ distribution did not show peculiarities and the $V \sin i$ distribution confirmed that most of the stars rotate slowly. The derived values can be found in Gazzano et al. (2010a).

[1] Laboratoire d'Astrophysique de Marseille (UMR 6110), OAMP, Université Aix-Marseille & CNRS, 38 rue Frédéric Joliot Curie, 13388 Marseille cedex 13, France
[2] Université Nice Sophia Antipolis, CNRS (UMR 6202), Observatoire de la Côte d'Azur, Laboratoire Cassiopée, BP 4229, 06304 Nice, France
[3] Institut d'Astrophysique de Paris (UMR7095) CNRS, Université Pierre & Marie Curie, 98bis Bd Arago, 75014 Paris, France
[4] Observatoire de Haute-Provence, CNRS/OAMP, 04870 St Michel l'Observatoire, France

Table 1. Properties of the three Galactic directions. The columns contain, the *CoRoT* field, the number of stars with derived atmospheric parameters, the mean Galactic longitude and latitude, and the r' magnitude (SDSS filter system, Fukugita et al. 1996) range.

Sample	N_{stars}	l ($^{\circ}$)	b ($^{\circ}$)	r'
LRa01	457	212.2	-1.9	[10.7 ; 15.0]
LRc01	555	37.5	-7.5	[11.5 ; 16.0]
SRc01	215	36.8	-1.2	[11.3 ; 15.8]
Total Sample	1 227	-	-	[10.0 ; 16.0]

2.1 MATISSE

We used the *MATISSE* (MAtrix Inversion for Spectral SynthEsis) algorithm described by Recio-Blanco et al. (2006), tested and applied in Gazzano et al. (2010a). This algorithm is based on the state of the art in model of stellar atmospheres (Gustafsson et al. 2008) and spectral synthesis technique to measure efficiently and in an automatic fashion atmospheric parameters, *i.e* the effective temperature ($T_{\rm eff}$), the surface gravity (log g), the overall metallicity content ([M/H]) and the α-elements enrichment ([α/Fe]). This algorithm was indeed originally developed for the spectral analysis of spectra to be observed with the Radial Velocity Spectrometer instrument of the Gaia mission (Lindegren et al. 2008). Hence it is a reliable and very fast algorithm perfectly suitable for the spectral analysis of our sample of 1914 stars. We calibrated the atomic lines list, modifying the oscillator strength for $\sim$ 300 atomic lines to reproduce the Kurucz solar spectrum described in Hinkle et al. (2003). We interpolated a grid of 10 000 spectra with $T_{\rm eff}$, log g and [M/H] randomly chosen, and added Gaussian noise to every spectrum to evaluate the internal precision of the algorihtm. Gazzano et al. (2010a) showed that the internal error only due to the method for spectra at a signal-to-noise ratio of 20, is $\Delta T_{\rm eff}\simeq$50 K, Δlog $g\simeq$0.08 dex, Δ[M/H]$\simeq$0.05 dex, and Δ[α/Fe]$\simeq$0.02 dex.

2.2 Literature comparison

In order to ensure the quality of the atmospheric parameters derived with *MATISSE*, we applied the entire procedure to several libraries of observed spectra analysed by different authors. We used the S^4N sample described by Allende Prieto et al. (2004), the Elodie 3.1 sample with parameters from Prugniel et al. (2007), a small sample of UVES spectra obtained in the context of the Paranal Observatory Project (POP, Bagnulo et al. 2003) and whose parameters could be also found in Prugniel et al. (2007) and giant stars spectra observed and analysed by Santos et al. (2009). We calculated the correlation between *MATISSE* and literature values for every parameter and found a correlation of 0.99 for the $T_{\rm eff}$, and 0.96 for [M/H] over the four samples mixed. The situation is not so good for the surface gravity. We found a correlation of 0.83 for the giant sample from Santos et al. (2009) and of 0.89 for the S^4N dwarfs. The latter might be due to the fact that we are comparing, for the S^4N sample spectroscopic (from *MATISSE*) and evolutionary surface gravity (derived from iso-chrones). This is not the case for the Santos et al. (2009) and this shows that it is much more difficult to derive spectroscopic gravity for giant stars. The discrepancy for [α/Fe] determination is higher, since the correlation between the two measurements is 0.75, but this might be due to the use of several abundance measures from Allende Prieto et al. (2004).

We compared this classification with the photometric one performed before *CoRoT* launch (in EXODAT, Deleuil et al. 2009) and found fairly good agreement for the brightest targets. This allowed us to characterise the population of the dwarfs in these *CoRoT* fields, to show that in the bin of magnitude r' 15 to 16, the number of dwarfs is highly underestimated by the photometric classification, particularly in the *LRc01* field. We also applied the relationship between metallicity and giant planet occurrence built during the ten past years (Udry & Santos 2007), and found a number of giant planets consistent with what *CoRoT* detected.

2.3 Absolute magnitude and stellar distances

We used the *MATISSE* atmospheric parameters to locate every star on a Y^2 iso-chrone (Demarque et al. 2004), and to derive the absolute visual magnitude. To illustrate that, we plotted on the left part of Fig 1 the logarithm

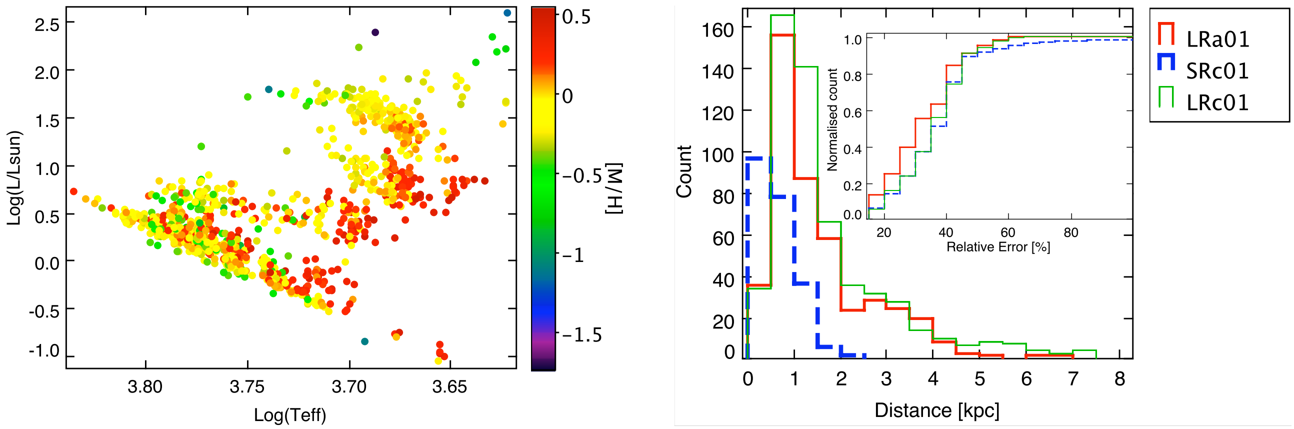

Fig. 1. Left: Hertzsprung-Russell diagram of the analysed stars with the overall metallicity colour coded. Right: distribution of the stellar distances derived by our procedure for the three Galactic directions.

of the luminosity with respect to the solar value* as a function of the effective temperature. It shows that we mostly observed main sequence F and G stars on the one hand, and K giants on the other hand. For the extinction determination, we used the *MATISSE* effective temperature with the new implementation of the infrared flux method using the 2MASS catalogue presented by González Hernández & Bonifacio (2009). This allowed us to measure the stellar distance with J band absolute and apparent magnitudes, and absorption. The derived values can be found in Gazzano et al. (2010b, in prep.). The distribution of the derived stellar distances is presented on the right part of Fig. 1. Most of the stars in the three fields are located within two kiloparsecs from the Sun. It also shows that the stellar distances are correctly determined, 80% of the entire sample having a relative error on the distance lower than 50%.

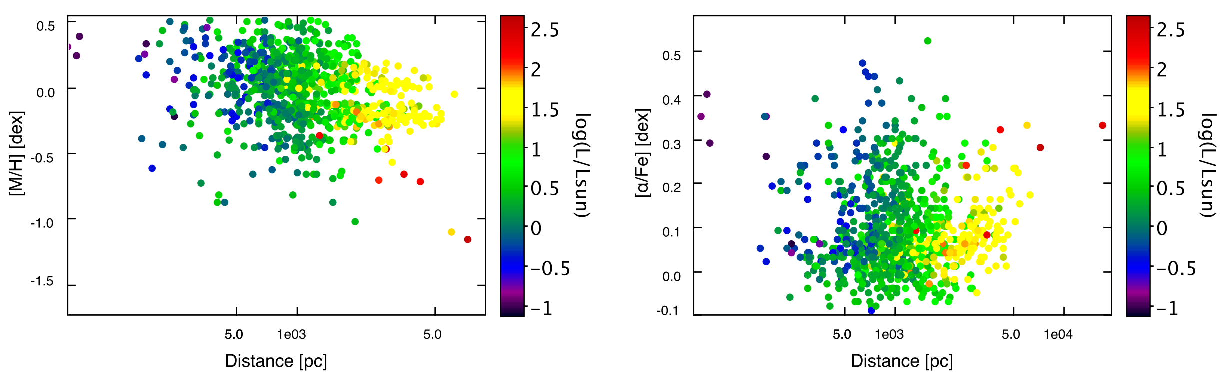

Fig. 2. Metallicity (left) and [α/Fe] (right) as a function of stellar distance from the Sun. This illustrates a possibility to study the metallicity Galactic gradient.

2.4 *Adding kinematical information*

When tracing the metallicity as a function of the stellar distance (Fig. 2 left), we see a correlation, probably linked to the Galactic metallicity gradient. This correlation does not appear that clearly for the [α/Fe] (Fig, 2 right).We matched the sample of stars with atmospheric parameters with the PPXML (Roeser et al. 2010) because these authors showed that the UCAC3 catalogue (Zacharias et al. 2010) has problems northern that $\delta = -20^\circ$. Besides, they argue that the proper motions they derived are as accurate or better than the UCAC2 catalogue (Zacharias et al. 2004). We found 1058 stars in common with errors around 0.4 arcsec per century.

*calculated from the absolute magnitude and choosing 4.83 for the absolute magnitude of the Sun

Combining these data with our $V_{\rm rad}$ and distance determination allowed us to measure the Galactic position and velocity components. We propagated the errors of every observational quantity either by deriving it analytically or using Monte-Carlo realisations. Galactic kinematics information allows to retrace stellar orbits of the stars and understand the structure and history, and link it to the chemistry of the Milky Way.

3 Conclusions and perspectives

We measured the atmospheric parameters and kinematical quantities for 1227 stars in the *CoRoT*/Exoplanet fields using the *MATISSE* algorithm (Gazzano et al. 2010a). We combined these results with isochrones and proper motions to estimate the absolute magnitude, distance, and Galactic kinematics of these stars (Gazzano et al. 2010b, in prep.; Kordopatis et al. 2010, in prep.). This opened the possibility to search for Galactic features such as the quantification of the Galactic metallicity gradient (Maciel & Costa 2010), Galactic population proportions from velocity components (Bensby et al. 2005) and take advantage of the [α/Fe] determination linked to Galactic kinematics. These points will be explored in a forthcoming paper (Gazzano et al. 2010b, in prep.). Finally, all these studies will be reproduced in other *CoRoT* fields and could be linked to the high quality *CoRoT* photometry.

We observed the spectra necessary for these studies at ESO/VLT. Computations have been done on the “Mesocentre SIGAMM” machine, hosted by Observatoire de la Côte d’Azur. We also thank C. Turon for her warnings about the proper motions from the UCAC3 catalogue, and V. Hill for our discussions.

References

Allende Prieto, C., Barklem, P. S., Lambert, D. L., & Cunha, K. 2004, A&A, 420, 183
Baglin, A., Auvergne, M., Boisnard, L., et al. 2006, in COSPAR, Plenary Meeting, Vol. 36,
Baglin, A., Auvergne, et al., 2007, Fifty Years of Romanian Astrophysics, 895, 201
Bagnulo, S., Jehin, E., Ledoux, C., et al. 2003, The Messenger, 114, 10
Baranne, A., et al. 1996, A&A, 119, 373
Bensby, T., Feltzing, S., Lundström, I., & Ilyin, I. 2005, A&A, 433, 185
Deleuil, M., et al. 2009, AJ, 138, 649
Demarque, P., Woo, J.-H., Kim, Y.-C., & Yi, S. K. 2004, ApJS, 155, 667
Fukugita, M., Ichikawa, T., Gunn, J. E., et al. 1996, AJ, 111, 1748
Gazzano, J.-C., de Laverny, P., Deleuil, M., et al. 2010, A&A, in press
Gazzano, J.-C., de Laverny, P., Recio-Blanco, A., et al. 2010, in preparation
González Hernández, J. I., & Bonifacio, P. 2009, A&A, 497, 497
Gustafsson, B., Edvardsson, B., Eriksson, K., et al. 2008,A&A, 486, 951
Hinkle, K., Wallace, L., Livingston, W., et al. 2003, in The Future of Cool-Star Astrophysics, Vol. 12, 851–856
Kordopatis, G. et al., A&A, in preparation
Lindegren, L., Babusiaux, C., Bailer-Jones, C., et al. 2008, in IAU Symposium, Vol. 248, 217–223
Maciel, W. J. & Costa, R. D. D. 2010, in IAU Symposium, Vol. 265, 317–324
Pepe, F., Mayor, M., Galland, F., Naef, D., Queloz, D., Santos, N. C., Udry, S., & Burnet, M. 2002, A&A, 388, 632
Prugniel, P., Soubiran, C., Koleva, M., & Le Borgne, D. 2007, ArXiv Astrophysics e-prints
Recio-Blanco, A., Bijaoui, A., & de Laverny, P. 2006, MNRAS, 370, 141
Robin, A. C., Reylé, C., Derrière, S., & Picaud, S. 2003, A&A, 409, 523
Robin, A. C., Reylé, C., Derrière, S., & Picaud, S. 2004, A&A, 416, 157
Roeser, S., Demleitner, M., & Schilbach, E. 2010, AJ, 139, 2440
Santos, N. C., Lovis, C., Pace, G., Melendez, J., & Naef, D. 2009, A&A, 493, 309
Udry, S., & Santos, N. C. 2007, ARA&A, 45, 397
Zacharias, N., Urban, S. E., et al. 2004, AJ, 127, 3043
Zacharias, N., Finch, C., Girard, T., et al. 2010, AJ, 139, 2184

SF2A 2010
S. Boissier, M. Heydari-Malayeri, R. Samadi and D. Valls-Gabaud (eds)

CHEMICALLY PECULIAR A/F STARS IN OPEN CLUSTERS OF THE MILKY WAY

M. Gebran[1] and R. Monier[2]

Abstract. Abundance anomalies have been determined at the surface of many field and open cluster A and F dwarfs. These abundance anomalies are most likely caused by microscopic diffusion at work within the stable envelopes of A stars. However diffusion can be counteracted by several other mixing processes such as convection, rotational mixing and mass loss. We present a short review of the surface abundance patterns of A/F stars in the Pleiades (100 Myr), Coma Berenices (450 Myr) and Hyades (650 Myr) open clusters. Real star-to-star variations of the abundances were found for several chemical elements in the A dwarfs in these clusters. The derived abundances are then compared to evolutionary models from the Montreal group. These comparisons strongly suggest the occurence of hydrodynamical processes at play within the radiative zones of these stars and hindering the effects of microscopic diffusion (mixing processes/mass loss). In the frame of Gaia mission, simulations are presented that predict the number of A stars and open clusters that Gaia will observe in the Galaxy.

Keywords: stars: abundances, stars: main sequence, stars: rotation, diffusion, Galaxy: open clusters and associations

1 Introduction

Abundance studies of A stars have mostly focused on the Chemically Peculiar A stars as their low projected rotationnal velocities facilitate abundance determinations. In contrast, little is known about the chemical composition of normal A stars. Star to star abundance variations have been found for a handful of normal A field stars (Lemke 1990, Hill & Landstreet 1993 and Hill 1995), definitely showing that these normal stars do not have a solar chemical composition.

Stars in open clusters originate from the same interstellar material (i.e. they have the same age and the same initial chemical composition) and as such are very useful to test the predictions of evolutionary models. Varenne & Monier (1999), Gebran et al. (2008), Gebran & Monier (2008) and Gebran et al. (2010) also found significant star to star abundance variations for most A stars members of the Pleiades, Coma Berenices and the Hyades. Elemental radiative diffusion is the main process to account for anomalous abundances in Am stars. However turbulence, mass loss, accretion and meridional circulation may play a role as well.

2 Results

We have derived abundances of several chemical elements using synthetic spectra in 21 A/F stars members of the Pleiades (100 Myr), 22 A/F stars members of Coma Berenices (450 Myr) and 44 A/F stars members of Hyades (620 Myr) open clusters. We display in Fig. 1 the abundance patterns for Am stars in these clusters. The typical underabundances of scandium and/or calcium and/or the overabundances of iron peak elements conspicuously show in these patterns.

We have found large star-to-star variations in abundances for several chemical elements among A stars (in contrast with the F stars). The largest spreads occur for Sc, Sr, Y and Zr while the lowest are for Mg, Si and Cr. The abundances of Ti, Cr, Ni, Sr, Y and Zr are correlated with the iron abundance. The ratios [C/Fe] and [O/Fe] are anticorrelated with [Fe/H]. Compared to normal A stars, Am stars appear to be more deficient in C

[1] Departament d'Astronomia i Meteorologia, Universitat de Barcelona, c/ Martì i Franquès, 1, 08028 Barcelona, Spain.

[2] Laboratoire Universitaire d'Astrophysique de Nice, UMR 6525, Université de Nice - Sophia Antipolis, Parc Valrose, 06108 Nice Cedex 2, France.

and O. No correlations exist between the abundances and $T_{\rm eff}$ nor between the abundances and $v_e \sin i$.
The derived abundances have been compared to the predictions of recent evolutionary models. These models are calculated with the Montréal stellar evolution code. Transport of chemical species includes several processes calculated from principles: radiative accelerations, turbulent diffusion, thermal diffusion and gravitational settling (for more details see Richard et al. 2001). None of the calculated patterns reproduces fully the shape of the observed patterns. The discrepancies between derived and predicted abundances could partly be due to non-LTE effects. However, the inclusion of other hydrodynamical processes acting within the radiative zone of these stars (mixing processes/mass loss) could hinder the effects of microscopic diffusion and improve the agreement between the observations and the predictions.

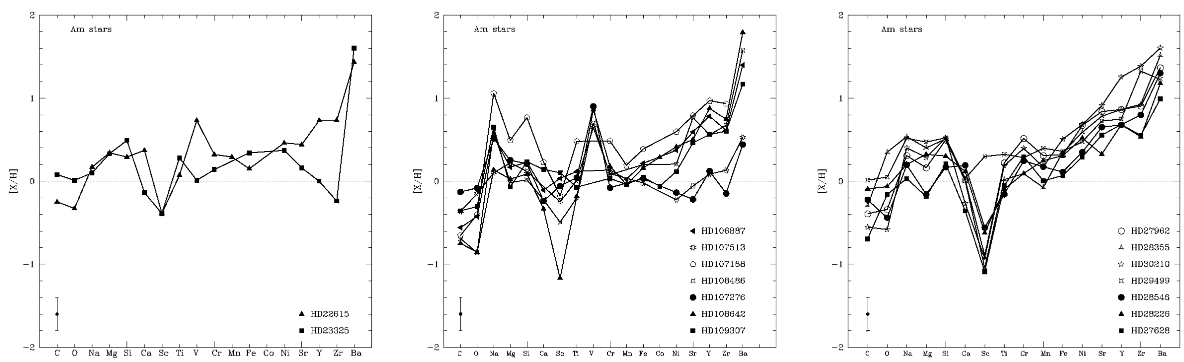

Fig. 1. Abundance patterns for Am stars in the Pleiades (left pannel), Coma Berenices (middle pannel) and Hyades (right pannel) clusters.

3 Gaia's predictions

Gaia's RVS and Astrometric Field will provide us valuable information concerning the statistics of A stars in the Galaxy. Am stars represent ∼12% of A stars. Simulations of RVS spectra show that we can disentangle between a normal A star and an Am star up to magnitude G_{RVS} ∼12-13 mag. This is due to the difference between the intensities of the calcium line in normal A and Am stars. At these magnitudes, we will have medium resolution spectra (R∼11500) for more than 1 million A stars. Among these stars, a group of Am stars (the one with low calcium abundances) can be identified. Once these stars are identified, on-ground observations will be needed to acquire high resolution and high signal-to-noise spectra in order to have detailed elemental abundance analyses. On the other hand, using the astrometry data, the distances to these stars and especially for members of open clusters will be determined with better accuracies. Then, using isochrones, we will have new estimation about the ages of the clusters and more constraints for the evolutionary models. For a magnitude V∼12-13 mag and for a typical A star, we can reach out to a distance of ∼3 kpc. There are about 900 open clusters with d<3 kpc according to the WEBDA database.

References

Gebran, M., & Monier, R. 2008, A&A, 483, 567

Gebran, M., Monier, R., & Richard, O. 2008, A&A, 479, 189

Gebran, M., Vick, M., Monier, R., & Fossati, L. 2010, arXiv:1006.5284

Hill, G. M. 1995, A&A, 294, 536

Hill, G. M., & Landstreet, J. D. 1993, VizieR Online Data Catalog, 327, 60142

Lemke, M. 1990, A&A, 240, 331

Richard, O., Michaud, G., & Richer, J. 2001, ApJ, 558, 377

Varenne, O., & Monier, R. 1999, A&A, 351, 247

SF2A 2010
S. Boissier, M. Heydari-Malayeri, R. Samadi and D. Valls-Gabaud (eds)

GALAXY STELLAR MASS ASSEMBLY BETWEEN $0.2 < Z < 2$ FROM THE S-COSMOS SURVEY

O. Ilbert[1], M. Salvato[2], E. Le Floc'h[3], H. Aussel[4], P. Capak[5], H.J. McCracken[6], B. Mobasher[7], J. Kartaltepe[8], N. Scoville[2], D.B. Sanders[8] and the COSMOS team

Abstract. We follow the galaxy stellar mass assembly by morphological and spectral type in the COSMOS 2-deg^2 field. We derive the stellar mass functions from $z = 2$ to $z = 0.2$ using 196,000 galaxies selected at $F_{3.6\mu m} > 1\mu Jy$ with accurate photometric redshifts ($\sigma_{(z_{phot}-z_{spec})/(1+z_{spec})} = 0.008$ at $i^+ < 22.5$). First, we find that the massive galaxies with the highest SSFR end their star formation phase first, following a downsizing pattern. Secondly, the mass function of the overall star-forming population doesn't evolve significantly at $z < 1$. Then, we find that the density of massive quiescent galaxies increases rapidly between $z = 2$ and $z = 1$ and this evolution slows down significantly after $z < 1$. The density of quiescent galaxies increases at low/intermediate masses. Adding the morphological information, we find that elliptical galaxies represents 80-90% of the massive quiescent galaxies at $z < 0.8$. Still, a significant fraction of quiescent galaxies present a Spi/Irr morphology at low mass (40-60% at $log(\mathcal{M}) \sim 9.5$). We find a population of blue elliptical galaxies which are mostly low mass galaxies at $z < 1$. This analysis is detailed in Ilbert et al. (2010).

Keywords: galaxies: luminosity function and mass function, galaxies: evolution, galaxies: formation

1 Introduction

A clear and comprehensive picture describing the physical processes which regulate stellar mass growth in galaxies is still missing in our understanding of galaxy evolution. Indeed, the stellar mass growth is regulated by a complex interplay between the radiative cooling of the gas (e.g. White 1978), cold accretion (e.g. Kereš et al. 2005), the spatial redistribution of the gas along the hierarchical growth of dark matter halos (e.g. Springel et al. 2006) and the feedback from supernovae and Active Galaxy Nuclei (e.g. Benson et al. 2003, Croton et al. 2006). Merging between galaxies is another central mechanism in stellar mass assembly. Indeed, mergers are expected to create new high-mass galaxies and to modify deeply galaxy properties (morphology and spectral type). The stellar mass function (MF) characterizes how star formation activity build the stellar mass and how mergers redistribute this stellar mass depending on the galaxy type.

We follow the evolution of the galaxy stellar mass function using the COSMOS survey (Scoville et al. 2007). The extensive multi-λ coverage of COSMOS provides accurate photometric redshifts (Ilbert et al. 2009). Combined with deep *Spitzer*/IRAC and NIR data (Sanders et al. 2007, McCracken et al. 2009), we estimate accurate stellar masses out to $z \sim 2$. Following the stellar mass assembly of a given galaxy population requires that the sample be split into well characterized galaxy types. We took special care to characterize the galaxy populations, using the specific star formation rate (SSFR) derived from SED fitting and a morphological classification carried out based on the HST/ACS images.

[1] Laboratoire d'Astrophysique de Marseille, Université de Provence, CNRS, BP 8, Traverse du Siphon, 13376 Marseille Cedex 12, France
[2] California Institute of Technology, MC 105-24, 1200 East California Boulevard, Pasadena, CA 91125
[3] CEA/DSM-CNRS, CEA, Saclay
[4] AIM Unité Mixte de Recherche CEA CNRS Université Paris VII UMR n158
[5] Spitzer Science Center, California Institute of Technology, Pasadena, CA 91125
[6] Institut d'Astrophysique de Paris, UMR7095 CNRS, Université Pierre et Marie Curie, 98 bis Boulevard Arago, 75014 Paris, France
[7] Department of Physics and Astronomy, University of California, Riverside, CA, 92521, USA
[8] Institute for Astronomy, 2680 Woodlawn Dr., University of Hawaii, Honolulu, Hawaii, 96822

2 Data

This analysis is based on a mass selected sample as generated from the $3.6\mu m$ IRAC catalogue of the S-COSMOS survey (Sanders et al. 2007). The IRAC data were taken during the Spitzer Cycle 2 S-COSMOS survey, which used 166 hrs to map the full 2-deg^2 COSMOS field. The source catalogue is extracted using the SExtractor software (Bertin & Arnouts, 1996). The source detection is performed at $3.6\mu m$. The IRAC catalogue is 90% complete at 5 μJy and 50% complete at 1 μJy.

We derive photometric redshifts using the *Le Phare*[1] code (Arnouts & Ilbert) with a χ^2 template-fitting method. The photo-z are computed using 31 bands (new H band data in comparison to Ilbert et al. 2009). The comparison between the photometric and spectroscopic redshifts from the zCOSMOS survey (Lilly et al. 2007) shows that the fraction of outliers is less than 1% and the accuracy is as good as $\sigma_{(z_{phot}-z_{spec})/(1+z_{spec})} = 0.008$ at $i^+_{AB} < 22.5$.

We cross-match the $3.6\mu m$ and photo-z catalogues by taking the closest counterpart within a radius of $1''$. We identify 2714 IRAC sources which are clearly non-detected in optical and are detected in the K-band selected catalogue. We measure a photo-z for these sources using NIR and IRAC data and an upper-limit was set in i^+.

Finally, we remove all of the sources flagged as star (χ^2 criteria) or AGN (detected with XMM-COSMOS). The final sample contains 196,000 galaxies at $F_{3.6\mu m} > 1\mu Jy$ over an effective area of 1.73-deg^2.

3 Method to compute the stellar mass function

We use stellar population synthesis (SPS) models to convert luminosity into stellar mass. The SED templates are generated with the stellar population synthesis package developed by Bruzual & Charlot (2003). We assume an universal IMF from Chabrier (2003), two different metallicities and an exponentially declining star formation history $SFR \propto e^{-t/\tau}$. Dust extinction is applied to the templates using the Calzetti et al. (2000) law. The difference between the stellar masses computed with the photometric and spectroscopic redshifts has a dispersion smaller than ~ 0.03 dex ($10\times$ smaller than the expected systematic uncertainties).

We measure the stellar mass functions using the tool ALF (*Algorithm for Luminosity Function*). This tool includes the STY parametric estimator, the $1/V_{max}$, the C^+ and the Step-Wise Maximum Likelihood. The estimators included in ALF are described in detail in appendix 2 of Ilbert et al. (2005). The low mass limits considered for the MF estimates are set in order to insure a complete and unbiased stellar mass sample with accurate photo-z (less than 30% of $i^+_{AB} > 25.5$ in the lowest stellar mass bin). Finally, we performed extensive simulations in order to propagate the photo-z uncertainties into the mass function.

4 Mass function by spectral and morphological type

First, we isolate "quiescent" galaxies based on the best-fit templates ($SSFR < 10^{-11}$) . Our "quiescent" population matches well with the red clump galaxies found by Williams et al. (2008) and we separate well "quiescent" galaxies and a dust-extincted star-forming population. Fig. 1 shows the MF of the quiescent galaxies (red curves). We find that: **i)** the density of "quiescent" galaxies more massive than $log(\mathcal{M}) > 11$ increases by a factor of ~ 14 between $z = 1.5 - 2$ and $z = 0.8 - 1$; **ii)** this evolution slows down significantly after $z < 1$ and the high-mass exponential cutoff does not increase by more than 0.2 dex at $z < 1$; **iii)** the density of quiescent galaxies increases at intermediate mass between $z = 0.8 - 1$ and $z = 0.2 - 0.4$ (continuous steepening of the slope α with time).

Secondly, we add the morphological information in our classification scheme. We use the high resolution HST/ACS images (Koekemoer et al. 2007) to perform a morphological classification of our galaxy sample and we separate E/S0 and Spi/Irr galaxies. At high mass, $log(\mathcal{M}) \sim 10.5$, the fraction of quiescent galaxies with an elliptical morphology is greater than 80% at $z < 0.8$ and decreases continuously toward low masses reaching 60% (40%) at $log(\mathcal{M}) \sim 9.5$. We find a similar MF evolution for the red ellipticals as for the quiescent galaxies: the most massive red elliptical galaxies show little evolution at $z < 1$ while their density still increases at low/intermediate masses. We also find a significant population of "blue elliptical" galaxies, which could be newly formed elliptical galaxies still consuming the gas of their progenitors. The fraction of "blue ellipticals" decreases towards high mass systems. The "blue elliptical" galaxies represent $< 20\%$ of the massive elliptical galaxies (at $log(\mathcal{M}) > 11$ and $z < 1$), but their contribution reaches 40-60% at $log(\mathcal{M}) \sim 10$.

[1] www.cfht.hawaii.edu/ arnouts/LEPHARE/cfht_lephare

Finally, we divide the star-forming sample into "intermediate activity" and "high activity" galaxies, which corresponds to two classes of SSFR ($10^{-11} < SSFR < 6.3 \times 10^{-10}$ and $SSFR > 6.3 \times 10^{-10}$, respectively). The slope of the "high activity" galaxies is always the steepest (blue curve in Fig. 1). The density of "high activity" galaxies decreases with cosmic time. The decrease is stronger for high mass galaxies. We do not observe significant changes in the MF of all star-forming galaxies, i.e. the sum of the "intermediate activity" and "high activity". The little evolution of the star-forming MF means that a fraction of star-forming galaxies is transferred to the quiescent population (as already noted by Arnouts et al. 2007 and is discussed in Peng et al. 2010, Boissier et al. 2010). It means also that the decrease with time of "high activity" galaxies is partly counter-balanced by the build up of the "intermediate activity" MF.

5 conclusion

We follow the galaxy stellar mass assembly by morphological and spectral type in the COSMOS 2-deg^2 field from $z = 2$ to $z = 0.2$.

Using a spectral classification, we find that $z \sim 1$ is an epoch of transition in the stellar mass assembly of quiescent galaxies. Their stellar mass density increases by 1.1 dex between $z = 1.5 - 2$ and $z = 0.8 - 1$, but only by 0.3 dex between $z = 0.8 - 1$ and $z \sim 0.1$. The high-mass end of the star-forming MF is shifted below the high-mass end of the quiescent MF at $z < 1$. Therefore, we interpret the slow down in the assembly of the most massive elliptical galaxies at $z < 1$ as being due to a "lack of supply" of massive star-forming galaxies available for "wet mergers" and a poor efficiency of "dry merging" (merger between quiescent galaxies) at high mass.

Then, we add the morphological information and find that 80-90% of the massive quiescent galaxies ($log(\mathcal{M}) \sim 11$) have an elliptical morphology at $z < 0.8$. Therefore, a dominant mechanism links the shutdown of star formation and the acquisition of an elliptical morphology in massive galaxies, as might be expected in galaxy merging and/or morphological quenching (Martig et al. 2009). Still, a significant fraction of quiescent galaxies present a Spi/Irr morphology at low mass (40-60% at $log(\mathcal{M}) \sim 9.5$). This significant fraction of quenched Spi/Irr leaves room for a mechanism which shuts down the star formation without transforming their morphology, such as the impact of AGN feedback on the satellite galaxies of a massive halo (e.g. Cattaneo et al. 2006).

We also split the star-forming galaxies into two SSFR classes: "intermediate activity" and "high activity" galaxies. We find that the most massive "high activity" galaxies end their high star formation rate phase first. Therefore, this redistribution of the star formation activity follows a clear "downsizing" pattern (Cowie et al. 1996) within the star-forming sample itself.

References

Arnouts, S. et al. 2007, A&A, 476, 137

Bertin, E. & Arnouts, S. 1996, A&AS, 117, 393

Boissier, S., Buat, V., Ilbert, O. 2010, A&A, in press, astro-ph/1005.5004

Bower, R.G., Benson, A.J., Malbon, R et al., 2006, MNRAS, 370, 645

Bruzual, A.G. & Charlot, S., 2003, MNRAS, 344, 1000

Calzetti, D., Armus, L., Bohlin R.C. et al., 2000, ApJ, 533, 682

Capak, P., Abraham, R.G., Ellis, R.S. et al., 2007, ApJS, 172, 284

Cattaneo, A., Dekel, A., Devriendt, J. et al., 2006, MNRAS, 370, 1651

Chabrier, G. 2003, PASP, 115, 763

Croton, D.J., Springel, V., White, S et al. 2006, MNRAS, 365, 11

Cowie, L.L., Songaila, A., Hu, E.M. & Cohen, J.G. 1996, AJ, 112, 839

Cowie, L.L. & Barger, A.J. 2008, ApJ, 697, 122

Ilbert, O., Tresse, L., Zucca, E. et al. 2005, A&A, 439, 863

Ilbert, O., Capak, P., Salvato, M. et al. 2009, A&A, 690, 1236

Ilbert, O., Salvato, M., Le Floc'h, E. et al. 2010, ApJ, 690, 1236

Kereš, D., Katz, N., Weinberg, D.H., & Davé, R. 2005, MNRAS, 363, 2

Koekemoer, A. M., Aussel, H., Calzetti, D. et al. 2007, ApJS 172, 196

Martig M., Bournaud F., Teyssier R. & Dekel A., 2009, ApJ, 707, 250

McCracken, H.J., Capak, P., Salvato, M. et al. 2009, ApJ, 708, 702

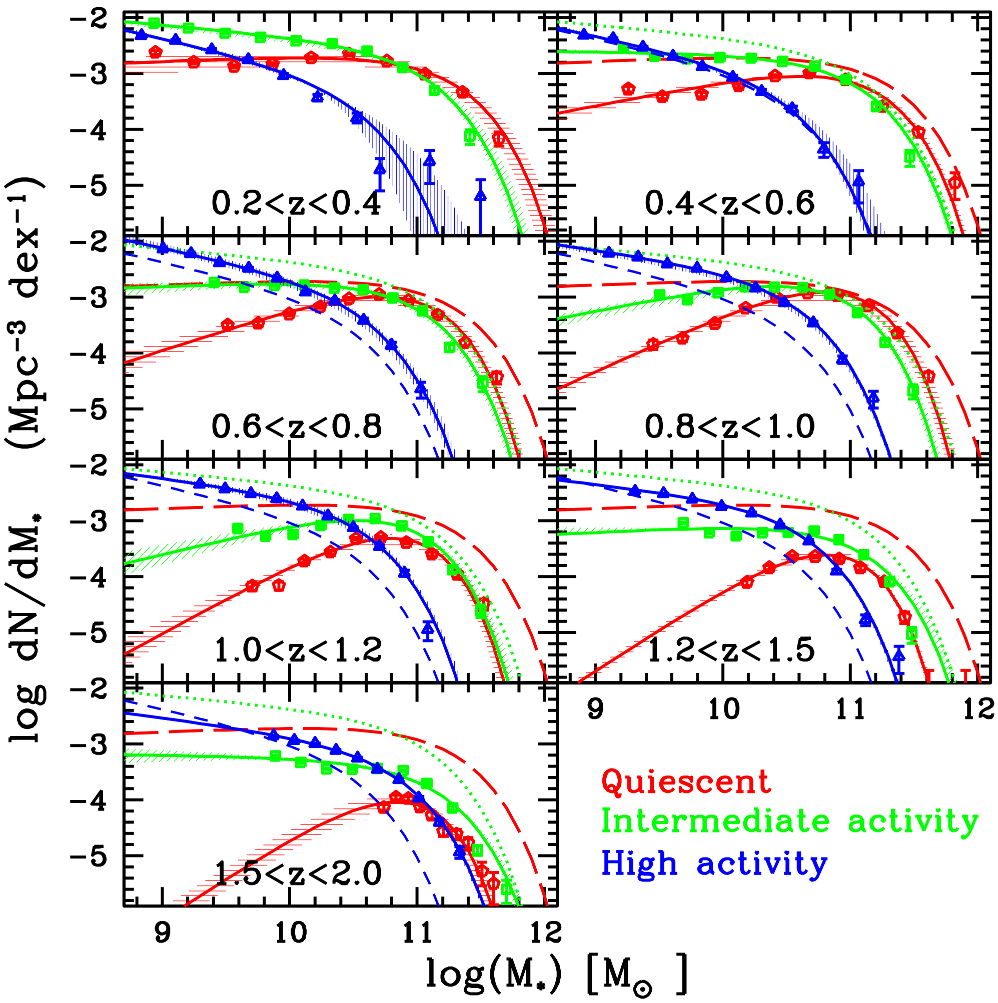

Fig. 1. MF by spectral type. The sample is split into "high activity" (blue vertical shaded area), "intermediate activity" (green oblique shaded area) and "quiescent" (red horizontal shaded area) galaxies. The blue short-dashed lines, the green dotted lines and the red long-dashed lines are the MFs measured at $z = 0.2 - 0.4$ for the "high activity", "intermediate activity" and "quiescent" galaxies, respectively.

Peng, Y.J., Lilly, S., Kovac, K. et al. 2010, ApJ, 721, 193
Sanders, D.B., Salvato, M., Aussel, H. et al. 2007, ApJS, 172, 86
Scoville, N. et al. 2007, ApJS, 172, 1
Springel, V., Frenk, C. S., & White, S. D. M. 2006, Nature, 440, 1137
White, S.D.M. & Rees, M.J. 1978, MNRAS, 183, 341
Williams, R.J., Quadri, R., F., Franx, M. et al., 2009, ApJ, 691, 1879

SF2A 2010
S. Boissier, M. Heydari-Malayeri, R. Samadi and D. Valls-Gabaud (eds)

SPECTRAL ANALYSIS OF A AND F DWARF MEMBERS OF THE OPEN CLUSTER M6: PRELIMINARY RESULTS

T. Kılıçoğlu[1], R. Monier[2] and L. Fossati[3]

Abstract. We present the first abundance analysis of CD-32 13109 (NGC 6405 47), member of the M6 open cluster. The photospheric abundances of 14 chemical elements were determined by comparing synthetic spectra and observed spectra of the star. Findings show that this star should be an Am star.

Keywords: stars: abundances, stars: chemically peculiar, open clusters and associations: individual: M6

1 Introduction

M6 (=NGC 6405, age = 100×10^{6} yrs) is an open cluster located about 500 pc away in the constellation Scorpio. The first photometric study of M6 including numbering system was performed by Rohlfs et al. (1959). In order to constrain physical processes such as radiative-gravitional settling and/or turbulence diffusion, previous abundance analysis of stars in open clusters have been performed by several authors, e.g. Varenne & Monier (1999), Monier (2005), Gebran et al. (2008), Gebran & Monier (2008). We have started to analyse the spectra of A and F type dwarf members of M6. We present detailed abundance determination of the star CD-32 13109 (NGC 6405 47) whose lines are sharp.

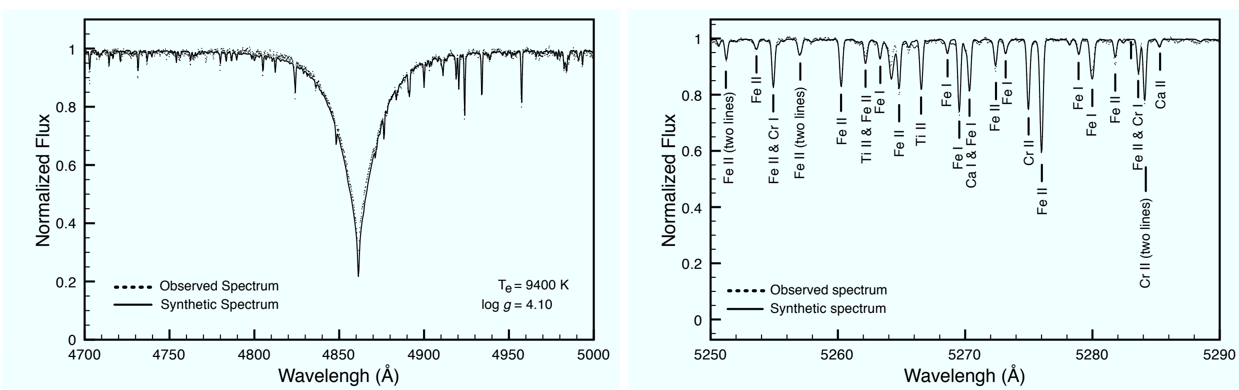

Fig. 1. Left: Comparison of the observed and the synthetic H_β profiles **Right**: Comparison of the observed and synthetic spectrum between 5250 Å and 5290 Å for [Fe/H] = 0.28 dex

2 Observations

The program stars have been observed using the FLAMES/GIRAFFE spectrograph with the MEDUSA fibers, mounted at UT2 (Kueyen), the 8 meter class VLT telescope in May and June, 2007. The spectral regions cover three wavelengh intervals: 4500 - 5100 Å, 5140 - 5350 Å and 5590 - 5840 Å at resolving powers of about 7500, 25900, 24200, respectively.

[1] Ankara University, Faculty of Science, Department of Astronomy and Space Sciences, 06100, Tandoğan, Ankara, Turkey
[2] Laboratoire Hippolyte Fizeau, Université de Nice - Sophia Antipolis, 06108 Nice Cedex 2, France
[3] Department of Physics and Astronomy, Open University, Walton Hall, Milton Keynes MK7 6AA, UK.

3 Atmospheric Parameters

Initial atmospheric parameters of 42 stars were derived from Geneva seven-color photometry measurements (WEBDA) using the CALIB code described in Kunzli et al. (1997). A reddening E(B2-V1) value of 0.13 $\pm$ 0.01 was adopted. In order to check the effective temperature and surface gravity derived from photometry, we compared the observed H_β profile of CD-32 13109 with synthetic models calculated with SYNSPEC48 (Hubeny & Lanz 1992). Finally, we adopted the values of T_e = 9400 K and log g = 4.10 for the star (Fig. 1, left).

4 Abundance Determinations

In order to obtain rotational broadened synthetic spectrum, the rotational velocity of 6.5 km s^{-1} is derived from the Fe II 5254.959 Å line. The photospheric abundances of 14 chemical elements of CD-32 13109 were derived by synthesizing unblended or weakly blended lines using SYNSPEC48 with ATLAS9 model atmospheres (Kurucz 1979). A sample of high resolution region is shown in Fig. 1, right. The comparison of the synthetic (solar) and the observed spectrum clearly establishes a Sc deficiency (Fig. 2, left).

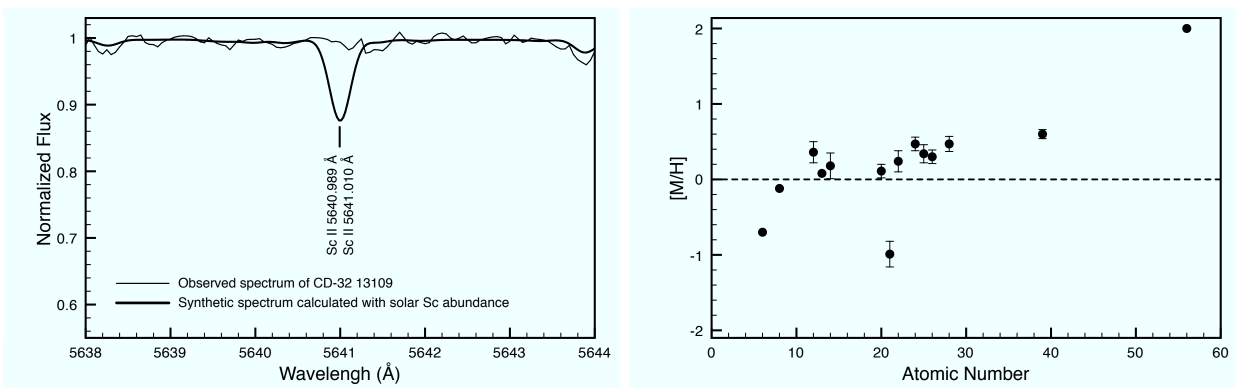

Fig. 2. Left: The difference between the observed spectrum and synthetic spectrum calculated for a solar Sc abundance **Right**: The derived atmospheric elemental abundances with respect to solar for CD-32 13109

5 Results

For CD-32 13109, the derived abundances (Fig. 2, right) for Mg and heavier atoms are greater than solar except for Sc which is very underabundant (-1.00 dex). We found striking overabundances (higher than 0.4 dex) for Cr, Ni, Y, and probably for Ba with respect to solar. Altogether these findings strongly suggest that this star is an Am star. The ongoing analysis of the other member stars will allow us to address the chemical heterogeneity (star to star variations) of A stars in this open young cluster.

We kindly thank Pierre North for making his code CALIB available. This research has used SIMBAD and WEBDA databases.

References

Gebran, M. & Monier, R. 2008, A&A, 483, 567
Gebran, M., Monier, R., & Richard, O. 2008, A&A, 479, 189
Hubeny, I. & Lanz, T. 1992, A&A, 262, 501
Kunzli, M., North, P., Kurucz, R. L., & Nicolet, B. 1997, A&AS, 122, 51
Kurucz, R. L. 1979, ApJS, 40, 1
Monier, R. 2005, A&A, 442, 563
Rohlfs, K., Schrick, K. W., & Stock, J. 1959, ZAp, 47, 15
Varenne, O. & Monier, R. 1999, A&A, 351, 247

SF2A 2010
S. Boissier, M. Heydari-Malayeri, R. Samadi and D. Valls-Gabaud (eds)

A SPARSE POPULATION OF YOUNG STARS IN CEPHEUS

A. Klutsch[1]

Abstract. Once mixed in the ambient galactic plane stellar population, young stars are virtually indiscernible because neither their global photometric properties nor the presence of nearby gas can help to disentangle them from older ones. Nevertheless, the study of the RasTyc sample revealed 4 lithium-rich field stars displaying the same space motion, which are located within a few degrees from each other on the celestial sphere near the Cepheus-Cassiopeia complex and at a similar distance from the Sun. Both physical and kinematical indicators show that all these stars are young, with ages in the range $10-30$ Ma. Multivariate analysis methods were used to select optical counterparts of XMM-Newton / ROSAT All-Sky Survey X-ray sources cross-identified with late-type stars around these 4 young stars. Recent intermediate- and high-resolution spectroscopic observations of this sample allowed to discover additional lithium-rich sources. The preliminary results show that some of them share the same space motion as the 4 original stars. They have properties rather similar to the members of the TW Hydrae association, although they are slightly older and located in the northern hemisphere. Nearby young stars in the field are of great importance to understand the recent local history of star formation, as well as to give new insight into the process of star formation outside standard star-forming regions and to study the evolution of circumstellar discs.

Keywords: stars: formation, stars: pre-main sequence, X-rays: stars, stars: kinematics and dynamics

1 Introduction

Most stars detected by the ROSAT mission are younger than 1 Ga (e.g. Motch et al. 1997). Taking account this property, Guillout et al. (1999) cross-correlated the ROSAT All-Sky Survey (RASS) with the Tycho catalogue creating the largest (≈ 14000 active stars) and most comprehensive set of late-type stellar X-ray sources, the so-called *RasTyc* sample. This stellar population can be used as a tracer of young local structures (Guillout et al. 1998). Presently, nine nearby ($30-150$ pc) young ($5-70$ Ma) associations are already identified in the southern hemisphere (see the reviews of Zuckerman & Song 2004, and Torres et al. 2008): e.g. the TW Hydrae association (TWA) around TW Hya (Gregorio-Hetem et al. 1992; Kastner et al. 1997). In particular, the SACY project (Torres et al. 2006, 2008) allowed to identify many of them and their members. Its sample can be considered as a sub-sample of the *RasTyc* population in this hemisphere. In the northern hemisphere, Guillout et al. (2009) identified 5 young stars among the optically bright *RasTyc* sources. They are located in various over-densities of the whole *RasTyc* sources, but none is near the largest one (Klutsch et al. 2010). The sky density of the youngest stars is fairly uniform (Klutsch 2008). The difference of more than one order of magnitude less than in the SACY survey is consistent with the significant asymmetry in the all-sky *RasTyc* distribution with respect to the galactic plane shown by Guillout et al. (1998).

2 Discovery of four comoving T Tauri stars

Using the optically faint sample, Klutsch (2008) and Guillout et al. (2010a) discovered an unusual group of 4 lithium-rich stars (green filled squares on Fig. 1) towards the Cepheus-Cassiopeia (Cep-Cas) complex. Although this sky area is rich in CO molecular regions (Dame et al. 2001) and dark clouds (Dobashi et al. 2005), these stars are projected several degrees off-clouds in front of a region devoid of interstellar matter, which correspond precisely to the sky area with the highest density of *RasTyc* sources (Fig. 1). They have all typical spectral signatures of young stars (Guillout et al. 2010a) as i) a Hα emission or a filled-in profile, ii) a strong lithium

[1] Universidad Complutense de Madrid, Departamento de Astrofísica, Facultad de Ciencias Físicas, 28040 Madrid, Spain

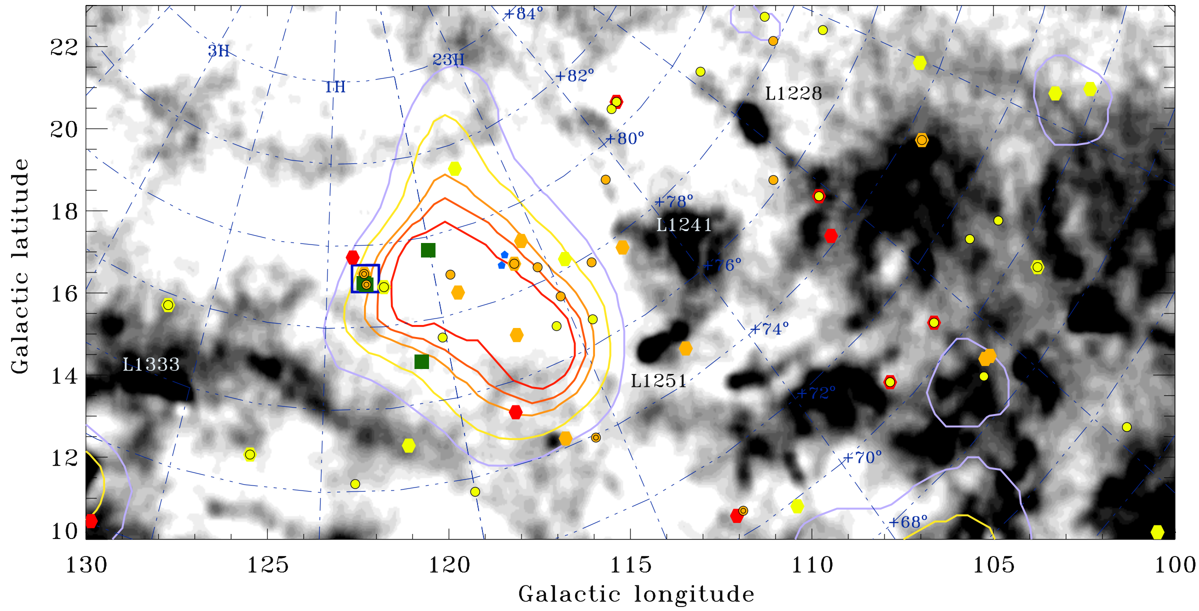

Fig. 1. Spatial distribution of stellar X-ray sources located near the 4 original comoving TTSs (green filled squares) as well as the naked TTS V368 Cep and its comoving companion (pentagons), which are over-plotted on the Dobashi et al. (2005) extinction (A_v) map. For selected targets (hexagons) as well as Tachihara et al. (2005) single stars (circles) and visual binaries (double circles), each symbol is filled in orange, red or yellow if the source displays a strong, moderate or no lithium line, respectively. The main clouds near the CO void region are labeled. I also indicated the density iso-contours for the whole *RasTyc* sources and the locus of an unusual concentration of at least 7 young stars (big blue open square) outside of SFRs.

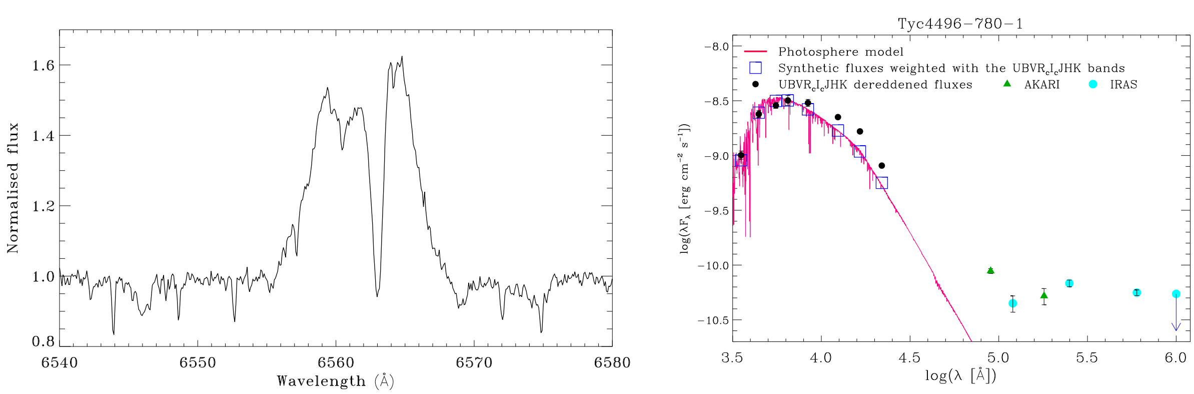

Fig. 2. *Left*: Spectrum of TYC 4496-780-1 displaying a strong Hα emission profile. *Right*: Spectral energy distribution of this source showing a near- and far-infrared excess, a typical signature of an accretion disc (Guillout et al. 2010a,b).

line corresponding to a lithium abundance close to the primordial one, and iii) a X-ray luminosity (L_X) of $\sim 10^{30.4}$ erg s^{-1} (within 0.2 dex), which is similar to that observed for weak-line T Tauri stars (WTTS) in Taurus-Auriga-Perseus star-forming regions (SFRs). Only TYC 4496-780-1, the star with a strong Hα emission profile (Fig. 2, left panel), displays a near- and far-infrared excess (Fig. 2, right panel). This feature is typical of class II infrared sources, i.e. T Tauri stars (TTSs) still surrounded by an accretion disc. Guillout et al. (2010b) characterized its properties because this star is the optical counterpart of one infrared source detected by both AKARI and IRAS missions. Because of the lack of relevant infrared excess, the 3 other sources are likely WTTS or post-T Tauri stars whose discs have already been dissipated as most stars with an age between $10 - 70$ Ma.

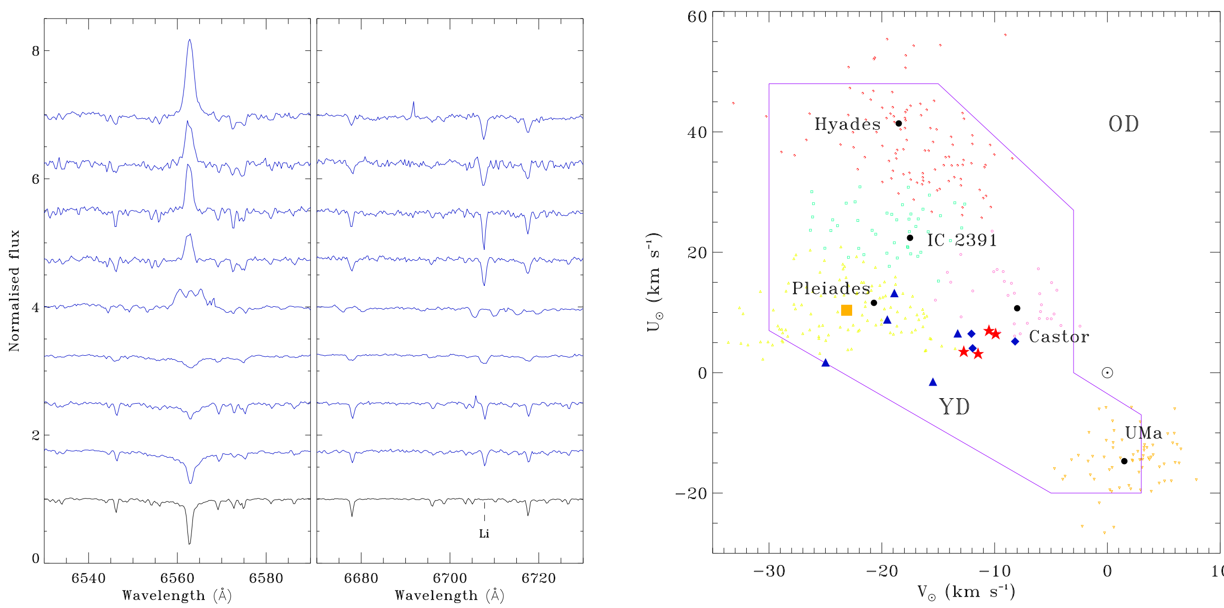

Fig. 3. *Left*: IDS spectra in the Hα (left panel) and lithium (right panel) spectral regions of 8 new lithium-rich stars. I also displayed the spectrum of a "non-active" standard star (black). *Right*: $U-V$ kinematic diagram for these 8 young comoving candidates seen as single stars (triangles) and spectroscopic systems (diamonds) with the cross-correlation technique. I also plotted the space velocities of the 4 original TTSs (star symbols), the naked TTS V368 Cep (square), some late-type members of some young stellar kinematic groups (SKG) as well as the average velocity components (dots) of these SKG. The loci of the young-disc (YD) and old-disc (OD) populations are also marked.

Unfortunately, their Tycho parallaxes are useless and one must rely on photometric distance estimations. To cover a wide range of possibilities, Guillout et al. (2010a) estimated two distances for each star. We considered that the *lower limit* is $80-100$ pc assuming the stars are on the zero-age main sequence and that the *upper limit* is $130-180$ pc assuming a stellar age of 15 Ma. Using a lower age would be in contradiction to our photometric observations showing that no stars suffer major interstellar extinction. Whatever the distance is, all these stars share the same kinematics (within a few km s^{-1}) proving that they form a homogeneous group with a common origin (Guillout et al. 2010a, Fig. 4) and they are unrelated with the naked TTS V368 Cep (Fig. 3, right panel).

We also consider a possible link with the Cep-Cas complex. We can not exclude that these stars are runaway objects originated in L1251, L1241 or L1228, but their high-escape velocity and their similar space motion cast doubt on this hypothesis. The more plausible explanation for the formation of these TTSs is the in-situ model.

3 New young stars in the CO Cepheus void

Selecting an appropriate sample of targets is the major difficulty for searching other young comoving stars in this sky area. Klutsch et al. (2010) picked optical counterparts of XMM-Newton / RASS X-ray sources cross-identified with stars using multivariate analysis methods (Pineau 2009) allowing to disentangle the stellar population from the extragalactic component (galaxies and quasars) also emitting in X-ray.

All candidates are in a region 30° wide around the 4 original TTSs and compile following selection criteria: i) late-type stars ($B-V>0.6$), ii) faint ($V>10$ mag), iii) X-ray luminous ($L_X>10^{30}$ erg s^{-1}), and iv) within 170 pc of the Sun. Our first intermediate- and high-resolution spectroscopic observations on this ongoing project [semester 2009B on T193/Sophie (OHP), 2.2m/FOCES (CAHA) and INT/IDS (La Palma)] showed that 25 and 23 sources (i.e. about 20 % and 18 % candidates already observed) display a strong lithium line similar to that of the original TTSs and a moderate lithium line, respectively. Out of 8 lithium-rich stars discovered with IDS (Fig. 3), 4 are good young comoving candidates, but 3 turn out to be spectroscopic binaries. Spectra of the remaining 17 are in the reduction/analysis phase. Most of the others are classified as M-type stars.

On Fig. 1, I showed the spatial distribution of selected stars (hexagons). Some of lithium-rich stars (including one of the original TTSs) were already identified as WTTS (orange filled circles) by Tachihara et al. (2005). All stars from this paper will be also included in the future observing runs to determine their radial velocity and kinematics for finding a possible connection with the 4 comoving TTSs. Presently, 15 stellar X-ray sources (i.e. 7, 5 and 3 stars discovered by this work, Tachihara et al. and both, respectively), located in the CO Cepheus void, are rich in lithium. Out of them, 3 are good young comoving candidates. I also detected an unusual concentration (blue open square on Fig. 1) of at least $7-8$ lithium-rich stars formed by two of the original TTSs (the visual binary, RasTyc0038+7903 or [TNK2005] 4, and the spectroscopic binary, RasTyc0039+7905) and another visual binary, [TNK2005] 5, for which one component turns to be a binary or a triple system. These preliminary results seem to confirm a possible link between many (not all) young stars of this region.

4 Conclusions and perspectives

TYC 4496-780-1 was classified as a class II young infrared source, i.e. a TTS still surrounded by an accretion disc. However, presently, few of these sources have been found outside of SFR's cores (e.g. TW Hya). This source share the same galactic motion as three comoving TTSs. They are located in a region devoid of dark clouds and near at least other 10 stellar X-ray sources displaying a strong lithium line. These properties are similar to the TWA, although slightly older and located in the northern hemisphere. The runaway hypothesis is highly improbable for explaining the formation of this homogeneous comoving group because of their kinematical properties and the identification of a great number of new T Tauri candidates in this sky area. Some of them also form an unusual concentration of $7-8$ lithium-rich stars. That raises the question of the in-situ star-formation scenario in low-mass cloud environments (as in many other SFRs). Afterwards the GAIA mission will certainly shed light on this issue and on the origin of this group which could be related to the Cep-Cas complex.

This work was supported by Universidad Complutense de Madrid (UCM), the Spanish Ministerio de Ciencia e Innovacin (MICINN) under grants AYA2008-00695, and "The Comunidad de Madrid" under PRICIT project S2009/ESP-1496 (AstroMadrid). My collaborators for this project are: D. Montes[1], P. Guillout[2], A. Frasca[3], F.-X. Pineau[2], N. Grosso[2], E. Marilli[3], and J. López-Santiago[1] ([1]UCM, Madrid, Spain; [2]Observatoire Astronomique de Strasbourg, Université de Strasbourg, CNRS, UMR 7550, 11 rue de l'Université, F-67000 Strasbourg, France; [3]INAF - Osservatorio Astrofisico di Catania, via S. Sofia, 78, 95123 Catania, Italy).

References

Dame, T. M., Hartmann, D., & Thaddeus, P. 2001, ApJ, 547, 792

Dobashi, K., Uehara, H., Kandori, R., et al. 2005, PASJ, 57, 1

Gregorio-Hetem, J., Lepine, J. R. D., Quast, G. R., et al. 1992, AJ, 103, 549

Guillout, P., Frasca, A., Klutsch, A., et al. 2010a, A&A, in press (ArXiv:1009.2587)

Guillout, P., Grosso, N., et al. 2010b, in preparation

Guillout, P., Klutsch, A., Frasca, A., et al. 2009, A&A, 504, 829

Guillout, P., Schmitt, J. H. M. M., Egret, D., et al. 1999, A&A, 351, 1003

Guillout, P., Sterzik, M. F., Schmitt, J. H. M. M., et al. 1998, A&A, 334, 540

Kastner, J. H., Zuckerman, B., Weintraub, D. A., & Forveille, T. 1997, Science, 277, 67

Klutsch, A. 2008, Ph.D. thesis, ULP and Strasbourg Observatory

Klutsch, A., Montes, D., Guillout, P., et al. 2010, Proceeding "16th Cambridge Workshop on Cool Stars, Stellar Systems, and the Sun", Astronomical Society of the Pacific Conference Series (Poster F02).

Motch, C., Guillout, P., Haberl, F., et al. 1997, A&AS, 122, 201

Pineau, F.-X. 2009, Ph.D. thesis, ULP and Strasbourg Observatory

Tachihara, K., Neuhäuser, R., Kun, M., & Fukui, Y. 2005, A&A, 437, 919

Torres, C. A. O., Quast, G. R., da Silva, L., et al. 2006, A&A, 460, 695

Torres, C. A. O., Quast, G. R., Melo, C. H. F., & Sterzik, M. F. 2008, in Handbook of Star Forming Regions, Volume II, edited by Reipurth, B., Astronomical Society of the Pacific Monograph Publications, 757

Zuckerman, B., & Song, I. 2004, ARA&A, 42, 685

SF2A 2010
S. Boissier, M. Heydari-Malayeri, R. Samadi and D. Valls-Gabaud (eds)

CHARACTERIZATION OF THE THICK DISC PROPERTIES UP TO 8 KPC THROUGH A SPECTROSCOPIC SURVEY

G. Kordopatis[1], A. Recio-Blanco[1], P. de Laverny[1], G. Gilmore[2], V. Hill[1], R.F.G. Wyse[3], A. Helmi[4], A. Bijaoui[1], C. Ordenovic[1], M. Zoccali[5] and O. Bienaymé[6]

Abstract. A spectroscopic survey of nearly 600 stars probing the Galactic Thick Disc far from the Solar neighbourhood is performed. The MATISSE (MATrix Inversion for Spectral SynthEsis) algorithm is developed and trained in order to automatically obtain the atmospheric parameters of the stars. The derived effective temperatures, surface gravities and overall metallicities are then combined to stellar evolution isochrones, radial velocities and proper motions to get the distances, kinematics and orbital parameters of the sample stars, up to 8kpc. The Galactic components Thin and Thick discs and Halo are then characterized. The velocity ellipsoid for the old Thin Disc is found at $(\sigma_u, \sigma_v, \sigma_w) = (39, 27, 20)$ km s^{-1} with a mean [M/H] ~ -0.12 dex, whereas the Thick Disc has a mean [M/H] ~ -0.4 dex and a rotational lag of V $\sim$-76 km s^{-1}

Keywords: galaxy: evolution, galaxy: kinematics and dynamics, stars: abundances, methods: observational

1 Introduction

The existence of a Thick Disc for the Milky Way (Gilmore & Reid 1983), and for other disc Galaxies (Yoachim & Dalcanton 2006) is rather clearly established nowadays. Nevertheless, its creation mechanisms still remain a riddle in the paradigm of a cold dark matter dominated Universe. For instance, Abadi *et al.* (2003) propose that the stars forming the Thick Disc mostly come from distrupted satelites, whereas Villalobos & Helmi (2008) predict that the pre-existing Thin Disc has been heated rapidly from successive accretions. On another hand, Brook *et al.* (2004) suggest that a gas rich merger brought the necessary gas to form *in situ* the Thick disc stars, before the gas have had completely settled into a thin disc. Finally, the simulations of Schönrich & Binney (2009) manage to form a Thick Disc without any external stimulus: stars migrate to larger heights from the inner parts of the Galaxy, due to resonances with the spiral arms and the central bar.

Typical F, G and K main sequence stars are particularly useful to study Galactic evolution, since they are both numerous and long-lived, and their atmospheres reflect their initial chemical composition. However, a direct measurement of their spatial distribution requires accurate estimates of stellar distances, which is a delicate step involving (if the parallax is not available) the determination of precise stellar parameters (effective temperatures $T_{\rm eff}$, surface gravities log g, and metal content [M/H]).

In order to put more constraints on the Thick Disc properties, we explore spectroscopically the stellar contents outside the Solar neighbourhood, owing to an extensive use of the Ojha (1994) catalogue in which are published the proper motions and U,B,V colours of several thousand stars. Here, based on the observations of 600 of these stars towards the galactic coordinates l$\sim$ 277°, b$\sim$ 47°, we present a kinematic and chemical characterization of the Galactic components.

[1] Université de Nice Sophia-Antipolis, CNRS, Observatoire de la Côte d'Azur, Dpt Cassiopée, UMR 6202, Nice, France
[2] Institute of Astronomy, University of Cambridge, Madingley Road, Cambridge CB3 0HA, UK
[3] Johns Hopkins University, Baltimore, MD, USA
[4] Kapteyn Astronomical Institute, University of Groningen, PO Box 800, 9700 AV Groningen, The Netherlands
[5] Departamento de Astronomía y Astrofísica, Pontificia Universidad Católica de Chile, Av. Vicu na Mackenna 4860, Casilla 306, Santiago 22, Chile
[6] Université de Strasbourg, Observatoire Astronomique, Strasbourg, France

2 The catalogue of stars

The target stars were selected having $14 \le m_v \le 18.5$ mag in order to probe the Galactic Thick Disc and have acceptable signal-to-noise ratios (S/N). According to the published values of Ojha (1994), the magnitude precisions range from 0.02 mag for the brightest, to 0.05 mag for the faintest stars. Associated errors for the proper motions are estimated to be 2 mas/year.

Radial velocities have been derived by cross-correlating the spectra with a binary template of a K0 type star, reaching a mean estimated error of 4.7 km s^{-1}. The observations were obtained with VLT/FLAMES feeding the GIRAFFE spectrograph with the LR08 grating (8206-9400 Å, R$\sim$6500). This setup contains the Gaia/RVS wavelength range (8475-8745 Å), and is similar to its low resolution mode. This survey can therefore be used as a complementary study of Recio-Blanco *et al.* (2006), to test with real spectra what information will be possibly retrieved from the Gaia/RVS low resolution mode (or its ground based follow up), with an automatic spectral analysis code such as the MATrix Inversion for Spectral SynthEsis (MATISSE, Recio-Blanco *et al.* 2006).

In that wavelength range, the IR CaII triplet is predominant for most of the spectral types and luminosity classes as well as for very metal poor stars. In addition, these strong features are still detectable even at a low S/N, allowing a good radial velocity ($V_{\rm rad}$) derivation and an overall metallicity estimation. Paschen lines are visible for stars hotter than G3. The MgI (8807 Å) line, which is a useful indicator of surface gravity, is also visible even for low S/N. Finally, molecular lines like TiO and CN can be seen for the cooler stars.

3 The derivation of the atmospheric parameters

We used the MATISSE algorithm to obtain the $T_{\rm eff}$, log g and [M/H] for our sample. MATISSE is a local multi-linear regression method that allows the determination of an atmospheric stellar parameter by a simple projection of an observed spectrum on vectors derived during a learning phase. In order to train MATISSE for the LR08 setup of FLAMES, we computed a library of 2905 synthetic spectra using the MARCS model atmospheres, and a linelist calibrated on the high resolution spectra of the Sun and Arcturus. The parameter ranges for the synthetic library were, $T_{\rm eff}$: [3000, 8000] K, log g: [0, 5] dex and [M/H]: [-5, +1] dex. We assumed a coupling between the overall metallicity and the α-elements abundances*, according to the commonly observed enhancements in the metal-poor Galactic stars.
The method has been tested on a set of 10^3 synthetic spectra not being part of the learning set of MATISSE, in order to establish the relative errors of our algorithm. We found that for an intermediate metallicity dwarf star, at S/N $\sim$ 50 (which is the mean S/N of our spectra), accuracies of $\sim$ 150 K, 0.3 dex and 0.2 dex are achieved for $T_{\rm eff}$, log g and [M/H], respectively. In addition, the algorithm has been applied on two observed stellar librairies, the S^4N and the CFLIB one, showing no particular biases according to the S/N, the spectral type of the star or the metallic content (Kordopatis *et al.* 2010).

4 Characterization of the observed stellar sample

Based on the position of the stars in the H–R diagram and an interpolated set of the Y^2 isochrones, we derived the line-of-sight distances, by assuming the interstellar extinction provided by the Schleggel data. Galactocentric positions† X,Y,Z and velocities U,V,W were derived, using the proper motions of Ojha (1994) and the derived by ourselves $V_{\rm rad}$. Errors have been propagated by running 5.10^3 Monte-Carlo simulations, taking as a final value the mean of the obtained realisations and as an error their dispersions. All the stars having S/N >10, relative errors on the distance less than 40%, and errors on $V_{\rm rad}$ less than 7 km s^{-1} have been selected.

In order to characterize the Galactic components, we made extensive use of the Besançon Model of the Milky Way (Robin *et al.* 2003), which supposes a scale height of 800 pc for the Thick disc. We obtained a catalog of simulated stars towards our line-of-sight and biased it according to our magnitude distribution. According to the model, stars till a Z-height above the plane of 600 pc are dominated (more than 80%) by the Thin Disc. Furthermore, a given star situated between 0.6 kpc and 1.1 kpc, has equal chances to belong to one of the two components. On the other hand, farther than 1.1 kpc, the Thick Disc is predominant and for 1.1 kpc<Z<4 kpc, more than 82 % of the stars should be from the Thick Disc. Farther away than 4 kpc, the inner Halo is no longer negligible, representing more than 40% of the total stars according to the model. Thus, we decided to select as

*The chemical species considered as α-elements are O, Ne, Mg, Si, S, Ar, Ca and Ti.

†We have adopted a right-handed reference frame, with the X axis pointed towards the Galactic centre

Galactic component	N	<U>; σ_U km s^{-1}	<V>; σ_V km s^{-1}	<W>; σ_W km s^{-1}	<[M/H]>; $\sigma_{[M/H]}$ dex
Thin Disc	108	(−22; 39)	(−12; 27)	(−7; 20)	(−0.12; 0.30)
Thick Disc	215	(−49; 72)	(−76; 57)	(−12; 59)	(−0.41; 0.26)
Inner Halo	30	(−24; 187)	(−257; 89)	(−135; 132)	(−0.66; 0.50)

Table 1. Column (2) shows the number of stars considered in order to characterize each Galactic component. Colums (3) to (6) show the mean values as well as the dispersion for the fitted Gaussians of the velocity and metallicity distributions. The Thin Disc stars have been selected as the ones having Z<600 pc, the Thick disc stars as the ones having $1.1 < Z < 4$ kpc, and the Halo stars the ones having $Z > 4$ kpc and V smaller than -180 km s^{-1} .

Thin Disc members the stars being closer than 600 pc, as Thick Disc stars the targets lying between 1.1 kpc and 4 kpc, and as inner halo members, all the stars above 4 kpc having an almost null rotational velocity (V smaller than −180 km s^{-1}). This selection separates out clearly each Galactic component in a Toomre diagram (see Fig. 1-d).

Gaussians fits have been applied to the velocities and metallicity distributions (see Fig. 1) of the Thin and Thick discs as well as the inner Halo. As summarized in Table 1, we found that the Thin Disc has (<U>; σ_U)=(−22; 39) km s^{-1}, (<V>; σ_V)=(−12; 27) km s^{-1}, (<W>; σ_W)=(−7; 20) km s^{-1} and (<[M/H]>, $\sigma_{[M/H]}$)=(−0.12; 0.30) dex. These values agree with the studies of for example Reddy *et al.* (2006) and Soubiran *et al.* (2003). As far as the Thick Disc is concerned, the Gaussian distributions are characterized by (<U>; σ_U)=(−49; 72) km s^{-1}, (<V>; σ_V)=(−76; 57) km s^{-1}, (<W>; σ_W)=(−12; 59) km s^{-1} and (<[M/H]>, $\sigma_{[M/H]}$)=(−0.41; 0.26) dex. Finally, let us note that the stars selected as belonging to the inner Halo, may still include a non negligible part of Thick Disc members. In addition, they are prone to bigger errors (because of the fact that they are giant stars), as well as to selection biases, since a lot of them might have been rejected due to either their low S/N, or their high relative error on the atmospheric parameters (and hence their distance). Indeed, the rejection of the targets based on their distance accuracies and their S/N, removes most of the metal poor stars, which may introduce a bias against low-metal stars. For the 30 stars selected as being part of the inner Halo, we find a mean [M/H] of ∼ -0.66 dex, but the number of the candidates is rather small to make reliable statitistics.

The eccentricity of the stars was computed by integrating their orbits up to several Galactic revolutions. The Milky Way potential is fixed, and is modelled with a Miyamoto-Nagai disc, a Hernquist bulge and a spherical logarithmic halo. The shape of the eccentricity distribution seems to rule out, according to Sales *et al.* (2009), a pure accretion scenario for the formation of the Thick Disc.

5 Conclusions

Results found for the Thin Disc are in very good agreement with the predictions of the Besançon model, or surveys made in the Solar neighbourhood (Reddy *et al.* 2006; Soubiran *et al.* 2003). On another hand, the rotational lag found for the Thick Disc is higher than the commonly admitted value for the Canonical Thick Disc of ∼-50 km s^{-1}. The issue whether or not this is due to a gradient of the rotational velocity with Z is still an open question.

The authors would like to thank the MESOCENTRE de l'Observatoire de la Cote d'Azur, for computing the grid of synthetic spectra. We are grateful to B. Plez for his molecular linelists and the improved Turbospec code, M. Irwin for letting us use the routine of sky subtraction and A. Robin for her useful advices on the use of the Besançon model. Finally, G.K. would like to thank the Centre National d'Etudes Spatiales (CNES) and the Centre National de Recherche Scientifique (CNRS) for the financial support

References

Abadi, M. G., Navarro, J. F., Steinmetz, M., and Eke, V. R.: 2003, ApJ, **591** , 499

Brook, C. B., Kawata, D., Gibson, B. K., and Freeman, K. C.: 2004, ApJ, **612**, 894

Gilmore, G. and Reid, N.: 1983, MNRAS, **202**, 1025

Gilmore, G., Wyse, R. F. G., and Norris, J. E.: 2002, ApJL, **574**, L39

Kordopatis, G., Recio-Blanco, A., de Laverny, P., *et al.* : 2010, A&A, in prep.

Ojha, D. K.: 1994, Ph.D. thesis, Université de Strasbourg

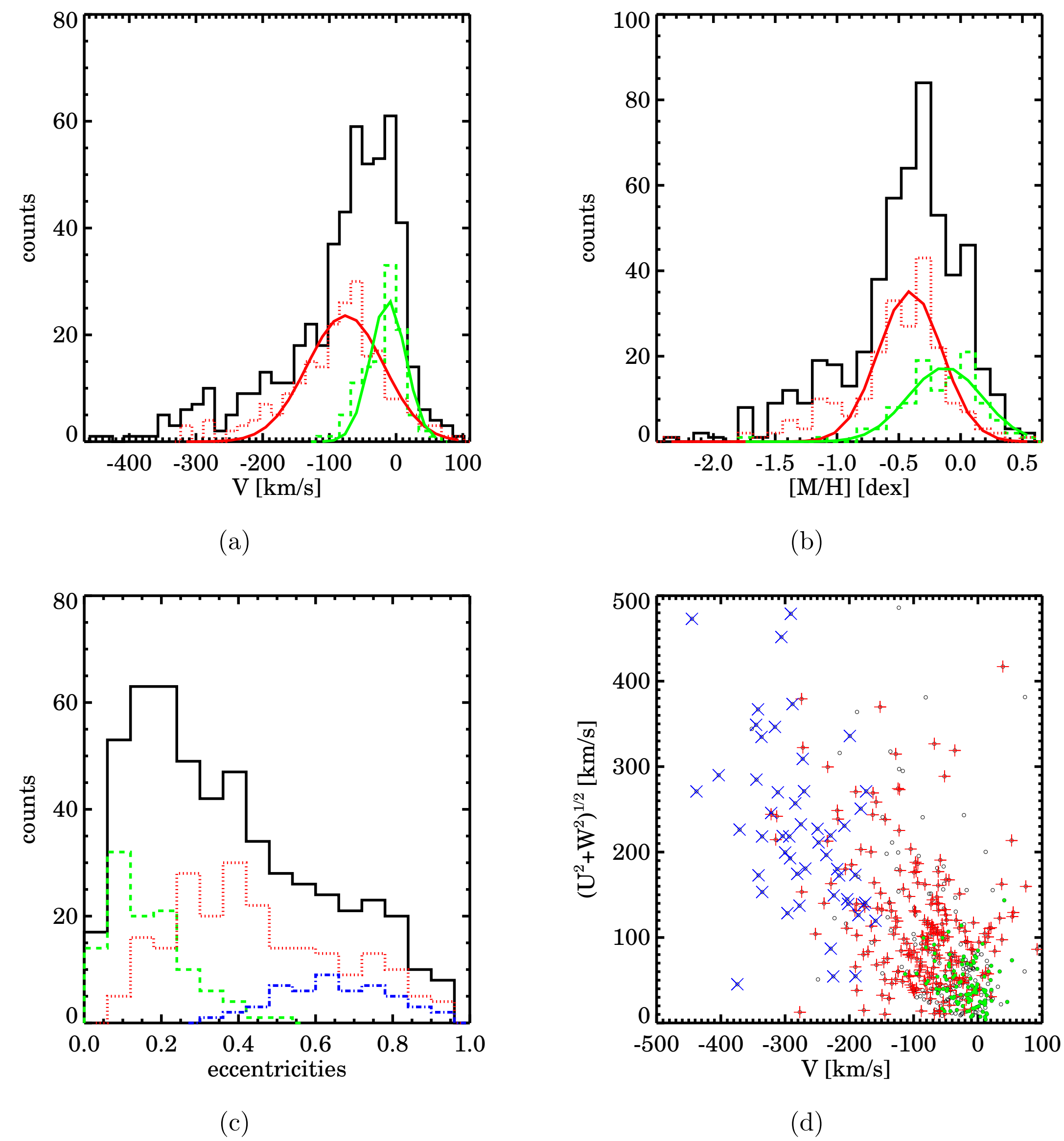

Fig. 1. Pannels (a), (b), (c) refer to the V-velocity, metallicity and eccentricity distributions for all the stars (continuous line), Thin Disc (dashed green line), Thick Disc (dotted red line) and Halo (blue dotted-dashed line). For panels (a) and (b) the halo distribution has not been shown for clarity reasons, since the counts are very few. Finally, pannel (d) shows the Toomre diagram, where each Galactic component separates out clearly. Thin disc stars are represented with filled green dots, Thick Disc stars with red plus signs and Halo stars with blue crosses. Open circles represent stars that could not be affiliated to any of the Galactic components.

Recio-Blanco, A., Bijaoui, A., and de Laverny, P.: 2006, MNRAS, **370**, 141

Reddy, B., Lambert, D., and Allende Prieto, C.: 2006, MNRAS, **367**, 1329

Robin, A. C., Reylé, C., Derrière, S., and Picaud, S.: 2003, A&A, **409**, 523

Sales, L., Helmi, A., Abadi, M., et al.: 2009, MNRAS, **400**, 61

Schönrich, R. and Binney, J.: 2009, MNRAS, **399**, 1145

Soubiran, C., Bienaymé, O., and Siebert, A.: 2003, A&A, **398**, 141

Villalobos, Á. and Helmi, A.: 2008, MNRAS, **391**, 1806

Yoachim, P. and Dalcanton, J.: 2006, AJ, **131**, 226

SF2A 2010
S. Boissier, M. Heydari-Malayeri, R. Samadi and D. Valls-Gabaud (eds)

HAVE WE SEEN DARK MATTER ANNIHILATION IN THE COSMIC-RAY ELECTRON AND POSITRON SPECTRA

J. Lavalle[1]

Abstract. Measurements of a rise in the cosmic positron fraction up to $\sim$ 100 GeV by the PAMELA satellite have triggered putative interpretation attempts in terms of dark matter (DM) annihilation or decay, even though generic DM particle models are not expected to contribute to this signal. Here, we review the tricks that have been invoked to make DM-induced signals fit the data. We also recall how considering conventional astrophysical sources — supernova remnants (SNRs) and pulsars — in a consistent cosmic-ray (CR) propagation framework can easily explain these observations, despite large theoretical uncertainties. Although this does not dismiss potential DM contributions, this unfortunately makes the related background far too difficult to control for discovery purposes. Though the positron puzzle appears qualitatively solved in terms of standard astrophysics, substantial improvements in the CR source and propagation modelings are now clearly necessary to improve our understanding of the Galactic CR lepton budget and associated multi-wavelength diffuse emissions.

Keywords: dark matter, cosmic-ray propagation, cosmic-ray sources, pulsars, supernova remnants

1 Introduction

Indications of an increase in the CR positron fraction above a few GeV have been collected for quite a long time (Fanselow et al. 1969; Golden et al. 1987; Barwick et al. 1997; Alcaraz et al. 2000), but the recent PAMELA measurements have reached an unprecedented statistics allowing much more detailed analyses (Adriani et al. 2009). It turns out that this increase can hardly be explained in terms of secondary positrons* (Moskalenko & Strong 1998; Delahaye et al. 2009), though peculiar spatial effects are still worth being investigated into more details (Shaviv et al. 2009) — see also the original proposal by Roberts (2010) about a possible solar magnetic lens effects.

Antimatter CR excess signals as potential probes of DM annihilation were first proposed by Silk & Srednicki (1984) after one became aware of the power of gamma-ray and CR observations to constrain the DM properties (*e.g.* Gunn et al. 1978; Stecker 1978; Zeldovich et al. 1980). Later, as already mentioned by Tylka (1989), Baltz & Edsjö (1998) showed in detail that annihilation of supersymmetric neutralinos, one of the most popular DM candidate so far, could hardly generate observable features in the local positron spectrum unless the annihilation rate is substantially boosted, suggesting that DM substructures could play this amplifier role, following the idea of Silk & Stebbins (1993). It was recently shown that such subhalos can actually hardly be at the origin of the large required enhancement (Lavalle et al. 2007, 2008b), and that even an isolated such dark source, as proposed in Cumberbatch & Silk (2007), would lead to tensions with current gamma-ray constraints (Bringmann et al. 2009). Despite this apparent failure of dark matter particle models to naturally yield CR positrons in sufficient amount, an impressive number of papers has been released in the past few years to try to explain the PAMELA data in terms of DM annihilation or decay. We will discuss a few aspects of the available proposals below, but it is already worth noticing that all these works assumed the absence of astrophysical sources of positrons but secondaries when fitting the data.

[1] Università di Torino & INFN, Dipartimento di Fisica Teorica, Via Giuria 1, 10125 Torino — Italia
(from Oct. 2010: Instituto de Física Teórica (IFT), Madrid — Spain). e-mail: `lavalle@in2p3.fr, lavalle@to.infn.it, julien.lavalle@uam.es`

*For the non-expert reader, a primary cosmic ray is produced — or/and accelerated — at sources, whereas a secondary cosmic ray originates from nuclear interactions between primary CR nuclei and the interstellar gas (ISG).

Although interpretations in terms of standard astrophysical sources were only a few in the past decades (*e.g.* Arons 1981; Harding & Ramaty 1987; Boulares 1989; Aharonian et al. 1995; Chi et al. 1996), they all relied on quite sound physical arguments: pulsars were already predicted to produce a significant amount of electron-positron pairs only few years after their discovery (*e.g.* Sturrock 1970), which is now indirectly proven from the more recent observations of gamma-rays originating from pulsar magnetospheres. Another way to generate primary-like positrons, also relying on standard astrophysics and recently widely surveyed, is to invoke the diffusive acceleration of those secondary positrons created at SNR shocks (*e.g.* Berezhko et al. 2003; Blasi 2009). Nevertheless, we will focus here on the pulsar solution when discussing standard astrophysical explanations of the positron excess.

The outline of this proceeding is the following. We first recall the bases of electron-positron propagation in the Galaxy. Then, we revisit the case for the DM interpretation of the cosmic positron excess, showing how contrived this attempt can be. Afterwards, we discuss the requirements a model of astrophysical CR electrons and positrons should obey. We emphasize that including pulsars as positron sources can naturally lead to a good fit of the PAMELA data, with quite reasonable parameters. Finally, we conclude and discuss a few perspectives.

2 Electron and positron propagation in the galaxy

Reviews and books on CR propagation are numerous, and we refer the reader to *e.g.* Strong et al. (2007) for a recent review, and to Berezinskii et al. (1990) and Longair (1992, 1994) for valuable books. A detailed description of CR electron[†]propagation can be found in Delahaye et al. (2010).

Once produced, stable charged CRs (among which electrons) in the GeV-TeV energy range may experience different processes. The dominant ones are diffusion in space (due to scattering with magnetic turbulences and to convective winds) and diffusion in momentum (energy losses — negligible for CR nuclei — and diffusive reacceleration — negligible above a few GeV). Electron propagation in this energy range is almost completely set by spatial diffusion and energy losses, the latter being due to inverse Compton interactions with the interstellar radiation field (ISRF, including the CMB) and the Galactic magnetic field (synchrotron). In steady state and when convection is neglected, the master propagation equation associated with an electron density $\mathcal{N} \equiv dn/dE$ reads $-\vec{\nabla}\left\{K(E,\vec{x})\,\vec{\nabla}\mathcal{N}(E,\vec{x})\right\} - \partial_E\left\{b(E)\,\mathcal{N}(E,\vec{x})\right\} = \mathcal{Q}(E,\vec{x})$, where $\mathcal{Q}$ is the source term, $K(E,\vec{x})$ is the diffusion coefficient, and $b(E) = -dE/dt$ is the energy loss rate; being set by Compton interactions,the latter strongly increases with energy ($b(E) \propto E^2$ in the Thomson approximation). The typical energy loss timescale is $\tau_l \approx 10^{16}$s at 1 GeV for Galactic electrons. Note that the diffusion coefficient can, in most of relevant situations, be considered as homogeneous, and is usually modeled as a power law, $K(E) \simeq K_0(E/E_0)^\delta$. The normalization and index can be determined from observed secondary-to-primary ratios of nuclei species which mostly depend on K_0/L, where L is the half-thickness of the diffusion zone (see *e.g.* Maurin et al. 2001; Putze et al. 2010) — values are usually found close to $K_0(E_0 = 1\,\mathrm{GeV}) \approx 3.4 \times 10^{27}\mathrm{cm}^2/\mathrm{s}$, $\delta \approx 0.7$ and $L \approx 4$ kpc. The above equation (without spatial boundaries) admits a solution in the form of a Green function $\mathcal{G}(E,\vec{x} \leftarrow E_s,\vec{x}_s) = \frac{\exp\left\{-\frac{(\vec{x}_s-\vec{x})^2}{\lambda^2}\right\}}{b(E)(\pi\,\lambda^2)^{\frac{3}{2}}}$ with $\lambda^2 \equiv 4\int_E^{E_s} dE'\,\frac{K(E')}{b(E')}$, where λ is mean propagation scale, of the order of $\sqrt{K_0\,\tau_l} \approx 2$ kpc, *i.e.* usually less than L (spatial boundaries can therefore be neglected to a good approximation): due to the very efficient energy losses, electrons with energies above a few tens of GeV are mostly local. This Green function allows the computation of the electron density at the Earth given a source term $\mathcal{Q}(E_s,\vec{x}_s)$ which features the spatial and energy distributions before propagation.

Primary and secondary CRs of astrophysical origin are injected in the Galactic plane, where the standard sources (SNRs and pulsars) and the ISG are located. For secondary positrons, which will constitute the "background" in the next sections of this proceeding, one can approximate the source term as a power law spectrum of index γ_s, reminiscent from the CR nuclei index, and flatly distributed in the Galactic plane, so that $\mathcal{Q}_s \propto E^{-\gamma_s}\delta(z)$. Thus (in the Thomson approximation for the energy losses), the secondary positron flux can be derived analytically: $\phi_s \propto \sqrt{\tau_l/K_0}\,E^{-\tilde{\gamma}_s}$, where $\tilde{\gamma}_s = \gamma_s + 0.5(\alpha+\delta-1)$ — $\alpha \equiv \ln(b(E)/b(E_0)/\ln(E/E_0)$, *i.e.* $\alpha = 2$ in the Thomson approximation. Note that this reasoning also holds for primaries when neglecting local discrete sources. By using the index inferred from considering CR nuclei interactions with the ISG, *i.e.* $\gamma_s \simeq 2.75$, one readily gets $\tilde{\gamma}_s \simeq 3.45$, quite close to the observed positron-only index (Delahaye et al. 2009, 2010). Nevertheless, predictions for the secondary positron flux fail to fit the positron fraction data — $f_{e^+} \equiv \phi_{e^+}/(\phi_{e^-} + \phi_{e^+})$ — leading instead to a fraction decreasing with energy (Delahaye et al. 2009, 2010). Nevertheless, taking into account the hardening in the proton spectrum above ~ 2 TeV recently observed by the CREAM experiment (Ahn et al. 2010) should result into a slightly harder secondary positron spectrum. This effect remains to be checked in detail though we do not expect it to amplify the secondary flux by more than 50%, while an enhancement factor $\gtrsim 5$ around 100 GeV is necessary to fit the data.

3 Dark matter interpretation of the positron excess

DM particle scenarios rely on physics beyond the standard model. In most of them, *e.g.* in the so-called weakly interacting massive particle (WIMP) paradigm, the total DM abundance is set by annihilation in the early universe (for reviews, see *e.g.* Jungman et al. 1996; Bergström 2000; Murayama 2007). Originally in thermal and chemical equilibrium with the primordial plasma after inflation, DM chemically decouples when the annihilation rate becomes smaller than the expansion rate of the universe. This usually has to happen before big bang nucleosynthesis (BBN), which must not be unsettled, when WIMPs are already non-relativistic — referred to as cold DM (CDM). Therefore, cosmology imposes strong constraints to the annihilation cross section, provided the expansion rate of the universe before BBN is taken standard[‡]. Typically, to get a relic abundance of $\Omega_{\rm DM} \approx 0.1/h^2$, WIMPs need a thermally averaged annihilation cross section of $\langle \sigma v \rangle \approx 3 \times 10^{-26}{\rm cm}^3/{\rm s}$.

Annihilation is revived after DM has collapsed to form galaxies, its density being large enough in these objects. WIMPs annihilation now occurs almost at rest and proceeds into pairs of standard model particles, some of them further hadronizing or decaying, usually leading to the injection of CRs with continuous energy spectra. Attempts to detect these annihilation products refer to as *indirect detection* (see *e.g.* Salati 2007). The knowledge of the DM density distribution is crucial to compute the induced CR fluxes, since the annihilation rate scales like the squared density; it is generally expressed in terms of the ratio of the mass density profile ρ to the particle mass m_χ, $n_\chi = \rho/m_\chi$, and constrained theoretically from N-body simulations and observationally from kinematic data (*e.g.* Klypin et al. 2002).

In the case of high energy positrons, which are short range CRs, the most relevant input is the local DM density set by $\rho_\odot \approx 0.3\,{\rm GeV/cm^3}$. At sufficiently high energy, positrons lose their energy before they substantially diffuse, so that one can neglect spatial diffusion to a good approximation, provided the injection rate does not fluctuate too much over short distances. In that case, the Green function defined earlier becomes $\mathcal{G}(E,\vec{x} \leftarrow E_s,\vec{x}_s) \stackrel{\lambda\to 0}{\approx} \delta^3(\vec{x}_s - \vec{x})/b(E)$. The positron flux at the Earth generated by DM annihilation is thus completely analytical: $\phi_{e^+}(E) \approx \frac{\beta\, c}{4\pi}\frac{\langle\sigma v\rangle}{2\,b(E)}\left[\frac{\rho_\odot}{m_\chi}\right]^2 \int_E^{m_\chi} dE_s\, \frac{dN_{e^+}}{dE_s}$ leading to:

$$\phi_{e^+}(E) \approx \phi^0_\chi \left[\frac{\langle\sigma v\rangle}{3\times 10^{-26}{\rm cm^3/s}}\right] \left[\frac{\tau_l}{10^{16}{\rm s}}\right] \left[\frac{\rho_\odot/(0.3\,{\rm GeV/cm^3})}{(E/1\,{\rm GeV})(m_\chi/100\,{\rm GeV})}\right]^2 \int_E^{m_\chi} dE_s\, \frac{dN_{e^+}}{dE_s}\ , \tag{3.1}$$

where we find $\phi^0_\chi = 3.2\times 10^{-6}$ ${\rm cm^{-2}}$ ${\rm s^{-1}}$ ${\rm GeV^{-1}}$ ${\rm sr^{-1}}$ — if WIMPs are Dirac fermions, an additional factor of 1/2 must be accounted for. Notice the dependence on energy and WIMP mass, which is explicit in this equation. We can further simplify it by assuming annihilation into electron-positron pairs, so that the injected spectrum $dN_{e^+}/dE_s = \delta(E_s - m_\chi)$. In this case, the positron flux associated with a WIMP mass of $m_\chi = 100$ GeV at an energy of 100 GeV is $\phi_\chi(E = m_\chi = 100\,{\rm GeV}) \approx 3.2\times 10^{-10}{\rm cm^{-2}}$ ${\rm s^{-1}}$ ${\rm GeV^{-1}}$ ${\rm sr^{-1}}$, amazingly close to the value predicted for the secondary background at this energy. This means that such a model, provided a small amplification (or *boost*) by a factor of a few, could very well explain the observed rise in the positron fraction (Pieri et al. 2009). Nevertheless, such an exclusive annihilation into lepton pairs is quite a contrived situation for WIMPs with masses greater than a few GeV, which can neither rely on sound particle physics motivations nor be easily cooked up. For other annihilation final states, like heavy quarks or massive gauge bosons, the required boost factor is much larger (see left panel of Fig. 2 in Lavalle 2010). Since the annihilation cross section is fixed by the relic abundance, this low positron flux is a quite generic prediction, valid for most of motivated DM particle scenarios like in supersymmetry or extra-dimensions (Lavalle et al. 2008a).

At this stage, the question is: are there ways to amplify the predicted signal which would be motivated by some physical arguments? Actually, there are three different tracks one can explore: (i) enhancing annihilation cross section; (ii) playing with CR propagation: theoretical uncertainties allow some freedom; (iii) considering extra (local) sources of DM.

[†]The term *electrons* will characterize both electrons and positrons when discussing general propagation features.
[‡]This could change *e.g.* in the context of quintessence as a solution to dark energy (*e.g.* Salati 2003).

3.1 Enhanced annihilation cross section

The physical motivation behind this possibility is that when WIMPs are much more massive than an exchanged virtual boson field during the annihilation process, then a resonance can occur, which can strongly amplify the cross section (referred to as *Sommerfeld enhancement*). This effect usually scales like the inverse squared velocity of WIMPs, so it is stronger in galaxies today than at the decoupling time in the early universe. Nevertheless, this effect concerns a very small part of the WIMP parameter space, and suffers severe constraints: all signals associated with the amplified final state are enhanced the same, which generally leads the predicted antiproton flux to overshoot the observational bounds, unless heavy DM particles annihilate only into leptons, which is quite contrived (Cirelli et al. 2009). Such a possibility has therefore poor relevance.

3.2 Impact of theoretical uncertainties in CR propagation

Since DM-induced CRs are produced everywhere in the Galaxy, enlarging the diffusion zone in the range permitted by theoretical uncertainties may increase the flux predictions. Nevertheless, for positrons, this would only affect the low energy part of the spectrum, since high energy positrons, bound to be short range by efficient energy losses, must originate from very local regions. Therefore, tuning the propagation parameters also fails to enhance the high energy positron flux (Lavalle et al. 2008b; Delahaye et al. 2008) — the energy loss parameters being quite well constrained.

3.3 Considering extra DM sources

The impact of DM substructures wandering in the Galactic halo was first emphasized by Silk & Stebbins (1993). Nevertheless, predicting the positron boost factor associated with these subhalos is not trivial, since it depends on both their inner properties and their spatial distribution (Lavalle et al. 2007). Even when spanning the full ranges for prescriptions coming from cosmological structure formation theory, it was actually shown that these Galactic subhalos could not increase the signal by a large factor, with an upper limit $\lesssim 20$ (Lavalle et al. 2008b). However, this upper bound is associated with a large statistical variance at high energy reflecting the fact that though the probability of finding a massive enough subhalo close to the Earth is vanishingly small, this would amplify the signal by a larger factor if this occurred. Nevertheless, even this tricky situation suffers strong constraints coming *e.g.* from gamma-ray observations which strongly disfavors it as an explanation of a rising positron fraction (Bringmann et al. 2009).

To conclude this section, we emphasize that the DM solution to the cosmic positron issue is by itself very contrived and lacks strong physical motivations. Likewise, most of attempts are now excluded by complementary constraints coming from other cosmic messengers.

4 Towards a consistent model of CR leptons

We have already underlined that pulsars have long been proposed as sources of CR positrons, and were even demonstrated, more than 15 years ago, to provide a good fit to the observed positron fraction above 5 GeV. Since there are also other astrophysical proposals beside pulsars that could provide additional positrons, the question is not really whether standard astrophysics can explain the data, but what a consistent CR model should look like — note that the whole set of data such a model has to fit must also include the individual spectra of electrons and positrons, and their sum as recently measured by Fermi and HESS up to TeV energies (Abdo et al. 2009; Aharonian et al. 2008). In fact, it is probably because it was wrongly believed that a *standard model* of CRs existed that PAMELA measurements triggered such a "buzz". Indeed, the most advertized CR model called `GALPROP` (Strong & Moskalenko 1998; Moskalenko & Strong 1998), which was too naively taken as a reference in the debate on positrons, (i) was not including any source of primary positrons at that time and (ii) was treating the injection of electrons with a smooth and continuous spatial distribution of SNRs associated with an empirical energy spectrum, which also led to the claim of an excess in the Fermi data. Aside from the lack of primary positrons in this model, it has been known for a long time that considering a smooth spatial distribution of sources for high energy electrons failed for local predictions, just because the discreteness of local sources has to manifest itself at high energy in the form of spectral fluctuations in the data (Shen 1970; Kobayashi et al. 2004). Yet, this confusion cannot be attributed to the `GALPROP` model itself, since one of its main goals was to investigate the diffuse Galactic multi-wavelength emissions originating from CR interactions with the interstellar medium (ISM), either hadronic and electromagnetic, rather than the local electron budget.

Therefore, while we can fairly talk about a *standard paradigm* for CR propagation and sources, a *standard model* is still far from achieved. A consistent prediction of the CR electron and positron fluxes at the Earth (or at any point in the Galaxy) should at least include the contributions of (i) secondaries, (ii) a smooth distribution of sources for the distant (and therefore low energy) primary component, with a radial cut-off set to a distance from the Earth for which the source discreteness effects can safely be averaged out ($\sim$ 2 kpc), and (iii) the discrete sources located inside this cut-off radius. For the latter contribution, different catalogs are available for pulsars and SNRs to constrain the relevant parameters, *e.g.* the position and age estimates (*e.g.* Manchester et al. 2005; Green 2009).

We have mostly discussed the spatial distribution that a consistent CR electron model. Nevertheless, there is still a major issue to mention: the injection from SNRs and pulsars. Indeed, though we can reasonably motivate an average power law spectrum associated with an injection rate set by the explosion rate of supernovæ and some energetics considerations for the distant component (*e.g.* Malkov & O'C Drury 2001), an accurate modeling of local sources is of paramount importance, since few of them might dominate the overall spectrum above $\sim$ 100 GeV. Thus, the overall spectrum piles up all individual contributions and likely departs from a simple power law. The individual amplitudes and spectral shapes strongly depend not only on the injected spectra, but also on the source distances and ages (Delahaye et al. 2010). Moreover, the dynamics of CR (both nuclei and electrons) injection into the ISM is still unclear (see discussion in *e.g.* O'C. Drury 2010; Blasi & Amato 2010). Nevertheless, the big advantage of local sources is that we have at hand a numerous multi-wavelength observations to build a rather constrained model for each of them (see an example in Tatischeff 2009). Such a thorough study involving sophisticated modelings for both local pulsars and SNRs remains to be achieved, though some preliminary efforts have already been undergone in this direction. Delahaye et al. (2010) have notably demonstrated that considering the observational properties of local sources is sufficient to explain the whole set of data on CR electrons and positrons despite the large theoretical uncertainties, without overtuning the parameters. This paves the road for further developments.

5 Conclusion

We have discussed the DM interpretation of the so-called electron and positron excesses, showing that it was likely too contrived to be supported from reasonable grounds, though one cannot formally exclude a DM contribution to the electron and positron spectra. We have also emphasized that consistently considering well known positron sources like pulsars can easily explain the current available data, despite the still large theoretical errors associated with the predictions. This not only means that the explanation to these excesses is no longer an issue, but also, unfortunately, that the positron channel is no longer an interesting discovery channel in frame of indirect DM detection. Indeed, the uncertainties affecting the predictions make the background to DM searches very hard to control.

Nevertheless, these new measurements of high energy CR electrons allow us to refine the current models of CR propagation and sources. Beside studying more sophisticated propagation treatments (*e.g.* Shalchi 2009), improving and testing the physics of CR injection from sources is likely an important topic for the next few years, which can now be implemented thanks to these unprecedented new data. Finally, clarifying our understanding of local CR electrons will have a paramount impact on the predictions for associated multi-wavelength electromagnetic diffuse emissions on the Galactic scale. Among interesting topics, this may provide novel approaches to study the Galactic magnetic fields through the synchrotron emission, and also the diffuse gamma-ray emission from the Galactic center. It is clear that the forthcoming lower frequency data expected from instruments like Planck or Herschel (Tauber et al. 2010; Walmsley et al. 2010) will be precious in this research field, as well as higher energy data on local electrons expected from AMS-02[§].

I am grateful to the PCHE scientific committee for having selected this topic among so many other interesting ones for the plenary PCHE talk. It is also a pleasure to thank some of my collaborators in this field for participation to the work itself and/or interesting discussions, namely T. Delahaye, R. Lineros, A. Marcowith, D. Maurin and P. Salati.

References

Abdo, A. A., Ackermann, M., Ajello, M., et al. 2009, Physical Review Letters, 102, 181101

[§] `http://ams.cern.ch/` `http://www.ams02.org/`

Adriani, O., Barbarino, G. C., Bazilevskaya, G. A., et al. 2009, Nature, 458, 607

Aharonian, F., Akhperjanian, A. G., Barres de Almeida, U., et al. 2008, Physical Review Letters, 101, 261104

Aharonian, F. A., Atoyan, A. M., & Voelk, H. J. 1995, A&A, 294, L41

Ahn, H. S., Allison, P., Bagliesi, M. G., et al. 2010, ApJL, 714, L89

Alcaraz, J., Alpat, B., Ambrosi, G., et al. 2000, Physics Letters B, 484, 10

Arons, J. 1981, in IAU Symposium, Vol. 94, Origin of Cosmic Rays, ed. G. Setti, G. Spada, & A. W. Wolfendale, 175–204

Baltz, E. A. & Edsjö, J. 1998, Phys. Rev. D, 59, 023511

Barwick, S. W., Beatty, J. J., Bhattacharyya, A., et al. 1997, ApJL, 482, L191

Berezhko, E. G., Ksenofontov, L. T., Ptuskin, V. S., Zirakashvili, V. N., & Völk, H. J. 2003, A&A, 410, 189

Berezinskii, V. S., Bulanov, S. V., Dogiel, V. A., & Ptuskin, V. S. 1990, Astrophysics of cosmic rays (Amsterdam: North-Holland, 1990, edited by Ginzburg, V.L.)

Bergström, L. 2000, Reports on Progress in Physics, 63, 793

Blasi, P. 2009, Physical Review Letters, 103, 051104

Blasi, P. & Amato, E. 2010, arXiv:1007.4745

Boulares, A. 1989, ApJ, 342, 807

Bringmann, T., Lavalle, J., & Salati, P. 2009, Physical Review Letters, 103, 161301

Chi, X., Cheng, K. S., & Young, E. C. M. 1996, ApJL, 459, L83

Cirelli, M., Kadastik, M., Raidal, M., & Strumia, A. 2009, Nuclear Physics B, 813, 1

Cumberbatch, D. & Silk, J. 2007, MNRAS, 374, 455

Delahaye, T., Donato, F., Fornengo, N., et al. 2009, A&A, 501, 821

Delahaye, T., Lavalle, J., Lineros, R., Donato, F., & Fornengo, N. 2010, arXiv:1002.1910

Delahaye, T., Lineros, R., Donato, F., Fornengo, N., & Salati, P. 2008, Phys. Rev. D, 77, 063527

Fanselow, J. L., Hartman, R. C., Hildebrad, R. H., & Meyer, P. 1969, ApJ, 158, 771

Golden, R. L., Mauger, B. G., Horan, S., et al. 1987, A&A, 188, 145

Green, D. A. 2009, Bull. Astron. Soc. Ind., 37, 45

Gunn, J. E., Lee, B. W., Lerche, I., Schramm, D. N., & Steigman, G. 1978, ApJ, 223, 1015

Harding, A. K. & Ramaty, R. 1987, in International Cosmic Ray Conference, Vol. 2, International Cosmic Ray Conference, 92

Jungman, G., Kamionkowski, M., & Griest, K. 1996, Phys. Rept., 267, 195

Klypin, A., Zhao, H., & Somerville, R. S. 2002, ApJ, 573, 597

Kobayashi, T., Komori, Y., Yoshida, K., & Nishimura, J. 2004, ApJ, 601, 340

Lavalle, J. 2010, in American Institute of Physics Conference Series, Vol. 1241, American Institute of Physics Conference Series, ed. J.-M. Alimi & A. Fuözfa, 398–407

Lavalle, J., Nezri, E., Athanassoula, E., Ling, F.-S., & Teyssier, R. 2008a, Phys. Rev. D, 78, 103526

Lavalle, J., Pochon, J., Salati, P., & Taillet, R. 2007, A&A, 462, 827

Lavalle, J., Yuan, Q., Maurin, D., & Bi, X.-J. 2008b, A&A, 479, 427

Longair, M. S. 1992, High energy astrophysics. Vol.1: Particles, photons and their detection (High Energy Astrophysics, by Malcolm S. Longair, pp. 436. ISBN 0521387736. Cambridge, UK: Cambridge University Press, March 1992.)

Longair, M. S. 1994, High energy astrophysics. Vol.2: Stars, the galaxy and the interstellar medium (Cambridge: Cambridge University Press, —c1994, 2nd ed.)

Malkov, M. A. & O'C Drury, L. 2001, Reports on Progress in Physics, 64, 429

Manchester, R. N., Hobbs, G. B., Teoh, A., & Hobbs, M. 2005, AJ, 129, 1993

Maurin, D., Donato, F., Taillet, R., & Salati, P. 2001, ApJ, 555, 585

Moskalenko, I. V. & Strong, A. W. 1998, ApJ, 493, 694

Murayama, H. 2007, arXiv:0704.2276

O'C. Drury, L. 2010, arXiv:1009.4799

Pieri, L., Lavalle, J., Bertone, G., & Branchini, E. 2009, arXiv:0908.0195

Putze, A., Derome, L., & Maurin, D. 2010, A&A, 516, A66

Roberts, J. P. 2010, arXiv:1005.4668

Salati, P. 2003, Physics Letters B, 571, 121

Salati, P. 2007, Proceedings of Science, Cargese 2007, 009

Shalchi, A. 2009, Nonlinear Cosmic Ray Diffusion Theories (Springer)

Shaviv, N. J., Nakar, E., & Piran, T. 2009, Physical Review Letters, 103, 111302

Shen, C. S. 1970, ApJL, 162, L181
Silk, J. & Srednicki, M. 1984, Physical Review Letters, 53, 624
Silk, J. & Stebbins, A. 1993, ApJ, 411, 439
Stecker, F. W. 1978, ApJ, 223, 1032
Strong, A. W. & Moskalenko, I. V. 1998, ApJ, 509, 212
Strong, A. W., Moskalenko, I. V., & Ptuskin, V. S. 2007, Annual Review of Nuclear and Particle Science, 57, 285
Sturrock, P. A. 1970, Nature, 227, 465
Tatischeff, V. 2009, A&A, 499, 191
Tauber, J. A., Mandolesi, N., Puget, J., et al. 2010, A&A, 520, A1
Tylka, A. J. 1989, Physical Review Letters, 63, 840
Walmsley, C. M., Bertout, C., Combes, F., et al. 2010, A&A, 521
Zeldovich, Y. B., Klypin, A. A., Khlopov, M. Y., & Chechetkin, V. M. 1980, Sov. J. Nucl. Phys., 31, 664

THE EROS-2 ARCHIVE: IMPLEMENTATION AND APPLICATIONS

J.B. Marquette[1], E. Lesquoy[1,2], J.P. Beaulieu[1] and P. Tisserand[2,3]

Abstract. We present the strategy adopted to make the EROS-2 data publicly available. Applications based on these data are presented as well.

Keywords: magellanic clouds, galactic center, spiral arms, EROS-2, surveys, photometry, light curves, metallicity

1 Introduction

The EROS-2 (Expérience de Recherches d'Objets Sombres) has observed in a wide field configuration more than 200 square degrees towards the Magellanic Clouds, the Galactic center and the Spiral arms in order to probe the baryonic dark matter in the Galactic halo. The photometric data were acquired between July 1996 and February 2003 using the MARLY telescope at La Silla (1 m Ritchey- Chrétien, f/5.14), with a dichroic beam-splitter; this allowed simultaneous imaging to be completed in two non-standard broad passbands, the so-called EROS filters B_E (420-720 nm, blue channel) and R_E (620-920 nm, red channel). Each camera consisted of a mosaic of eight 2K 2K LORAL CCDs with a pixel size of 0.6 arcsec, and a field of view of 0.7 deg (right ascension) times 1.4 deg (declination). It resulted a unique set of more than 87 million stellar light curves and a collection of about 15 Tb of science images which are worth publishing for public uses.

2 Architecture

It is planned to have three levels:

1. The light curves were transferred at the Time Series Center of the Harvard University (Cambridge, Massachusetts, USA; PI: Pavlos Protopapas) for future availability through a web interface shared with other surveys like MACHO or OGLE2. More details on the TSC and its projects can be found at the URL `http://timemachine.iic.harvard.edu/`

2. The catalogues describing the 87 million stellar objects will be published in the near future through the CDS (Strasbourg). The paper describing these catalogues is in preparation.

3. The science images obtained during the 7 years of observation were transferred on a dedicated RAID system at the IAP for systematic astrometric calibration and filtering process. They will be published in the future on a VO system to be defined.

[1] Institut d'Astrophysique de Paris, CNRS, UMR7095, UPMC Univ Paris 06, 98bis Bd Arago, F-75014, Paris, France
[2] CEA, DSM, DAPNIA, Centre d'Etudes de Saclay, F-91191 Gif-sur-Yvette Cedex, France
[3] Research School of Astronomy & Astrophysics, Mount Stromlo Observatory, Cotter Road, Weston ACT 2611, Australia

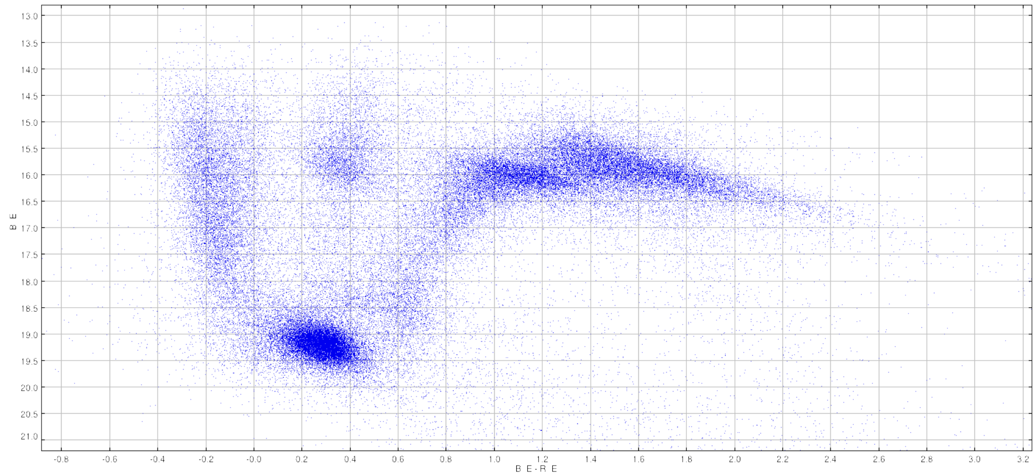

Fig. 1. Color-magnitude diagram (B_E vs. $B_E - R_E$) of the variables identified in the LMC (71620 objects are visible).

3 Applications

We have used the EROS-2 database for various applications, some of them are detailed below:

1. Search for periodic variables: we have conducted a systematic search of periodic objects using a dedicated pipeline based on a periodogram method (Analysis of Variance, see Schwarzenberg-Czerny (2003)). The figure 1 shows a color-magnitude diagram (B_E vs. $B_E - R_E$) of the variables identified in the LMC (71620 objects are visible). These objects will be published in the catalog paper cited above.

2. R Coronae Borealis: we have conducted a systematic search of R Coronae Borealis objects in the database. R Coronae Borealis stars (RCB) are a rare type of evolved carbon-rich supergiant stars that are increasingly thought to result from the merger of two white dwarfs, called the Double degenerate scenario. This scenario is also studied as a source, at higher mass, of type Ia Supernovae (SnIa) explosions. Therefore a better understanding of RCBs composition would help to constrain simulations of such events (Tisserand et al. 2004, 2008, 2009).

3. Double mode Cepheids: We have conducted a systematic search of double mode Cepheids (beat Cepheid, BC) in the Magellanic Clouds (Marquette et al. 2009). A double mode Cepheid pulsates either in the first overtone and fundamental modes (FO/F), or in the second and first overtone modes (SO/FO). It is clearly established that the period ratio (higher to lower mode) of the FO/F pulsators is around 0.72, while that of SO/FO objects is near 0.80. For the FO/F pulsators it is well known that the period ratio depends on the metallicity Z. We identify 74 FO/F BCs in the LMC and 41 in the SMC, and 173 and 129 SO/FO pulsators in the LMC and SMC, respectively; 185 of these stars are new discoveries. For nearly all the FO/F objects we determine minimum, mean, and maximum values of the metallicity.

References

Marquette, J. B., Beaulieu, J. P., Buchler, J. R., et al. 2009, A&A, 495, 249

Schwarzenberg-Czerny, A. 2003, in Astronomical Society of the Pacific Conference Series, Vol. 292, Interplay of Periodic, Cyclic and Stochastic Variability in Selected Areas of the H-R Diagram, ed. C. Sterken, 383

Tisserand, P., Marquette, J. B., Beaulieu, J. P., et al. 2004, A&A, 424, 245

Tisserand, P., Marquette, J. B., Wood, P. R., et al. 2008, A&A, 481, 673

Tisserand, P., Wood, P. R., Marquette, J. B., et al. 2009, A&A, 501, 985

SF2A 2010
S. Boissier, M. Heydari-Malayeri, R. Samadi and D. Valls-Gabaud (eds)

IMPROVEMENT OF ATOMIC MODELS FOR NLTE RADIATIVE TRANSFER IN ATMOSPHERES OF LATE TYPE STARS

T. Merle[1], F. Thévenin[1], B. Pichon[1] and L. Bigot[1]

Abstract. We present our first results on NLTE line transfer for Mg I, Ca I and Ca II in atmospheres of late type stars. This work prepares for the analysis of future spectroscopic data of the Gaia mission. To do this, we have updated atomic models of magnesium and calcium. This work on NLTE effects will also be applied to correct the determination of LTE chemical abundances for late type stars.

Keywords: radiative transfer, stars: abundances, stars: atmospheres, stars: late type

1 Introduction

The determination of stellar chemical abundances is an important clue to understand chemical evolution of galaxies. The classical line formation synthesis is based on a strong assumption: the Local Thermodynamic Equilibrium (LTE) which means that Boltzmann and Saha laws are verified everywhere in the line forming region. This assumption leads to consider independently all the lines of the same element as two level atom models. But several radiative mechanisms can affect a level population using all the other excited levels or other ionization stages making the two level atom model poorly realistic. To improve accuracy in the abundance analyses, we relax the assumption of LTE and build atoms taking into account as many energy levels as possible with all available radiative and collisional transitions between them: this is the Non LTE (NLTE) approach.

In this work, we focus on α elements, starting with magnesium and calcium, because they are good tracers of stellar populations in galaxies, with several optical and Infra-Red (IR) lines. Moreover, these elements are crucial for the Gaia spatial mission (Katz et al. 2004). A medium resolution spectrograph RVS (Radial Velocity Spectrometer) will observe in the region of the Ca II IR triplet lines with few iron, silicon and magnesium lines, doing hundreds of million of spectra to analyze. Therefore, it will be necessary to have a grid of synthetic spectra and NLTE corrections for realistic abundance determination.

In the first part, we present the atom modelling, then we test the validity of these model atoms on solar line profiles and finally we present the NLTE computations for a grid of stellar parameters using the NLTE 1D radiative transfer code MULTI (Carlsson 1986) and the MARCS model atmospheres (Gustafsson et al. 2008).

2 Atom modelling

In order to model an atom, one has to collect:

– the excited levels with their energies, statistical weights and electronic configurations;

– the ionization cross sections of these levels caused by the radiative field and by the collisions;

– the oscillator strengths and spectral broadening parameters of the radiative transitions;

– the cross-sections (when available, otherwise semi-empirical formulae) for the collisional transitions.

We have developed a code that compiles data from atomic databases like NIST*, TopBase†, VALD‡, Kurucz§, from literature for electronic collisional cross-sections (Burgess et al. 1995; Samson & Berrington 2001), Van

[1] Université de Nice Sophia-antipolis, Laboratoire Cassiopée (UMR 6202 du CNRS), Observatoire de la Côte d'Azur (OCA), B.P. 4229, 06304 Nice Cedex 4, France

*available at: `http://physics.nist.gov/asd3`

†available at: `http://cdsweb.u-strasbg.fr/topbase/topbase.html`

‡available at: `http://vald.astro.univie.ac.at/$\sim$vald/php/vald.php`

§available at: `http://www.cfa.harvard.edu/amp/ampdata/kurucz23/sekur.html`

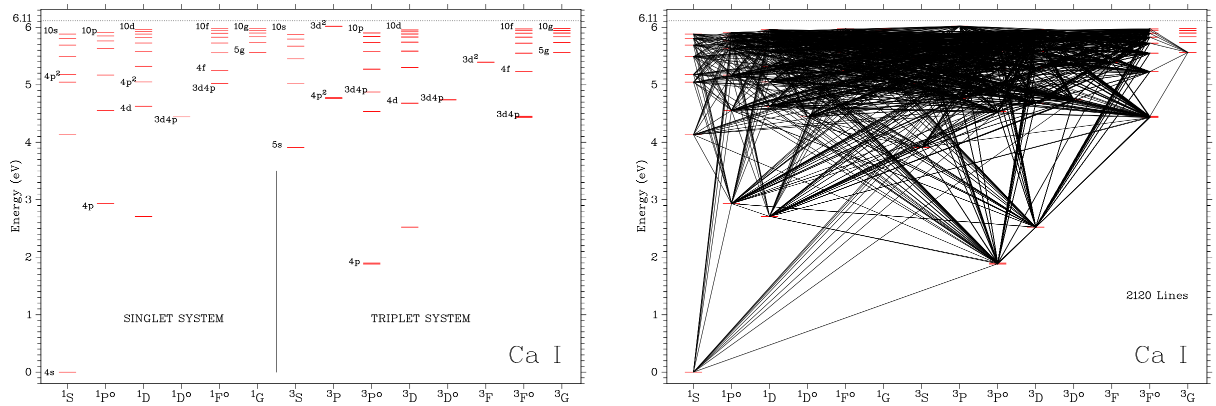

Fig. 1. Grotrian diagram of Ca I. Neutral calcium is a two-electron atom which implies two multiplicity systems: a singlet system and a triplet system where each level contains three fine levels except for ^{3}S terms. Left panel: energy levels; fine structure is presented but not visible at this scale. Right panel: radiative transitions; all transitions between fine levels considered are identified from VALD.

der Waals broadening parameter (Anstee & O'Mara 1995; Barklem & O'Mara 1997, 1998) and semi-empirical formulae for electronic collisional transitions (Van Regemorter 1962; Seaton 1962). In this work, we have neglected the contribution of inelastic collisions with neutral hydrogen (because there is a lack of accurate quantum mechanical calculations to determine their importance) and the Stark effect in the line broadening parameters. Some of the best complete atoms for Mg I and Ca I/II were constructed respectively by Przybilla et al. (2001) and by Mashonkina et al. (2007) but without taking the fine structure into account. We have included it for all levels until $n = 10$ and $l = 4$ for Mg I, Ca I and Ca II. An example of a Grotrian diagram for Ca I is presented in Fig. 1.

We have tested model atoms on solar lines, using theoretical LTE 1D MARCS solar atmosphere, chemical mixture from Grevesse et al. (2007) and opacities from the Uppsala package (Gustafsson 1973). The code MULTI2.2 (Carlsson 1986), slightly modified for the collisional transition part, solves the radiative transfer and statistical equilibrium equations consistently and computes line intensities, equivalent widths and contribution functions for all the radiative transitions. We are able to reproduce the main solar lines for Mg I, Ca I and Ca II in a good agreement with the LTE computations and solar atlas¶ from Brault & Neckel (1987), except for the Mg I optical triplet (5167, 5172, 5183 Å) and the line cores of Ca II IR triplet because they are formed in atmospheric layers not included in the theoretical MARCS models (see Merle et al., in prep., for more details).

3 NLTE equivalent width corrections for a grid of stellar parameters

We have selected stellar parameters for late type stars with an effective temperature range of $[5000, 7000]$ K with a 500 K step, a logarithm of surface gravity of 3, 4 and 4.5 and a range of metallicity of $[-3, 0]$ with 1 dex step. Plane parallel model atmospheres with standard composition from the MARCS site‖ (Gustafsson et al. 2008) have been adopted. We have computed LTE equivalent widths W^* and NLTE equivalent widths W for all lines of Mg I, Ca I and Ca II model atoms. Fig. 2 and Fig. 3 show variations of the W/W^* ratio for the Mg I 8736 Å and the Ca II 8542 Å lines with stellar parameters. We have chosen these lines because they are in RVS wavelength range.

For stars with solar abundance [Fe/H] $= 0$, we can see a negligible deviation from LTE whatever the effective temperature and surface gravity for Ca II 8542 Å line. Concerning the Mg I 8736 Å line, we find a deviation from LTE of about +20%. As shown in the other panels of Fig. 2 and Fig. 3 and for late type stars with [Fe/H]< -1, the general trend is that the LTE deviation increases with the decreasing metallicities for both lines but not in the same way; this implies a negative correction for the magnesium LTE abundance deduced from the 8736 Å line and a positive correction for the calcium LTE abundance deduced from the 8542 Å line. At metallicity of

¶available at: ftp://ftp.hs.uni-hamburg.de/pub/outgoing/FTS-Atlas

‖available at: `http://marcs.astro.uu.se`

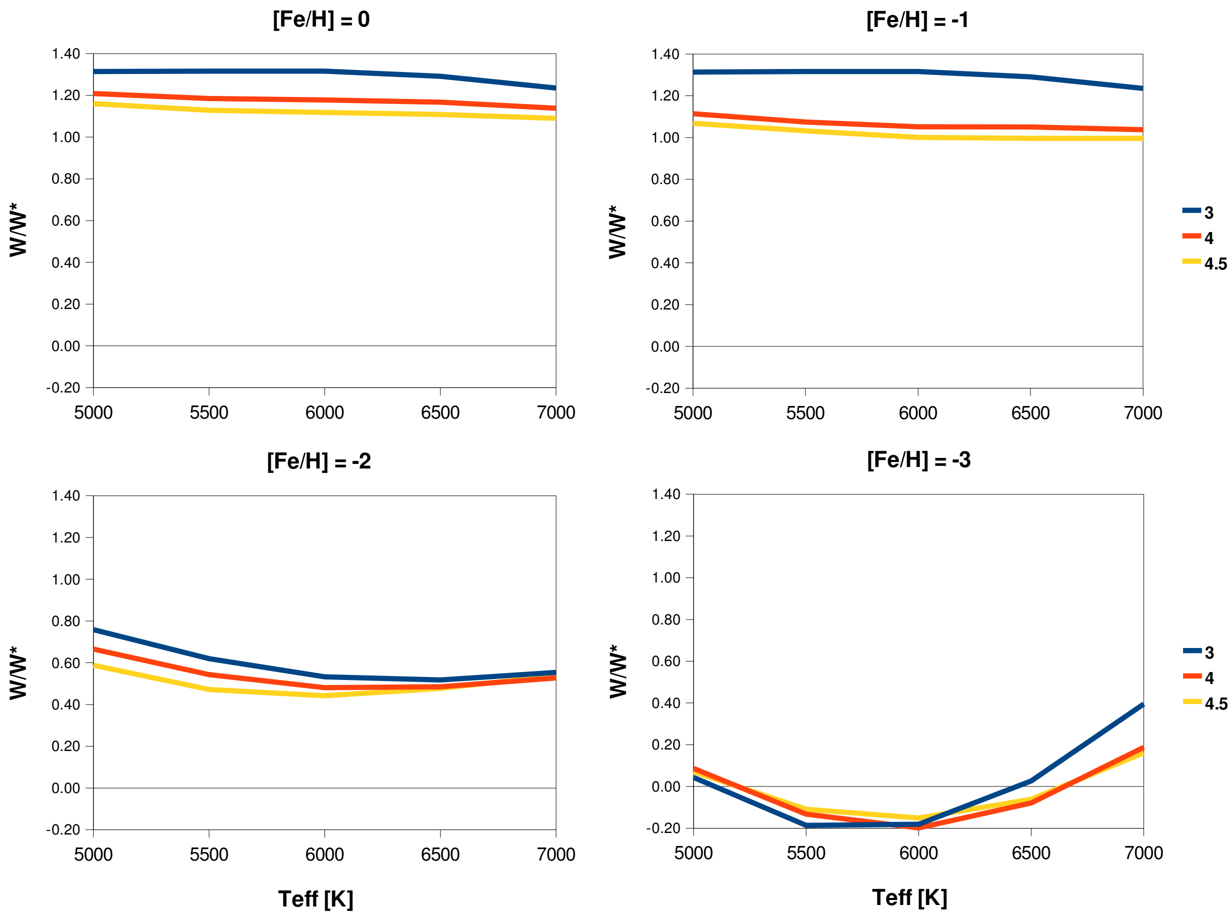

Fig. 2. W/W^* ratio vs effective temperature $T_{\rm eff}$ for Mg I 8736 Å. W stands for the NLTE theoretical equivalent width whereas W^* is the LTE theoretical one. Each of the four panels corresponds to a global metallicity [Fe/H] as indicated. The W/W^* are plotted for surface gravities: $\log g = 3$ (blue), $\log g = 4$ (red) and $\log g = 4.5$ (yellow).

[Fe/H] $= -3$, the W/W^* ratio of Mg I 8736 Å line has negative values corresponding to an emission line but it may not be observable since the line is very weak. The W/W^* corrections for more lines in optical and RVS domains will be available in Merle et al. (in prep).

4 Conclusions

We have performed a realistic atom modelling for Mg I, Ca I and Ca II with more energy levels, more transitions than we can be found in the literature, taking into account fine structure of energy levels, and the best physics available concerning photo-ionization, electronic collisions and hydrogen elastic collisions. Then, we computed a grid of NLTE equivalent width corrections for late type stars that will be useful to study galactic abundances and its evolution. We confirm that NLTE effects are important for metal poor stars, but need to be studied line by line for a quantitative prediction of the error on the LTE abundance determinations.

TM is granted by OCA and Région PACA. This work was supported by the "Action Spécifique Gaia". We thank the SAM collaboration for helpful discussions.

References

Anstee, S. D., O'Mara, B. J. 1995, MNRAS, 276, 859

Barklem, P. S., O'Mara B. J. 1997, MNRAS, 290, 102

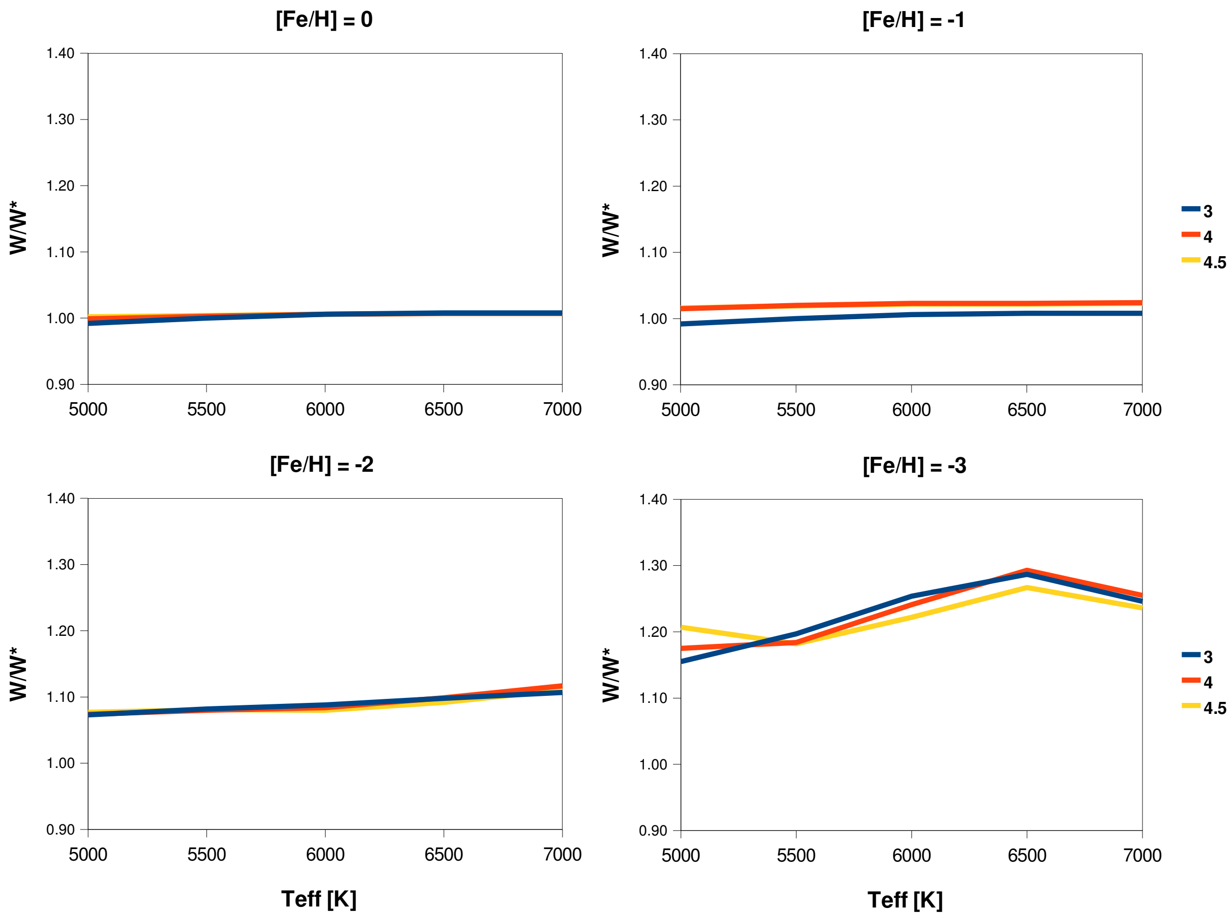

Fig. 3. W/W^* ratio vs effective temperature $T_{\rm eff}$ for Ca II 8542 Å. W stands for the NLTE theoretical equivalent width whereas W^* is the LTE theoretical one. Each of the four panels corresponds to a global metallicity [Fe/H] as indicated. The W/W^* are plotted for surface gravities: $\log g = 3$ (blue), $\log g = 4$ (red) and $\log g = 4.5$ (yellow).

Barklem, P. S., O'Mara B. J. 1998, MNRAS, 300, 863

Brault, J. & Neckel, H. 1987, Spectral atlas of the Sun intensity/flux from 3290 to 12510Å, unpublished

Burgess, A., Chidichimo, M. C., Tully, J. A. 1995, A&A, 300, 627

Carlsson, M. 1986, Uppsala Astronomical Observatory Report, 33

Grevesse, N., Asplund, M., Sauval, A. J. 2007, Space Sci Rev, 130, 105

Gustafsson, B. 1973, Uppsala Astr. Obs. Ann., 5, No. 6

Gustafsson, B., Edvardsson, B., Eriksson, K. et al. 2008, A&A, 486, 951

Katz, D., Munari, U., Cropper M. et al. 2004, MNRAS, 354, 1223

Mashonkina, L., Korn, A. J., Przybilla, N. 2007, A&A, 461, 261

Merle, T., Thévenin, F., Bigot, L., Pichon, in prep., MNRAS

Przybilla, N., Butler, K., Becker, S. R., Kudritzki, R. P. 2001, A&A, 369, 1009

Samson, A. M. & Berrington, K. A. 2001, ADNDT, 77, 87

van Regemorter, H. 1962, ApJ, 136, 906

Seaton, M. J. 1962, Proc. Phys. Soc., 79, 1105

SF2A 2010
S. Boissier, M. Heydari-Malayeri, R. Samadi and D. Valls-Gabaud (eds)

A SINFONI INTEGRAL FIELD SPECTROSCOPY SURVEY FOR GALAXY COUNTERPARTS TO DAMPED LYMAN-α SYSTEMS

C. Péroux[1], N. Bouché[2], V. P. Kulkarni[2], D. G. York[3] and G. Vladilo[4]

Abstract. Details of processes through which galaxies convert their gas into stars need to be studied in order to obtain a complete picture of galaxy formation. One way to tackle these phenomena is to relate the H I gas and the stars in galaxies. Here, we present dynamical properties of Damped and sub-Damped Lyman-α Systems identified in H-α emission with VLT/SINFONI at near infra-red wavelengths. While the DLA towards Q0302−223 is found to be dispersion-dominated, the sub-DLA towards Q1009−0026 shows clear signatures of rotation. We use a proxy to circular velocity to estimate the mass of the halo in which the sub-DLA resides and find $M_{halo}=10^{12.6}$ $M_{\odot}$. We also derive dynamical masses of these objects, and find $M_{dyn}=10^{10.3}$ $M_{\odot}$ and $10^{10.9}$ $M_{\odot}$. For one of the two systems (towards Q0302−223), we are able to derive a stellar mass of $M_{*}=10^{9.5}$ $M_{\odot}$ from Spectral Energy Distribution fit. The gas fraction in this object is $1/3^{rd}$, comparable to similar objects at these redshifts. Our work illustrates that detailed studies of quasar absorbers can offer entirely new insights into our knowledge of the interaction between stars and the interstellar gas in galaxies.

Keywords: galaxies: kinematics and dynamics, quasars: absorption lines, quasars: individual: Q0302−223, Q1009−0026

1 Introduction

Tremendous progress has been made over the last decade in establishing a broad cosmological framework in which galaxies and large-scale structure develop hierarchically over time, as a result of gravitational instabilities in the density field. The next challenge is to understand the physical processes of the formation of galaxies and structures and their interactions with the medium surrounding them. Of particular importance are the processes through which these galaxies accrete gas and subsequently form stars (Putman et al. 2009). The accretion of baryonic gas is complex. Recently, several teams (Birnboim & Dekel 2003, Keres et al. 2005) have realized that, in halos with mass $< 10^{11.5-12}$ $M_{\odot}$, baryonic accretion may not involve the traditional shock heating process of White & Rees (1978). Similarly, details of processes through which galaxies convert their gas into stars are still poorly understood. But the observational evidences for accretion are scarce. A related signature is that the total amount of neutral gas in the Universe, Ω_{HI}, is almost constant over most of the cosmic time (Prochaska, Herbert-Fort & Wolfe 2005, Péroux et al. 2005, Noterdaeme et al. 2009), unlike the history of the star formation rate which peaks around z=1 (Hopkins & Beacom 2006 and references therein). This shows the importance of ongoing global gas accretion and the conversion of atomic gas to molecular gas in the star formation process (Hopkins, Rao & Turnshek 2005, Bauermeister et al. 2010).

One way to tackle these problems is to relate the H I gas and the stars in galaxies. While radio observations now provide detailed constraints on the H I content of large sample of galaxies (Zwaan et al. 2005), they are still limited to redshift z∼0. Conversely, the study of quasar absorbers, the galaxies probed by the absorption they produce in a background quasar spectrum, is insensitive to the redshift of the object (Wolfe et al. 1995). Indeed, the H I content of the strongest of these quasar absorbers, the so-called Damped Lyman-α systems (DLAs), have been measured in samples of several hundreds of objects from the Sloan Digital Sky Survey (SDSS). However, studying the stellar content of these systems has proven very challenging until now.

[1] Laboratoire d'Astrophysique de Marseille, OAMP, Université Aix-Marseille & CNRS, 38 rue Frédéric Joliot Curie, 13388 Marseille cedex 13, France
[2] Department of Physics, University of California, Santa Barbara, CA 93106, USA.
[3] Dept. of Astronomy and Astrophysics, Univ. of Chicago, 5640 S. Ellis Ave, Chicago, IL 60637, USA.
[4] Osservatorio Astronomico di Trieste - INAF, Via Tiepolo 11 34143 Trieste, Italy.

Table 1. Summary of the properties of two absorber galaxies detected with SINFONI.

Quasar	$z_{\rm abs}$	$\log N(H\ i)$ [atoms/cm^2]	[Zn/H] [km/s]	F(H-α) [erg/s/cm^2]	Lum(H-α) [erg/s]	SFR ^{a} [M$_\odot$/yr]
Q0302−223	1.009	$20.36^{+0.11}_{-0.11}$	-0.51 ± 0.12	$7.7\pm2.7\times10^{-17}$	$4.1\pm1.4\times10^{41}$	1.8 ± 0.6
Q1009−0026	0.887	$19.48\ ^{+0.05}_{-0.06}$	$+0.25\pm0.06$	$17.1\pm6.0\times10^{-17}$	$6.6\pm2.3\times10^{41}$	2.9 ± 1.0

^{a}**:** The SFR estimates are not corrected for dust extinction.

2 SINFONI detections of H-α emission

The observations presented were carried out at the European Southern Observatory with the near-infrared field spectrometer SINFONI on Unit 4 of the Very Large Telescope. In Péroux et al. (2010a), we have reported two secure detections of the redshifted H-α emission of high H I column density quasar absorbers: a DLA with log $N(H\ i)$=20.36±0.11 at $z_{\rm abs}$=1.009 towards Q0302−223 and a sub-DLA with log $N(H\ i)$=$19.48^{+0.05}_{-0.06}$ at $z_{\rm abs}$=0.887 towards Q1009−0026 (see Table 1). We detect galaxies associated with the quasar absorbers at impact parameters of 25 and 39 kpc away from the quasar sightlines, respectively.

For field Q0302−223 where the quasar is bright enough, we have used the quasar itself as a natural guide star for adaptive optics in order to improve the spatial resolution (see Table 1). The two data sets have a resulting Point Spread Function (PSF) of 0.7” and 1.0”. Both the objects in our study have well-determined absorption line properties determined from spectra of the background quasars. Thus, the metallicities are well-determined for both of our target absorbers. An estimate of the emission metallicities is made based on the N II/ H-α parameter (Pettini & Pagel 2004): the galaxy with the smaller absorption line metallicity also has the smaller emission-line metallicity. The absorber toward Q0302−223 is the more gas-rich absorber, while that toward Q1009−0026 is the more metal-rich absorber.

Using the H-α luminosity we then derived the star formation rate assuming the Kennicutt (1998) flux conversion corrected to a Chabrier (2003) initial mass function. We find low star formation rates (not corrected for dust extinction), of 1.8±0.6 and 2.9±1.0 M$_\odot$/yr (see Table 1). These values of star formation rates are among the lowest that have ever been possible to detect in quasar absorber searches with ground-based observations at z$\sim$1 and 2.

3 Kinematics and mass estimates

In addition to the identification and redshift confirmation of the galaxy responsible for the quasar absorbers, the SINFONI data allow for a study of the dynamical properties of the galaxies (Péroux et al. 2010b). We find that galaxy associated with the DLA identified towards Q0302−223 shows little signs of rotation and significant amounts of dispersions. Moreover, the light profile and morphology provide further evidence that this galaxy is dispersion dominated, albeit it already has a disky morphology. This is indicative of a young object which is confirmed by results from a SED fit or could be due to the blending of the two components detected with HST interacting together. On the contrary, the galaxy associated with the sub-DLA towards Q1009−0026 has a morphology and kinematics consistent with that of a disk, with a normal dispersion profile peaking at the center and flattening out in the outer-parts. This object shows clear signatures of rotation with systematic velocity gradients which is not typical of local disk galaxies, but the systematic gradient still favors a spiral galaxy. It remains to be understood why such high $N(H\ i)$ column densities are found at large impact parameters (up to b=39kpc) from galaxies. The results of these are shown in Table 2.

Overall, we conclude that of the two absorbers studied, the less metal-rich absorber toward Q0302−223 arises in a gas-rich system with H-α luminosity consistent with that of a disk, while the more metal-rich absorber toward Q1009−0026 arises in a lower gas mass system but with higher total mass showing clear signs of rotation. With the limitations of small number statistics, our findings are consistent with the suggestion (Khare et al. 2007; Kulkarni et al. 2007) that the metal-rich sub-DLAs may arise in more massive galaxies compared to the DLAs, which are usually metal-poor by comparison. Our work illustrates that detailed studies of quasar absorbers can offer entirely new insights into our knowledge of the interaction between stars and the interstellar gas in galaxies.

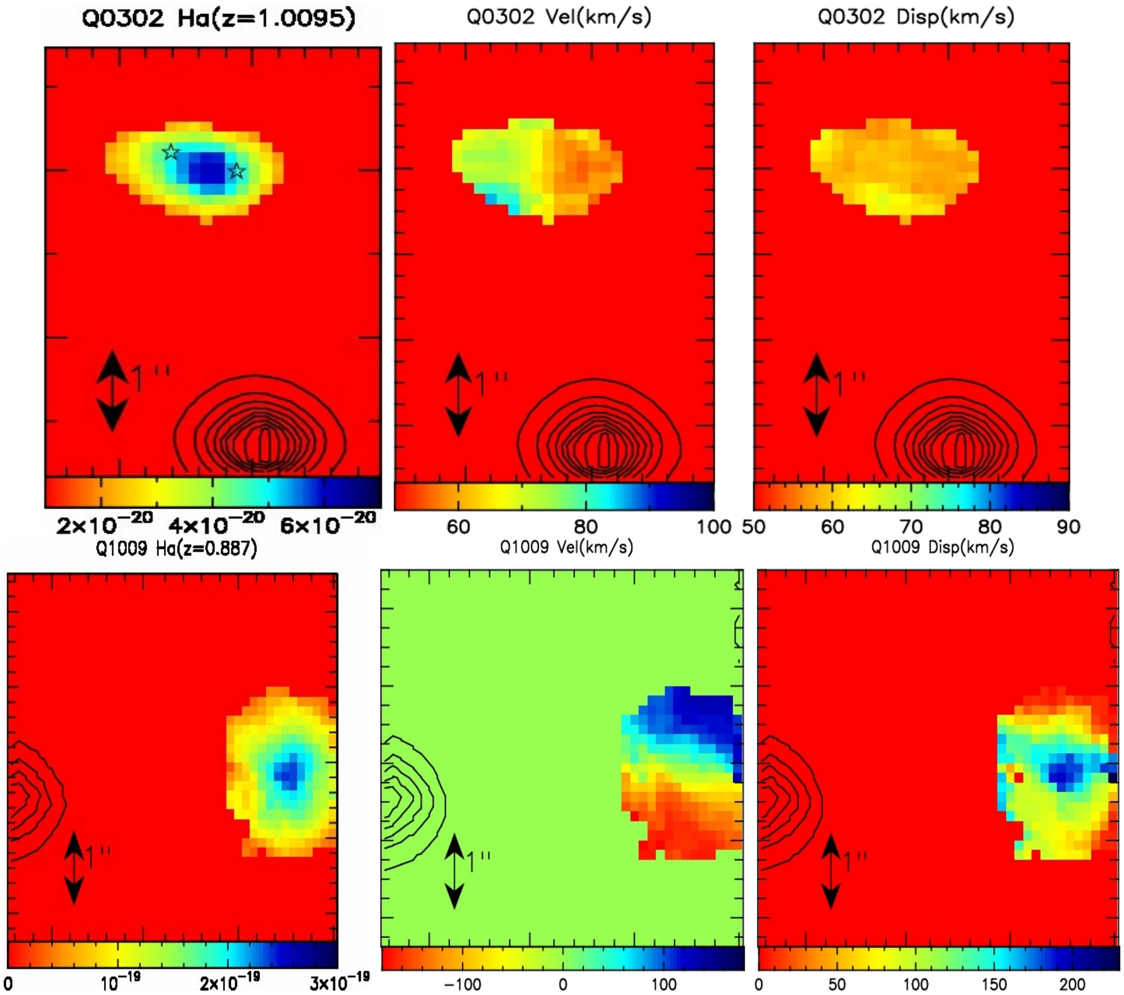

Fig. 1. H-α flux map, H-α velocity field and H-α velocity dispersion maps of the two quasar absorbers. The colour-scale indicates the flux in erg/s/cm^2 in the H-α flux map on the left and the velocities or velocity dispersions in km/s for the middle and right set of panels. North is up and east is to the left. The thin lined, black contours indicate the position of the quasar and the arrow represents 1 arcsec which corresponds to 8.1 kpc in the case of Q0302−223 and 7.8 kpc in the case of Q1009−0026. The system at the top (Q0302−223) is dispersion-dominated with H-α luminosity consistent with that of a disk. The system at the bottom (Q1009−0026) shows a blueshifted and redshifted component of the gas on its velocity map. This pattern is a clear characteristic of a rotating disk.

4 Conclusions

In conclusion, the observational set-up of SINFONI has demonstrated the power of integral field spectroscopy for deriving a number of emission properties for quasar absorbers, a type of high-redshift galaxies that have been difficult to identify in the past. Detailed dynamical properties of these galaxies with known gas characteristics could be derived. These new tools are now available to systematically study these objects. We find that the two absorbers studied here have kinematical properties similar to other galaxies studied in the same way at these and others redshifts (Epinat et al. 2009, Förster-Schreiber et al. 2006, Genzel et al. 2006, Förster-Schreiber et al. 2009).

We would like to thank the LOC for organising a very enjoyable meeting.

References

Bauermeister, A., Blitz, L. & Ma, C., 2010, ApJ, 717, 323

Table 2. Kinematic properties and mass estimates of the two $N(H\ i)$ absorbers detected.

Quasar	sin i	v/σ	$r_{1/2}$ ["]	Σ_{SFR} [$M_\odot$/yr/kpc^2]	M_{dyn} [$M_\odot$]	Σ_{gas} [$M_\odot$/pc^2]	M_{gas} [$M_\odot$]	M_{halo} [$M_\odot$]	M_* [$M_\odot$]
Q0302−223[a]	0.88	0.19	0.7	0.13	$10^{10.3}$	$10^{1.9}$	$10^{9.1}$	–	$10^{9.5}$
Q1009−0026	0.60	1.45	0.5	0.31	$10^{10.9}$	$10^{2.2}$	$10^{9.2}$	$10^{12.6}$	–

Note: The inclination is the main source of uncertainties and is estimated to be around 30%.

[a]**:** The higher-resolution HST/WFPC2 data from Le Brun et al. (1997) clearly shows that the object is subdivided into two sub-components, consistent with the elongated shape seen in the SINFONI data presented here. In this table, however, the object is treated as only one.

Birnboim, Y. & Dekel, A., 2003, MNRAS, 345, 349

Epinat, B., Contini, T., Le Fevre, O., Vergani, D., Garilli, B., Amram, P., Queyrel, J., Tasca, L. & Tresse, L., 2009, A&A, 504, 789

Förster Schreiber, N. M., Genzel, R., Lehnert, M. D., Bouché, N., Verma, A., Erb, D. K., Shapley, A. E., Steidel, C. C., Davies, R., Lutz, D., Nesvadba, N., Tacconi, L. J., Eisenhauer, F., Abuter, R., Gilbert, A., Gillessen, S. & Sternberg, A., 2006, ApJ, 645, 1062

Förster Schreiber, N. M., Genzel, R., Bouché, N., Cresci, G., Davies, R., Buschkamp, P., Shapiro, K., Tacconi, L. J., Hicks, E. K. S., Genel, S., Shapley, A. E., Erb, D. K., Steidel, C. C., Lutz, D., Eisenhauer, F., Gillessen, S., Sternberg, A., Renzini, A., Cimatti, A., Daddi, E., Kurk, J., Lilly, S., Kong, X., Lehnert, M. D., Nesvadba, N., Verma, A., McCracken, H., Arimoto, N., Mignoli, M., Onodera, M., 2009, ApJ, 706, 1375

Hopkins, A. M., Rao, S. M. & Turnshek, D. A., 2005, ApJ, 630, 108

Hopkins, A. M. & Beacom, J. F., 2006, ApJ, 651, 142

Keres, D., Katz, N., Weinberg, D. H. & Davé, R., 2005, MNRAS, 363, 2

Khare, P., Kulkarni, V. P., Péroux, C., York, D. G., Lauroesch, J. T. & Meiring, J. D., 2007, A&A, 464, 487

Kulkarni, V. P., Khare, P., Péroux, C., York, D. G., Lauroesch, J. T. & Meiring, J. D., 2007, ApJ, 661, 88

Le Brun, V., Bergeron, J., Boisse, P., Deharveng, J. M., 1997, A&A, 321, 733

Mo, H. J. & White, S. D. M., 2002, MNRAS, 336, 112

Noterdaeme, P., Petitjean, P., Ledoux, C., Srianand, R., 2009, A&A, 505, 1087

Péroux, C., McMahon, R. G., Storrie-Lombardi, L. J. & Irwin, M., 2003, MNRAS, 346, 1103

Péroux, C., Dessauges-Zavadsky, M., D'Odorico, S., Kim, T. S. & McMahon, R. G., 2005, MNRAS, 363, 479

Péroux, C., Bouché, N., Kulkarni, V. P., York, D. G. & Vladilo, G. 2010a, in press (astro-ph/1009.0025)

Péroux, C., Bouché, N., Kulkarni, V. P., York, D. G. & Vladilo, G. 2010b, in press (astro-ph/1009.0027)

Pettini, M., Ellison, S. L., Steidel, C. C., Shapley, A. E. & Bowen, D. V., 2000, ApJ, 532, 65

Pettini, M & Pagel, B. E. J., 2004, MNRAS, 348L, 59

Prochaska, J. X., Herbert-Fort, S. & Wolfe, A. M., 2005, ApJ, 635, 123

Putman, M.E., et al. 2009, "How do galaxies accrete gas and form stars?", The Astronomy & Astrophysics Decadal Survey 2010

White, S. D. M. & Rees, M. J., 1978, MNRAS, 183, 341

Wolfe, A. M., Lanzetta, K. M., Foltz, C. B. & Chaffee, F. H., 1995, ApJ, 454, 698

Zwaan, M. A., Meyer, M. J., Staveley-Smith, L.; & Webster, R. L., 2005, MNRAS, 359L, 30

SF2A 2010
S. Boissier, M. Heydari-Malayeri, R. Samadi and D. Valls-Gabaud (eds)

STELLAR ROTATION IN OPEN CLUSTERS

L. Santoro[1]

Abstract.
The goal of this work is the analysis of rotation impact on the age determination of open clusters. In this preliminary study we discuss on a statistical method to know the key parameter V_{rot}. Then we use V_{rot} estimate in stellar evolution computations (Cesam2k code) with implemented Maeder-Zahn's theory of stellar rotation.

Keywords: rotating star, statistical distribution

1 Introduction

Open clusters (OCs), young and metal rich, have an advantage on Globular clusters: they host a wide variety of stellar masses. If one want to test the influence of rotation of stars on the structure of the HR diagram and on the change of properties of stars induced by rotation, one will adopt to work on OCs. The limit of these OCs as laboratories is in the distribution of chemical abundances, most of them being close to solar abundances within a factor 3. If we prefer to test stellar physics influenced by the opacity one would use the oldest ones: the Globular clusters. In the present work we are concerned by the distribution of rotational velocities varying with the mass of the stars within a cluster and to perform test of macroscopic properties of the rotating stars induced by this parameter.

To understand how the impact of stellar rotation affect the star evolution we need to handle two difficulties: on one hand an adequate formulation of the rotation implemented in 1D stellar codes and on the other hand how we can test the theory with observations. The stellar rotation has an impact on the star evolution and on the position of the star in the HR diagram. Vega (α Lyr) had its rotational velocity ignored during all the 20th century because its spectrum did not exhibit evidence of rotation distortion of the shape of the lines. Recently interferometric measurements revealed its oblateness and its V_{rot} estimate was possible thanks to very high resolved spectrograph (Peterson et al. 2006).

In 1998, Maeder & Zahn (Maeder and Zahn 1998) have proposed a formulation of the theory of the stellar rotation adapted to 1D models. This theory has permitted some progresses in the comprehension of the HR diagrams with stellar mass above $1M_{\odot}$. For test on OCs we have to estimate the real distribution of Vrot with mass.

Why to test the Cesam2k code with the implemented theory of stellar rotation? It takes place in the ESA mission Gaia context and in particular this work is related to the group FLAME (Final Luminosity Age Mass Estimation) of CU8 (Coordination unit 8 for the astrophysical parameters) of DPAC (Data Process Analysis Consortium). Here we propose to estimate the difference on age determinated of OCs and then of stars when one use or not the rotation in the 1D codes.

2 How estimate V_{rot}

As metioned above, we need to estimate the rotational velocity to test the theory implemented in the code and then to predict the discrepancies with previous work ignoring this parameter. V_{rot} does't come from observations in a direct way. In fact the spectrum of a star gives only the projected component of rotation on the line of

[1] Université de Nice Sopha-Antiopolis, Laboratoire Cassiopée (UMR 6202 du CNRS), Observatoire de la Côte d'Azur, B.P. 4229, 06304 Nice Cedex 4, France

Parameters	Pleiades	Hyades
q	1.38	1.51
σ	8.75	4.27

Table 1. The results of our statistic analysis for Hyades and Pleiades clusters. Row 1 and row 2 represented the results of χ^2 test for the distribution parameters: the shape parameter q and the standard deviation σ.

sight: ($V_{rot}\sin i$) for which "i" is generally unknown. The position on HR diagram of rotating star is affected by this inclination factor of $\sin i$ (Kraft and Wrubel 1965) (Maeder 1998). In cluster stars in which we are interested, we consider the random distribution of the inclination angle i (Struve 1945) and we follow the work of Chandrasekhar and Munch (1950) to estimate V_{rot}. Following this work, we have an integral relation between the distributions of $V_{rot}\sin i$ and V_{rot} that allow us to estimate V_{rot} for each cluster star. The problem turn out in finding the mathematical expression of the distribution that describes both the observed distribution (Fig. 1) built with the data from catalogues (as for example Mermilliod et al. (2009) and WEBDA database, `http://www.univie.ac.at/webda/`).

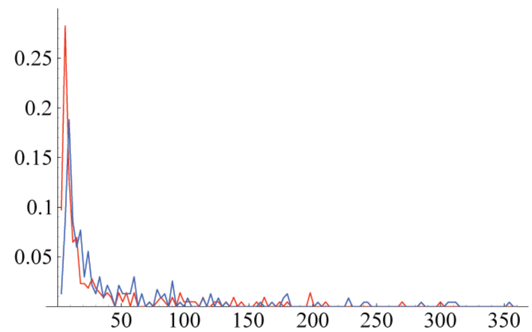

Fig. 1. V_{rot} distribution for Hyades (red) and Pleiades (blue) clusters. In x-axis there is $V_{rot}\sin i$ in km/s and in the y-axis there is the frequency normalized to 1. The important features of the distributions are a peak in the low-rotators zone and very flat in the fast-rotators zone

The Hyades cluster among several open clusters was choosen for the following reasons: its distance, its metallicity and its helium content are known with good accuracies, and there is an accurate set of measures of $V_{rot}\sin i$ also for several binary systems with well known orbital parameters, masses (Patience et al. 1988; Cayrel de Stroebel et al. 1997; Perryman et al. 1998; Lebreton et al. 2001). The $V_{rot}\sin i$ distribution shows two important features (fig. 1): it has a peak in the low rotators zone and it is very flat in the fast rotators zone. Such distribution were studied in the past and several attempts were done to fit the observed one. Chandrasekhar and Munch (1950) used a gaussian function in their pionnering work, later Deutsch (1970) proposed to use a maxwellian function to try to fit the the $V_{rot}\sin i$ distribution, but they failed to fit the whole velocities range. Similar work was done by Gaigé (1993) with a non-uniform function. For the Pleiades cluster Soares et al (2006) found a good distribution with a uniform function (Tsallis distribution) to fit the $V_{rot}\sin i$ data set. Here we follow the work of Soares et al (2006) and we use the Tsallis distribution on the Hyades and Pleiades clusters. This distribution has some parameters that we calculated through a χ^2 for the Hyades and the Pleiades clusters. We confront our results for Pleiades and we found the same values as Soares et al (2006) with a different test of convergence and a different data set. But we found different results between Hyades and Pleiades clusters, as shown in table 1, and we are investigating to understand where the difference is coming from (Santoro et al. in preparation).

Thanks to these parameters we built the uniform function that describe the $V_{rot}\sin i$ distribution and we use the relation given by Chandrasekhar and Munch (1950), in order to get the distribution of V_{rot} for all cluster stars. Besides of this, we use binary stars of the Hyades cluster to test the statistical procedure described before, we have all the orbital information for those particular system. Adding an hypothesis that the star rotational axis orientation is perpendicular to the orbital plane of the binary system(Peterson & Solensky 1988; Torres et al. I 1997; Torres et al. II 1997). we deduce two different V_{rot} estimates for the binary stars and the results are presented in the table 1 of Santoro (2010). Applying this method on the OC we estimate the ages of the OCs and we compare them with those obtain when ignoring the rotation of star in the stellar evolution codes. Non neligeable discreapencies exist and lead us to conclude that for the inversion of the HR diagram in the context of Gaia ignoring rotation lead for single stars to wrong mass (without rotation the mass are underestimated) and age estimate reach 15 percent older.

3 Conclusions

Adding this information in Cesam2k code with implemented theory of rotation of Maeder and Zahn (1998) we can evaluate the impact of rotation on cluster age determination. Now we need to introduce the von Zeippel's effect which change the uniformity of the temperature and the gravity at the surface of fast rotators. In a near future we shall work on multiple stars binary or with more components to validate all these concept and derive tables of corrections for star cluster ages whan ignoring this parameter.

We thanks ELSA project to have supported this research

References

Cayrel de Strobel, G., Soubiran, C., Friel, E., D., Ralite, N., Francois, P. 1997, A&AS, 124, 229

Chandrasekhar, S., Munch, G. 1950, ApJ, 111, 142

de Bruijne, J., H., J., Hoogerwerf, R., de Zeeuw, P., T. 2001, A&A, 367, 111

Deutsch, A., J. 1970,in Stellar rotation, IAU Colloquium, A. Sletteback, ed. (Dordrecht:Reidel), p. 207

Gaigé, Y. 1993, A&A, 269, 267

Kraft, R., P., & Wrubel, M., H. 1965, ApJ, 142, 703

Lebreton, Y., Fernandes, J., Lejeune, T. 2001, A&A, 374, 540

Maeder, A. 1998, ASPC, 131, 85

Maeder, A., & Zahn, J.-P. 1998, A&A, 334, 1000

Mermilliod, J.-C., Mayor, M., Udry, S. 2009, A&A, 498, 949

Morel, P. & Thévenin, F. 2002, A&A, 390, 611

Patience, J., Ghez, A., M., Reid, N., I., Weinberger, A., J., Matthews, K. 1988, AJ, 115, 1972

Perryman, M., A., C., Brown, A., G., A., Lebreton, Y., Gomez, A., Turon, C., Cayrel de Strobel, G., Mermilliod, J.-C., Robichon, N., Kovalevsky, J., Crifo, F. 1998, A&A, 331, 81

Peterson, D., & Solensky, R. 1988, ApJ, 333, 256

Peterson, D., M., Hummel, C., A. Pauls, T., A. *et al.* 2006, Nat, 440, 896

Santoro, L. 2010, in ELSA conference "Gaia: at the frontiers of astrometry", Sèvres, Paris, June 2010, EDP Sciences (EAS Series), editors C. Turon, F. Arenou &, F. Meynadier, in press

Soares, B., B., Carvalho, J., C., do Nascimiento Jr., J., D., De Medeiros, J., R. 2006, Physica A, 364, 413

Struve, O. 1945, Pop. Astr., 53, 202

Torres, G., Stefanik, R., P., Latham, D., W. 1997, ApJ, 485, 167

Torres, G., Stefanik, R., P., Latham, D., W. 1997, ApJ, 479, 268

UNCOVERING THE NATURE OF TIDAL TAILS IN PALOMAR 14

D. Valls-Gabaud[1], A. Sollima[2], D. Martínez-Delgado[3] and J. Peñarrubia[4]

Abstract. We have detected in deep CFHT images a pair of tidal tails extending over one degree around the distant globular cluster Palomar 14. Their characteristic S-shape and association with an extended power-law departure from the usual density profile makes this surprising detection unambiguous. We briefly discuss the mechanisms that could give rise to these tails at such large galactocentric distances and the implications for the nature of this globular cluster.

Keywords: globular clusters, stellar populations, galaxy, galactic halo, statistical methods

1 Introduction

Palomar 14 stands out as one of the most interesting globular clusters of the outer Galactic halo. Faint, extended, sparse but distant, it turns out to be an ideal site for testing gravitation in the weak acceleration régime (Baumgardt et al. 2005; Jordi et al. 2009; Sollima & Nipoti 2010; Küpper & Kroupa 2010). The properties of this globular cluster are therefore essential to assess the suitability of the system to test gravitation at these scales.

Discovered in 1960 (Arp and van den Bergh 1960), it was soon established as being distant (~ 70 kpc) and relatively metal rich ([Fe/H]~ -1.5) for a globular cluster in the outer halo.

At this large distance, SDSS data (e.g. Jordi and Grebel 2010) appear to be too shallow to detect faint features, as they can only probe the sparsely populated upper RGB. Deep observations, reaching well below the turn off, are required, as well as over a wide field (e.g. Chun et al. 2010).

Within the framework of a systematic campaign to explore the outer Galactic halo (Martínez Delgado et al. 2004), we have carried out CFHT observations of a series of clusters to disentangle internal evolutionary effects (stellar mass loss, binary heating, two-body relaxation) from external effects (tidal shocks, tidal stripping). Both effects lead to the eventual disruption of the cluster through a continuous loss of stars, which may be forming characteristic tails around the cluster. Naively, one would expect these tails to be more important at small galactocentric distances, as indeed observations have revealed in an increasingly larger fraction of globular clusters (Grillmair et al. 1995; Leon et al. 2000; Odenkirchen et al. 2001, 2003; Grillmair & Dionatos 2006; Belokurov et al. 2006; Zou et al. 2009).

2 Tidal tails in Palomar 14

Our CFHT observations of Palomar 14, covering a wide area to a depth comparable with previous HST observations (Dotter et al. 2008), reveal a pair of tails, extending over one degree (see Fig. 1), and Sollima et al. 2011, for details). Using the isochrones from Marigo et al. (2008) and adopting as priors the observed metallicity [Fe/H]$=-1.6$ (Armandroff et al. 1992) and [α/Fe]$=+0.3$ Ferraro et al. (1999), we used the Bayesian inference method developed by Hernandez & Valls-Gabaud (2008) to measure the maxima of the marginalised posterior distribution probability functions of age ($t = 13.2 \pm 0.3$ Ga) and distance ($d = 71 \pm 2$ kpc).

[1] CNRS, Observatoire de Paris, 5 Place Jules Janssen, 92195 Meudon, France
[2] Instituto de Astrofísica de Canarias, 38205 La Laguna, Spain
[3] Max Planck Institut für Astronomie, Königstuhl 17, 69117 Heidelberg, Germany
[4] Institute of Astronomy, Madingley Road, Cambridge CB3 0HA, United Kingdom

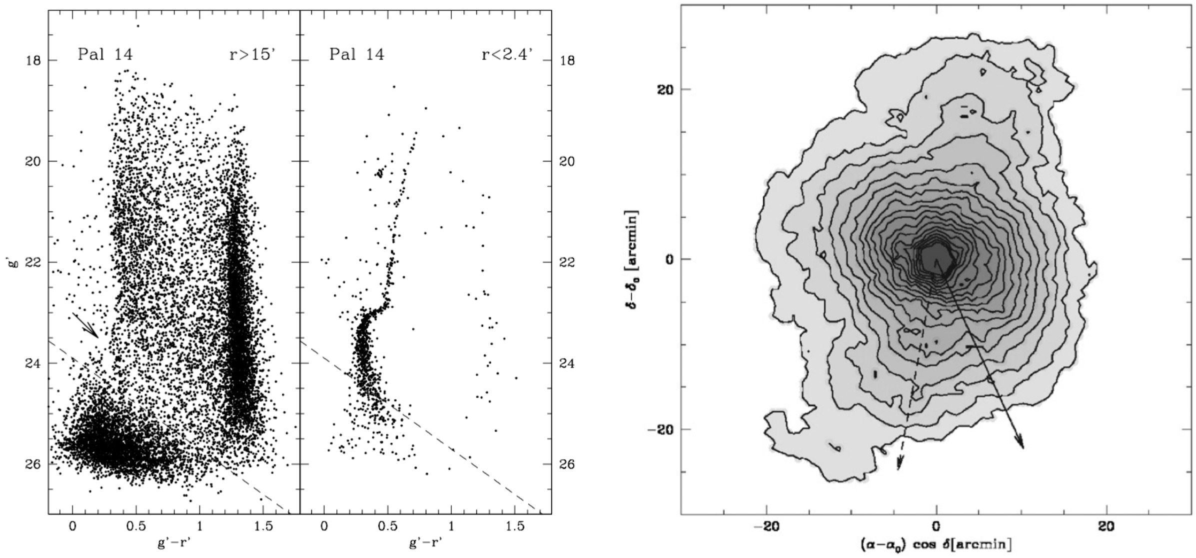

Fig. 1. *Left*: Colour-magnitude diagram (CMD) of Palomar 14. The right panel shows the CMD of the inner area within $2'.4$, while the left panel presents the CMD of stars lying beyond a radius of $15'$ from the centre. The arrow indicates a subtle excess of stars just below the turn off region. The dashed line is the approximate boundary where DAOPHOT does not discriminate between stars and (compact) galaxies. *Right*: Adaptively-smoothed maps of the stellar density around Palomar 14, from 3 to 20 times the average dispersion in background number counts using a matched filter provided by the inner CMD of Pal 14. The solid arrow gives the direction of the Galactic centre, while the dashed arrow shows the predicted proper motion direction in the Lynden-Bell & Lynden-Bell (1995) scenario where Pal 14 belongs to a stream with Fornax and Pal 15. See Sollima et al. (2011) for further details.

The density profile extends the one obtained by Trager et al. (1995) and McLaughlin & van der Marel (2005) and reveals that while the core radius remains unchanged by our observations, both the maximum Roche lobe radius and tidal radius are increased nearly four-fold. The maximum Roche radius, assuming the Galatic potential from Johnston et al. (1995), the above mentioned distance, total mass of 15,500 $M_{\odot}$and radial velocity of 72.3 km s^{-1}(Jordi et al. 2009), turns out to be $8'.2$, much less than the estimated tidal radius of about $25'$and implies that a substantial amount of stars will be lost along the orbit. The half-light radius is almost twice larger than previous measures ($2'.23 \pm 0'.14$ versus $1'.22$). There are only 9 clusters in the updated list by Harris (1996)* which have larger half-light angular radii (NGC 5139, $5'.0$; NGC 4161, $4'.33$; NGC 4372, $3'.91$; Terzan 1, $3'.82$; NGC 104, $3'.17$; NGC 3201 and HP 1, $3'.10$; NGC 6366, $2'.92$; Pal 5, $2'.73$). Given the distance of Palomar 14, however, this scale translates into a linear radius of 46.1 ± 2.9 pc, which makes it the largest in physical terms within the Milky Way. In fact, combined with its luminosity of 8130 $L_{\odot}$, this revised measure makes Pal 14 to stand as a transition object filling in the gap between the positions of classical globular clusters of the Milky Way and the ones of its satellites (see Fig. 9 and its discussion in Sollima et al. 2011).

We also detect a clear power-law extension from the classical profile (Plummer 1911), from about $10'$ to $25'$, with an exponent of -1.6 which is very similar to the one measured in several clusters (e.g Grillmair et al. 1995; Leon et al. 2000; Testa et al. 2000; Lee et al. 2003) as well as in numerical simulations (Johnston et al. 1999).

We used a matched filter algorithm (Rockosi et al. 2002) to quantify the extension and direction of the tails, through an adaptive density estimation (Silverman 1986), and a new statistic based on the ratio of Poisson number counts (Cerviño & Valls-Gabaud 2003). Fig. 2 shows the characteristic S-shape of tidal tails, where the inner isopleths appear twisted with respect to the outer ones in a way similar to the expectations from numerical simulations (e.g. Montuori et al. 2007; Peñarrubia et al. 2008; Klimentowski et al. 2009; Peñarrubia et al. 2009).

*2010 revision available at `http://physwww.physics.mcmaster.ca/~harris/mwgc.dat`

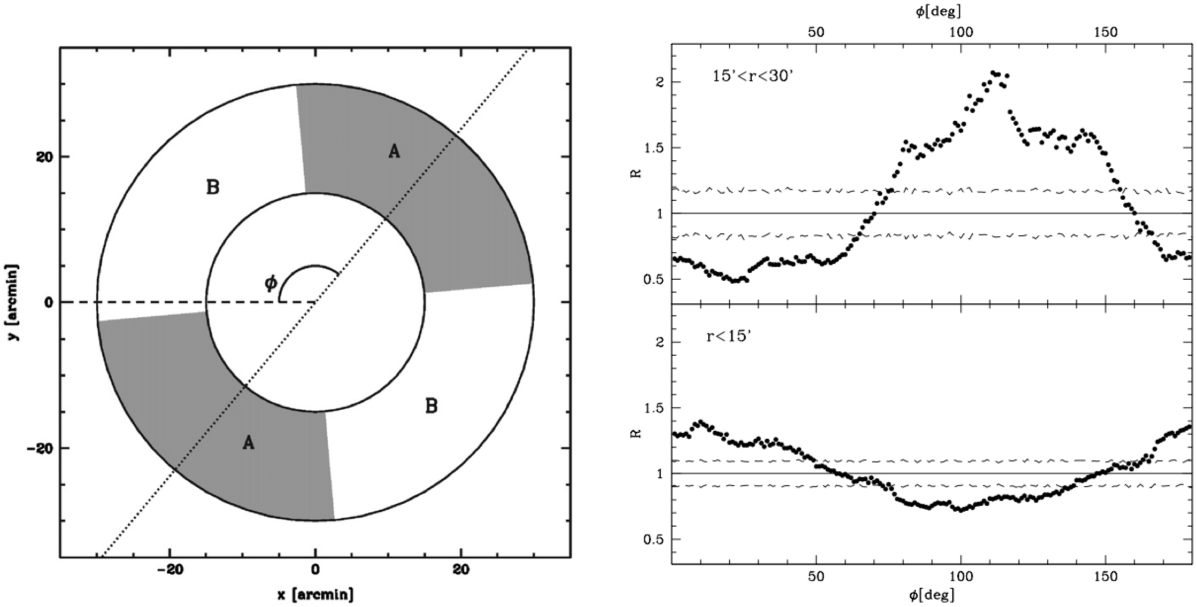

Fig. 2. *Left*: To assess the statistical significance of the anisotropic distribution of stars around Pal 14 (see Fig. 1), number counts in sectors A and B, oriented by an angle ϕ, are compared through the normalised ratio $\mathcal{R}(\phi) = (N_c^A\, N_f^B)/(N_f^A\, N_c^B)$ of counts in sectors A and B for field (f) and cluster members (c). *Right*: Dependence of the normalised ratio $\mathcal{R}$ as a function of position angle, for the inner (*bottom*) and outer (*top*) areas. The variation range for $\mathcal{R}$ around unity for an isotropic distribution is given by the dashed lines, which were obtained with 1,000 Monte Carlo simulations. In both the inner and outer areas, the test statistic is significantly larger than the null value for an isotropic distribution. Note that contiguous points are heavily correlated due to the common stars from one position angle to the next, yet the trend is unambiguous. Moreover, the maximum value in the inner area appears to differ in position angle by 100° to the one in the outer region, quantifying in a meaningful way the S-shape of the isopleths (Fig. 1). See Sollima et al. (2011) for further details.

3 Conclusions

An intriguing feature of the inferred isopleth map (Fig. 1 right), which characterises the typical S-shape of tidal tails detected in Palomar 14, is that the outer contours appear to be roughly in the proper motion direction expected in the cluster is part of a large-scale stream comprising Fornax and Palomar 15, as tentatively predicted by Lynden-Bell & Lynden-Bell (1995). Whether deeper observations will yield a better determination of the twisting of the outer isophotes and future measures of proper motions will confirm this association remain unclear at this point, yet we also note that Palomar 14 lies close to the large “disc of satellites” system which comprises most of the satellites of the Milky Way (e.g. Metz et al. 2009).

The ensemble of properties of Pal 14 reinforces this interpretation, which challenges the standard picture of globular clusters (Mateo 1998; Mackey & Gilmore 2004; Prieto & Gnedin 2008). Indeed, in the globular system of M31, new observations (McConnachie et al. 2009) have also revealed that most, if not all, of the globular clusters beyond a projected radius of about 30 kpc are associated with large coherent stellar streams (Mackey et al. 2010).

It would therefore not be very surprising if Palomar 14 provides further evidence within our Galaxy (e.g. Cohen et al. 2010) that outer halo globular clusters are part of a population that was accreted during the formation of the Milky Way.

Based on observations obtained with Megacam, a joint project of CFHT and CEA/DAPNIA, and processed in part with the TERAPIX facilities. This work was supported by grants MICINN/AYA2007-65090, CNRS/MAE PICASSO, and ANR POMMME (ANR 09-BLAN-0228).

References

Armandroff, T.E., Da Costa, G.S., Zinn, R. 1992, AJ, 104, 164
Arp, H.C. and van den Bergh, S. 1960, PASP, 72, 48
Baumgardt, H., Grebel, E. K., & Kroupa, P. 2005, MNRAS, 359, L1
Baumgardt, H., et al. 2010, MNRAS, 401, 1832
Belokurov, V., et al. 2006a, ApJ Lett, 637, L29
Cerviño, M., & Valls-Gabaud, D. 2003, MNRAS, 338, 481
Chun, S.-H., et al. 2010, AJ, 139, 606
Cohen, J.G. et al. 2010, ApJ, 725, 288
Dotter, A., Sarajedini, A., & Yang, S.-C. 2008, AJ, 136, 1407
Ferraro, F.R. et al. 1999, AJ, 118, 1738
Girardi, L., et al. 2005, A&A, 436, 895
Grillmair, C. J., & Dionatos, O. 2006, ApJ Lett, 641, L37
Grillmair, C. J., et al. 1995, AJ, 109, 2553
Harris, W. E. 1996, AJ, 112, 1487
Hernandez, X., & Valls-Gabaud, D. 2008, MNRAS, 383, 1603
Hilker, M. 2006, A&A, 448, 171
Johnston, K. V., Sigurdsson, S., & Hernquist, L. 1999, MNRAS, 302, 771
Johnston, K. V., Spergel, D. N., & Hernquist, L. 1995, ApJ, 451, 598
Jordi, K., et al. 2009, AJ, 137, 4586
Jordi, K., & Grebel, E.K. 2010, A&A, 522, A71
Klimentowski, J., et al. 2009, MNRAS, 400, 2162
Küpper, A. H. W., & Kroupa, P. 2010, ApJ, 716, 776
Lee, K. H., Lee, H. M.,Fahlman, G. G., & Lee, M. G. 2003, AJ, 126, 815
Leon, S., Meylan, G., & Combes, F. 2000, A&A, 359, 907
Lynden-Bell, D. & Lynden-Bell, R.M. 1995, MNRAS, 275, 429
Mackey, A. D., & Gilmore, G. F. 2004, MNRAS, 355, 504
Mackey, A.D. et al. 2010, ApJ, 717, L11
McLaughlin, D. E., & van der Marel, R. P. 2005, ApJ Suppl, 161, 304
Marigo, P. et al. 2008, A&A, 482, 883
Martínez Delgado, D. et al. 2004, in *Satellites and Tidal Streams*, ASP Conf. Series, Vol. 327, 255
Mateo, M. L. 1998, ARAA, 36, 435
McConnachie, A. W., et al. 2009, Nature, 461, 66
Metz, M. et al. 2009, MNRAS, 394, 2223
Montuori, M., et al. 2007, ApJ, 659, 1212
Odenkirchen, M., et al. 2001, ApJ Lett, 548, L165
Odenkirchen, M., et al. 2003, AJ, 126, 2385
Peñarrubia, J., Navarro, J. F., & McConnachie, A. W. 2008, ApJ, 673, 226
Peñarrubia, J., et al. 2009, ApJ, 698, 222
Plummer, H. C. 1911, MNRAS, 71, 460
Prieto, J. L., & Gnedin, O. Y. 2008, ApJ, 689, 919
Rockosi, C. M., et al. 2002, AJ, 124, 349
Silverman, B. W. 1986, *Density estimation for statistics and data analysis* (London: Chapman and Hall)
Sollima, A., & Nipoti, C. 2010, MNRAS, 401, 131
Sollima, A., Martínez-Delgado, D., Valls-Gabaud, D. and Peñarrubia, J. 2011, ApJ, 726, 47
Testa, V., et al. 2000, A&A, 356, 127
Trager, S. C., King, I. R., & Djorgovski, S. 1995, AJ, 109, 218
Zou, H., Wu, Z.-Y., Ma, J., & Zhou, X. 2009, RAA, 9, 1131

GALEX NUV LYMAN BREAK GALAXIES

G. M. Williger[1], L. Haberzettl[2], M. D. Lehnert[3], N. P. H. Nesvadba[4] and D. Valls-Gabaud[3]

Abstract. Lyman Break Galaxies (LBGs) have been the benchmarks against which other samples of high redshift galaxies have been compared for the last 2 decades. They are unique in that no other selection mechanism allows us to study galaxies selected in a consistent manner over redshifts $0.5 \lesssim z \lesssim 7$. An important remaining gap is the redshift range $z \sim 1.5 - 2.5$, which includes NUV-band dropouts. We searched for LBGs at this epoch using very sensitive multi-wavelength data from the FUV to mid-IR in the GOODS-S. We combined the dropout technique with color selection to identify star-forming galaxies at $1.5 \lesssim z \lesssim 2.5$. We find only a small overlap with the BM/BX selection method (Adelberger et al. 2004), and our sample of ~ 200 $z \sim 2$ LBG candidates includes a significant number of relatively redder LBGs. By comparing our results to other selection methods for star-forming galaxies at $z \sim 2$ (BM/BX, BzK), we can show that the use of true dropout selection results in a cleaner, more efficient sample of LBG candidates. Our selected $z \sim 2$ LBG candidates are more consistent with LBG samples at $z \leq 3$ than BM/BX and BzK galaxies, despite our sample including relatively younger, lower mass systems.

Keywords: galaxies: star formation, galaxies: high redshift, galaxies: evolution

1 Selection criteria

Our optical color selection criteria (Haberzettl et al. 2010, in prep.) for LBGs at $1.5 \lesssim z \lesssim 2.5$, combined with the NUV dropout technique, are analogous to the Steidel et al. (1996) method, used for $z \sim 3$ LBGs. Until recently, only proxies which are based solely on optical colors like the BM/BX and BzK methods (Adelberger et al. 2004; Daddi et al. 2004) have been used to identify star-forming galaxies at this epoch. The BM/BX color criteria were derived from $z \sim 3$ template SEDs, and are optimized to identify samples of very blue star-forming galaxies (Fig. 1). We consider both true NUV dropouts ($2 < z < 2.5$) and, to probe to as low redshift as possible with the available data, partial NUV dropouts (NUV selected, $1.5 < z < 2$).

2 NUV dropouts and NUV selected vs. the BM/BX and BzK methods

While the BzK-selection is able to pick out redder, dustier, more massive star-forming galaxies, it has difficulties to distinguish between star-forming and evolved galaxies at faint ($K_s \gtrsim 20$) magnitudes. A comparison of model SEDs with the BM/BX color-selection box (Fig. 1), shows that the BM/BX selection has only slight overlap with the template SEDs of moderate star-forming galaxies at $1.5 \lesssim z \lesssim 2.5$. We created the template SEDs using the single stellar population models of Bruzual & Charlot (2003, red+black diamonds) and the chemically consistent evolution models from PEGASE (Fioc & Rocca-Volmerange 1997, green+blue diamonds). We included in our models a variety of star formation histories from starbursts to exponentially decreasing star formation rates, and cases with and without dust extinction. We devised color selection parameters to not only include the BM/BX selected galaxies, but also our template SEDs with redshifts $1.5 \leq z \leq 2.5$ (Fig. 1).

[1] Lab. Fizeau, Univ. de Nice, UMR 6525, 06108 Nice
[2] Dept. of Physics & Astronomy, U. Louisville, KY, USA
[3] GEPI, Obs. de Paris-Meudon, 5 Pl. Janssen, 92195 Meudon
[4] IAS, U. Paris-Sud, 91405 Orsay

3 LBG samples

We calculated photometric redshifts for our NUV-dropout and NUV-selected samples for those cases where no spectroscopic redshifts were available, then performed SED analyses. We eliminated stellar interlopers by cross-correlating a stellar catalogue for the CDF-S from Groenewegen (2001), and did consistency checks with a subsample with spectroscopic redshifts. Given the selection boxes from Fig. 1, we found 157 candidates from the NUV dropout method and 44 NUV selected systems. See Haberzettl et al. (2010, in prep.) for details and results of SED analyses.

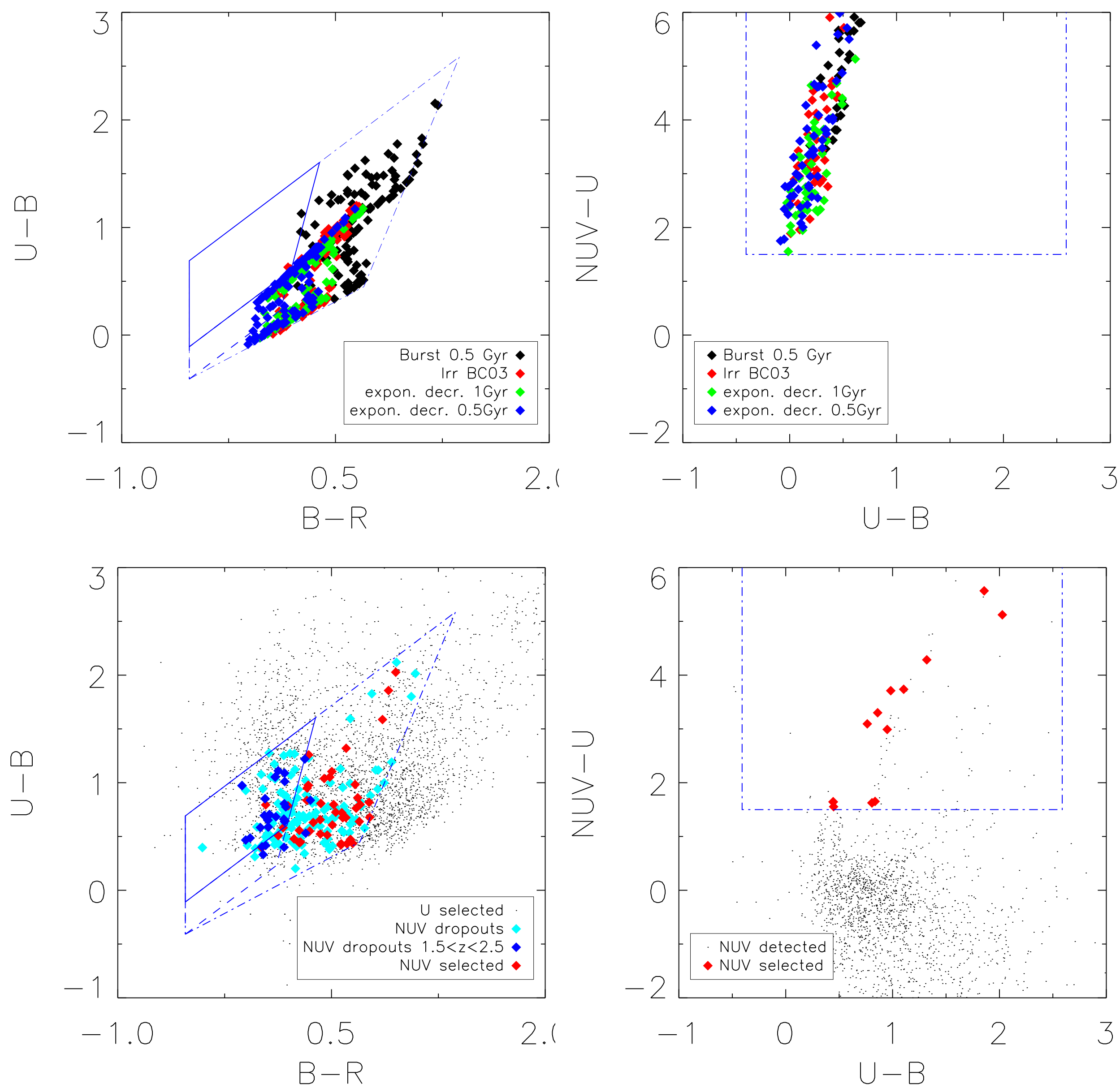

Fig. 1. Comparison of BM/BX vs. LBG color selection criteria for $1.5 < z < 2.5$ LBGs from the CDF-S. *Top panels:* large dot-dashed boxes show the locations of model colors of star-forming galaxies in the two color plane. *Upper left:* selection boxes for BM/BX galaxies (solid+small dashed boxes). We determined selection parameters from model colors of star forming galaxies at $1.5 < z < 2.5$ using the GaBoDS filter set (Hildebrandt et al. 2005). *Bottom panels:* the resulting samples of 157 NUV dropout ($2 < z < 2.5$, *cyan diamonds*, lower left) and 44 NUV selected ($1.5 < z < 2$, *red diamonds*, lower panels) LBG candidates. *Black dots:* other galaxies selected in U or NUV.

References

Adelberger, K.L. Steidel, C. C., Shapley, A. E. et al. 2004, ApJ, 607, 226
Bruzual, G. & Charlot, S. 2003, MNRAS, 344, 1000
Daddi, E., Cimatti, A., Renzini, A. et al. 2004a, ApJ, 617, 746
Fioc, M. & Rocca-Volmerange, B. 1997, A&A, 326, 950
Groenewegen, M. A. T., Girardi, L., Hatziminaoglou, E. et al. 2002, A&A, 392, 741
Hildebrandt, H., Bomans, D. J., Erben, T. et al. 2005, A&A, 441, 905
Steidel, C.C., Giavalisco, M., Pettini, M. et al. 1996, ApJ, 462, L17

SF2A 2010
S. Boissier, M. Heydari-Malayeri, R. Samadi and D. Valls-Gabaud (eds)

THE MATISSE ANALYSIS OF LARGE SPECTRAL DATASETS FROM THE ESO ARCHIVE

C. Worley[1], P. de Laverny[1], A. Recio-Blanco[1], V. Hill[1], Y. Vernisse[1], C. Ordenovic[1] and A. Bijaoui[1]

Abstract. The automated stellar classification algorithm, MATISSE, has been developed at the Observatoire de la Côte d'Azur (OCA) in order to determine stellar temperatures, gravities and chemical abundances for large datasets of stellar spectra. The Gaia Data Processing and Analysis Consortium (DPAC) has selected MATISSE as one of the key programmes to be used in the analysis of the Gaia Radial Velocity Spectrometer (RVS) spectra. MATISSE is currently being used to analyse large datasets of spectra from the ESO archive with the primary goal of producing advanced data products to be made available in the ESO database via the Virtual Observatory. This is also an invaluable opportunity to identify and address issues that can be encountered with the analysis large samples of real spectra prior to the launch of Gaia in 2012. The analysis of the archived spectra of the FEROS spectrograph is currently underway and preliminary results are presented.

Keywords: stars:fundamental parameters, astronomical databases, methods: data analysis

1 Introduction

Galactic archæology is the study of large datasets of stellar spectra in the search for underlying structures and populations within the Galaxy. Identification of such structures and populations allows astronomers to test theories of galactic formation and evolution. The main tool that is created by the assimilation of this information is a kinematic and chemical chart of the Galaxy. This chart is contructed using the key stellar parameters of radial velocity, proper motion, distance, effective temperature, surface gravity, metallicity and chemical abundances.

The current and future generations of telescopes and instruments have, and will, create large spectral datasets over a wide range of resolutions, wavelengths and signal-to-noise (SNR). This wealth of data can be used to derive kinematic and chemical signatures for the observed stars, providing unprecedented detail of the surrounding Galaxy. The analysis of such large datasets cannot be carried out 'by hand' and so it is essential that automated stellar classification algorithms are developed in order to provide a consistent and efficient analysis of these data.

The Gaia satellite is at the forefront of astronomical technology and, once launched, it will observe approximately a billion stars in the Galaxy. For this sample Gaia will measure stellar distances to new precisions at milliarcsecond accuracies. Of the three instruments that Gaia will carry, the Radial Velocity Spectrometer (RVS) will observe spectra at two different resolutions (R$\sim$11500 and R$\sim$7000) over the wavelength domain from 847 nm to 874 nm. This wavelength region includes several key spectral features which will be used to determine the stellar parameters for at least 25 million stars.

[1] Université de Nice Sophia Antipolis, CNRS (UMR 6202), Observatoire de la Côte D'Azur, Cassiopée, B.P.4229, 06304 Nice Cedex 04, France

Table 1. Details of the ESO spectrographs and publicly available archived spectra that are part of the AMBRE project.

Spectrograph	Resolution	Wavelength Range (nm)	No. Spectra
FEROS	48,000	350 – 920	∼ 23,000
HARPS	115,000	378 – 691	∼ 40,000
UVES	40,000 – 110,000	300 – 1100	∼ 35,000
Flames/GIRAFFE	5,600 – 46,000	370 – 900	∼ 100,000

2 The AMBRE project: tests of MATISSE

The stellar classification algorithm, MATISSE, is being developed at the Observatoire de la Côte d'Azur (OCA) (Recio-Blanco et al. 2006). It has been selected by the Gaia Data Processing Consortium (DPAC) as one of three stellar classification codes that will be used to analyse the RVS spectra for classification of the Gaia stellar sample. The AMBRE project team at OCA oversees the development of MATISSE and the work being carried out by AMBRE is formally connected to the Gaia DPAC under the Generalized Stellar Parametrizer-spectroscopy (GSP-spec) Top Level Work Package which is overseen by Coordination Unit 8 (CU8).

The AMBRE Project is the analysis of the archived spectra of four European Southern Observatory (ESO) spectrographs under a contract between ESO and OCA. The characteristics of the four spectrographs in question are listed in Table 1. The stellar parameters of effective temperature (T_{eff}), surface gravity (log g), metallicity ([M/H]), and α element abundances ([α/Fe]) will be derived for each of the archived stellar spectra. These will be delivered to ESO for inclusion in the ESO database and then made available to the astronomical community via the Virtual Observatory in order to encourage greater use of the archived spectra.

This analysis of the archived spectra of four separate instruments is a unique opportunity to test the performance of MATISSE on large datasets of real spectra. The datasets also include the Gaia RVS wavelength domain and resolutions and this will enable rigorous testing of MATISSE on general and Gaia-like spectra. This is necessary in order to optimise the performance of MATISSE in the Gaia analysis pipeline that is being compiled at the Centre National d'Etudes Spatiales (CNES). As such the AMBRE project has been formally designated as a sub-work package under GSP-spec.

3 MATISSE & FEROS

MATISSE (MATrix Inversion for Spectral SynthEsis) is an automated stellar classification algorithm based on a local multi-linear regression method. It derives stellar parameters ($\theta = T_{eff}$, log g, [M/H], individual chemical abundances) by the projection of an input observed spectrum on a vector $B_\theta(\lambda)$. The $B_\theta(\lambda)$ vector is an optimal linear combination of theoretical spectra calculated from a synthetic spectra grid. Key features in the observed spectrum due to a particular θ are reflected in the corresponding $B_\theta(\lambda)$ vector indicating the particular regions which are sensitive to θ (Recio-Blanco et al. 2006; Bijaoui et al. 2008).

A grid of high resolution synthetic spectra has been calculated using the MARCS stellar atmosphere models (Gustafsson et al. 2008) for $T_{eff} < 8000$ K. The grid spans the entire optical domain across the following stellar parameter range: 3,000 K $< T_{eff} <$ 8,000 K; 0.5 < log g < 5.0; −5 < [M/H] < +1.

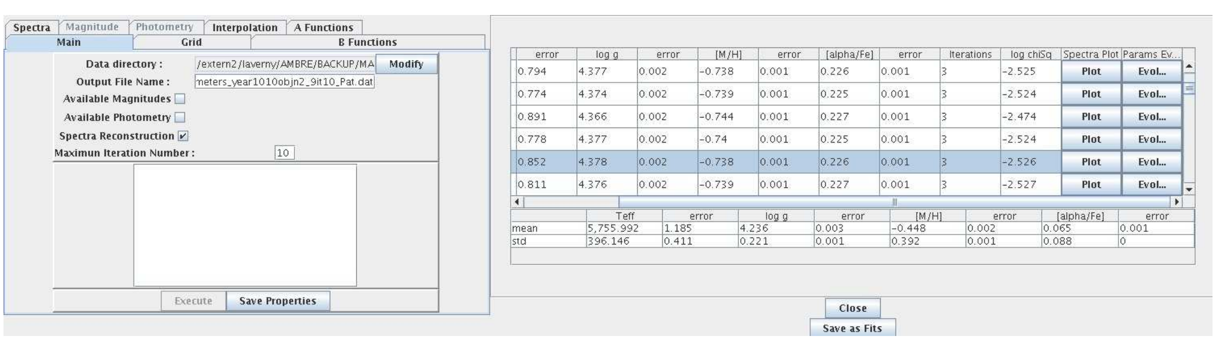

Fig. 1. Matisse java application showing input interface and results display.

MATISSE has been developed for integration into the CNES pipeline and also as a standalone java appli-

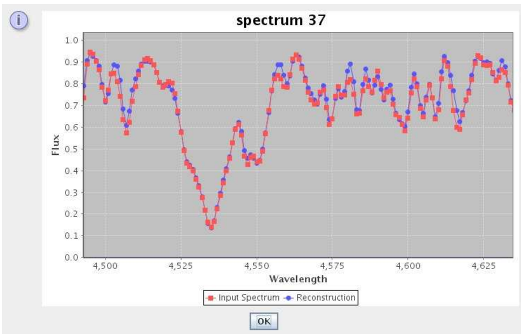

Fig. 2. Example of the comparison between the observed spectrum and the synthetic spectrum reconstructed at the stellar parameters of the corresponding MATISSE solution.

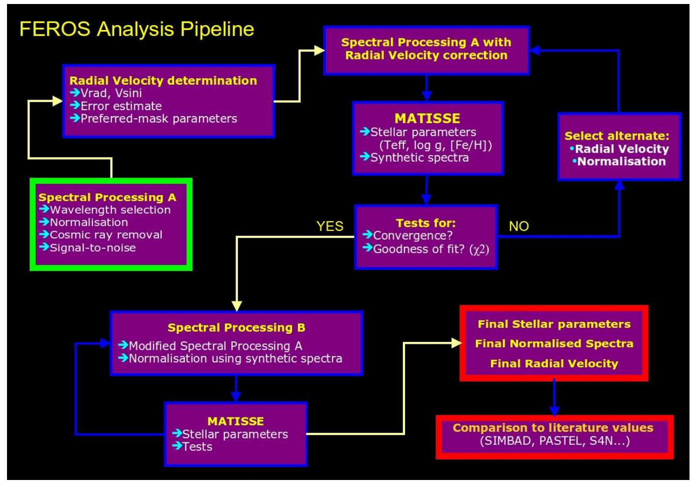

Fig. 3. Flowchart showing the different stages of analysis that the observed spectra undergoes in the FEROS analysis pipeline.

cation for use in a wide variety of projects. The archived spectra of the FEROS spectrograph (see Table 1) are currently being analysed using the java application. A picture of the java interface is shown in Figure 1. To the left is the user input where the observed spectra, signal-to-noise and photometric files can be specfied. To the right is the results display showing the parameters derived for the spectra as well as functions that enable the visual comparison of the observed spectrum with synthetic spectrum generated at the derived stellar parameters. An example of this is shown in Figure 2.

The java application can also be integrated into a local analysis pipeline, and such a pipeline has been developed for the FEROS spectra. Figure 3 shows a flowchart of the key stages of analysis in the FEROS pipeline. After initial normalisation and cleaning of the observed spectra the radial velocities are determined using a cross-correlation programme which compares the observed spectrum to masks created from synthetic spectra (private communication, C. Melo). A second stage of normalisation then occurs which includes the radial velocity correction to shift the spectra to laboratory wavelengths. The next stage is inital MATISSE analysis and the resulting stellar parameters are tested for convergence and for goodness of fit using a χ^2 test between the observed spectrum and the reconstructed synthetic spectrum. Potential issues regarding normalisation and radial velocity corrections are identified and remedied at this stage.

An iterative procedure is then executed which again cleans and normalises the observed spectrum but now normalisation is made relative to the reconstructed spectrum of the previous MATISSE analysis. This newly normalised spectrum is entered into MATISSE to derive new stellar parameters. This analysis cycle between normalisation and stellar parameter derivation is repeated ten times in order to converge on the final stellar parameters. Ultimately the procedure produces the final stellar parameters, the final normalised observed spectrum and the final reconstructed synthetic spectrum. This final observed normalised spectrum is entered into the radial velocity programme to confirm the radial velocity and determine the final radial velocity errors.

A crucial stage which is currently underway is the identification of previously analysed stars within the FEROS dataset. Key databases such as the S^4N library (Allende Prieto et al. 2004) have been used to identify reference samples within the FEROS dataset in order to compare the results of MATISSE with previous studies. Figure 4a compares the radial velocities calculated in the AMBRE-FEROS pipeline with the reported S^4N values. There is good agreement between the two sets of values.

Stellar parameters were determined for the S^4N sample using the AMBRE-FEROS pipeline and the comparison of the derived effective temperatures (T_{eff}) of AMBRE-FEROS with the S^4N values is shown in Figure 4b. There is good agreement between the two sets of T_{eff} values. Further investigation of other reference samples is also being pursued for a comprehensive comparison between MATISSE and other extended studies.

4 Conclusion

As part of the AMBRE Project we have developed a comprehensive analysis pipeline for the FEROS dataset that feeds the cleaned and normalised stellar spectra into MATISSE for derivation of the stellar parameters.

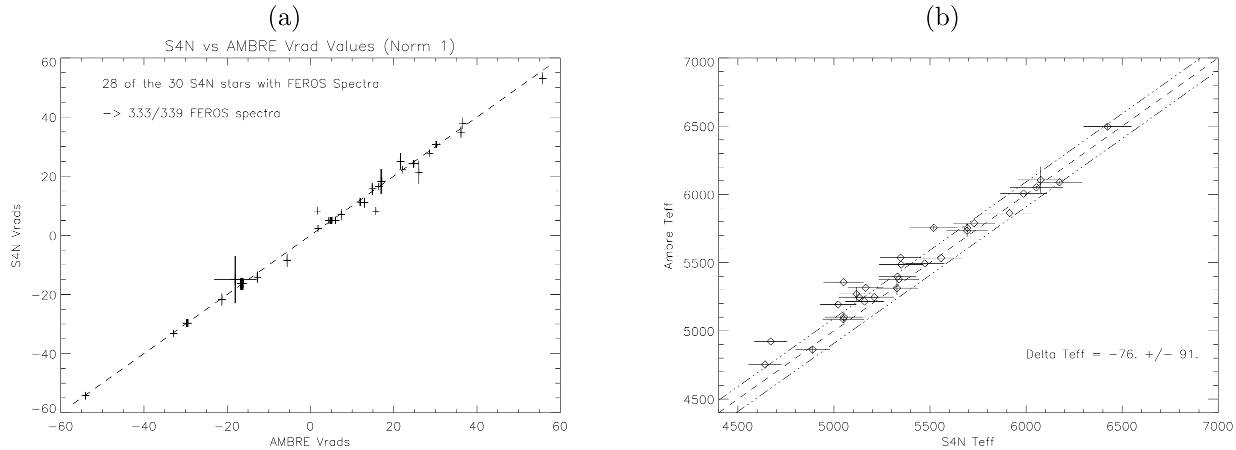

Fig. 4. a) Comparison of the radial velocity values reported in S^4N with those determined in the AMBRE-FEROS pipeline for the S^4N stars found in the FEROS dataset. Errorbars for each set are also shown. b) As for a) but for the effective temperature (T_{eff}).

This pipeline can be tailored to the specifications of the other three instruments that are also to be analysed in this project.

The preliminary results from the AMBRE-FEROS analysis show the great potential of MATISSE as a stellar classification tool for stand-alone projects and also for large-scale endeavours such as Gaia RVS spectra. The analysis of the ESO archive provides a unique opportunity to rigorously test MATISSE on RVS wavelengths and resolutions using large datasets of real stellar spectra in order to optimise its performance in the CNES pipeline.

The primary outcome of the AMBRE Project is to deliver to ESO the advanced data products (the stellar parameters) of the archived spectra for each of the four spectrographs, FEROS, UVES, HARPS and Flames/GIRAFFE. Considered as a whole this will be a homogeneous determination of stellar parameters for the archived spectra which will add an extra layer of key information to the ESO database. These parameters will in turn be made available to the astronomical community via the Virtual Observatory. The stellar parameters of these archived spectra will also create a galactic chemical chart which can be used to study stellar structures within the Milky Way in the pursuit of galactic archæology.

The authors wish to thank the Observatoire de la Côte d'Azur and the LOC/SOC of SF2A for their financial support which enabled C. Worley to attend this meeting.

References

Allende Prieto, C., Barklem, P. S., Lambert, D. L., and Cunha, K.: 2004, A&A, 420, 183

Bijaoui, A., Recio-Blanco, A., and de Laverny, P.: 2008, in C. A. L. Bailer-Jones (ed.), American Institute of Physics Conference Series, Vol. 1082 of American Institute of Physics Conference Series, p 54-60

Gustafsson, B., Edvardsson, B., Eriksson, K., Jørgensen, U. G., Nordlund, Å., and Plez, B.: 2008, A&A, 486, 951

Recio-Blanco, A., Bijaoui, A., and de Laverny, P.: 2006, MNRAS, 370, 141

Author Index